

NASA TECHNICAL  
MEMORANDUM

NASA TM X-64726

LARGE SPACE TELESCOPE  
PHASE A FINAL REPORT

Volume IV - Scientific Instrument Package

By Program Development  
(This volume prepared by Kollsman Instrument  
Corporation)

December 15, 1972

NASA

**CASE FILE  
COPY**

*George C. Marshall Space Flight Center  
Marshall Space Flight Center, Alabama*

## DOCUMENT CONTENTS

### Volume I – Executive Summary

- Chapter I – Introduction
- Chapter II – Mission Analysis
- Chapter III – LST Configuration and Systems Design
- Chapter IV – Maintenance Analysis
- Chapter V – Conclusions and Recommendations

### Volume II – Mission Description and System Design Characteristics

- Chapter I – Scientific Uses of the LST
- Chapter II – Phase A Study Approach
- Chapter III – Mission Analysis
- Chapter IV – LST Configuration and System Design
- Chapter V – Configurations and System Alternatives
- Chapter VI – Interfaces
- Chapter VII – Low Cost Considerations
- Chapter VIII – Program Implementation
- Chapter IX – Conclusions and Recommendations
- Appendix A – Alternate LST Structural Design Employing Graphite/Epoxy Shells
- Appendix B – Solar System Observations
- Appendix C – LST Configuration Concept Comparison

### Volume III – Optical Telescope Assembly

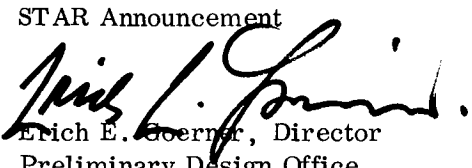
- Section A – Introduction
- Section B – System Considerations
- Section C – System Design

### Volume IV – Scientific Instrument Package

- Section 1 – Introduction
- Section 2 – General Scientific Objectives
- Section 3 – SIP System Analysis
- Section 4 – Scientific Instrumentation
- Section 5 – Ancillary Subsystems
- Section 6 – Imaging Photoelectric Sensors
- Section 7 – Environmental Considerations of the Scientific Instrumentation Design
- Section 8 – Scientific Instrument Package Physical Description
- Section 9 – Interface Considerations
- Section 10 – Reliability and Maintainability
- Section 11 – Program Planning
- Appendix A – Resolvable Element Size vs Pointing Parametric Analysis
- Appendix B – Signal-to-Noise Ratio

### Volume V – Support Systems Module

- Chapter I – Configuration and System Design
- Chapter II – Structures
- Chapter III – Thermal Control System
- Chapter IV – Electrical System
- Chapter V – Communication and Data Handling
- Chapter VI – Attitude Control System
- Chapter VII – Maintainability Analyses
- Chapter VIII – Reliability Analysis
- Chapter IX – Conclusions
- Appendix A – LST Contamination Control
- Appendix B – Scientific Data Gathering Efficiency
- Appendix C – Derivation of Optimum Readout Bandwidth for Preamplifier of SEC Vidicon

1. REPORT NO. TM X- 64726		2. GOVERNMENT ACCESSION NO.		3. RECIPIENT'S CATALOG NO.	
4. TITLE AND SUBTITLE Large Space Telescope Phase A Final Report Volume IV -- Scientific Instrument Package				5. REPORT DATE December 15, 1972	
				6. PERFORMING ORGANIZATION CODE	
7. AUTHOR(S) By Program Development*				8. PERFORMING ORGANIZATION REPORT #	
9. PERFORMING ORGANIZATION NAME AND ADDRESS  George C. Marshall Space Flight Center Marshall Space Flight Center, Alabama 35812				10. WORK UNIT NO.	
				11. CONTRACT OR GRANT NO.	
				13. TYPE OF REPORT & PERIOD COVERED  Technical Memorandum	
12. SPONSORING AGENCY NAME AND ADDRESS  National Aeronautics and Space Administration Washington, D.C. 20546				14. SPONSORING AGENCY CODE	
15. SUPPLEMENTARY NOTES  Prepared by Program Development  * This volume prepared by Kollsman Instrument Corporation					
16. ABSTRACT  This document is a report of the Phase A study of the Large Space Telescope (LST). The study defines an LST concept based on the broad mission guidelines provided by the Office of Space Science (OSS), the scientific requirements developed by OSS with the scientific community, and an understanding of long range NASA planning current at the time the study was performed.  The LST is an unmanned astronomical observatory facility, consisting of an optical telescope assembly (OTA), scientific instrument package (SIP), and a support systems module (SSM). The report consists of five volumes: Volume I is an executive summary, Volume II is a summary of the entire report, and Volumes III, IV, and V contain the analyses and conceptual designs of the OTA, SIP, and SSM, respectively. The report describes the constraints and trade off analyses that were performed to arrive at a reference design for each system and for the overall LST configuration.  The LST will be launched into low earth orbit by the Space Shuttle and operated for 10 to 15 years. The Shuttle will also be used to maintain the LST and to update the scientific instrument complement. Several maintenance modes have been investigated, including on-orbit pressurization of the SSM to provide a shirtsleeve environment for maintenance, and earth return of the LST.  The LST will provide the scientific community with several fundamentally unique capabilities which will permit the acquisition of new and important observational data. Its location in space permits observations over the entire spectrum from about 100 nm to the far infrared.  A low cost design approach was followed in the Phase A study. This resulted in the use of standard spacecraft hardware, the provision for maintenance at the black box level, growth potential in systems designs, and the sharing of Shuttle maintenance flights with other payloads.					
17. KEY WORDS Large Space Telescope Scientific Satellite Astronomy Payload High Resolution Astronomy Faint Object Detection Conceptual Satellite Design Shuttle Maintenance Spacecraft				18. DISTRIBUTION STATEMENT STAR Announcement  Erich E. Goerner, Director Preliminary Design Office	
19. SECURITY CLASSIF. (of this report) Unclassified		20. SECURITY CLASSIF. (of this page) Unclassified		21. NO. OF PAGES 647	22. PRICE NTIS

## LIST OF ACRONYMS

A/D	analog to digital
ACN	Ascension Island (tracking station)
ACS	attitude control system
AFO	Announcement for Flight Opportunity
AGC	automatic gain control
AGO	Santiago, Chili (tracking station)
ALU	arithmetic logic unit
AM	airlock module
AOS	acquisition of signal
APP	antenna position programmer
ASCS	attitude sensing and control system
ASR	automatic send/receive
ASTAM	automated system test and monitor
ATM	Apollo Telescope Mount
ATS	Applications Technology Satellite
AVE	Mojave, California (tracking station)
BDA	Bermuda (tracking station)
BECO	Teledyne-Brown Engineering Company
BER	bit error rate
BITE	built-in test equipment
BOL	beginning of life
BOM	basic operating module
BUR	Johannesburg, South Africa (tracking station)
C&DH	communications and data handling

## LIST OF ACRONYMS (Continued)

C& DHS	communications and data handling system
C&W	caution and warning
CAM	computer address matrix
CCD	charge couple device
CCS	contamination control system
CDR	critical design review
CG, C.G.	center of gravity
CMG	control moment gyro
CMOS	complementary metal oxide semiconductor
CPU	central processor unit
CRO	Carnarvon (tracking station)
CSS	coarse sun sensor
CTU	command and telemetry unit
CYI	Canary Islands (tracking station)
D/A	digital to analog
DAU	data acquisition unit
DDT& E	design, development, test, and engineering
DEA	drive electronics assembly
DG	double gimbal
DGCMG	double gimbal CMG
DOD	depth of discharge
DPA	digital processor assembly
DSIF	Deep Space Instrumentation Facility
DTPL	domain tip propagation logic

## LIST OF ACRONYMS (Continued)

DTU	data transmission unit
ECA	electrical control assembly
EC/LSS	environmental control/life support system
EDS	electrical distribution subsystem
EDU	electrical distribution unit
EIRP	effective isotropic radiated power
EM, em	electromagnet; engineering model
EMC	electromagnetic control
EMI	electromagnetic interference
EOL	end of life
EOM	end of mission
EPS	electrical power subsystem
ERTS	Earth Resources Technology Satellite
ESE	electrical support equipment
ETC	Engineering Training Center, Greenbelt, Maryland
EVA	extravehicular activity
EVLSS	extravehicular life support system
FGS	fine guidance system
FHST	fixed-head star tracker
FM	frequency modulated
FMEA	failure mode effects analysis
FOV	field of view
FRUSA	flexible, rollup solar array
FST	fixed star tracker

## LIST OF ACRONYMS (Continued)

GAC	Grumman Aerospace Corporation
GDN	ground data network
GDSX	Goldstone (tracking station)
GESE	ground electrical support equipment
ghu	gyro hang-up
GMT	Greenwich mean time
GRARR	Goddard range and range rate
GSE	ground support equipment
GSFC	Goddard Space Flight Center
GST	gimbaled star tracker
GWM	Guam (tracking station)
HAW	Hawaii (tracking station)
HEAO	High Energy Astronomy Observatory
HEPA	high efficiency particulate air
HPI	high performance insulation
HSK	Honeysuckle Creek, Australia (tracking station)
I/O	input/output
I. D.	inside diameter
IESE	in-space electrical support equipment
IOCC	integrated operations control console
IOP	in the orbit plane
ISA	interstage adapter; interface systems adapter
IVA	intravehicular activity
LCP	left circular polarized
LOHARR	Lockheed heat rate program
LOS	line of sight

## LIST OF ACRONYMS (Continued)

LSI	large scale integration
LST	Large Space Telescope
MAC	maximum allowable concentration
MAD	Madrid, Spain (tracking station)
MCC	mission control center
MCF	Mating/Checkout Facility
MIB	minimum impulse bit
MIL	Merritt Island, Florida (tracking station)
MMS	micrometeoroid shell
MNOS	metal nitride oxide silicon
MOJAVE	tracking station at Barstow
MOS/LSI	metal oxide semiconductor/large-scale integrated
MSFC	Marshall Space Flight Center
MSFN	Manned Space Flight Network
MSS	magnetometer sensing system
MT	magnetic torquer
MTBF	mean time between failures
MTE	magnetic torquer electronics
MTF	modulation transfer function
MTS	magnetic torquing system
MTU	magnetic tape unit
NASCOM	National Aeronautics and Space Administration Communications Network
NASO	National Astronomical Space Observatory
NDRO	nondestructive readout
NEA	noise equivalent angle



## LIST OF ACRONYMS (Continued)

NFL	St. John's, Newfoundland (tracking station)
OAAR	other activities as required
OAQ	Orbiting Astronomical Observatory
OAS	Orbit Adjust Stage
OMS	orbit maneuvering system
OOC	observatory operation center
ORRX	Orroral Valley (tracking station)
OSR	optical solar reflector
OTA	optical telescope assembly
OWS	Orbital Workshop
PCM	phase change material; pulse code modulator
PCS	peripheral communication system
PCU	power converter unit
PDR	preliminary design review
PEP	perpendicular to the ecliptic plane
PGA	pressure garment assembly
PM	pulse modulated
POP	perpendicular to the orbit plane
PRR	preliminary requirements review
PSD	power spectral density
PSK	phase shift keyed
PSU	power switch unit
QUI	Quito, Equador (tracking station)
R&D	research and development
RAM	research applications module (studies); reference alignment mode

## LIST OF ACRONYMS (Continued)

RBV	return beam vidicon
RCD	remote command decoder
RCP	right circular polarized
RCS	reaction control system
REC	recurring costs
RF	radio frequency
RFI	radio frequency interference
RGA	reference gyro assembly
ROM	read-only-memory
ROS, ROSMAN	tracking station at Rosman, North Carolina
RSDP	remote site data processer
RTV	room temperature vulcanizing
RW	reaction wheel
SAA	South Atlantic anomaly
SBU	sensor buffer unit
SCAMA	switching, conferencing, and monitoring arrangement
SEC	secondary electron conduction
SFP	solicitation for proposal
SG	single gimbal
SGCMG	single gimbal CMG
SI	science instrument
SIP	scientific instrument package
SIT	silicon intensified target
SMS	secondary mirror sensor
SPD	solar power distributor

## LIST OF ACRONYMS (Continued)

SPEH	special purpose equipment handler
SPF	single-point failure
SPG	single-point ground
SSM	support systems module
SSP	Space Station prototype
STADAN	Space Tracking and Data Acquisition Network
STDN	Spaceflight Tracking and Data Network
2-SPEED	two scissored pair ensemble explicit distribution
TA	transfer assembly
TACS	thrust attitude control system
TAN	Tananarive, Malagasy Republic (tracking station)
TBC	The Boeing Company
TCS	thermal control system
TDRS	tracking and data relay satellite (network)
TEX	Corpus Christi, Texas (tracking station)
TMR	triple modular redundancy
TOOMBA	tracking station at Cooby Creek
TRW	TRW Systems, Incorporated
TTY	teletypewriter
TWT	traveling wave tube
ULA	Fairbanks, Alaska (tracking station)
UPD	update buffer
USB	unified S-band
USBE	unified S-band equipment
VAB	Vertical Assembly Building
VGP	vehicle ground point

## LIST OF ACRONYMS (Concluded)

VPM	variable permanent magnet
W-R	Wolf-Rayet
WASS	wide angle sun sensor
WFE	wavefront error
WNK	Winkfield, United Kingdom (tracking station)
XPDR	transponder

## TABLE OF CONTENTS

<u>Section</u>		<u>Page</u>
1	INTRODUCTION . . . . .	1-1
1.1	BACKGROUND . . . . .	1-1
1.2	STUDY OBJECTIVES AND APPROACH . . . . .	1-2
1.3	SYSTEMS DESCRIPTION . . . . .	1-7
	1.3.1 Configuration . . . . .	1-7
	1.3.2 Focal Plane Arrangement . . . . .	1-9
	1.3.3 Imagery . . . . .	1-9
	1.3.4 Spectral Response . . . . .	1-12
1.4	INSTRUMENT PACKAGE EFFECTIVENESS . . . . .	1-12
1.5	STUDY SUMMARY . . . . .	1-13
2	GENERAL SCIENTIFIC OBJECTIVES . . . . .	2-1
3	SIP SYSTEM ANALYSIS . . . . .	3-1
3.1	INTRODUCTION . . . . .	3-1
3.2	STUDY INPUTS . . . . .	3-6
	3.2.1 Committee Recommendations . . . . .	3-6
	3.2.2 Technological Inputs . . . . .	3-8
3.3	GENERAL INSTRUMENT DESIGN PARAMETERS . . . . .	3-14
	3.3.1 Camera Analysis . . . . .	3-14
	3.3.2 Spectrograph Analysis . . . . .	3-17
3.4	INSTRUMENT DESIGN PARAMETERS . . . . .	3-19
	3.4.1 High Resolution Camera . . . . .	3-19
	3.4.2 Wide Field Camera . . . . .	3-22
	3.4.3 High Resolution Spectrograph . . . . .	3-22
	3.4.4 Faint Object Spectrograph . . . . .	3-28
	3.4.5 Mid IR (Fourier) Interferometer . . . . .	3-29

TABLE OF CONTENTS (Cont.)

<u>Section</u>	<u>Page</u>
3.5	ERROR BUDGETS . . . . . 3-31
3.5.1	High Resolution Camera . . . . . 3-31
3.5.2	Wide Field Camera . . . . . 3-33
3.5.3	High Resolution Spectrograph . . . . . 3-33
3.5.4	Faint Object Spectrographs . . . . . 3-35
3.6	THROUGHPUT ANALYSIS . . . . . 3-36
3.6.1	Wide Field Camera . . . . . 3-39
3.6.2	High Resolution Camera (f/96) . . . . . 3-42
3.6.3	High Resolution Spectrograph . . . . . 3-45
3.6.4	Faint Object Spectrograph . . . . . 3-52
3.7	SYSTEM OPERATIONAL, HARDWARE AND RELIABILITY CONSIDERATION . . . . . 3-59
3.7.1	Role of the Astronaut and its Implications . . . . . 3-57
3.7.2	Data Handling . . . . . 3-60
3.8	EFFECT OF IMPROVED SENSORS ON INSTRUMENT PERFORMANCE . . . . . 3-61
4	SCIENTIFIC INSTRUMENTATION . . . . . 4-1
4.1	INTRODUCTION . . . . . 4-1
4.2	HIGH SPATIAL RESOLUTION CAMERA ASSEMBLY . . . . . 4-5
4.2.1	General Description . . . . . 4-5
4.2.2	Description of Optics . . . . . 4-7
4.2.3	Tolerance Analysis . . . . . 4-14
4.2.4	Sensors . . . . . 4-18
4.2.5	Signal To Noise Analysis . . . . . 4-19
4.3	HIGH RESOLUTION SPECTROGRAPHS . . . . . 4-26
4.3.1	General Description . . . . . 4-26
4.3.2	Description of Optics . . . . . 4-26
4.3.3	Tolerance Analysis - High Resolution Spectrograph . . . . . 4-43
4.3.4	Detector . . . . . 4-44
4.3.5	Signal-to-Noise Ratio and Slit- Width Selection . . . . . 4-50
4.4	FAINT OBJECT SPECTROGRAPH . . . . . 4-57
4.4.1	General Description . . . . . 4-57
4.4.2	Description of Optics . . . . . 4-67
4.4.3	Detector . . . . . 4-92

## TABLE OF CONTENTS (Cont.)

<u>Section</u>	<u>Page</u>
4.4.4 Signal-To-Noise Analysis . . . . .	4-93
4.5 MID-IR INTERFEROMETER . . . . .	4-98
4.5.1 General Description . . . . .	4-98
4.5.2 Description of Optics . . . . .	4-100
4.5.3 Servo Control System . . . . .	4-103
4.5.4 Detector and Internal Sources . . . . .	4-106
4.5.5 Signal-to-Noise Analysis . . . . .	4-107
4.5.6 Output Data Prediction . . . . .	4-112
4.6 WIDE FIELD CAMERA (f/12) . . . . .	4-113
4.6.1 General Description . . . . .	4-113
4.6.2 Description of Optics . . . . .	4-113
4.6.3 Sensor . . . . .	4-122
4.6.4 Signal-To-Noise Ratio . . . . .	4-123
5 ANCILLARY SUBSYSTEMS . . . . .	5-1
5.1 INTRODUCTION . . . . .	5-1
5.2 SLIT JAW CAMERA . . . . .	5-2
5.2.1 Purpose . . . . .	5-2
5.2.2 Description . . . . .	5-2
5.2.3 Slit Jaw Camera - S/N Considerations . . . . .	5-12
5.2.4 Alternative Approaches . . . . .	5-14
5.3 MECHANISMS . . . . .	5-21
5.3.1 Servo Considerations . . . . .	5-21
5.3.2 Mechanical Considerations . . . . .	5-23
5.3.3 Additional Functions (Slit Mechanism) . . . . .	5-29
5.3.4 Field Select Mirror Assembly . . . . .	5-32
5.4 ELECTRONIC SUPPORT . . . . .	5-34
5.4.1 Mechanism . . . . .	5-34
5.4.2 Packaging Approach . . . . .	5-35
5.4.3 Sensor Electronics . . . . .	5-42
5.4.4 SIP Harnessing . . . . .	5-45

## TABLE OF CONTENTS (Cont.)

<u>Section</u>	<u>Page</u>
6	IMAGING PHOTOELECTRIC SENSORS . . . . . 6-1
6.1	INTRODUCTION . . . . . 6-1
6.2	PERFORMANCE CRITERIA USED IN SENSOR SELECTION . . . . . 6-1
6.3	CAMERA TUBE DISCUSSION . . . . . 6-4
	6.3.1 Single Exposure Mode . . . . . 6-4
	6.3.2 Camera Tubes Comparison . . . . . 6-5
6.4	WINDOW AND PHOTOCATHODE COMBINATIONS. . . . 6-6
	6.4.1 Window Materials . . . . . 6-7
	6.4.2 Photocathodes . . . . . 6-8
	6.4.3 Final Selections . . . . . 6-13
6.5	TARGET MATERIAL . . . . . 6-15
6.6	ELECTRON-OPTICS . . . . . 6-15
6.7	MAGNETIC EFFECTS . . . . . 6-17
6.8	SPACE RADIATION . . . . . 6-20
6.9	PACKAGING CONSIDERATIONS . . . . . 6-22
6.10	SIT-VIDICON CAMERA TUBE . . . . . 6-22
6.11	ADDITIONAL WORK ON THE SEC-VIDICON . . . . 6-25
7	ENVIRONMENTAL CONSIDERATIONS OF THE SCIENTIFIC INSTRUMENTATION DESIGN . . . . . 7-1
7.1	INTRODUCTION . . . . . 7-1
7.2	THERMAL CONSIDERATIONS . . . . . 7-1
	7.2.1 Conditions of Investigation . . . . . 7-2
	7.2.2 Description of the Thermal Models . . . . 7-3
	7.2.3 Input Power . . . . . 7-3
	7.2.4 Method of Analyses. . . . . 7-3
	7.2.5 Temperature Results . . . . . 7-11
	7.2.6 Time Response . . . . . 7-13
	7.2.7 Detailed Thermal Design . . . . . 7-14
	7.2.8 Performance Effects . . . . . 7-15
	7.2.9 Detector Tube Assembly . . . . . 7-25
7.3	STRUCTURAL CONSIDERATIONS . . . . . 7-48
	7.3.1 Dynamic Environments . . . . . 7-48
	7.3.2 Stability of Instruments . . . . . 7-49



<u>Section</u>	<u>Page</u>
7.3.3	Design Criteria . . . . . 7-49
7.3.4	Material Properties . . . . . 7-51
7.3.5	Structural Analysis . . . . . 7-51
7.3.6	Structural Considerations - High Resolution Spectrograph . . . . . 7-68
7.3.7	Structural Considerations - Faint Object Spectrograph . . . . . 7-71
7.4	RADIATION . . . . . 7-73
7.5	OTHER ADVERSE ENVIRONMENTS . . . . . 7-75
8	SCIENTIFIC INSTRUMENT PACKAGE OVERALL
	PHYSICAL DESCRIPTION . . . . . 8-1
8.1	INTRODUCTION . . . . . 8-1
8.2	DESCRIPTION OF THE SIP . . . . . 8-1
8.3	DEVELOPMENT OF THE STRUCTURAL CONFIGURATION . . . . . 8-7
8.3.1	General Philosophy . . . . . 8-7
8.3.2	Design Criteria . . . . . 8-7
8.3.3	Design Evolution (Alternate Approaches) . . . . . 8-9
8.4	STRUCTURAL MATERIAL . . . . . 8-15
8.4.1	Material Selection . . . . . 8-15
8.4.2	Fabrication Methods . . . . . 8-16
8.4.3	Assembly Concepts . . . . . 8-19
8.5	STRUCTURAL ANALYSIS . . . . . 8-21
8.5.1	Analytical Model . . . . . 8-21
8.5.2	Thermal Sensitivity Analysis . . . . . 8-21
8.5.3	Launch and Reentry Loads . . . . . 8-48
8.5.4	Resonant Frequency . . . . . 8-48
8.6	SIP THERMAL DESIGN AND ANALYSIS . . . . . 8-48
8.6.1	Introduction . . . . . 8-48
8.6.2	Thermal Control Concepts . . . . . 8-49
8.6.3	Results of Thermal Model Studies . . . . . 8-58
8.6.4	Discussion of Results . . . . . 8-62

## TABLE OF CONTENTS (Cont.)

<u>Section</u>	<u>Page</u>
9	INTERFACE CONSIDERATIONS . . . . . 9-1
9.1	INTRODUCTION . . . . . 9-1
9.1.1	Optical Interface . . . . . 9-2
9.1.2	Mechanical Interface . . . . . 9-3
9.2	FINE GUIDANCE ASSEMBLY . . . . . 9-4
9.3	DATA HANDLING AND ELECTRONICS DATA . . . . . 9-6
9.3.1	Data . . . . . 9-6
9.3.2	Power . . . . . 9-28
9.3.3	Summary Document . . . . . 9-34
9.3.4	EMC . . . . . 9-38
10	RELIABILITY AND MAINTAINABILITY . . . . . 10-1
10.1	RELIABILITY . . . . . 10-1
10.1.1	Introduction . . . . . 10-1
10.1.2	Bases for Reliability Analysis . . . . . 10-2
10.1.3	LST-SIP Operational Reliability Block Diagram . . . . . 10-4
10.1.4	LST-SIP Instrument Utilization Profile . . . . . 10-7
10.1.5	Reliability Block Diagrams and Mathematical Models . . . . . 10-12
10.1.6	Reliability Predictions . . . . . 10-15
10.1.7	Conclusions . . . . . 10-22
10.1.8	Recommendations . . . . . 10-27
10.2	MAINTAINABILITY . . . . . 10-28
10.2.1	Introduction . . . . . 10-28
10.2.2	Basic Approach . . . . . 10-29
10.2.3	Maintainability Analysis . . . . . 10-29
10.2.4	Maintenance Action Schedule . . . . . 10-30
10.2.5	Maintenance Action Environment . . . . . 10-31
10.2.6	General Design for In-Orbit Maintenance . . . . . 10-32
10.2.7	SIP Layout and Hardware Mounting Considerations . . . . . 10-33
10.2.8	Tolerances for In-Service Replaceability . . . . . 10-43
10.2.9	Growth Provisions . . . . . 10-44
10.2.10	Failure Identification . . . . . 10-44
10.2.11	Provisioning . . . . . 10-49
10.2.12	Training . . . . . 10-50
10.2.13	Conclusions . . . . . 10-50
10.2.14	Recommendations . . . . . 10-51

TABLE OF CONTENTS (Cont.)

APPENDIX A - RESOLVABLE ELEMENT SIZE VS. POINTING PARAMETRIC ANALYSIS . . . . .	A-1
APPENDIX B - SIGNAL-TO-NOISE RATIO . . . . .	B-1
APPENDIX C - SIGNAL-TO-NOISE ANALYSIS, FAINT OBJECT SPECTROGRAPH NUMBER 3 . . . . .	C-1

## LIST OF ILLUSTRATIONS

<u>Figure No.</u>		<u>Page</u>
1-1	SIP Configuration . . . . .	1-8
1-2	Focal Plane Arrangement . . . . .	1-10
1-3	Scientific Instrument Package, Functional Block Diagram . . . . .	1-11
3-1	System Analysis Flow Diagram . . . . .	3-3
3-2	Family Tree, System Analysis . . . . .	3-5
3-3	Spectrograph Format, Area Presentation (Echelle) . . . . .	3-12
3-4	Spectrograph Format, Line Presentation . . . . .	3-12
3-5	Grating Efficiency . . . . .	3-13
3-6	Camera Performance at 300 nm and 500 nm With SEC Vidicon Detector . . . . .	3-16
3-7	Effect of Pointing Instability on Field Camera Resolution . . . . .	3-20
3-8	Effect of Telescope Image on Spectral Resolution . . . . .	3-25
3-9	Relative Energy as a Function of Aperture Size . . . . .	3-27
3-10	S/N as a Function of Image Size . . . . .	3-27
3-11	Effect of Telescope Image on Spectral Resolution . . . . .	3-30
3-12	Effect of Image Size Increase on Resolvable Element Size . . . . .	3-34
3-13	Spectral Reflectance of Haas-1 Coating $R=f(n)$ With $n$ = number of Reflective Surfaces/normal Incidence . . . . .	3-37
3-14	High Resolution Spectrograph, Optics Reflectance . . . . .	3-38
3-15	Spectral Reflectance of Silver Coating $R = f(\lambda)$ Shown for a $45^\circ$ Incidence Angle, $\alpha$ . . . . .	3-38

LIST OF ILLUSTRATIONS (Cont.)

<u>Figure No.</u>		<u>Page</u>
3-16	Dichroic Mirror, Transmittance and Reflectance = $F(\lambda)$ . . . . .	3-40
3-17	Available Far-UV Filters . . . . .	3-41
3-18	LST Wide Field Camera Throughput for Zero Mag. Star . . . . .	3-43
3-19	LST High Resolution Camera (f/96) (Range I) Throughput for Zero Mag. Star . . . . .	3-44
3-20	LST High Resolution Camera (f/96) (Range II) Throughput for Zero Mag. Star . . . . .	3-46
3-21	LST High Resolution Camera (f/96) (Range III) Zero Mag. Throughput . . . . .	3-47
3-22	High Resolution Spectrograph, Range I Efficiency, Center of Order . . . . .	3-49
3-23	LST High Resolution Spectrograph, Zero Mag. Throughput . . . . .	3-50
3-24	High Resolution Spectrograph Instrument Efficiency . . . . .	3-51
3-25	LST Faint Object Spectrograph, Zero Mag. Throughput	3-53
3-26	LST Faint Object Spectrograph No. 2, Double Flat Grating/Dichroic Separation, Zero Mag. Throughput .	3-55
3-27	LST Faint Object Spectrograph Instrument No. 3, Zero Mag. Throughput . . . . .	3-56
4-1	High Resolution Camera Assembly . . . . .	4-6
4-2	High Resolution Camera Assembly Functional Schematic . . . . .	4-8
4-3	High Resolution Camera Assembly Family Tree . . . . .	4-9
4-4	Camera Assembly Optical System Record . . . . .	4-11
4-5	High Resolution Camera Axial MTF at 300 nm . . . . .	4-12

LIST OF ILLUSTRATIONS (Cont.)

<u>Figure No.</u>		<u>Page</u>
4-6	High Resolution Camera MTF at 25 mm Height on Image Tube . . . . .	4-13
4-7	S/N Ranges I and II Curves, High Resolution Camera.	4-23
4-8	High Resolution Camera, Range III, Signal-to-Noise Ratio as a Function of Star Magnitude and Integration Time . . . . .	4-25
4-9	High Resolution Spectrograph, Functional Schematic.	4-27
4-10	High Resolution Spectrograph, Family Tree, I or II.	4-28
4-11	High Resolution Spectrograph, Error Budget for Various Camera Mirror and Grating Parameters . . .	4-30
4-12	High Resolution Spectrograph Range 1 (115 to 180 nm) . . . . .	4-32
4-13	High Resolution Spectrograph Range 2 (180 to 350 nm) . . . . .	4-33
4-14	High Resolution Spectrograph . . . . .	4-34
4-15	High Resolution Spectrograph Spectral Formats . . .	4-36
4-16	Lower Wavelength High Resolution Spectrograph Spot Diagram . . . . .	4-37
4-17	Lower Wavelength High Resolution Spectrograph Spot Diagram . . . . .	4-38
4-18	Lower Wavelength High Resolution Spectrograph Spot Diagram . . . . .	4-39
4-19	Upper Wavelength High Resolution Spectrograph Spot Diagram . . . . .	4-40
4-20	Upper Wavelength High Resolution Spectrograph Spot Diagram . . . . .	4-41
4-21	Spectral Resolution versus Total Image Blur Diameter . . . . .	4-42

LIST OF ILLUSTRATIONS (Cont.)

<u>Figure No.</u>		<u>Page</u>
4-22	Spectral Resolution versus Total Image Blur Diameter . . . . .	4-45
4-23	High Resolution Spectrograph Range I S/N Ratio as a Function of Star Magnitude and Integration Time . . . . .	4-54
4-24	High Resolution Spectrograph Range II S/N Ratio as a Function of Star Magnitude and Integration Time (t) for Three Slit Width Values . . . . .	4-56
4-25	Faint Object Spectrograph No. 1, Physical Layout . .	4-58
4-26	Faint Object Spectrograph 110-160 nm (1A), 160-220 nm (1B) . . . . .	4-59
4-27	Faint Object Spectrograph 220 to 350 nm, 350 to 660 nm, 660 to 1000 nm . . . . .	4-60
4-28	Faint Object Spectrograph 220-350 nm, 350-660 nm .	4-61
4-29	Faint Object Spectrograph Family Tree (110 to 220 nm) . . . . .	4-63
4-30	Faint Object Spectrograph Family Tree (220 to 660 nm) . . . . .	4-64
4-31	Faint Object Spectrograph Family Tree . . . . .	4-65
4-32	Faint Object Spectrograph 660-1000 nm . . . . .	4-66
4-33	Faint Object Spectrograph Optical System Record . .	4-70
4-34	Faint Object Spectrograph Range 1A (115 to 160 nm).	4-72
4-35	Spot Diagram - Faint Object Spectrograph Range 1A (115 to 160 nm) . . . . .	4-73
4-36	Spot Diagram - Faint Object Spectrograph Range 1A (115 to 160 nm) . . . . .	4-74
4-37	Spot Diagram - Faint Object Spectrograph Range 1B (160 to 220 nm) . . . . .	4-75

LIST OF ILLUSTRATIONS (Cont.)

<u>Figure No.</u>		<u>Page</u>
4-38	Spot Diagram - Faint Object Spectrograph Range 1B (160 to 220 nm) . . . . .	4-76
4-39	Spot Diagram - Faint Object Spectrograph Range 1B (160 to 220 nm) . . . . .	4-77
4-40	Faint Object Spectrograph Optical System Record . . . . .	4-79
4-41	Faint Objective Spectrograph Spot Diagram, Range 2B (350 to 660 nm) . . . . .	4-81
4-42	Faint Object Spectrograph Spot Diagram, Range 2B (350 to 660 nm) . . . . .	4-82
4-43	Faint Objective Spectrograph Spot Diagram, Range 2B (350 to 660 nm) . . . . .	4-83
4-44	Spot Diagram - Faint Object Spectrograph, Range 2A (220 to 350 nm) . . . . .	4-84
4-45	Spot Diagram - Faint Object Spectrograph, Range 2A (220 to 350 nm) . . . . .	4-85
4-46	Faint Objective Spectrograph Spot Diagram, Range 2A (220 to 350 nm) . . . . .	4-86
4-47	Optical Record . . . . .	4-88
4-48	Faint Objective Spectrograph No. 3, Spot Diagram; Spectral Range 660 to 1000 nm . . . . .	4-89
4-49	Faint Objective Spectrograph No. 3, Spot Diagram; Spectral Range 660 to 1000 nm . . . . .	4-90
4-50	Faint Objective Spectrograph No. 3, Spot Diagram; Spectral Range 660 to 1000 nm . . . . .	4-91
4-51	Faint Object Spectrograph No. 1, S/N Ratio as a Function of Star Magnitude (11.000K) and Integra- tion Time (t) SEC-Vidicon Oper. Temp. 300K; 20 LP/mm at 50% MTF . . . . .	4-96
4-52	Faint Object Spectrograph No. 2, S/N Ratio as a Function of Star Magnitude (11.000K) and Integra- tion Time (t) SEC-Vidicon Oper. Temp. 300K; 20 LP/mm at 50% MTF	4-97



LIST OF ILLUSTRATIONS (Cont.)

<u>Figure No.</u>		<u>Page</u>
4-53	Foreoptics of Interferometer . . . . .	4-99
4-54	Optical Diagram of Interferometer . . . . .	4-99
4-55	Mid-IR (Fourier) Interferometer . . . . .	4-101
4-56	Mid-IR (Fourier) Interferometer . . . . .	4-103
4-57	Interferometer Servo Control System . . . . .	4-105
4-58	Wide Field Camera Tube Assembly . . . . .	4-114
4-59	Wide Field Camera Layout . . . . .	4-115
4-60	Wide Field Camera Family Tree . . . . .	4-116
4-61	Ritchey-Chretien Astigmatism (f/12) . . . . .	4-118
4-62	Wide Field Camera, Bottom of Format . . . . .	4-119
4-63	Wide Field Camera, Middle of Format . . . . .	4-120
4-64	Wide Field Camera, Top of Format . . . . .	4-121
4-65	Wide Field Camera Signal-to-Noise Ratio, as a Function of Star Magnitude and Integration Time . .	4-124
5-1	Reference Slit Jaw Camera, Family Tree . . . . .	5-3
5-2	Reference Slit Jaw Camera, Optical Schematic . . .	5-5
5-3	Optical Schematic Slit Jaw Camera and Field Select Mirrors . . . . .	5-6
5-4	Slit Jaw Camera, Mechanical Layout . . . . .	5-8
5-5	Field Select Mirrors, Mechanical Layout (Sheet 1 of 2) . . . . .	5-9
5-5	Field Select Mirrors, Mechanical Layout (Sheet 2 of 2) . . . . .	5-10
5-6	Slit Jaw Camera, Early Version . . . . .	5-16

LIST OF ILLUSTRATIONS (Cont.)

<u>Figure No.</u>		<u>Page</u>
5-7	Deleted	5-20
5-8	Slit Mechanism . . . . .	5-24
5-9	Spectrograph Selector . . . . .	5-25
5-10	Spectrograph Calibration Source . . . . .	5-30
5-11	Calibration Source Display . . . . .	5-31
5-12	Field Select Mirror Assembly Family Tree . . . . .	5-33
5-13	High Resolution Camera, Block Diagram . . . . .	5-36
5-14	Aft Spectrographs, Block Diagram . . . . .	5-37
5-15	Faint Object Spectrograph No. 2, Block Diagram . . . . .	5-38
5-16	Faint Object Spectrograph No. 3, Block Diagram . . . . .	5-39
5-17	Mid-IR Interferometer, Block Diagram . . . . .	5-40
5-18	Wide Field Camera, Block Diagram . . . . .	5-41
5-19	Typical Electronics Assembly . . . . .	5-43
5-20	Sensor Electronics . . . . .	5-44
5-21	LST-SIP Harness Interconnect Schematic . . . . .	5-46
5-22	LST-SIP Harness Interconnect Layout (Sheet 1 of 2). . . . .	5-48
5-22	LST-SIP Harness Interconnect Layout (Sheet 2 of 2). . . . .	5-49
6-1	Spectral Responses, Photocathode Window in the UV . . . . .	6-9
6-2	Spectral Responses, Photocathode Window in the Visible and UV . . . . .	6-11
6-3	Photocathode Dark Current Vs. Temperature . . . . .	6-12
6-4	Spectral Responses, Reflective III-V Photocathodes. . . . .	6-14

LIST OF ILLUSTRATIONS (Cont.)

<u>Figure No.</u>		<u>Page</u>
6-5	Magnetic Fields for Two LST Desaturation Magnet Designs . . . . .	6-21
6-6	SEC-Vidicon, Physical Parameters . . . . .	6-23
7-1	Faint Object Spectrograph, Thermal Model . . . . .	7-4
7-2	High Resolution Camera, Thermal Model . . . . .	7-5
7-3	High Resolution Spectrograph, Thermal Model . . . . .	7-6
7-4	High Resolution Camera Thermal Response Diagram . . . . .	7-21
7-5	Detector Tube Assembly Model . . . . .	7-28
7-6	Detector Tube Assembly, Power Distribution . . . . .	7-31
7-7	Temperature Distribution Case 1 . . . . .	7-34
7-8	Temperature Distribution Case 2 . . . . .	7-35
7-9	Temperature Distribution Case 3 . . . . .	7-36
7-10	Temperature Distribution Case 4 . . . . .	7-37
7-11	Temperature Distribution Case 5 . . . . .	7-38
7-12	Temperature Distribution Case 6 . . . . .	7-39
7-13	Power Lost Thru Contact Area Vs. Contact Area . . . . .	7-40
7-14	Axial Gradient on Conduction Sleeve Vs. Wall Thickness . . . . .	7-41
7-15	Temperature History . . . . .	7-42
7-16	Focus Coil Case Temp. (Average Vs. P Radiated) . . . . .	7-43
7-17	Camera Energy Balance . . . . .	7-45
7-18	f/96 Camera Structure Model . . . . .	7-53
7-19	Influence Coefficient Matrix . . . . .	7-56
7-20	Natural Frequencies and Mode Shapes . . . . .	7-57

LIST OF ILLUSTRATIONS (Cont.)

<u>Figure No.</u>		<u>Page</u>
7-21	Peak Random Responses (Shuttle Launch Levels) . . .	7-60
7-22	Shock Response . . . . .	7-60
7-23	Transmissibility Plot - f/96 Camera, Mass Point 9, Damping Factor = $\mu = 2\rho = 0.1$ . . . . .	7-62
7-24	Dynamic Loads . . . . .	7-63
7-25	Internal Loads . . . . .	7-64
7-26	Structural Model, High Resolution Spectrograph . .	7-69
7-27	Structural Model Faint Object Spectrograph . . . .	7-72
8-1	LST-SIP Assembly Layout (Sheet 1 of 2) . . . . .	8-2
8-1	LST-SIP Assembly Layout (Sheet 2 of 2) . . . . .	8-3
8-2	Support Structure (Sheet 1 of 2) . . . . .	8-4
8-2	Support Structure (Sheet 2 of 2) . . . . .	8-5
8-3	Concept No. 1 . . . . .	8-10
8-4	Concept No. 2 . . . . .	8-12
8-5	Concept No. 3, Present Design . . . . .	8-13
8-6	Production Concept for Strut . . . . .	8-17
8-7	Four-Piece Mold for Open Structural Sections . . .	8-18
8-8	Itek Concept SIP Ease Beam Projection . . . . .	8-22
8-9	Thermal Model, Rings 2 and 3 . . . . .	8-25
8-10	Structure Deformations, Case C . . . . .	8-41
8-11	Structural Shifts at f/96 Camera Mounting . . . .	8-47
8-12	Outer Thermal Control Surface - Nodal Network . . .	8-52
8-13	Pressure Cylinder Wall - Nodal Network . . . . .	8-53

## LIST OF ILLUSTRATIONS (Cont.)

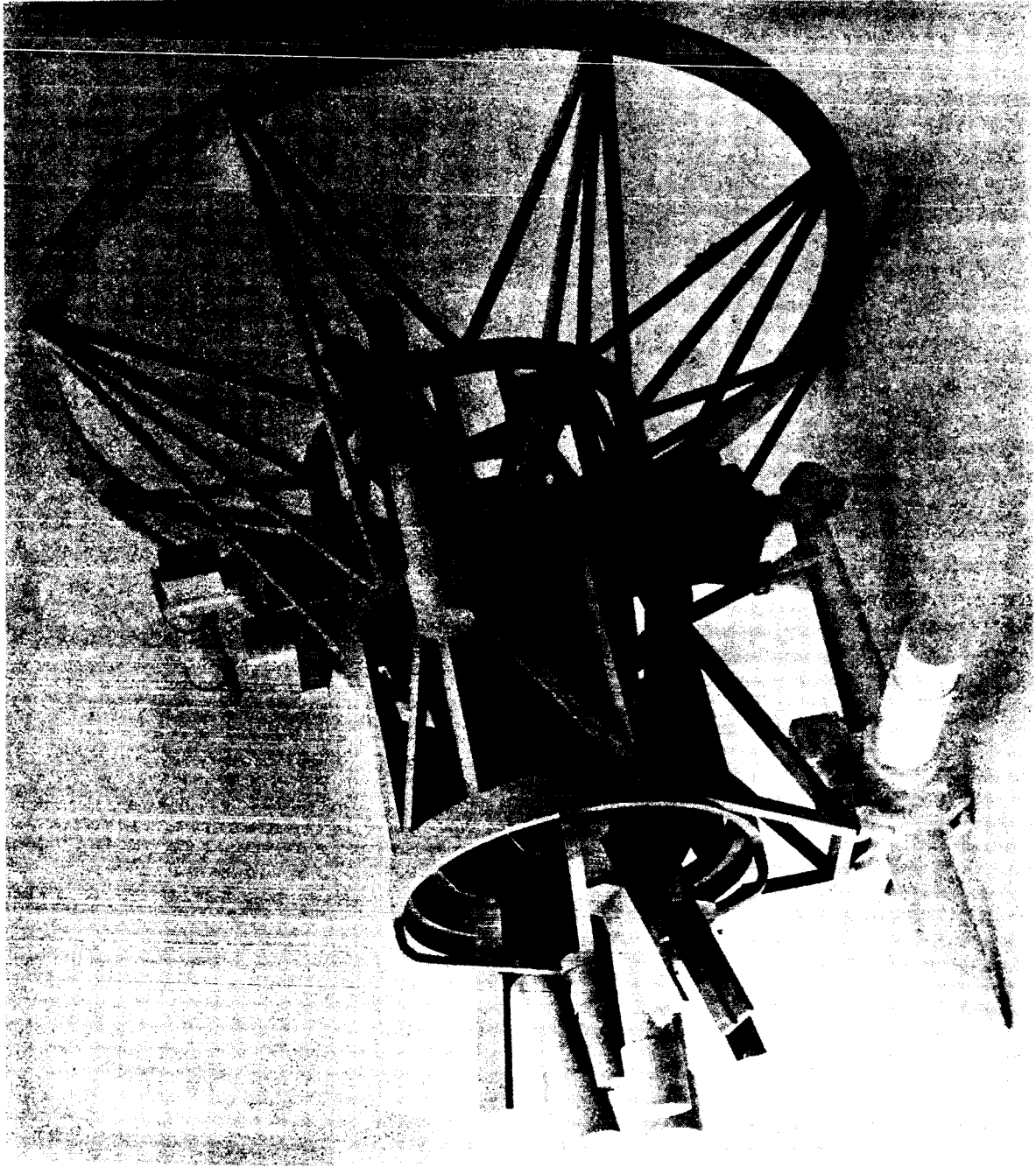
<u>Figure No.</u>		<u>Page</u>
8-14	Radial Truss Nodal Network . . . . .	.8-54
8-15	Nodal Network - Axial Truss . . . . .	.8-55
9-1	Scientific Data Flow . . . . .	.9-7
9-2	Sampled Data Spectrum . . . . .	.9-8
9-3	Power Profile Examples . . . . .	.9-30
10-1	LST/SIP Operational Reliability Block Diagram. . .	.10-5
10-2	SIP Series Model . . . . .	.10-16
10-3	F/96 Camera Assembly Operational Reliability Block Diagram and Math Models . . . . .	.10-17
10-4	Spectrography Operational Reliability Block Diagram and Math Models. . . . .	.10-18
10-5	F/12 Camera Assembly Operational Reliability Block Diagram and Math Models . . . . .	.10-19
10-6	SIP Series Model Evaluation. . . . .	.10-20
10-7	SIP Series Model Evaluation. . . . .	.10-21
10-8	Initial Maintenance Layout (Sheet 1 of 2). . . . .	.10-34
10-8	Initial Maintenance Layout (Sheet 2 of 2). . . . .	.10-35
10-9	Maintenance Layout (Sheet 1 of 2). . . . .	.10-37
10-9	Maintenance Layout (Sheet 2 of 2). . . . .	.10-38
10-10	Installation Provisions for Axially Located Instrumentation. . . . .	.10-40
10-11	Radial Instrument Installation . . . . .	.10-41

LIST OF ILLUSTRATIONS (Cont.)

<u>Figure No.</u>		<u>Page</u>
10-12	f/96 Camera, Maximum Outline . . . . .	10-45
10-13	Radial Instrument, Maximum Outline . . . . .	10-46
10-14	High Resolution Spectrometer Instrument Replacement, Maximum Outline . . . . .	10-47
10-15	Faint Object Spectrograph Instrument Replacement, Maximum Outline . . . . .	10-48

## ABSTRACT

This report presents the results of a study (NAS-5-23068) which establishes that it is feasible to design and build a Scientific Instrument Package (SIP) for the Large Space Telescope (LST) capable of diffraction limited imagery and high spectral resolution for a large range of celestial bodies. The instrument will be useable for several decades and will obtain scientific data not available on the ground. The SIP will be capable of growth and in-orbit repair and modification in response to the requirements of the scientific community.



Frontispiece. Scientific Instrument Package, Large Space Telescope



## FOREWORD

This document is the final report of the Kollsman Instrument Corporation phase A study of the Large Space Telescope (LST) Scientific Instrument Package (SIP). This study was performed under NASA Contract No. NAS-5-23068 for Goddard Space Flight Center under the technical direction of Mr. Raymond Melcher. It is the primary product of an LST Optical Instruments System Study Program as defined by Dr. Kenneth Hallam of the G.S.F.C. Laboratory for Optical Astronomy and sponsored by Dr. Rodney Johnson through the Experiment Definition Program Office of the NASA Office of Manned Space Flight, in cooperation with Mr. M. J. Aucremanne of the Physics and Astronomy Program Office of the NASA Office of Space Science. Mr. Edward Chin of G.S.F.C. provided basic guidance for systems integrity during the course of the study.

Kollsman wishes to acknowledge the support of the Itek Corporation which performed the overall structural and thermal analysis and the Martin Marietta Corporation which provided support in several areas.

In addition, Kollsman extends its appreciation to John Lowrance of Princeton University, and John Butler, James Heyer and Jean Olivier of the Marshall Space Flight Center for their support.

## Section 1

### INTRODUCTION

#### 1.1 BACKGROUND

During the past decade the scientific community has been considering the vast potential of a Large Space Telescope which could be placed in orbit for a long period of time to gather astronomical data not available from the ground. In 1969 the Ad Hoc Committee of the Large Space Telescope, appointed by the Space Science Board of the National Academy of Science, concluded that the LST would make valuable and significant contributions to our knowledge of cosmology and astronomy.

In 1970 NASA-Goddard Space Flight Center (GSFC) conducted a study of the LST Instrumentation Package and in November, 1970 published "Instrumentation Package for a Large Space Telescope" (X-670-70-480). This study examined the appropriateness of providing a system with general purpose space astronomy instrumentation. Its objective was to exploit the observational opportunities unique to the Large Space Telescope (LST). The instrument package configuration was designed to be consistent with an unpressurized modular replacement concept.

In January 1972 Kollsman Instrument Corporation, with team members Itek Corporation and Martin Marietta Corporation, was awarded a study contract (NAS-5-23068) for the LST Scientific Instrument Package (SIP). The formal objectives of this study are to (1) incorporate into the Research and Application Module (RAM) configuration the instrumentation described in GSFC Report No. X-670-70-480, (2) define the instrument complement and the performance of each instrument, and (3) provide trade-off analyses which optimize a Scientific Instrument Package configuration.

The Marshall Space Flight Center was later designated the NASA center responsible for the overall LST conceptual design and fabrication. The MSFC studies showed that the Scientific Instrument Package would be most effective if it were pressurized during the instrument maintenance and replacement periods. In addition, it was decided that the SIP configuration was to be modeled to be consistent with both a Titan-III and a Shuttle launch vehicle. The SIP instrument complement to be used in the study was to be in accordance with the primary LST Instrument Recommendations of the NASA LST Science Steering Committee.

This study report reflects the latest NASA concepts. This report develops specialized technical data, confirms the feasibility of, and provides a reference design for the SIP and thereby, aids in the establishment of the LST as a National Astronomical Facility. The LST will make a major contribution to the understanding of the content, structure, scale, and evolution of the universe. The LST is the next natural and logical step for the continued growth of our nation's astronomic and observational capability.

## 1.2 STUDY OBJECTIVES AND APPROACH

The objective of this study is to incorporate the instruments recommended by the NASA LST Science Steering Committee (Table 1-1) into a viable scientific instrument package system. The instrument configurations and bandwidth selections analyzed here are not to be construed as the final or optimized choice for the LST. Rather, they provide typical design parameters which serve as a reference to study packaging, structural and thermal problems, to expose maintenance problems and to establish tolerance and stability parameters. It is also necessary to explore the interaction of pointing, optical performance (spatial and spectral) and detector capability and the effect of each on the design parameters of the overall system. A further objective of the study is to define a reference instrument complement in sufficient detail to develop

costs, schedules, and milestones, and to identify any supporting research that is necessary to fulfill the technology requirements of the instrument package. Each system's alignment, in-orbit maintenance, and accessibility is also evaluated as a major objective to determine the desired degree of man's participation.

TABLE 1-1  
SUMMARY LST STEERING COMMITTEE RECOMMENDATIONS

Instrumentation	Resolution	Operating Range	Field
I High Spatial Resolution Camera	Match Telescope Performance	110 to 1,100 nm	Largest Field Consistent with Detector Capability and Selectable Filters
II High Spectral Resolution Spectrograph	$\frac{\lambda}{\Delta\lambda} = 3 \times 10^4$	110 to 350 nm	Slit Size Adjustable (max. 72 x 72 $\mu$ rad)
III Faint Object Spectrograph	$\frac{\lambda}{\Delta\lambda} = 10^3$	110 nm to 5 $\mu$ m	Same as II

The complement of scientific instruments that was evaluated during this study is listed in Tables 1-2 through 1-4. The instruments are responsive to the LST scientific objectives and to the above committee recommendations. Reliability, maintainability, instrument placement and system configuration are responsive to instrument priorities established by the committee.

TABLE 1-2  
FIELD CAMERAS

Camera f/No.	Equivalent Focal Length Meters	Plate Scale $\mu\text{rad}/\text{mm}$	Reciprocal Plate/Scale $\mu\text{m}/\mu\text{rad}$ ( $\mu\text{m}/\text{Arc Sec}$ )	Field of View mrad	Limiting Resolution nrad ( $> 27 \text{ mag}$ $\lambda = 300 \text{ nm}$ )	Limiting Magnitude $m_v$ ( $S/N = 2$ )
f/12	36	27.8	36 (175)	1.39	840	30.5
f/96	288	3.48	288 (1400)	0.173	160	32.5

TABLE 1-3  
HIGH SPECTRAL RESOLUTION SPECTROGRAPHS

	Spectral Range $\lambda_1 - \lambda_2$ (nm)	Dispersion at $\lambda_1$ nm/mm	Plate Scale $\mu\text{rad/mm}$	Spectral Resolution $\lambda_1/\Delta\lambda$	Limiting Magnitude $m_v$ ( $S/N = 2$ )
High Spectral Resolution Spectrograph I	110*-180	0.06	33.2	$4.5 \times 10^4$	17.2
High Spectral Resolution Spectrograph II	180 - 350	0.12	33.2	$3.0 \times 10^4$	19.7
* Sensor window material requires $\lambda_1 > 115$ nm					

TABLE 1-4  
 FAINT OBJECT SPECTROGRAPHS

Instrument	Spectral Range $\lambda_1 - \lambda_2$ (nm)	Dispersion at $\lambda_1$ nm/mm	Plate Scale $\mu\text{rad/mm}$	Spectral Resolution $\lambda_1/\Delta\lambda$	Limiting Magnitude $m_v$ (S/N = 2)
Faint Object Spectrograph I	A 115* - 160	1.67	37.0	$1.25 \times 10^3$	21
	B 160 - 220	2.00	37.0	$1.75 \times 10^3$	22.5
Faint Object Spectrograph II	A 220 - 350	4.40	27.3	$1.23 \times 10^3$	25
	B 350 - 660	10.27	27.3	$0.75 \times 10^3$	25
Faint Object Spectrograph III	660 - 1000	11.33	27.3	$1.5 \times 10^3$	22
Mid-IR Interferometer	1 - 5 $\mu\text{m}$	NA	NA	NA	13

\* Sensor window material requires  $\lambda_1 > 115$  nm

It is recognized that growth is an important configuration consideration. Therefore, flexibility, unused volume, replacement methods and hardware designs which allow for maximum state of the art updating, both during initial detail designs as well as after launch, have been considered in this study.

### 1.3 SYSTEMS DESCRIPTION

The Scientific Instrument Package is an energy selection, analyzing and processing system that has been tailored to match a 3 meter diameter, f/12 Ritchey-Chretien type telescope. Energy reaching the focal plane is selectively imaged on a variety of detectors or spectrographs. The selection and design of the individual instruments is the result of preliminary trade-off studies of several system configuration concepts.

#### 1.3.1 Configuration

The general SIP configuration is shown in Figure 1-1. The basic structure consists of three (3) rings which are tied together by trusses to provide bending and torsional stability. The stability of the structure is independent of the rigidity of the instruments. The three-ring assembly is attached to the OTA/SSM main ring at eight points. The open truss work permits access to all areas of the package. The instruments have been systematically arranged to allow for the removal of an individual instrument without disturbing any other. Self-aligning devices and insertion guiderails are provided for replacing instruments in order to minimize the need of astronaut dexterity and specialized maintenance skills. Moreover, all of the image sensors can be replaced and accurately repositioned without removing the associated optical elements or affecting any other subassembly of any instrument. The instruments located between the 2nd and 3rd rings are removed axially. The instruments between the 1st and 2nd rings are removed radially. The configuration of the unit mounting pads is designed to allow for a maximum variety of instrument configurations and potential for interchange. Sufficient instrument



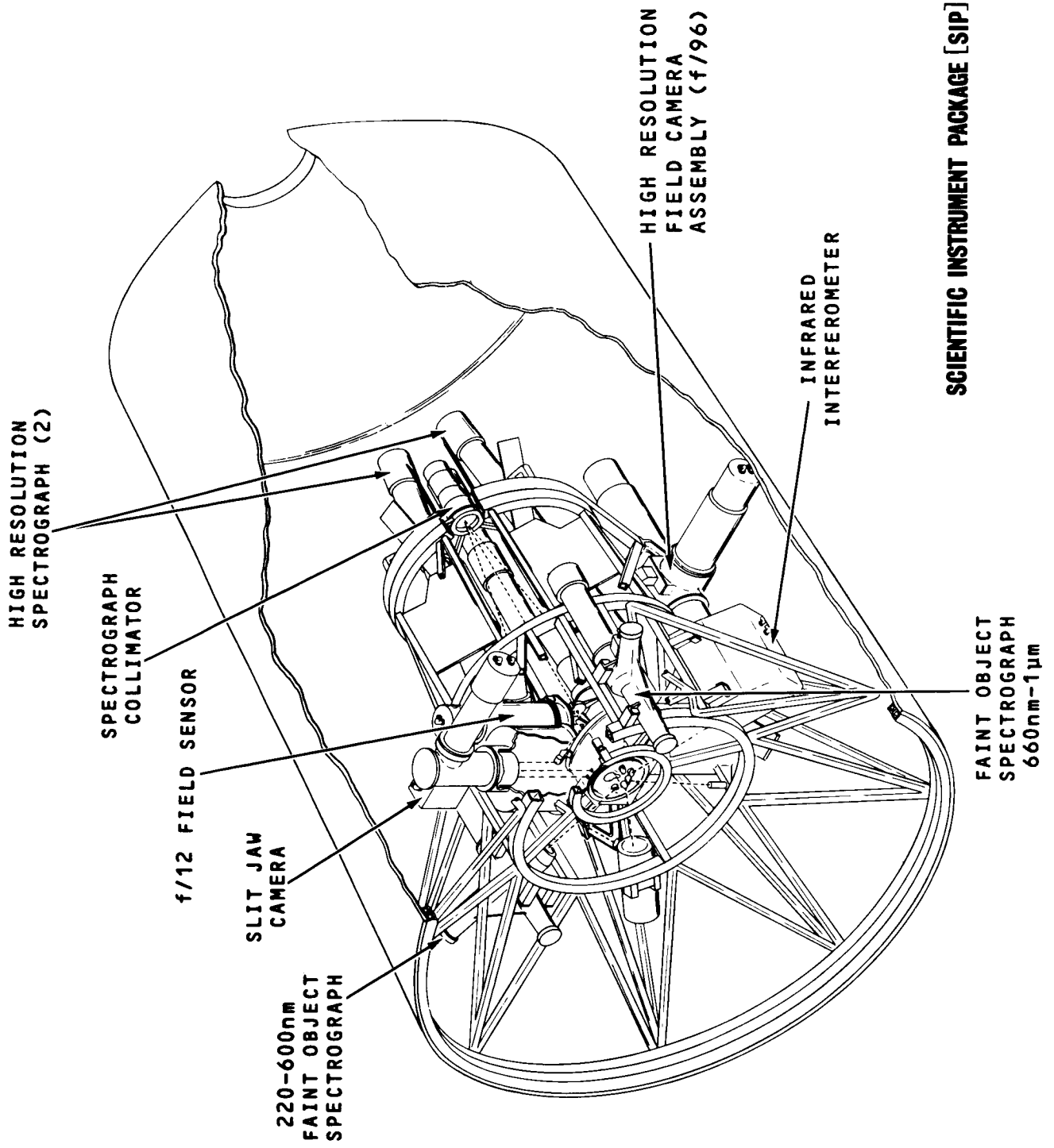


Figure 1-1. SIP Configuration

positions are provided for adding a supplemental, redundant or "yet to be conceived" instrument, besides those explicitly included in the complement studied herein.

### 1.3.2 Instrument Feed System

The light focused by the telescope is apportioned to each instrument according to each instrument's entrance aperture requirements and instrumental priority. Refer to Figure 1-2 for the schematic layout of the focal surface. A large diagonal mirror and five smaller fold mirrors each divert the light from the telescope image to the High Resolution Camera, the Wide Field Camera, the Fine Guidance Error Sensor and the Spectrograph mounted in the fore section of the SIP. The five fold mirrors are rigidly mounted on a quartz window. This window has holes to permit the direct passage of ultra-violet radiation. The High Spatial Resolution Camera system (f/96) is located directly on the telescope's optical axis to obtain maximum resolution over the greatest potential field of view. The offset fine guidance error sensors are fed by the same large diagonal mirror as the f/96 Camera to provide common mode error rejection. Their field coverage consist of an annulus 4.6 mrad ID by 7.0 mrad OD. The entrance slit assembly for the High Resolution Spectrograph and Faint Object Spectrograph is located 800  $\mu$ rad off the telescope optical axis. The center of the Wide Field Image Camera is 2 mrad off the telescope axis and has a local field of view of 1.4 mrad. The five (5) fold mirrors are mounted equidistantly at a radius of 1.2 mrad from the telescope axis and forward of the guidance and f/96 diagonal mirror. Each of the fold mirrors has a correction for astigmatism to extend its local field of view. A slit jaw camera (f/36) views the front face of all spectrograph entrance slits for target alignment and centering. Figure 1-3 is a functional block diagram of the Scientific Instrument Package which

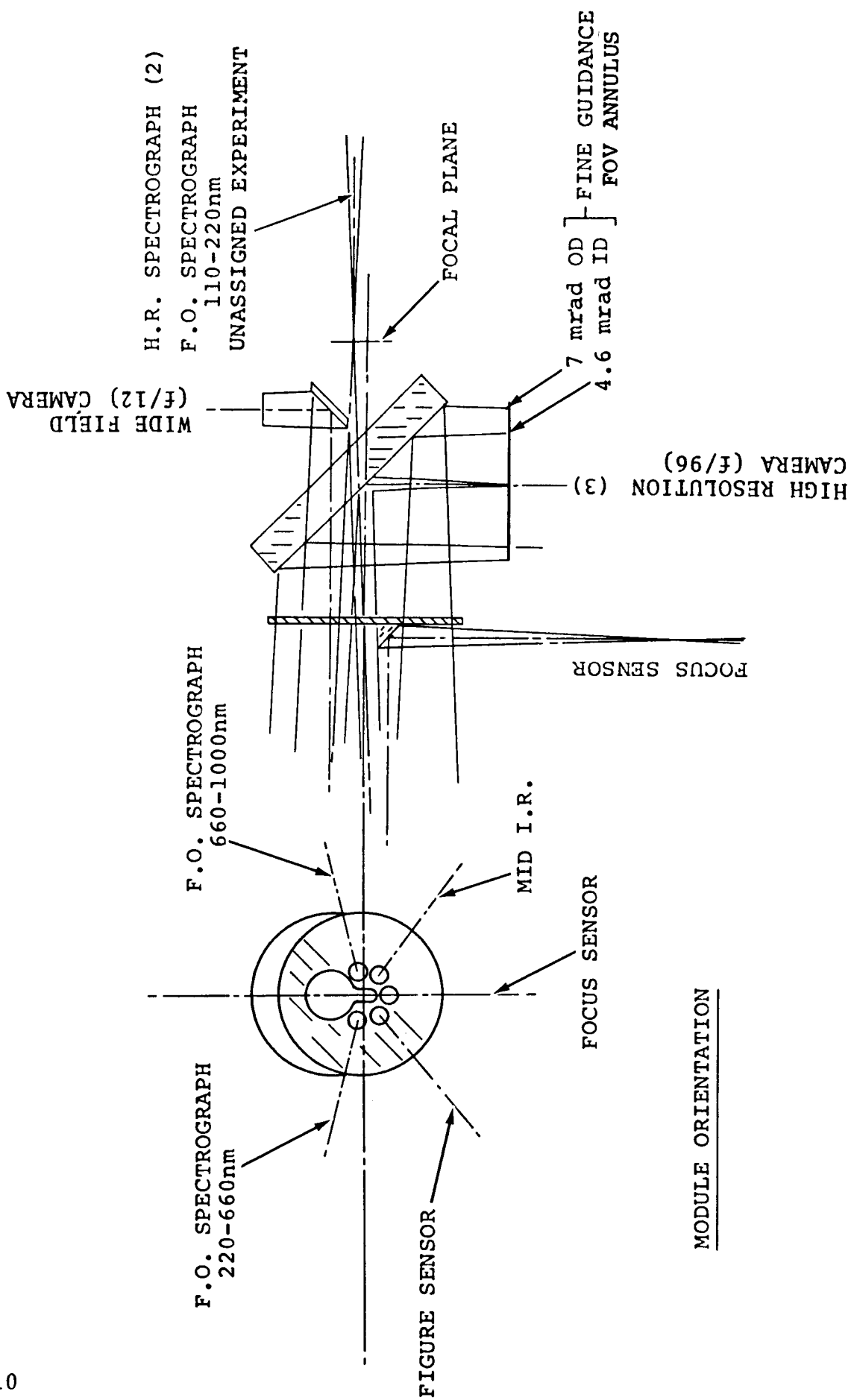


Figure 1-2. Focal Plane Arrangement

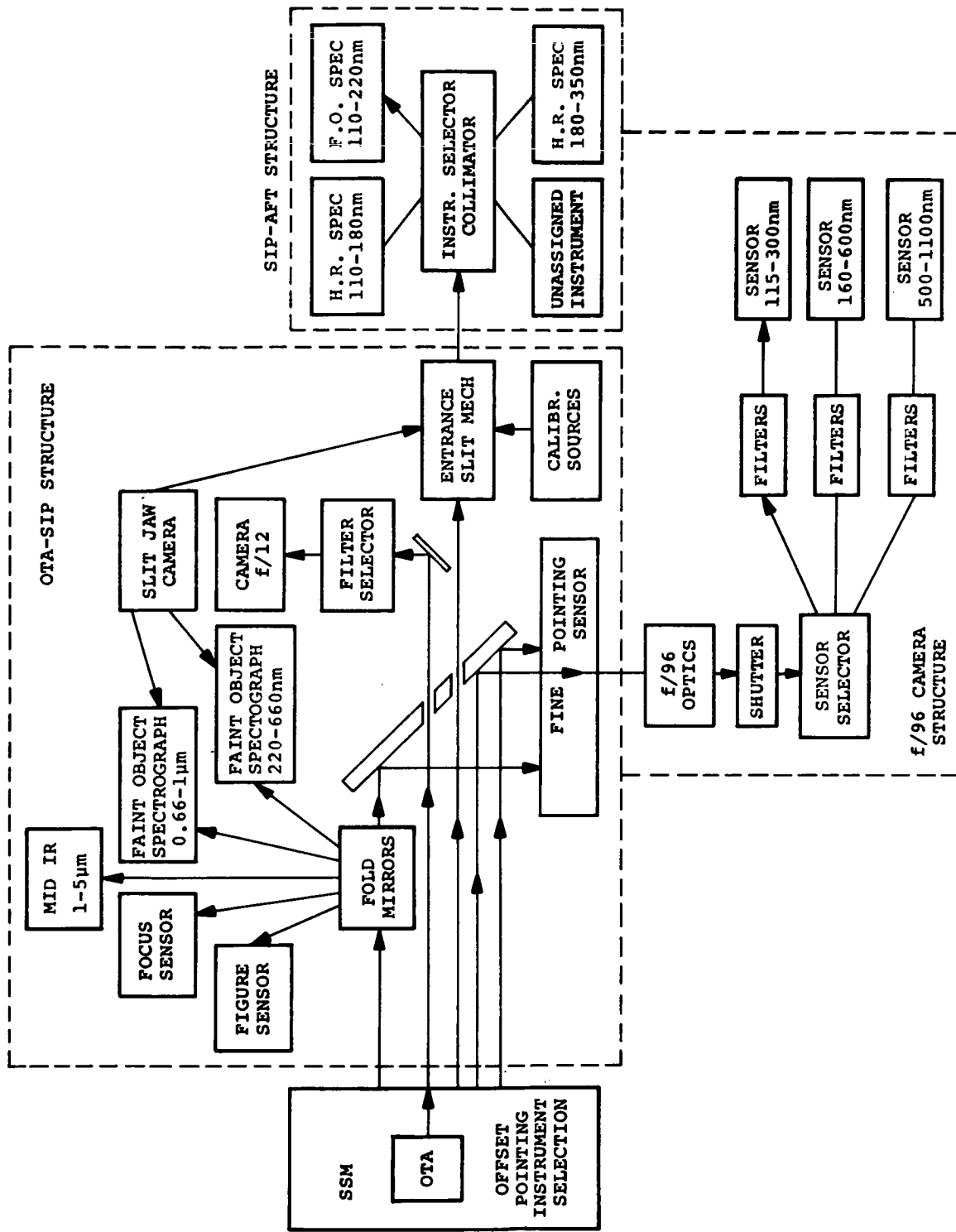


Figure 1-3. Scientific Instrument Package, Functional Block Diagram

shows the means by which light flows from the OTA into each scientific instrument.

### 1.3.3 Imagery

In order that the resolution from the image sensor of the High Resolution field cameras is not significantly less than that imposed by the diffraction limit of the telescope, the equivalent focal length of the cameras must provide focal scale consistent with the linear resolution of any given image sensor. In the case of the design reference SEC TV sensor, the High Resolution Camera has been designed to be f/96. The faster f/12 beam is used without re-imaging to provide a large field, limited only by image sensor format size and resulting in proportionately less angular resolution for a given sensor than when used in the f/96 Camera. The off-axis f/12 field camera location can be used to accommodate photon-counting or higher spatial resolution sensors yet to be developed, until off-axis aberrations predominate.

### 1.3.4 Spectral Response

The useful wavelength sensitivity range of the reference instrument complement is from 115 nm to 5  $\mu$ m. A spectral resolution ( $\lambda/\Delta\lambda$ ) of  $10^3$  is provided over the entire spectral range. In the spectral band between 115 and 350 nm, a spectral resolution of  $3 \times 10^4$  is also available.

## 1.4 INSTRUMENT PACKAGE EFFECTIVENESS

The SIP is to be capable of operational use for at least ten years. In order to maintain the capability of the LST instruments over that extended period of time, the SIP has built-in design features such as independence of instrument assemblies and subsystem accessibility despite the apparently dense packaging. The accessibility of the modules permits periodic maintenance, repair and replacement in orbit, which also allows the overall performance to be upgraded with improved instruments.

## 1.5 STUDY SUMMARY

This study has shown that it is feasible to design and build a Scientific Instrument Package for the LST capable of near diffraction limited imagery and high spectral resolution. The instrument can be usable for several decades and be capable of growth and modification in accordance with the requirements of advancing technology. This general purpose instrument can be available to the astronomical community by 1980.

The recommendations that should be considered in the next phase of the LST-SIP development are summarized as follows:

1. For the assumptions which were used in this study, there exists a family of non-critical instrument design concepts:

- a) An f/96 design for the high resolution camera and a f/12 design for the wide field camera.
- b) An f/9 to f/12 range for the spectrographs. An area presentation should be used for the high resolution spectrograph applications. A line presentation should be used for the low resolution spectrograph applications.
- c) A memory is required for the Mid IR 1-5 micrometer Faint Object Spectrometer.

2. Two assumptions which have significant impact on the design are that (1) the camera tube resolution is 20 lp/mm and (2) the minimum allowable single grating efficiency is 80%. If the tube development yields a superior resolution, e.g., 60 lp/mm, the high resolution camera f number can be reduced to 32 and higher spectral resolution can be achieved by the spectrographs. If the allowable grating efficiency is reduced, fewer gratings will be needed for the spectrographs.

3. Some LST parameters have much greater impact on one type of instrument than another, i.e., the High Resolution Camera determines the LST pointing stability requirements. The High Resolution Spectrographs determine the LST pointing accuracy requirements.

4. The "limiting magnitude" based on a S/N ratio of two is roughly +30 magnitude for the camera, +18 for the high resolution spectrograph and +20 for the faint object spectrograph.

5. Man's major role will be that of replacement/repair. Most of the troubleshooting and diagnosis will be done on the ground, therefore a sufficient amount of diagnostic data should be made available.

6. The instruments must be designed

- a) such that no alignment/calibration is performed by the astronaut
- b) to be readily replaced in the SIP. This maintenance concept will be a major driver of the mechanical, electronic and harness design.

7. An improved sensor design can:

- a) permit a closer approach to the background limit in the spectrographs.
- b) result in lower focal ratios and a smaller package size.
- c) improve the resolution of the present designs.
- d) ease the thermal constraints on sensors.
- e) ease the structural problems of the high resolution camera

8. Further work is required on the image motion compensation for the high resolution camera.

9. Further work is needed on the near IR photocathode development (III-V compounds).

10. Further work is required on the slit jaw monitor mode of operation and its sensor.

11. Additional packaging studies of the 50 by 50 millimeter SEC vidicon, including cooling, magnetic shielding, and circuitry are required.

12. A study of previous target problems (UVICON) and an investigation of Ebic targets is recommended.

13. A more detailed evaluation of calibration sources should be made.

14. A comprehensive review of the assumptions and the trade-off options available to the astronomer as a result of this study should be made. The astronomers and engineering community should do this in close liaison in order to optimize the SIP design in terms of performance and cost effectiveness.



Section 2  
GENERAL SCIENTIFIC OBJECTIVES

This section will be found in Volume 2 of this Report.

## SECTION 3 SIP SYSTEM ANALYSIS

### 3.1 INTRODUCTION

This section describes the approach and methods used for establishing criteria for the total SIP performance. The performance of each instrument is analyzed with respect to the OTA capabilities, guidance, environment and cost effectiveness. Scientific use priorities, accuracy and maintainability are carefully weighed in the instrument selection and configuration evaluations. Once the reference SIP configuration is established, an analysis is made for each instrument and component to determine an error budget. Finally specifications and design guide lines are established for the scientific instruments. These reference instruments are described in detail in Section 4. New or yet to be designed scientific instruments should be evaluated against the same design guide lines and methods that are described here.

The approaches utilized in the analyses which follow are based on certain assumptions, some of which pertain to the devices used, and others are concerned with desired levels of performance. The former are based on the desire to provide a design which would best utilize the devices expected to be available by the time the LST is flying. The latter are used whenever firm input information was not available.

The designs are not "sharply tuned", therefore the design or the performance will not be significantly altered by small changes in these assumptions. Significant changes in these assumptions will affect the performance or change the basic design. The basic assumptions and the performance desired by the astronomers is an area of critical importance, and a close and continuous liaison between the engineering and the astronomy communities must be maintained in this area if the design of the SIP is to be optimized.

The performance criteria are broken into two major areas, resolution and signal-to-noise (S/N) ratio. The resolution is a measure of the ability to separate two point objects in the cameras or two spectral lines in the spectrographs. The S/N is a measure of the ability of the instrument to separate two amplitude (intensity) levels. The "limiting magnitude" of an instrument is here defined as that resulting from the input intensity for which the S/N ratio is 2.

The process by which the SIP systems analysis is carried out can be seen from Fig. 3-1, the System Analysis Flow Diagram. The system design is initiated by using the astronomy committee recommendations as criteria, and the technological inputs as a basis for establishing the assumptions used to evaluate a particular design concept. The design concept is evaluated for its resolution, S/N ratio, size, weight, etc. If the design meets the criteria specified, it becomes a candidate for an instrument, as shown by the designations candidate #1, #2 and #3 in Fig. 3-1. If it does not meet the specifications, a modification decision is made. If the decision is no, that particular design is discarded. If the decision is yes, the assumptions/criteria/designs/ are modified, and the process continues until either the conceptual design is accepted as a candidate, or discarded.

The next step in the process is to evaluate all the candidates for a particular instrument and select the best one, based on the criteria utilized to evaluate a conceptual design.

When a weighted judgment is made, the "best" design is used as an input for the SIP evaluation. At this system level, the major considerations are the system interaction parameters of all of the instruments, such as: reliability, maintainability, priority of instruments, cost effectiveness and future growth potential.

At this juncture another acceptability judgment is made. If the decision is yes, the reference SIP System goal has been reached. If the answer is no, the existence of candidates other than those

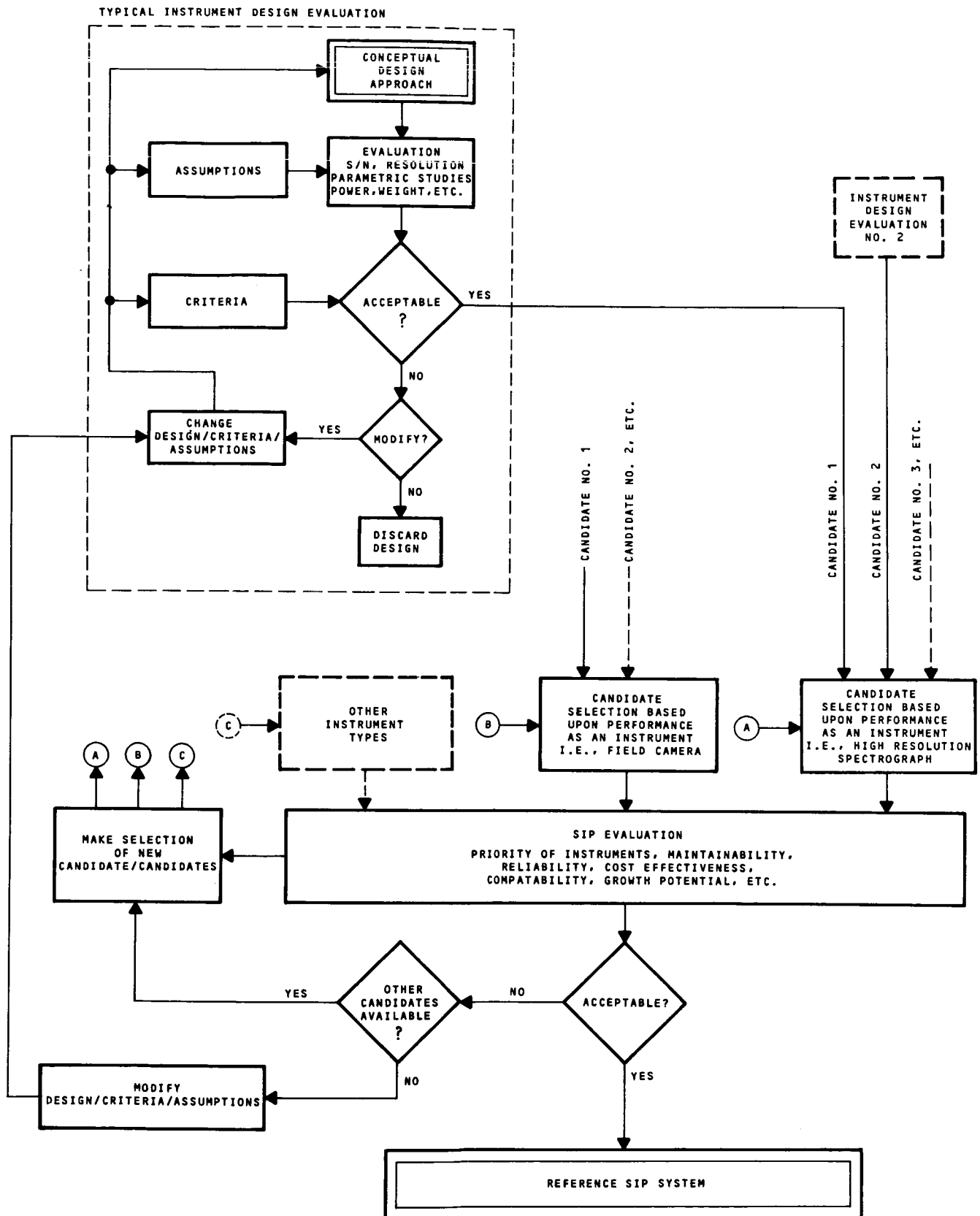


Figure 3-1. System Analysis Flow Diagram

which were entered into the SIP evaluation is determined. If there are, then a new candidate or candidates is selected, based upon the information gleaned from the initial SIP evaluation. The new set of candidates is evaluated and the process continues until either a reference SIP System is achieved or the number of candidates is exhausted.

At this point, the design/criteria/assumptions for any or all of the instruments may change; or an instrument type may be added to or deleted from the SIP package as a result of the SIP System evaluation. It should be noted that this is a continuing process. As the state of the art changes, and as the subsystems are designed in greater detail, information becomes available which can change the assumptions/criteria to the point where either certain instruments or the entire SIP system should be re-evaluated.

Figure 3-2, the system analysis family tree, is also illustrative of the analytical process. It does not indicate the exact order and flow of the analysis, that is the purpose of the System Analysis Flow Diagram. It does show, in greater detail, the assumptions and criteria used in the analysis, and the output resulting from the analysis.

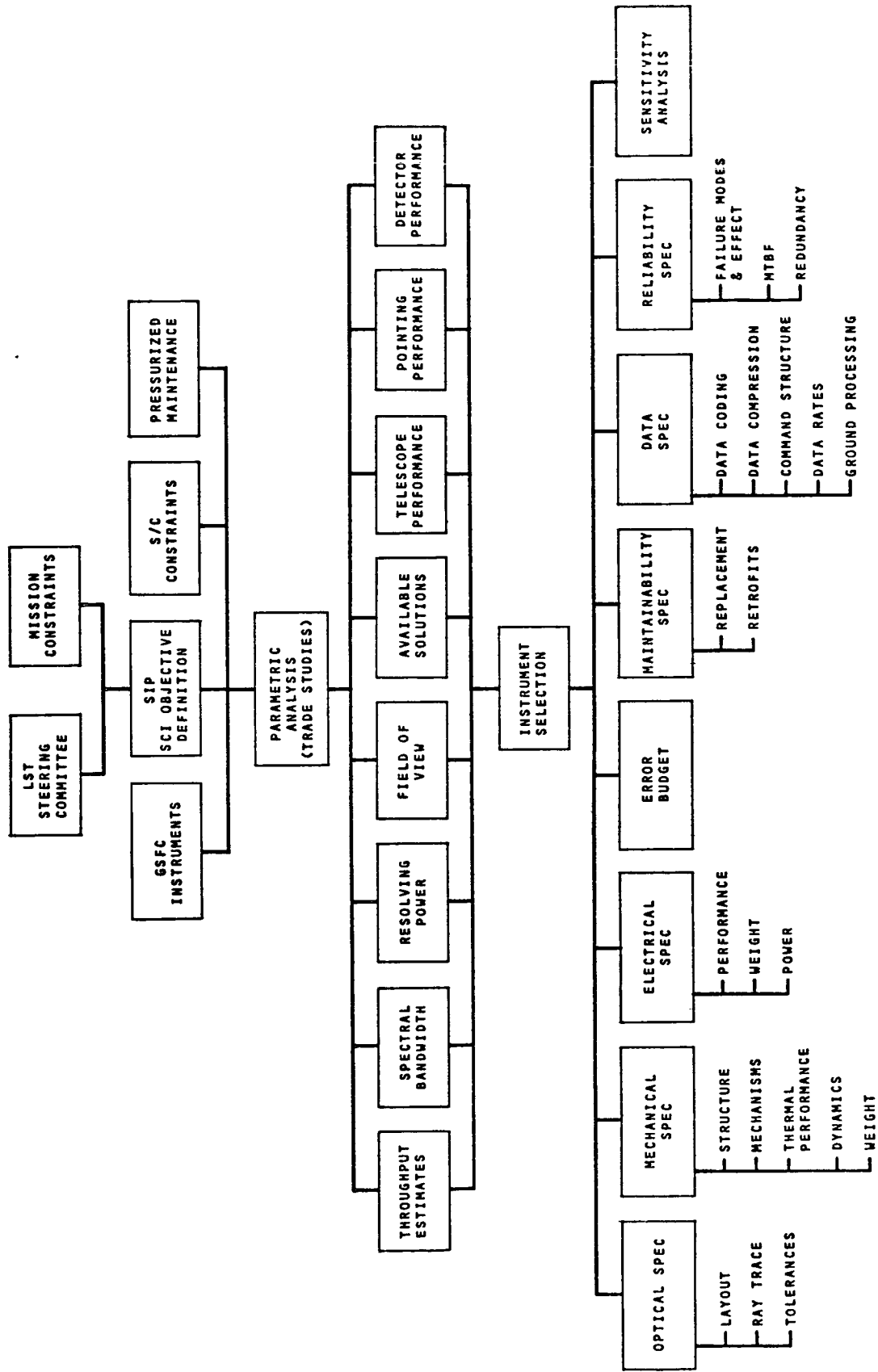


Figure 3-2. Family Tree, System Analysis

## 3.2 STUDY INPUTS

### 3.2.1 Committee Recommendations

The LST steering committee chaired by Dr. N. Roman of NASA Headquarters provided recommendations for the LST measurement capabilities.

The instruments were divided into primary and secondary priority groups. Table 3-1 is a summary of the instruments; instruments I, II and III are the primary instruments.

The effort was therefore concentrated on the first set of requirements which called for a field camera to match the resolving power of the telescope and two sets of spectrographs - one to provide resolving power of  $3 \times 10^4$  in the spectral interval from 110 nm to 350 nm and a second to provide resolving power of  $10^3$  in the spectral interval from 110 nm to 5000 nm (5  $\mu$ m). (Although the committee did not require sets of instruments to cover these spectral regions, it will become clear that the limitations of diffraction gratings and detectors require that the regions be broken into sub-regions if reasonable transmission efficiencies are to be obtained.) An f/12 Camera was added to the instrument complement for several reasons: the f/12 focal plane is the prime focal plane of the system and is preceded by only three optical surfaces; the plate scale at f/12 would permit a field of view as large as 1.4 mrad which could act as a "discovery field"; and an improvement in detector spatial frequency response by a factor of two to three would make f/12 the matching focal ratio, approximately, for best camera system S/N Ratio.

TABLE 3-1. SUMMARY LST STEERING COMMITTEE RECOMMENDATIONS

Instrument	Resolution	Operating Range	Notes
PRIMARY OBJECTIVES			
I. High Spatial Resolution Camera	Match Telescope Performance	110 to 1,100 nm	Largest Field Consistent with Detector Capability-Selectable Filters
II. High Spectral Resolution Spectrograph	$\frac{\lambda}{\Delta\lambda} = 3 \times 10^4$	110 to 350 nm	Slit Size Adjustable Max 72 x 72 $\mu$ rad
III. Low Spectral Resolution Spectrograph	$\frac{\lambda}{\Delta\lambda} = 10^3$	110 nm to 5 $\mu$ m	Slit Size Adjustable Max 72 x 72 $\mu$ rad
SECONDARY PRIORITY OBJECTIVES			
IV. Very High Spectral Resolution Spectrograph	$\frac{\lambda}{\Delta\lambda} = 3 \times 10^5$	-	P.I. responsibility 2nd generation implementation
V. Polarimeter	-	ultraviolet	P.I. responsibility 2nd generation implementation
VI. Photometer	TBD	-	High time resolution at $\Delta t \approx 1-10 \mu$ sec
VII. Low Spatial Resolution Camera		UV to 3-5 $\mu$ m	Further study required.



The committee made additional recommendations during review sessions as follows:

1. Provide means for compensating for relative shifts between the guidance focal plane and the high resolution camera focal plane; the optical paths to the two systems shall contain as many common elements as possible.
2. Provide a variety of slits for the spectrographs, including slits adequate to separate just resolvable binaries (approximately 250 mrad).
3. Provide a slit jaw camera, or cameras, so that the position of the experiment object in the slit can be verified.

The committee recommendations were entered as inputs to the system analysis program. The result of this study shows that all of the committee recommendations can be accommodated in the reference SIP system. A means of providing compensation for relative shifts between the guidance and the high resolution camera focal plane needs further study. Several techniques such as a compensating coil in the SEC were considered, but most produced more problems than the ones they were endeavoring to eliminate. This reference design limits the relative motion between the guidance and the high resolution camera rather than compensate for it.

### 3.2.2 Technological Inputs

As mentioned in the discussion of the system analysis flow diagram, Figure 3-1, the technological inputs are used to form the assumptions needed to evaluate a candidate instrument design concept. The majority of the technological inputs are concerned with components, such as detectors, diffraction gratings, photocathodes and optical coatings. The other technological input which influences the assumptions is the pressurized maintenance concept. A brief summary of the impact of each of the technological inputs follows in paragraph (a) through (d).

a. Detectors

There is general agreement in both the astronomical and engineering communities that the most practical detector for a long term space experiment is a television camera tube. Photograph film, commonly used in ground based astronomy, is not favored for extended space use because it is difficult:

1. to protect from cosmic radiation for long periods;
2. to retrieve the film from orbit.
3. to carry enough for long term unattended operation.

At the present time the tube which most nearly meets the qualifications for an astronomical detector is the SEC vidicon. The principal characteristics wanted in an astronomical detector are:

1. High quantum efficiency
2. Long integration time
3. Low noise
4. High spatial frequency response
5. Reliability

Secondary desirable characteristics are:

1. Large detector area
2. Low power consumption
3. Light weight
4. Ruggedness

The principal characteristics of the SEC Vidicon tube are:

Quantum efficiency - 5-30% depending on photocathode.

Integration time - 10 hours at 300K, longer with moderate cooling.

Noise - essentially photon noise limited for inputs greater than 100 photoelectrons per TV line (resolution element).

Spatial frequency response - the amplitude vs. frequency plot is approximately a gaussian curve with an amplitude of 1 at a spatial frequency of 0 and an amplitude of 0.5 at a spatial frequency of 20 line pair/millimeter

Although higher performance tubes appear to be theoretically possible, they are not presently under hardware development. A tube which can operate in the photon counting mode could provide a substantial improvement in LST capability, as could higher spatial frequency response. The development of higher performance tubes should be pursued. However, the SEC Vidicon performance, stated above, is used in the parametric studies of the instruments that require a television detector. If an improved tube should become available early enough, the parametric analyses provide the basis for modifying an instrument design. Consideration is given in section 3.8 to the performance improvements which would be gained by simply inserting an improved detector into an instrument designed for the reference tube.

#### b. Diffraction Gratings

The expected performance of diffraction gratings for use in spectrograph design has a significant influence on the particular configuration used to satisfy a given performance requirement. The availability of lasers resulted in the interferometric control of ruling engines. This in turn has greatly improved the performance of gratings particularly in the area of "ghosts" (periodic ruling errors). In addition, interferometric control has made possible the ruling of high quality echelle gratings which can be used in high orders. This development makes it possible to design two grating spectrographs which produce a television raster like display of the spectrum which makes effective use of the rectangular detector area of a TV tube. This type of instrument

is known as a crossed echelle spectrograph or simply echelle spectrograph (see Figure 3-3). In some cases one of the gratings can be replaced by a prism.

Echelle designs are especially useful for resolving powers greater than  $10^4$ . For resolving powers of  $10^3$  and lower, echelle designs are more difficult to implement because they limit the bandwidth achievable in a single instrument. We therefore turn to single grating instruments to meet the requirement for lower resolution. This results in single line formats, shown in Figure 3-4, and the rectangular detector area available in a TV sensor is not required. Therefore, only a few TV lines will be scanned to read the data from the line presentation gratings. For some spectral regions it should be possible to develop line arrays of detector elements which would be more efficient than TV tubes in terms of size, weight and power. Microchannel plates coupled to self-scanned arrays may be one possibility.

Another advantage of interferometrically ruled gratings is that it is possible to predict the efficiency with somewhat better accuracy than previously. When the ruling space is large compared to the wavelength, geometrical optics gives reasonable predictions provided the reflectivity of the grating coating is taken into account.

Geometrical optics (scalar wave equation) predicts a grating efficiency as shown in Figure 3-5. The parameter is not linear in wavelength, necessitating a non-linear scale of  $\lambda$  for first order gratings. For high order gratings ( $n \gg 1$ ) such as echelles, the bandwidth  $\frac{\lambda}{n+1}$  is small so that a linear scale is sufficiently accurate.

#### c. Photocathodes and optical coatings

The third class of technological inputs which strongly influences the system design are the characteristics of available photocathodes which can be used as detector surfaces and the efficiency of optical coatings as a function of wavelength. Various

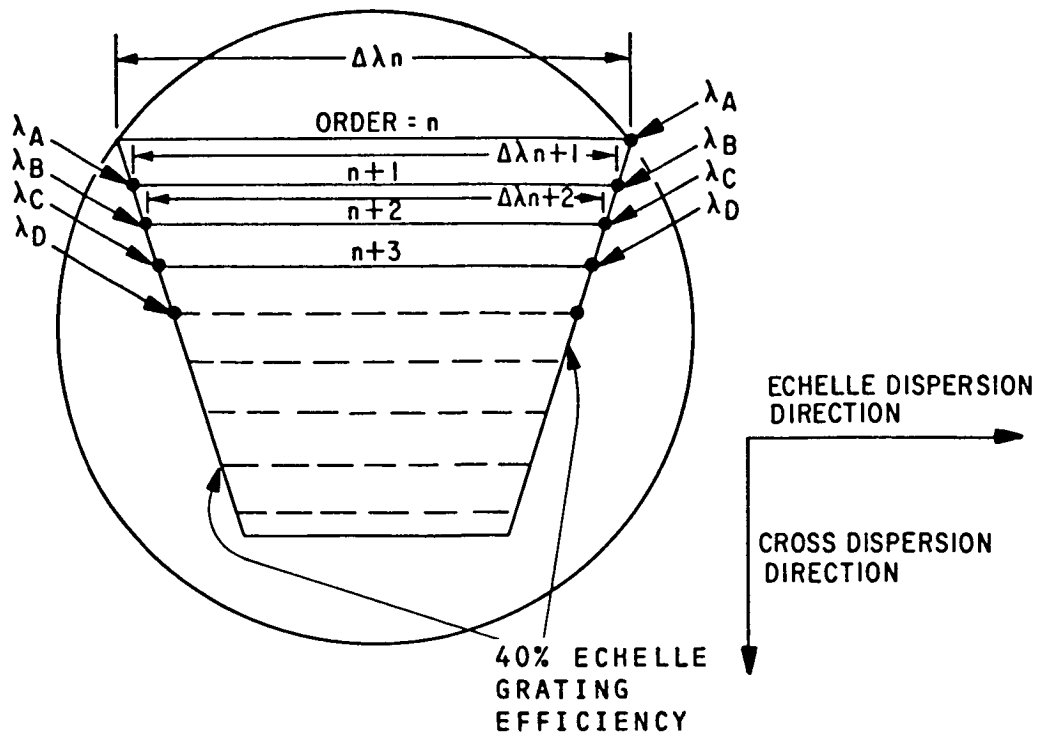


Figure 3-3. Spectrograph Format, Area Presentation (Echelle)

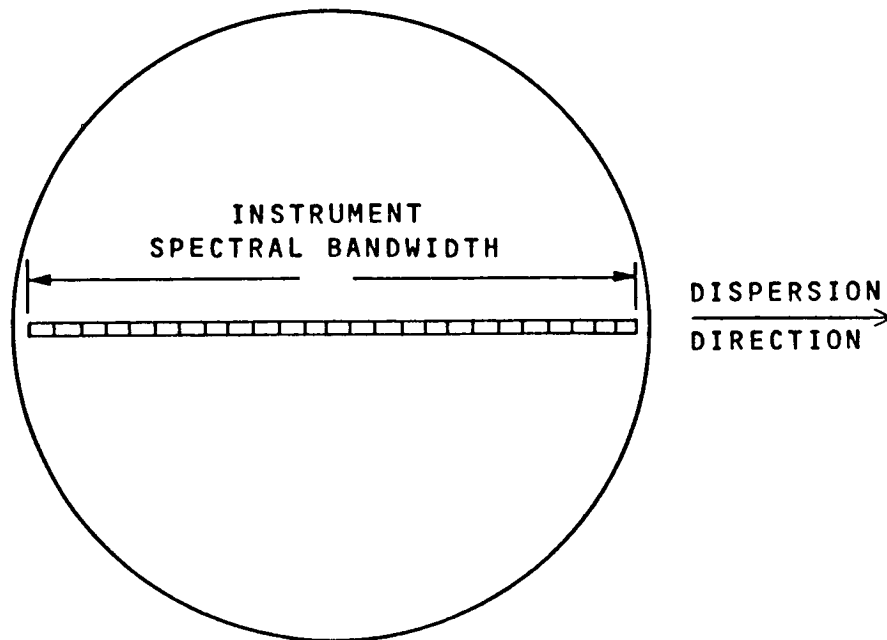


Figure 3-4. Spectrograph Format, Line Presentation

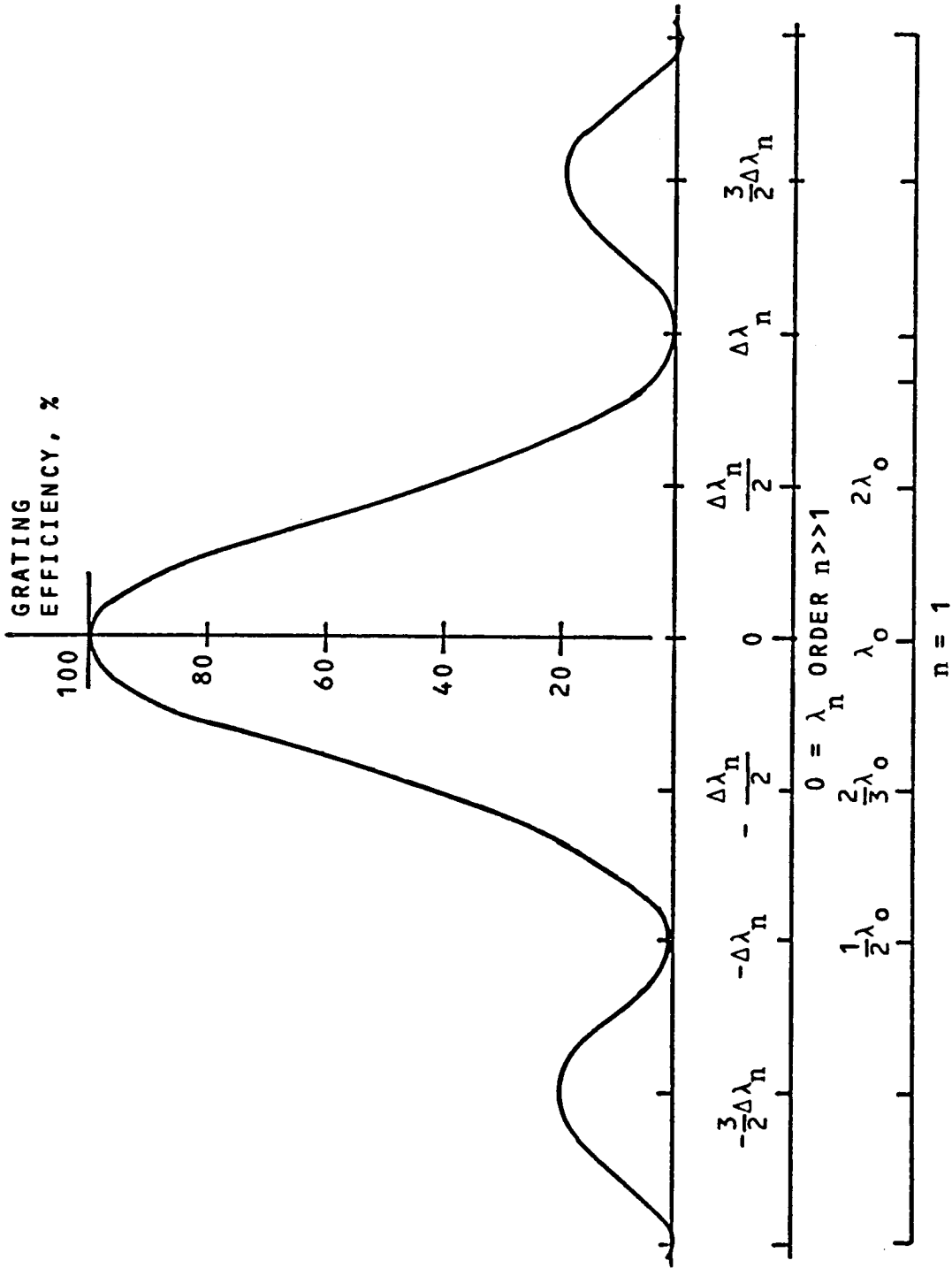


Figure 3-5. Grating Efficiency

combinations of detector photocathodes and optical coatings were evaluated by multiplying their efficiencies point-by-point over the entire spectrum of the instruments. S/N ratio evaluations were performed for star black body temperatures of 70,000K to 1,000K. The photocathode and coatings were chosen using an 11,000K star as a reference. Thus, the coatings and photocathodes used in the reference instruments have been optimized for an 11,000K star, and the selection of materials could change if a different reference star is chosen. Typical throughputs are shown in Figures 3-18, 3-19, 3-20 and 3-21.

#### d. Pressurized Maintenance Concept

A guideline was supplied by MSFC that the instrument package should be optimized from a maintenance point of view, for a "shirt sleeved astronaut" in a pressurized compartment. Accordingly, the SSM can be sealed off from the telescope and pressurized. A hatch at the end of the SSM provides access for the astronaut and provides an opening through which instruments or subassemblies can be removed to the Shuttle. It was also postulated that maintenance activity be limited to three operations so far as the SIP was concerned: removal and replacement of entire instruments; replacement of detector assemblies; or replacement of major electronic subassemblies.

This maintenance concept, along with the optical requirements, guided the placement and arrangement of the instruments within the SIP.

### 3.3 GENERAL INSTRUMENT DESIGN PARAMETERS

#### 3.3.1 Camera Analysis

The design of a field camera involves two relatively independent areas. First, parameter values must be determined which will optimize the performance in the spatial domain and second, the optimum compromise between detector spectral bandwidth and

detector efficiency must be made. Spatial performance has three features of interest: the resolving power, which measures the smallest detectable separation between two point sources; the detectivity, or the faintest object which can be detected; and field of view or the largest sky area which can be seen on one exposure. The dynamic range of the detector is also of interest but is generally a specific characteristic of the detector and not under the control of the system designer. The dynamic range of this system can be extended by multiple exposures.

The concept of resolving power can be generalized to the modulation transfer function (MTF) which specifies the ratio of output to input contrast as a function of spatial frequency. The resolving power of a system is generally taken to be the point on the MTF curve where the contrast transfer falls to 3%. For cascaded independent subsystems the individual MTF's may be multiplied together point by point to get the system MTF. An example of this procedure is shown in Figure 3-6, which shows individual and combined MTF's for a SEC Vidicon and three meter telescope with an f/96 focal plane. Telescope performance is shown at two wavelengths. The pointing error characteristics of the telescope can also be presented as an MTF and combined with the telescope and detector MTF's to get a system MTF. The MTF taken with signal to noise ratio (SNR) calculation permit prediction of overall performance.

To maximize the camera resolving power, we must first require that the pointing error is small compared with the telescope image size. This makes the pointing MTF much wider than the telescope MTF so that the product of the two is essentially the same as the telescope MTF alone. Since high accuracy pointing is expensive, the pointing requirement should not be tightened beyond the point where significant improvement is obtained. The resolving power is also maximized by increasing the F number. This broadens the spatial frequency response, as shown in Figure 3-6. But increasing



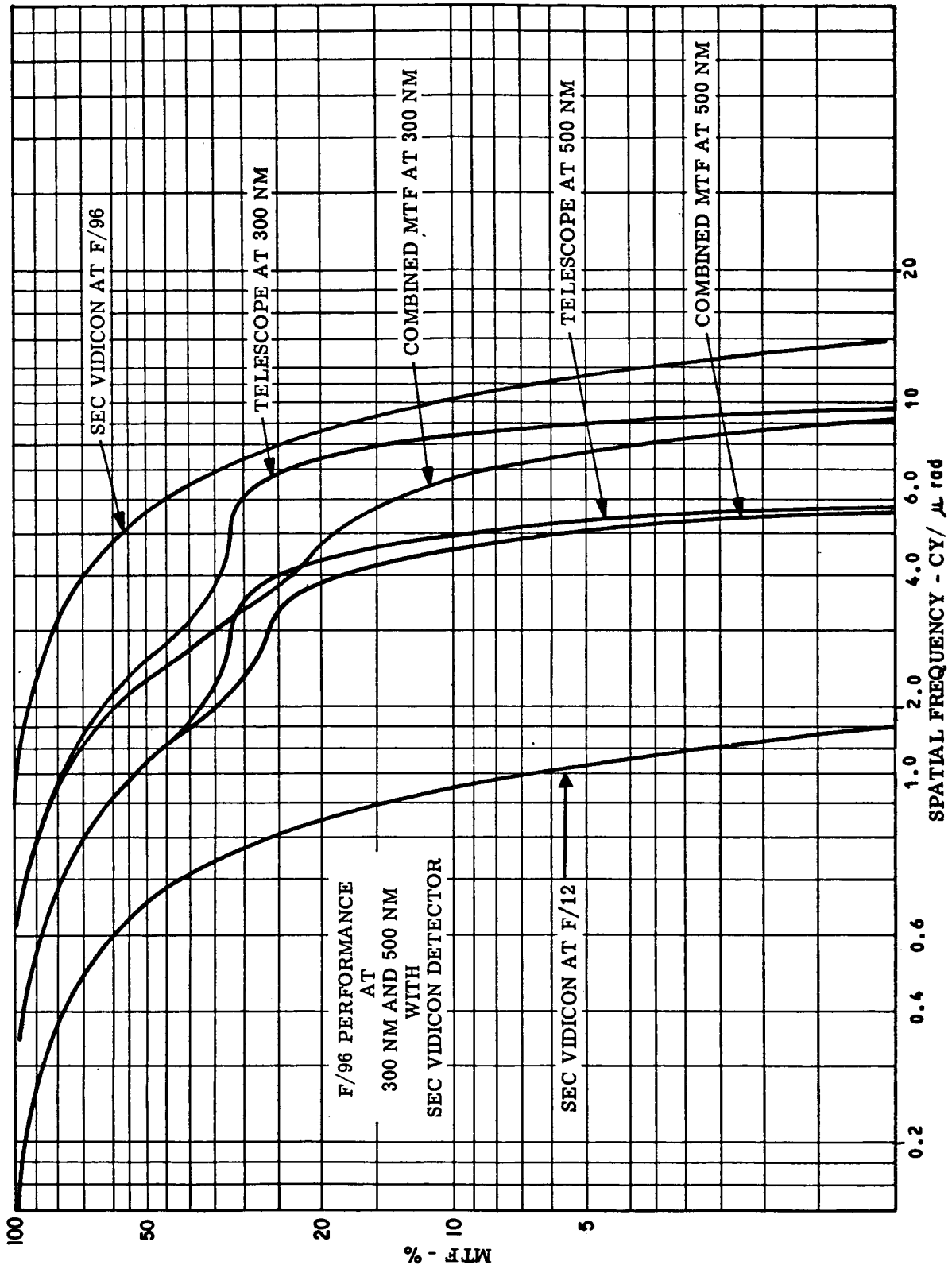


Figure 3-6. Camera Performance at 300 nm and 500 nm With SEC Vidicon Detector

the F number tends to decrease the S/N ratio and adds to instrument length, so that the F number should not be increased beyond the point where reasonable improvement in resolution is obtained. The details of the analysis are in Section 3.4.1. The F number chosen is f/96, and the pointing accuracy is 25 nanoradians.

Optimizing for the best detectivity requires the S/N ratio be maximized. This is achieved by matching the detector MTF to the combined pointing and telescope MTF. Physically, the image size on the sensor surface is made equal to a line pair. For a 20 l.p/mm detector this corresponds to an f number of 30 to 40. For the SIP three options are possible. The first involves changing the scan of the sensor in the f/96 camera so that a line pair corresponds to the image, or approximately 150 x 150 micrometers. The second is to use the f/12 camera with an electronic zoom, so that an effective f number of 30-40 is achieved. The third method would be to add an optical magnifier of 3 to the instrument complement. At this writing, the first method is the most likely candidate for a 1980 launch date.

Selecting photocathodes for the camera system involves trading off spectral bandwidth with quantum efficiency and background to get good performance with a small number of detectors. The trade-off technique involves plotting the overall throughput of various photocathodes taking into account all the preceding optical surfaces and their coatings. This trade-off is shown in Section 3.4.1.

### 3.3.2 Spectrograph Analysis

Spectrographs are designed to achieve a specified resolving power over a given bandwidth. The measure of the effectiveness of a given design is related to the instrument efficiency and throughput

over the spectral range, the number of spectral elements which are measured simultaneously, the tolerance allowed for image motion and growth and the method of measuring the background for the purpose of cancelling it. The variables under control of the designer are the spectrograph types, size (within limits), the angular dispersion, and the linear dispersion. The input f/no. and the choice of detector characteristics are not under control of the designer. As a matter of fact, the detector is a major "driver" of the design and determines the linear dispersion required. Another driver is the grating efficiency which limits the wavelength ratio to about 1.7 for an echelle and to less than 3 for a single grating system. This bandwidth limitation is the reason that echelle systems are not attractive for low resolution requirements. Both the high dispersion and the small bandwidths are undesirable. These bandwidth limitations, which are usually more stringent than the detector bandwidth limitations require that the desired spectral coverage be broken up into intervals which meet the wavelength ratio restrictions, and which also fit within the photocathode pass-band.

After the wavelength ranges have been optimized, parametric studies determine the remaining variables by selecting from the family of solutions, the one which maximizes overall tolerance for the instrument. The results of a typical study of this type are shown in Figure 4-10 and show that a compact system has greater tolerance than a larger one for this case. The allowable error derived here must then be apportioned among the system elements by determining the image growth sensitivity of the various component errors such as tilt, figure, focus and decentering.

A discussion of the various design choices is contained in sections 3.4, 3.5, 3.6 and 4.

### 3.4 INSTRUMENT DESIGN PARAMETERS

#### 3.4.1 High Resolution Camera

Studies were made to determine the desired parameters and the performance of the High Resolution Camera, and the sensitivity of instrument performance to variation in parameters. These studies include the number and size of the sensors, influence of pointing and f number, and the resolution and S/N ratio achievable.

Throughput studies indicate that at least two sensors (SEC Vidicons) are necessary to cover the wavelength range from 110 to 1000 nm. If three vidicon tubes are used, the efficiency in the far UV is almost doubled and the narrower spectral range associated with each sensor tube reduces the background noise, improving the S/N ratio. Configuration studies showed that the three tubes could be packaged within the available space, and this design was adopted for the High Resolution Camera. Computerized studies were made to determine the optimum optical coatings. Details of this study are in subsection 3.6.

The f/number is determined in two ways. The first considers that a tube line pair corresponds to 50 micrometers. If two images of equal intensity, each containing 73% of their energy in two Airy disc radii, are separated by 1.45 Airy radii, the sensor readout beam contrast is 20%. Assuming this contrast is sufficient, the 1.45 Airy radii separation corresponds to 174 nrad at 300 nm. To separate the two images by 174 nrad and a line pair (50  $\mu\text{m}$ ), a focal length of  $f = \frac{S}{\theta} = \frac{50 \times 10^{-6} \text{ m}}{174 \times 10^{-9} \text{ rad}}$ , or 288 meters is required. For a three meter telescope diameter, the resulting f/number is f/96.

The second method involved a parametric study of resolvable element size versus pointing accuracy, for various values of f number. The assumptions used in the analysis, and the mathematics involved are shown in Appendix A. A partial result of the study is shown in Figure 3-7. F numbers above f/96 are not shown, because they are close to the f/96 curve.

As a result of both studies, the f/number chosen for the high resolution camera is f/96.

$\lambda = 300 \text{ nm}$   
 APERTURE = 3 METERS  
 OBSCURATION 30%  
 WFE =  $0.1\lambda$   
 DETECTOR MTF = 50% @ 20 L.P./mm  
 1 AIRY DISC = 120 nrad RADIUS

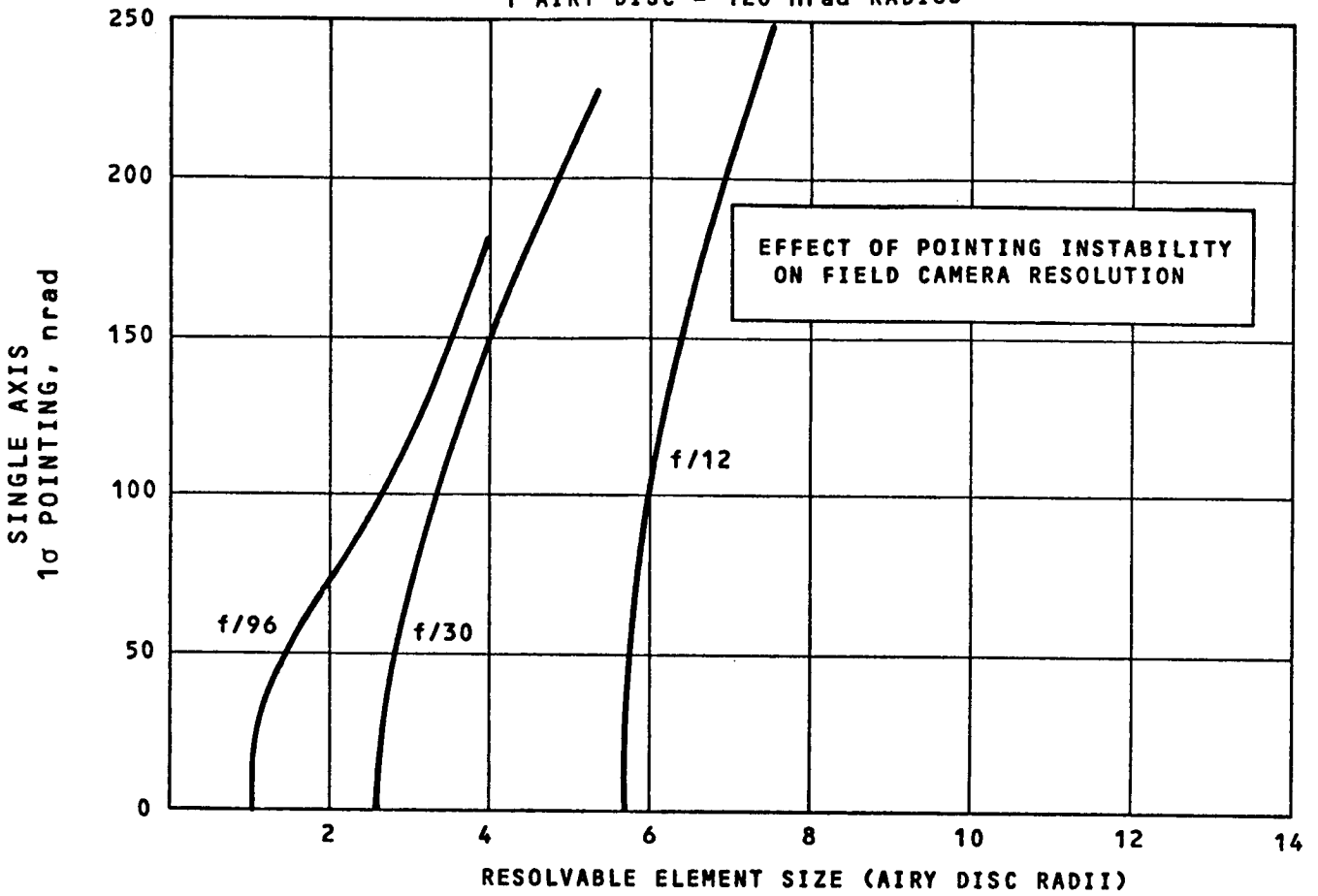


Figure 3-7. Effect of Pointing Instability on Field Camera Resolution

An examination of Figure 3-7 for an f/number of 96 leads to the choice of desired pointing stabilization error. The knee of the curve occurs at 25 nanoradians. Smaller stabilization errors result in a very limited improvement in overall performance, since a 13% decrease in resolvable image size results if the pointing stabilization error decreases from 25 nanoradians to zero. Stabilization errors above 25 nrad degrade overall performance. In addition, allowance must be made for degradations resulting from mechanism errors, thermal shifts, etc. Therefore, the pointing stabilization error is assumed to be 25 nrad,  $1\sigma$ . An error of 31 nrad (section 3.5.1) budgeted to all internal error sources, yields in an "Equivalent Pointing Error" of 40 nrad,  $1\sigma$ . The resulting resolvable element size is 1.3 Airy disc radii, compared to a perfect system with a resolution of 1.0 Airy disc radius. Further application of this analysis is shown in sub-section 3.5 where the effect of increased image size is given.

The High Resolution Camera was analyzed to determine its "limiting magnitude". Unfortunately, it is difficult to arrive at a single number to characterize the "limiting magnitude", because magnitude varies with the type of star chosen as a target, the S/N ratio taken as the criteria of recognition, the spectral range of interest and the exposure time consumed in gathering information. The S/N ratio obtained during various exposures, for an 11,000K star, and for various magnitudes is shown in Figure 4-7. If a ten hour exposure and a S/N of two are chosen as criteria, the "limiting magnitude" is approximately 32 for spectral ranges I and II.

The astronomy Committee has requested that the cameras possess the largest field of view possible consistent with f/number, therefore, the SEC Vidicon with a 50 x 50 mm cathode is chosen for both field camera applications.

### 3.4.2 Wide Field Camera

One SEC Vidicon is used for this wide angle application, though the use of more sensors would improve the performance as it does for the High Resolution Camera. Two or more tubes, however, would require the addition of a mechanism for selecting the desired sensor. Also, the Wide Field Camera is located in the same area as instruments of much high priority, and two or more tubes would consume additional space, impacting on the design of the higher priority instruments.

The f/number was chosen as 12 to provide the widest field of view possible at the prime focus, and to allow for future improvements in sensor technology. If the tube resolution goes from the present 20 l.p./mm to 60 l.p./mm, an f/12 camera will achieve the maximum S/N ratio.

As in the High Resolution Camera, the 50 mm SEC Vidicon tube is used to provide the largest field of view available at this time.

### 3.4.3 High Resolution Spectrograph

It is desirable to consume the least possible time to view an object, to eliminate mechanisms which must move during an observation, and to obtain the high dispersion needed to meet the resolution requirement. The detector is a TV type integrating tube. For these conditions, the Echelle spectrograph is a better choice than either a scanning or line presentation spectrograph. It is capable of high dispersion, has no parts which move during an observation, and presents the information in an area format, utilizing the area of the tube to the fullest.

The theoretical efficiency of a reflecting grating is a function of the wavelength ratio as shown in Figure 3-5, page 3-13. To achieve a good efficiency over the 110 to 350 nm range, two cross disperser gratings are incorporated in the design.

Two sensor tubes are used to obtain a high efficiency, particularly in the far UV, and to improve the S/N ratio by additional filtering of the background.

Two separate instruments are chosen for the High Resolution spectrograph. Since there is a need for two cross dispersers and two tubes, the use of two separate instruments does away with the requirement for a grating select mechanism for the cross disperser. It also permits the use of two Echelle gratings. If one Echelle and two cross dispersers are used, the width of the format of the low wavelength grating would be shortened to  $\lambda_L/\lambda_H$  times the width of the long wavelength grating, where  $\lambda_L$  and  $\lambda_H$  are the longest wavelengths associated with the short and long wavelength gratings, respectively. Thus, the use of two instruments permits more efficient usage of the sensor area.

The use of two instruments does call for some mechanism to select between them, seemingly negating the advantage of eliminating the cross disperser selector mechanism. But there are several instruments in the aft section of the SIP, and a common mechanism is needed to select the desired instruments. Therefore, the collimator mirrors for both instruments of the High Resolution spectrograph have been incorporated in the Aft Spectrograph Selector Mechanism.

The design parameters for the spectrographs are obtained by assuming that the telescope image conforms to Figure 3-9, page 3-27. As mentioned in Appendix A, the final image is close to Gaussian. Therefore, the spectrographs were designed such that the  $2\sigma$  (70% of encircled energy) diameter of the total image, including the effects of the telescope image and degradations in the spectrograph, is 50  $\mu\text{m}$ . The justification for this procedure follows. The detector MTF ( $A_d(w)$ ) is close to Gaussian. For a Gaussian MTF with a 50% response at 20 line pair/millimeter, the point spread function is a Gaussian with  $2\sigma$  equal to 18.6  $\mu\text{m}$ . The total



point spread function is then  $\sqrt{(25)^2 + (18.6)^2}$  or 31  $\mu\text{m}$ . If two Gaussian point spread functions with a  $2\sigma$  value of 31  $\mu\text{m}$  are separated by 50  $\mu\text{m}$ , the contrast ratio, (MAX-MIN)/MAX, is 0.5. Thus, if we wish to resolve two wavelengths of the spectrograph that are separated by a  $\Delta X$  of 50  $\mu\text{m}$  at its photocathode, a S/N ratio of two or greater is required.

Parametric studies are then made of allowable spectrograph component angular tolerances, as a function of effective focal length and grating size, which will limit the  $2\sigma$  diameter point spread to 50  $\mu\text{m}$ .

The results of the study (see Figure 4-11) show that an f/10 system is the optimum. Layout studies further show that the f/10 system can be packaged in the allotted space and therefore, this system is incorporated in the present design.

Throughput studies were made to determine the best choice of materials for this instrument. The details of the study and the materials chosen for cathodes and coatings are in subsections 3.6 and 4.3.

Figure 3-8 is also a result of a parametric study and it demonstrates the relative insensitivity of the spectrometer resolution to changes in telescope image size. For instance, a 100% increase in telescope image size results in approximately 10% loss in spectral resolution. The rationale for the study follows:

Assuming no reduction in image size is obtained for wavelengths less than 350 nm in the worst case, 70% of the telescope image's energy is contained in a diameter of 0.44  $\mu\text{rad}$ . Assuming that the tolerance of a total blur of 50  $\mu\text{m}$  (minimum resolvable distance) or 1.67  $\mu\text{rad}$  is met, the tolerance for the spectrograph is  $\sqrt{(1.67)^2 - (0.44)^2}$  or 1.60  $\mu\text{rad}$ . If the image diameter is 1.60  $\mu\text{rad}$ , the total image diameter will be  $I_{\text{TOT}} = \sqrt{(1.6)^2 + I_{\text{TEL}}^2}$  where  $I_{\text{TEL}}$  is the effective telescope image. The spectral resolution  $\frac{\lambda}{\Delta\lambda}$  of the telescope is related to the total image diameter by the dispersion,  $\frac{d\lambda}{d\theta}$ , of the spectrograph. Therefore, growth in the

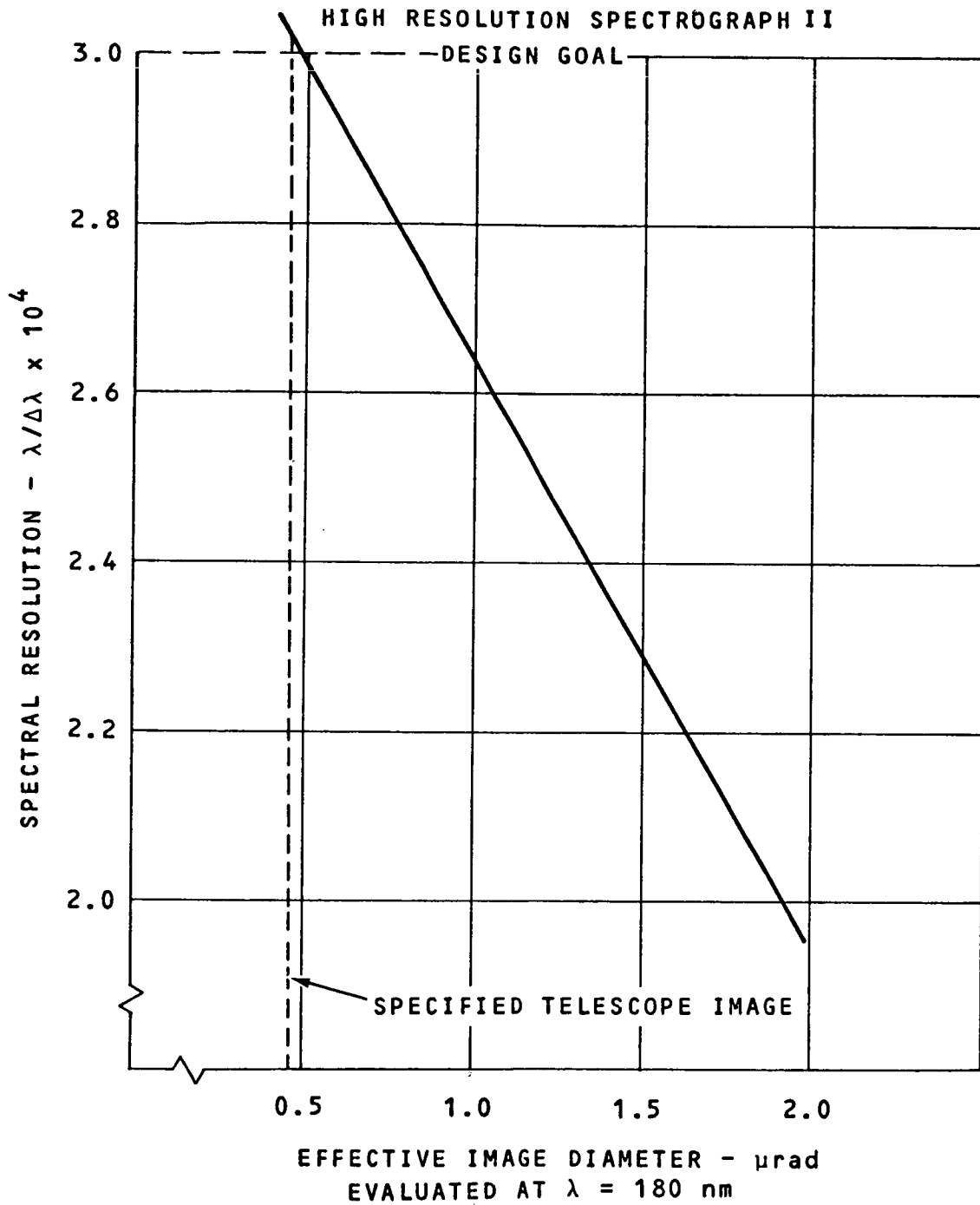


Figure 3-8. Effect of Telescope Image on Spectral Resolution

"effective telescope image", which is obtained when pointing instability or other factors appear to increase the optical image size, has a second order effect on the Spectrometer's resolution, again as shown in Figure 3-8.

A study was made of S/N ratio as a function of star magnitude, using exposure time and slit width as parameters. The details are in Section 4.3; the results are shown in Figure 4-23 and 4-24. If a 10 hour exposure time and a S/N of 2 are taken as criteria, the "limiting magnitudes" of the High Resolution Spectrograph are 16 (Range 1) and 18 (Range 2).

An increase of telescope image beyond the size of the entrance slit does not effect the instrument's spectral resolution. However, the resulting reduction in energy passed through the slit to the detector causes a reduction in the signal-to-noise ratio with consequently reduced data quality.

This will be illustrated by an example: consider the High Resolution Spectrograph in Range I, operating with a slit width  $w_1 = 0.25 \mu\text{rad}$ , at a target magnitude  $m = 10.6$  and a wavelength  $\lambda = 180 \text{ nm}$ . For these conditions, subsection 4.3 predicts a  $S/N = 10$  after an integration time of  $t = 10^3 \text{ s}$ .

An Airy disc radius  $\delta = 1.22\lambda/D = 122 \text{ nrad}$  for  $\lambda = 300 \text{ nm}$ . The specified telescope image,  $R_1$  is 1.5 Airy discs or 183 nrad. For the case of a half slit width of  $(w_1/2) = 125 \text{ nrad}$ , the equivalent slit-to-image ratio is 125/183 or 0.66 Airy discs radii. Figure 3-9 shows the enslitted energy,  $E_{in}$ , for this case to be 0.6. If we define  $\Delta R = (R_2 - R_1)/R_1$  as the growth in image size, the value of  $E_{in}$  for  $\Delta R = 0$  is 0.6. Similar energy values may be derived from Figure 3-9 for other values of  $\Delta R$ , and used to calculate the S/N ratio. Figure 3-10 shows the S/N change with image growth. It is assumed that a signal noise limited condition exists, and that the S/N ratio varies as the  $\sqrt{S}$ .

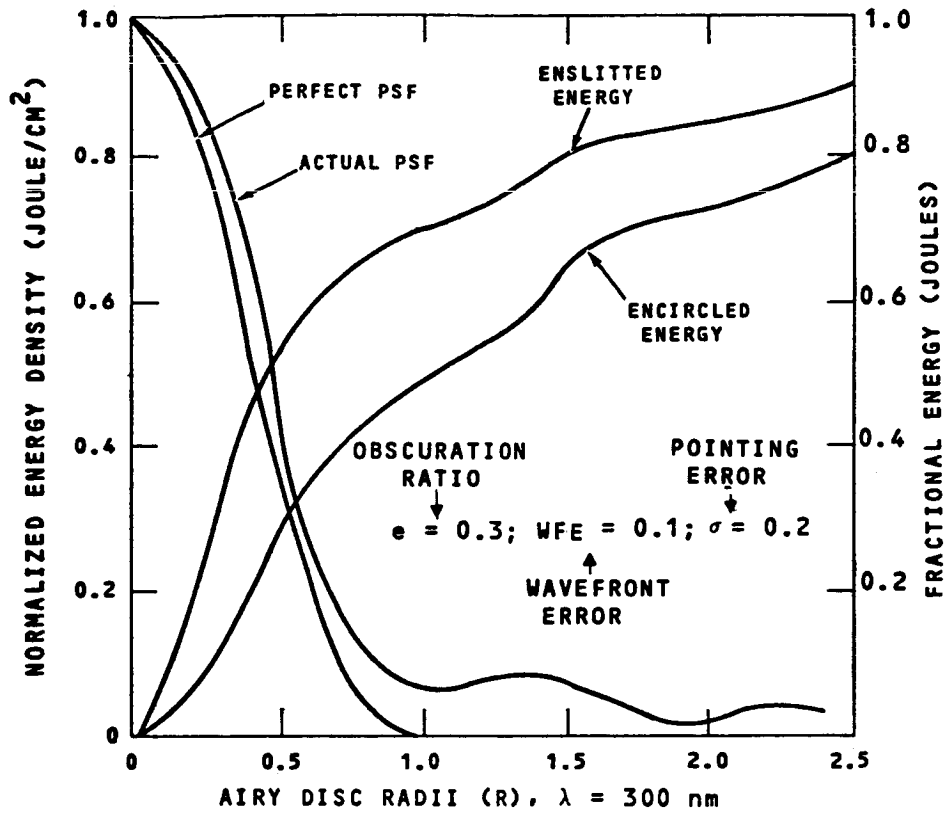


Figure 3-9. Relative Energy as a Function of Aperture Size

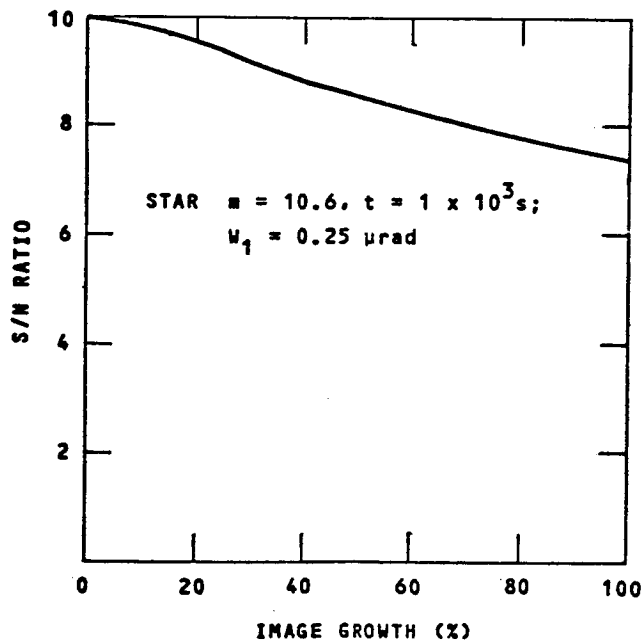


Figure 3-10. S/N as a Function of Image Size

#### 3.4.4 Faint Object Spectrograph

The purpose of this spectrograph is to analyze very faint celestial objects. This instrument provides a much wider operating spectral range than the High Resolution Spectrograph - 115 to 1000 nm. Therefore, its efficiency should be the maximum possible over its operating range. From Figure 3-5, it is apparent that to keep the efficiency above an assumed value of 0.8, the wavelength range of a grating must not exceed a ratio of 1.67 to cover the 9 to 1 ( $\frac{1000 \text{ n.m.}}{110 \text{ n.m.}}$ ) range of the faint object spectrographs. Therefore  $1.67^N \geq 9$ , or  $N \geq 5$ . Five gratings and their associated wavelength ranges are used in the design. The values of the ranges are based on the throughput of the coatings used on surfaces, the efficiencies of the cathodes employed, and the desire to keep the wavelength ratio below 1.67. The details are in subsection 4.4.

A line presentation type grating is used for this application because it meets the resolution requirement of  $10^3$ , and has a higher efficiency than the Echelle. To cover the range from 110 to 220 nanometers, one tube, two gratings and a grating select mechanism are employed. (The presently available long-lived sensor window material limits measurement quality at wavelengths lower than 120 nm.) In the range of 220 to 660 nm, it is possible to utilize a dichroic to separate the spectra. The dichroic directs the energy to the two gratings, saving a mechanism. One tube may be used over this range. The final range of 660 to 1000 nanometers is obtained from one grating and one sensor.

Parametric studies of S/N ratio, similar to the studies of the High Resolution Spectrograph (Figure 4-29) indicate that f/10 is the optimum for this application. A study of the figure indicates that the choice of f-number is not critical, and that a change of f number from 9 to 12 would have only a minor effect on the image growth tolerance. It should also be kept in mind (see Section 3.1) that this "optimum" f-number is based upon certain assumptions, and

that a significant change in these assumptions could change not only the optimum f number but the number of gratings used in the faint object spectrograph design. For the range of 110 to 220 nanometers, an f/9 system is employed because the length of an f/10 system is in conflict with the space allotted. For the range of 660 to 1000 nanometers, the f/number of 12 is selected to allow some of the light beams to clear surfaces. In either case, the effect on the allowable component tolerances is small, as shown in subsection 4.4.

Throughput studies are made to determine the optimum cathode materials, coatings, etc. The details are in subsection 3.6. Parametric S/N studies are made for all ranges of the Faint Object Spectrographs, for various slit widths, integration times, and for a 11,000K star and are given in detail in subsection 4.4. Table 1-4 shows the "limiting magnitudes" of the Faint Object Spectrograph, if a 10 hour exposure time and a S/N of 2 are taken as criteria.

The curve of Figure 3-11 provides the relationship of resolution to image size and demonstrates the relative insensitivity of the Faint Object Spectrograph's spectral resolution to changes in the "effective telescope image" size: a 100% increase in telescope image size causes only a 15% loss in spectral resolution.

#### 3.4.5 Mid I-R (Fourier) Interferometer

This instrument provides spectral data in the mid infra-red wavelength range of 1 to 5  $\mu\text{m}$ . It is chosen in preference to a grating system mainly because an IR TV type sensor is not presently available. Further, if scan type gratings were used, three such gratings would be necessary to cover the 5-to-1 wavelength range. This would result in a much greater volume occupied and additional complexity from grating mechanisms compared to the Fourier Interferometer. The design and operation of this instrument are explained in subsection 4.5.

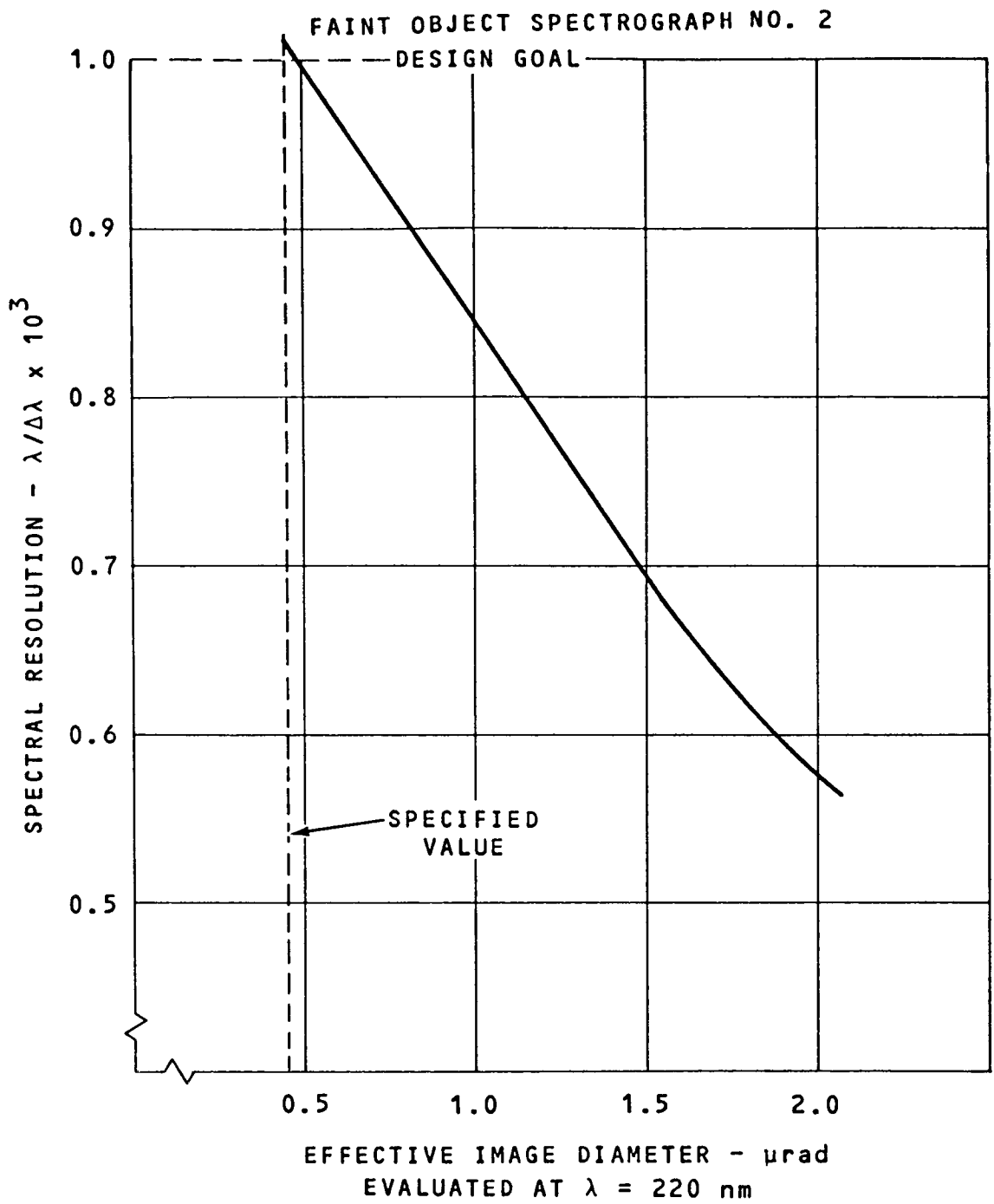


Figure 3-11. Effect of Telescope Image on Spectral Resolution

## 3.5 ERROR BUDGETS

### 3.5.1 High Resolution Camera

The errors in the system are broken into two main sections for the purposes of interface definition: (1) telescope errors and (2) instrument errors. The system error budget is based upon the notion of apportioning tolerances such that the camera performance comes as close to diffraction limited as possible without placing undue strain on any subsystem. The method chosen is to use the curves of Figure 3-7, page 3-20, as a guide in initially setting the specifications for the various subsystems. The subsystems are then investigated to determine the components and tolerances required to meet the specifications. Where necessary, the initial specifications are revised to reflect what the subsystems are capable of achieving. This process, and some conclusions, are discussed in more detail in the paragraphs which follow.

Other than optical and pointing errors, the errors in the system tend to be small or randomly distributed. This is due to the fact that they are caused primarily by thermal changes, which do not take place in a matter of minutes. Over a short time then, the thermal change, which should cycle periodically with orbit, has a small effect. Over the long exposures of many orbits, the errors will tend to fluctuate randomly within a given bound. When apportioning tolerances for an error budget, the bounds of operation must be specified. Therefore the other system errors may be treated as equivalent pointing errors which are root sum squared with the pointing error.

If the instrument were perfect, the effect of the  $0.1\lambda$  wavefront error of the telescope optics and 25 nanoradian pointing instability would be a resolvable element size of 1.13 Airy Disc



radii (138 nrad) as shown in Figure 3-7. If the degradation of the instrument itself is such that it produces the effect of total equivalent pointing error of 40 nanoradians, the resolvable image size would be 1.33 Airy disc radii or 160 nrad. The error budget is computed as follows:

$$\begin{aligned} \text{The instrument error} &= \sqrt{(40)^2 - (25)^2} \\ &= 31 \text{ nanoradians} \end{aligned}$$

This must be divided between the 8X multiplier, the structure, and the selector mechanism within the camera. If each of them contributes an equal amount, then each may have an error of  $31/\sqrt{3}$  or 18 nanoradians.

Therefore, the target goals are set at 25 nanoradians-1 $\sigma$  for the telescope pointing, and 31 nanoradians-1 $\sigma$  for the instrument. Neither specification is easily met, and more detailed investigations on the subsystem levels are required. A change in the performance of one subsystem could effect the specifications placed on the other. As an example, if the structural and thermal phenomena preclude an instrument error of less than 50 nanoradians, then the specification for the pointing would be loosened unless it was apparent that 25 nanoradians-1 $\sigma$  pointing is easily achievable. The reason for this is that the total error would then be  $\sqrt{50^2 + 25^2}$  or 55 nanoradians. To allot 50 out of 55 nanoradians to the instrument is unrealistic. Under this condition, if the pointing error were specified as 40 nanoradians, the total error would be 64 nanoradians, or an increase of 30% over the instrument error, and the resolvable image size is 1.83 Airy discs.

From the above example, it is seen that the system error budget must be constantly monitored to reflect changes in the state of the art and information pertaining to the desired use of the instrument by the astronomers. It is our opinion that further tradeoff studies in this area would be most useful to both the engineering and scientific community.

In line with this thinking, the question may be asked, "What happens if the image size is different than the specified value?" Theoretically, to get an exact answer, it would be necessary to take the Fourier transform of the out-of-specification image point spread function and determine the new image MTF. This MTF would then be used in the analysis procedure outlined in Appendix A to determine the resolvable image size vs. pointing curve. Since this is not a practical approach at this time, an alternate method has been chosen.

It is assumed that the image degradation, whether in the telescope or SIP section, is due to unpredictable phenomena, resulting in random errors. Therefore, increases in image size may be treated as "equivalent pointing errors", and room sum squared with the true pointing error. For example, if the image grows by 50 nanoradians on a diameter, the total "equivalent pointing error" is  $\sqrt{(25)^2 + (40)^2}$  or 47 nanoradians, and the resolvable image size from Figure 3-7 is 1.4 Airy disc. Figure 3-12 is a plot of resolvable element size vs. angular image increase beyond the budgeted 1.33 Airy radius (160 nrad). Further, the effect of image increase is the same irrespective of cause (optics, control system, environmental, etc.).

### 3.5.2 Wide Field Camera

The rationale for this camera is the same as for the High Resolution Camera. Assuming that the resolvable element size is to be no greater than 7 Airy disc radii (840 nrad), the total equivalent pointing error is 200 nrad. If this is divided equally between the telescope and instrument, it results in a 140 nrad tolerance for each. There is no optical multiplier or selector mechanism in the Wide Field Camera, therefore the 140 nanoradian tolerance may be divided among the optics and structure.

### 3.5.3 High Resolution Spectrograph

During the slit mode of operation, a 250 nrad slit is placed around the image. The Itek telescope design indicated that a

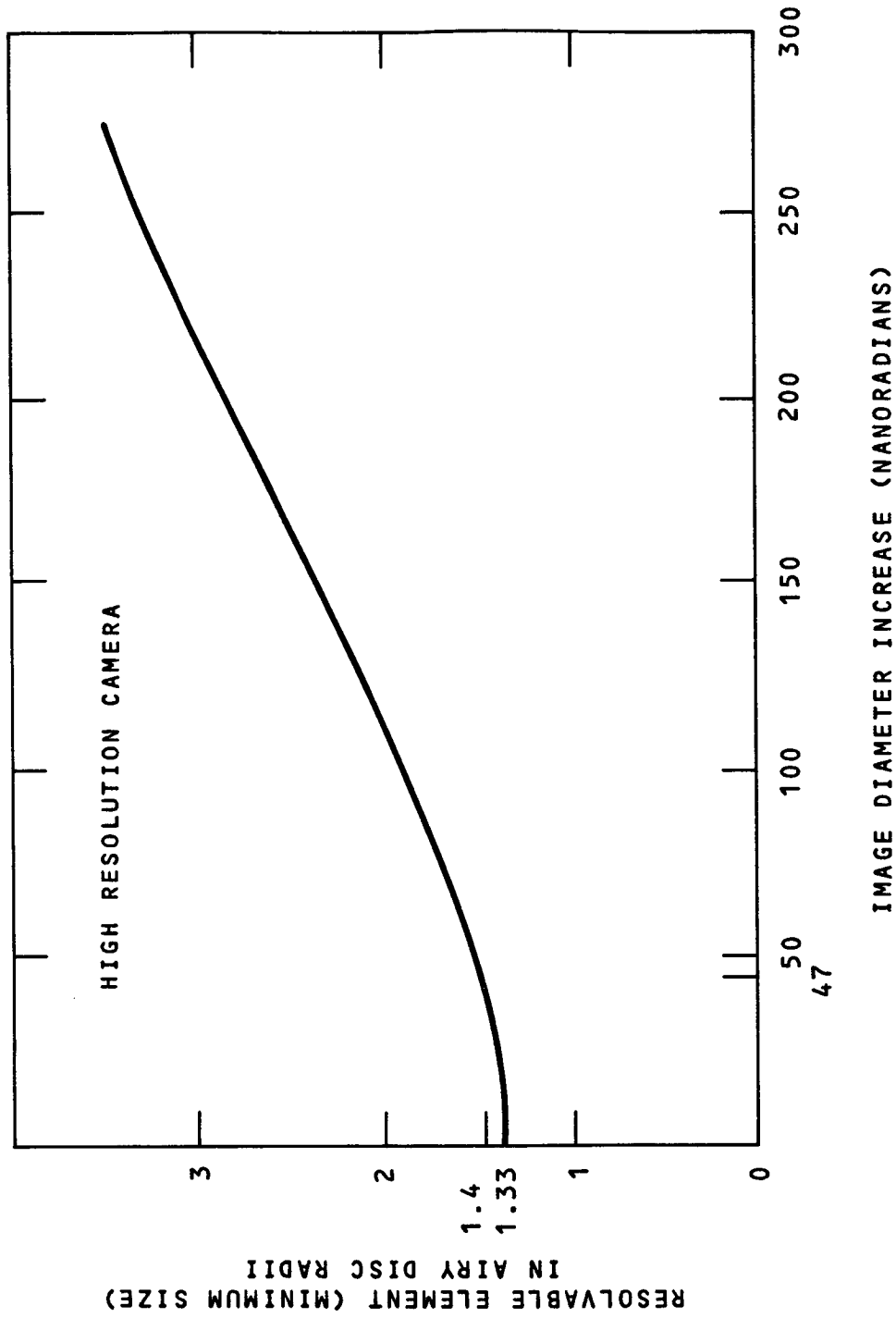


Figure 3-12. Effect of Image Size Increase on Resolvable Element Size

telescope with a  $0.1\lambda$  WFE error and 25 nanoradians pointing stability is feasible, and would have 50% of its energy within one Airy disc diameter (240 nrad at 300 nm). This performance is sufficient for use with the 240 nanoradian slit, and has been chosen as the performance criteria for the High Resolution Spectrograph.

The spectrograph errors were allotted such that 73% of a slitless telescope image would remain within the bounds of 50 micrometers. Further breakdowns of the errors within the High Resolution Spectrograph will be found in subsection 4.3.

#### 3.5.4 Faint Object Spectrographs

The considerations for error budgeting the Faint Object Spectrographs are identical to those of the High Resolution Spectrographs, and the error budgets for the telescope and instrument were made the same as for the High Resolution Spectrographs. The detailed error budgets for the Faint Object Spectrographs are found in subsection 4.4.

### 3.6 THROUGHPUT ANALYSIS

One of the evaluation parameters of individual SIP instruments is the spectral throughput.

This computation derives the photocathode output photo-electron density, using as an input to the telescope a zero magnitude star at various color temperatures. Optical and electrical efficiencies of all intermediate components in the path of individual instruments are applied and outputs are plotted in terms of electron density per unit time for each of the instruments. Tradeoffs between the most promising sensors are made.

For this computation the telescope (OTA) primary diameter  $d = 3$  m and obscuration ratio  $\epsilon = 0.30$  are used. The OTA primary and secondary mirror coatings and all SIP optical surfaces, used down to the present tentative limiting wavelength of 115 nm (dictated by the photodetector window -  $\text{MgF}_2$ ), were optimized based on Haas<sup>(1)</sup> (2). For normal incidence, a fresh aluminum layer thickness,  $t_{al} = 65 \pm 2$  nm, is overcoated with a magnesium fluoride,  $t_{m1} = 25 \pm 1$  nm. The two coatings, successively applied in vacuum prevent losses due to aluminum oxidation, making the transmission loss negligible. The graph of Figure 3-13 is used for better appreciation of the overall optical reflection efficiency as a function of the number of identical surfaces (Haas-1).

A second type of UV-coating (Haas-2) is used in the computation for surfaces operating above 180 nm. This one is aluminum  $t_{a2} = 55 \pm 2$  nm and  $\text{MgF}_2$ ,  $t_{m2} = 45 \pm 2$  nm. Comparison of the two Haas coatings is shown in Figure 3-14 for a typical SIP instrument.

The SIP reflective optical surfaces which operate in the near- and mid-IR range are assumed to have an optimized silver coating shown in Figure 3-15.

---

(1) G. Haas, J.E. Waylonis JOSA 51, 719 (1961)

(2) A.P. Bradford, G. Haas, J.F. Osantowski, A.R. Taft: Preparation of Mirror Coatings for the Vacuum U.V. Appl. Optics 8.6 p. 1183 (1969)

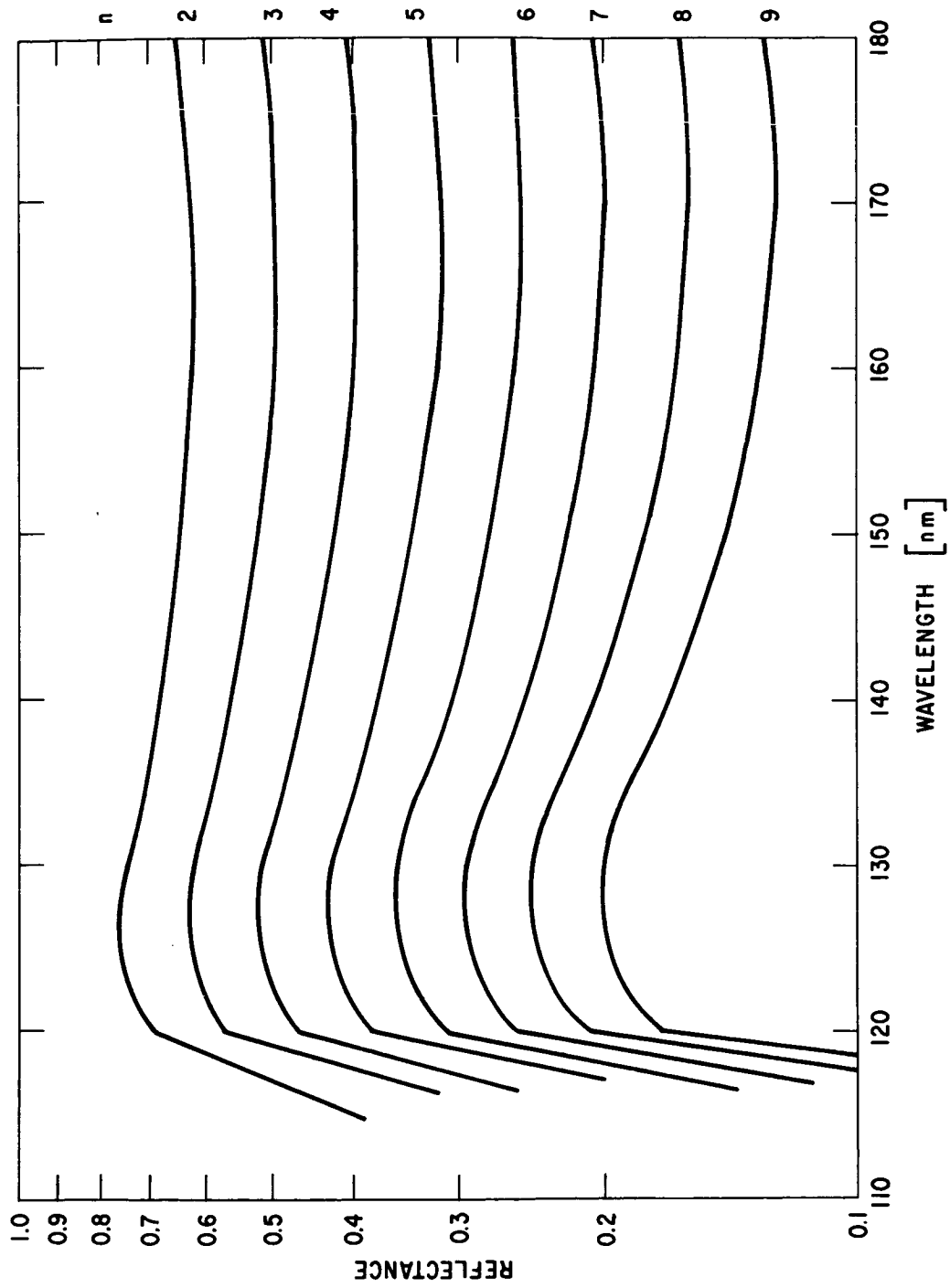


Figure 3-13. Spectral Reflectance of Haas-1 Coating  $R=f(n)$   
 [with  $n$  = number of reflective surfaces/normal incidence]

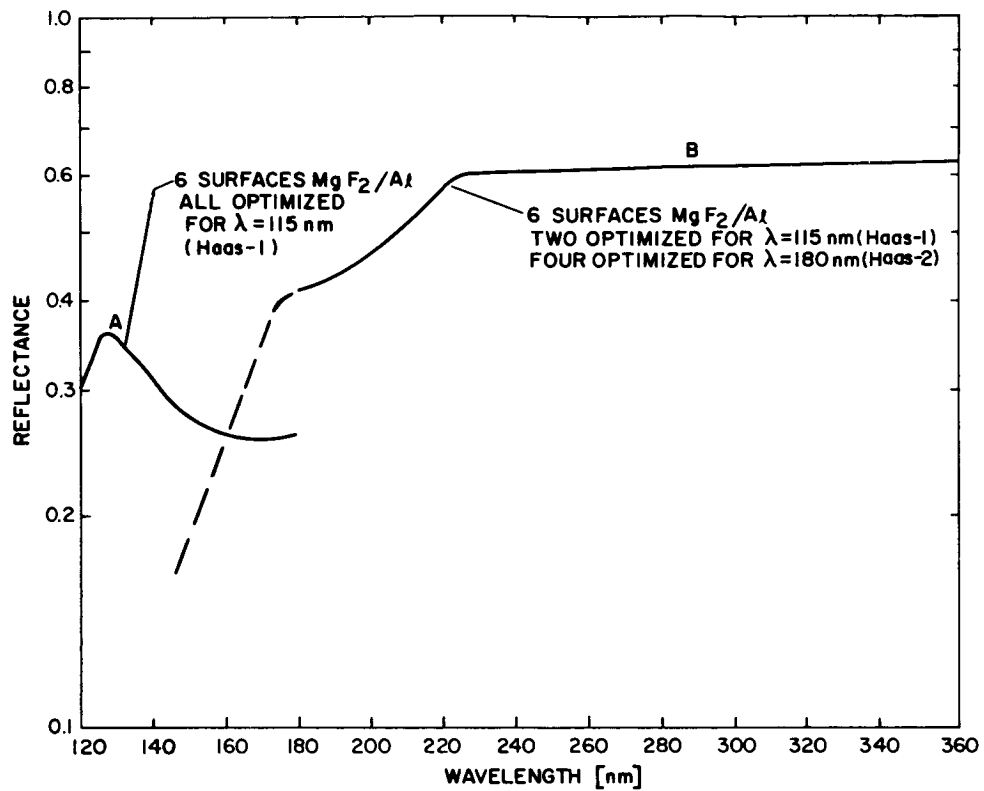


Figure 3-14. High Resolution Spectrograph, Optics Reflectance

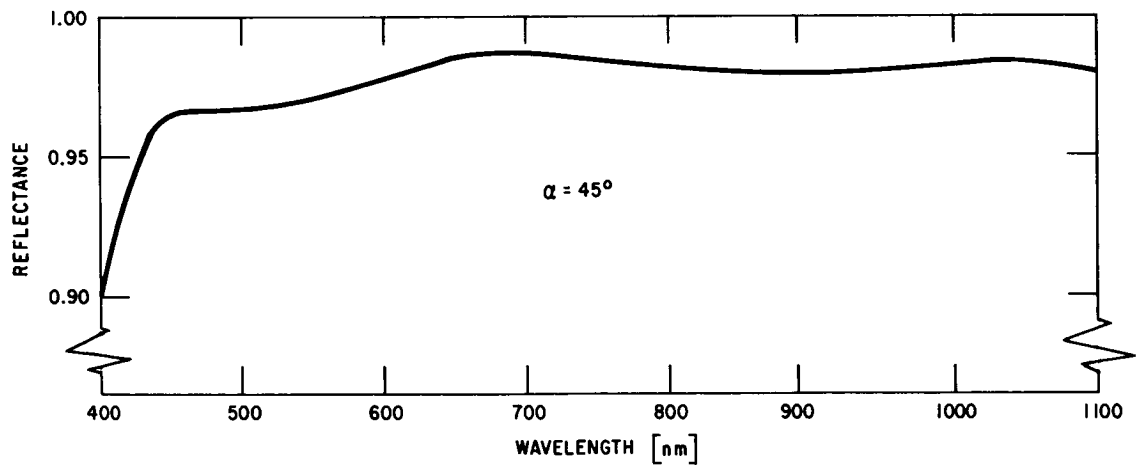


Figure 3-15. Spectral Reflectance of Silver Coating  
 $R = f(\lambda)$ . Shown for a 45° Incidence Angle,  $\alpha$

The Faint Object Spectrograph No. 2 (220-660nm) uses a dichroic mirror (DM-1) of the type shown in Figure 3-16 for separation of its two adjacent spectral ranges.

For computation of the spectrograph throughputs, grating blaze efficiencies according to Figure 3-5, Page 3-13, are used. These efficiencies are multiplied by the appropriate coating efficiency and the form-factors (smear) derived from actual data of comparable gratings. More than one grating blaze-angle is used in some cases to arrive at the optimum throughput.

Photodetector quantum efficiencies for individual instruments are in accordance with the specifications and graphs given in Section 6. From the number of photocathode/window combinations reviewed, two are used for throughput computation and final reference selection is based on S/N analyses in Section 4. For the projected semitransparent III-V photocathode (near-IR), Q.E. data available for the reflective  $\text{Ga}_{1-x}\text{In}_x\text{As-O}$  for  $0.52 < x < 0$  is used, assuming that the actual development under SR & T will be accomplished on time and will fulfill the prediction.

The reference design provides means for interchangeable spectral filters for the cameras. Examples of available vacuum - UV filters are shown in Figure 3-17. However, a selection of spectral bandwidth and number of filters will be made by the astronomy community. Hence, no filters were included in the camera throughput computations.

### 3.6.1 Wide Field Camera

The throughput calculations are based on the tables which follow. The first item in the table is the photocathode type(s). The items which follow are the coatings which are applied to the various surfaces, and the product of the coatings efficiencies is used. The calculations are based on a zero magnitude black body star model at various temperatures. The incoming photon rate is multiplied by the photocathode efficiency and the total coating efficiency.



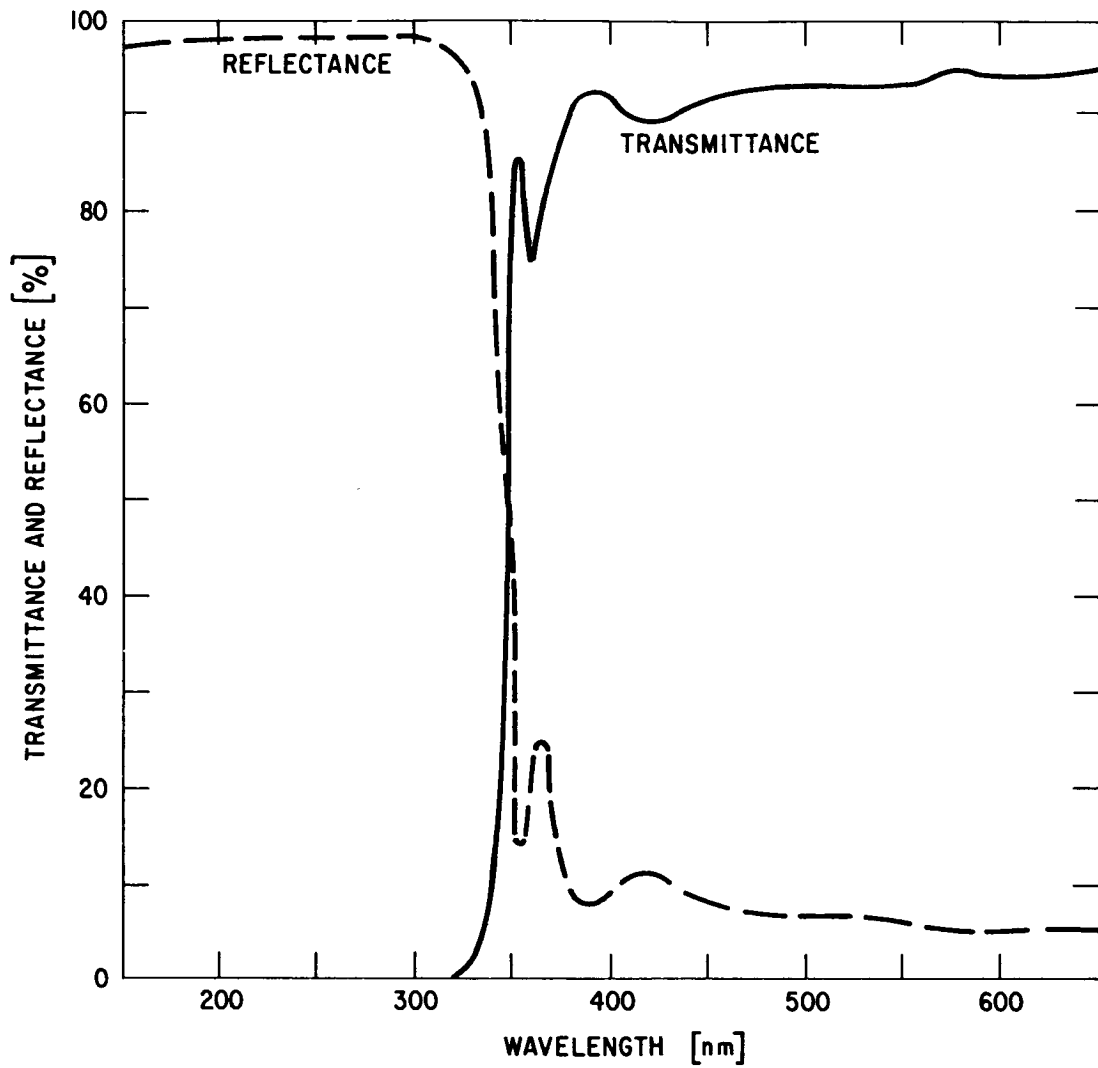


Figure 3-16. Dichroic Mirror, Transmittance and Reflectance =  $F(\lambda)$

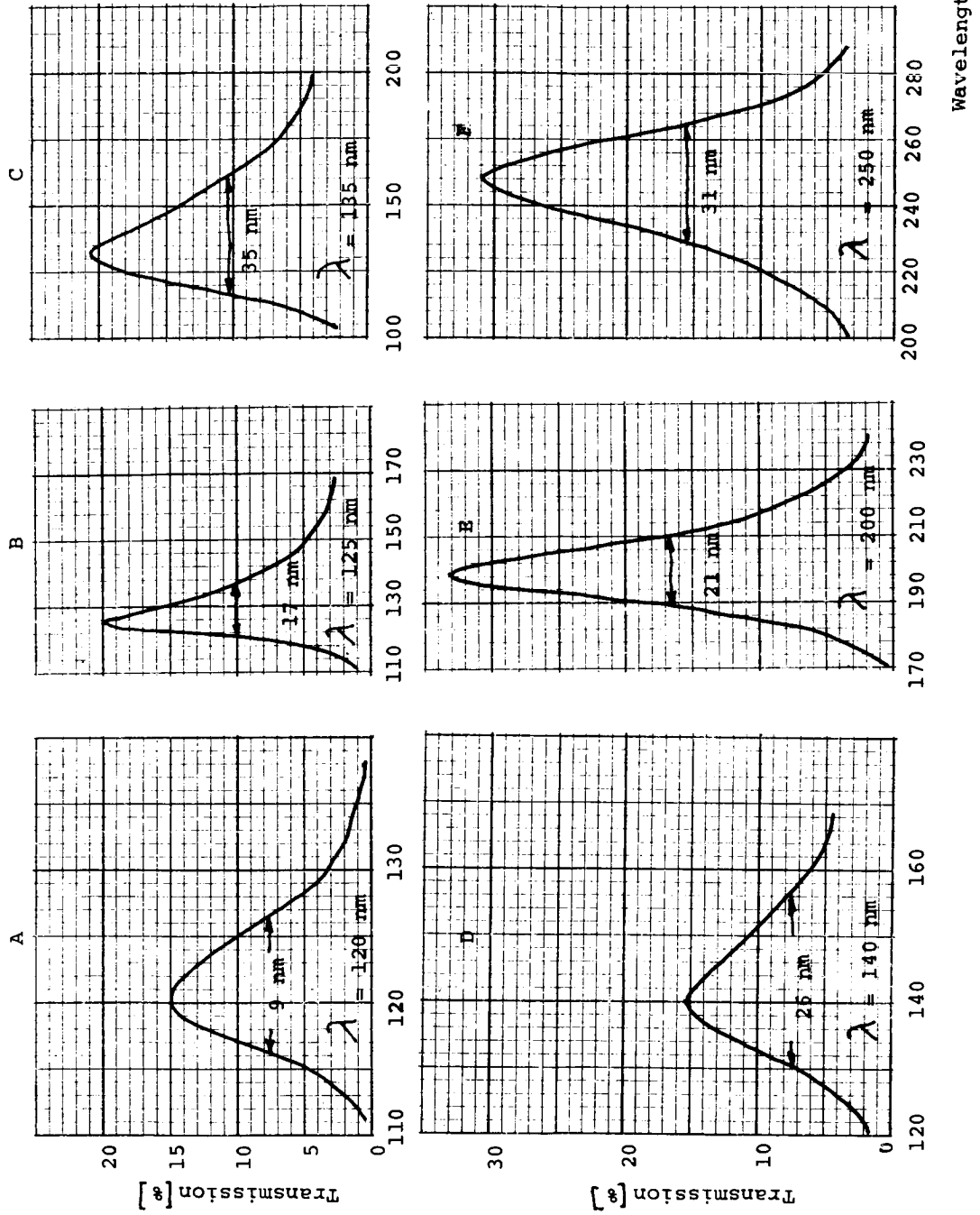


Figure 3-17. Available Far-UV Filters

(a) Photocathode	Bialkali/MgF <sub>2</sub>
OTA (Telescope) Coatings	(Haas-1) <sup>2</sup>
Diagonal Mirror* Coating	(Haas-1) <sup>1</sup>
Coating Total	<u>(Haas-1)<sup>3</sup></u>
(b) Photocathode	S-20/Fused Silica
Telescope	Same as (a) above
Diagonal Mirror* Coating	(Haas-2) <sup>1</sup>
Coating Total	<u>(Haas-1)<sup>2</sup> + (Haas-2)<sup>1</sup></u>

Computed throughputs are shown in Figure 3-18. Selection is made, based on the S/N computations and a review of the upper wavelength requirements in Section 4.

### 3.6.2 High Resolution Camera (f/96)

#### Range I

(a) Photocathode	CsI/MgF <sub>2</sub>
OTA (Telescope) Coatings	(Haas-1) <sup>2</sup>
8X Magnifier Coatings	(Haas-1) <sup>2</sup>
Diagonal Coatings	(Haas-1) <sup>2</sup>
Coating Total	<u>(Haas-1)<sup>6</sup></u>
(b) Same as (a) above, except for the photocathode, which is CsTe/MgF <sub>2</sub> .	

Comparison of the (a) and (b) throughputs is shown in Figure 3-19. In the final evaluation the CsTe/MgF<sub>2</sub> is selected based on S/N analysis.

#### Range II

(a) Photocathode	Bialkali/MgF <sub>2</sub>
OTA (Telescope) Coatings	(Haas-1) <sup>2</sup>

---

\*For all diagonals, the incidence angle is  $\pi/4$  rad. The coating thicknesses are modified to yield an effective reflectance equivalent to that shown for normal incidence.

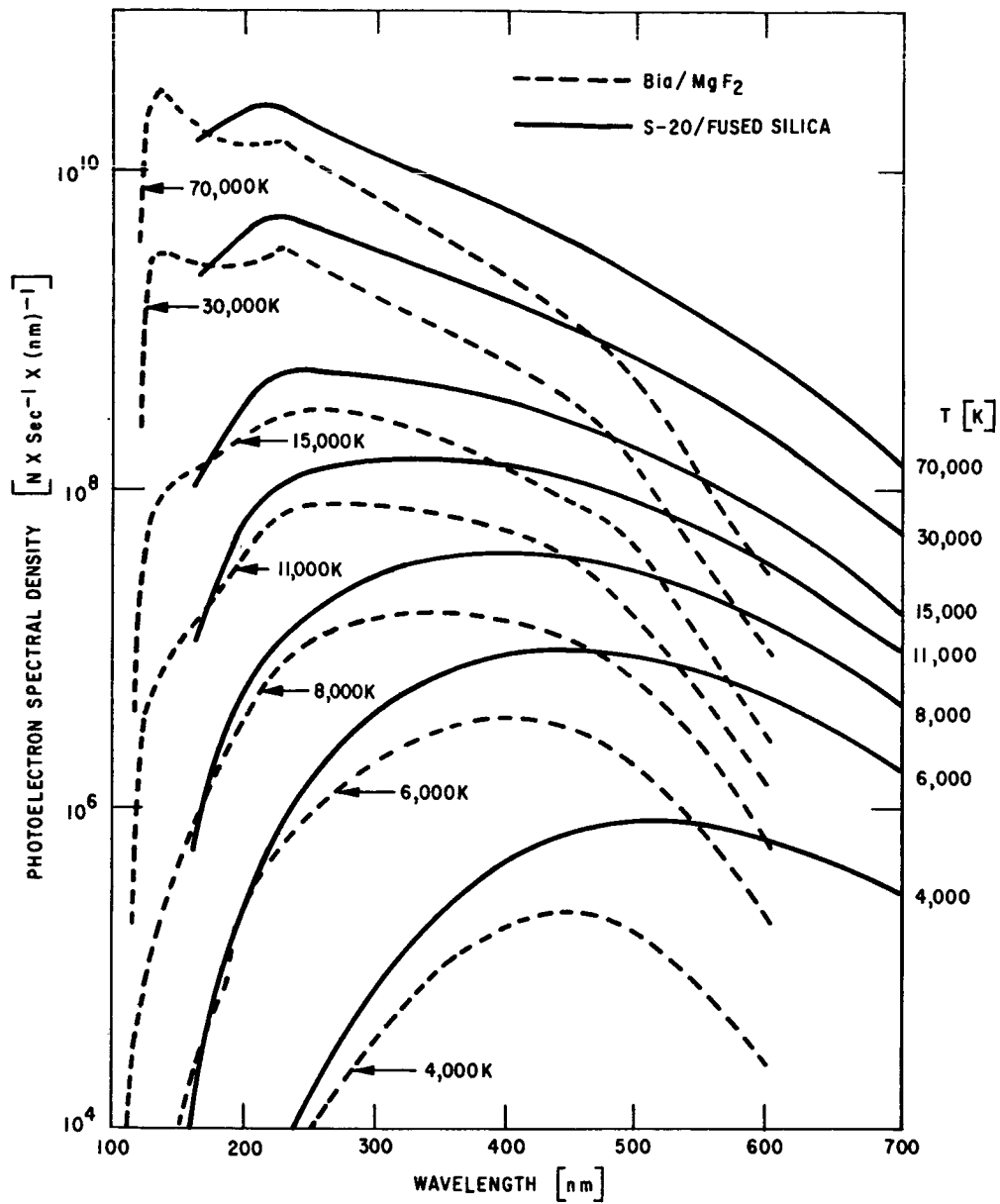


Figure 3-18. LST Wide Field Camera Throughput for Zero Mag. Star

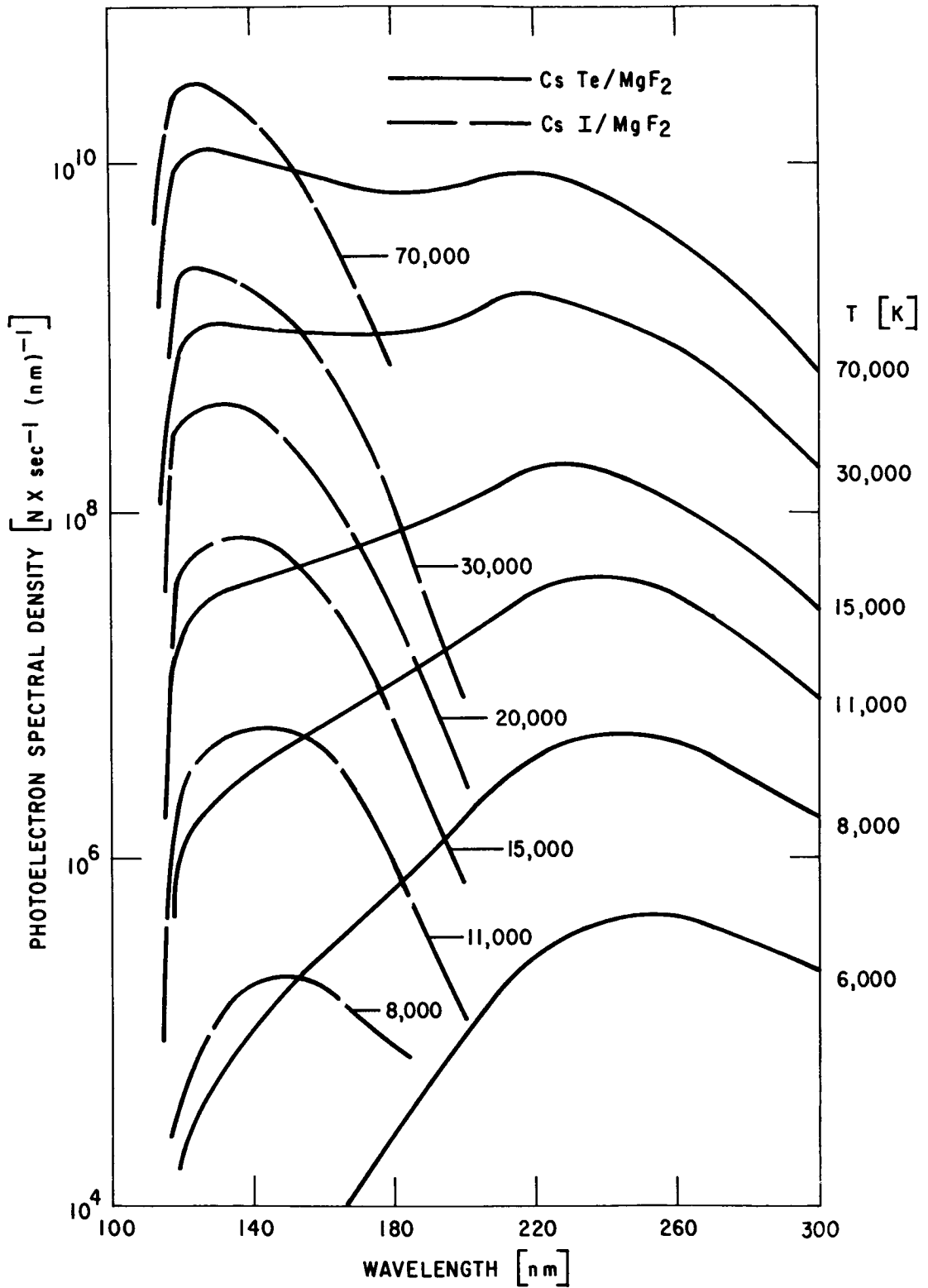


Figure 3-19. LST High Resolution Camera (f/96) (Range I) Throughput for Zero Mag. Star

8X Magnifier Coatings	(Haas-1) <sup>2</sup>
Diagonal Coating	(Haas-1) <sup>2</sup> <u>(Haas-2)<sup>1</sup></u>
Coating Total	(Haas-1) <sup>6</sup> times (Haas-2) <sup>1</sup>

(b) Same as (a) above, except the photocathode, which is S-20/Fused Silica. Due to this window, cutoff occurs at 160 nm at the low end, however, it is substantially extended at the high end, which indirectly leads to increased noise, especially at temperatures above 300K. Comparison of the (a) and (b) throughputs is shown in Figure 3-20.

### Range III

Photocathode	Cesiated Gallium-Indium-Arsenide (III-V)/glass
OTA (Telescope) Coatings	(Haas-1) <sup>2</sup>
8X Magnifier Coatings	(Haas-1) <sup>2</sup>
Diagonal Coatings	(Haas-1) <sup>2</sup> <u>(Haas-2)<sup>1</sup></u>
Coating Total	(Haas-1) <sup>6</sup> times (Haas-2) <sup>1</sup>

The throughputs computed for above conditions are shown in Figure 3-21.

### 3.6.3 High Resolution Spectrograph

Range I  $110 < \lambda < 180$  nm

Photocathode	Bialkali/MgF <sub>2</sub>
Optical Coatings	
OTA (Telescope) Coatings	(Haas-1) <sup>2</sup>
Collimator, Echelle, Cross-Disperser, Camera Mirror - four surfaces	<u>(Haas-1)<sup>4</sup></u>
Coatings Total	(Haas-1) <sup>6</sup>

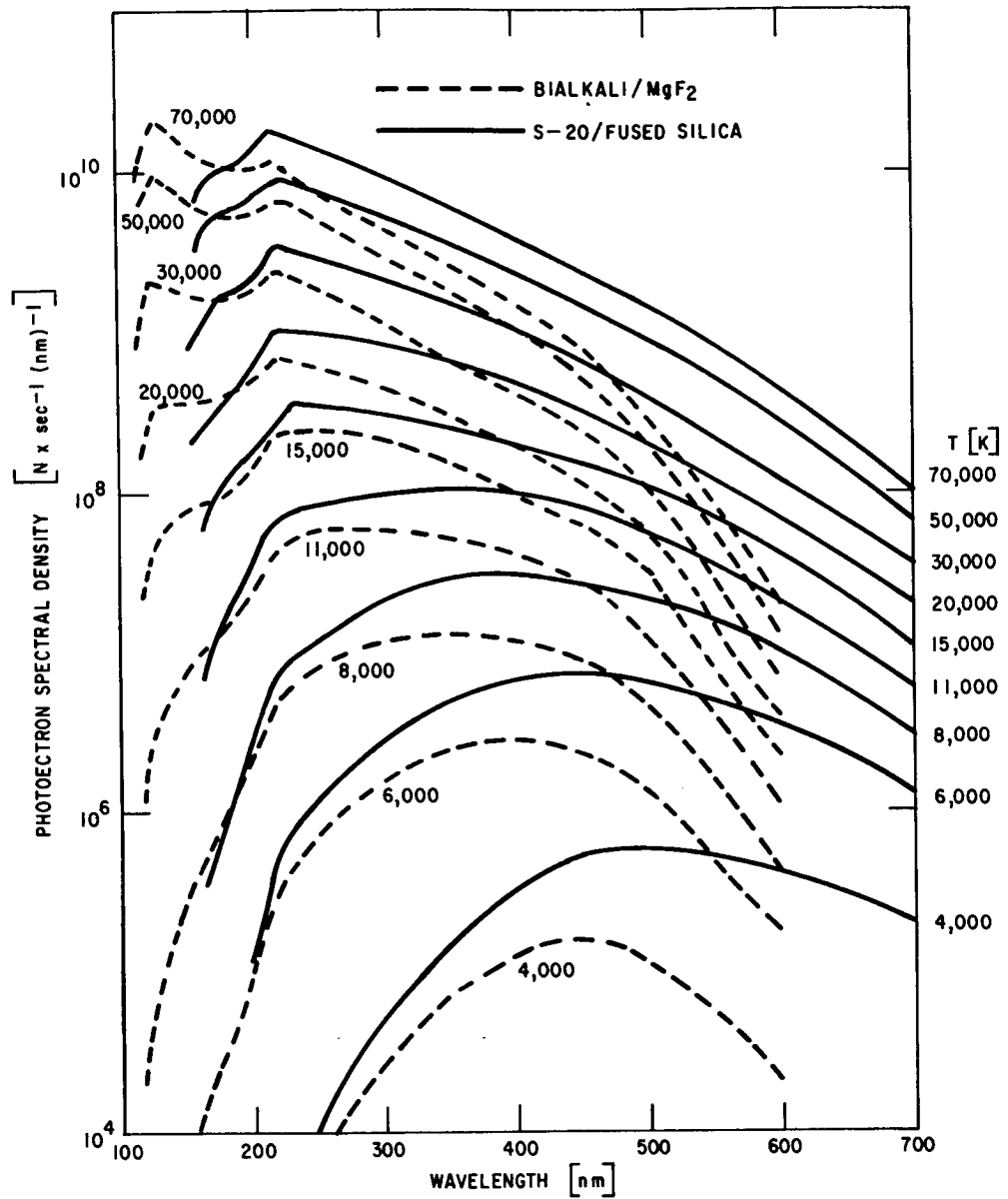


Figure 3-20. LST High Resolution Camera (f/96) (Range II) Throughput for Zero Mag. Star

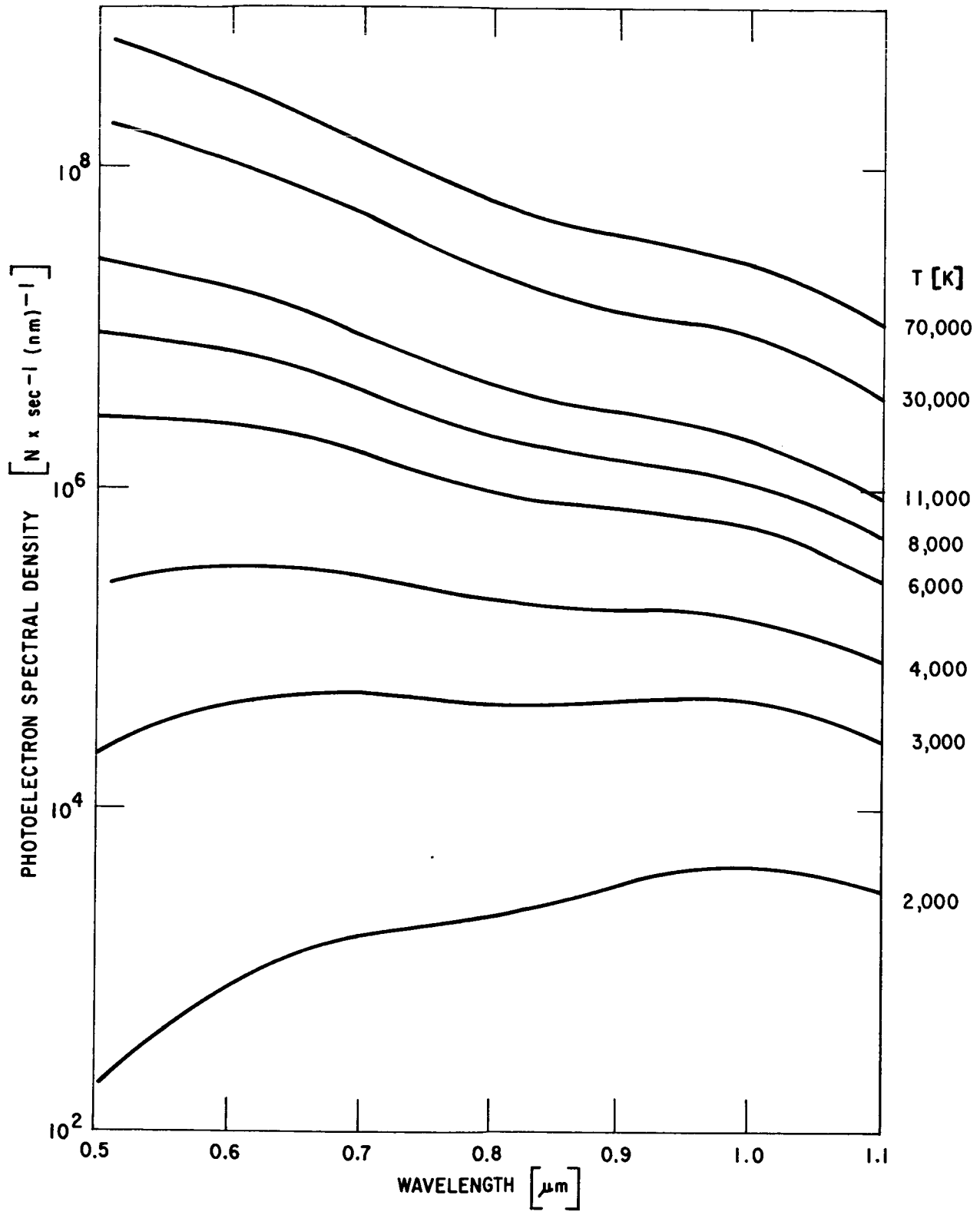


Figure 3-21. LST High Resolution Camera (f/96)  
Range III Zero Mag. Throughput



The Echelle grating is used at high orders (106-166). Near the center of each order, it is assumed to have a peak efficiency of 0.8 (smear factor) as shown normalized to unity in Figure 3-5, page 3-13. At the useable limits, each order is assumed to have an overall efficiency of 0.32 (not including the effect of the optical coating).

The Cross-Disperser also follows the curve of Figure 3-5 but with a peak efficiency of 0.6 at the center order. However, it exhibits a fall-off to 0.48 at the lowest and highest operating wavelengths. Based on the calculated efficiency as a function of blaze angle, shown in Figure 3-22, a grating blaze was optimized for  $\lambda_p = 115$  nm.

The overall throughput in terms of photoelectron spectral density per second for several incident black body inputs is shown on the left side of Figure 3-23. (center of order is shown)

Range II	180 < $\lambda$ < 350 nm
Photocathode	Bialkali/Fused Silica
Optical Coatings	
OTA (Telescope) Coatings	(Haas-1) <sup>2</sup>
Collimator, Echelle, Cross-Disperser, Camera Mirror	(Haas-2) <sup>4</sup>

The Echelle grating, used at high orders (80-155) is assumed to have a peak efficiency of 0.8 near the center of each order. The useful spectral range at the ends of each order is assumed to be at an overall efficiency of 0.32.

The efficiency of the Cross-Disperser is evaluated at three blaze angles for  $\lambda_p = 180, 200$  and  $240$  nm. Based on the results shown in Figure 3-24, the blaze angle for  $\lambda_p = 240$  nm is selected. The Cross-Disperser efficiency also follows the curve of Figure 3-5 with a peak efficiency of 0.7 and 0.5 at the limiting order.

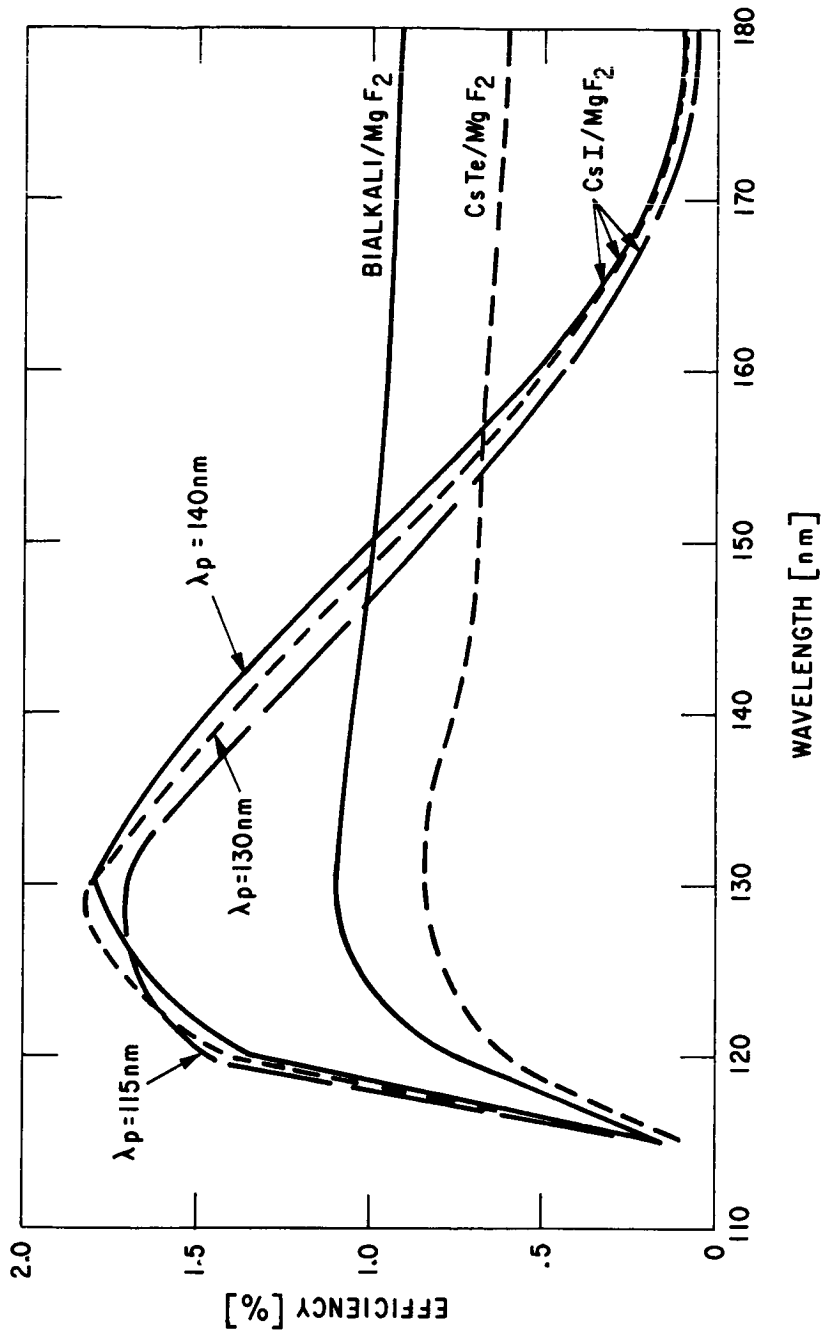


Figure 3-22. High Resolution Spectrograph, Range I Efficiency, Center of Order

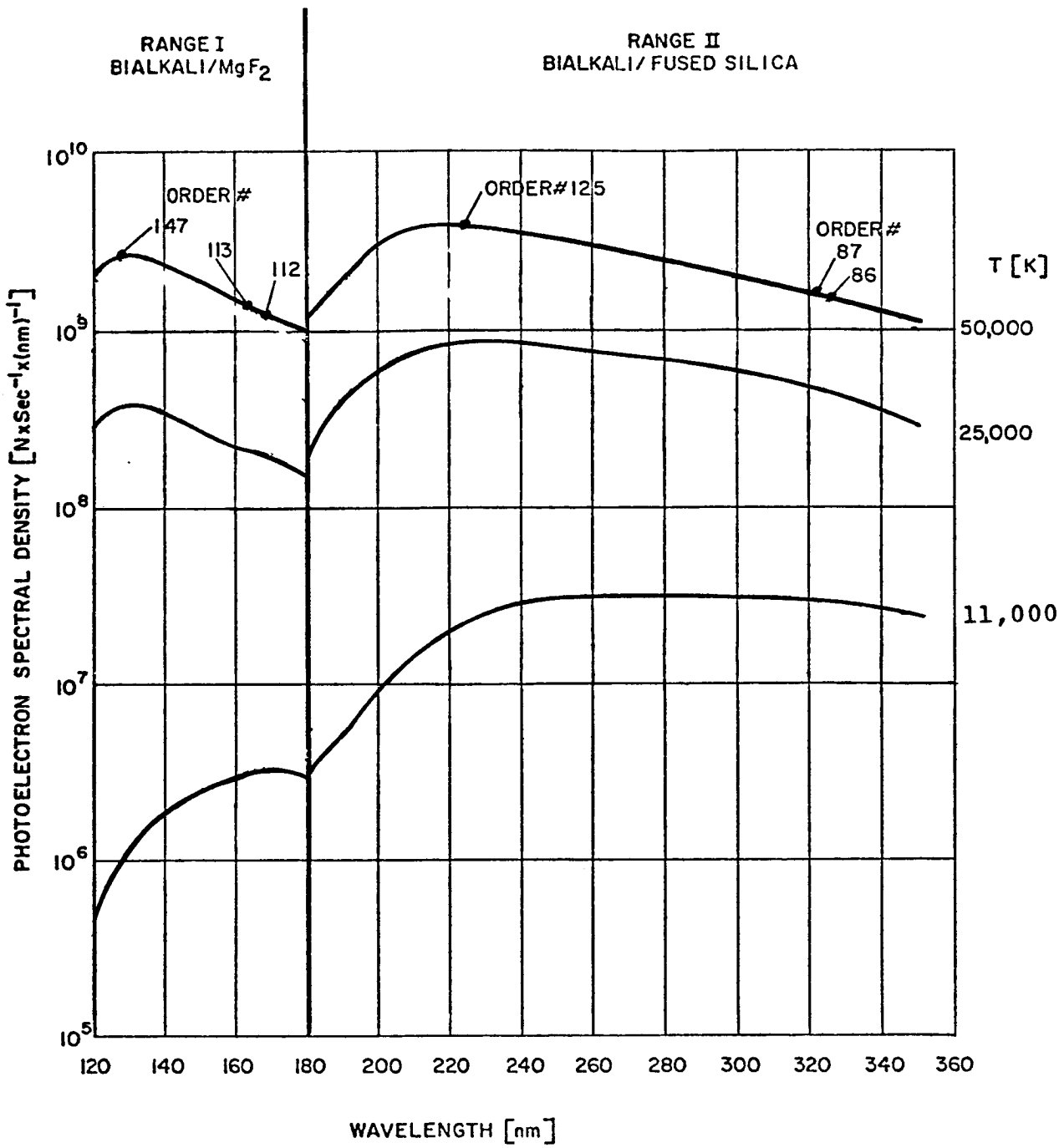


Figure 3-23. LST-High Resolution Spectrograph, Zero Mag. Throughput

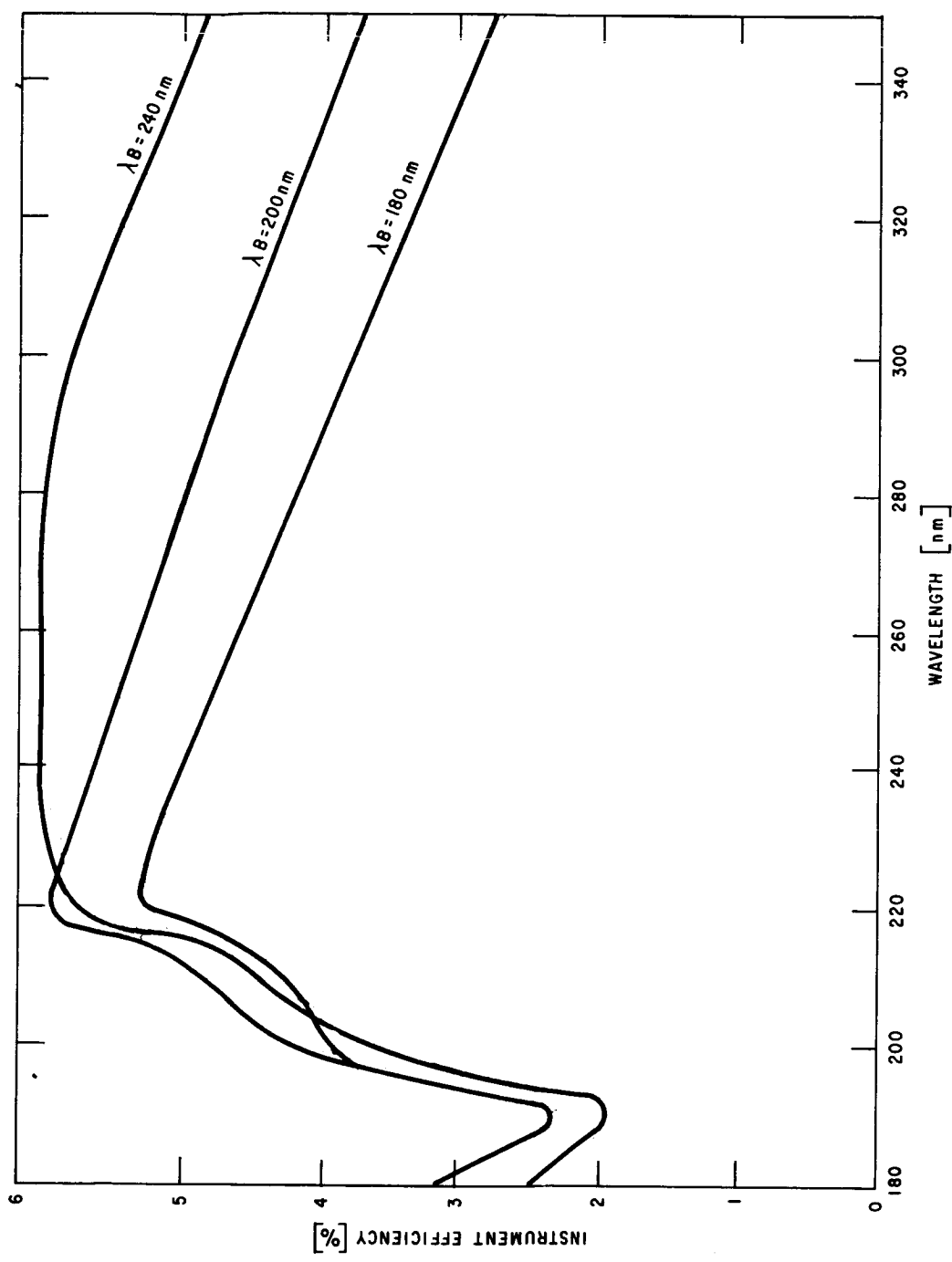


Figure 3-24. High Resolution Spectrograph Instrument Efficiency

The overall throughput in terms of photoelectron spectral density per second for several incident black body inputs is shown on the right side of Figure 3-23 (center of order).

### 3.6.4 Faint Object Spectrograph

The baseline system uses three camera tubes, one each in the three instruments with following spectral range coverage:

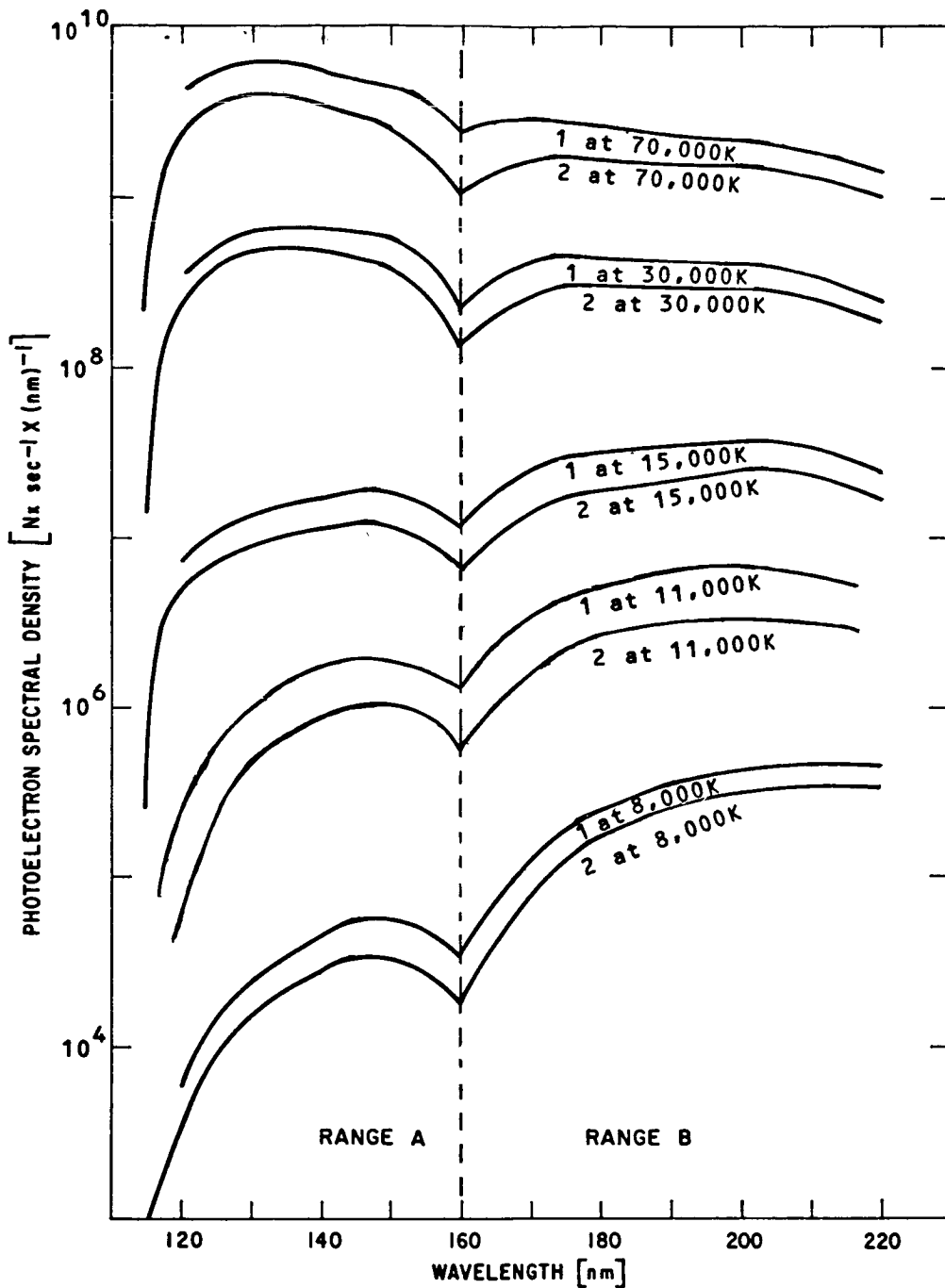
Instrument No. 1	A	115 < $\lambda$ < 160 nm
	B	160 < $\lambda$ < 220 nm
No. 2	A	220 < $\lambda$ < 350 nm
	B	350 < $\lambda$ < 660 nm
No. 3		660 < $\lambda$ < 1,000 nm

#### FOS Instrument No. 1

a) Photocathode	Bialkali/MgF <sub>2</sub>
OTA Coatings	(Haas-1) <sup>2</sup>
Collimator	(Haas-1) <sup>1</sup>
Flat Grating	(Haas-1) <sup>1</sup>
Folding Mirror	(Haas-1) <sup>1</sup>
Camera Mirror	(Haas-1) <sup>1</sup>
	<hr/>
Coating Total	(Haas-1) <sup>6</sup>
b) Photocathode	CsTe/MgF <sub>2</sub>
Coatings (same as a above)	(Haas-1) <sup>6</sup>

Each grating blazing is computed to render the specified spectral coverage in a 30 mm linear trace with the low and high wavelength limits, yielding an 80% normalized blaze efficiency, see Figure 3-5. The grating peak efficiency (smear) of 60% is used, which does not include the surface coating efficiency, previously accounted for.

Results of this computation, shown in Figure 3-25 do not include the slit losses.



1) Bi-alkali/MgF2 (Higher Throughput)

2) CsTe/MgF2

Figure 3-25. LST Faint Object Spectrograph,  
Zero Mag. Throughput

FOS Instrument No. 2

This instrument provides simultaneous coverage in two spectral ranges, A and B, rendering two linear spectral traces on a single sensor.

A common off-axis paraboloid directs the collimating bundle to a dichroic filter which separates the two ranges, A and B, into two separate paths - A, using the reflected and B, using transmitted energy. Based on the optical details in Section 4.3, following efficiencies are assigned:

<u>Range A</u>		<u>Range B</u>
(Haas-1) <sup>2</sup>	OTA (two reflective surfaces)	(Haas-1) <sup>2</sup>
(Haas-2) <sup>3</sup>	Diagonal, collimator, grating Folding mirror	(Haas-2) <sup>3</sup> (Haas-2) <sup>1</sup>
Reflectance	Dichroic filter, see Figure 3-16	Transmittance
S-20/SiO <sub>2</sub> (fused)	Common Sensor	S-20/SiO <sub>2</sub> (fused)
$\lambda_p = 270 \text{ nm};$ $\eta_{sm} = 0.56$	Flat grating blazed for $\lambda_p$ smear efficiency	$\lambda_p = 500 \text{ nm};$ $\eta_{sm} = 0.56$

Each of the two flat gratings is computed to render its respective spectral coverage in a 30 mm linear trace with the low and high wavelength limits having a 50% normalized blaze efficiency, see Figure 3-5.

The results of this computation, shown in Figure 3-26, do not include the slit losses.

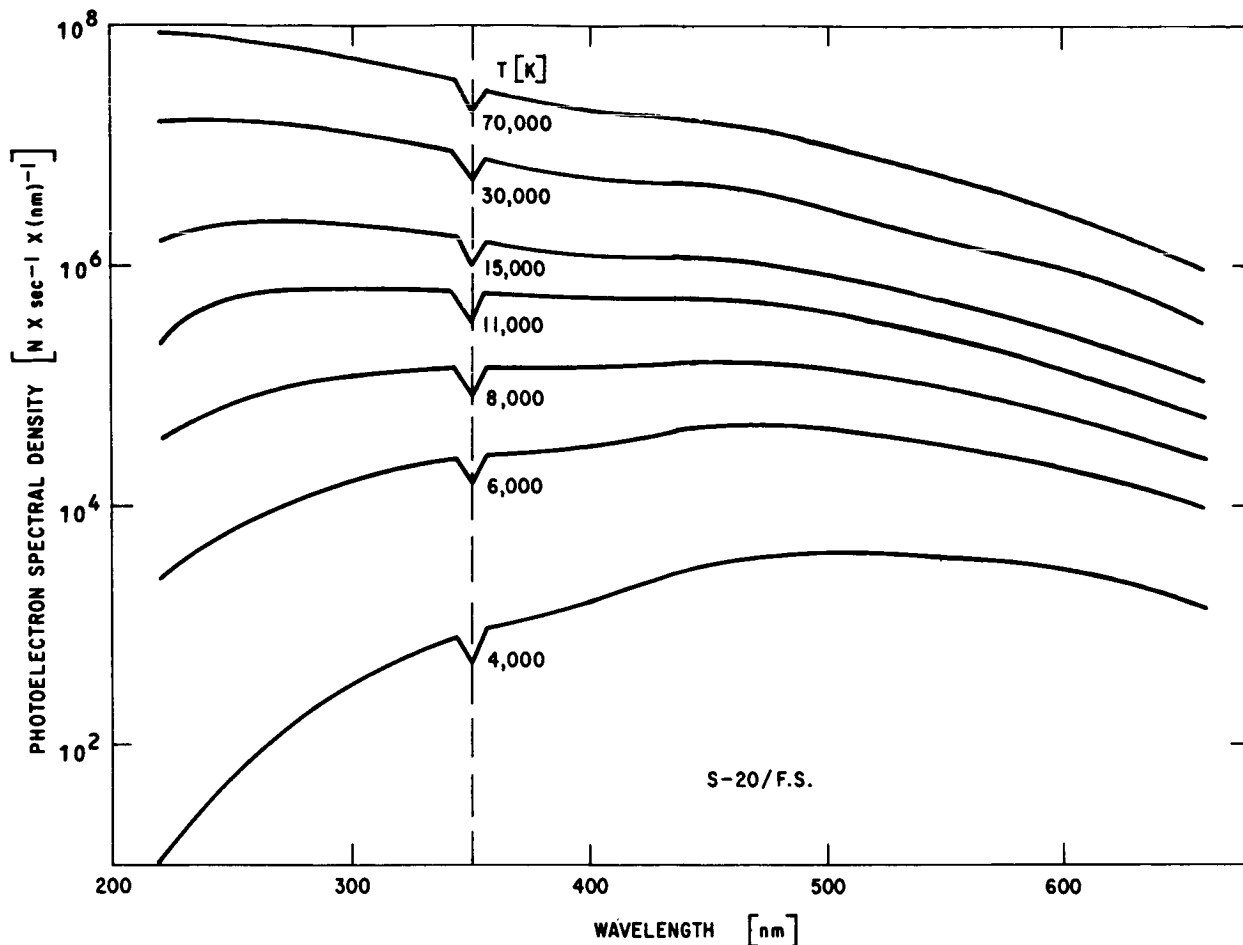


Figure 3-26. LST Faint Object Spectrograph, No. 2 Double Flat Grating/  
Dichroic Separation, Zero Mag. Throughput

Instrument No. 3       $660 < \lambda < 1,000 \text{ nm}$

Reflective photocathode                       $\text{Ga}_{1-x}\text{In}_x\text{As}:\text{CsO}/\text{glass}$

Optical Coatings

OTA (Telescope)                               $(\text{Haas-1})^2$   
two surfaces

Diagonal     $(\text{Silver})^1$

Collimator, Grating, Folding  
Mirror, three surfaces                           $(\text{Silver})^3$

Grating spectral response, see Figure 3-5 with  $\lambda_p = 900 \text{ nm}$ ,  
shape efficiency (smear) = 0.7.

Throughput data is plotted in Figure 3-27.

Slit losses are not included in this computation.



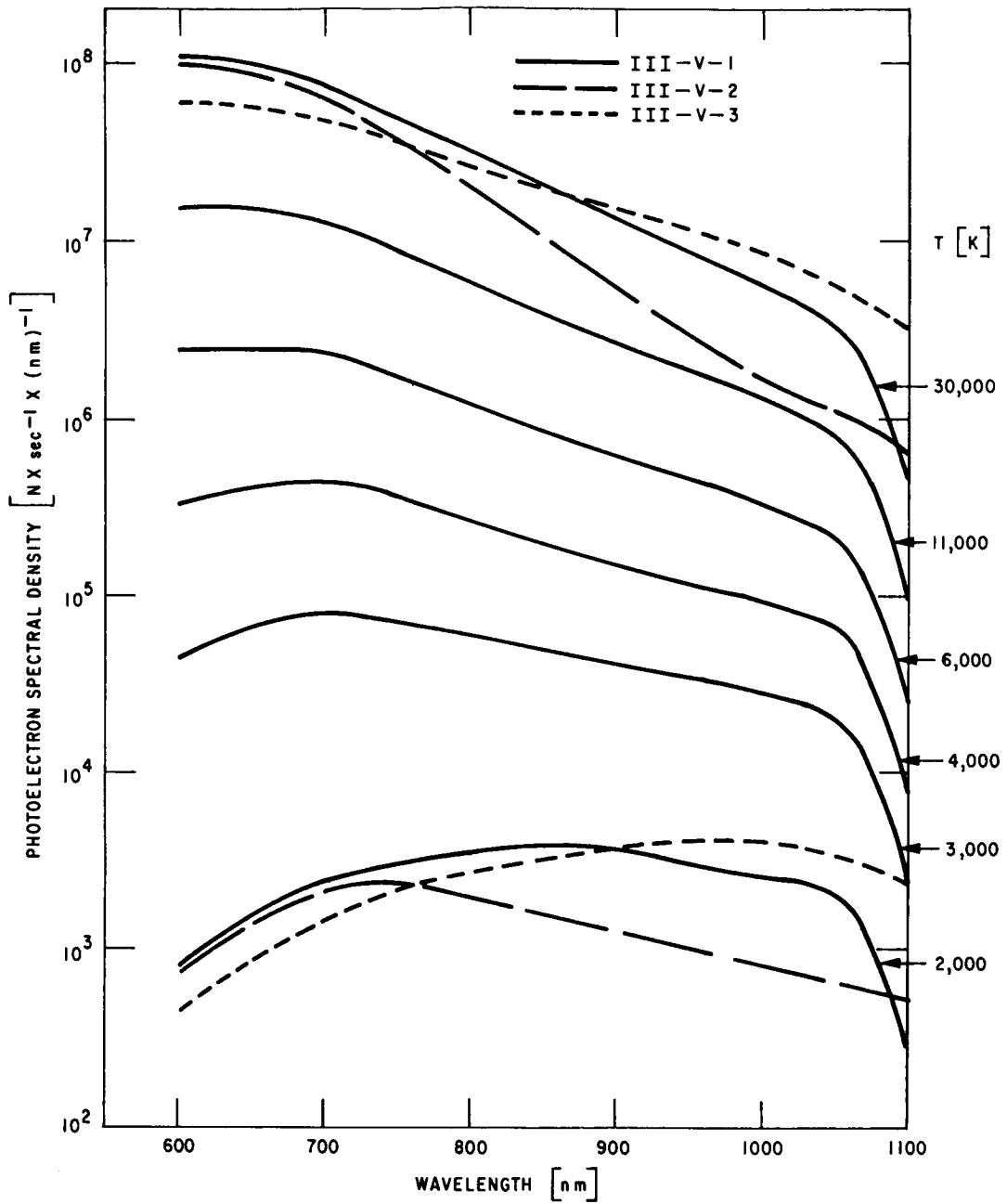


Figure 3-27. LST Faint Object Spectrograph Instrument No. 3, Zero Mag. Throughput

### 3.7 SYSTEM OPERATIONAL, HARDWARE AND RELIABILITY CONSIDERATION

These factors are discussed together here because they are all interrelated on the systems level. The main driving factors are (1) the role of the astronaut and the implications of that role; and (2) the problems of data handling, which are somewhat affected by the role of the astronaut.

#### 3.7.1 Role of the Astronaut and Its Implications

Other than checking for broken cables and performing other visual, on-the-spot inspections, the astronaut is not expected to function as a troubleshooter. His main role is presently envisioned as one of replacement/repair effector.

The implication of such a role is that the major troubleshooting will be performed on the ground. This notion is further reinforced when consideration is given to the thought that some time will elapse between the disclosure of an anomaly, and the dispatch of an astronaut for replacement/repair. Such time could and would be used for ground evaluation.

When evaluating a suspected anomaly, it must be kept in mind that those devices which monitor system performance are themselves subject to error or failure. This leads the designer to one of two possible approaches:

- (a) The first is to have a simple status monitoring system. The advantage of this approach is that the data handling problems and the instrument monitoring design problems are simplified. It minimizes the interface problems, and requires less power consumption and available space. The drawback of such an approach is a lower confidence in the diagnosis since several possible failures could cause the same symptoms. This might necessitate the carrying of several extra parts to be sure that the proper repair could be effected. Further, it could mean the needless

replacement of an entire instrument if the trouble could not be pinpointed. It also increases the probability of false alarm, since a failure in the monitoring system could be interpreted as an instrument failure and could lead to the needless replacement of a working assembly. Considering the expense of a Space Shuttle flight, this could be serious.

- (b) The second approach is to design a system with a good deal of monitoring. The various bits of information can be weighed, one against the other, for the purpose of forming a judgement as to where the problem is. This will maximize the probability of pinpointing the trouble, and minimize the possibility that an error in a single monitoring device could cause a false alarm. Narrowing the list of possible causes of failure means that less equipment need be taken aboard the Shuttle to effect a repair, and it lessens the probability that an entire instrument be replaced to effect a repair. The drawbacks of this approach are the increased power consumption, volume, and power, and the need for more sophisticated data handling and evaluation. There is also the problem of defining a limit to the supply of monitoring equipment.

After careful consideration, Kollsman studied the implementation of the second approach. Data handling and packaging studies indicated that neither the volume, power consumption or data handling requirements were excessive, and this approach is recommended.

To aid in the replacement/retrofit, and to provide for differing future needs and instrument improvements, each instrument is separately removable. The packaging of the electronics is made integral with each instrument, although it is possible to remove the

electronics associated with each instrument without removing the instrument itself. The advantage of such an approach is that the electronics may be tailored to each instrument, so that the electronic design of one instrument does not impact another. For non-redundant systems, this is a more reliable concept than a system which shares electronics. It also means that there is a minimum amount of wiring and connectors on each instrument (each instrument requires only power and command lines), which is an important factor in replacement/repair.

It is not clear at this time which approach consumes more power. If all of the experiments were on, then the central electronics system would use less power. But the present concept calls for the non-operating units to use standby power, and the additional standby power used must be balanced against the greater dissipation of the supplies of the central system. The central system definitely uses less parts, for a non-redundant system. But packaging studies show that the power and volume consumed by the electronics are within the desired range, and are small compared to the volume and power consumed by the SEC Vidicon tubes. Therefore, Kollsman considers that the added ease of design, the flexibility for future growth, the easing of the repair/retrofit problem, and the increased reliability are worth the small increase in overall size, and the electronics for each instrument are designed and packaged separately.

This does not mean that every instrument uses different parts however. Where possible, common circuits are used throughout to simplify the design and spare parts problem.

The tube electronics are packaged integrally with the tube components. It is not desirable to run high voltage leads over any length, and the readout preamplifier must be packaged physically close to the tube to prevent noise problems. At the present time, the state-of-the-art of the SEC Vidicon requires that power supply output voltages (or currents) power supplies be trimmed to each tube

to ensure proper operation. The final consideration is that of reliability. Current estimate is that the tube is the most likely device to require replacement; therefore it is desirable to reduce the number of wires and connectors to an absolute minimum.

As a further step in reducing the number of wires and connectors, all information going to and transmitted from an instrument is in serial digital format.

The replacement/repair philosophy is based on two concepts, depending on the type of problem. The Science Committee has formulated a priority list for the various instruments. If an instrument should fail catastrophically, there are still others which can be used to gather data. If one or two low priority instruments were to fail, the effectiveness of the LST would not be seriously impaired, whereas impairment would follow the failure of several high priority items. The criterion for repair/replacement is then based on a weighted average number below which the total system reliability may not go. The details of this approach are found in Section 10.

### 3.7.2 Data Handling

It is shown in Section 9 that the number of scientific data bits is quite large:  $8 \times 10^7$  bits for the 50 millimeter tube. Presently, there are no memories available which can handle this large volume of data that are suitable for use on the LST. The data must be stored on the SEC Vidicon target until contact is made with a ground station; it is then read out. The bit error rate of the down link transmission system is low ( $10^{-5}$ ) but it is desirable to use some means of encoding the data. If ten bits are used to encode each of 500 scan lines, the number of bits used for encoding scan lines is only 0.2 percent of the total number of bits required for transmitting the scientific data. Therefore each scan line of the tube is encoded when transmitting scientific data.

Housekeeping data, which is expected to be transmitted at intervals greater than 30 minutes, is transmitted in its entirety even if it is not used or considered useful at the time of transmission. The number of housekeeping bits is about 2000 for all the instruments, which is small compared to the number of scientific bits. In fact, it is less than one-half the number of bits used to encode the scan lines for the 25 millimeter SEC Vidicon. This data is very helpful in checking on gradual deterioration of an instrument which might not be detected immediately, or in verifying data after it has been received. If such data is on file, it can be referred to for evaluation. If it is not transmitted, it is forever lost.

### 3.8 EFFECT OF IMPROVED SENSORS ON INSTRUMENT PERFORMANCE

The statement was made at the beginning of Section 3 that the purpose of the system analysis was to take the maximum advantage of the 3 meter telescope. It soon became apparent that to do this, the system parameters had to be manipulated to conform to conditions imposed by one important driver - the sensor. The purpose of this subsection is to evaluate the impact on system performance and operation of improvements in sensor performance.

The effect that improved sensors would have on instrument performance is evaluated for two kinds of improvements: (1) those which may reasonably be expected in the present sensor, and (2) those which require a technological breakthrough.

Section 6 treats the subject of possible improvements in the present sensor in detail. The four improvements to be expected are (1) a decrease in focus coil power (presently 25 watts), (2) an increase in the target gain by a factor of 10 to 20X, (3) an increase in target capacity in terms of photoelectrons at saturation, and (4) an increase in spatial resolution. A decrease in focus power would simplify the cooling problems. It would also lessen the electronic

power supply design problems. An increase in the target gain by a factor of 10 to 20 will diminish the effect of preamplifier noise. For the cameras, although sensitivity to dimmer targets is not improved (the cameras are background noise limited), increased target gain permits the preamplifiers to generate more noise, which implies that the preamplifier may be operated at a higher temperature. For the spectrographs, which are tube and preamplifier noise limited, an increase in target gain permits the viewing of dimmer objects by achieving a closer approach to background or photon noise limited operation.

An increase in target capacity improves the S/N ratio during a single scan by (1) decreasing the relative uncertainty in the signal, which varies as  $1/\sqrt{S}$ , where S is the signal photoelectrons; and (2) by increasing the ratio of signal to amplifier noise.

The effect of an increase in spatial resolution may be seen by observing the curves in Figs. 3-6 and 3-7. If the general shape of the MTF curve ( $e^{-b^2w^2}$ ) remains the same and the limiting frequency increases, then the effect on instrument resolution caused by a change in limiting frequency on the MTF plot is identical to a corresponding change in f/number. For example, if the limiting frequency doubled, an f/48 system would yield the same resolution as the present f/96. The use of an f/48 system would simplify the thermal, structural, and the mechanical problems associated with the high resolution camera and the optical multiplier, and would probably result in a smaller package size.

Among the possible improvements which are not expected from the present tube is a decrease in tube noise. This would permit the viewing of dimmer objects in the spectrographs, which at present are sensor and preamplifier noise limited. The ultimate improvement in this regard would be the development of a photon counting image tube. In this device, the photodetector is scanned

and erased continuously. Thus, the accumulation of dark charge is prevented from obscuring the signal. When a photon arrives, it is detected and transformed into a digital pulse which is accumulated in a memory. As long as tube noise is not greater than the signal, it has no effect. The advantage of a tube such as this is that it is capable of operating the spectrographs at the background limit, instead of the present tube and preamplifier noise limit.

To employ a photon counting tube, a memory capable of handling about  $10^9$  bits must be developed which is suitable for operation in the LST. At present memories of this size are not available, although some, such as the magnetic bubble memory, are under development. The development of such a memory would also open the sensor field to devices such as the return beam vidicon, which has a greater resolution capability than the SEC vidicon, but saturates on dark current within minutes.



SECTION 4  
SCIENTIFIC INSTRUMENTATION

4.1 INTRODUCTION

Following the requirements inherent in the Objectives (Section 2) and using the results of the parametric analyses discussed and displayed graphically in Section 3, a tentative Scientific Instrument Package configuration is developed; its purpose is to provide a design whose realization could perform the necessary measurements. Moreover, the design serves as a reference from which departures to alternate, and, perhaps, more advantageous configurations can be made.

The discussion of fabrication, assembly and dynamic tolerances and the ensuing discussion of those tolerances (Table 4-1 through 4-3) name dynamic tolerances which effect image motion as the largest and most difficult to hold.

The high resolution camera is designed to provide in a compact package a maximum field of view and high UV-efficiency over the 115nm - 1100nm spectral range. To maintain high resolution, the camera formats each of three spectral ranges, one at a time, onto one of three 50 x 50 mm cathode surfaces each of which has a cathode/window material combination chosen to maximize response and efficiency in its range. Signal-to-noise ratio characteristics govern the tradeoffs leading to the cathode/window material selection.

To avoid an unacceptably large image format and to maintain acceptable efficiency, the high resolution spectrograph covers the 115nm - 350nm spectral range with two instruments. Each one employs an echelle grating followed by a cross disperser, a combination which yields a rectangular image format.

An optimization of system parameters with respect to their relative effect (through aberrations and tolerances) upon image size recommends the use of an f/10 camera mirror with a 120mm diameter. The spot diagrams of the recommended spectrograph configurations show the redistribution of image energy as it is effected by image location in the overall format.

The three instrument complement of the faint object spectrograph contains

1. a single dispersion instrument whose two interchangeable gratings divide the 110-220 nm range at 160 nm; a twenty-five millimeter square, bialkali/MgF<sub>2</sub> cathode records either of the two 30 mm-long line spectra;
2. a single instrument for the 220-660 nm range utilizing a dichroic beamsplitter to separate the collimated beam at 350 nm. Two curved gratings then disperse the beams and focus them into two nearly parallel 30 mm long line spectra on a 25 x 25 SEC-Vidicon sensor. An S-20/SiO<sub>2</sub> photocathode/window provides the required spectral coverage for simultaneous data integration in both lines.
3. a single grating instrument which forms a 30 mm-long line spectra of the 660-1000 nm range on a glass window protecting a III-V semi-transparent photocathode. Signal-to-noise calculations, based on recommended slit widths, determine the limiting apparent magnitude (stars) detectable with each instrument.

Selection rationale and evaluation (characteristic spot diagrams) are given for each instrument.

The unsuitability of dispersive systems to examine the 1000 to 5000 nm spectral region leads to the use of Fourier interferometry. Measures of the incoming radiation's intensity and temporal coherence combine to define an interferogram whose Fourier transform yields the spectrum. The instrument design, including optics and servo control system, and the necessity of exploring slower stepping rate modes to allow more efficient overall operation are discussed and explained.

For initial target survey and for mapping, a wide field camera of high sensitivity and adequate resolution is designed. Several

detection systems are mentioned citing the relative advantages of each (sensitivity, resolution). The selected reference instrument uses an S-20/SiO<sub>2</sub> photocathode; an alternate is cited.

Current scientific objectives and technological capabilities--existing or anticipated-- have, to a large extent, lead to the tentative inclusion of the following instrumentation subsystems into the Scientific Instrumentation Package:

- a. High (Spatial) Resolution Camera (f/96).
- b. Two High Resolution Spectrographs
- c. Three Faint Object Spectrographs
- d. Fourier Interferometer
- e. Wide Field Camera (f/12).

The instruments described here are not to be construed as the final choice of instrumentation for the LST. Rather, as chosen, they represent a configuration which:

1. Provides a means of broad range observational capability.
2. Allows the study of packaging problems.
3. Exposes hidden problems.
4. Permits the establishment of tolerance ranges.
5. Provides a reference to explore the interaction of spacecraft pointing, optical performance and detector capability on the overall Scientific Instrumentation system.

Tolerances are assigned to components and subassembly to insure the system will function as predicted in actual operation. In general the system tolerances are the difference between the theoretically possible performance and the required performance. This margin must then be apportioned among all the elements of the system which may cause degradation. The contributors to variation may be divided into three groups.

Group 1. Fabrication Tolerances

Group 2. Assembly Tolerances

Group 3. Dynamic Tolerances

The first group has to do with the radii, surface figure, grating spacing, etc. The second group deals with the placement of elements into the system, alignments and focusing. Group three deals with the motion of components (tilts, decentration defocusing, etc.) that may occur due to thermal changes. This movement of components will have two effects. One is to degrade the image and the other to move it. If the movement time constant is less than the exposure time then the movement is equivalent to an image degradation.

There are two major philosophies which are generally used to apportion tolerances: worst case and statistical. The worst case approach assumes that many units of a small number of components will be used to build the system and that the specifications of the units permit significant variation; it is important that any combination of components fulfill the specifications. The statistical approach assumes negligible the probability of all tolerances of the system acting in concert to maximize the error, and accepts a statistical risk that some system element might have to be remade in order to meet system specifications. The assumption that errors root sum square is the hallmark of this approach. It is considered that this approach is appropriate to the LST instrumentation.

Among the many parameters that may effect image quality, some, if held within tolerances compatible with normal shop practice, have a negligible effect. Such tolerances may then be assigned to these parameters (without increasing cost), which are then entered into a non-relevant (NR) category of our tolerance analysis. Similar parametric variations, whose effects may be compensated for by simple adjustments, may also be entered into a non-relevant category. The tolerances available are then apportioned among the remaining parameters.

## 4.2 HIGH SPATIAL RESOLUTION CAMERA ASSEMBLY

### 4.2.1 General Description

The high resolution camera is a cross-shaped cylinder mounted to the outboard side of the SIP structure. Its optical input is the f/12 bundle at the same focal plane as the fine guidance sensor. This energy bundle is re-imaged by the camera optics (f/96) to a focal plane at the selected sensor's cathode. The 50 x 50 mm cathode image format produces a field of view of 174 x 174  $\mu$ rad in object space. A layout of this assembly is shown in Figure 4-1. The estimated weight of the depicted assembly is 240 kg.

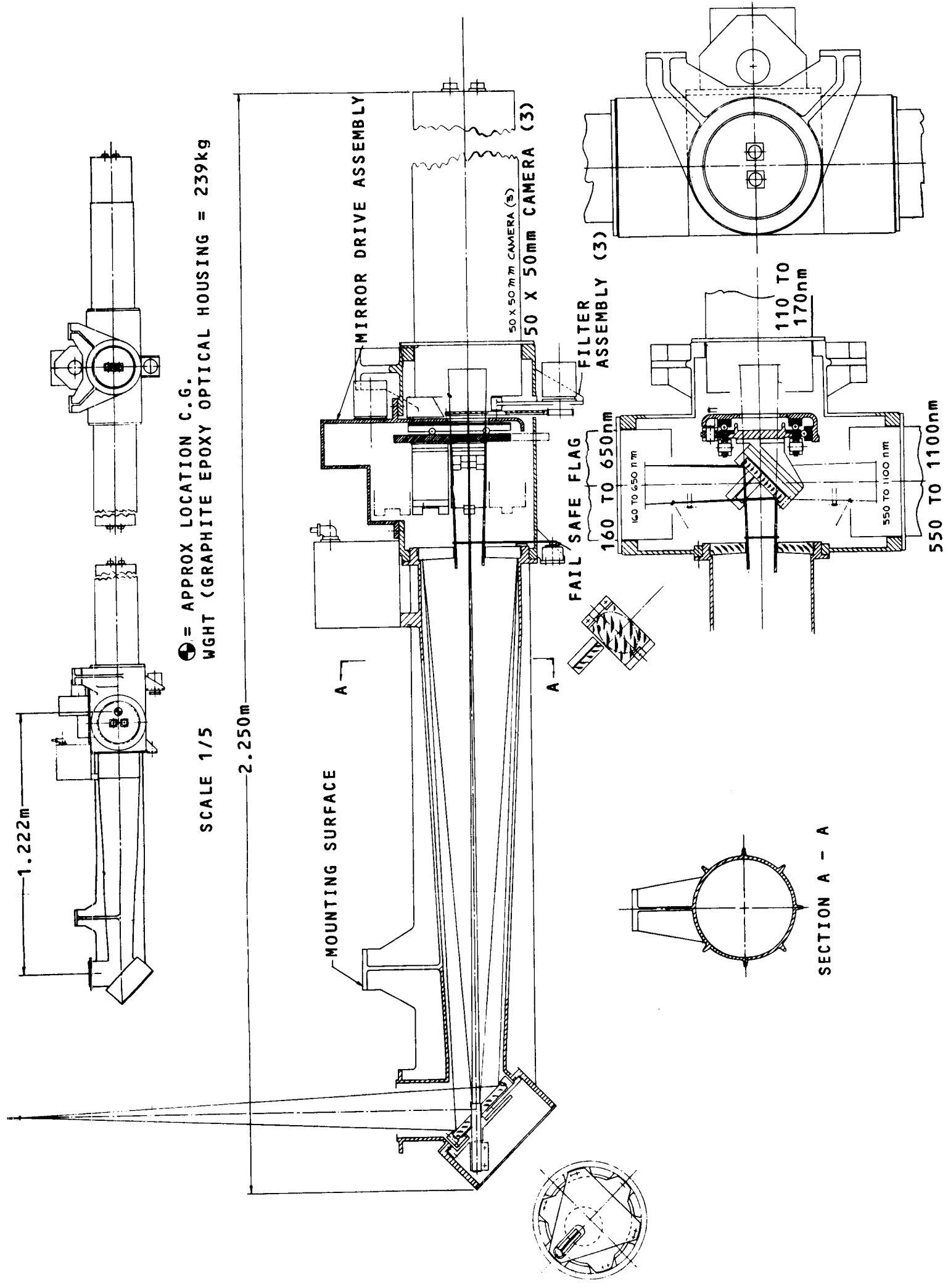


Figure 4-1. High Resolution Camera Assembly

The camera contains three sensors from which the experimenter can choose for response in a particular spectral range of interest or, by successive observations, to explore the total available spectral range. The spectral bands or ranges are as follows:

Range I - 115- 300 nm

Range II - 160- 600 nm

Range III - 500-1100 nm

Each of the three sensors is provided with a filter select mechanism which permits the inclusion of up to four spectral filters. The actual band-pass characteristics of the several filters are not specified at this time.

The positioning of the high resolution camera energy bundles on the desired sensor's cathode is controlled by the Mirror Select and Drive Assembly.

A shutter capable of occulting the energy entering the sensor area is provided to protect the sensors and to permit measurement of sensor dark noise.

A functional schematic of the High Resolution Camera Assembly is shown in Figure 4-2. A family tree, indicating the subassembly sequence and major constituents of the Camera Assembly, is shown in Figure 4-3.

#### 4.2.2 Description of Optics

##### a. Design Consideration

The high resolution camera is intended to achieve the full resolution capability of the OTA over the spectral range of 115 to 1100 nm. Further desirable properties of this instrument are:

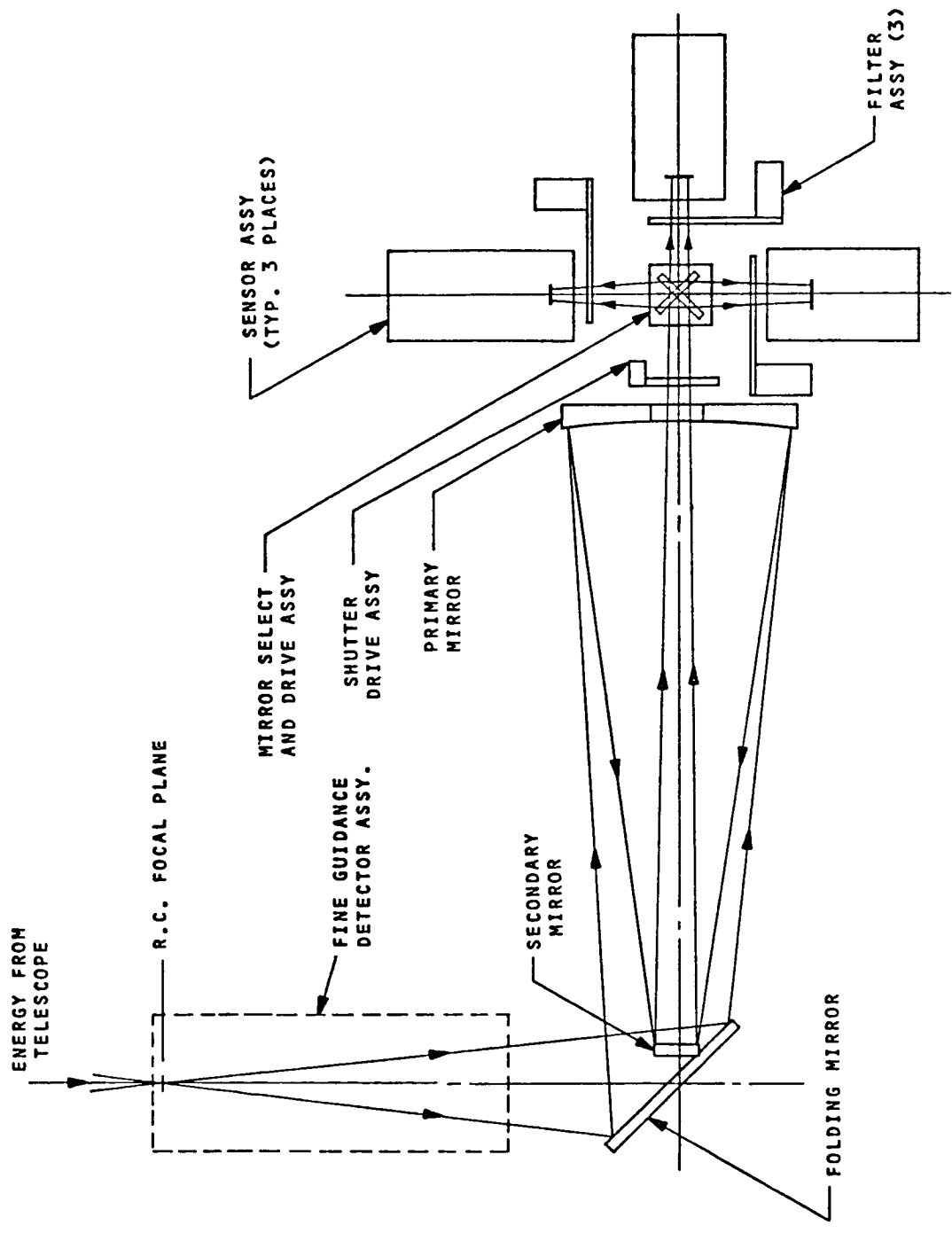


Figure 4-2. High Resolution Camera Assembly Functional Schematic



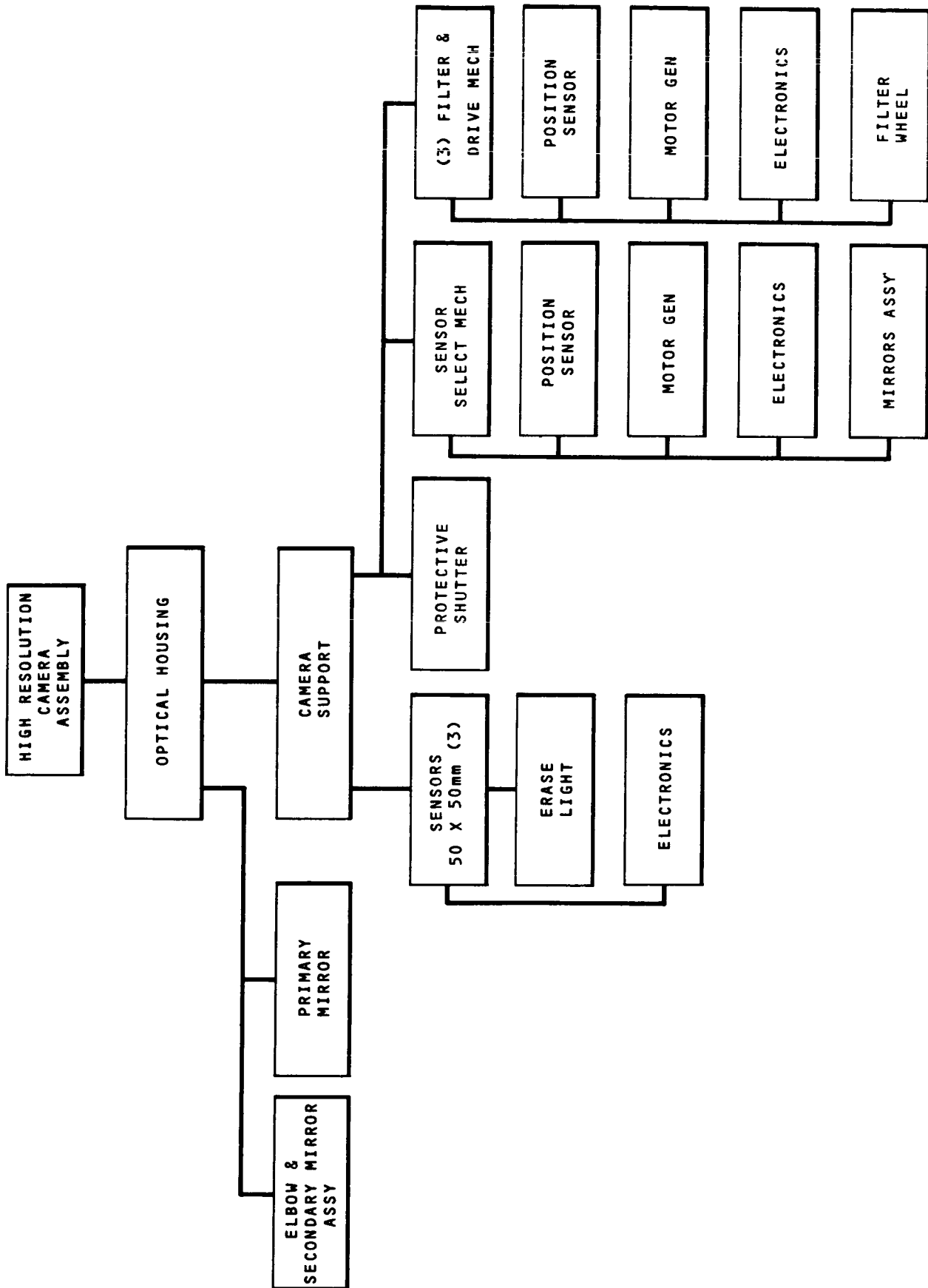


Figure 4-3. High Resolution Camera Assembly Family Tree

1. Maximum field of view.
2. Minimum number of reflections (ultra violet efficiency).
3. Compact as possible.

The broad spectral band demands that a reflective system be used for this instrument. The proposed system is a two mirror inverse Cassegrain that serves both to relay the f/12 image of the Ritchey-Chrétien and to magnify it eight times, forming an f/96 image on the face of a 50 x 50 mm camera tube sensor.

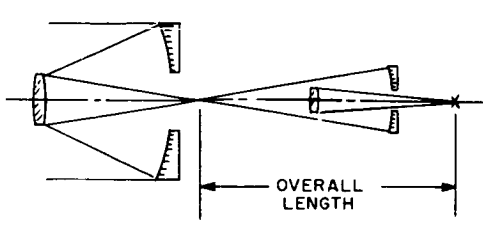
#### b. Optical Path

The high resolution system has been given the highest priority among the LST instruments. It has therefore been kept on axis with respect to the telescope. A diagonal mirror folds the optical path of the camera to a side bay along with the field of the fine guidance. The optical path of the instrument then passes through the center of the fine guidance detector assembly. A second diagonal is introduced to fold the path (avoiding mechanical interferences with the wall of the package) at a right angle. The energy then strikes the primary of the inverse Cassegrain, returns to the secondary, which is mounted inside the folding flat, and then passes through a hole in the primary and images on the tube. The path is shown schematically in Figure 4-2. The optical data for the high resolution camera is given in Figure 4-4.

#### c. Performance

The performance of the high resolution camera may be given in terms of the modulus of the system's Optical Transfer Function. This is given in Figures 4-5 and 4-6. It can be seen that the system is essentially diffraction limited. However, a certain amount of (1) degradation due to tolerancing, and (2) image movement due to pointing instability will occur. See Section 3.

### OPTICAL SYSTEM RECORD

TITLER. C. TELESCOPE WITH 8 X INCA	JOB NO. 100193	DATE 8/10/72
UNITS - ALL DIMENSIONS IN ( )	INSTRUMENT Large Space Telescope f/96 Camera	
	EFL = 2880.0	APER. STOP SURF NO. 1
	BFL = 134.6	ENT. PUPIL DIA. = 302.4
	FFL = -	EXT. PUPIL DIA. = -
	f/NO. 96.0	ENT. PUPIL LOC = 00
	SEMI FIELD ANGLE 9.7μrad	EXT. PUPIL LOC = -
	SPEC. RANGE 200-1000 nm	MAGNIFICATION 8X
	OVERALL LENGTH 220.98	DESIGNED BY M. Amon

SURF NO.	RADIUS		THICKNESS		CLEAR AP	OUTSIDE DIA	GLASS	
	TEST PLATE	CALCULATED ± TOL	CENTER ± TOL				CODE	MELT NO. OR ± TOL.
1		-1320.0	-527.838		303.1		Refl.	
2		-323.6616	720.883		64.6		Refl.	
3	R. C. focus	∞	186.690		-		Air	
4		-138.647	-100.330		17.8		Refl.	
5		-21.464	134.620		7.6		Refl.	
6	f/96 focus	∞			-		Air	
7								
8								
9								
10								
11								
12								
13								
14								
15								
16								
17								
18								
19								
20								

$\lambda_1$	$\lambda_2$	$\lambda_3$	NOTES	Surf No.	Conic Constant
SEIDEL COEFFICIENTS				1	-1.016843
SPH. =				2	-2.253951
COMA =				4	-0.049232
AST =				5	-0.393627
DIST =					
PET =					
LEHR =					
TCHR =					

KOLLSMAN INSTRUMENT CORPORATION

Figure 4-4. Camera Assembly Optical System Record

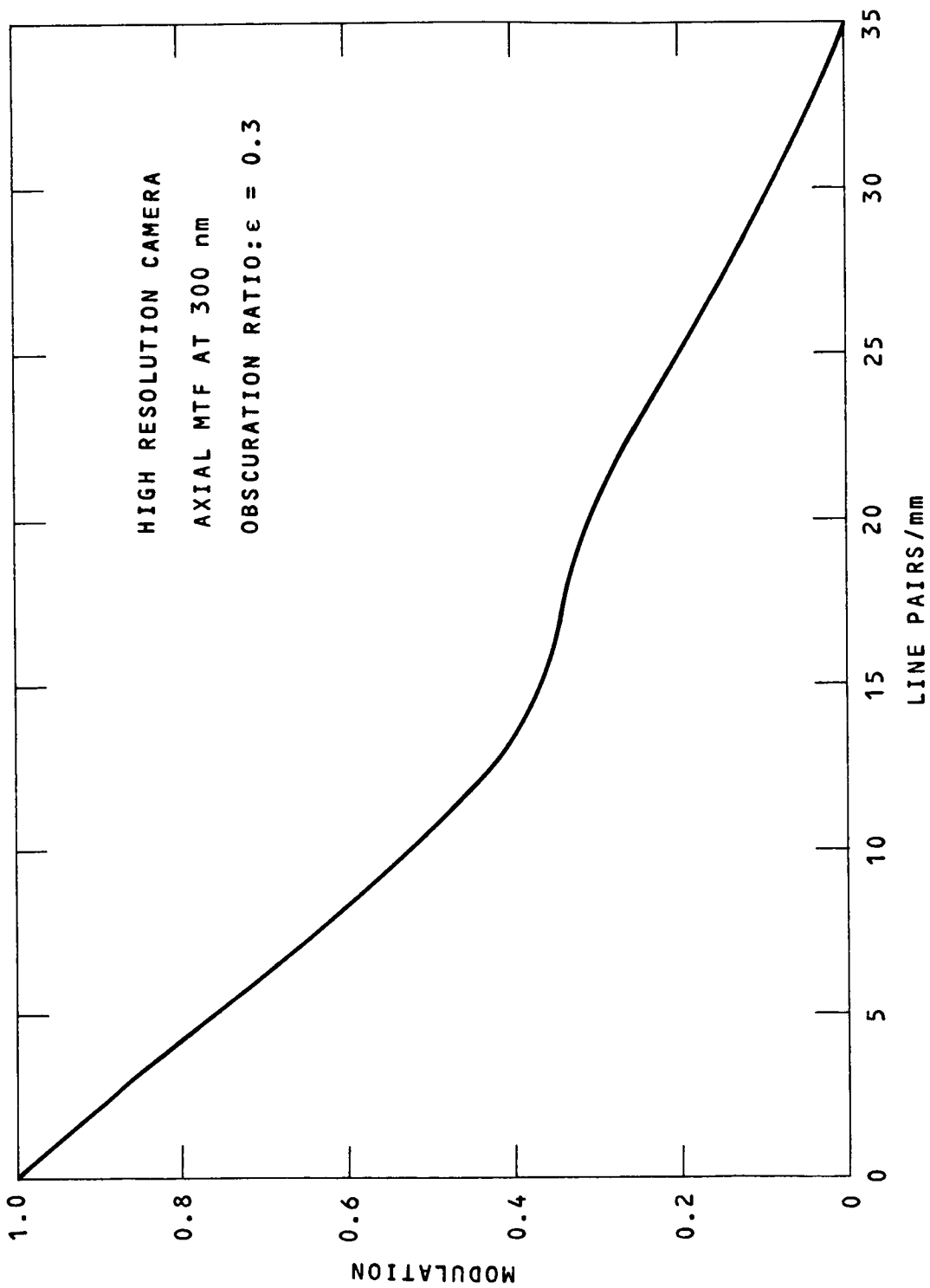


Figure 4-5. High Resolution Camera Axial MTF at 300 nm

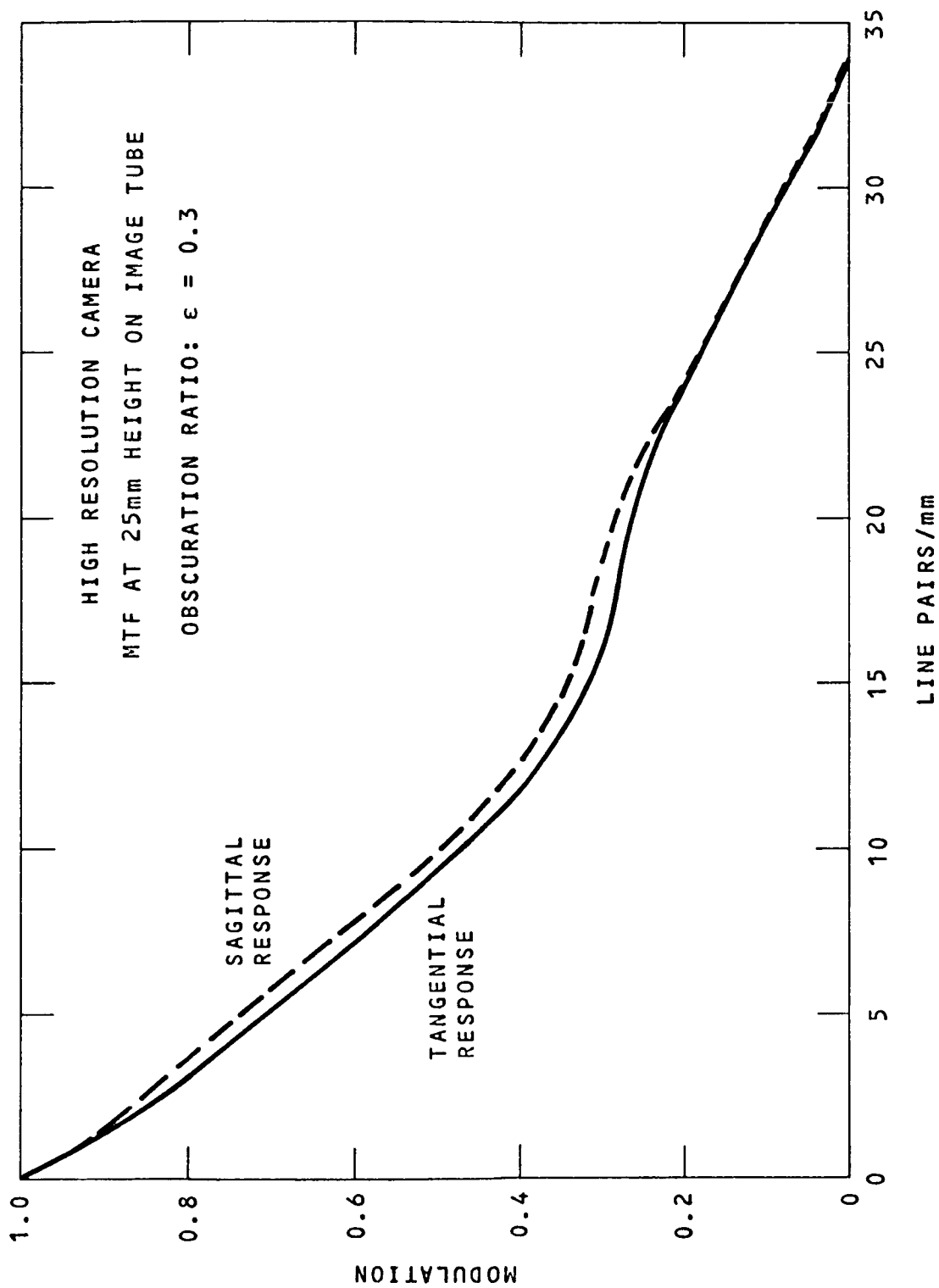


Figure 4-6. High Resolution Camera MTF at 25 mm Height on Image Tube

The reference system is essentially unvignetted out to 25 mm off axis, while vignetting, equivalent to a loss of 1.8 star magnitude, is accepted at 35 mm off axis. A similar system could be designed to give an unvignetted field out to 70 mm, corresponding to the corners of the 50 x 50 mm tube. However, the length of the system must be increased substantially (280 cm) over the proposed 221 cm in order to achieve this.

#### 4.2.3 Tolerance Analysis

The diameter of input image blur, containing 70 percent of the total collected energy, is 1.5 times the Airy disc diameter. At  $\lambda = 300$  nm the diameter of the image blur,  $D_b$ , in the f/96 focal plane is

$$D_b = 2.44 \lambda (f/\text{number}) (1.5)$$

$$D_b = 105 \mu\text{m}$$

A budget of 25  $\mu\text{m}$  additional growth or movement has been established by systems analysis in Section 3 and is used in the prediction of the camera's overall performance.

To establish component tolerances within the camera optics, influence coefficients were determined. These coefficients ( $\delta$  blur) establish the image motion or growth that would occur as a result of a change in a given parameter. The parameters and their respective coefficients ( $\delta$  blur) are given in Tables 4-1 through 4-3 for manufacturing, assembly and dynamic tolerances respectively. From the tabulated data it is clear that manufacturing and assembly tolerances have only small effects on the image and may be entered into a non-relevant category. The dynamic tolerances which indicate the motion of the image during the extended exposure have rather large effects. Five parameters in all have significant effect on the image size or position.

TABLE 4-1. MANUFACTURING TOLERANCES, HIGH RESOLUTION CAMERA

	Starting Value	$\delta$ Value	$\delta$ Blur ( $\mu\text{m}$ )	Tolerance
Radius (Primary)	1386.47 mm	4 mm	0.4	$\pm$ 4.0 mm NR
Radius (Secondary)	214.64 mm	2 mm	1.2	$\pm$ 2.0 mm NR
Conic Constant (Primary)	-0.049232	0.001	5.4	$\pm$ .002 NR
Conic Constant (Secondary)	-0.393627	0.010	1.0	$\pm$ .01 NR
Surface Figure (Primary)				$\lambda/10$ NR
Surface Figure (Secondary)				$\lambda/10$ NR
Surface Figure (Flat)				$\lambda/10$ NR

TABLE 4-2. ASSEMBLY TOLERANCES, HIGH RESOLUTION CAMERA

	Starting Value	$\delta$ Value	$\delta$ Blur ( $\mu\text{m}$ )	Tolerance
Separation f/12 Focus to Primary	7208.88 mm	1.0 mm	0.6	$\pm$ 0.1 mm NR
Separation Primary to Secondary	1003.3 mm	1.0 mm	0.6	$\pm$ 0.1 mm NR
Tilt Primary	0.0	870 $\mu\text{rad}$	50	49 $\mu\text{rad}$ NR
Tilt Secondary	0.0	870 $\mu\text{rad}$	2	49 $\mu\text{rad}$ NR
Decentration Primary	0.0	0.1 mm	4	0.1 mm NR
Decentration Secondary	0.0	0.1 mm	4	0.1 mm NR



TABLE 4-3. DYNAMIC TOLERANCES, HIGH RESOLUTION CAMERA

	Starting Value	$\delta$ Value	$\delta$ Blur (mm)	Normalized	Tolerances
Separation f/12 Focus to Primary	1866.9 mm	1.0	0.625	.112 mm	0.07 mm
Separation Primary to Secondary	1003.3 mm	1.0	1.6	.044 mm	0.026 mm
Separation to f/96 Focus	1346.2 mm	1.0	0.0002	-	1.0 mm
Tilt Primary	0.0	870 $\mu$ rad	26.0	0.835 $\mu$ rad	0.4 $\mu$ rad
Tilt Secondary	0.0	870 $\mu$ rad	2.35	9.7 $\mu$ rad	4.3 $\mu$ rad
Decentration Primary	0.0	0.1 mm	2.16	0.011 mm	0.005 mm
Decentration Secondary	0.0	0.1 mm	1.26	0.019 mm	0.008 mm

The separation between primary and secondary, the tilt, and the de-centration of each component of the Inca are the significant tolerances. The relevant changes are then normalized to values that would give a 25  $\mu\text{m}$  change in the image. These values are then divided by the square root of five (5) and are then assigned as tolerance for these parameters. The impact of this analysis upon the structural design is discussed in Section 7.

#### 4.2.4 Sensors

Among the desired performance parameters of this field camera are a spectral coverage from 110 to 1100 nm and the largest field of view consistent with detector format. Based on the latter parameter, the 50 x 50 mm SEC-Vidicon presently under development is tentatively selected for this application.

Based on the detailed study shown in Section 6, the candidate photocathode-window types and their respective spectral coverage in nanometers reviewed for this application are:

- |                               |                         |
|-------------------------------|-------------------------|
| a. CsI - $M_gF_2$             | 115 < $\lambda$ < 180   |
| b. CsTe - $M_gF_2$            | 115 < $\lambda$ < 300   |
| c. Bialkali - $M_gF_2$        | 115 < $\lambda$ < 600   |
| d. Bialkali - $SiO_2$ (fused) | 160 < $\lambda$ < 600   |
| e. S-20 - $SiO_2$ (fused)     | 160 < $\lambda$ < 700   |
| f. III-V - Glass              | 500 < $\lambda$ < 1,100 |

The above cathode/window combinations suggest the possibility of a two sensor tube complement, c and f, to accommodate the spectral requirements of the high resolution camera. However, improved performance results from the use of three sensor tubes. This is particularly true in the UV range where spectral selectivity is supplemental to that obtainable by the inclusion of yet to be determined spectral filters; the selectivity effectively eliminates the deleterious influence of space background which affects a wide spectral response cathode (bialkali or trialkali). Quantitatively, the S/N curves for Range I, shown in the next sub-section, are valid even in regions of the sky where the background is an order of magnitude greater than the assumed average background of one +23 magnitude star in 25 psr.

Further considerations in the sensor selection are the partial redundancy and cross-calibration capability offered by the overlapping of the several spectral ranges.

Additional considerations relative to the high resolution camera's sensors, detailed in Section 6, are:

1. Three different III-V cathode types are reviewed. All require development for a semitransparent photocathode. Additionally, present information suggests that a temperature lower than 250K is required for stability of these negative electron affinity detectors.
2. Window material, suitable for long-lived space application, effectively limits the shorter wavelength response to 120 nm for the dimmest stars and to possibly 115 nm for the very bright targets.

#### 4.2.5 Signal To Noise Analysis

Based on the general equation derived in Appendix B, a signal-to-noise ratio is computed for each of the three spectral ranges. In ranges I and II, a comparison between two photocathode/window combinations is made in each range; a single combination covers range III.

The throughput analysis in subsection 3.6 derives the photoelectron spectral density per second for several cathode materials. Considering the fact that the semitransparent photocathodes exhibit a lower quantum efficiency than the reflective type of the same material (a single conversion path is used compared to a double path in the reflective type), a one-third loss in Q.E. is assumed in the semitransparent version of the III-V (Range III) photocathode.

a. Range I

Two possible photocathode-window combinations:

CsTe/MgF<sub>2</sub>

CsI/MgF<sub>2</sub>

are used in the signal-to-noise computations. The throughput data in Figure 3-19 yields the spectral current density,  $N_o(\lambda)$ , computed for the high resolution camera and a zero magnitude star. From this, the total signal,  $S_m$ , is computed for the assumed magnitude  $m$ :

$$S_m = (2.51)^m t \int_{\lambda_1}^{\lambda_2} N_o(\lambda) d\lambda$$

with  $\lambda_1$  and  $\lambda_2$  the corresponding integration limits

CsTe/MgF<sub>2</sub>

CsI/MgF<sub>2</sub>

$$\lambda_1 = 115 \text{ nm}, \lambda_2 = 300 \text{ nm}; \quad \lambda_1 = 115 \text{ nm}, \lambda_2 = 180 \text{ nm}$$

and  $t = 3.6 \times 10^4$  s (10 hrs) the maximum assumed integration time for both choices. Different magnitudes were assumed for the two choices in order to arrive at a comparable S/N ratio:

$$m = 29 \quad ;$$

$$S_{29} = 325 \text{ pe} \quad ;$$

$$m = 26$$

$$S_{26} = 337 \text{ pe}$$

At the above signal levels the background noise and the dark noise are negligible compared to the quantum noise and readout noise ( $n_R = 11.3 \text{ pe rms}$ ).

The general formula for S/N, discussed in Appendix B, simplified for the high resolution camera, Range I conditions, is:

$$S/N_m = \frac{S_m}{\sqrt{S_m + (n_R)^2}},$$

from which the signal to noise values are:

$$S/N_{29} \cong 15.3 \text{ for CsTe/MgF}_2; \text{ and } S/N_{26} \cong 15.7 \text{ for CsI/MgF}_2$$

Conclusion: in Range I, CsTe provides better S/N characteristics.

#### b. Range II

##### 1. Bialkali/MgF<sub>2</sub>

Using the throughput values from Figure 3-20, and  $\lambda_1 = 120 \text{ nm}$ ,  $\lambda_2 = 600 \text{ nm}$  and  $t = 3.6 \times 10^4 \text{ sec}$ .

$$N_o(t) = \int_{120}^{600} N_o(\lambda) d\lambda = 1.44 \times 10^{10} \text{ pe/sec}$$

$$S_o = t N_o(t) = 5.18 \times 10^{14} \text{ pe}$$

The solid angle,  $\Omega$ , subtended by the image (at 300 nm) is 0.1 psr.

$$S_\beta = \frac{0.1}{25} S_{23} = 1300 \text{ pe}$$

The photocathode area occupied by the star image is

$$a = \Omega(f)^2 = 8.3 \times 10^{-5} \text{ cm}^2$$

At room temperature the dark count is

$$N_D = a Nt = 120$$

$$\text{The readout count } (n_R)^2 = 128$$

$$S_{\text{lim}} = 2 + 2 \sqrt{1549} = 81$$

$$m_{\text{lim}} = 2.5 \text{ Log } \frac{5.18 \times 10^{14}}{0.81 \times 10^2} = 32$$

## 2. S-20/SiO<sub>2</sub>

Using the same procedure outlined above, and

$$\lambda_1 = 160 \text{ nm}, \lambda_2 = 700 \text{ nm}, \text{ and } t = 3.6 \times 10^4 \text{ sec}$$

$$S_o = 1.07 \times 10^{15} \text{ pe} \quad (n_R)^2 = 128$$

$$S_\beta = 2690 \quad S_{\text{lim}} = 129$$

$$N_D = 1200 \quad m_{\text{lim}} = 32.3$$

The results of the range II calculations are summarized in Figure 4-7. As can be seen the S-20/SiO<sub>2</sub> is the preferred cathode material for this application.

## c. Range III

### Signal:

From the throughput computation in Figure 3-21, the values of  $N_o(\lambda)$  for  $T = 11,000\text{K}$  and  $m = 0$  star are integrated between the wavelength limits  $\lambda_1 = 500 \text{ nm}$  and  $\lambda_2 = 1.100 \text{ }\mu\text{m}$  resulting in a zero magnitude signal:

$$S_o = 3.2 \times 10^{14} \text{ photoelectrons for an integration time}$$

$$t = 3.6 \times 10^4 \text{ s (10 hrs.)}$$

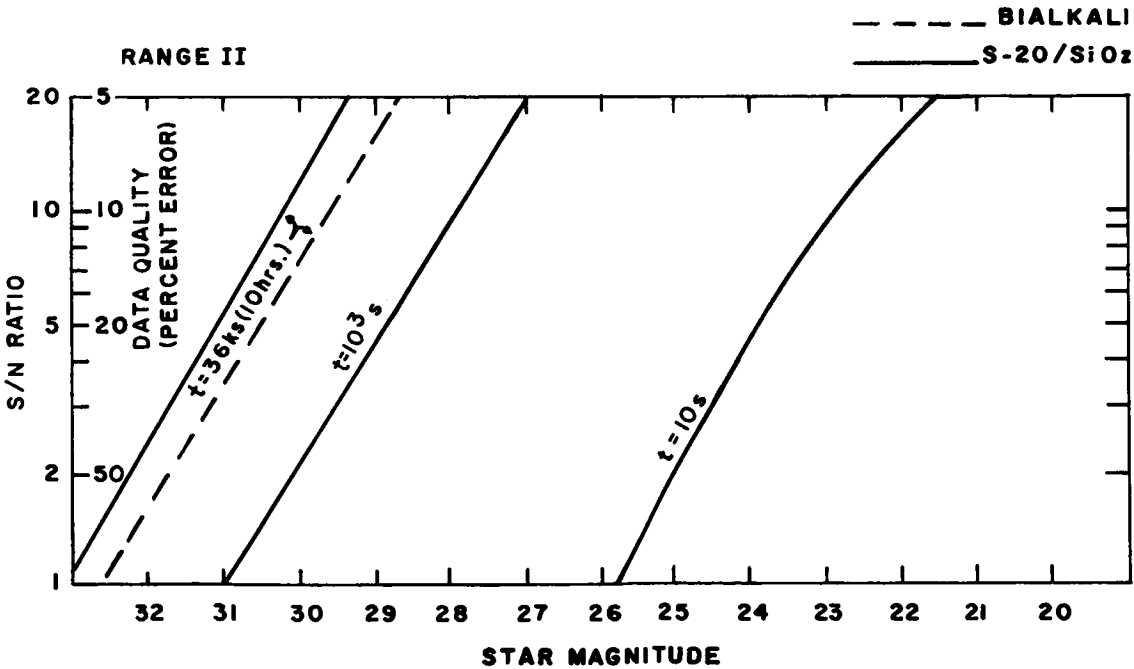
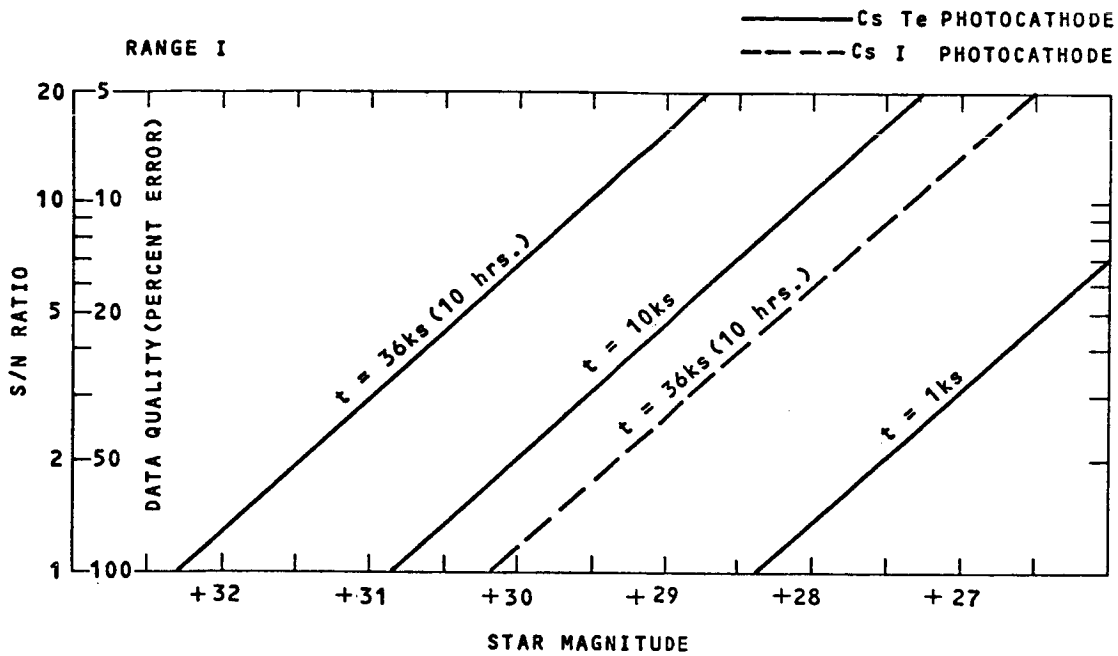


Figure 4-7. S/N Ranges I and II Curves, High Resolution Camera

For an assumed star magnitude  $m = +28$ , the signal is

$$S_{28} = 6.25 \times 10^{-12} S_0 = 2,000 \text{ photoelectrons.}$$

It should be noted that the signal does not saturate the target despite the apparent saturation level, since the image area at the center wavelength  $\lambda = 800 \text{ nm}$ , is approximately seven times larger than the image at  $\lambda = 300 \text{ nm}$ , used in Range II (the image subtends 24 pixels, each  $25 \mu\text{m}$  in size). Section 6 states saturation begins at 1.0 electrons per  $\mu\text{m}^2$  or 625 electrons per pixel.

Noise:

$$\text{Background noise count: } S_B = S_{23} \frac{\Omega}{25}$$

The solid angle subtended by the image is  $\Omega \approx 0.7[\text{psr}]$

$$S_{23} = 6.25 \times 10^{-10} S_0 = 2 \times 10^5 [\text{pe}], \text{ hence } S_B = 5600 (\text{pe})$$

$$\text{Dark count: } N_D = aNt$$

$$\text{The image area: } a \approx 1.5 \times 10^{-4} [\text{cm}^2]$$

$$t = 3.6 \times 10^4 [\text{s}]$$

$$\text{at } T = 293\text{K}^{(1)} \quad N \approx 4 \times 10^3 [\text{pe/cm}^2\text{-s}]$$

(Fig. 6-3)

$$N_n = 2 \times 10^4 [\text{pe}] \quad (833 \text{ pe/pixel} - \text{slightly saturated})$$

The readout (noise) count,  $(n_R)^2 = 128 \text{ pe}$ , is negligible.

At the above levels of signal and noise, the S/N ratio is:

$$S/N = \frac{2000}{\sqrt{2000 + 5600 + 2 \times 10^4}} \approx 13$$

Additional points were computed for brighter stars and shorter integration times. Figure 4-8 shows these plots.

The limiting magnitude ( $S/N = 2$ ) is  $m \approx 30$ , obtained with a cesiated gallium-indium-arsenide (III-V)/glass photocathode/window combination.

---

(1) May require cooling to  $T = 250 \text{ K}$ .



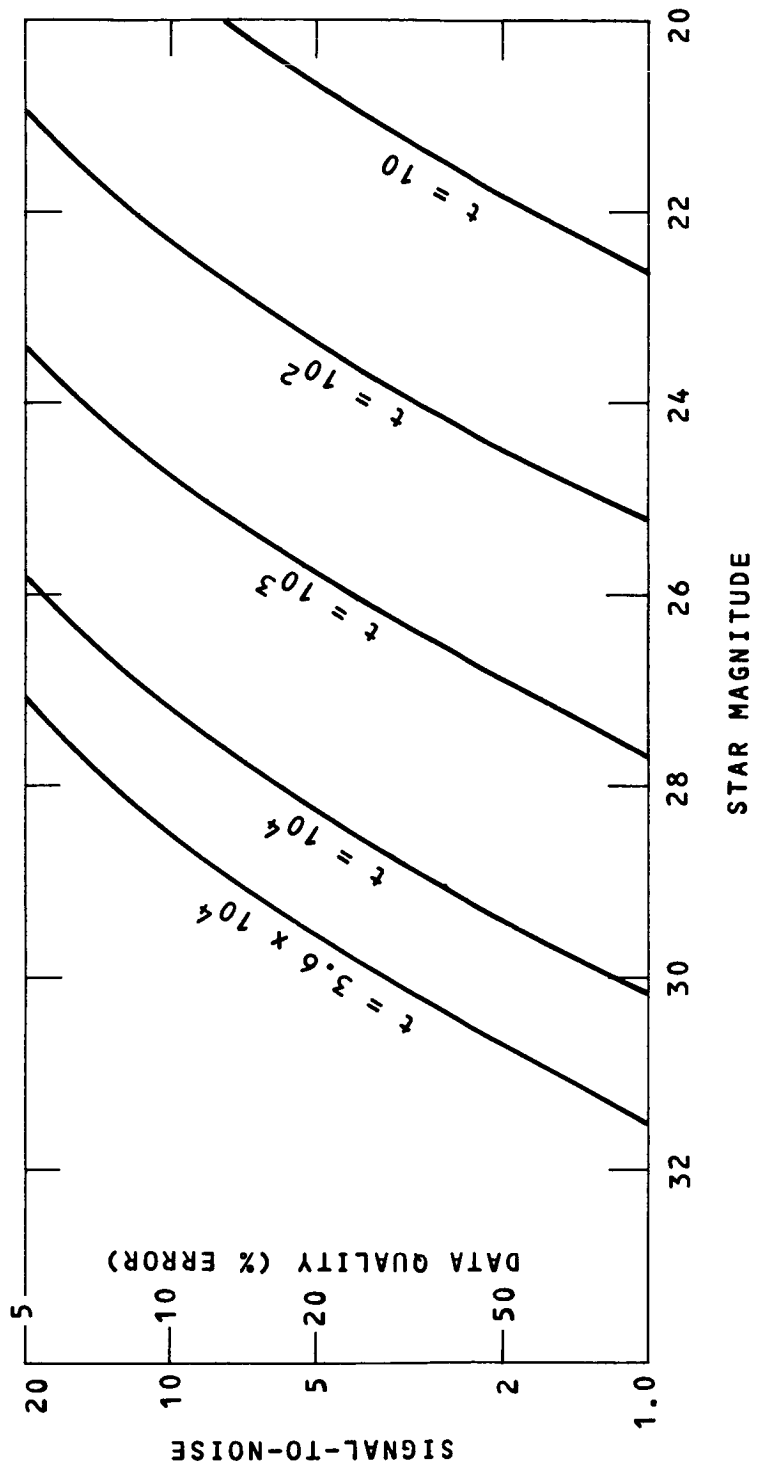


Figure 4-8. High Resolution Camera, Range III, Signal-to-Noise Ratio as a Function of Star Magnitude and Integration Time

## 4.3 HIGH RESOLUTION SPECTROGRAPHS

### 4.3.1 General Description of the Reference Configuration

The reference High Resolution Spectrograph consists of two nearly identical instruments, one which covers the spectral range 110 to 180 nm, and one which covers the spectral range 180 to 350 nm. The major differences in the instruments are the grating ruling frequencies and the photocathodes of the detectors. Referring to Figure 4-9, the input is the f/12 bundle which passes through the entrance aperture to the off-axis parabola which collimates the light and directs it to the echelle grating. The dispersed light leaving the echelle falls on the cross disperser which disperses the light at right angles to the direction of the echelle dispersion. The doubly dispersed light then falls on the camera mirror which focuses the trapezoidal array of orders on the 25 mm detector photocathode.

The two spectrographs are the largest of the instrument group and are located in the aft section of the SIP, as shown in Figure 1-1. Each instrument weighs 62.4 kg. Instrument selection in the aft section is accomplished by first offsetting the LST so that the object of interest passes through the slit. Then the off-axis collimator is rotated about the telescope axis to the position which directs the light to the selected echelle grating.

A functional schematic is shown in Figure 4-9 and the family tree in Figure 4-10.

### 4.3.2 Description of Optics

#### a. Design Considerations

In a single line spectrograph with a spectral resolution of  $\frac{\lambda}{\Delta\lambda} = 3 \times 10^4$ , the image format is over three meters long. An effort to keep this data within a more reasonable format size inevitably leads to an echelle spectrograph. The echelle grating

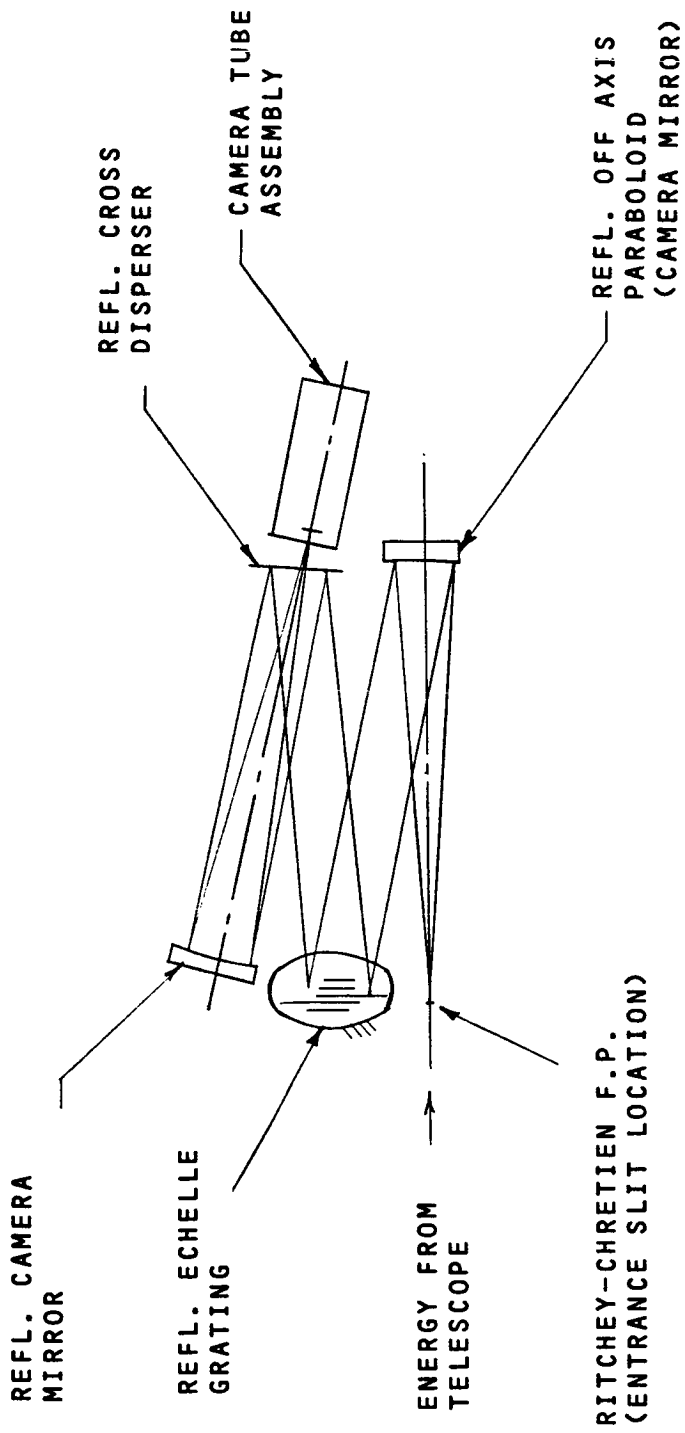


Figure 4-9. High Resolution Spectrograph, Functional Schematic

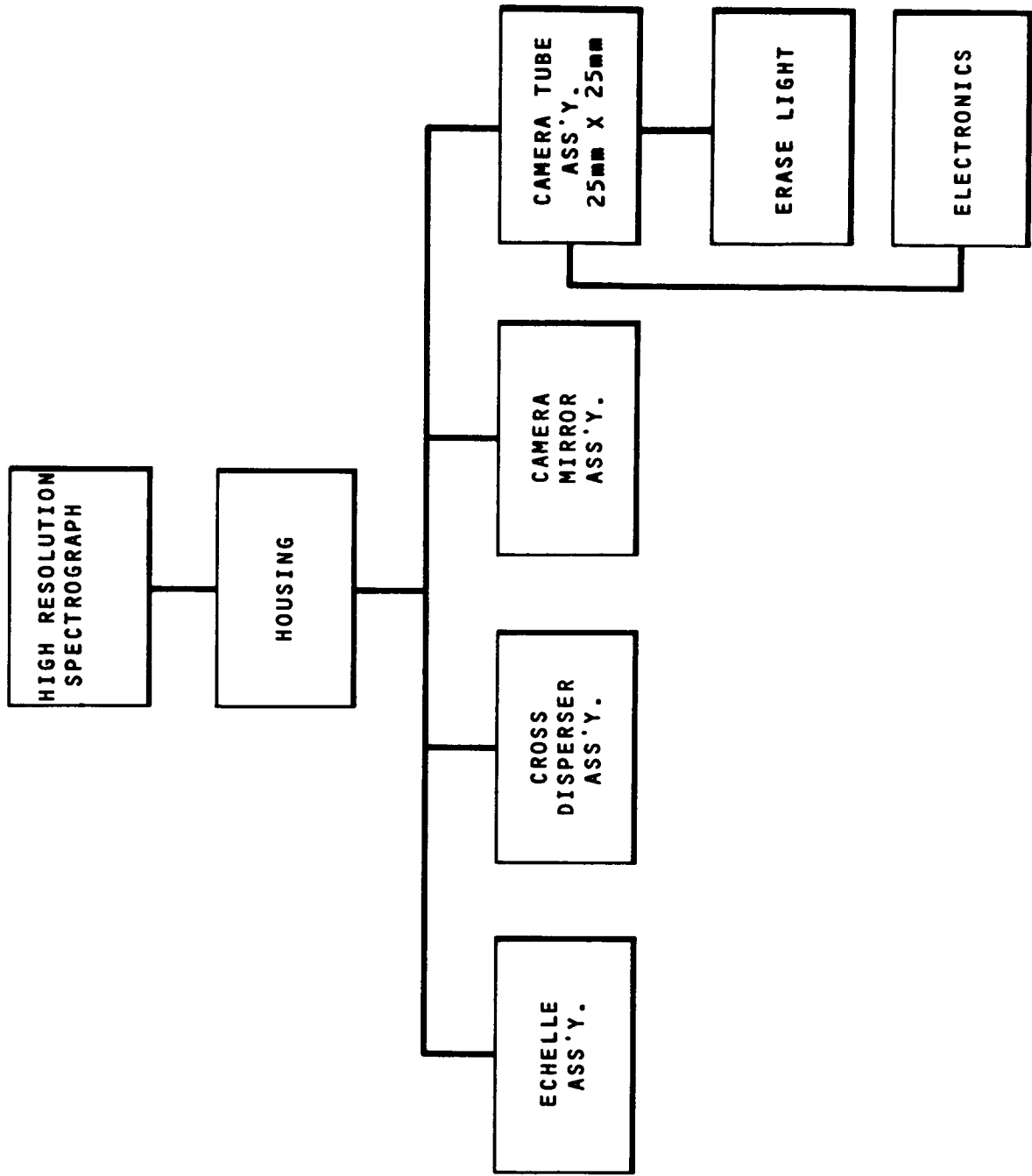


Figure 4-10. High Resolution Spectrograph, Family Tree, I or II

can supply the necessary dispersion, but it works at very high orders and the orders overlap. A second grating (known as a cross disperser) is required to separate the overlapping orders.

The efficiency of an echelle and cross disperser combination causes an energy loss that increases rapidly with spectral bandwidth. Figure 3-5 shows an intensity curve as a function of wavelength for an echelle and normal grating. If the spectrum extends beyond  $\frac{2}{3} \lambda_0$  to  $2 \lambda_0$ , the system operates near the bottom of the intensity curve. It is for this reason that we are forced to divide the spectral range of 115 to 350 nm between two instruments. The first covers the spectral band from 115 to 180 nm and the second from 180 to 350 nm.

The spectral and angular resolution for each instrument is consistent with the 50  $\mu\text{m}$  length of a detector resolution cycle (two TV lines) at 50% MTF. A rather extensive study was carried out to determine the optimum configuration for the spectrographs. A series of echelle spectrographs was designed and the image size due to aberrations, diffractions and telescope tolerances was determined. This was done as a function of the camera mirror focal length and diameter, yielding a family of solutions shown in Figure 4-11. There is an optimum condition at f/10: it yields the smallest image regardless of the diameter of the camera mirror. It would be attractive from a packaging point of view to use as small an instrument as possible. However, the camera mirror forms the final image through a hole in the cross disperser, and this hole forms an obscuration. As long as this obscuration is less than or equal to the obscuration formed by the secondary mirror, no additional energy is lost. A 120 mm diameter is the minimum that may be used and still conform with this requirement.

#### b. Optical Path

Both instruments function in the same manner. An off-axis paraboloid accepts the energy from the star image formed by

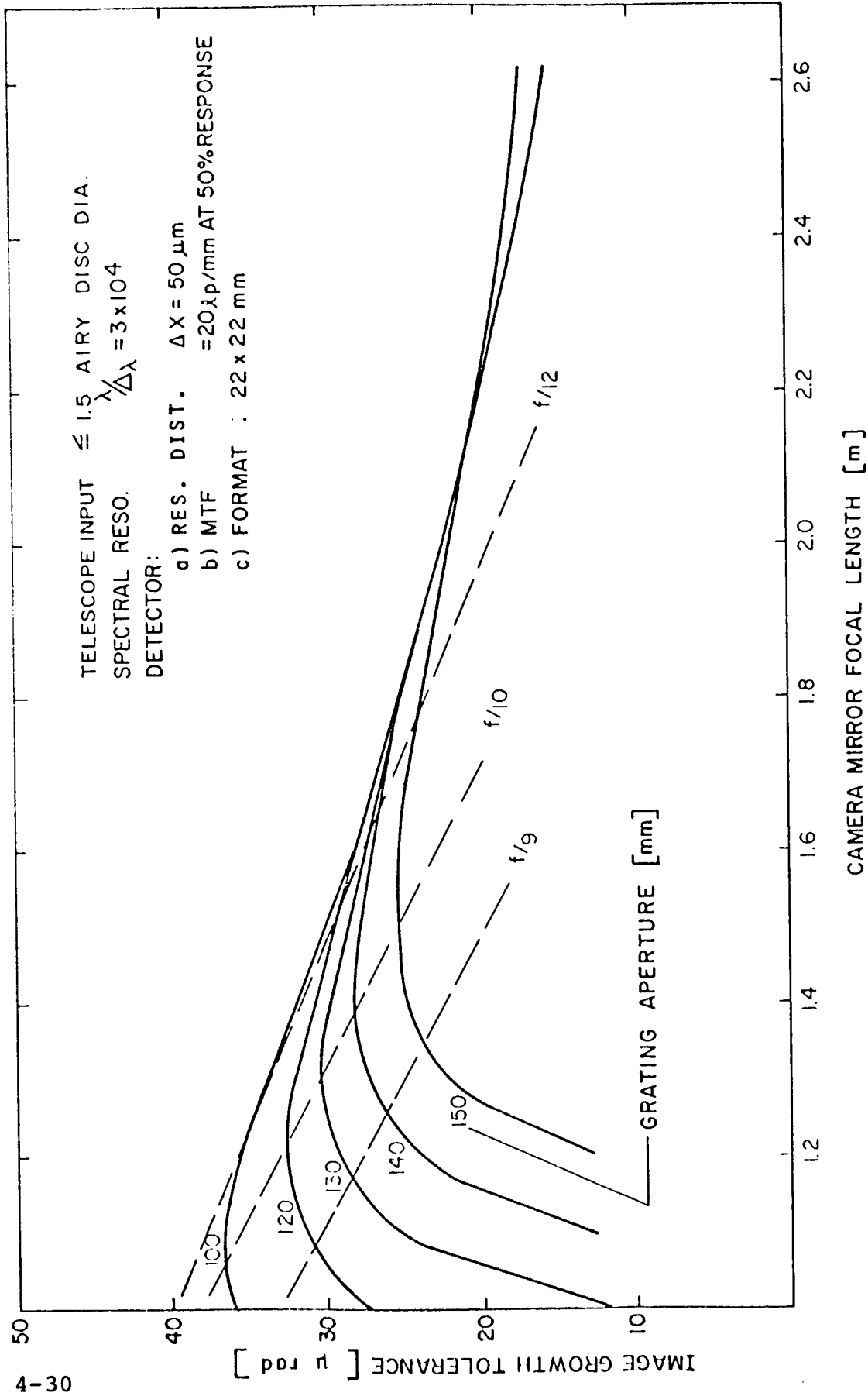


Figure 4-11. High Resolution Spectrograph, Error Budget For Various Camera Mirror and Grating Parameters

the telescope and renders the light parallel. The paraboloid may be pivoted to feed either one of the high resolution spectrographs (It will also be used to feed a faint object spectrograph). The collimated bundle is then dispersed by the echelle grating and again by the cross disperser. The energy is then focused by a camera mirror operating at  $f/10$  through a hole in the cross disperser. It is essential to have the camera mirror operate on axis. The coma and astigmatism of a spherical mirror increase very rapidly with the field angle. The detailed design data for the lower and upper wavelength echelle is given in Figures 4-12 and 4-13, respectively.

c. Baffles

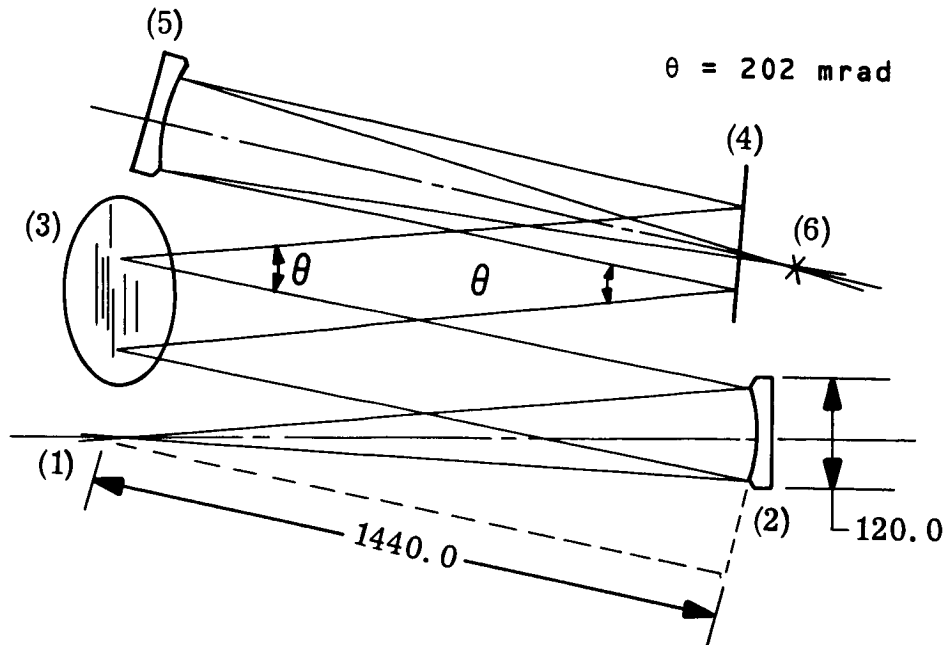
Unwanted illumination may enter the focal plane of the instrument in two ways. The first and most serious is unfocused light that may come off a reflective surface and impinge directly on the tube. Light may also reflect from the walls and structural parts and find its way to the focal surface.

Figure 4-14 shows a cut away view of the high resolution spectrograph. It is necessary to block the dispersed energy that leaves the echelle and passes directly through the hole in the cross disperser. The baffle used is a tubular structure cut away on one side so that it prevents energy from passing through the hole in the cross disperser, yet does not introduce any additional vignetting or obscuration; it is shown in Figure 4-9. This would be the only direct source of unwanted illumination on the tube.

The structure itself is open at only one end to receive the collimated light from the off-axis paraboloid. This provides a natural shielding; furthermore, all of the structure is kept well outside the field of view so that energy will not be scattered by the walls and find its way into the focal plane. The slit itself shields out energy from stars and background in the vicinity of the star under investigation.

# HIGH RESOLUTION SPECTROGRAPH

RANGE 1 (115 to 180 nm)



Surface No.	Radius*	Conic Constant	Thickness*	
(1)	$\infty$	-	1440.00	Ritchey-Chretien F.P.
(2)	-2880.0	-1.0	1335	Ref1. Off Axis Paraboloid
(3)	$\infty$	-	1035	Ref1. Echelle Grating
(4)	$\infty$	-	1130	Ref1. Cross Disperser
(5)	2410.0	-	1205	Ref1. Camera Mirror
(6)	$\infty$	-	-	Tube*

Surface 3: Echelle Rulings = 73.04 lines/mm; Blaze Angle = 765 mrad.

Surface 4: Cross Disperser = 260.8 line/mm; Blaze Angle = 13.8 mrad.

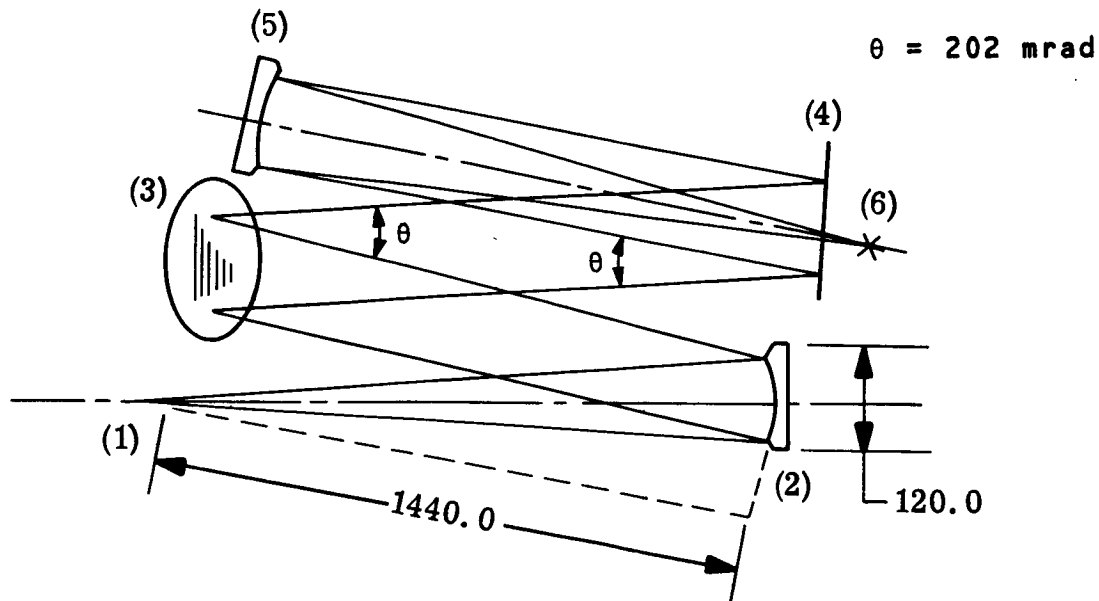
\* Image format 22 x 22; (all dimensions in millimeters)

Figure 4-12. High Resolution Spectrograph  
Range 1 (115 to 180 nm)



# HIGH RESOLUTION SPECTROGRAPH

RANGE 2 (180 to 350 nm)



Surface No.	Radius*	Constant	Thickness*	
(1)	$\infty$	-	1440.00	Ritchey-Chretien F.P.
(2)	-2880.00	-1.0	1335	Ref1. Off Axis Paraboloid
(3)	$\infty$	-	1035	Ref1. Echelle Grating
(4)	$\infty$	-	-1130	Ref1. Cross Disperser
(5)	2410.0	-	1205	Ref1. Camera Mirror
(6)	$\infty$	-	-	Tube*

Surface 3: Echelle Rulings = 45.77 lines/mm; Blaze Angle = 502 mrad.

Surface 4: Cross Disperser = 107.39 lines/mm; Blaze Angle = 17.5 mrad.

\* Image format 22 x 22; (all dimensions in millimeters)

Figure 4-13. High Resolution Spectrograph  
Range 2 (180 to 350 nm)

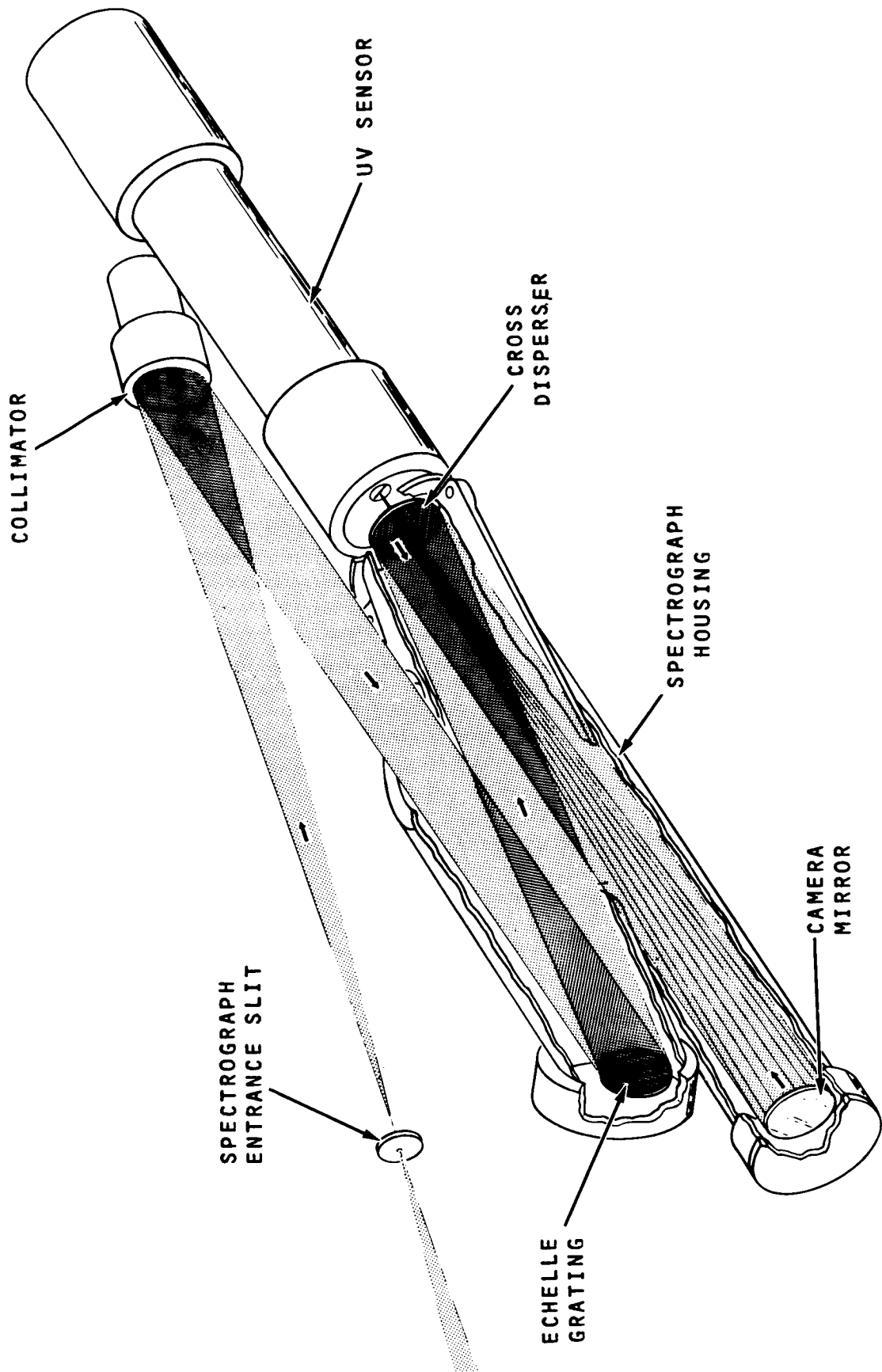


Figure 4-14. High Resolution Spectrograph

The baffle which shields the tube from the echelle's illumination may itself be a source of indirectly scattered energy which reaches the image plane. The dispersed energy from the echelle and cross disperser will carry part of the light outside the tube's field of view; this energy may strike the inner walls of the baffle and scatter. The baffle cannot be made thick enough to use rings or light traps without introducing some additional obscuration or vignetting. Further study in Phase B is required to eliminate this problem.

#### d. Performance

Sample wavelengths were traced through the Ritchey Chretien telescope and the high resolution spectrographs to determine the size and shape of the image. Figure 4-15 shows the spectral format for the High Resolution Spectrograph. Figures 4-16 through 4-18 are spot diagrams of sample wavelengths covering the entire spectral range of the lower wavelength echelle spectrograph. They show the image size and dispersion of the instrument at the top, middle, and bottom of the image format. The procedure is repeated for the upper wavelength High Resolution Spectrograph. The results are shown in Figures 4-19 to 4-21.

The spot diagrams indicate that the image will be considerably smaller than the 0.05 mm line pair. These spot diagrams are the result of geometric ray traces. The effects of aperture diffraction and tolerances required for the telescope and instruments will also contribute to the image size. Thermal gradients could cause relative motion between components of the system during extended exposure times (up to 10 hours) and further degrade the image.

The image size is estimated to be about 0.025 millimeters. Therefore, the image may double in size and still remain within a resolution element. It would appear that this is a generous tolerance for the spectrograph. However, any angular motions that occur

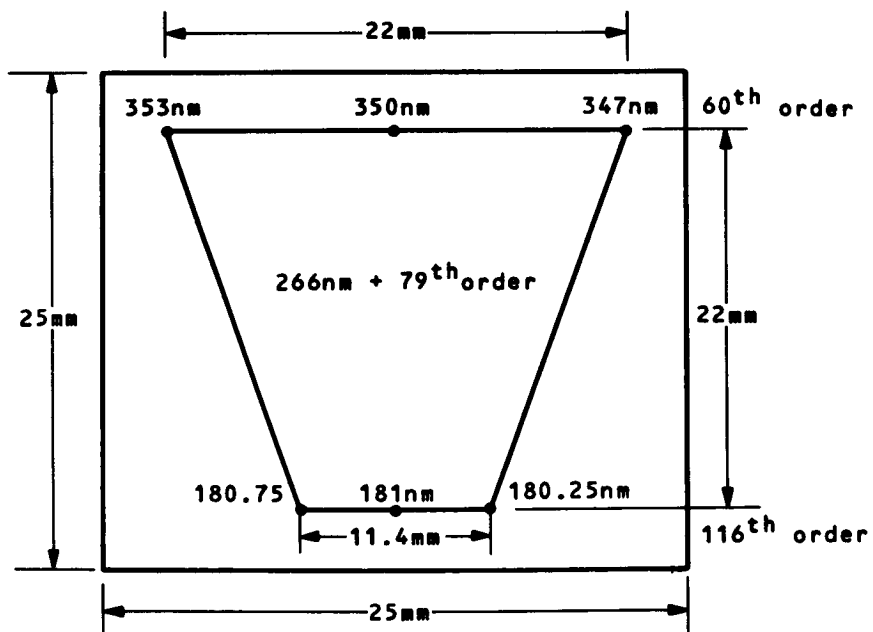
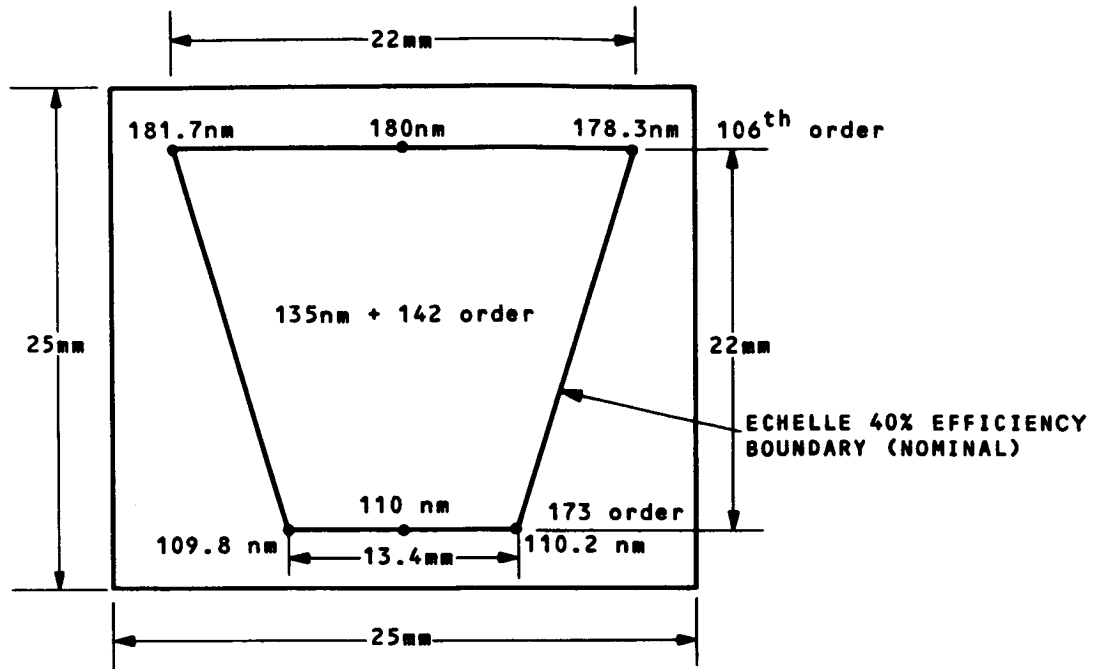


Figure 4-15. High Resolution Spectrograph Spectral Formats

$$\lambda = 180 \text{ nm} \pm 6.0 \times 10^{-3} \text{ nm}$$

106 ORDER

$$\frac{\lambda}{\Delta \lambda} = 4.5 \times 10^4 \text{ Resolution}$$

TOP OF IMAGE FORMAT

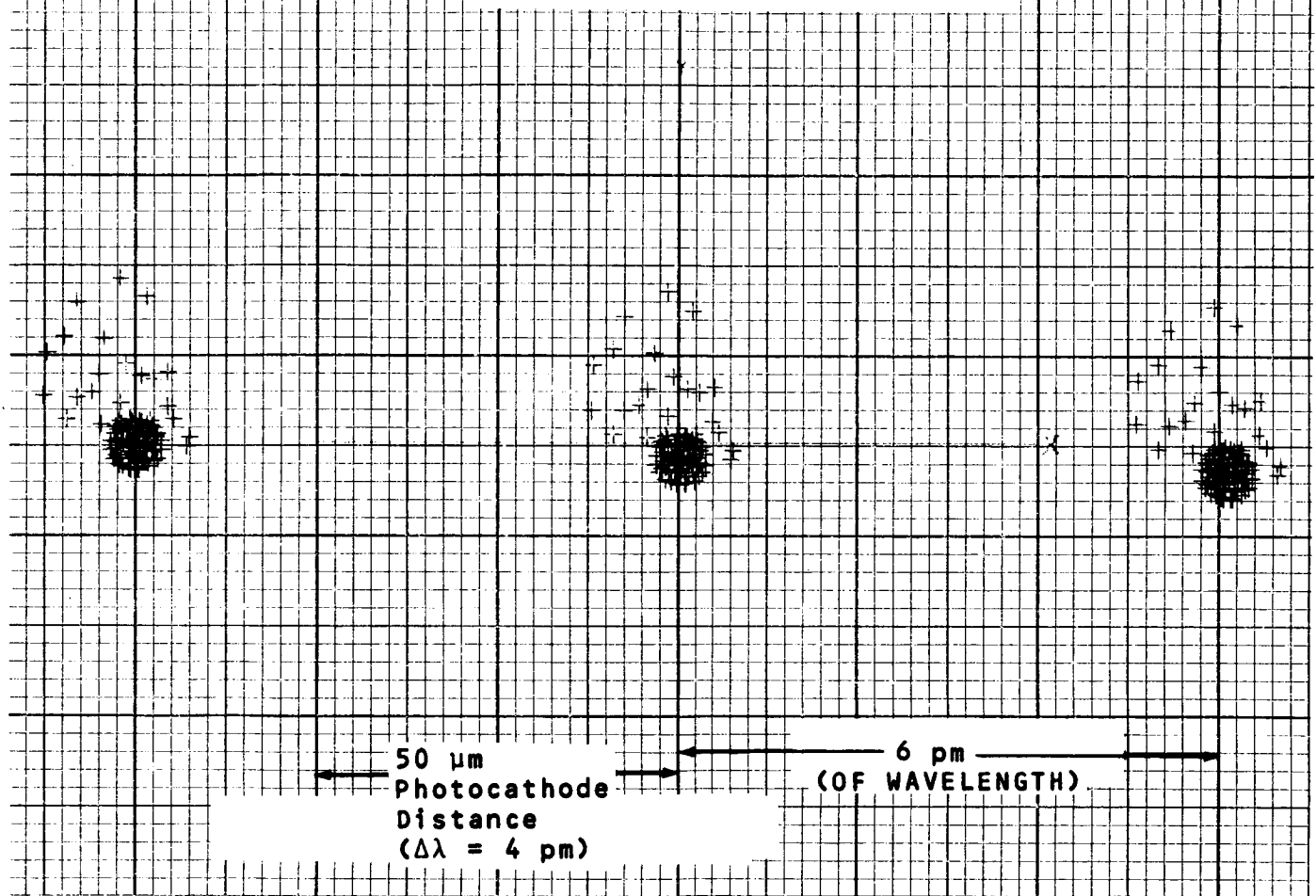


Figure 4-16. Lower Wavelength High Resolution Spectrograph Spot Diagram

$$\lambda = 135 \text{ nm} \pm 4.5 \times 10^{-3} \text{ nm}$$

142 ORDER

$$\frac{\lambda}{\Delta \lambda} = 4.5 \times 10^4$$

MIDDLE OF IMAGE FORMAT

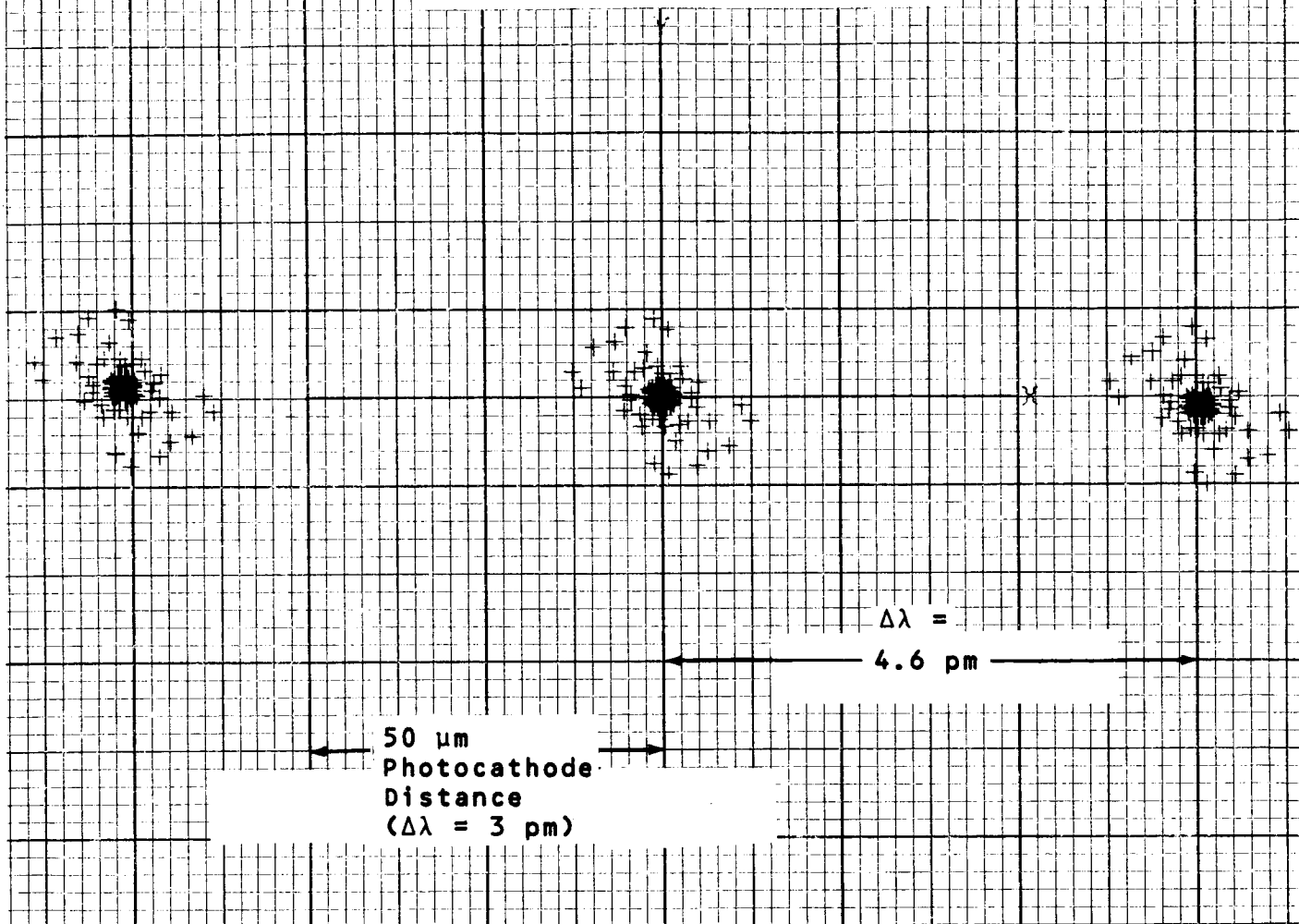


Figure 4-17. Lower Wavelength High Resolution Spectrograph Spot Diagram

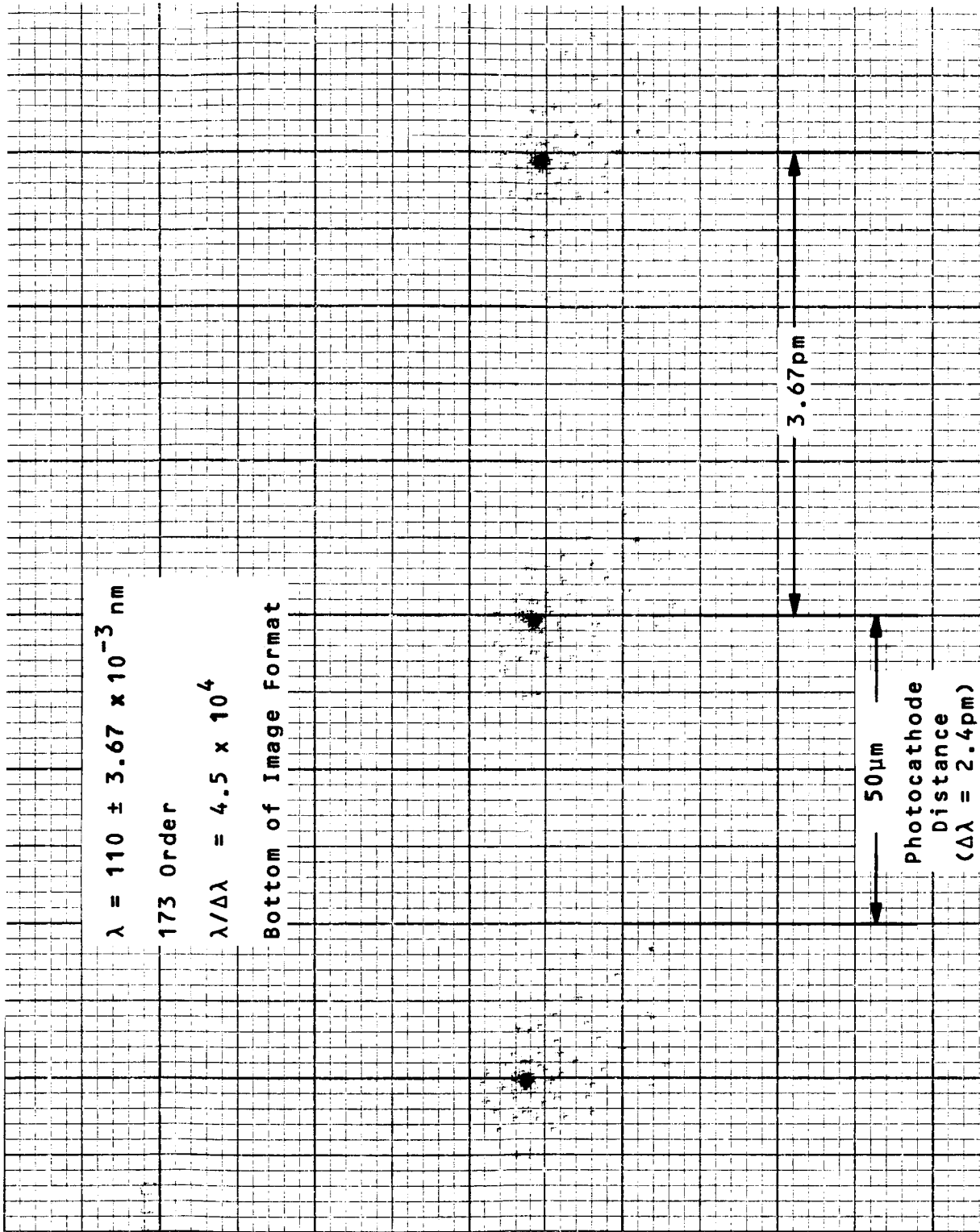


Figure 4-18. Lower Wavelength High Resolution Spectrograph Spot Diagram

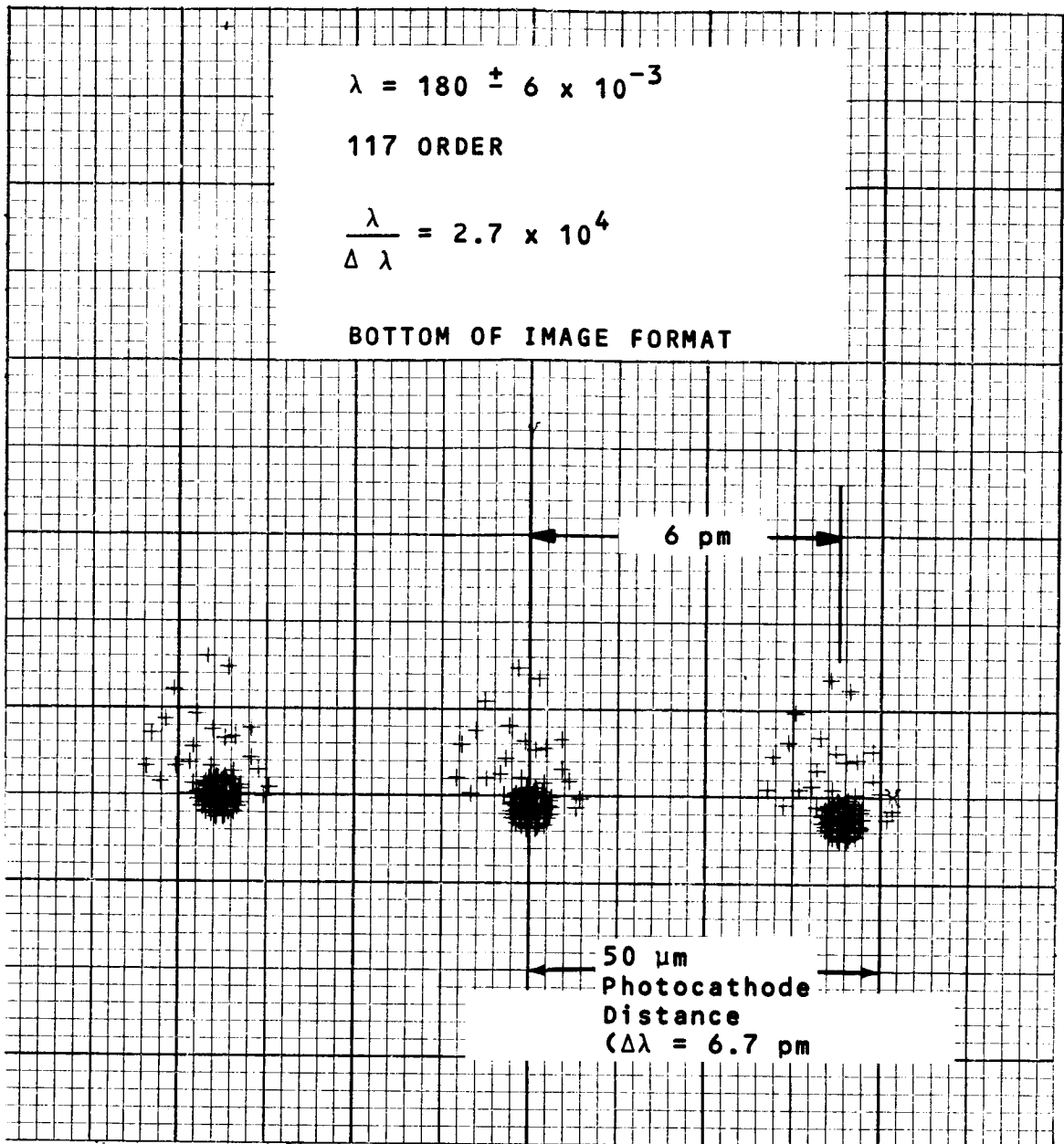


Figure 4-19. Upper Wavelength High Resolution Spectrograph Spot Diagram



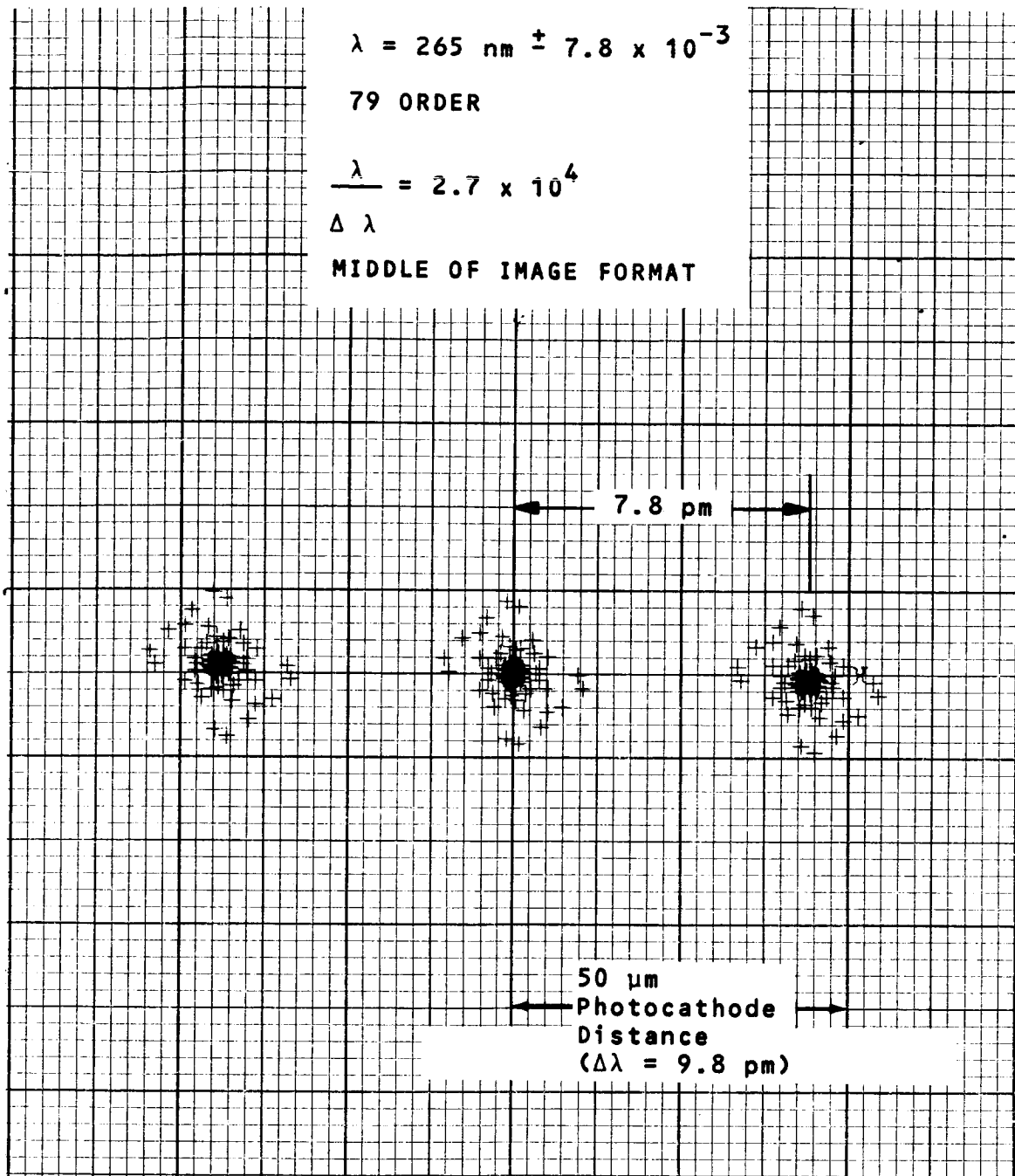


Figure 4-20. Upper Wavelength High Resolution Spectrograph Spot Diagram

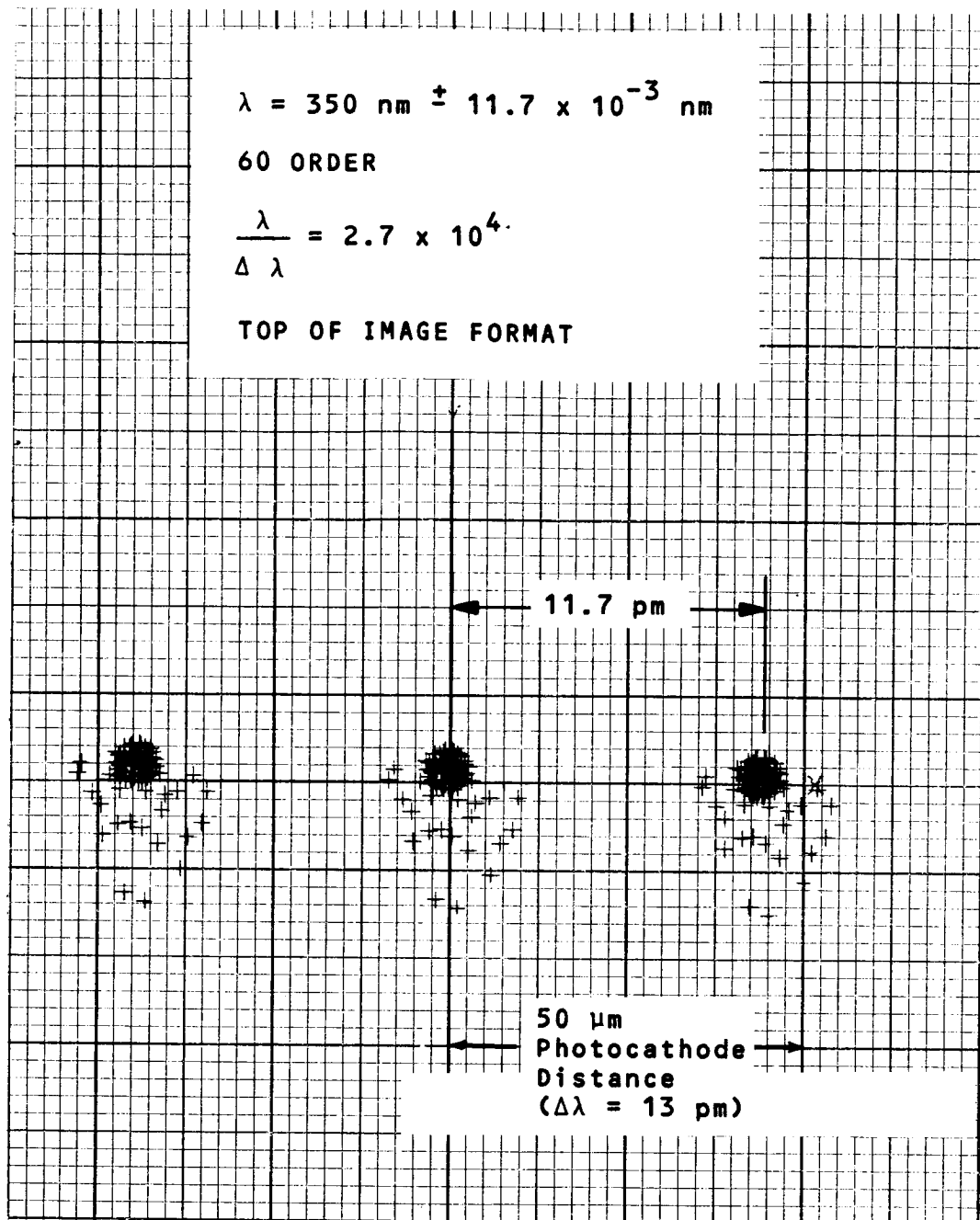


Figure 4-21. Upper Wavelength High Resolution Spectrograph Spot Diagram

during exposure periods would use this tolerance up very rapidly. Thirty  $\mu$ rad of image error (not space angle) is available but a motion of 15  $\mu$ rad would completely use up this tolerance (the angle doubles for a reflective element). This tolerance cannot be given to one component but must be distributed among the four elements of the spectrograph.

#### 4.3.3 Tolerance Analysis - High Resolution Spectrograph

The manufacturing tolerances may be classified as non-relevant. If the radius of the paraboloid is not exactly that of the theoretical value, it may be compensated for at assembly time. However, a change in this radius which may result from thermal variations is equivalent to a defocus; this is considered a dynamic tolerance. In assembly as well, it can be seen that most parameters are insensitive to variations that would occur under normal shop tolerancing. The paraboloid renders the beam collimated and it remains collimated to the echelle and cross disperser; it is then focused by the camera mirror. The echelle grating and cross disperser are flat, albeit grooved elements and therefore have little or no effect on the image quality due to tilt or decentration. The cross disperser may also be tilted or decentered through a small angle without degrading the image. These same changes will move the image during an exposure; as stated earlier, a displacement is equivalent to enlarging the image. It can easily be seen from the table that the bulk of the tolerance must be reserved for the dynamic group. The spot diagram indicates that the image due to geometric aberrations is about .010 mm as determined by geometric ray tracing. The diffraction blur is comparable in size. Allowing two (2) Airy discs for the telescope at the 180 nm wavelength, the diffraction blur size is obtained from (2) (2.44) ( $\lambda$ ) (f/#):

$$(2) \times 2.44 \times .000180 \times 10 = 0.01 \text{ mm}$$

By a combination of linear sum and R.S.S., these image values are approximately .013 millimeters. The  $\Delta\lambda$  is 0.05 mm; this leaves 0.037 mm of tolerance to be divided among the relevant tolerances. Since it is expected that the dynamic tolerances will be more difficult to hold, they are given a larger share. The manufacturing and assembly tolerances are allowed 0.012 millimeters; the dynamic tolerances are allowed 0.025 millimeters. In combination, they should never exceed 0.050 mm. Each relevant tolerance is then normalized to the maximum blur size. In the case of assembly tolerance, it is 0.012 mm and 0.025 mm for the dynamic tolerance. The tolerance then assigned is that value divided by the square root of the total number of relevant tolerances.

If we allow these tolerances to be exceeded, the spot would grow still further. Figure 4-22 is a plot of spectral resolution versus total spot diameter, the spot size resulting from the effects of physical optics, tolerances, and thermal and mechanical disturbances, all of which are integrated over a time which is large with respect to the natural period of each. The figure shows that a total blur diameter limited to 50  $\mu\text{m}$  results in a spectral resolution of  $4.5 \times 10^4$ ; an increase to 75  $\mu\text{m}$  (fifty percent larger than a 50  $\mu\text{m}$  resolution element) brings the resolution down to the minimum allowable design value:  $3 \times 10^4$ .

This graph may be used to determine the spectral resolution as the spot grows in size. It may be considered independent of the cause of image growth.

The error budget for manufacturing assembly, and for dynamic tolerances are given in Tables 4-4 through 4-6.

#### 4.3.4 Detector

The High Resolution Spectrograph uses an echelle grating in conjunction with a cross disperser for order separation. This results in a trapezoidal rendition of the spectral range on the 25 x 25 mm photocathode of an all magnetic SEC-Vidicon detector.

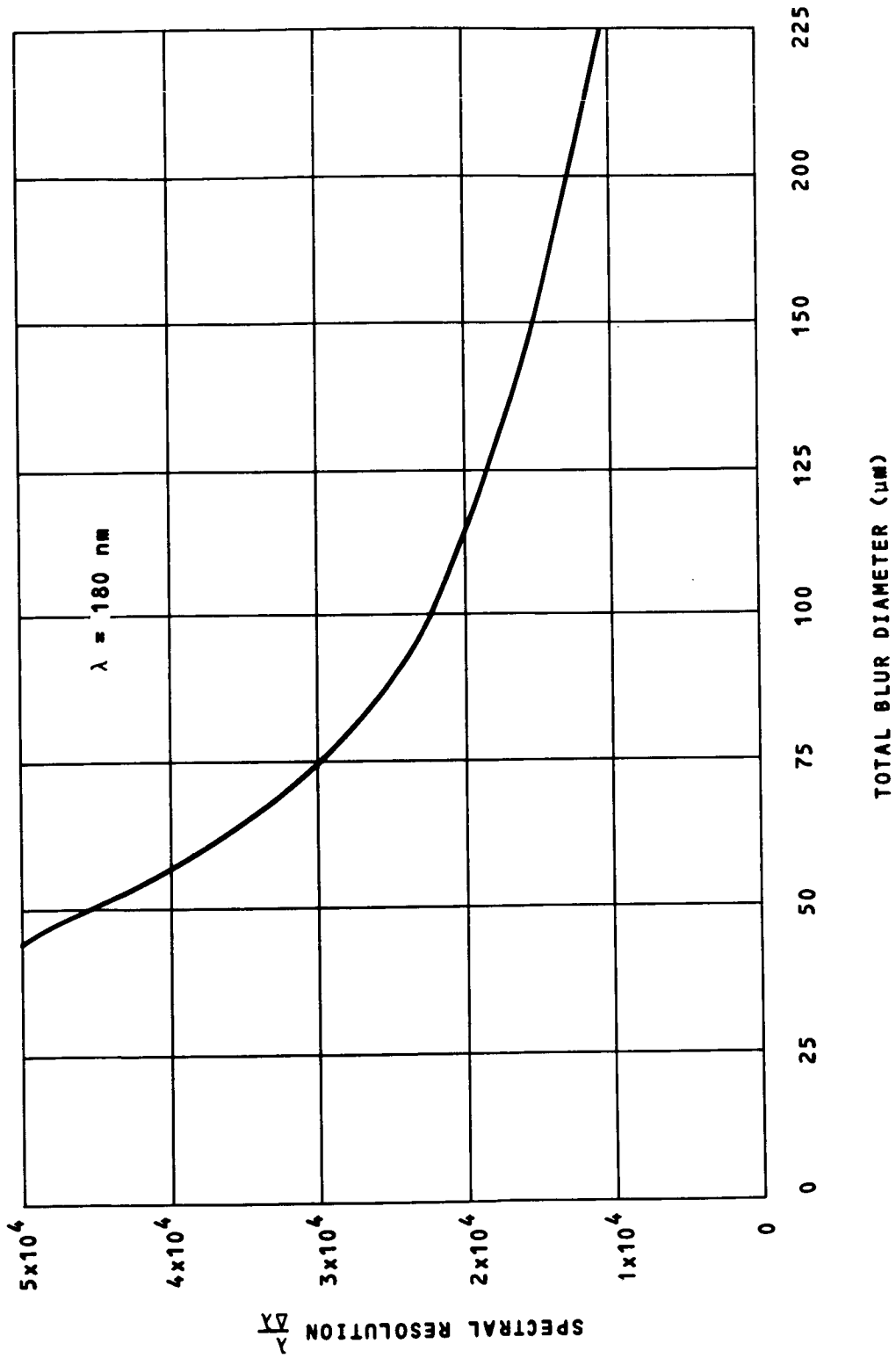


Figure 4-22. Spectral Resolution versus Total Image Blur Diameter

TABLE 4-4. MANUFACTURING TOLERANCES, HIGH RESOLUTION SPECTROGRAPH

	Starting Value	$\delta$ Parameter	$\delta$ Blurr (mm)	Tolerance	Non Relevant
Radius of Paraboloid	2880 mm	1.0 mm	0.0	$\pm 30$ mm	NR
Conic Constant	-1.0	0.001	0.0025	$\pm 0.0005$	
Radius of Imaging Mirror	2160 mm	1.0 mm	0.0	$\pm 30$ mm	NR

TABLE 4-5. ASSEMBLY TOLERANCES, HIGH RESOLUTION SPECTROGRAPH

	Starting Value	$\delta$ Parameter	$\delta$ Blurr (mm)	Tolerance	Non Relevant
Focus of Paraboloid	1440	.05 mm	.002	0.15 mm	
Tilt of Paraboloid	0.0	50 $\mu$ rad	.00085	6 $\mu$ rad	
Decentration of Paraboloid	0.0	0.025 mm	.0003	$\pm$ 0.5 mm	
Separation of Echelle	1335	1.0 mm	0.0	1.0 mm	NR
Separation Echelle to Cross Disperser	1306	1.0 mm	0.0	60 mm	NR
Separation Cross Disperser to Camera Mirror	1130	1.0 mm	0.0	1.0 mm	NR
Sep. Camera Mirror to Focus	1205	1.0 mm	0.006	$\pm$ 1.0 mm	
Tilt Echelle	0.0	300 $\mu$ rad	0.0	300 $\mu$ rad	NR
Tilt Cross Disperser	0.0	300 $\mu$ rad	0.0	300 $\mu$ rad	NR
Tilt Camera Mirror	0.0	300 $\mu$ rad	0.0	300 $\mu$ rad	NR
Decentration Echelle	0.0	0.1 mm	0.0	0.1 mm	NR
Decentration Cross Disperser	0.0	0.1 mm	0.0	0.1 mm	NR
Decentration Camera Mirror	0.0	0.1 mm	0.0	0.1 mm	NR

TABLE 4-6. DYNAMIC TOLERANCES, HIGH RESOLUTION SPECTROGRAPH

	Starting Value	$\delta$ Parameter	$\delta$ Blurr (mm)	Tolerance	Non Relevant
Radius of Paraboloid	-2880 mm	0.1 mm	0.002	0.6 mm	
Focus of Paraboloid	1440.0 mm	0.05 mm	0.002	0.3 mm	
Tilt	0.0	50 $\mu$ rad	0.060	7.5 $\mu$ rad	
Separation to Echelle	1335 mm	1.0 mm	0.0	1.0 mm	NR
Separation Echelle to Cross Disperser	1035 mm	1.0 mm	0.0	1.0 mm	NR
Separation Cross Disperser to Camera Mirror	1130 mm	1.0 mm	0.0	1.0 mm	NR
Separation Camera Mirror to Focus	1205 mm	1.05 mm	0.006	0.075 mm	
Tilt Echelle	43.93°	50 $\mu$ rad	0.060	7.5 $\mu$ rad	
Tilt Cross Disperser	0.0	50 $\mu$ rad	0.060	7.5 $\mu$ rad	
Tilt Camera Mirror	0.0	50 $\mu$ rad	0.060	7.5 $\mu$ rad	
Decentration Echelle	---	0.1 mm	0.0	0.1 mm	NR
Decentration Cross Disperser	---	0.1 mm	0.0	0.1 mm	NR
Decentration Camera Mirror	---	0.1 mm	0.0	0.1 mm	NR



Two instruments are used to accommodate the required spectral coverage. Accordingly, a suitable photocathode/window combination was selected after an initial investigation, as discussed in Section 6 of this document:

Range I  $110 < \lambda < 180 \text{ nm}$       Bialkali/MgF<sub>2</sub>

Range II  $180 < \lambda < 350 \text{ nm}$       Bialkali/Fused SiO<sub>2</sub>

Target: KCl - short lag; susceptible to shock and vibration;  
Gain: 50-100, Life: 3 years<sup>(1)</sup>

Target Size: 25 x 25 mm

Operation Mode:

1. Exposure to irradiance (unscanned) with field mesh potential up to 1000 VDC.
2. Single raster scan readout.
3. Target erasure cycle - preparation for subsequent exposure.

Maximum Integration Time:  $t_s = 36 \text{ ks}$  (10 hrs)

Image Section: Fixed Focus

Resolution: 20 cycles/mm at 50% MTF

Readout Scan Time: 25 seconds

Data Transmission Link: 0.5 megabits/sec

Size:  $1 \times 10^{-2} \text{ m}^3$

Weight: 25 kg

Power Dissipation: 14W (64W incl. Cooling)

Operating Temperature: 260-293K

Temperature Stability during data integration:  $\Delta T = \pm 2\text{K}$  (max.)

---

<sup>(1)</sup>J. Lowrance, Princeton U. Current work on improved resolution target and electron optics. Private communication (1972)

#### 4.3.5 Signal-to-Noise Ratio and Slit-Width Selection

Based on the general equation derived in Appendix B, a signal-to-noise ratio is computed for the two spectral ranges of the high resolution spectrograph. Three values of slit width  $W_1 = 0.25 \mu\text{rad}$ ,  $W_2 = 0.5 \mu\text{rad}$  and  $W_3 = 1.0 \mu\text{rad}$  are used for this computation. The slit length  $L = 6.3 \mu\text{rad}$  is established as the maximum for which the spectrometer will be free from order overlap when operation with an extended body target is performed.

##### 4.3.5.1 Slit Selection

Evaluation of slit size requirements for the high resolution spectrograph results in a fixed slit length and three selectable slit width values.

The selected slit length,  $L = 6.3 \mu\text{rad}$ , in the reference configuration allows observation of extended bodies without overlap of adjacent orders. The selected slit width value,  $W_1 = 0.25 \mu\text{rad}$ , permits low background spectrographic evaluation of point sources with still acceptable slit losses; the widest slit,  $W_3 = 1.0 \mu\text{rad}$  is suitable for observation of extended sources wherein the instrument sensitivity is enhanced. The medium slit width,  $W_2 = 0.5 \mu\text{rad}$ , may be used on brighter extended source targets or at the upper spectral limit in the case of an unpredictable image size increase.

The above slit selection satisfies the high resolution requirements. In addition, a preliminary review of a continuously adjustable slit disclosed a high degree of mechanical complexity with a possible adverse effect upon the reliability. Hence, the selectable slit width approach was chosen.

##### 4.3.5.2 Signal-to-Noise Ratio

For each wavelength of interest, the limiting object magnitude  $m_{\text{lim}}$ , is established by postulating a desired signal-to-noise ratio of 2 ( $S/N = 2$ ) for the longest target integration time,  $t$ . Subsequent  $S/N$  values are computed for brighter objects using various

integration times. For each wavelength of interest, the zero magnitude signal,  $S_o$ , is determined:

$$S_o = \frac{E_W}{E_T} t \int_{\lambda - \Delta\lambda/2}^{\lambda + \Delta\lambda/2} N_o(\lambda') d\lambda' \cong \frac{E_W}{E_T} t N_{o\lambda} \Delta\lambda$$

where

$E_W$  = Energy passing the slit W

$E_T$  = Energy in the f/12 OTA image

$E_W/E_T$  = Enslitted energy, see Figure 3-9

t = integration time in seconds

$\Delta\lambda = \frac{1}{3} \times 10^{-4} \lambda$  is the instrument spectral precision

$N_o(\lambda)$  = photoelectron spectral density listed in Figure 3-23 for the wavelength of interest.

Also,  $S_{lim}$  = minimum signal (at the photocathode output) which provides a S/N ratio equal in value to two. It must reside, then, between  $\lambda - \frac{\Delta\lambda}{2}$  and  $\lambda + \frac{\Delta\lambda}{2}$ , i.e., in  $\Delta\lambda$ .

The limiting magnitude,

$$m_{lim} = 2.5 \log \left( \frac{S_o}{S_{lim}} \right), \text{ and the minimum signal required,}$$

$$S_{lim} = 2 \left( 1 + \sqrt{1 + S_B + N_D + (n_R)^2} \right), \text{ are determined for each range:}$$

a. Range I

Examples are computed for:	$\lambda_1 = 120$	$\lambda_2 = 180 \text{ (nm)}$
Spectral bandwidth of	$\Delta\lambda_1 = 4 \times 10^{-3}$	$\Delta\lambda_2 = 6 \times 10^{-3} \text{ (nm)}$
Photoelectron spectral density (Fig. 3-23)	$N_{O1} = 6 \times 10^5$	$N_{O2} = 4 \times 10^6 \text{ (pe/s/nm)}$
Integration time	$t = 3.6 \times 10^4$	$t = 3.6 \times 10^4 \text{ (s)}$
Enslitted energy for $W_1$	$E_W/E_T = 0.8$	$E_W/E_T = 0.75$
The zero magnitude signal	$S_{O1} = 6.9 \times 10^7$	$S_{O2} = 6.5 \times 10^8 \text{ (photoel)}$
The +23 mag signal	$S_{23} \cong 4.3 \times 10^{-2}$	$0.4 \text{ (pe)}$
Solid angle subtended by the image (Resolution Cycle)	$\Omega \cong 2$	$\Omega \cong 2 \text{ (psr)}$
Background count	$S_{B1} \cong 4 \times 10^{-3}$	$S_{B2} \cong 3 \times 10^{-2} \text{ (pe)}$
$S_B = S_{23} \frac{\Omega}{25}$ ; both of $S_{B1}$ and $S_{B2}$ are negligible.		
Dark Count	$N_{D1} \cong 36$	$N_{D2} \cong 36 \text{ (pe)}$
$N_D = aNt$ with		
$a = 2.5 \times 10^{-5} \text{ cm}^2$ , the area of the image, and		
$N \cong 40 \text{ el/s-cm}^2$ , the dark count for Bialkali at $T = 293\text{K}$ (see Figure 6-3.)		
Readout noise count	$(n_R)^2 = 128$	$(n_R)^2 = 128 \text{ (pe)}$
Limiting Signal	$S_{lim} \cong 28$	$S_{lim} \cong 28 \text{ (pe)}$
Limiting Magnitude	$m_{lim} \cong +16$	$m_{lim} \cong +18.5 \text{ star mag.}$

Target saturation occurs at a signal count of 2500 pe with a  $S/N = 50$ .

In addition, the S/N is computed for brighter objects at  $t = 3.6 \times 10^4$  s (and shorter) from the equation

$$\frac{S}{N} = \frac{S_m}{\sqrt{S_m + S_B + N_D + (n_R)^2}}$$

Corresponding values for the two wavelengths are shown in Figure 4-23 for  $W_1$ ,  $W_2$  and  $W_3$ .

The above examples were derived under the assumption that the selected wavelengths are located in the center of their respective orders (echelle). If these, or other wavelengths of interest are at the beginning or end of their respective order, the results are shifted by about one star magnitude toward brighter objects (40% level on the skirt of the grating response in Figure 3-5).

b. Range II

$$\lambda_1 = 180 \quad \lambda_2 = 350 \text{ [nm]}$$

$$\Delta\lambda_1 = 6 \times 10^{-3} \quad \Delta\lambda_2 = 1.17 \times 10^{-2} \text{ [nm]}$$

From Figure 3-23:  $N_{01} = 4 \times 10^6 \quad N_{02} = 3 \times 10^7 \text{ [pe/s-nm]}$

$$t = 3.6 \times 10^4 \quad t = 3.6 \times 10^4 \text{ [s]}$$

For  $W_1 = 0.25 \mu\text{rad}$   $\frac{E_W}{E_T} = 0.75 \quad \frac{E_W}{E_T} = 0.65$

$$S_{01} = 6.5 \times 10^8 \quad S_{02} = 8.2 \times 10^9 \text{ [pe]}$$

$$S_{23} = 0.4 \quad S_{23} = 5.1 \text{ [pe]}$$

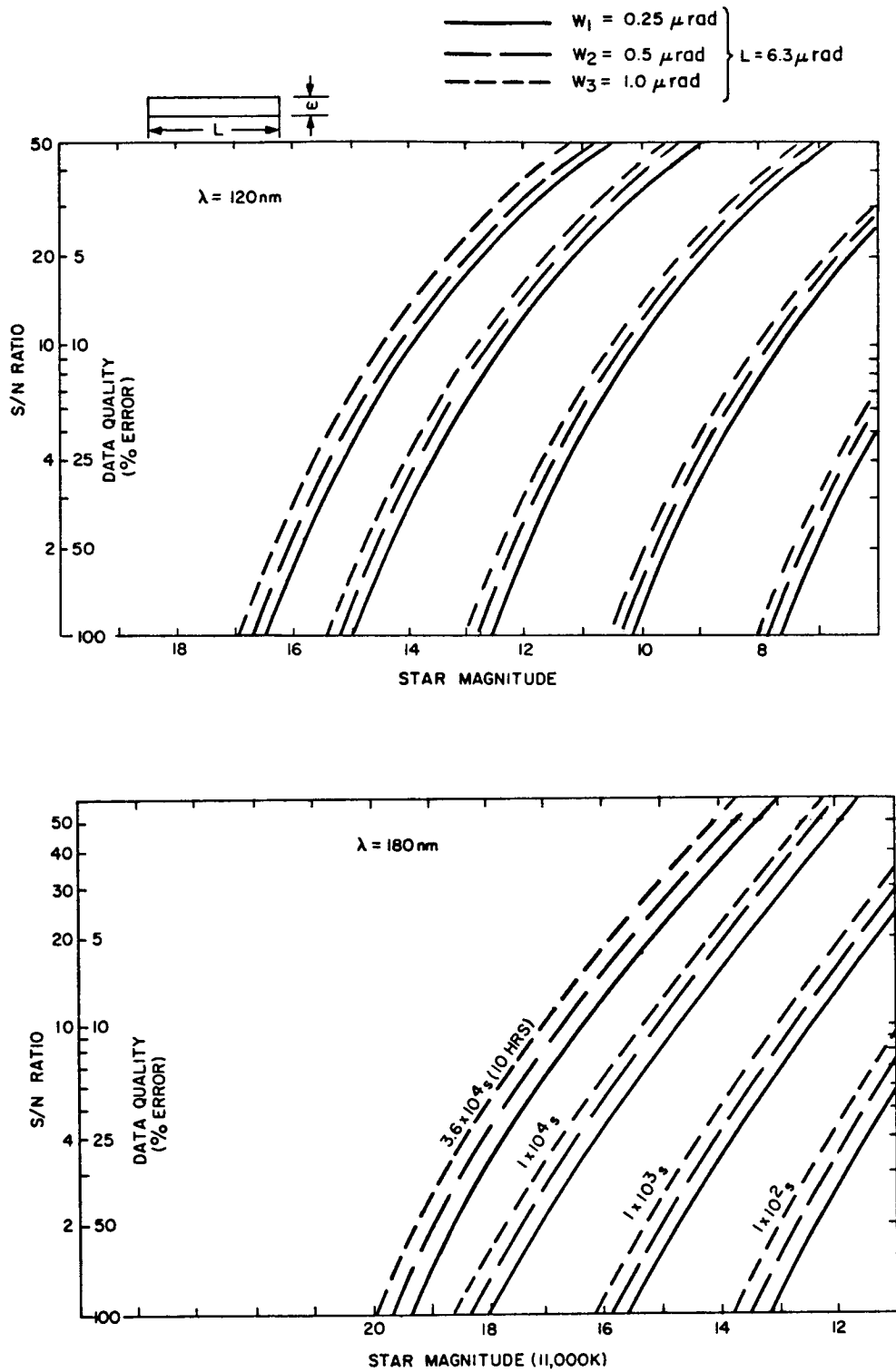


Figure 4-23. High Resolution Spectrograph Range I  
 S/N Ratio as a Function of Star Magnitude  
 and Integration Time

$\Omega \approx 2$ psr as in Range I	$S_{B1} = 3 \times 10^{-2}$ negl.	$S_{B2} = 0.4$ negl. [pe]
$N_D$ , as in Range I	36	36 [pe]
Readout Noise Count	$(n_R)^2 = 128$	$(n_R)^2 = 128$ [pe]
Limiting Signal	$S_{lim} = 28$	$S_{lim} = 28$ [pe]
Limiting Magnitude	$m_{lim} \approx +18.5$	$m_{lim} \approx +21$ star mag.

In addition, the S/N was computed for brighter objects for  $t = 3.6 \times 10^4$  s and for shorter integration times using the same relations as in Range I. Corresponding values for the two wavelengths in Range II are shown in Figure 4-24 for  $W_1$ ,  $W_2$  and  $W_3$ .

As in Range I, the S/N at saturation is 50.

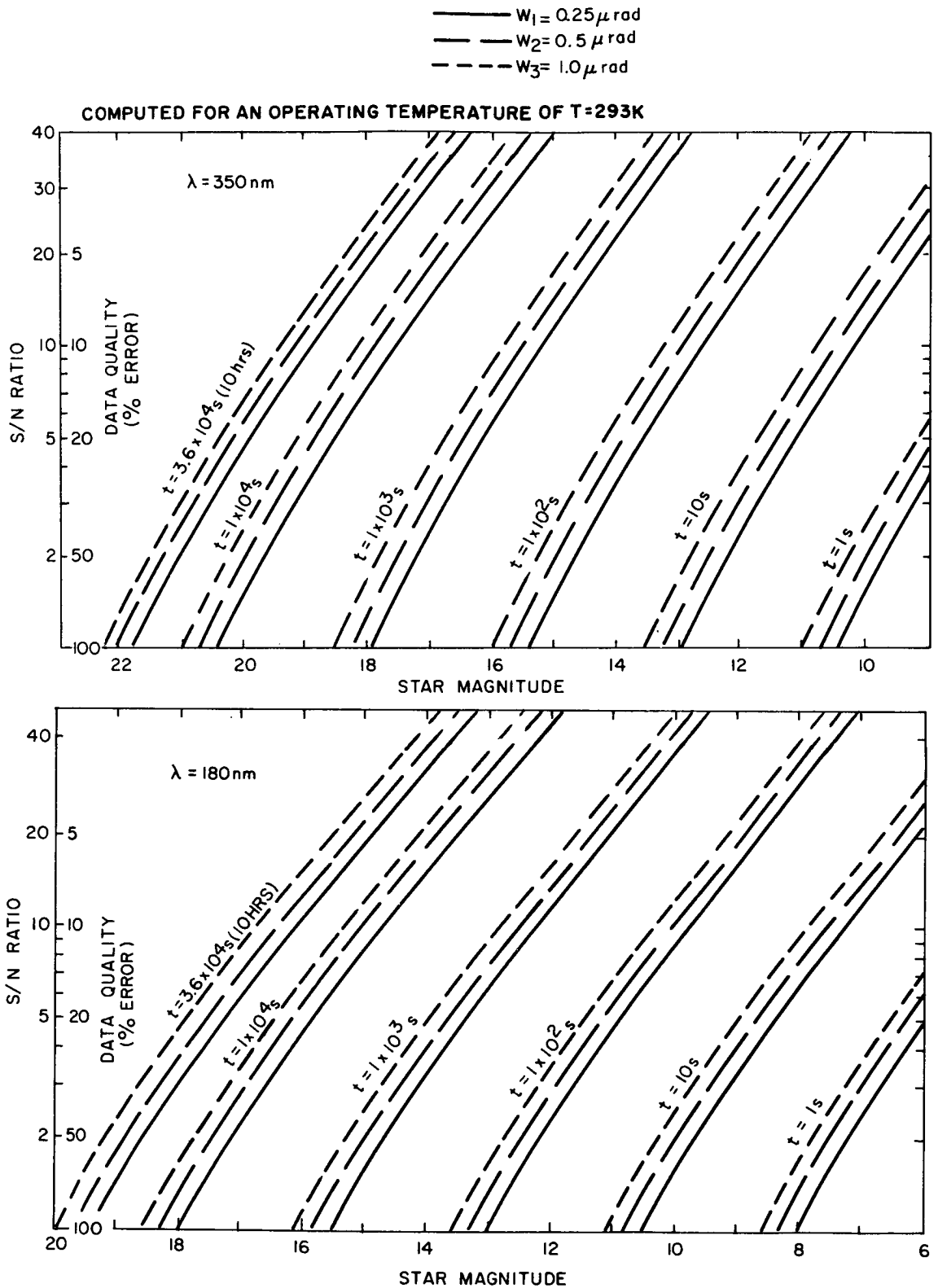


Figure 4-24. High Resolution Spectrograph Range II S/N Ratio as a Function of Star Magnitude and Integration Time (t) for Three Slit Width Values



## 4.4 FAINT OBJECT SPECTROGRAPH

### 4.4.1 General Description

The faint object spectrograph, whose resolving power is  $10^3$ , covers the spectral range from 110 to 1000 nm with three instruments. The first is a single dispersion instrument which covers the range 110-220 nm using two interchangeable gratings to break up the spectrum into two intervals; 110 to 160 nm and 160-220 nm. The physical layout of this instrument is shown in Figure 4-25. This unit is located in the aft section of the SIP with the high resolution instruments and is accessed with the same collimator mirror. As shown in Figure 4-26, the telescope f/12 bundle of light from the object to be studied passes through the slit assembly at the focal plane (F.P.), and is collimated by the collimator mirror. The light is then reflected from a flat mirror to the grating which has a central hole that matches the telescope obscuration. The dispersed light then falls on the camera mirror which focusses the spectrum on the 25 mm square detector photocathode after passing through the hole in the grating. The hole in the grating allows the camera mirror to operate on or near its optical axis with much improved images compared to off axis operation without a hole in the grating. After the exposure is complete the second grating may be moved into place by the grating drive assembly and a second exposure made to record the other spectral interval. The weight of this instrument is 64.2 Kg.

The other two units which complete the faint object spectrograph use the same package outline and are smaller than the first. They have the form of an unsymmetrical T as shown in Figure 4-27, and use a 25 mm square photocathode. These instruments are located in the forward section of the SIP and each is accessed by a small pickoff mirror located about 1.2 mrad off axis. The telescope is offset to select one of these mirrors. Figure 4-28 shows the

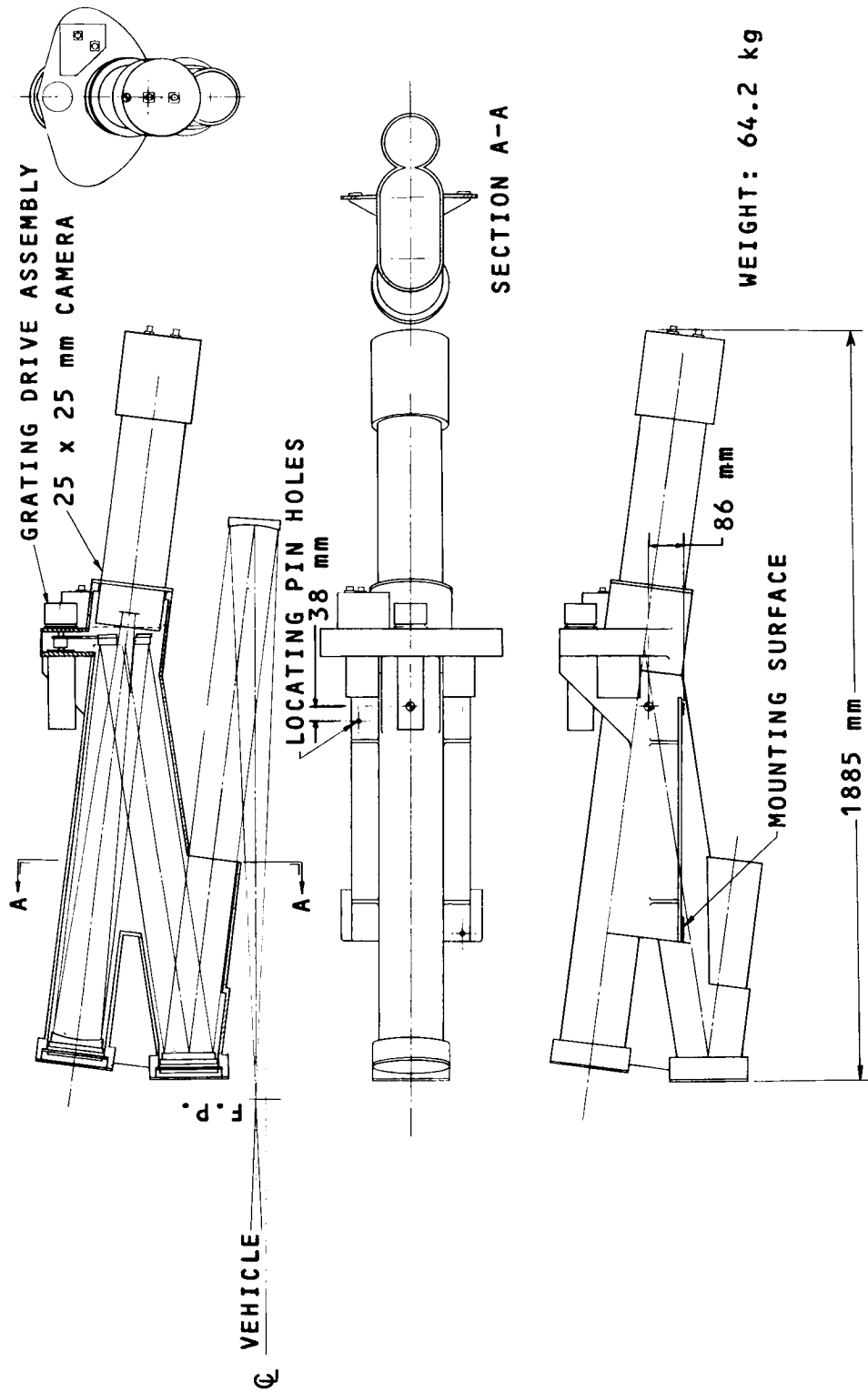


Figure 4-25. Faint Object Spectrograph No. 1, Physical Layout

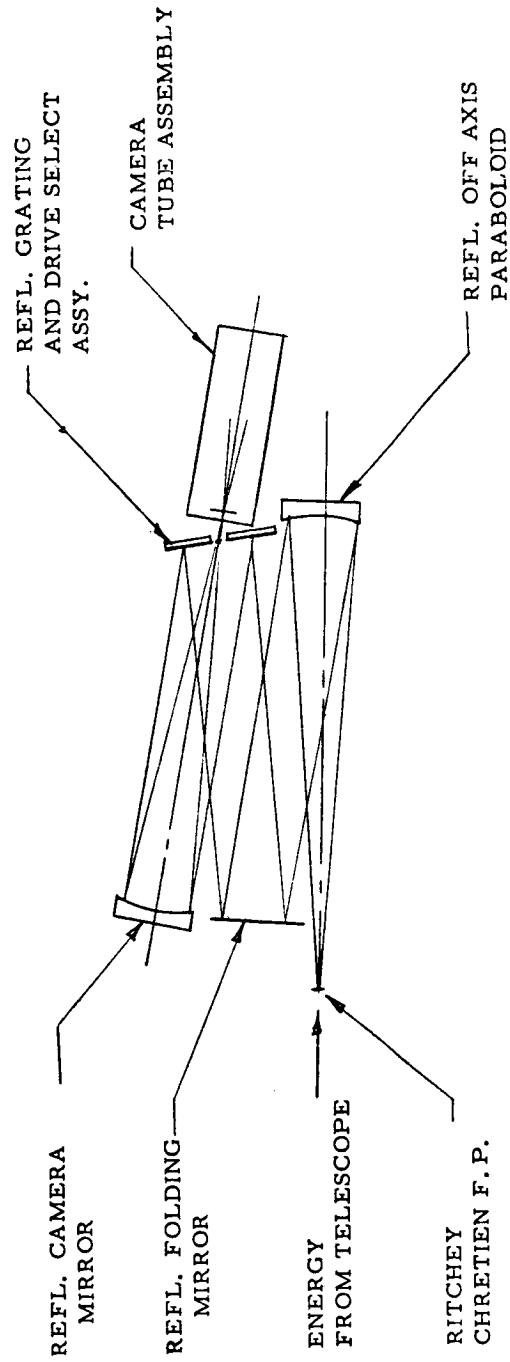
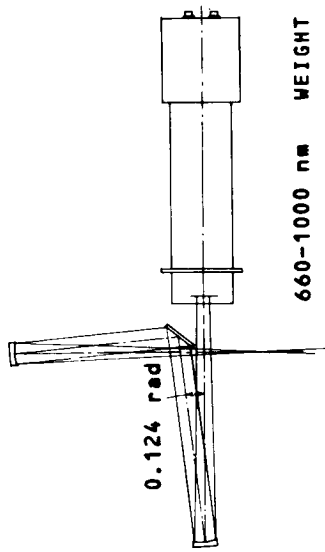


Figure 4-26. Faint Object Spectrograph 110-160 nm (1A)  
160-220 nm (1B)



660-1000 nm WEIGHT = 48 Kg

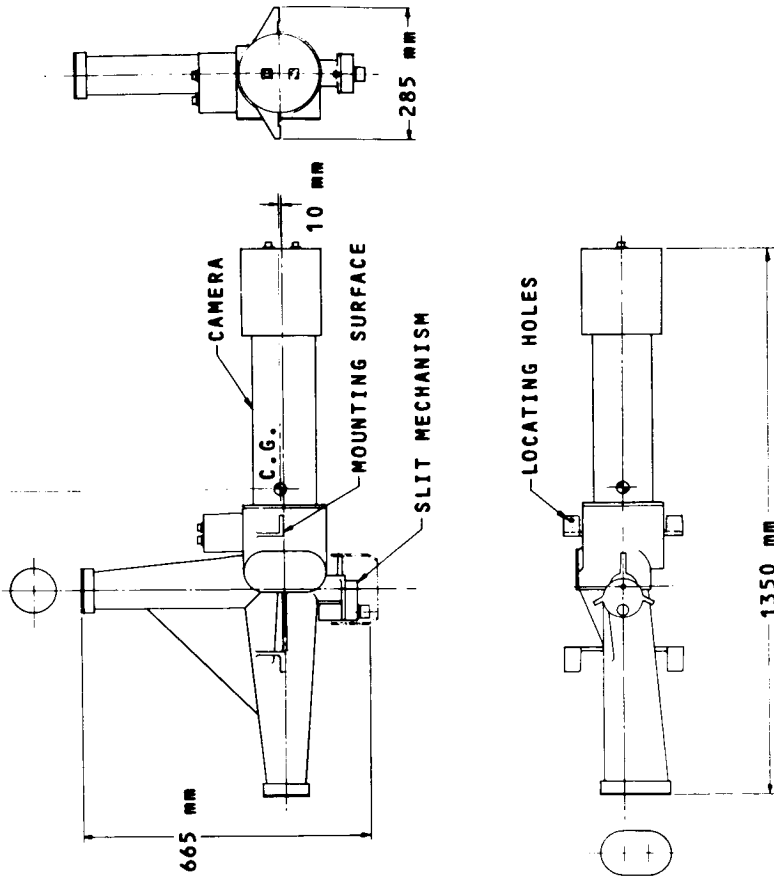
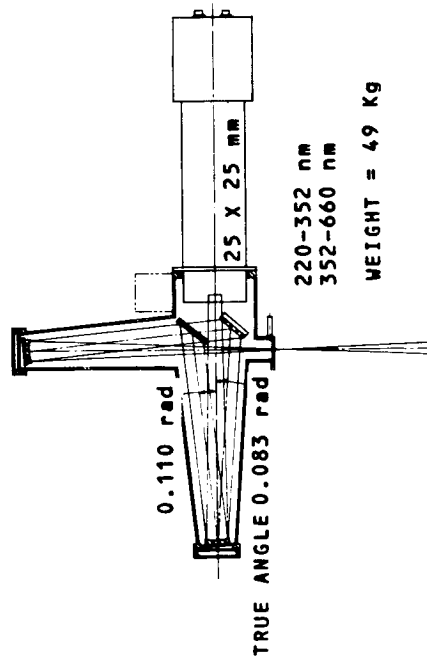


Figure 4-27. Faint Object Spectrograph  
220 to 350 nm, 350 to 660 nm, 660 to 1000 nm

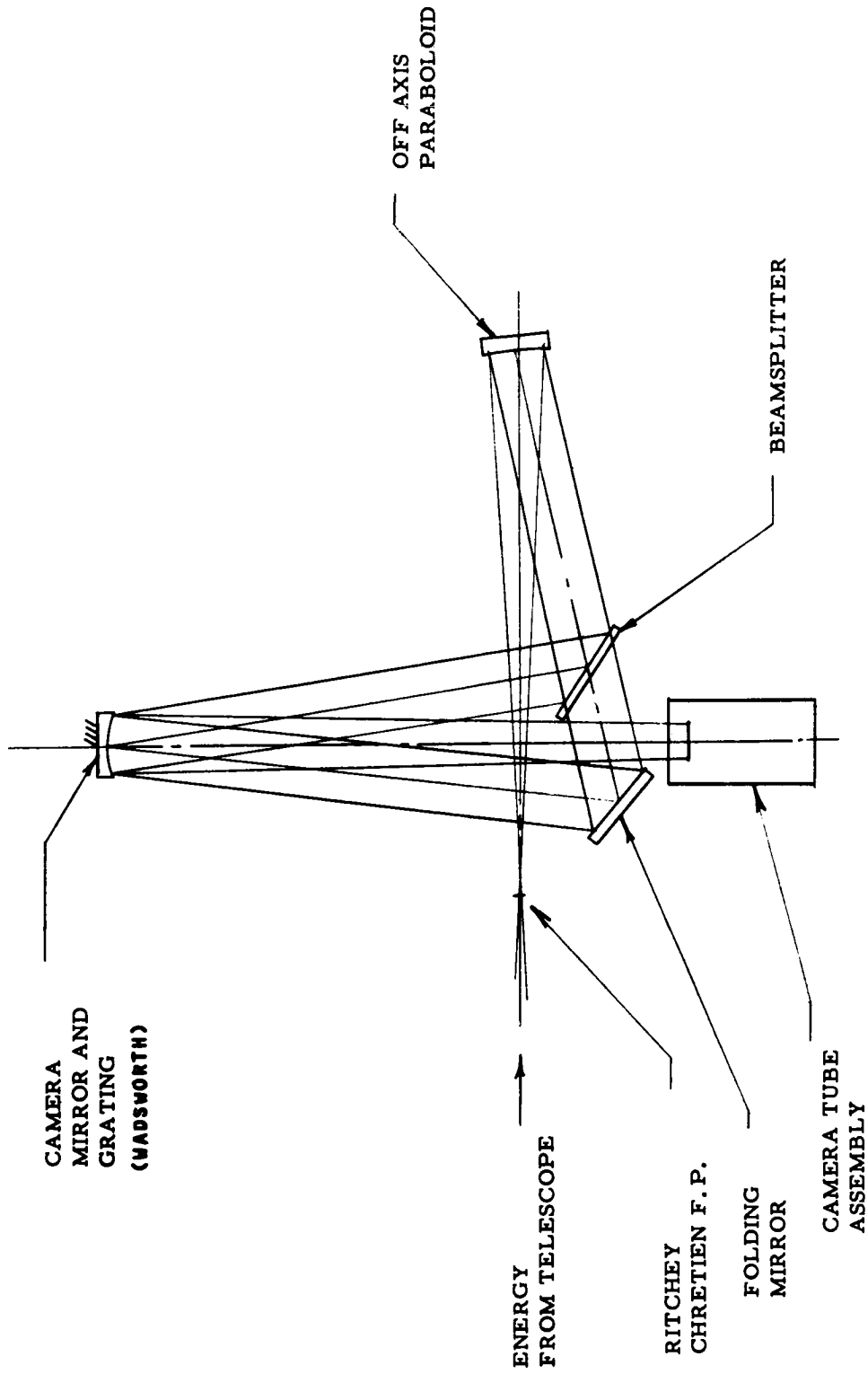


Figure 4-28. Faint Object Spectrograph  
220-350 nm, 350-660 nm

optical schematic of the 220-660 nm instrument. The light is picked off in front of the telescope focal plane and directed to the collimator mirror. After reflection the beam falls on a dichroic beamsplitter which reflects the light in the 220 to 350 nm range and transmits the light in the 350 to 660 nm range. The reflected light falls on a grating which is curved and focusses the light on the photocathode as well as dispersing it. The transmitted light falls on the flat folding mirror and is reflected to the second curved grating, and forms a second spectral image on the photocathode below the first image. This arrangement is possible because a high efficiency dichroic beamsplitter is available and the photocathode can cover the complete spectral range with good efficiency. The use of a single grating to cover this range would require a larger photocathode or the development of a linear detector array. It would also result in a much larger variation in grating efficiency. The weight of this instrument is 49 Kg.

The third instrument of the faint object spectrograph is a single grating version of the previous instrument with a grating selected to cover the range 660 to 1000 nm. This instrument requires a III-V photocathode which is presently early in the development cycle. The optical schematic is shown in Figure 4-32. The weight is 48 Kg.

All of the reflecting surfaces are chosen to maximize the transmission of the appropriate wavelength band. The components of the spectrographs are shown in the following family tree diagrams, Figures 4-29, 4-30 and 4-31.

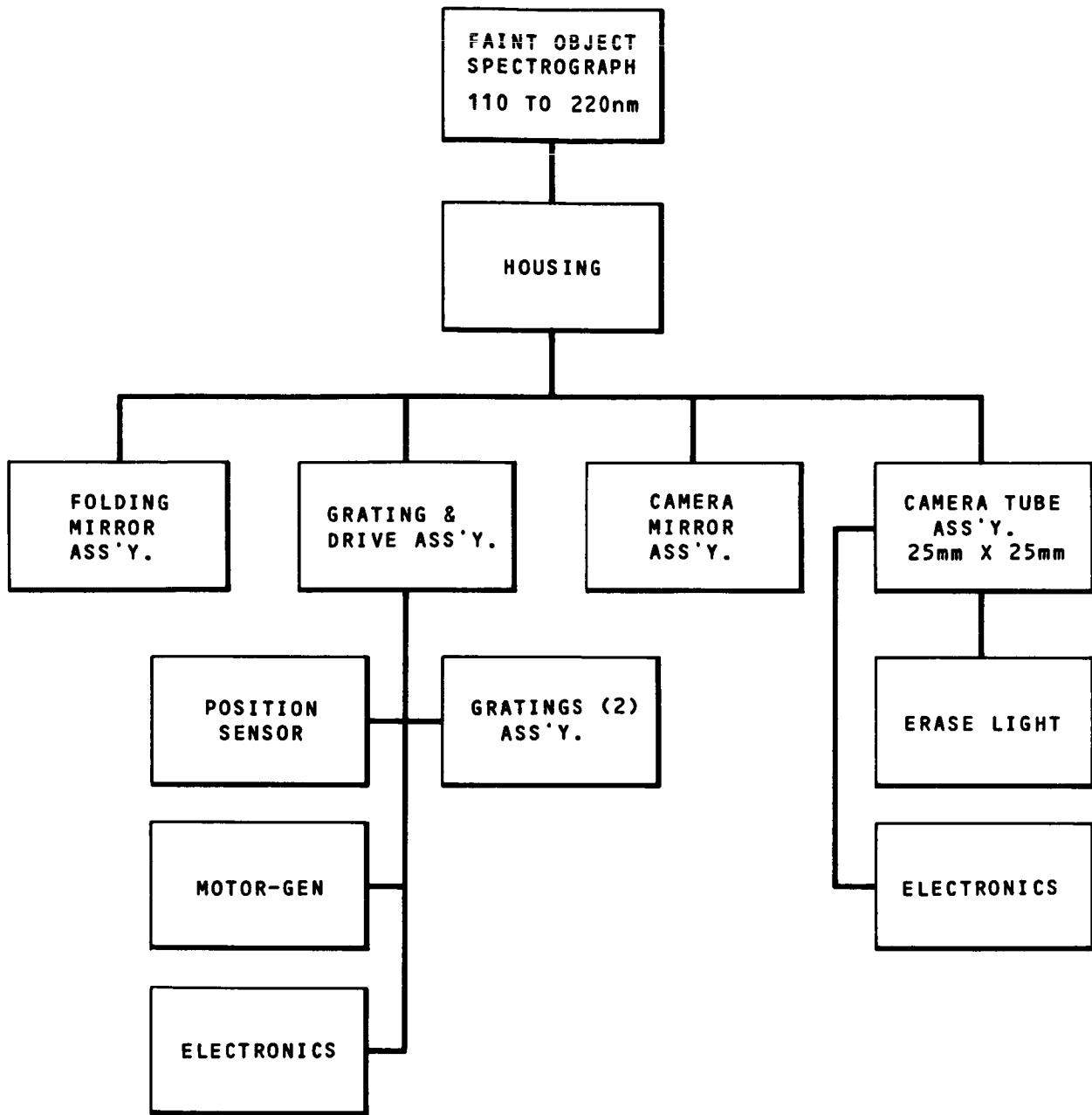


Figure 4-29. Faint Object Spectrograph Family Tree  
(110 to 220 nm)

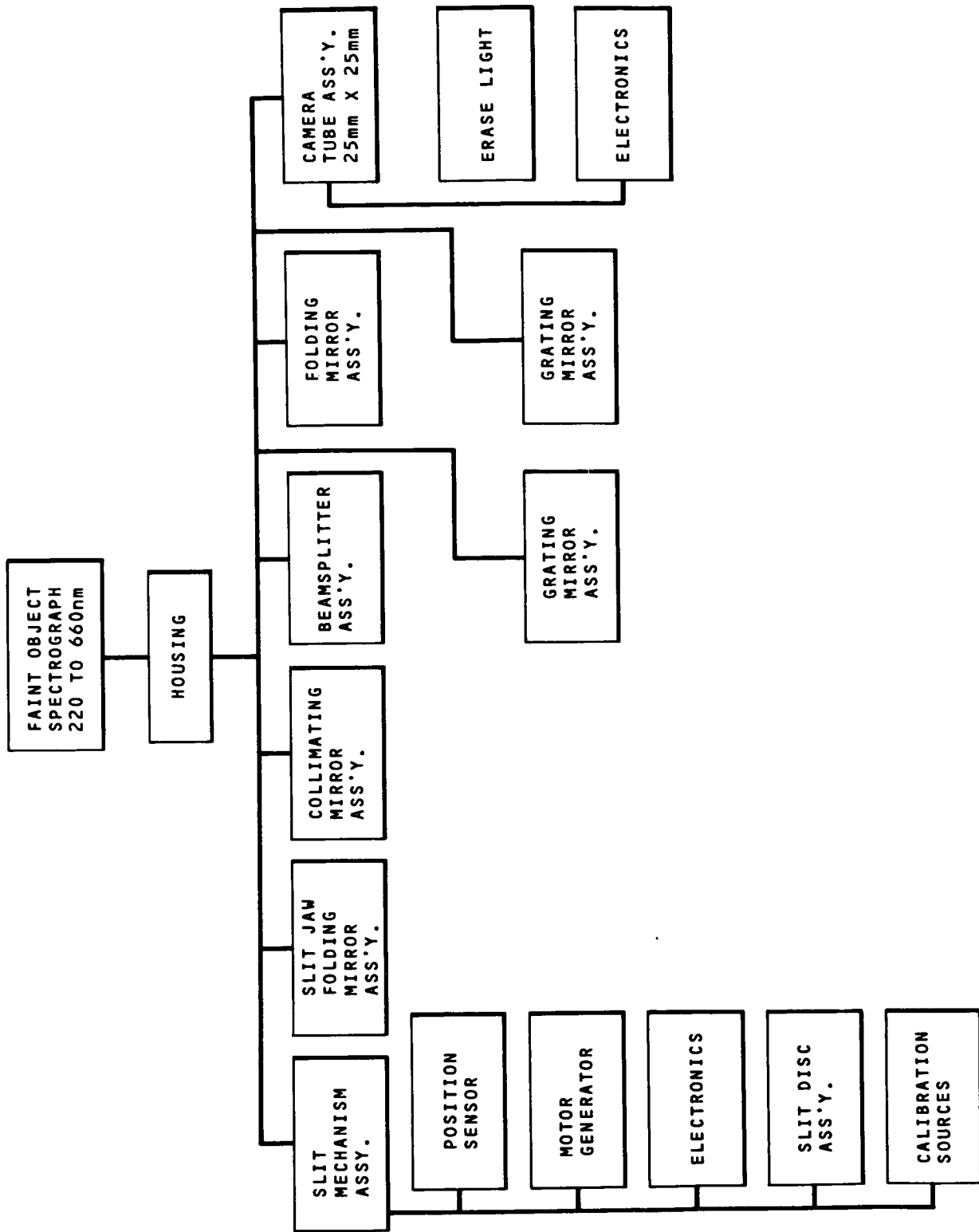


Figure 4-30. Faint Object Spectrograph Family Tree (220 to 660 nm)



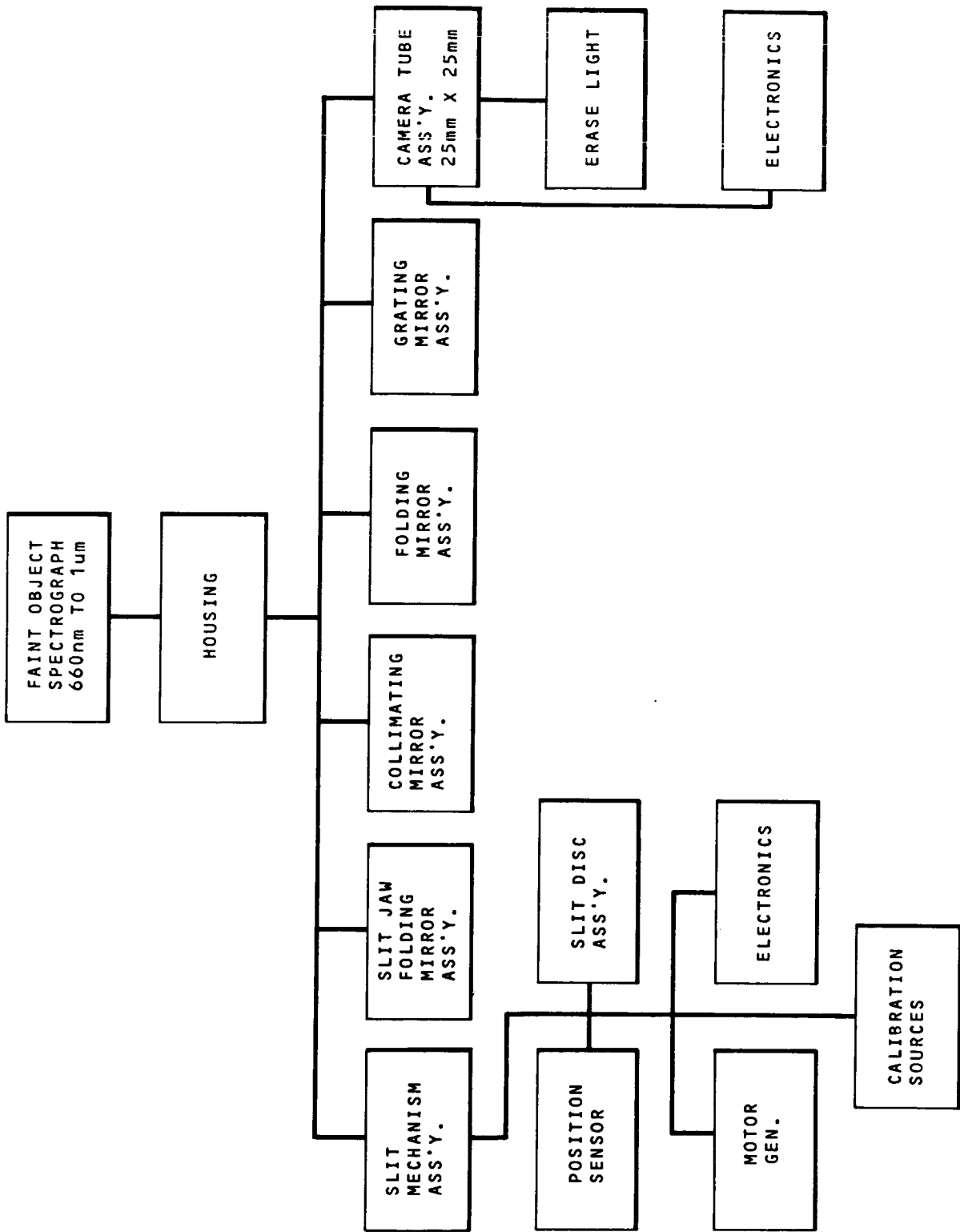


Figure 4-31. Faint Object Spectrograph Family Tree

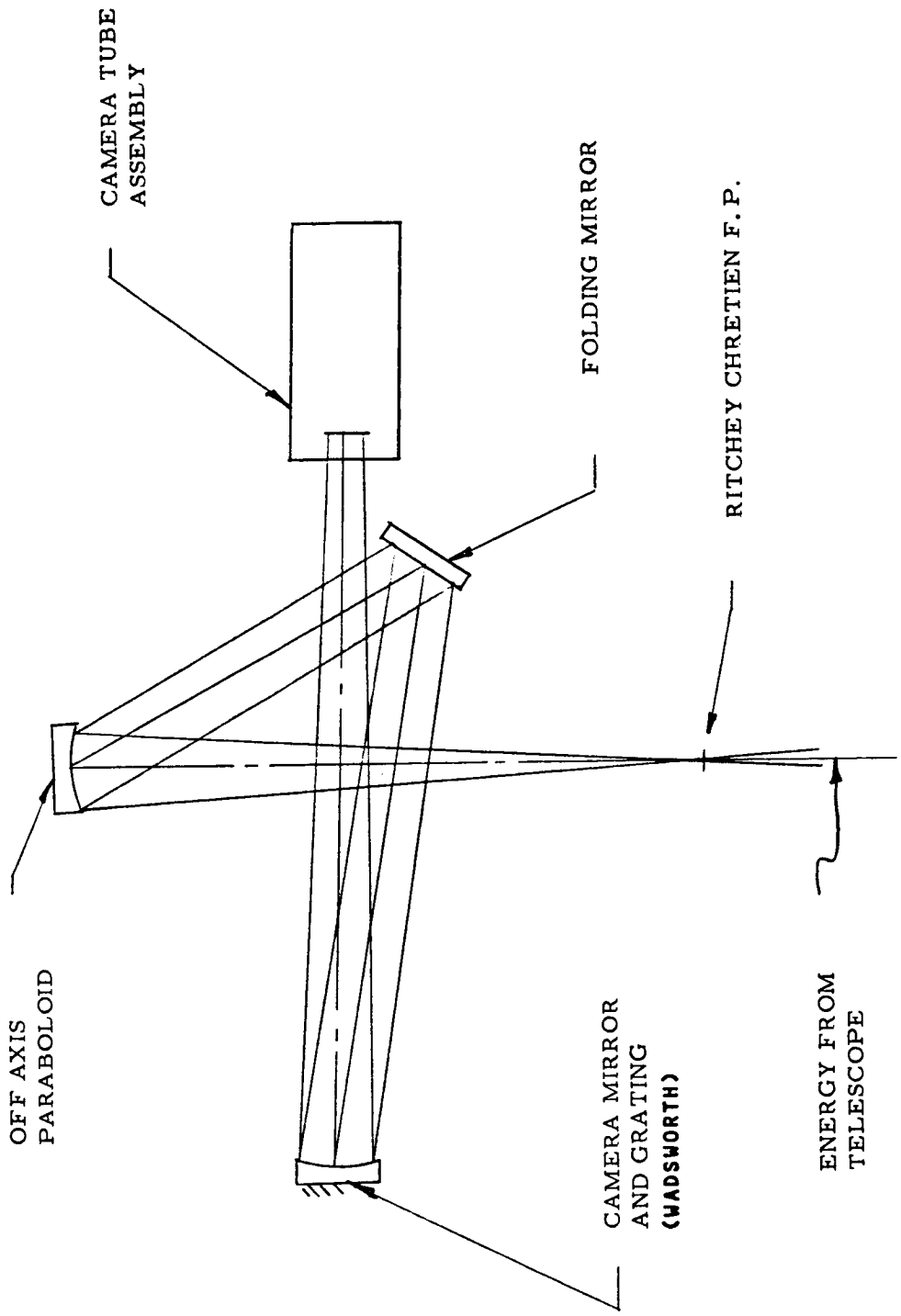


Figure 4-32. Faint Object Spectrograph 660-1000 nm

#### 4.4.2 Description of Optics

##### a. Discussion

A series of instruments has been studied for obtaining spectral data of faint objects in the spectral region of 115 to 1000 nm with spectral resolution of  $\lambda/\Delta\lambda = 10^3$ .

The number of instruments required to cover this spectral range at the desired spectral resolution is a function of:

1. Detector format size.
2. Detector resolvable element size.
3. Detector spectral range.
4. Efficiency of the grating system.

It is desirable to minimize the number of instruments required to cover this broad spectral range. At the same time one must also consider the size, weight, complexity and efficiency of the proposed spectrograph as well as its adaptability to the modular concept envisioned for the LST instrumentation.

In terms of a line spectrum (single grating) a large image format is desirable in order to compress onto a single focal plane as much of the dispersed spectra as possible. A double grating system such as the echelle spectrograph proposed for the High Resolution Spectrograph was considered, but the energy throughput of a two grating system is greatly reduced and thus defeats the purpose of gathering data from faint objects.

Image tubes with a 50 x 50 mm format provide a 70 mm diagonal for a line of spectrum. However, the size and weight of such a tube is unattractive; this tube weighs about 59 Kg; the smaller 25 x 25 mm tube weighs only 25 Kg. In order to provide room for the image to pass through the grating to the focal plane, a larger hole is required. This means the grating diameter must increase to preclude an increase in obscuration.

The smaller tube provides only a 30 millimeter diagonal; this forces the use of more instruments or combinations of instruments which fold the dispersed spectra onto the same tube. The faint object spectrographs that are presented in this report provide a viable solution in that they cover the spectral range, consistent with the resolution required, and may be packaged in accordance with the LST modular concept. They provide a baseline for consideration of size, weight, tolerancing, power requirements, etc. They also provide a baseline for comparison of alternate configurations.

Three instruments have been designed to cover the spectral range of 110 to 1000 nm.

<u>Faint Object Spectrograph</u>	<u>Spectral Range</u>
No. 1A	110 to 160 nm
1B	160 to 220 nm
No. 2A	220 to 350 nm
2B	350 to 660 nm
No. 3	660 to 1000 nm

#### 4.4.2.1 Faint Object Spectrograph (1A and 1B)

The same study used to determine the optimum f/number for the high resolution spectrographs holds equally well for the faint object spectrographs, since they also use a camera mirror operating on axis and both have a 30 mm diagonal on the image format. However, packaging layout problems are eased by using an f/9.0, rather than an f/10 camera mirror.

It is apparent from the family of curves in Figure 4-11 that the tolerance increases as the aperture decreases. However, the obscuration also increase, as does the dispersion required of the

grating. This means a higher ruling frequency is needed; and as the ruling frequency increases, more and more energy is lost to the zero order. Ruling frequencies up to 600 lines/mm can be expected to be excellent. Therefore the spectrographs proposed use gratings with ruling frequencies of less than 600 lines/mm.

The spectral range of 115 to 220 nm requires 60 millimeters of image format. This may be accomplished by using:

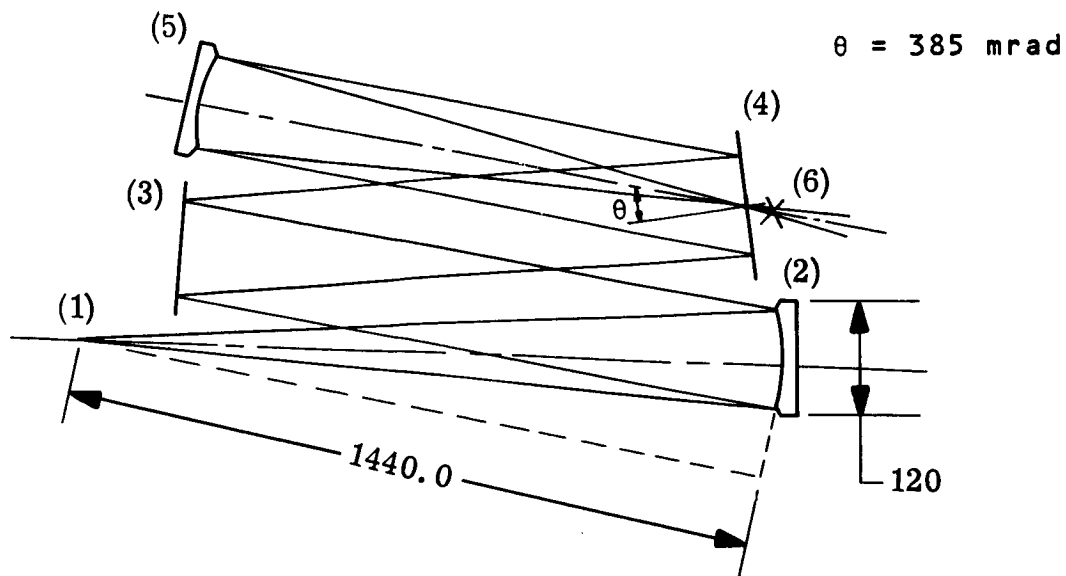
1. Separate systems.
2. Exchanging Gratings.
3. Splitting the aperture at the grating.
4. Folding the image so that the spectral lines lie next to one another.

All of these possibilities were considered. None of them is completely satisfactory. The proposed system changes gratings so that the camera mirror and tube may be shared. Placement of the grating is not critical because this would only produce a lateral shift in the location of the spectrum. However, once the grating has been inserted it must be held in that position during exposure. The dynamic tolerances, as determined for the high resolution spectrograph, hold equally well for this spectrograph.

#### a. Optical Path

The same off axis paraboloid which feeds collimated light into the High Resolution Spectrographs is positioned to send a collimated bundle into this faint object spectrograph. The light is then reflected by a folding mirror and then dispersed by whichever one of the two gratings is in position at the line of operation. The light then goes to the camera mirror, which images the dispersed spectra through a hole in the grating. The prescription for this spectrograph is given the Optical System Record, Figure 4-33.

SPECTRAL RANGE 1A (110 to 160 nm)  
 1B (160 to 220 nm)



<u>Surface No.</u>	<u>Radius</u>	<u>Constant</u>	<u>Thickness</u>	
(1)	-	-	1440.0	Ritchey-Chretien F.P.
(2)	-2880.0	-1.0	1335	Refl. Off Axis Paraboloid
(3)	-	-	1035	Refl. Folding Mirror
(4)	-	-	1000	Refl. Grating
(5)	2160.0	-	1080.0	Refl. Camera Mirror
(6)	-	-	-	Tube*

Surface No. 4

1st Grating Frequency = 555.6 lines/mm Blaze Angle = 31.4 mrad

2nd Grating Frequency = 463.0 lines/mm Blaze Angle = 38.5 mrad

\* Image format 30 mm; (all dimensions in millimeters)

Figure 4-33. Faint Object Spectrograph Optical System Record

## b. Performance

A single 30 mm line spectrum is spread across the image tube. At the edges of the format the camera mirror is operating at an effective semi-field angle of 13.8 mrad. The spot diagrams shown in Figures 4-34 through 4-39 show the shape of the image and the spectral resolution (separation in nanometers) of the system at the center and at either end of the spectrum for both system 1A and 1B. The resolution requirement here is  $\lambda/\Delta\lambda = 10^3$ , a value exceeded in the ultraviolet region of the spectrum. It will be shown later that we pay a penalty in the visual region, but there is an assumed lesser interest in the data gathered in that region of the spectrum. A slightly different distribution of spectral bands among the spectrometers would allow them all to conform to the  $\lambda/\Delta\lambda = 10^3$  spectral resolution. It was decided for the baseline system, however, to favor the UV spectrometers.

## c. Tolerancing

This faint object spectrograph is similar to the echelle in size, number of reflections and basic configuration. Essentially the same component tolerances, determined for the high resolution spectrograph, apply equally well to this spectrograph (Section 4.3.3).

## d. Baffles

The only difference between this spectrograph and the high resolution spectrograph is that a folding mirror is used in place of the echelle grating; therefore, the same internal shields are required. Figure 4-25 shows a cutaway view of the spectrograph from which it can be seen that the focal plane must be shielded from the reflected light of the folding mirror. With the exception of the folding mirror, the spectrograph is handled the same as the high resolution spectrograph (see 4.3.2.b).

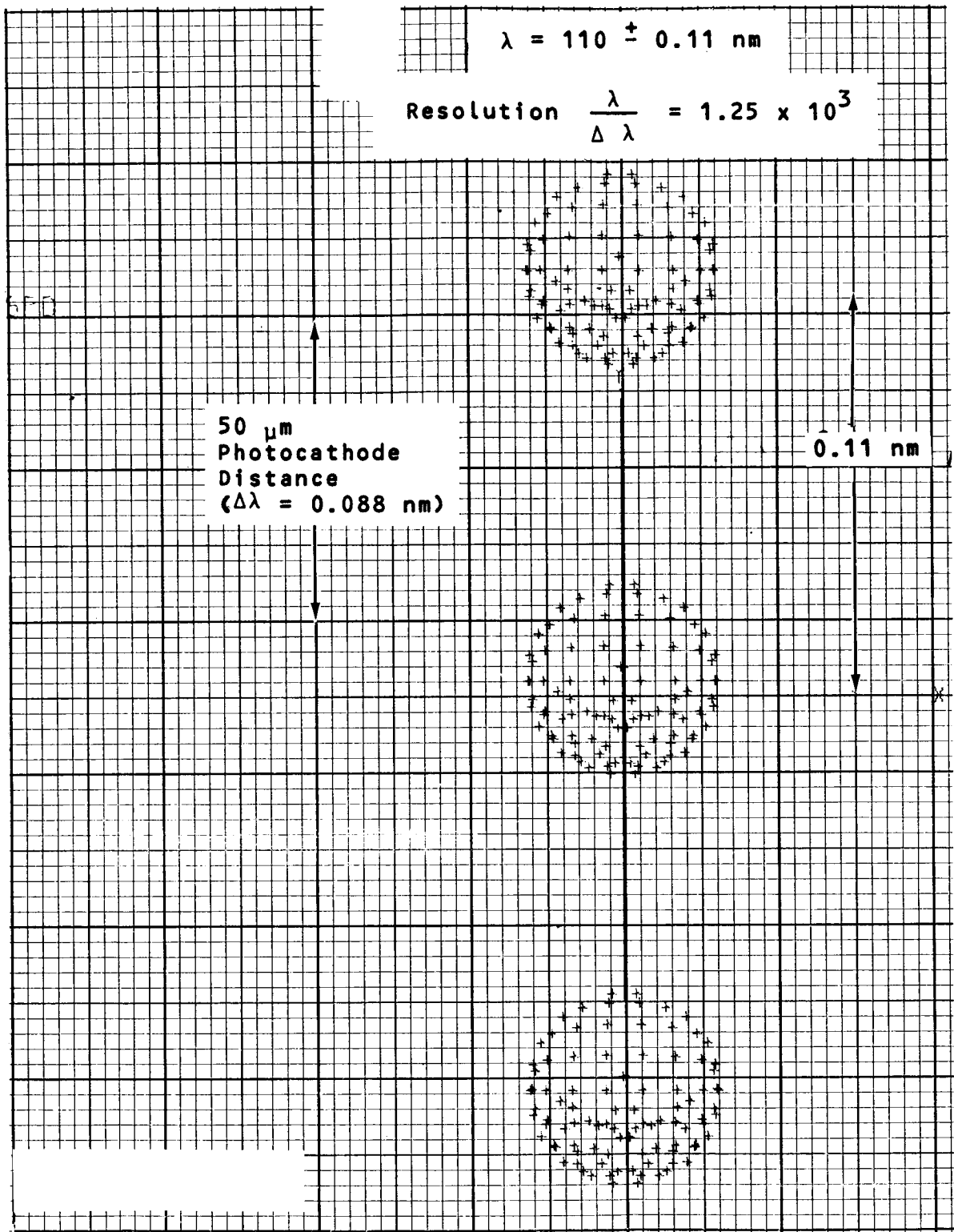


Figure 4-34. Faint Object Spectrograph  
Range 1A (115 to 160 nm)



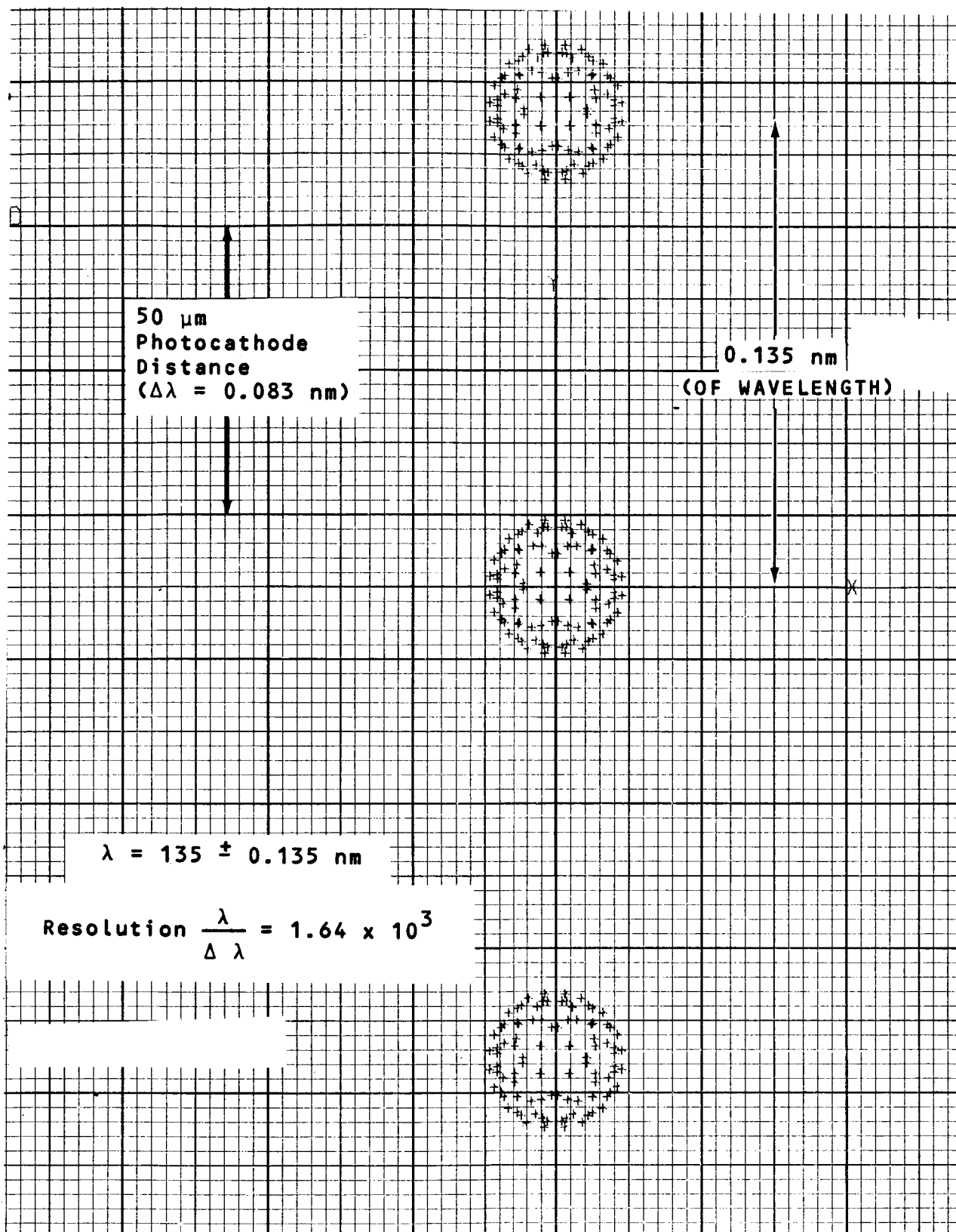


Figure 4-35. Spot Diagram - Faint Object Spectrograph  
Range 1A (115 to 160 nm)

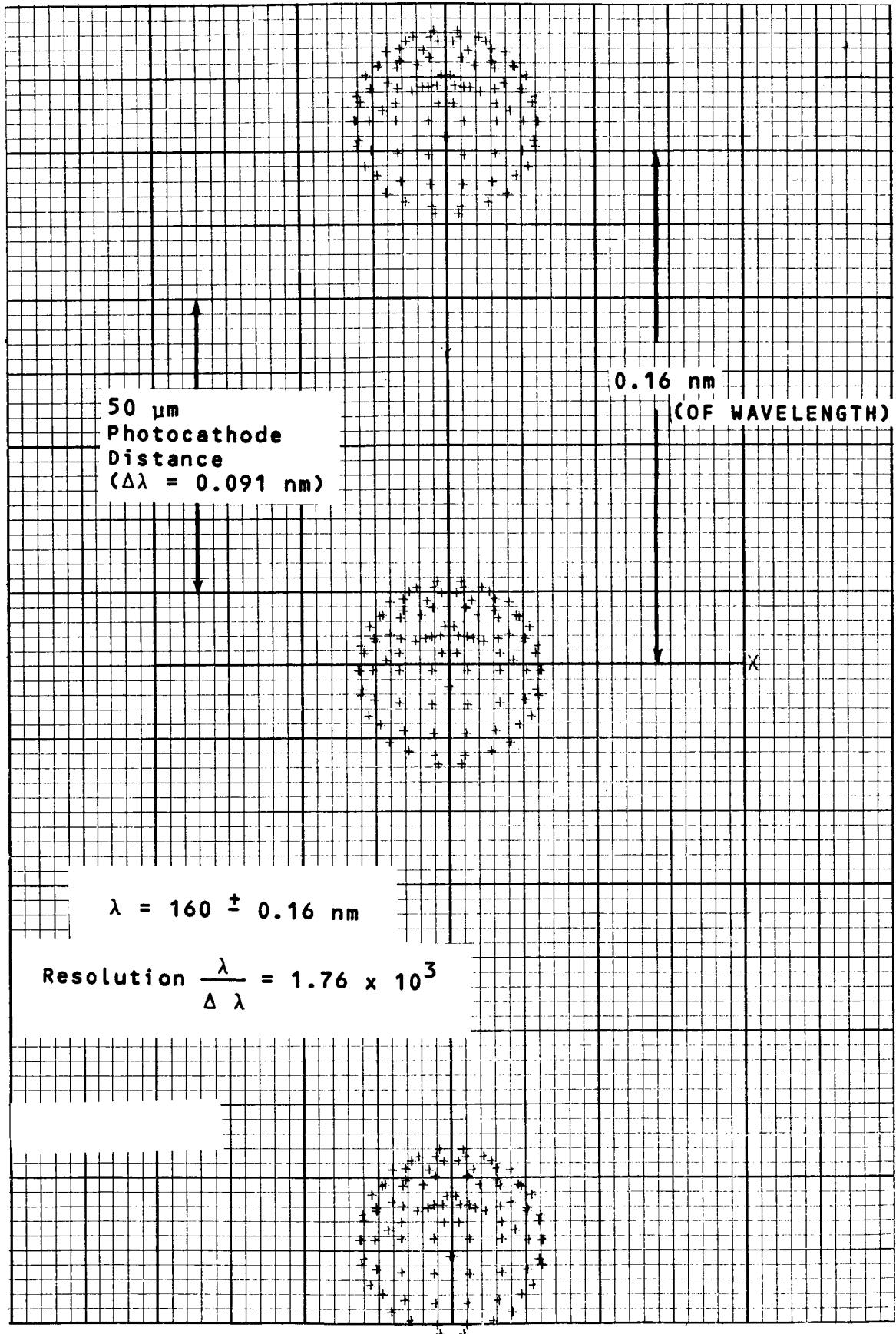


Figure 4-36. Spot Diagram - Faint Object Spectrograph  
Range 1A (115 to 160 nm)

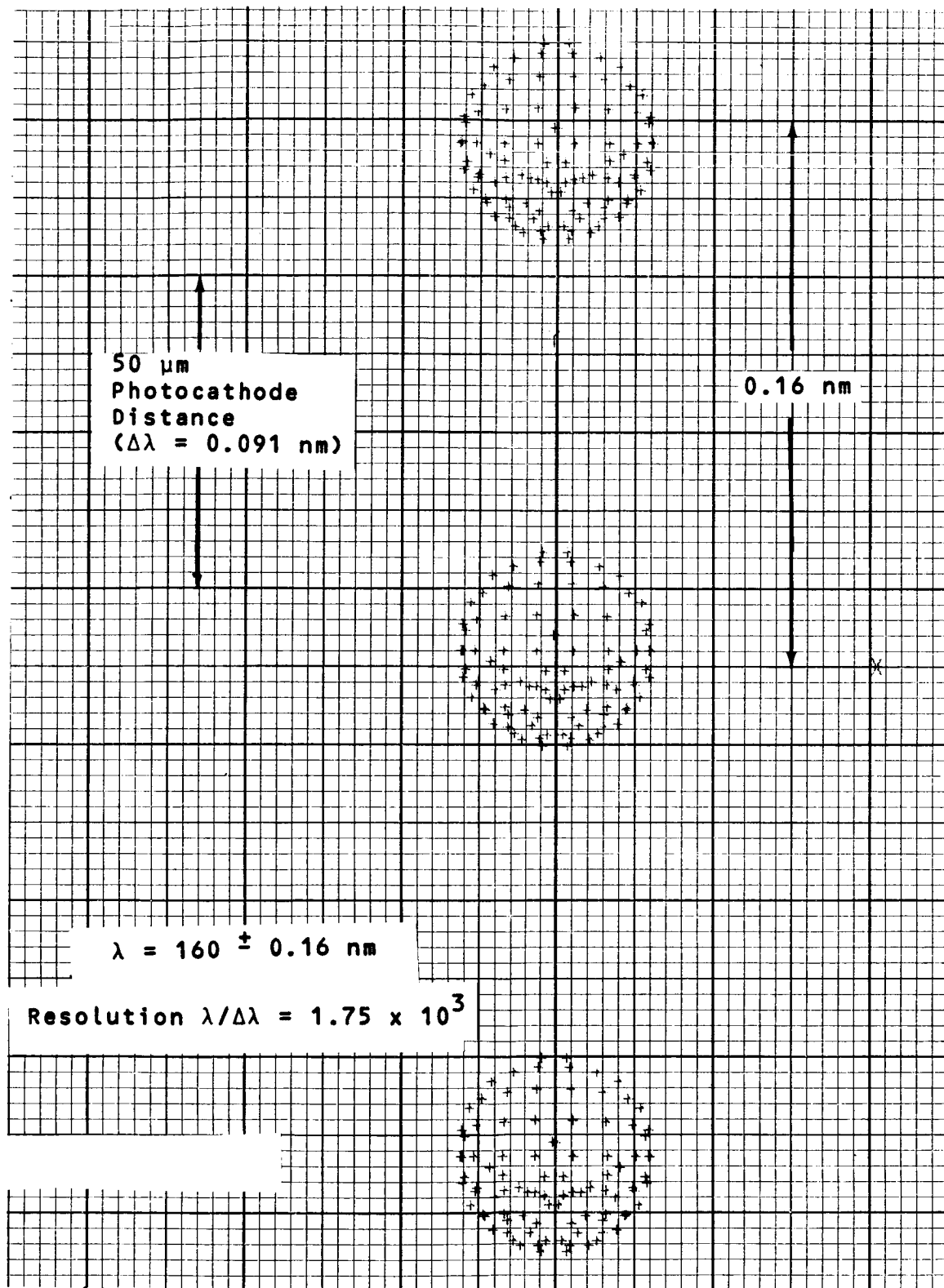


Figure 4-37. Spot Diagram - Faint Object Spectrograph  
Range 1B (160 to 220 nm)

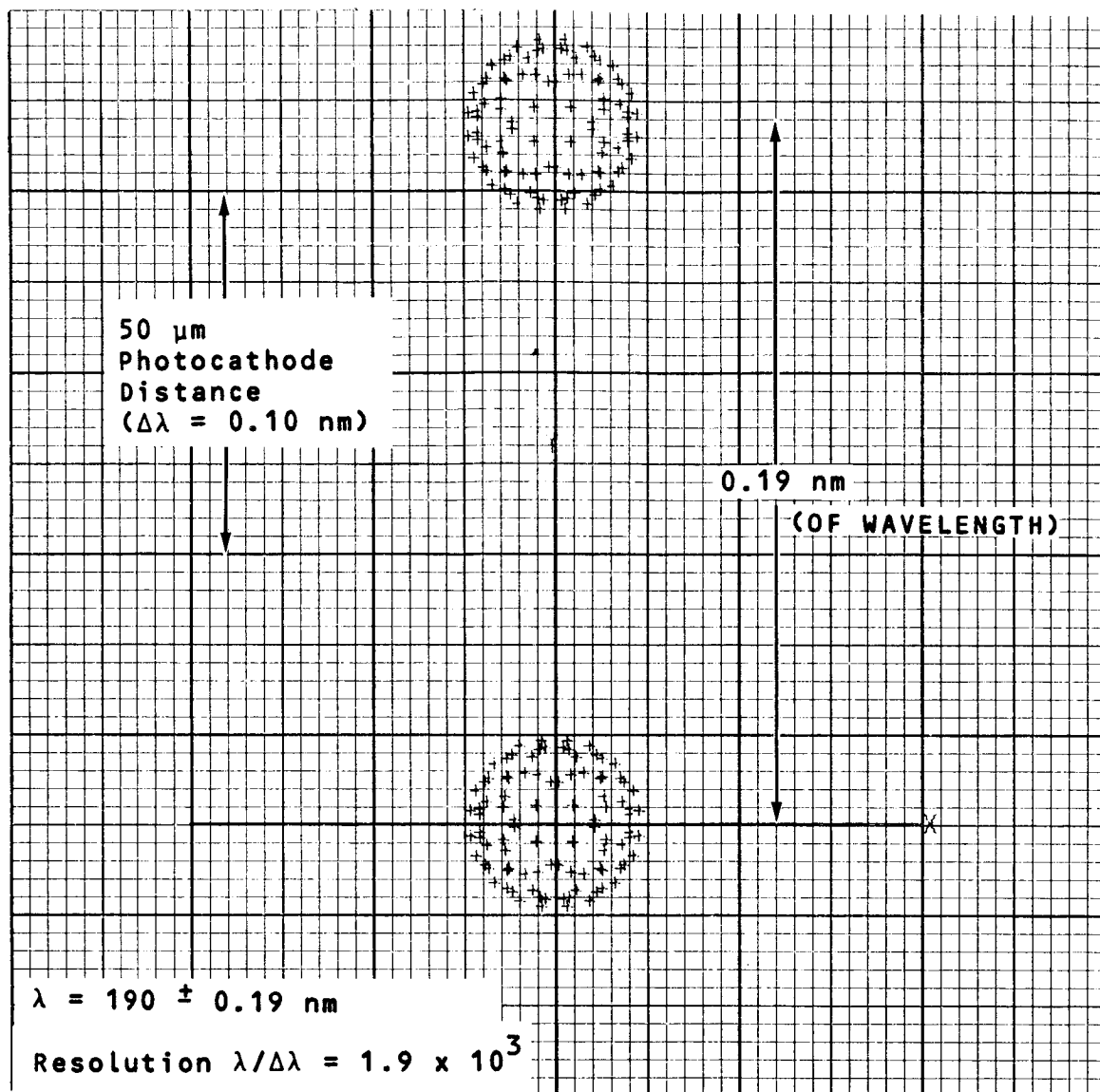


Figure 4-38. Spot Diagram - Faint Object Spectrograph  
Range 1B (160 to 220 nm)

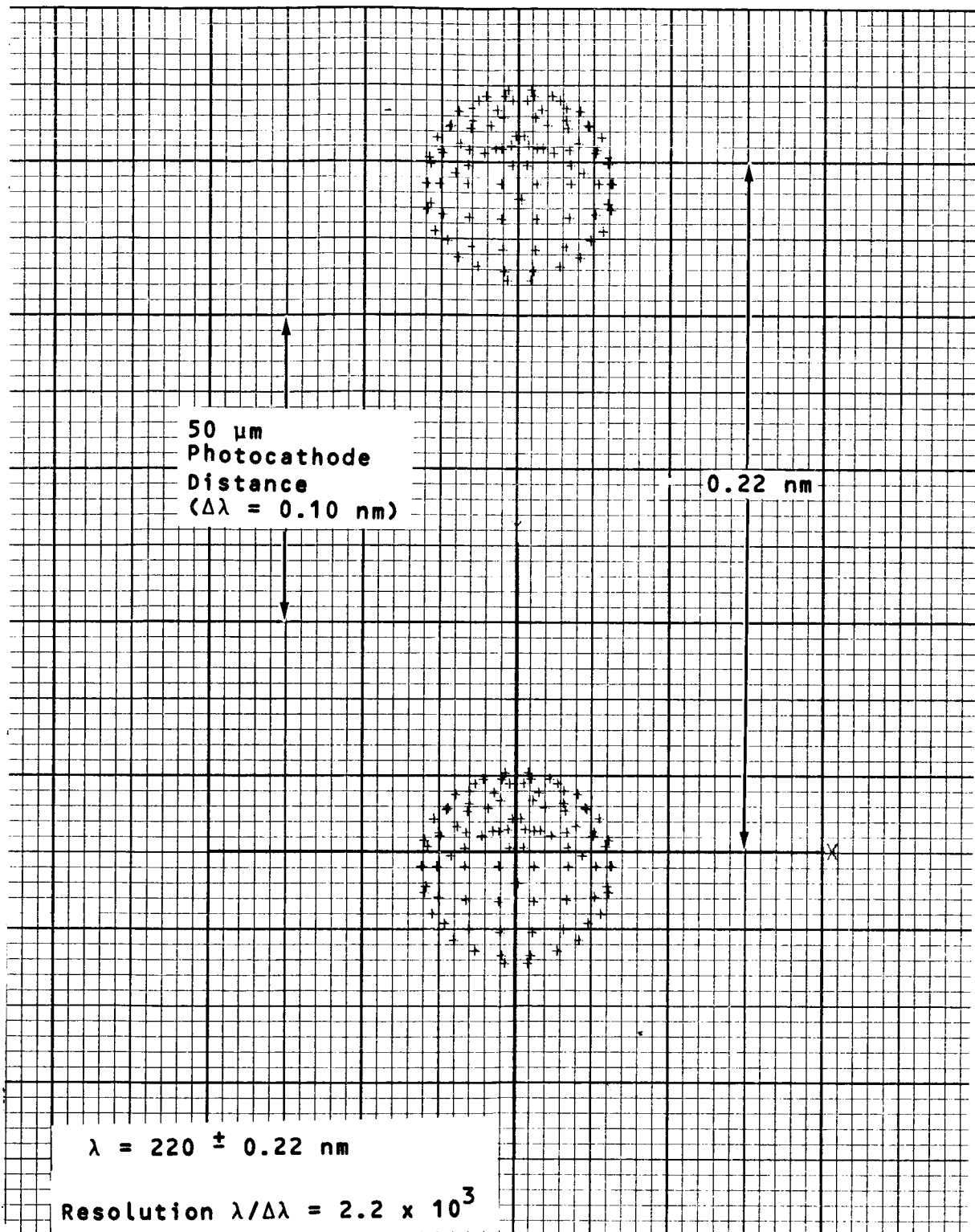


Figure 4-39. Spot Diagram - Faint Object Spectrograph  
Range 1B (160 to 220 nm)

#### 4.4.2.2 Faint Object Spectrograph (2A and 2B)

Two separate instruments are required to cover the range from 220 to 660 nm. However, since less dispersion is required (fewer grooves per millimeter) smaller diameter gratings may be used. These two systems are combined into a single housing and share the same image tube. In this case, the grating is ruled right onto the spherical surface of the camera mirror which is designed such that the central wavelength emerges parallel to the axis after diffraction. Mathematically, the grating equation fulfills this condition when  $\theta_2 = 0$ .

$$m\lambda = d (\sin \theta_1 + \sin \theta_2)$$

where  $m$  = the order number

$\lambda$  = wavelength

$d$  = groove spacing

$\theta_1$  and  $\theta_2$  = angle of incidence and diffraction

##### a. Optical Path

Figure 4-24 is the optical schematic. Light enters the spectrograph at f/12 and is rendered parallel by an off axis paraboloid. The light then strikes a dichroic beamsplitter. Energy below 350 nm is reflected to a camera mirror, while the energy above 350 passes on to a folding mirror and a different camera mirror. Each bundle is then focused onto the same image tube.

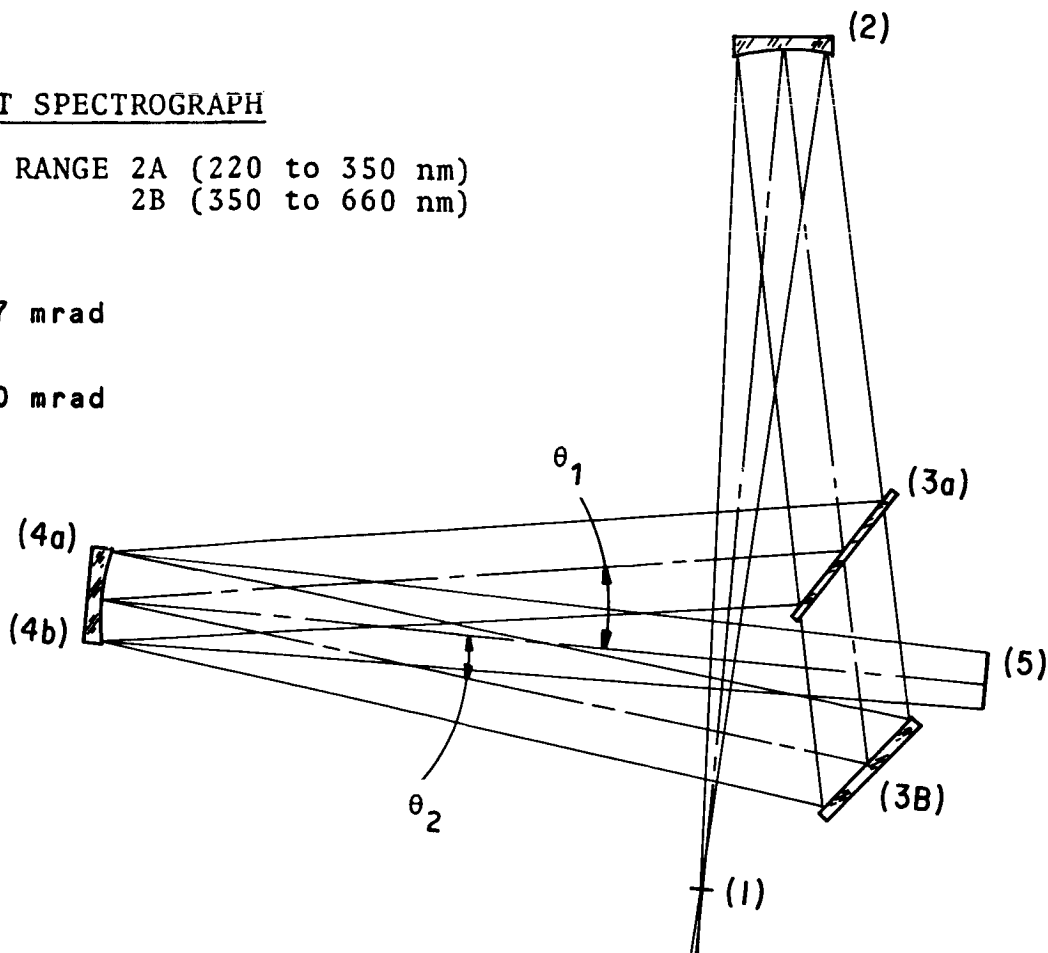
The image presentation is a two line format and may be set along side one another. The advantages of combining these two spectrographs are obvious. It eliminates an extra instrument, saving space, weight and power; it also allows for simultaneous operation of the two instruments, which is not true for any of the other instruments of the package. The design data for these instruments are given in Figure 4-35. It should be noted that these instruments have an f/12 camera mirror.

FAINT OBJECT SPECTROGRAPH

SPECTRAL RANGE 2A (220 to 350 nm)  
2B (350 to 660 nm)

$\theta_1 = 107 \text{ mrad}$

$\theta_2 = 80 \text{ mrad}$



Surface No.	Radius	Conic Constant	Thickness	
(1)	$\infty$		609.6	Ritchey-Chretien F.P.
(2)	-1219.2	-1.0	a. 395.0	Off Axis Paraboloid
(3a.)	$\infty$		b. 487.5	Beamsplitter
(3b.)	$\infty$		a. 515.0	Folding Mirror
(4a.)	1219.2		b. 527.5	Camera Mirror and Grating
(4b.)	1219.2		609.6	Camera Mirorrand Grating
(5)	$\infty$			Tube (30 mm image format)

SURFACE NO. 4

No. 2A 372.9 lines/mm 220 to 350 nm Blaze Angle = 54.2 mrad

No. 2B 159.8 lines/mm 350 to 660 nm Blaze Angle = 40.3 mrad

Figure 4-40. Faint Object Spectrograph Optical System Record

## b. Performance

Figures 4-41 through 4-46 are spot diagrams for the No. 2A and 2B faint object spectrograph. They show the imagery and dispersion at the corners and the center of the field. The spot diagrams for the center wavelengths are symmetrical, since the camera mirrors are effectively on axis. In the corners the effects of coma can be seen. In this case, the effective semi-field angle to the corner of the format is 24.4 mrad. Figure 4-46 shows that this spectrograph falls short of the desired spectral resolution of  $\lambda/\Delta\lambda = 10^3$ . The following distribution could be substituted for the spectral ranges of the spectrographs and conform to the requirement throughout the range:

No. 1A	115 to 160 nm
1B	160 to 250 nm
2A	250 to 400 nm
2B	400 to 640 nm
3	640 to 1000 nm

This would require that the spacings on the gratings be changed, but nothing else.

The penalty was accepted to enhance the spectral resolution of the ultraviolet spectrometers.

## c. Tolerancing

Each of the faint object spectrographs 2A and 2B has only three reflecting components which must share the total tolerance. In all other respects, the tolerancing procedure is the same as outlined in Section 4.3.3 for the high resolution spectrograph.

## d. Baffles

At this time, no additional internal baffles are required for this faint object spectrograph. The instrument geometry, which



$$\lambda = 506 \pm 0.506 \text{ nm}$$

$$\text{Resolution} = \frac{\lambda}{\Delta \lambda} = 1.0 \times 10^3$$

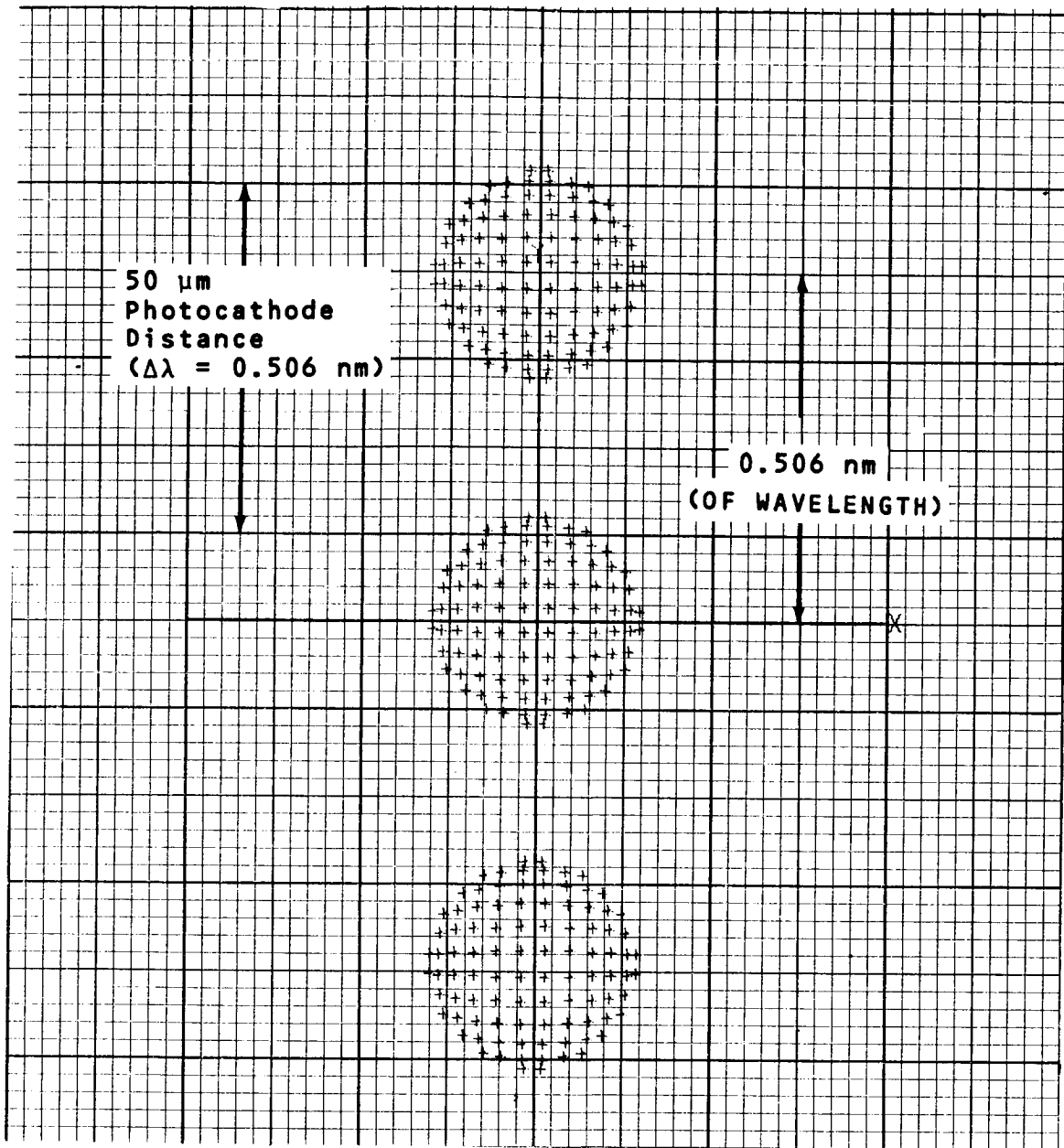


Figure 4-41. Faint Objective Spectrograph Spot Diagram,  
Range 2B (350 to 660 nm)

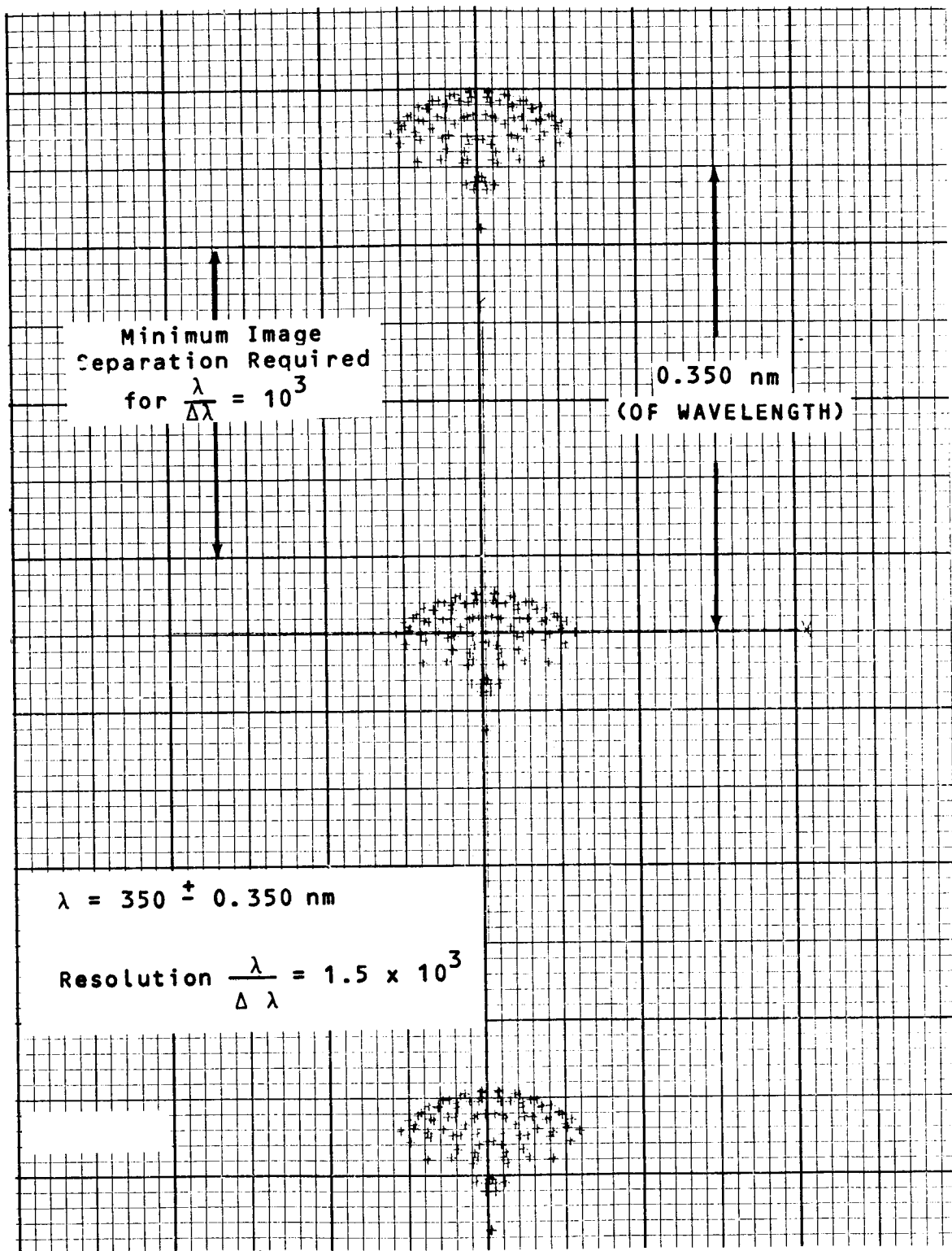


Figure 4-42. Faint Objective Spectrograph Spot Diagram, Range 2B (350 to 660 nm)

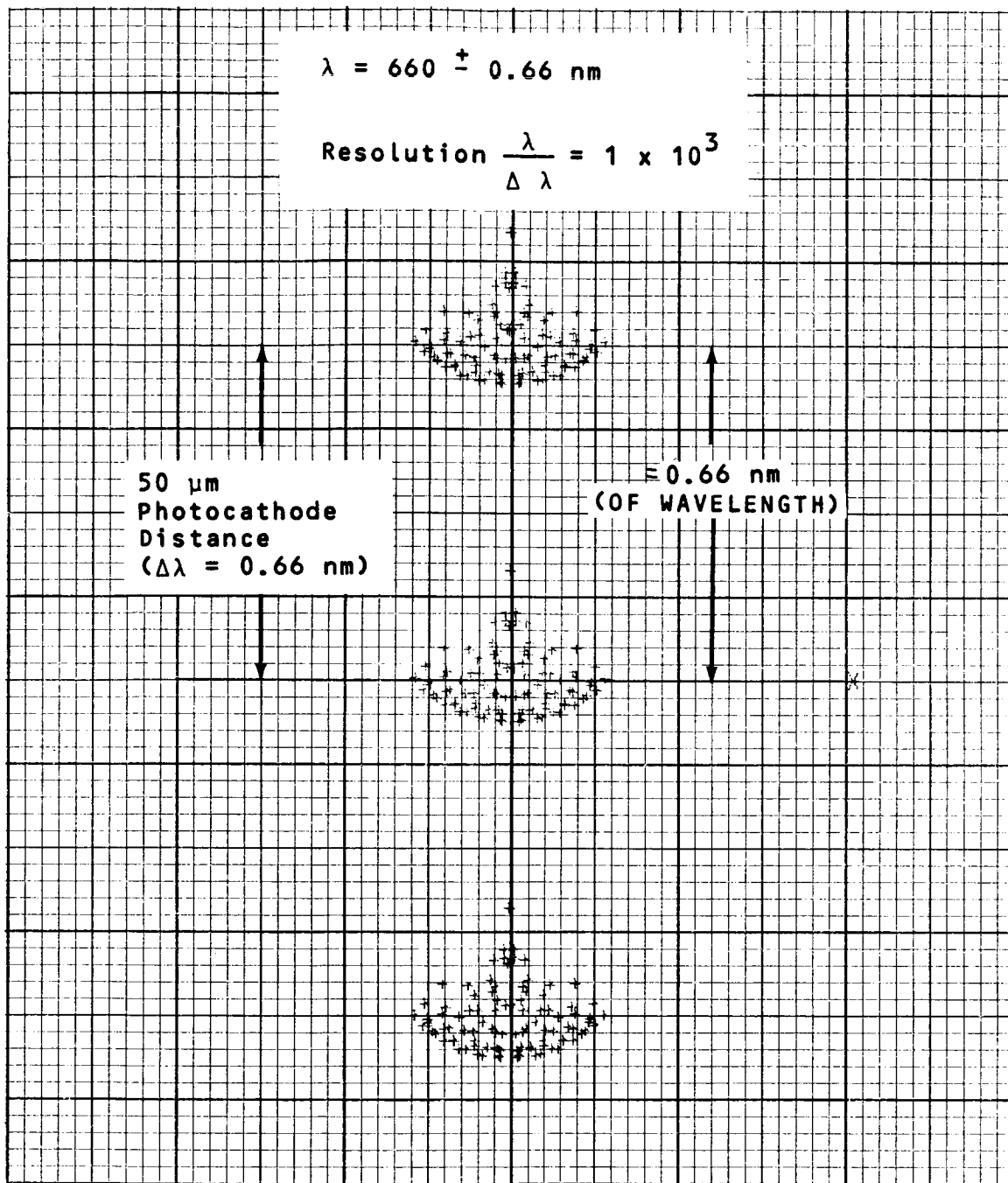


Figure 4-43. Faint Objective Spectrograph Spot Diagram, Range 2B (350 to 660 nm)

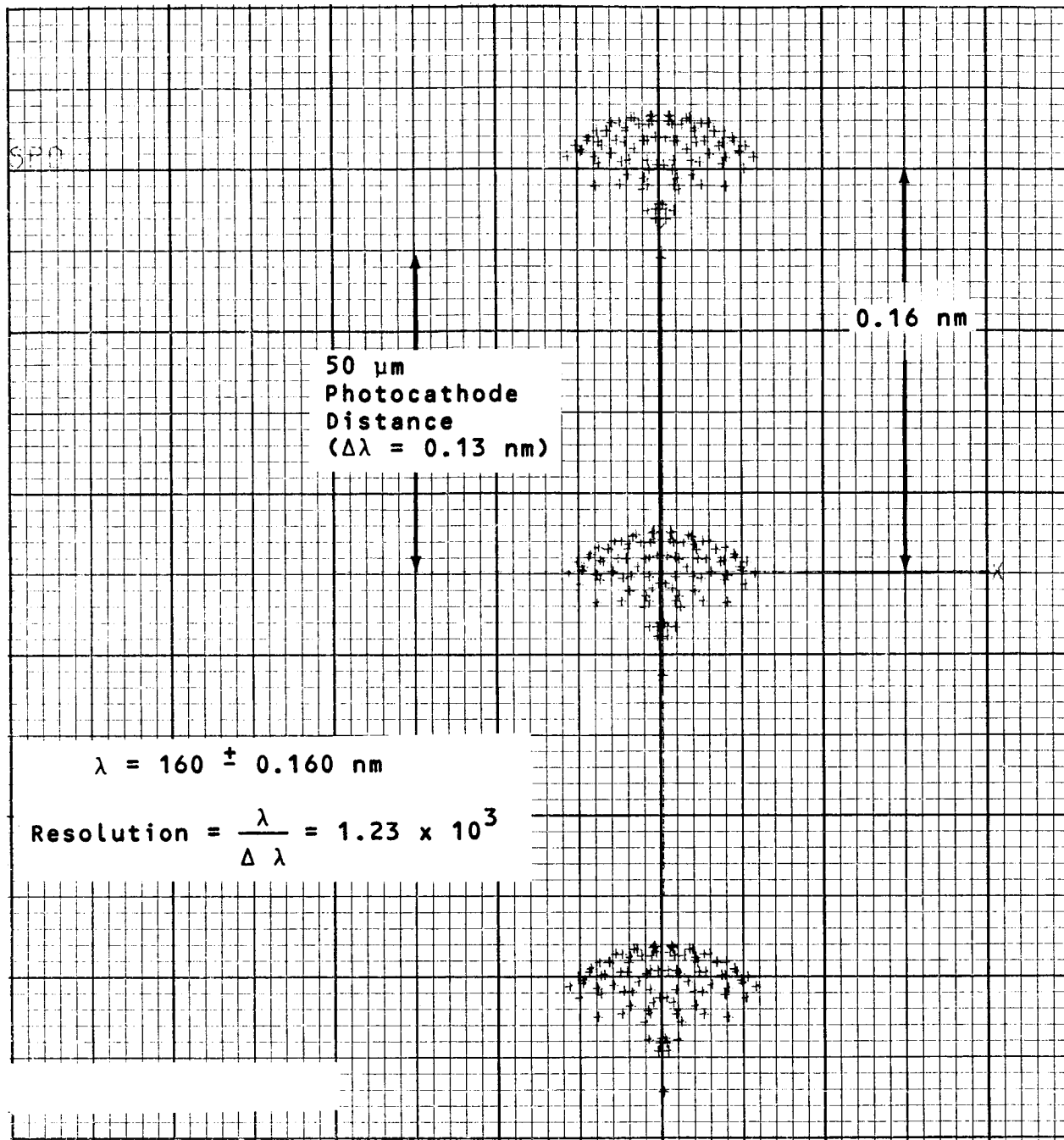


Figure 4-44. Spot Diagram - Faint Object Spectrograph,  
Range 2A (220 to 350 nm)

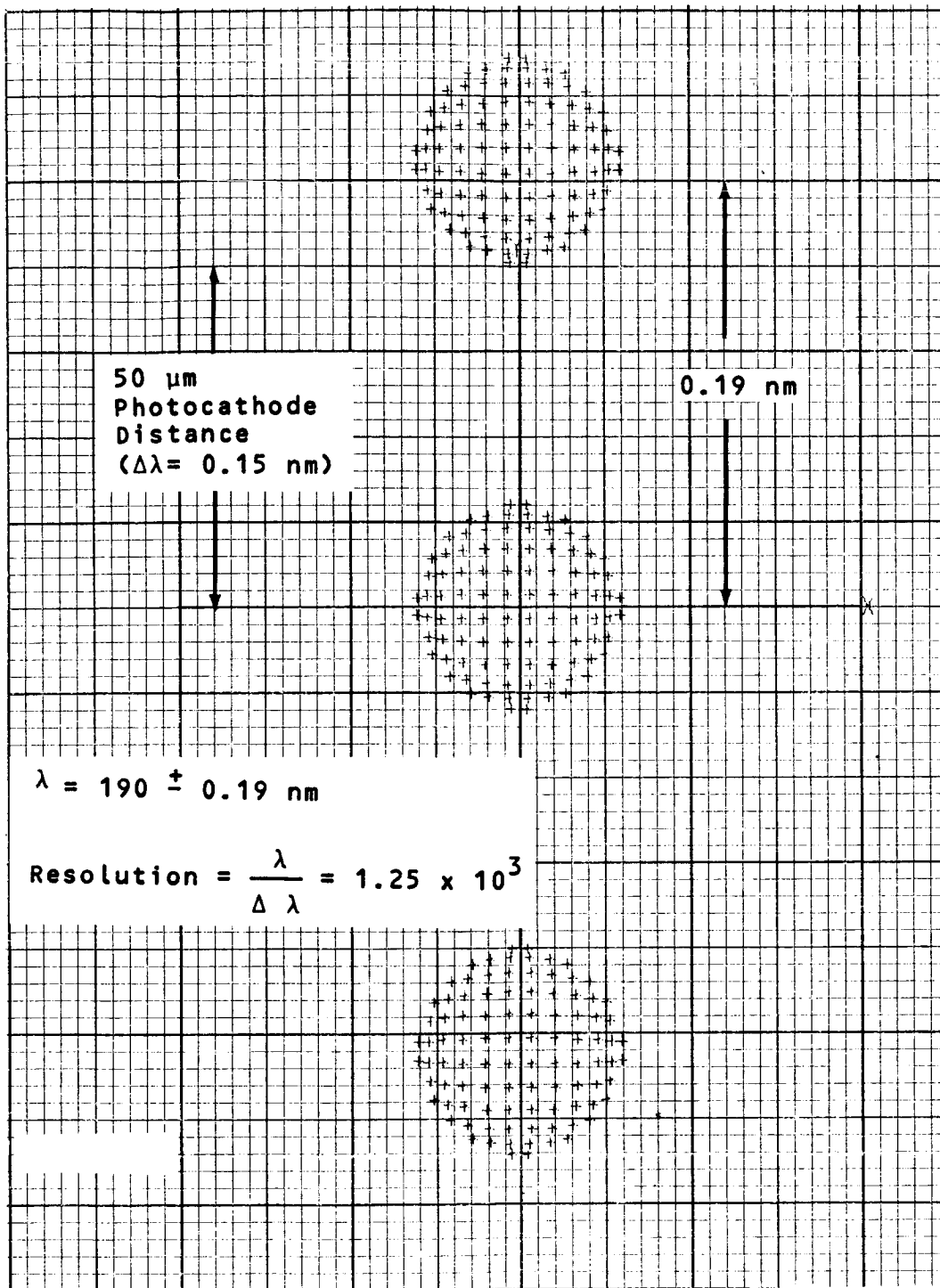


Figure 4-45. Spot Diagram - Faint Object Spectrograph,  
Range 2A (220 to 350 nm)

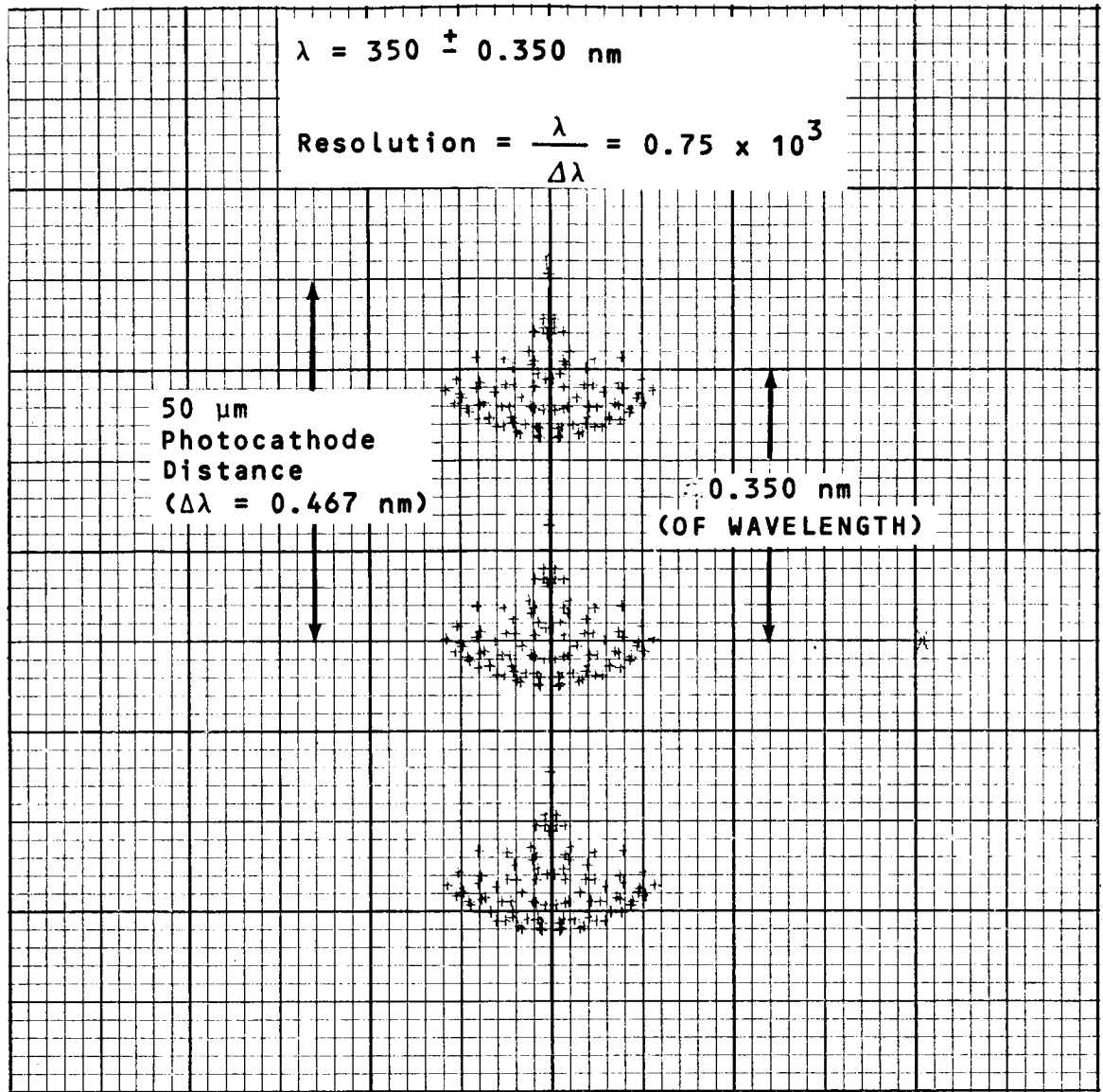


Figure 4-46. Faint Objective Spectrograph Spot Diagram, Range 2A (220 to 350 nm)

places the image tube at right angles to the entrance slot, minimizes the possibility of any light finding its way to the focal plane from any reflective surface, other than the camera mirror.

#### 4.4.2.3 Faint Object Spectrograph No. 3 (660 to 1000 nm)

##### a. Discussion

This spectrograph is similar in construction to that of Case No. 2. It would be desirable to extend the concept of using a dichroic beamsplitter one step further by combining the three instruments into one housing. The dichroic beamsplitter is not capable of covering such a broad spectral band effectively. A separate instrument is therefore needed to cover the near IR range.

##### b. Optical Path

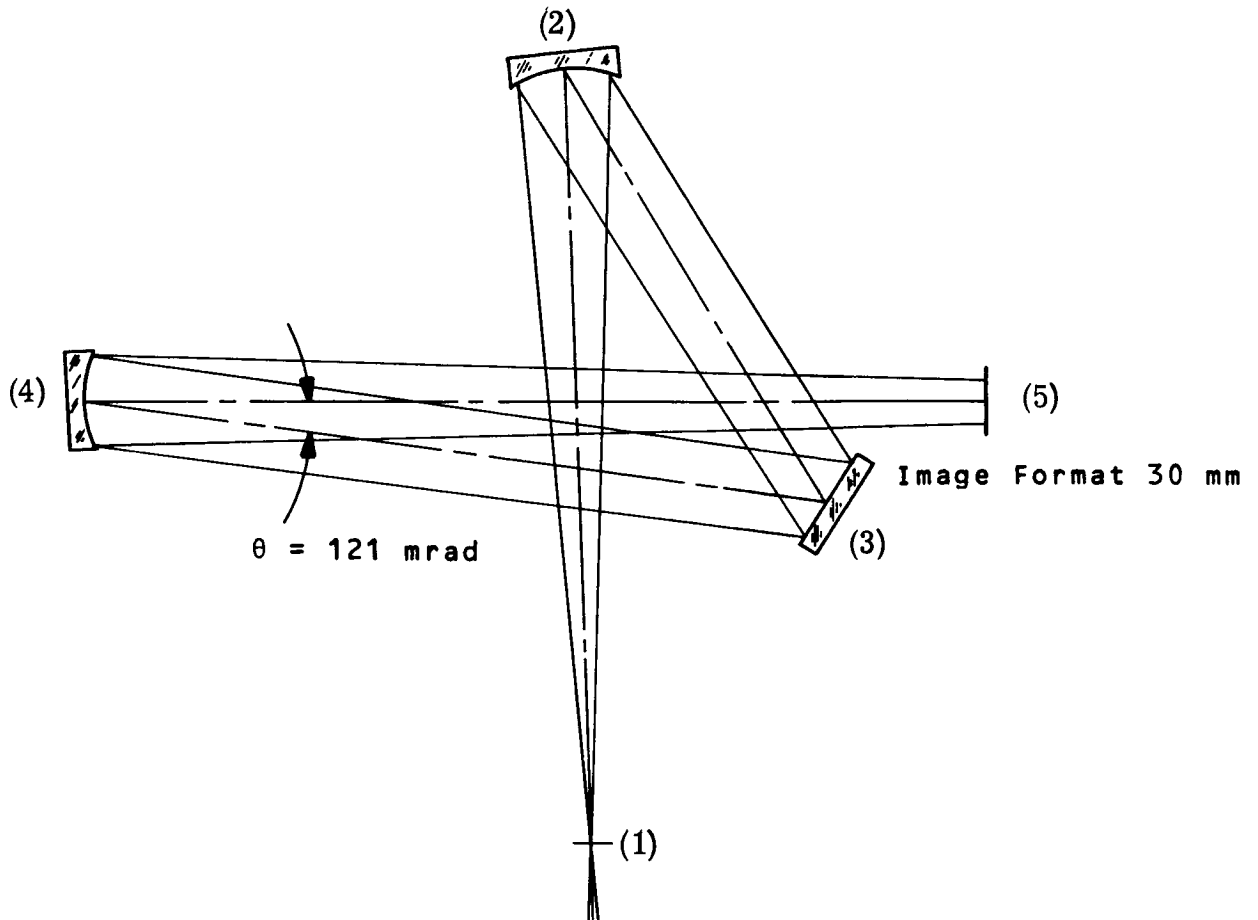
An off-axis collimating mirror renders parallel the light from the f/12 Ritchey Chretien. This energy is then folded toward the camera mirror. The grating is nulled on the camera mirror. As in the previous case, dispersion is set to fill a 30 millimeter format and the central wavelength emerges on axis. Figure 4-47 gives the optical data required for this system.

##### c. Performance

This system uses an f/12 camera mirror as does the No. 2A and 2B spectrographs. The performance is therefore similar. Figures 4-48, 4-49 and 4-50 are spot diagrams showing the performance of the spectrograph at the edges and center of the format.

FAINT OBJECT SPECTROGRAPH NO. 3

SPECTRAL RANGE ③ (660 to 1000 nm)



<u>Surface No.</u>	<u>Radius</u>	<u>Conic Constant</u>	<u>Thickness</u>	
(1)			609.6	Ritchey-Chretien F.P.
(2)	-1219.2	-1.0	442.5	Off Axis Paraboloid
(3)			515.0	Folding Mirror
(4)	1219.2		609.6	Camera Mirror and Grating
(5)				Tube 30 mm Image Format

SURFACE NO. 4

144.7 lines/mm Blaze Angle = 60.2 mrad

Figure 4-47. Optical Record



$$\lambda = 660 \pm 0.66 \text{ nm}$$

$$\text{Resolution } \frac{\lambda}{\Delta \lambda} = 1.25 \times 10^3$$

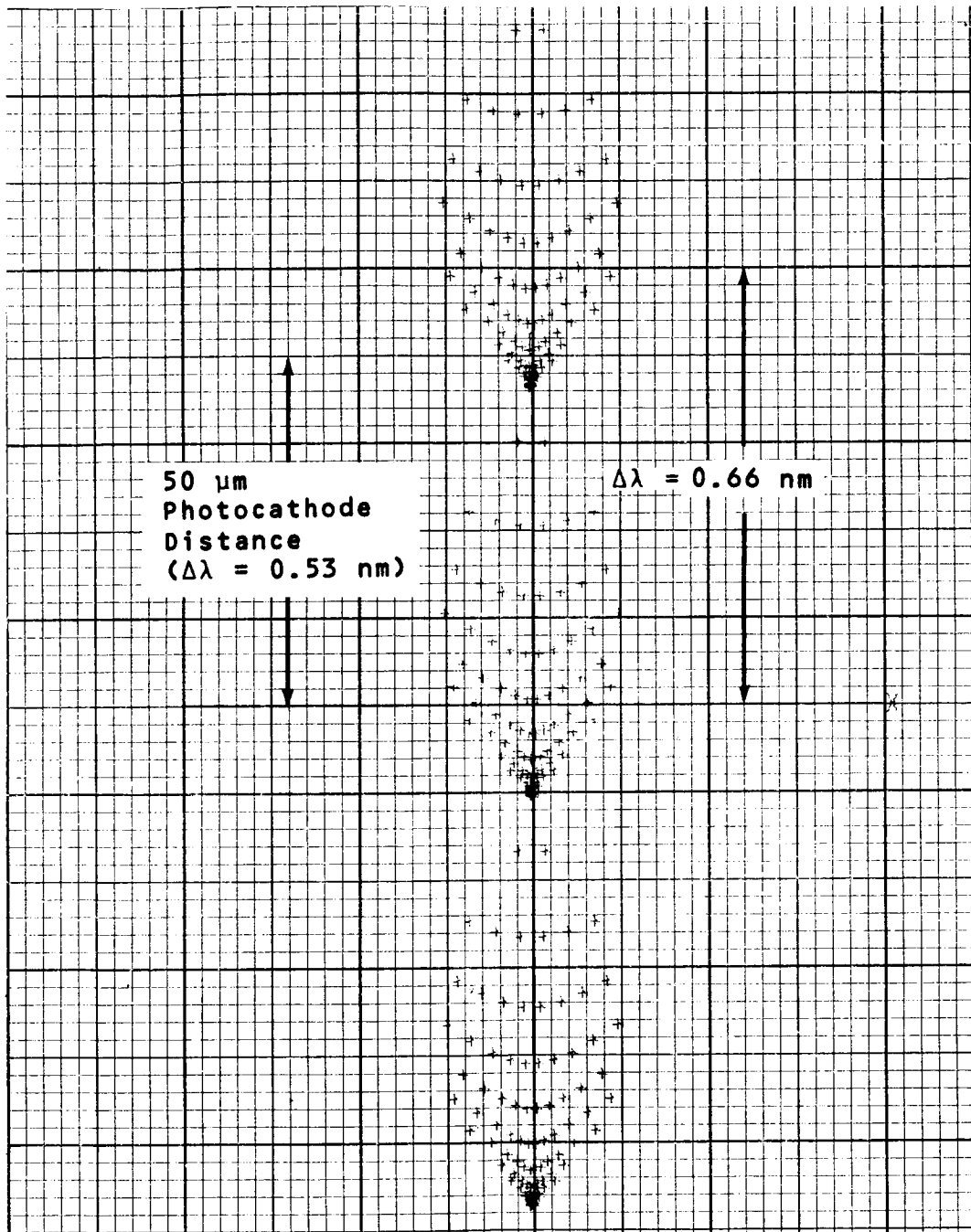


Figure 4-48. Faint Objective Spectrograph No. 3,  
Spot Diagram; Spectral Range 660 to 1000 nm

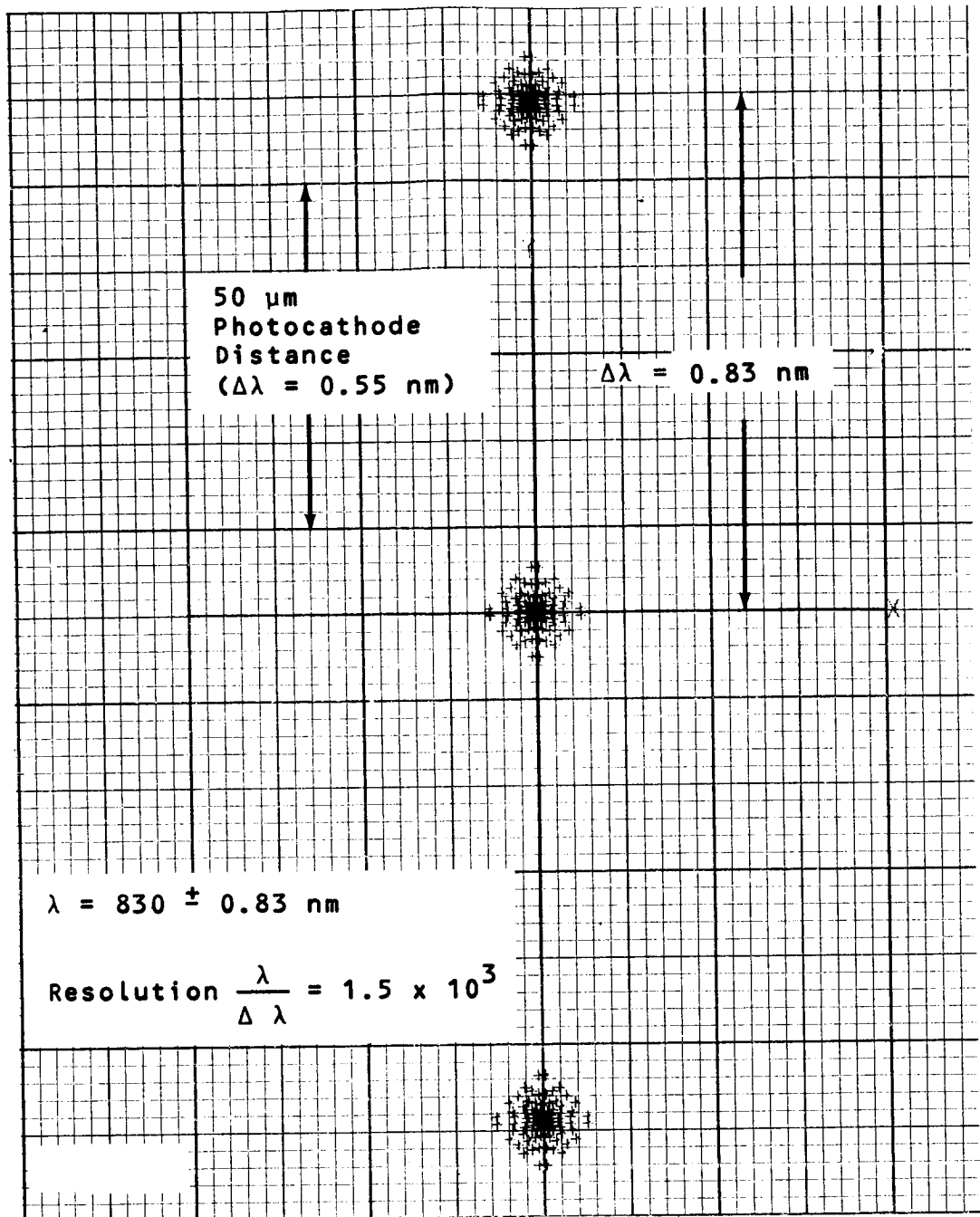


Figure 4-49. Faint Objective Spectrograph No. 3,  
Spot Diagram; Spectral Range 660 to 1000 nm

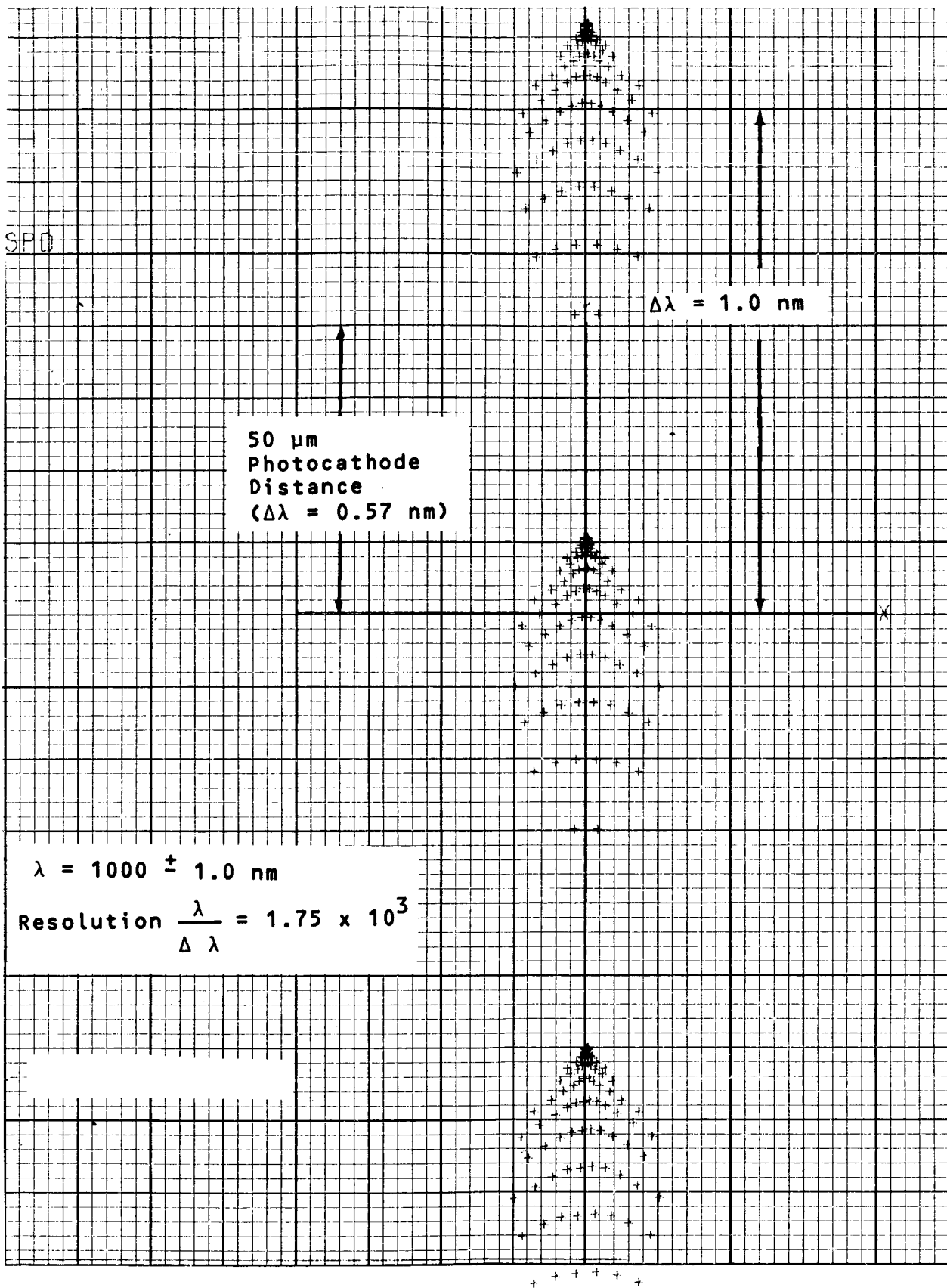


Figure 4-50. Faint Objective Spectrograph No. 3,  
Spot Diagram; Spectral Range 660 to 1000 nm

#### 4.4.3 Detector

The Faint Object Spectrograph is required to provide a spectral range from 115 nm to 1.1  $\mu\text{m}$ <sup>(1)</sup>. For the instrument No. 1 (A and B), covering a spectral range from 115 to 220 nm, two cathode types were evaluated:

- a. CsTe/MgF<sub>2</sub>
- b. Bialkali/MgF<sub>2</sub>

Based on the results of the throughput analysis, the bialkali photocathode was selected for this range (curve 1 in Figure 3-25). This instrument uses two flat gratings, operating one at a time, which generate a line spectrum approximately 30 mm long, fitting the diagonal of a 25 x 25 mm SEC-tube.

Instrument No. 2, which covers the two ranges

- A. from 220 to 350 nm and
- B. from 350 to 660 nm,

used in the initial design two separate camera tubes with different photocathodes. After the updating of the instrument design, one photocathode is used to cover the total range A and B in two parallel spectral line displays, similar to a dual trace in a CRT. Each display is approximately 30 mm long, hence this instrument can also use a 25 x 25 mm SEC-Vidicon with an S-20 photocathode deposited over a fused silica (SiO<sub>2</sub>) window.

Instrument No. 3 will also use a 25 x 25 mm SEC-Vidicon for detection of the single spectral line trace approximately 30 mm long. For accommodation of the specified spectral coverage up to 1.1  $\mu\text{m}$ , this instrument will use a glass window and a III-V semi-transparent photocathode.

All physical parameters and performance of this detector are identical to the one described in Section 4.2.3.

---

(1) Same as in para. 4.2.3.

#### 4.4.4 Signal-To-Noise Analysis

The Faint Object Spectrograph S/N analysis was computed similarly to the High Resolution Spectrograph, except that the appropriate throughput values (from Section 3.6) were used. For the Faint Object Spectrograph, a slit length of 75  $\mu$ rad was selected. This is the maximum recommended by the LST Steering Group<sup>(1)</sup> and the maximum which could be used for work on an extended target in instrument No. 2, where a maximum of two 75  $\mu$ rad wide traces (2.7 mm in f/12), each approximately 30 mm long, will fit diagonally on a 25 x 25 mm format. Results for both recommended slit width values ( $W = 0.25$  and  $0.50$   $\mu$ rad) are shown in Figures 4-51 and 4-52 for instruments No. 1 and No. 2, respectively, each for various star magnitudes (11,000K), integration times ( $t$ ) and an operating temperature of  $T = 293K$ .

For all cases, the background influence is negligible (scattering was not included in the computation). Instrument No. 1 is quantum noise limited except where the total number of integrated counts falls below 120, i.e., where the amplifier noise predominates and the dark count of the photocathode starts to appear. Instrument No. 2 is dark count limited at room temperature. Cooling its detector's cathode to approximately 250K achieves a 1.0 to 1.5 star magnitude sensitivity improvement.

Another noise factor, to be established during the sensor breadboard evaluation, is the camera tube wall's contribution to the noise count. This is assumed to limit the tube integration time to  $t = 36$  ks (10 hours).

LIMITING SIGNAL AND MAGNITUDE (as in Section 4.3.5)

##### a. Instrument No. 1

Wavelength	$\lambda_1 = 140$	$\lambda_2 = 180$ [nm]
Spectral bandwidth (contained in one spectral line image)	$\Delta\lambda_1 = 0.14$	$\Delta\lambda_2 = 0.18$ [nm]

<sup>(1)</sup> Summary of LST Instrument Recommendations (Appendix I)(Table 3-1)  
Received from S. Sobieski, Sec'y, LST Steering Group

Spectral density (From Figure 3-25) for Bialkali/MgF <sub>2</sub>	$N_{O1} = 1.5 \times 10^6$	$N_{O2} = 6 \times 10^6$
Exposure time	$t = 3.6 \times 10^4$	$t = 3.6 \times 10^4$ [s]
Enslitted energy for $W_1 = 0.25 \mu\text{rad}$ $\approx d_{\text{Airy Disc}}$ at $\lambda = 0.3 \mu\text{m}$	$\frac{E_W}{E_T} = 0.7$	$\frac{E_W}{E_T} = 0.7$
Zero magnitude signal	$S_{O1} = 5.3 \times 10^9$	$S_{O2} = 2.7 \times 10^{10}$ [pe]
23 magnitude signal	$S_{23} \approx 3.3$	$S_{23} \approx 16.9$ [pe]
The solid angle* $\Omega \approx 0.5 \text{ psr}$ for $W_1 = 0.25 \mu\text{rad}$	$S_{B1} \approx S_{23} \frac{\Omega}{25}$ $\leq 6.6 \times 10^{-2}$ negl.	$S_{B2} \approx 0.34$ [pe] negl.
The dark count $a = 2.5 \times 10^{-5} \text{ cm}^2$ $N = 40 \text{ el/cm}^2\text{-sec}$	$N_D = 36$	$N_D = 36$
Readout noise count	$(n_R)^2 = 128$	$(n_R)^2 = 128$ [pe]
Limiting signal** for $S/N = 2$	$S_{\text{lim}} \approx 28$	$S_{\text{lim}} \approx 28$ [pe]
Limiting magnitude for $S/N = 2$	$m_{\text{lim}} \approx +21$	$m_{\text{lim}} \approx +22.5$ star mag.

Figure 4-51 illustrates the above data and other computed points for the Faint Object Spectrograph, Instrument No. 1, using various star magnitudes and integration times.

b. Instrument No. 2

Wavelength	$\lambda_1 = 300$	$\lambda_2 = 500$ [nm]
Spectral bandwidth	$\Delta\lambda_1 = 0.3$	$\Delta\lambda_2 = 0.5$ [nm]

\* The spectrograph background noise (per sensor resolution element) is limited by the solid angle,  $\Omega$ . This angle is established by the angular slit width in one direction, and by the angular height of the sensor resolution element's image in the slit plane.

\*\*Target saturation occurs at a signal count of 2500 pe with a  $S/N = 50$ .

Integration time	$t = 3.6 \times 10^4$	$t = 3.6 \times 10^4$ [s]
Spectral density (from Figure 3-26)	$N_{O1} = 6 \times 10^7$	$N_{O2} = 4 \times 10^7$ [pe/s-nm]
Enslitted energy For $W_1 = 0.25 \mu\text{rad}$	$\frac{E_W}{E_T} = 0.7$	$\frac{E_W}{E_T} = 0.6$
Zero magnitude signal	$S_{O1} = 4.5 \times 10^{11}$	$S_{O2} = 4.3 \times 10^{11}$ [pe]
+23 magnitude signal	$S_{23} = 285$	$S_{23} = 280$ [pe]
Solid angle* For $W_1 = 0.25 \mu\text{rad}$	$\Omega_1 = 0.4$	$\Omega_2 = 0.4$ [psr]
Background signal	$S_B = S_{23} \times \frac{\Omega}{25} = 4$	$S_B = 3$ [pe]
$N_D = a N t$ with $N = 400 \text{ el/s-cm}^2$ for S-20 photo- cathode	$a_1 = 2.5 \times 10^{-5}$ $N_{D1} = 360$	$a_2 = 2.5 \times 10^{-5}$ [cm <sup>2</sup> ] $N_{D2} = 360$ [pe]
Readout noise count	$(n_R)^2 = 128$	$(n_R)^2 = 128$ [pe]
Limiting signal for $S/N = 2$	$S_{lim} = 47$	$S_{lim} = 47$ [pe]
Limiting magnitude for $S/N = 2$	$m_{lim} = +25$	$m_{lim} = 25$ star mag.

Figure 4-52 illustrates the above data and other computed points for the Faint Object Spectrograph, Instrument No. 2, using various star magnitudes and integration times.

---

\* The spectrograph background noise (per sensor resolution element) is limited by the solid angle,  $\Omega$ . This angle is established by the angular slit width in one direction, and by the angular height of the sensor resolution element's image in the slit plane.

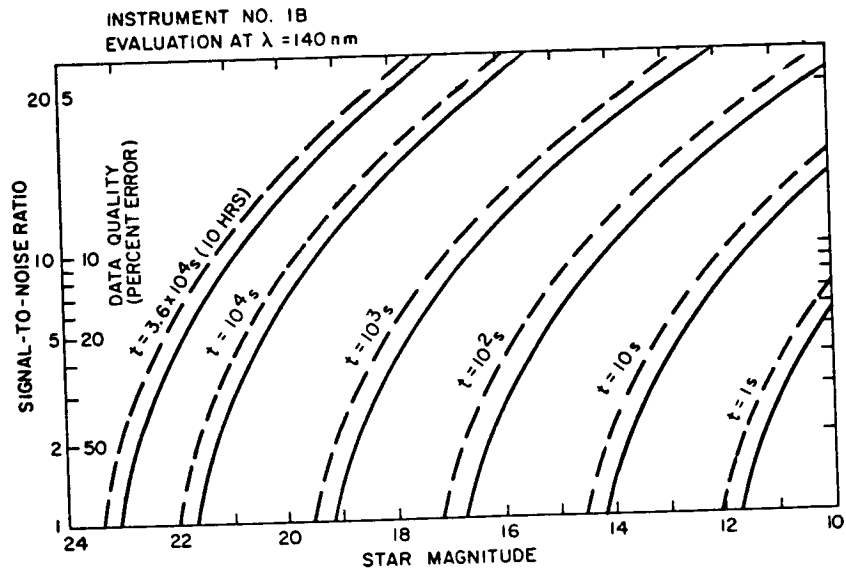
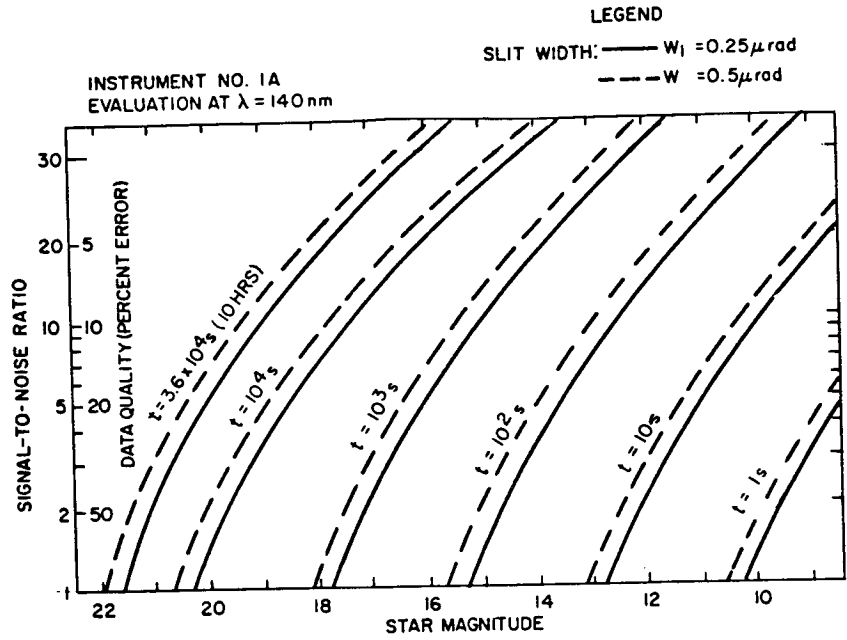


Figure 4-51. Faint Object Spectrograph No. 1, S/N Ratio as a Function of Star Magnitude (11,000K) and Integration Time (t) SEC-Vidicon Oper. Temp. 293K; 20 LP/mm at 50% MTF



INSTRUMENT NO. 2A  
EVALUATION AT  $\lambda = 300 \text{ nm}$

INSTRUMENT NO. 2B  
EVALUATION AT  $\lambda = 500 \text{ nm}$

LEGEND

—  $W_1 = 0.25 \mu\text{rad}$   
- - -  $W_2 = 0.5 \mu\text{rad}$

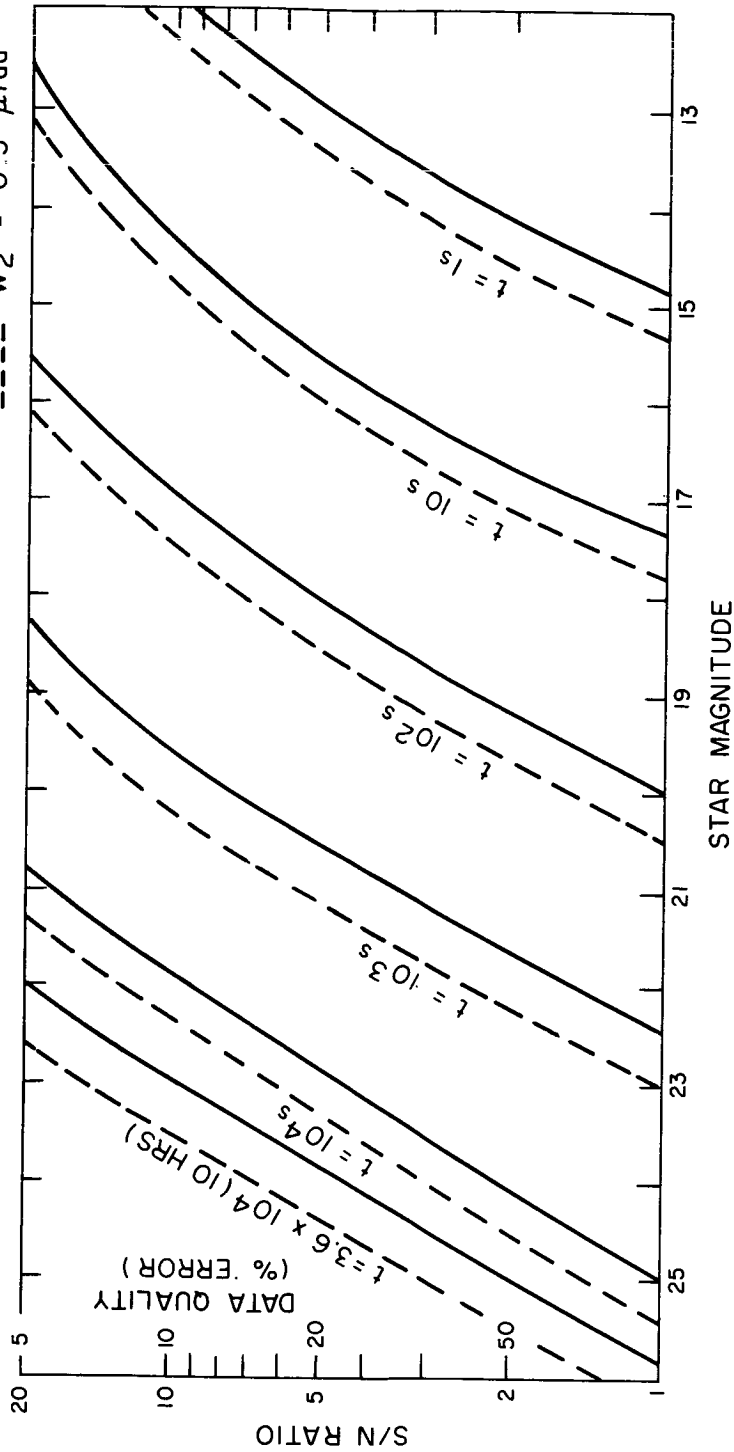


Figure 4-52. Faint Object Spectrograph No. 2, S/N Ratio as a Function of Star Magnitude (11,000K) and Integration Time (t) SEC-Vidicon Oper. Temp. 293K; 20 LP/mm at 50% MTF

## 4.5 MID-IR INTERFEROMETER

The unavailability of noncryogenic vidicon tubes capable of efficient operation in the middle infrared range (1  $\mu\text{m}$  to 5  $\mu\text{m}$ ) and of a single dispersive system for that range preclude the use of spectrographs of the type described in Sections 4.3 and 4.4.

An advantageous replacement is the modified Michelson interferometer. The interferometer is used to generate the interferogram of the source. A Fourier transform program, performed by ground computer, converts that interferogram into the power spectrum of the source.

A discussion of the system proposed to obtain the middle infrared spectra is given below. The discussion was abstracted from two basic references<sup>(1)</sup> in which the successful design and implementation of the system is thoroughly discussed.

### 4.5.1 General Description

The interferometer assembly consists of the foreoptics, reference sources, a modified Michelson interferometer with laser controlled stepping unit, the output detection system and the data handling system.

Referring to Figure 4-53, the entrance slits, ES, accepts the input beam from the f/12 telescope. The beam is modulated by the foreoptics and passed to the interferometer entrance aperture, EA. Division of amplitude within the beamsplitter cube produces two beams, a reference beam and a signal beam, shown in Figure 4-54. After each beam double-passes its retroreflecting cat's eye, the two beams are recombined and collimated onto the face of the signal detector. A record of intensity versus optical path

---

(1) (a) Schindler, R.A., Applied Optics, Feb. 1970, Vol 9, No. 2.  
(b) NASA/JPL Space Programs Summaries  
37-43, Vol IV 1967; 37-56 Vol III, 1969; 37-52, Vol III 1968.

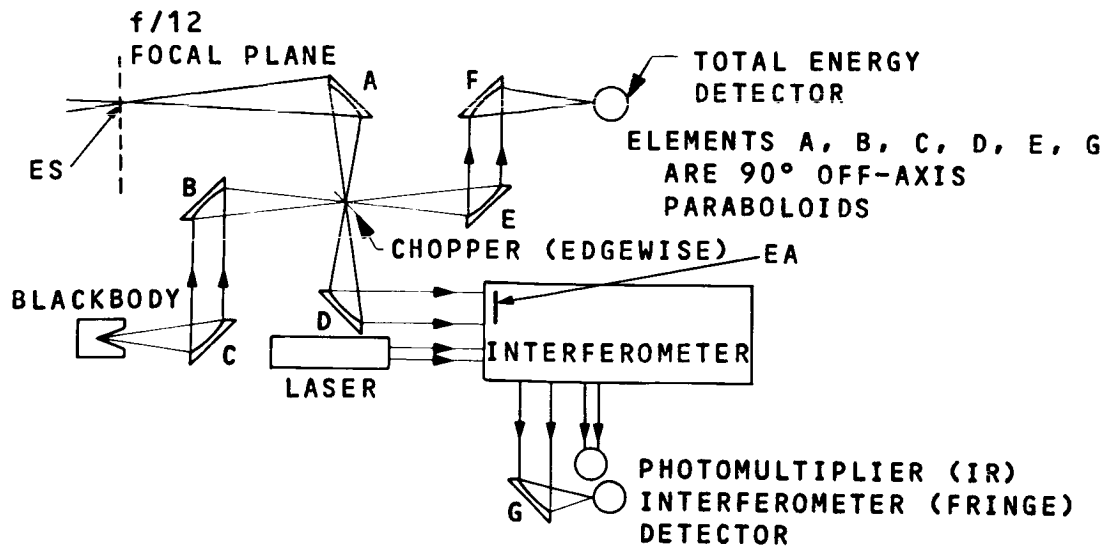


Figure 4-53. Foreoptics of Interferometer

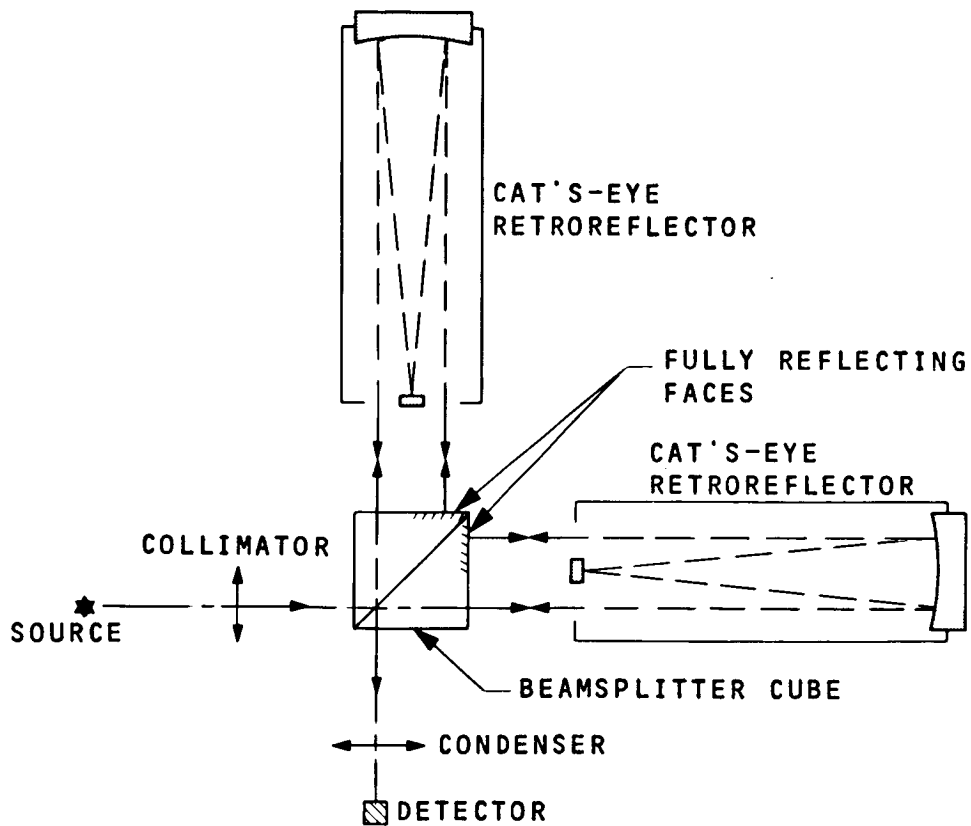


Figure 4-54. Optical Diagram of Interferometer

difference (existing at that intensity), called the interferogram, is thereby constructed. The movable signal arm is indexed by a servo loop system described below.

#### 4.5.2 Description of Optics

The family tree and design layout of the Mid-IR Interferometer assembly are shown in Figures 4-55 and 4-56, respectively.

##### a. Foreoptics

The foreoptics of the system consist of an entrance slit and two crossed, unit magnification relay systems having at their common intermediate focal plane a tuning fork chopper which alternates the field of view of the interferometer between a reference black body radiator and the signal passing through the entrance slit. The imaging optics, F and G of Figure 4-53, are  $f/2.5$ ,  $\pi/2$  rad, off-axis ellipsoids and paraboloids, respectively, of focal length 50 mm; with this field of view, they form 1.1 mm diameter images on their respective detectors. The 1000 Hz\* tuning fork chopper has a  $\text{CaF}_2$  (calcium fluoride) blade, half gold coated to allow the converging beams from either side to be simultaneously reflected or transmitted. On the first half of the chopper cycle, the chopper transmits to the interferometer the incoming signal in the  $f/12$  beam and transmits to the total power detector the reference black body radiation. During the second half of the chopper cycle, incident signal radiation is reflected to the total power detector and reference radiation is reflected to the interferometer.

The prime function of the foreoptics is to present a 22 mrad field of view to the 30 mm by 20 mm semiaperture of the cat's eye and to provide a (1000 Hz) signal modulation. The tuning fork chopper eliminates the need for a high-speed chopper-motor, a source of objectionable vibrations.

---

\* The chopping frequency may be reduced to one-third this value.

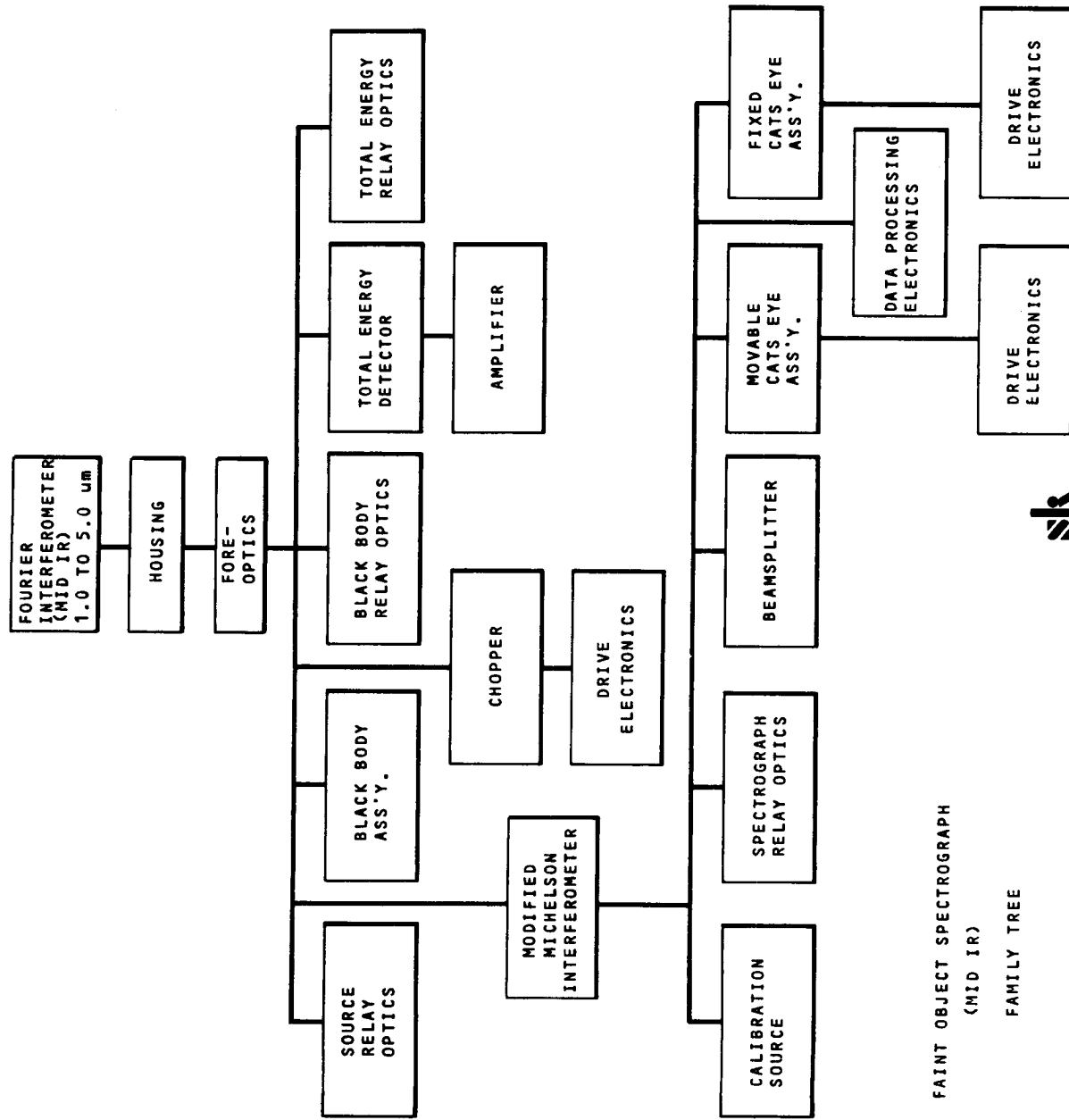
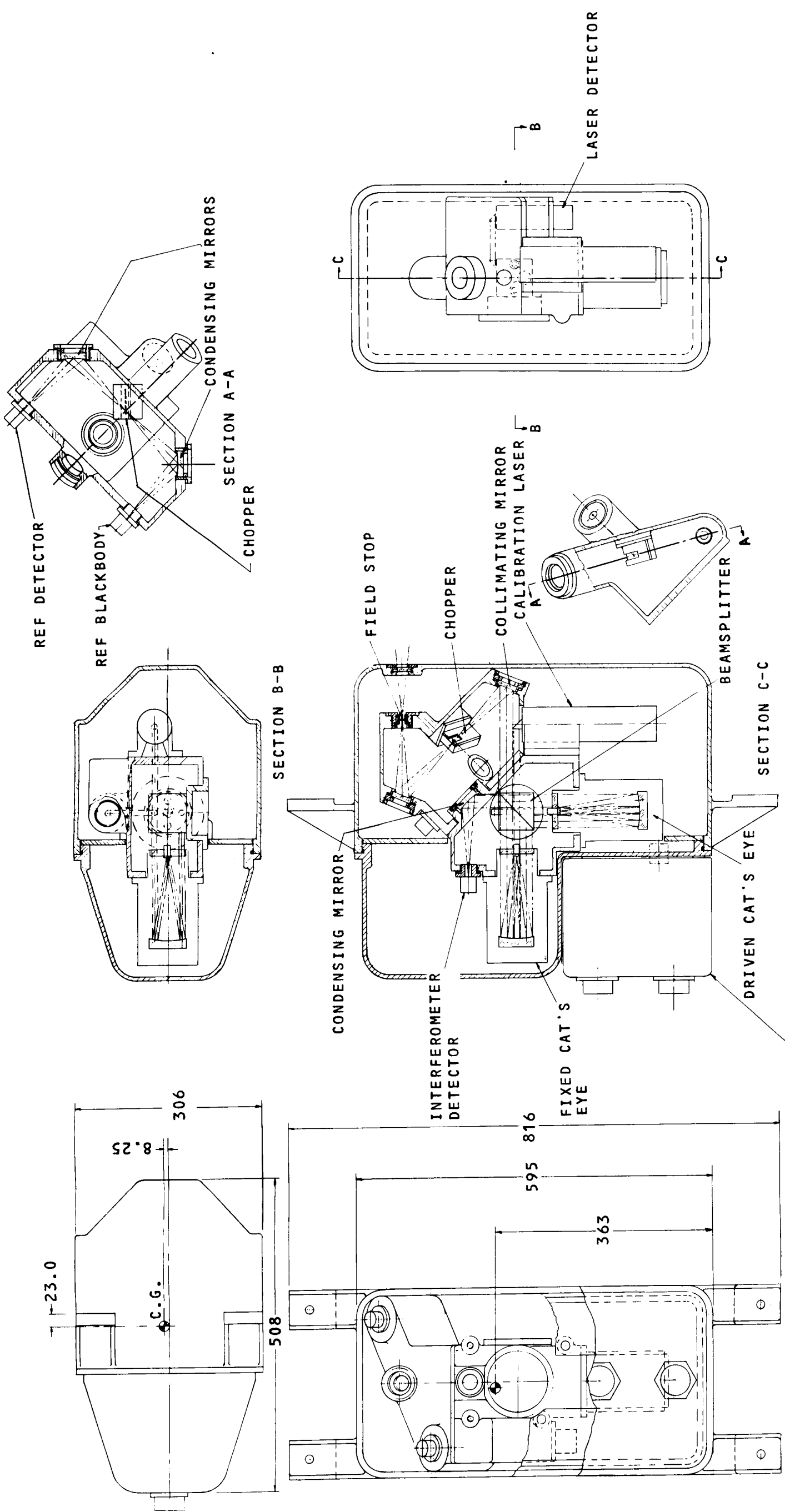


Figure 4-55. Mid-IR (Fourier) Interferometer



NOTE: 1. ALL DIMENSIONS IN MILLIMETERS  
 2. ESTIMATED WEIGHT 52.73 Kg

Figure 4-56. Mid-IR (Fourier) Interferometer

## b. Modified Michelson Interferometer

The important output data is generated by the two beam interference of the interferometer. In place of the standard plane mirrors, two cat's eye retroreflectors are employed, one each in the signal (movable) and reference (stationary) arms of the instrument. The retroreflectors and the associated double pass render the instrument insensitive to both angular and lateral motions of the moving element.

The cat's eye mirrors have a 132.5 mm focal length and a 60 mm diameter. The secondary mirrors are 5 mm in diameter.

Collimated radiation from the foreoptics enters the interferometer. Each of the two beams produced by amplitude division in the beamsplitter double passes its cat's eye retroreflector. This double pass through the cat's eye induces an optical path difference of four times the displacement of the moving signal arm instead of twice as in the classical (single pass) Michelson interferometer. An image of the Haidinger rings associated with the interferometer at this path difference falls onto the interferometer's lead-selenide detectors. The resulting output, a measure of the intensity of the signal radiation and its temporal coherence, is amplified, demodulated, integrated and sent to the analog-to-digital converter after which preprocessing it is accepted by the pulse-code modulation system.

### 4.5.3 Servo Control System

The laser source shown in Figure 4-54 generates a strong monochromatic fringe which serves to null the moving cat's eye servo system. The fixed reference arm's secondary mirror and its piezoelectric transducer form the resonant element of the local oscillator circuit.

The secondary mirror of the cat's eye (in the fixed arm) is vibrated by a piezoelectric crystal, producing a peak-to-peak fringe

position variation of approximately 8 nm at a frequency of 480 KHz; a photomultiplier senses the fringe intensity. The resulting photomultiplier output is nominally a fundamental of 480 KHz with amplitude and phase varying with the cat's eyes average position. Using the oscillator as a reference, the signal is phase sensitively demodulated and filtered to produce the derivative of fringe intensity with respect to optical path difference. This servo-error signal, having null points at fringe maxima or minima, is amplified and fed to a moving coil actuator which drives the signal arm's cat's eye until a minimum fringe intensity is produced. Selection of the minimum intensity for null condition reduces photomultiplier noise. A second coil on the actuator develops a voltage proportional to the moving element's velocity; the voltage is amplified and fed back to the drive coil to provide velocity damping and vibration immunity. The other part of the demodulated error signal is amplified (as shown in Figure 4-57) and fed to the secondary mirror transducer of the movable cat's eye, thus completing the crystal oscillator circuit. Hence, the monochromatic source is seen to provide:

- (1) a measure of optical path difference (one wavelength of HeNe per optical path difference between the two arms) and
- (2) a sinusoidally varying derivative signal to drive the actuator coil and bring the moving cat's eye back to the minimum fringe intensity position.

Upon command, a ramp voltage is added to the error signal, overpowering the servo-loop and forcing the cat's eye to move toward the next null position, i.e., to the next fringe. A reversible fringe counter, operated by the two in phase quadrature signals (mixer output and DC component of the photomultiplier output) keeps track of the actual fringe count. Since fringe count yields optical path difference, an accurate record of mirror position, critical to the generation of accurate spectra, is automatically provided.



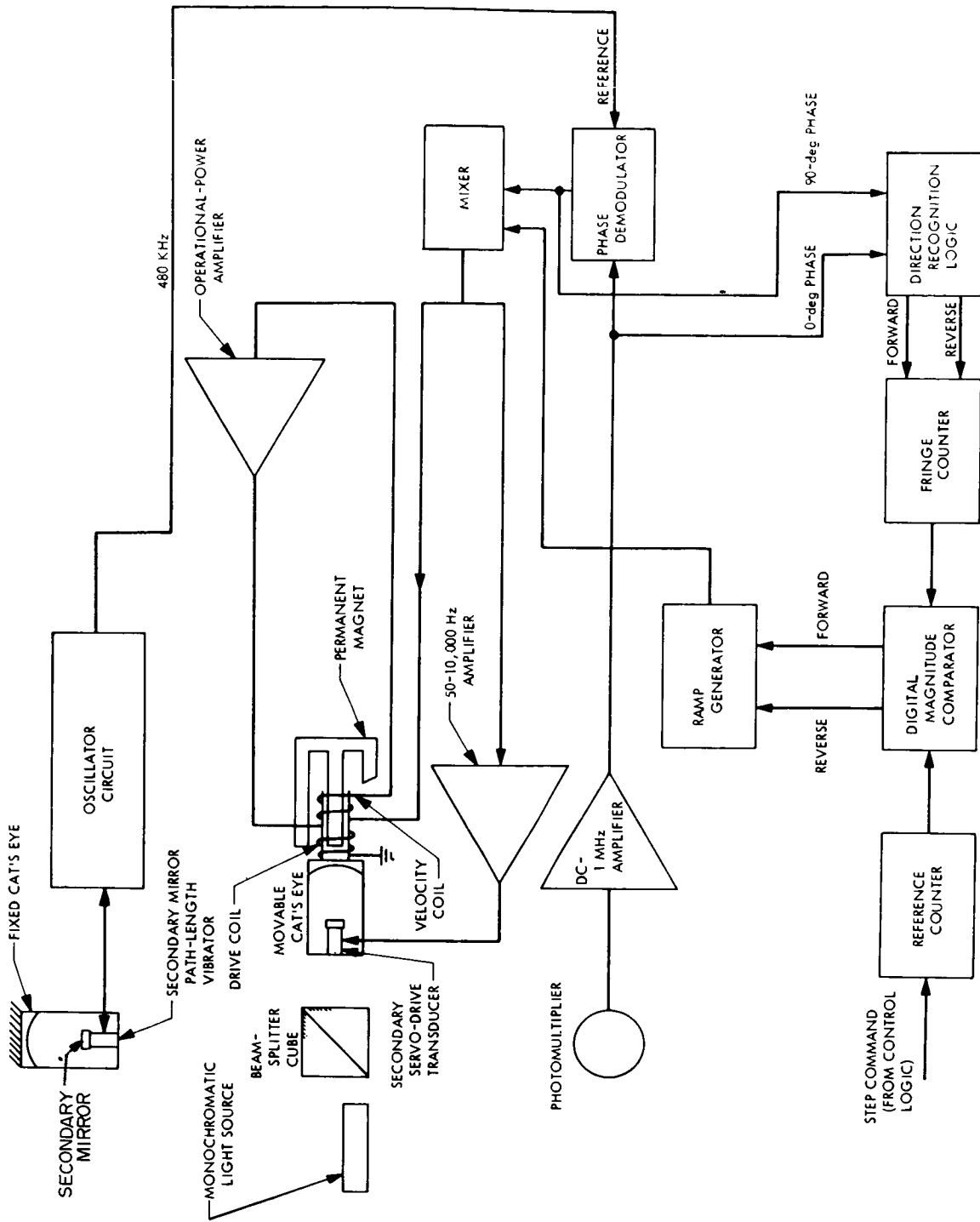


Figure 4-57. Interferometer Servo Control System

#### 4.5.4 Detector and Internal Sources

The Fourier Interferometer uses a 1.3 x 1.3 mm sensor element to detect the fringe intensity in a spectral band of 1-5  $\mu\text{m}$ .

Based on the system thermal analysis, the sensor operating point of 300K is predicted without cooling and an operating temperature reduction down to 270K may be achieved by means of a Peltier cooler. Further temperature reduction with the present cooling technology is considered cumbersome in the SIP, if possible at all.

The two candidate sensors are Lead Sulphide and Lead Selenide. Response times of the two sensors at two different temperatures are:

	<u>T = 295K</u>	<u>T = 193K</u>
PbS:	100 - 500 $\mu\text{s}$	5 ms
PbSe:	2 $\mu\text{s}$	30 $\mu\text{s}$

From the above data, the selection of PbSe is justified when detector operation at a chopping frequency of 1 kHz is desired, and cooling to 270 K will provide the spectral coverage in conjunction with a peak detectivity of  $D^* = 10^{10} \text{ cm Hz}^{\frac{1}{2}} \text{ W}^{-1}$ .

The interferometer's detection system consists of two PbSe detectors and their associated signal processing electronics. One detector senses the total power signal; the other the interferometer signal. On the first half cycle, these two detectors simultaneously measure black body reference radiation and total signal radiation so that a comparison of the two can be made in the A/D converter. On the second half of the cycle, the total black body reference radiation and the interferometer signal radiation are measured.

A black body source, whose temperature must be monitored at each data point, provides a datum from which absolute, radiometric data are deduced.

A laser source (HeNe: 632.8 nm) provides a high intensity, monochromatic beam from which the interferometer creates a high visibility, sinusoidal fringe. This laser radiation is detected by a photomultiplier, amplified, differentiated with respect to optical path difference and used to null the cat's eye stepping servo-system at each of 1000 path length increments in sequence.

#### 4.5.5 Signal-to-Noise Analysis

To compute the minimum object signal detectable by the interferometer detector, the noise equivalent power of that detector is found and added to the other sources of noise in the system, including radiation from the components and the background accompanying the target signal. Calculation of the background (Celestial) radiation, within the region of 1  $\mu\text{m}$  to 5  $\mu\text{m}$ , which reaches the PbSe detector in the image plane of the interferometer, proceeds along the same lines as the background calculations for the spectrographs. The average of background radiation was set at 23 mag/25 psr. For a zero magnitude star at 11,000K, the photon flux in the visible range is set at  $N_o = 10,000$  photon/sec-cm<sup>2</sup>-nm\*. The same star radiates approximately one per cent of that flux in the infrared region of interest (the star model is an 11,000K black body); hence, we have for input flux,  $N_{ir}$ :

$$N_{ir} = \frac{1}{100} (2.51)^{-23} (10,000) \frac{1}{25} \frac{\text{Photon}}{\text{sec-nm-cm}^2 \text{ psr}}$$

or,

$$N_{ir} = 2.5 \times 10^{-9} \frac{\text{Photons}}{\text{sec-nm-cm}^2 \text{ psr}}$$

---

\* Scientific Uses of the Large Space Telescope, National Academy of Sciences, 1969, Appendix A.

$N_{ir}$  is then the spectral flux per picosteradian (psr) solid angle due to the ir content of the background stellar radiation. The field of view of the detector in psr is calculated by finding the size of the image of the interferometer detector in the focal plane of the f/12 assembly. This size,  $D^1$ , subtends an angle  $\alpha$  at a distance of 36 meters from the second principal plane of the OTA. The solid angle subtended by the detector image in the object is then

$$\Omega = \alpha^2 = \left( \frac{D^1}{f_e} \right)^2 = \left[ \frac{(f/\#)_1}{(f/\#)_2} \right]^2 \left( \frac{d^2}{f_e^2} \right)$$

where

$$(f/\#)_1 = \begin{array}{l} \text{f number of the interferometer detector's} \\ \text{imaging mirror (labeled G in the Figure 4-53)} \\ = 2.5 \end{array}$$

$$(f/\#)_2 = \text{OTA f/number} = 12$$

$$d = \text{interferometer detector size} = 1.3 \text{ mm} = 1.3 \times 10^{-3} \text{ m}$$

$$f_e = \text{focal length of the OTA} = 36 \text{ meter}$$

Using the above formula  $\Omega$  becomes

$$\Omega = 57 \text{ psr}$$

The optical efficiency  $F(\lambda)$  of the total Mid-IR Interferometer system expressed as a fraction of the input photons surviving at the interferometer detector follows from multiplication of the reflectances and transmittances of the components.

$$F(\lambda) = R_{uv}^2(\lambda) R_{au}^{11}(\lambda) t_{bs}^2(\lambda) t_f(\lambda)$$

where

$R_{uv}(\lambda)$  = spectral reflectance of the mirrors coated with u.v. reflecting material (2)

$R_{au}(\lambda)$  = spectral reflectance of those elements coated with gold (11)

$t_{bs}(\lambda)$  = transmittance of the beamsplitter (double pass)

$t_f(\lambda)$  = transmittance of the tuning fork (overfull cycle)

Assuming the values  $R_{au}(\lambda) = 0.995$ ,  $R_{uv}(3.3 \mu\text{m}) = 0.5$ ,  $t_{bs}(\lambda) = 0.50$ ,  $t_f(\lambda) = 0.48$ , the value of  $F(\lambda)$  at the wavelength selected ( $\lambda = 3.3 \mu\text{m}$ ) is  $F(\lambda) = 0.03$ .

The general expression for the surviving photons, using an integration time  $t$  and an effective collecting area of  $0.91A_p$  as the area of the OTA primary mirror, is:

$$N_b = t (0.91)A_p \Omega \int_{\lambda_1}^{\lambda_2} N_{ir} F[\lambda] d\lambda$$

$$(0.91)A_p = 6.4 \times 10^4 \text{ cm}^2 = A'_p$$

$$N_{ir} = 2.5 \times 10^{-9} \text{ photon/sec-cm}^2\text{-nm-psr}$$

$$\Omega = 57 \text{ psr}$$

$$(\lambda_1, \lambda_2) = (1 \mu\text{m}, 5 \mu\text{m}) = (1 \times 10^3 \text{ nm}, 5 \times 10^3 \text{ nm})$$

$$F(\lambda) \cong 0.03 \text{ output photon/input photon}$$

using the approximation implicit in the estimates of  $F(\lambda)$ ,  $N_{ir}$ , etc., and assuming a total exposure of  $3.6 \times 10^4$  seconds, the average number of photons arriving at the interferometer detector in each step's dwell time  $t = 36 \text{ sec}$  is

$$N_b = t A' \Omega N_{ir} F[\lambda] (\lambda_2 - \lambda_1)$$

$$N_b \cong 40 \text{ photons (per data point)}$$

We can conclude that the noise due to an average space background is entirely negligible compared to the noise equivalent power of the PbSe detector as calculated below:

$$\text{NEP} = \frac{\sqrt{A_d \Delta f}}{D^*(\lambda, f, T)}$$

where

$$A_d = \text{area of detector } (\pi d^2/4).$$

$$\Delta f = \text{bandwidth of filter circuit (as deduced from the maximum integration time per data point)}$$

$$\Delta f = \frac{1}{2\pi\tau} = 4.4 \times 10^{-3} \text{ Hz}$$

$$D^*(\lambda, f, T) = \text{the detectivity of PbSe at the wavelength, chopping frequency and temperature indicated; here: } D^*(3.0 \mu\text{m}, 10^3, 295\text{K})$$

$$= \frac{10^{10} \text{ cm Hz}^{1/2}}{\text{watts}}$$

Using a detector diameter of  $1.3 \times 10^{-1}$  cm, the NEP becomes:

$$\text{NEP} = 7.7 \times 10^{-13} \text{ watts (J sec}^{-1}\text{)}$$

Converting to photons/second at the mean wavelength implicit in  $D^*$  and calling that power  $N(t)$  photon/sec; we have, with the energy per photon  $E_p$  given by

$$E_p = \frac{hc}{\lambda_m}$$

$$\text{where } h = \text{Planck's constant} \\ = 6.63 \times 10^{-34} \text{ J-sec}$$

$$c = 3 \times 10^8 \text{ m/sec}$$

$$\lambda_m = 3 \times 10^{-6} \text{ m}$$

$$E_p = 6.63 \times 10^{-20} \text{ joules/photon}$$

$$N(t) = \frac{\text{NEP}}{E_p} = \frac{7.7 \times 10^{-13} \text{ joules/sec}}{6.63 \times 10^{-20} \text{ joules/photon}}$$

$$N(t) = 1.16 \times 10^7 \text{ photons/sec}$$

In an integration time  $t = 36$  sec, as before, the detector contributes the equivalent of  $N_d$  average photons to the detection noise where  $N_d$  is

$$N_d = N(t) t$$

$$N_d = 4.18 \times 10^8 \text{ photons (per data point)}$$

The noise  $N_t$  affecting detection is the variance in sum of detector equivalent photons  $N_d$  and the signal photons  $S_m$  or

$$N_t = \sqrt{N_d + S_m}$$

The detection process must be able to resolve information at points of wave interference. Assuming that at such points an 80% reduction in the average energy level at the detector occurs and in these cases a minimum signal to noise ratio of two exists the signal photons thus required is the limiting signal  $s_{lim}$  or

$$(S/N) = 2 = \frac{S_{lim}}{N_t} = \frac{S_{lim}}{\sqrt{N_d + S_{lim}}}$$

$$S_{lim} = 4 \times 10^4 \text{ photons}$$

Considering the geometric and specular parameters used to calculate the arriving photons from the sky background, a zero magnitude, 11,000K star would produce a signal photon rate at the detector of  $N_o^1$ , given by

$$N_o^1 = \frac{1}{100} A_p^1 F[\lambda] N_o$$

$$N_o^1 = 1.92 \times 10^5 \text{ photon/sec-nm}$$

In the integration time and wavelength interval used above the signal photons from the zero magnitude star  $S_0$  is

$$S_0 = N_0^1 (\lambda_2 - \lambda_1) t$$

$$S_0 = 2.77 \times 10^{10} \text{ photons (in 36 sec)}$$

At the point of interference this star produces  $S_0^1$  photons where  $S_0^1 = 0.2 S_0$  or

$$S_0^1 = 5.5 \times 10^9 \text{ photons (in 36 sec)}$$

The limiting star magnitude  $M_{lim}$  which produces the above  $S_{lim}^1$  is

$$M_{lim} = 2.5 \log \frac{S_0^1}{S_{lim}}$$

$$M_{lim} = 13$$

#### 4.5.6 Output Data Prediction

The data exiting the pulse-code-modulation system consists of normalized signal intensity and interferometer optical path length difference. Approximately thirty-six bits accommodate these data. An existing Fourier transform converts the data (i.e., the interferogram) into the power spectrum displayed as relative magnitude versus wave number.

Further studies should explore operation of the cat's eye at a far slower stepping rate, allowing longer integration times, smaller bit rate and enhanced signal-to-noise.



## 4.6 WIDE FIELD CAMERA (f/12)

### 4.6.1 General Description

The Wide Field Camera is at the Cassegrain focus of the telescope and receives its light after only three reflections. It covers a field of 1.39 mrad which is centered 2 mrad off the telescope axis. The camera is accessed by offsetting the telescope. The light passes through the large hole in the main diagonal to the second diagonal which reflects the light to the 50 mm square photocathode. (See Figure 5-58.) If a detector with a larger photocathode becomes available, the design of the main diagonal can be changed so that a larger field is made available to the camera. In this case, those parts of the field which are farthest off axis would have some detectable image growth. The weight of the camera is 70 Kg. The camera mechanical design, showing the six position filter wheel, is shown in Figure 5-59. The family tree is displayed in Figure 4-60.

### 4.6.2 Description of Optics

The Wide Field Camera consists of a Ritchey-Chretien Cassegrain, a folding flat and a vidicon camera with a 50 x 50 mm image format. The radii and separation of the primary and secondary mirrors are chosen to deliver the desired first order quantities, such as focal length, back focus and obscuration, while the aspheric terms describing the shape of the mirrors are chosen to correct spherical aberration and coma. Both the primary and secondary must be hyperboloids in order to achieve this condition.

#### a. Optical Path

The central portion of the telescope field is used for the High Resolution Camera and several spectrographic instruments. A diagonal mirror located above the axis folds a portion of the Ritchey-Chretien field-of-view off to a TV tube located in a radial bay.

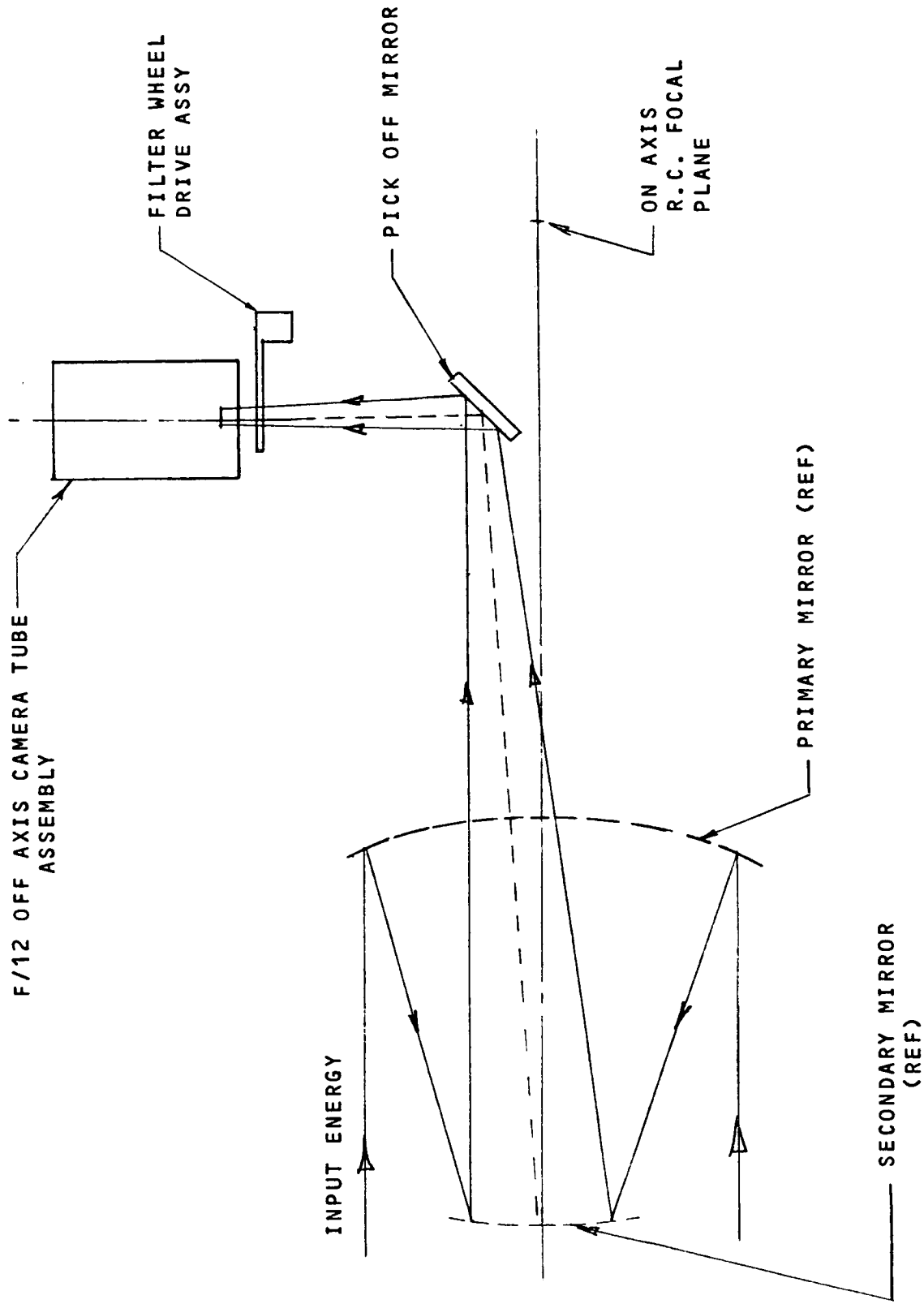


Figure 4-58. Wide Field Camera Tube Assembly

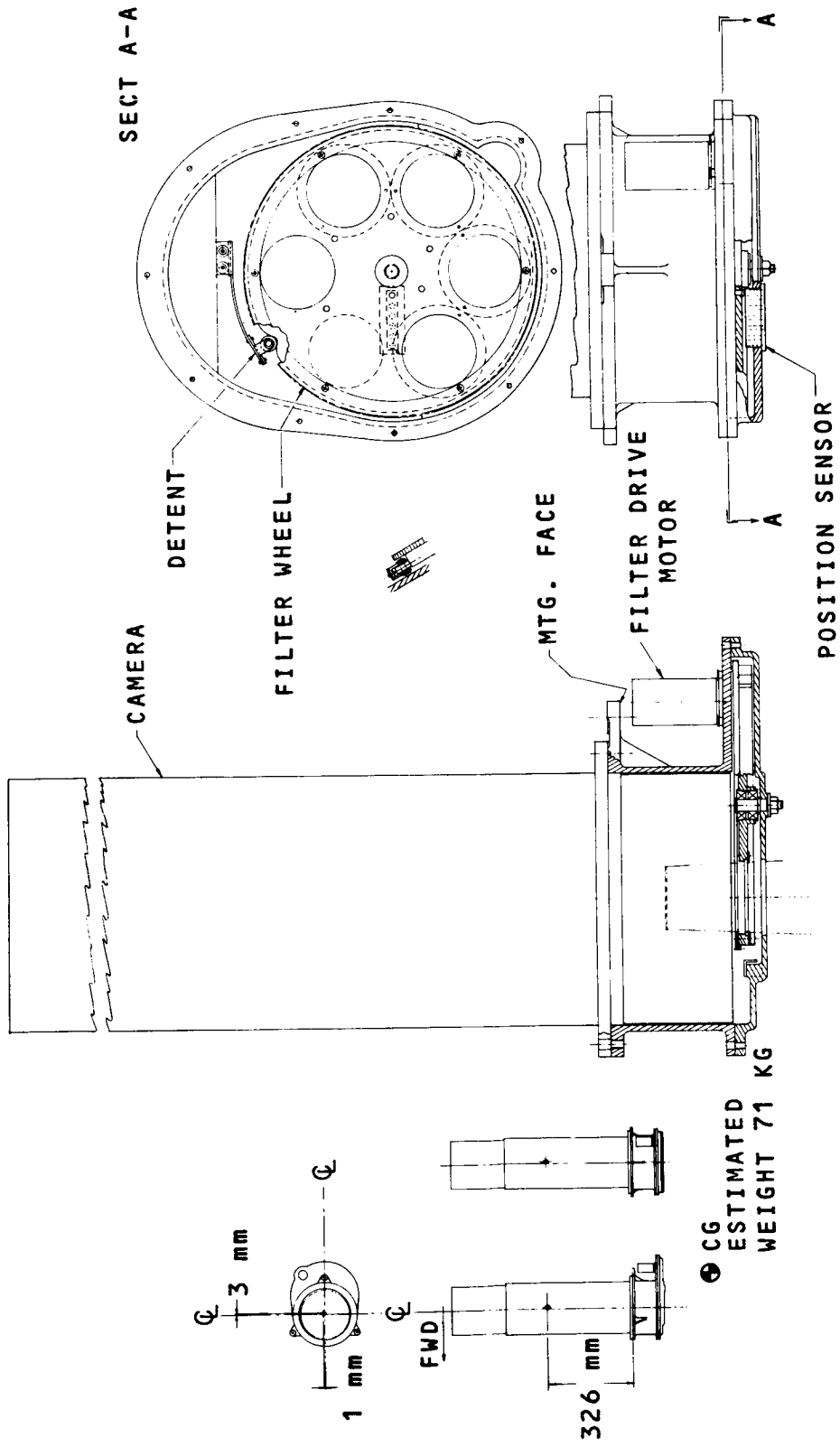


Figure 4-59. Wide Field Camera Layout

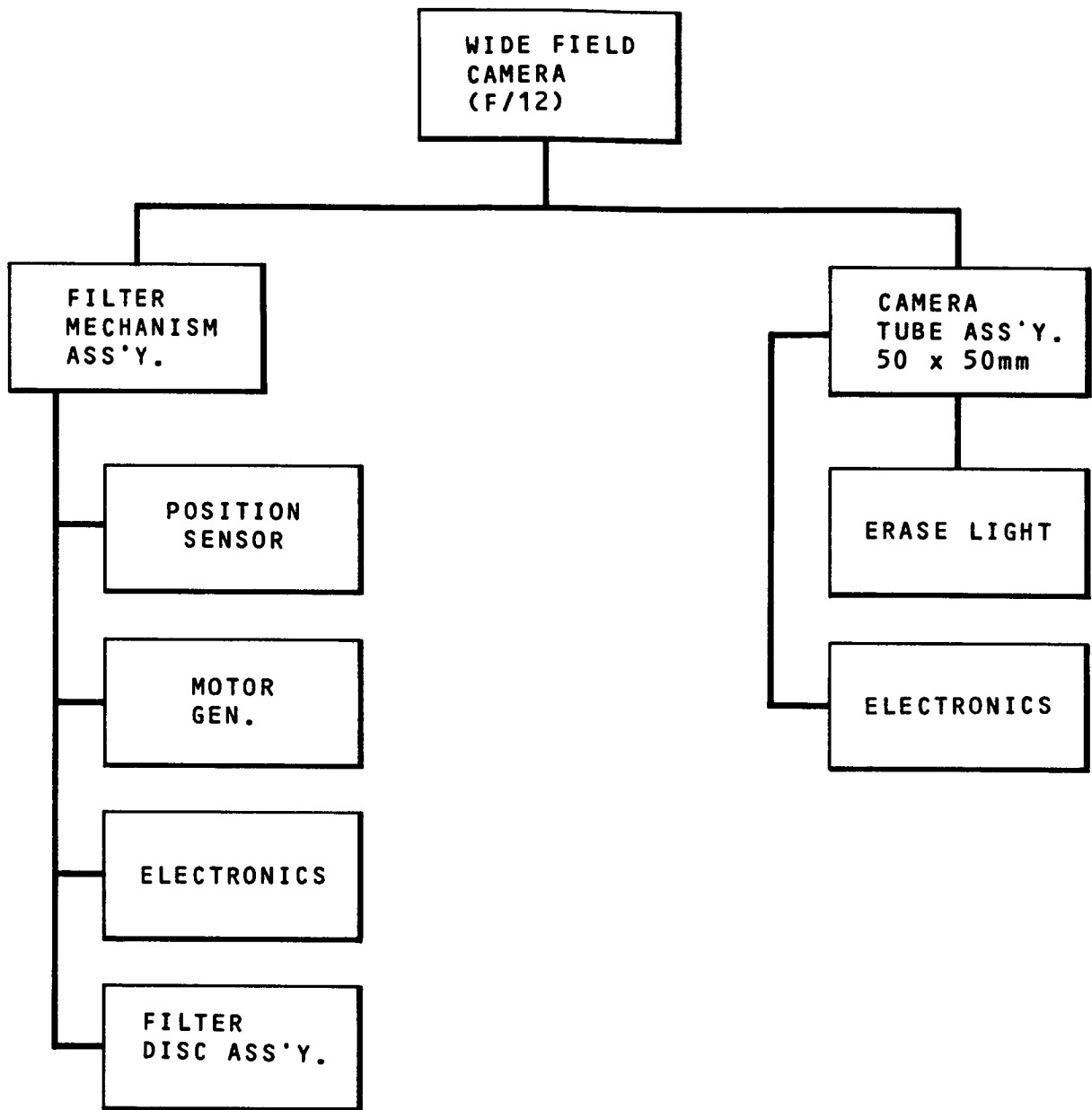


Figure 4-60. Wide Field Camera, Family Tree

## b. Performance

It is well known that at this field angle the astigmatism of the Ritchey-Chretien becomes troublesome. Figure 4-61 gives a plot of the sagittal and tangential foci of the Ritchey-Chretien. On a flat focal plane the imagery would be seriously degraded. In this case, the tube may be tilted and focused between the sagittal and tangential foci. This yields acceptable imagery for the Wide Field Camera as is demonstrated by the MTF curves in Figures 4-62, 4-63 and 4-64.

## c. Tolerancing

As with the other instruments, the most significant tolerances in the Wide Field Camera are those which involve motion of one component relative to another due to thermal and/or mechanical changes that will cause a movement of the image. Since the OTA and one pick-off mirror comprises the wide field camera's optical system, it is required to maintain only the stability of the sensor relative to the OTA during an observation (dynamic tolerance). The replaceability tolerance for sensor assembly is 0.15 mm to assure that photocathode surface is within the depth of focus of the telescope.

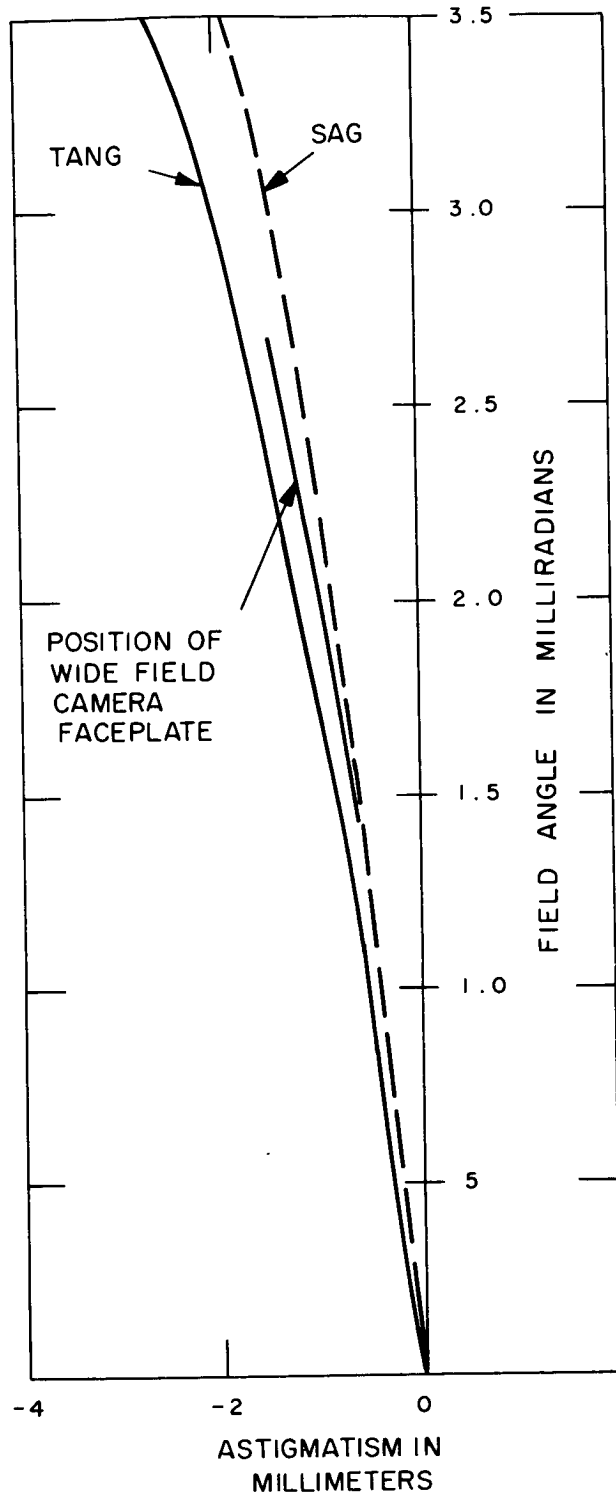


Figure 4-61. Ritchey-Chretien Astigmatism (f/12)

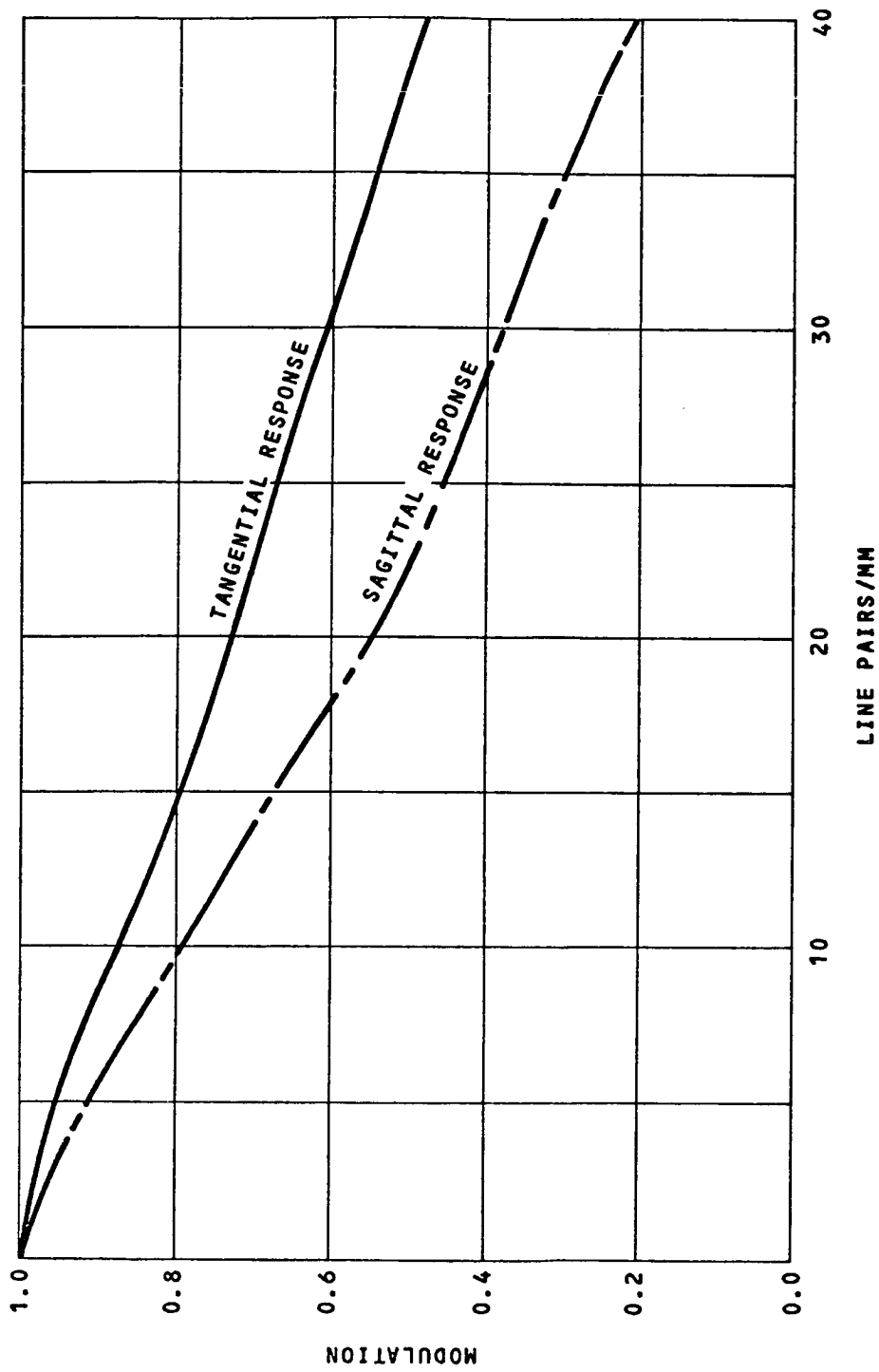


Figure 4-62. Wide Field Camera, Bottom of Format

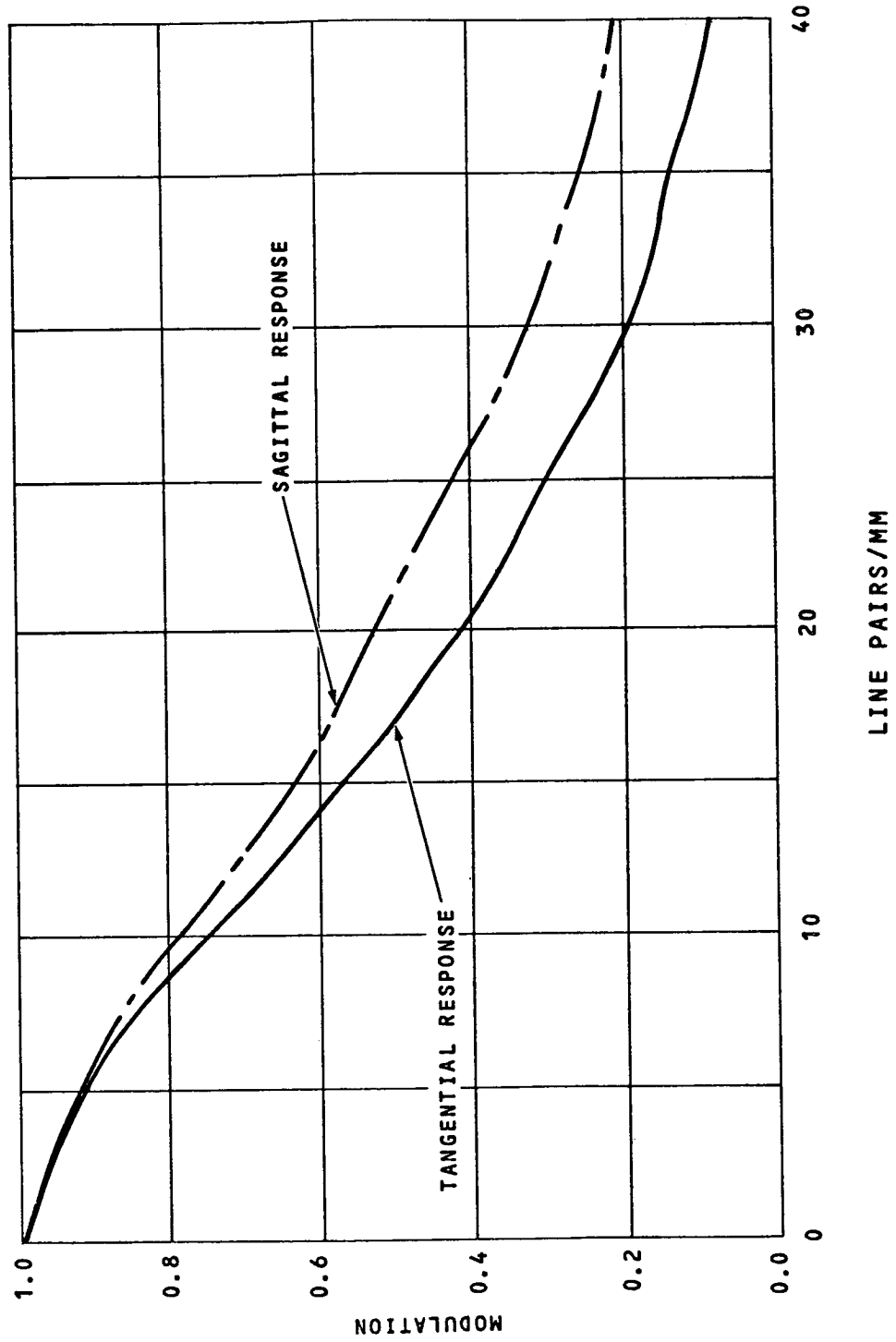


Figure 4-63. Wide Field Camera, Middle of Format



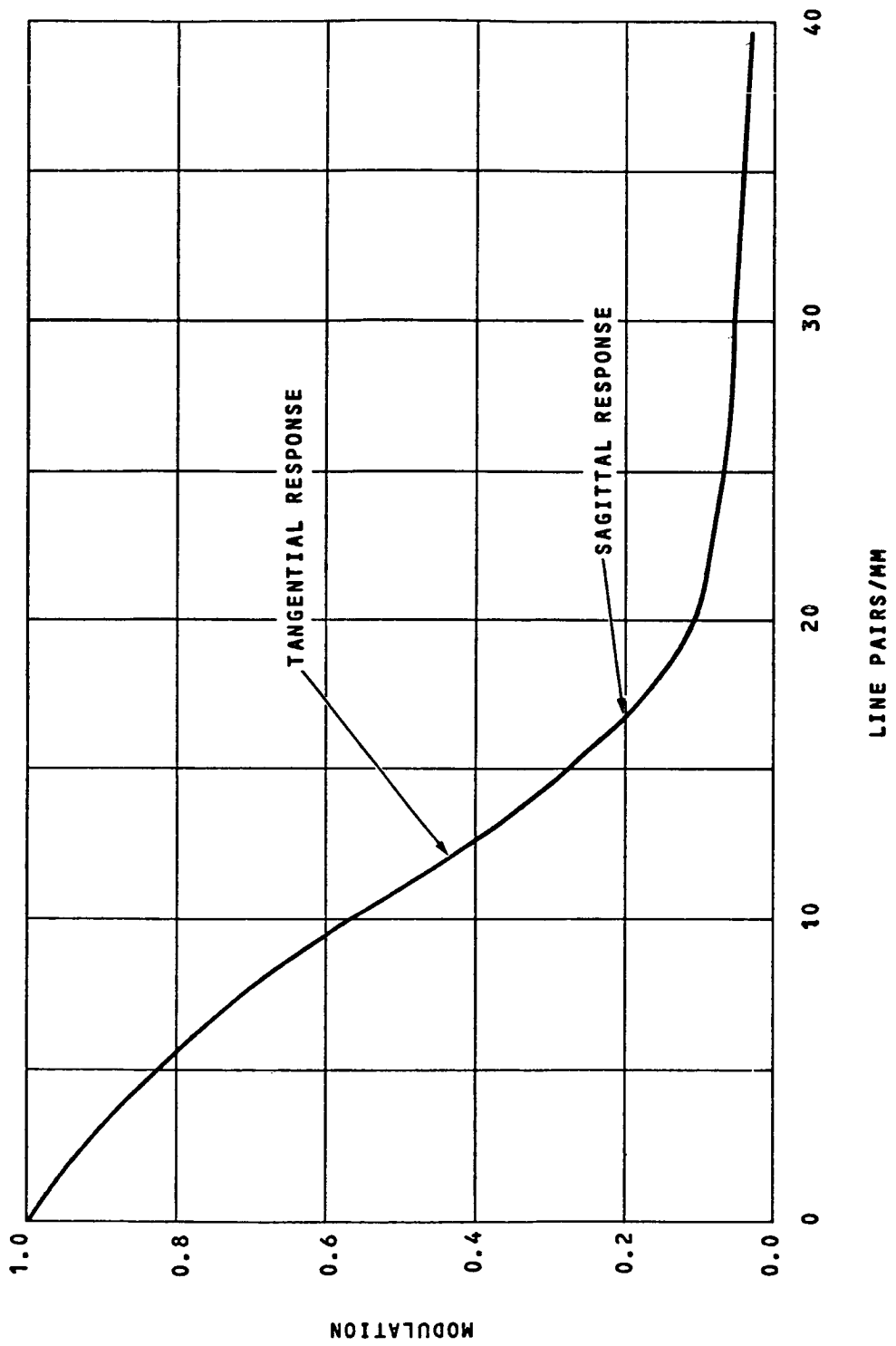


Figure 4-64. Wide Field Camera, Top of Format

#### 4.6.3 Sensor

The purpose of the Wide Field Camera is to provide an initial coarse survey of preselected parts for the celestial sphere for better location of dim scientific targets already obtained from other space experiments or from radio-astronomy. Consequently, a high sensitivity and the largest possible field of view are desirable. A short focal length and a large format of the sensor determine the field of view, however, the sensitivity depends upon the matching capability of the sensor and optics resolution. From these considerations the SEC Vidicon with a 50 x 50 mm photocathode was selected as a reference sensor<sup>(1)</sup> and the f/12 telescope as the fastest applicable optics. Since the sensitivity may best be judged by the signal-to-noise ratio, the ratio, the two photocathodes used as basis for the throughput estimates<sup>(2)</sup> were further evaluated for their effect upon the S/N ratio. Based on this computation (see following subsection), the selected reference instrument uses S-20/SiO<sub>2</sub> combination. The bialkali photocathode with a magnesium fluoride window is an alternate and may be used if more refined temperature data indicates cathode temperature in excess of 300K (without active cooling).

In addition to the SEC tube, the developmental work by Bendix which pertains to a camera tube with 100 mm photocathode, an electron multiplier microchannel plate and a silicon target<sup>(3)</sup> will be monitored. The projected advantage of the latter sensor not only increases the field of view but, in addition, increases the internal gain, making the preamplifier noise and the silicon target leakage negligible through photon counting operation. This in turn will highly increase (approximately double) the sensor resolution as

---

(1) See Sensor discussion in Section 6.

(2) See Section 3.6.1.

(3) Dr. Johnson, C.B., Bendix Research Laboratories: development work sponsored by NASA - GSFC (Private communication 1972).

compared to the SEC, assuming that a high degree of focus sophistication both in the image section and in the readout section is used. Such an electron optics system was developed<sup>(4)</sup> and is applicable to this sensor. However, with the higher resolution and a larger photocathode a rapid increase of data rates will result which may only be used in conjunction with a large data storage (over  $10^9$  bits). Using the present total transmission rate capabilities of the LST one megabit/second, a readout time of over  $10^3$  seconds results which could only be obtained by means of the single picture readout split between two successive ground stations.

#### 4.6.4 Signal-To-Noise Ratio

The wide field camera signal-to-noise computation is performed for two photocathode/window combinations:

1. Bialkali/MgF<sub>2</sub>
2. S-20/SiO<sub>2</sub>

Using the general S/N formulae in Appendix B and the zero apparent magnitude star throughput data,  $N_o(\lambda)$  (pe/s-nm), at  $T = 11,000K$  from Figure 3-18, limiting star magnitudes are computed for one hour exposures since the background radiation causes target saturation for longer exposures. In addition, the target gain is reduced to allow  $2 \text{ pe}/\mu\text{m}^2$  electron cathode density without saturation.

- a. Bialkali/MgF<sub>2</sub>

$\lambda_1 = 120 \text{ nm}$ ,  $\lambda_2 = 600 \text{ nm}$  are the limit wavelengths

$$S_o = t \int_{\lambda_1}^{\lambda_2} N_o(\lambda) d\lambda$$

From figure 3-18,  $\int_{120}^{600} N_o(\lambda) d\lambda = 1.9 \times 10^{10} \text{ pe/sec.}$

(4) O.H. Schade Sr., Electron Optics and Signal Readout of High - Definition Return-Beam Vidicon Camera RCA Review, March 1970.

for  $t = 3.6 \times 10^3$  [s]  
 $S_o = 6.9 \times 10^{13}$  [pe] the zero magnitude signal  
 $S_B = \frac{\Omega}{25} S_{23} = 870$  [pe] for  $\Omega = 0.5$  psr from a pixel of  
 25 x 25 $\mu$ m in 36m focal length  
 $N_D = aNt = 1$  pe where  $a = 6.25 \times 10^{-6}$  cm<sup>2</sup> and  
 $N = 40$  e1/cm<sup>2</sup>-sec  
 $(n_R)^2 = 128$  (pe) readout count  
 $S_{lim} \cong 66$  (pe) for S/N = 2  
 Result:  $m_{lim} \cong +30$  star magnitude

b. S-20SiO<sub>2</sub> (used in the selected reference instrument)

$\lambda_1 = 160$  nm;  $\lambda_2 = 700$  nm  
 for  $t = 3.6 \times 10$  (s)  
 $S_o = 1.36 \times 10^{14}$  (pe) is the zero magnitude signal  
 $S_B = \frac{\Omega}{25} S_{23} = 1710$  (pe) for  $\Omega = 0.5$  psr  
 $N_d = aNt = 10$  (pe) where  $a = 6.25 \times 10^{-6}$  cm<sup>2</sup>,  
 $N = 400$  pe/cm<sup>2</sup>-sec  
 Readout count,  $(n_R)^2 = 128$  (pe)  
 $S_{lim} \cong 88$  (pe) for S/N = 2  
 Result:  $m_{lim} \cong +30.5$  star magnitude

The S/20 photocathode offers a slightly better performance. Other computed points are shown in Figure 4-65.

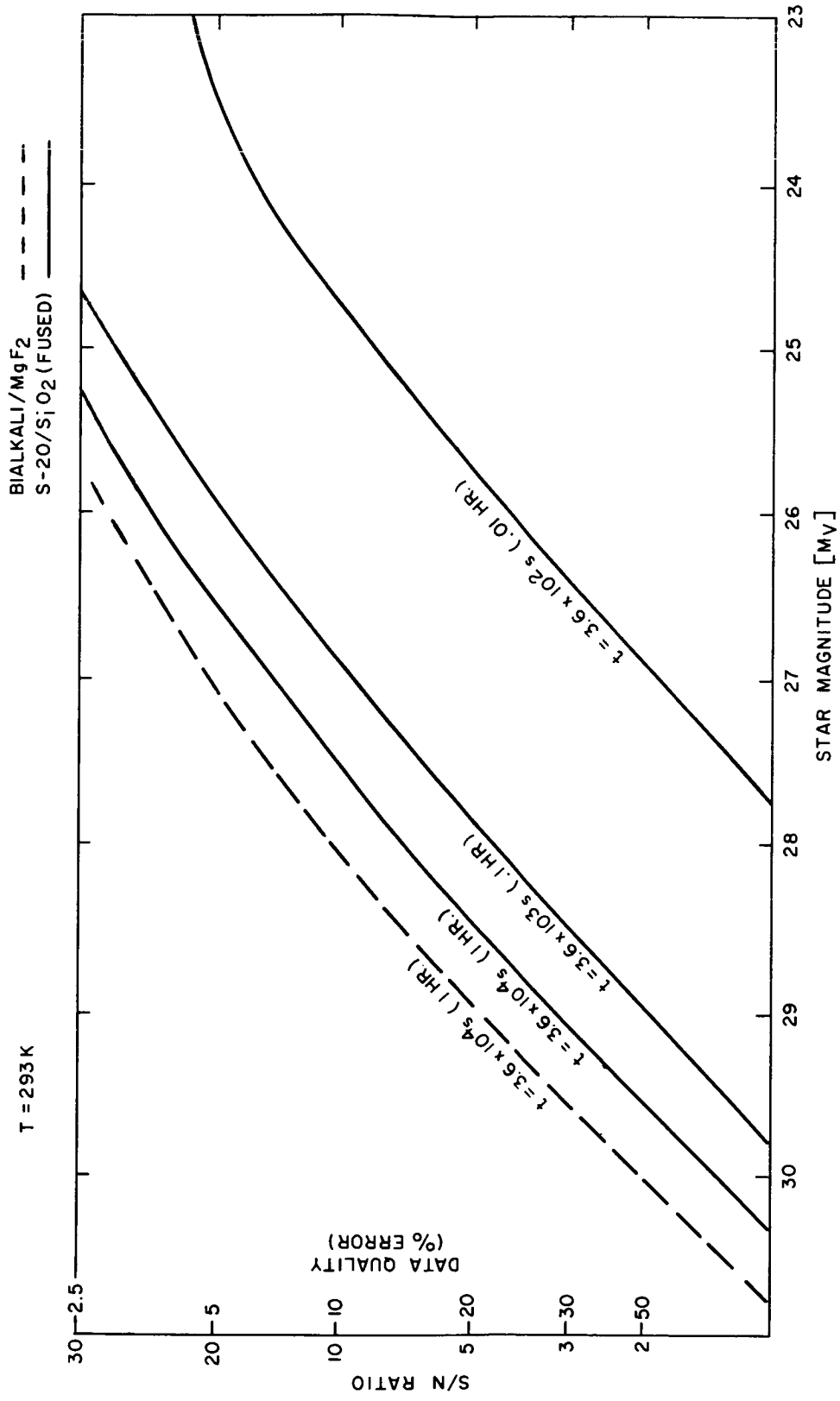


Figure 4-65. Wide Field Camera Signal-to-Noise Ratio, as a Function of Star Magnitude and Integration Time

Section 5  
ANCILLARY SUBSYSTEMS

5.1 INTRODUCTION

This section contains analyses of the subsystems required to support the operation of the LST instruments. These ancillary subsystems are grouped as:

- Slit Jaw Camera
- Mechanisms
- Electronics

The initial paragraphs of this section describe the Slit Jaw Camera, the objective of which is to recognize the spectrograph object position with respect to each entrance slit. This position information is used for image centering within the slit. Two concepts of acquisition and error generation are discussed.

In the first concept, a picture of the slit and all images in the surrounding field of view are displayed in the ground station. The experimenter makes an observation of the field of view and generates pointing correction commands.

In the second concept, a narrow instantaneous field of view is programmed to search around the entrance slit and detect the object which matches the commanded threshold level. In this concept, the sensor generates position error signals which cause the attitude control to reposition the telescope in a close loop, until the desired image location is achieved.

There is a trade-off between the two concepts. The first approach provides a wide field of view and permits selection of point objects, extended bodies or their details. The second concept provides a higher sensitivity and therefore may be used for

continuous and automatic pointing during the entire data integration time. However, problems occur when more than one object of the selected magnitude is within the search field.

In addition to the above two basic concepts, various approaches to the optics are treated and trade-offs, including a single versus three separate sensors as well as the sensor type, are presented.

The various mechanisms, used to position slits, filters and mirrors in the optical path of the SIP instruments, are then described.

The final paragraphs of this section cover consideration of electronics support of the instruments and mechanisms. Included are discussions of modularity for ease of maintenance, packaging techniques, system block diagrams and SIP harnessing.

## 5.2 SLIT JAW CAMERA

### 5.2.1 Purpose

None of the spectrographs in the reference design is equipped to acquire a target's image or to hold an image in its slit. With the aid of the Field Select Mirror Assembly (Section 5.3.5), the image acquisition and maintenance is performed by the Slit Jaw Camera. In the reference system the camera views the object field, which has already been imaged in the immediate vicinity of the spectrograph slit, and displays that view at a remote (ground) station. The experimenter analyses the display and, if necessary, originates the appropriate orientation commands to position the target's image into the slit, admitting light to the spectrograph.

### 5.2.2 Description

The organization of the several parts of the reference Slit Jaw Camera system is shown on the accompanying family tree, Figure 5-1, and the family tree of the Field Select Mirror Assembly, Figure 5-12. The optical layout drawing of the camera is shown in

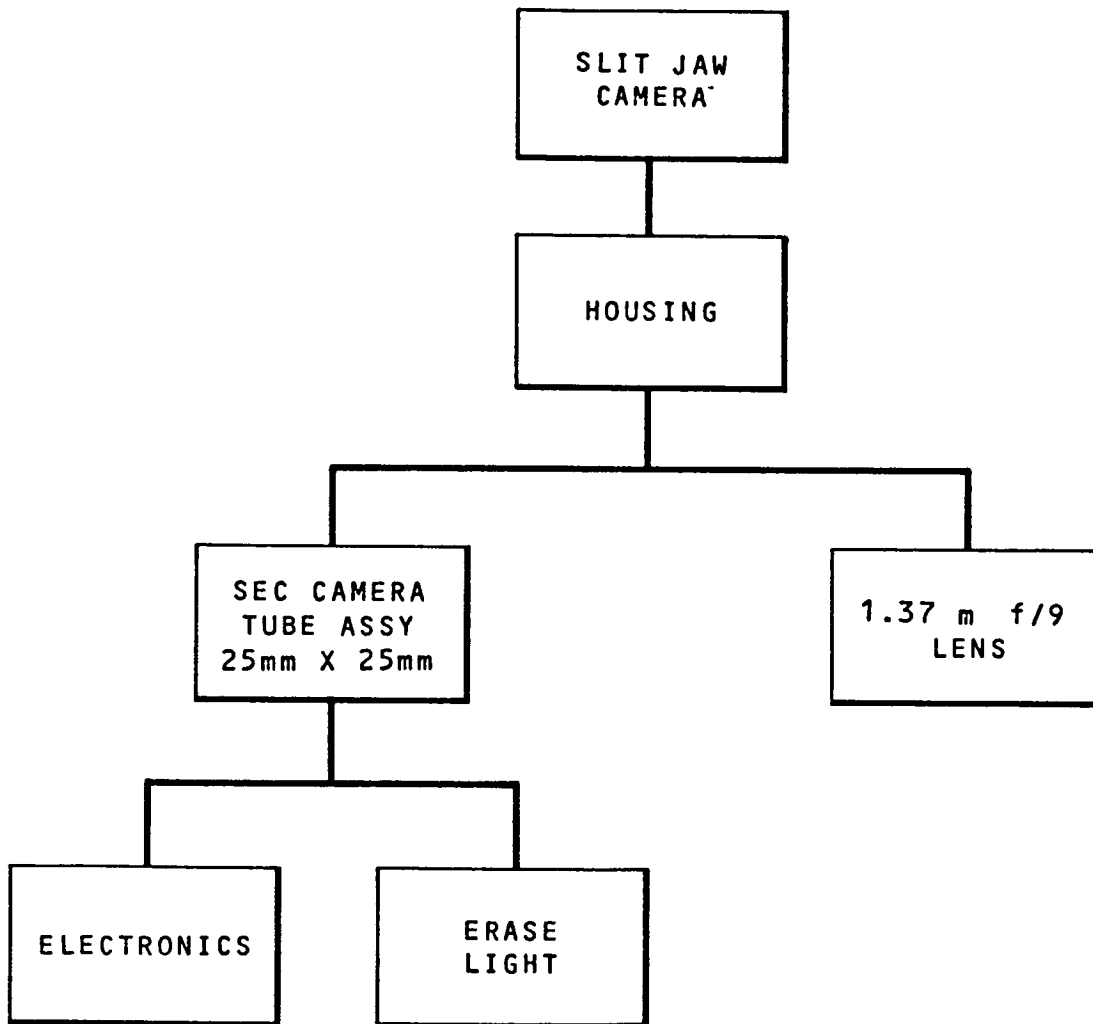


Figure 5-1. Reference Slit Jaw Camera, Family Tree



Figure 5-2, which includes the camera tube and its lens, and one of three collimators which are physically part of the Field Select Mirror Assembly, Figure 5-3.

The camera proper consists simply of a 25 x 25mm camera tube mounted to a housing which contains a 1.37m f/9 catadioptric lens of the Wynn-Rosin form. The refracting elements of fused quartz have no net power beyond that of correcting the coma and astigmatism of the reflecting paraboloid. Therefore, the spectral range for acceptable color correction is sufficient to give the rapid readout necessary for making star to slit adjustments during a single pass over a ground station. The entrance aperture of the catadioptric is fed by three different collimators and uses the unshaded area as shown in Figure 5-2.

The construction of the three slit collimators and the optics to combine their outputs around the entrance annulus of the slit camera lens is more complex. Each slit assembly is a high quality, flat, low scatter, first surface mirror with the slits cut through it. This mirror is tilted 100 mrad to the optical axis with the axis of this tilt being the long dimension of the slit at the spectrograph entrance.

The star image and slit fields are directed into the reflecting collimators by small diagonals with one additional mirror in the case of the collimator for the rear instrument slit. The diagonals are cemented into central holes in the larger diagonals (see Figure 5-3), by which the collimator slits and star fields are directed onward toward the camera lens. The last mirror, in two of the paths toward the camera lens, is mounted on the rear face of the same window that supports the first reflecting diagonals for directing the OTA telescope output toward the radial instrument's slits. The third path, from the rear instrument's slit, is folded toward the camera lens by a pair of elbow mirrors. The three arrangements result in three collimated beams equally spaced

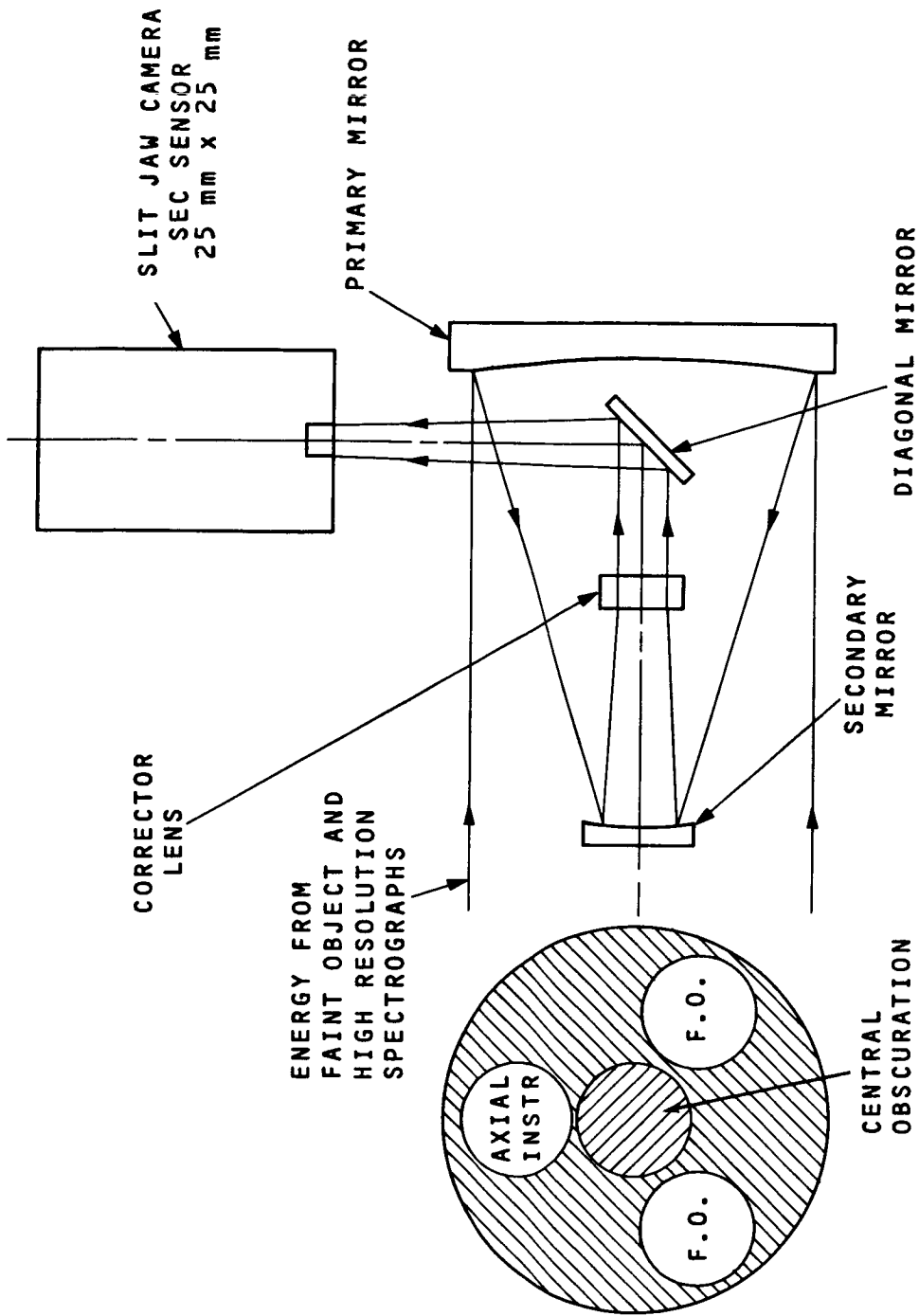


Figure 5-2. Reference Slit Jaw Camera, Optical Schematic

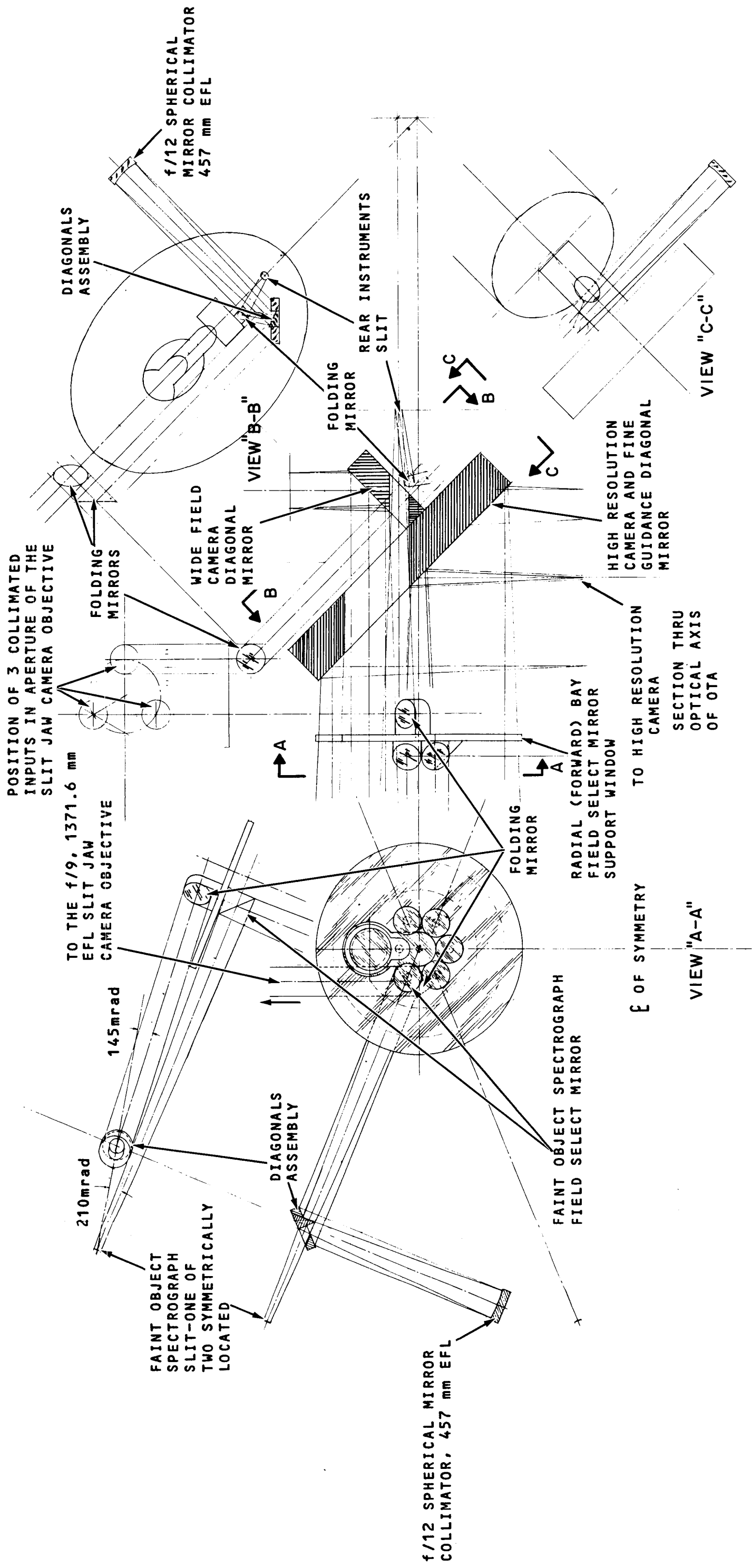


Figure 5-3. Optical Schematic Slit Jaw Camera and Field Select Mirrors

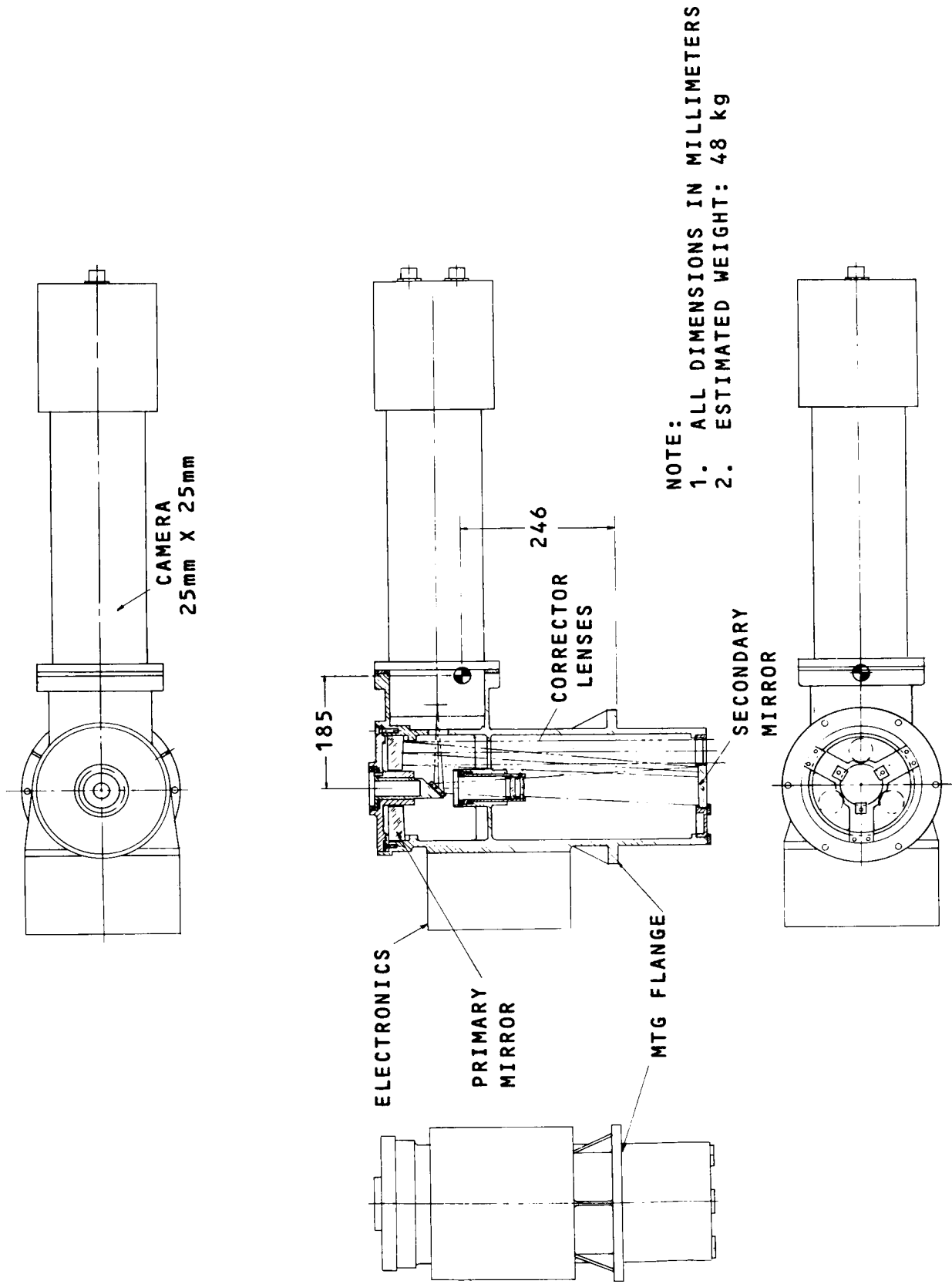
in the annular aperture of the camera lens system, see Figure 5-2. Effectively only the unshaded areas are used to form an image at  $f/36$  on the image tube. Both the star and a slit, which may be back illuminated, are imaged by any one of these instruments.

The slit is made visible by a faint light source shining through the slit in the direction of the reflected star field. This source is shown in Figure 5-8, accompanying the description of the Slit Mechanism. The fine attitude correction vernier causes the image to enter the slit and, at least partially, to disappear from the slit jaw sensor. At this time, the tritium activated slit light source must be capped by the shutter so that the minute reflections from the edge of the slit will not be confused with the star signal in the spectrograph. It should be noted that since the slit jaw fields of view share the camera, the slits not in use should not be imaged on the camera.

The optical performance of the collimators must be optimized separately from the optics of the camera because they are not concentric with each other. In the case of the collimators, spherical mirrors suffice as the power elements. The imagery of the more complex camera optics is close to diffraction limited for the full  $f/9$  aperture and therefore was not further investigated for the  $f/36$  aperture sub-divisions used here.

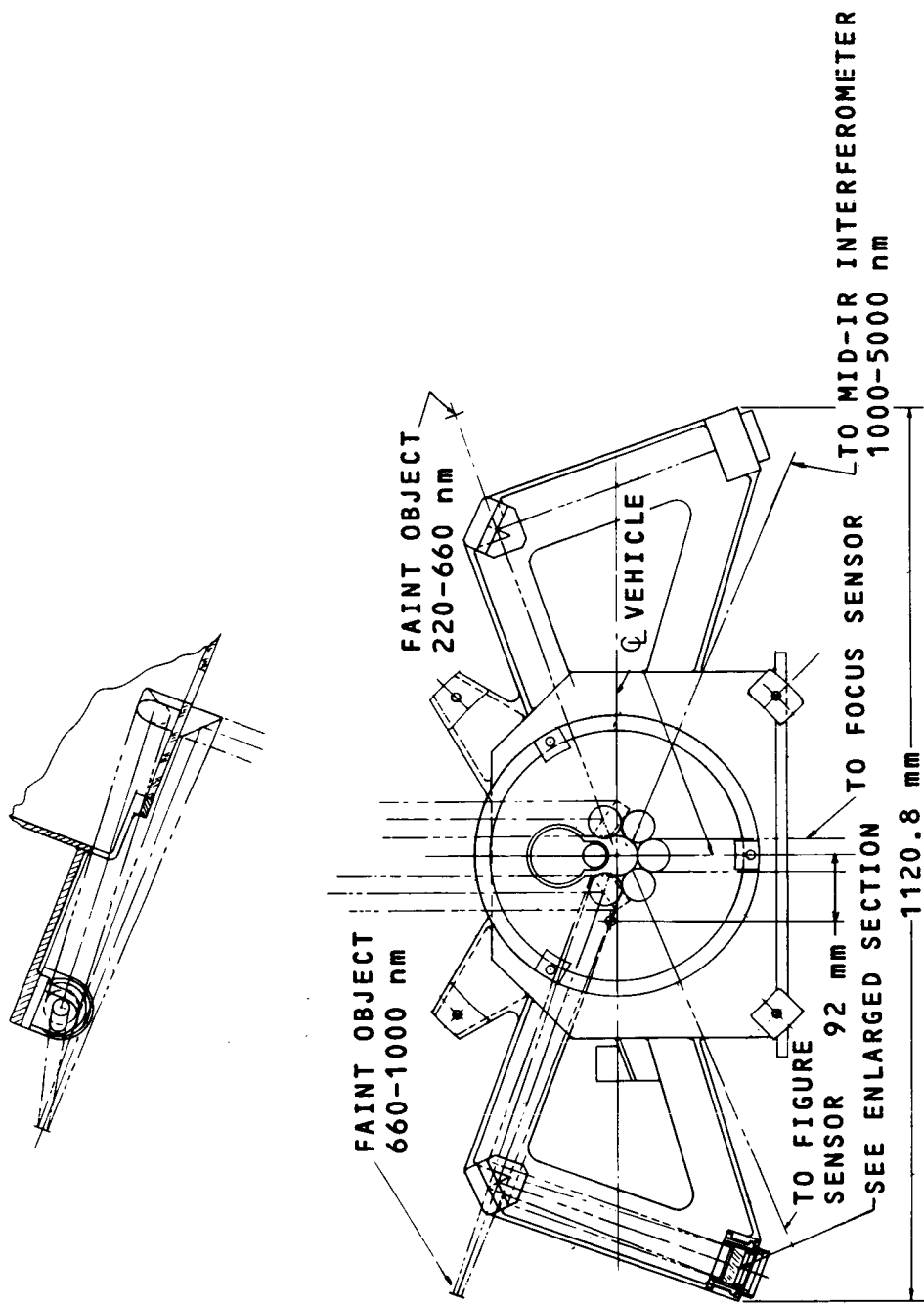
The controls of the slit jaw camera are only those associated with the camera electronics including the erase light. The electronics of the spectrograph and slit mechanisms are essential to the working of the slit jaw camera. The thermal requirements of the slit jaw camera do not differ in principle from any of the spectrographs, but the latitude for variation is greater.

The mechanical layouts of the Slit Jaw Camera and the Field Select Mirror Assembly are included as Figures 5-4 and 5-5, respectively. Structural considerations are the same as for other instruments with relaxed limits, especially on the mounting of the

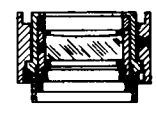


NOTE:  
 1. ALL DIMENSIONS IN MILLIMETERS  
 2. ESTIMATED WEIGHT: 48 kg

Figure 5-4. Slit Jaw Camera, Mechanical Layout



NOTE:  
 ALL DIMENSIONS IN MILLIMETERS  
 ESTIMATED WEIGHT: 37.6 kg



TYPICAL REFLECTING  
 LENS MOUNT

Figure 5-5. Field Select Mirrors, Mechanical Layout (Sheet 1 of 2)

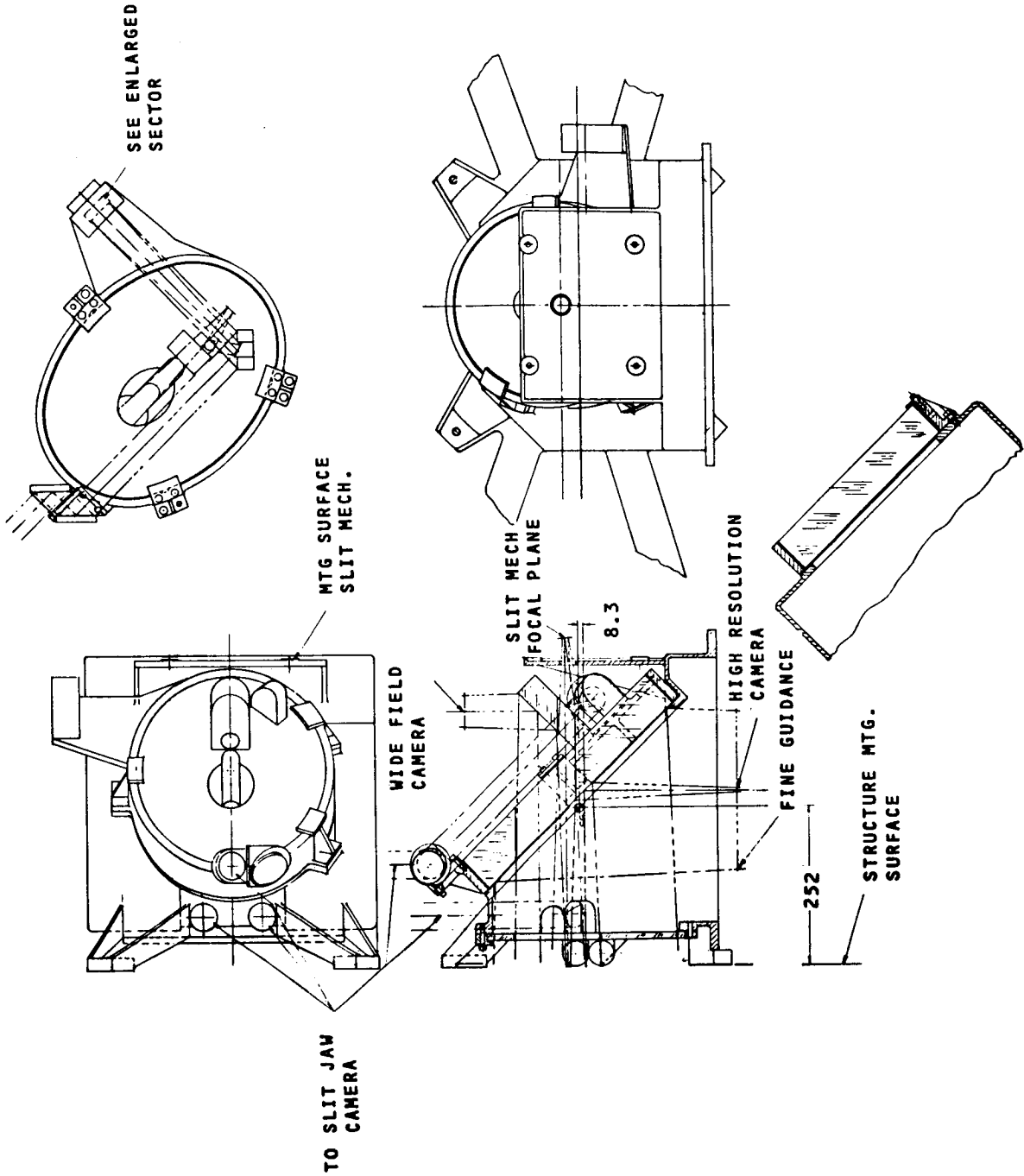


Figure 5-5. Field Select Mirrors, Mechanical Layout (Sheet 2 of 2)

camera proper since it operates in collimated space. The collimating optics are all mounted as part of the field select mirrors assembly and any construction that is stable in accord with that function will suffice for the slit jaw collimators. In each train only the collimating mirror itself is adjustable for both focus and centration.

The Slit Jaw Camera is an observing device which contributes no errors to the experiment results. Further work may result in a change of the camera magnification versus the field of view, the latter being maximized in the foregoing description.

The specifications for the foregoing Slit Jaw Camera system are:

1. FOV  $230\mu\text{rad}$  at each slit (in telescope object space).
2. Camera FOV  $25\text{mm} \times 25\text{mm} = 230\mu\text{rad}$  at each slit (in which the above FOV is displayed).
3. Optical efficiency:  $f/12$  on axis, 50% maximum vignetting at  $115\mu\text{rad}$  off axis; all mirrors high efficiency coated; all refracting elements quartz, high efficiency anti-reflection coated.
4. Focal length of collimators 457mm (18 inches).
5. Focal length of camera lens 1371.6mm (54 inches).

The analysis of the foregoing Slit Jaw Camera optical arrangement suggests that the optical complexity to provide a single camera with a field of view of  $230\mu\text{rad}$  for each of the three slit assemblies results in a marginal capability of detecting the faintest objects within the time span available for making pointing adjustments.

To create a more favorable balance between (1) the requirements for pointing corrections on the faintest spectrograph objects and (2) the desire to cover the maximum field for the identification of stars in an expanded field, alternate systems are the subject of continuing study.



### 5.2.3 Slit Jaw Camera - S/N Considerations

A number of solutions to accommodate the precision guidance of the image into the relatively narrow spectrograph entrance slits was reviewed. It was immediately recognized that this task is most difficult for the dimmest experiment target, which will be the case of the limiting magnitude of the Faint Object Spectrograph No. 2B, (350-660 nm) as is shown in Section 4.3.4.

#### a. Signal

The presented reference configuration consists of a single SEC sensor assembly selectively viewing one of the spectrographs entrance slits. A number of reflective surfaces (8-9 including the slit jaw) and two refractors in addition to the two OTA surfaces and a diagonal mirror (in some instruments) made mandatory the use of protected, silver coating on all components outside of the optical path of the UV spectrographs. The silver offers high efficiency in the visible range; however, it cuts off rapidly below 450 nm (see Figure 3-15). Hence, for eight surfaces and two refractors, an optical efficiency of  $\eta = 0.6$  may be used at wavelength above 450 nm in conjunction with the previously computed throughput data (Section 3). This data also includes the OTA and one diagonal, a configuration which applies to the most sensitive spectrograph, No. 2B. From the listed data, an S-20 photocathode yields an average spectral photoelectron density of  $N_0 = 5 \times 10^7$  pe/s - nm for a zero magnitude star ( $m_v = 0$ ) at  $T = 11,000K$  between the wavelengths of 450 and 700 nm. Using the additional optics efficiency  $\eta = 0.6$ , the S-20 photocathode will yield a total target star signal of:  $S_0 = N_0 \eta \Delta \lambda$

$$S_0 = 5 \times 10^7 \times 0.6 \times 250 = 7.5 \times 10^9 \text{ pe/s, for a zero mag.star;}$$

$$S_{20} = S_0 \times 10^{-8} = 75 \text{ pe/s, for a +20 mag. star;}$$

$$S_{22} = 12 \text{ pe/s, for a +22 mag. star;}$$

$$S_{24} \cong 2 \text{ pe/s, for a +24 mag. star.}$$

For an f/36 system, the diffraction limited image diameter at  $\lambda = 600 \text{ nm}$  is  $a \cong 2.44\lambda \times f/\# = 55 \text{ }\mu\text{m}$ . The actual image, however, is expected to be  $2a$  or  $110 \text{ }\mu\text{m}$ , approximately two times the diffraction limited diameter due to the jaw and intermediate optics. With a SEC 50% MTF pixel size of  $d = \mu\text{m}$ , only 0.05 of the point source current will be collected on each resolution element, assuming a flat distribution. This yields target signals of:

$$S'_{20} \cong 4 \text{ pe/s}$$

$$S'_{22} \cong 0.6 \text{ pe/s}$$

$$S'_{24} \cong 0.1 \text{ pe/s}$$

b. Dark Count

From Figure 6-3, the photocathode dark current for S-20 uncooled ( $T = 293 \text{ K}$ ):  $400 \text{ pe/s-cm}^2$  or  $N_D \cong 0.003 \text{ pe/s}$ .

c. Background

An average of one  $m_V = +23$ rd magnitude star lies in a solid angle of  $\Omega_B = 25 \text{ psr}$ . Since the pixel subtends a solid angle of  $\Omega_p = 0.04 \text{ psr}$ , the average background per pixel is reduced to approximately one  $m_V = +30$  star which is negligible compared with the usable star magnitudes.

d. Readout Noise

The preamplifier noise constitutes the predominant component of the readout noise. Measured in electrons per resolution element (pixel), after reduction by the target gain, the readout noise at the photocathode  $n_R = 8\sqrt{2}$  electrons rms or an average noise count of  $N_R = (n_R)^2 = 128$  photoelectrons.

e. Summary of S/N

Based on the foregoing calculations (a through d above), the following tabulation lists the integration time,  $t$ , required to attain a signal to noise ratio of two for an object of apparent magnitude  $m_v$ :

<u><math>m_v</math></u>	<u>S/N</u>	<u>t (seconds)</u>
20	2	6
22	2	38
24	2	250

It is noted that the Slit Jaw Camera is sensitive to that portion of the star image which is not passed by the slit. This means that an increase in slit width increases the difficulty the SEC will experience in attempting to track dimmer than 24th magnitude images. The slit position may be obtained by means of the described back-lighting source which is inactivated during data taking.

In the above examples, the sensitivity limitation is set by the preamplifier noise and the photo collecting efficiency which is determined by the optics coating and by the 0.3 mrad field of view obtained with a 25 mm x 25 mm SEC target.

5.2.4 Alternative Approaches

The preceding analysis indicates low optical efficiency of the Slit Jaw Camera system. The resulting long integration periods and inability to detect faint stars is due to the spillover of energy when the target is partially into the spectrograph slit. In the following discussion of ways to make the optical system more efficient, there are trade-offs involving the field of view. In general, it will be seen that a roughly inverse relation between field of view and integration time exists and that

this relation results from detector characteristics as well as from the optical designs. The optical design alternatives will be discussed first.

#### 5.2.4.1 Alternate Optics Systems

An example of alternative optical arrangements is an earlier version shown in Figure 5-6. This system has four reflections following the slit jaw compared to eight or nine reflections and four refracting surfaces in the reference system. It has approximately half the field of the reference system. Defocus and vignetting increase with field angle as a consequence of converging the three systems onto a single camera tube face and of the proportions of the Inca mirror system resulting from the space constraints. These same constraints also force the proportions far from the ideal Schwarzschild systems with their aplanatic imagery using all spherical surfaces\*. The system shown in Figure 5-6 has aspheric surfaces but it does not violate any basic precepts of good design. Therefore, as a compromise between the largest field of view and the best economy of signal for reducing integration time necessary to display faint targets, this system offers good possibilities as an ultimate approach.

Further gains in reduction of integration time are possible as the field of view is still further reduced. These gains are not as much a matter of optical efficiency as of the type of sensor. Nevertheless, the number of reflections can be reduced by one or two, which is significant in improving the transmission of shorter wavelengths. The reduction in reflecting surfaces is gained by eliminating those used only to bring the three fields of view to a common detector. The ultimate reduction in the number of reflecting surfaces is obtained using three separate sensors. For

---

\*S. Rosin: Inverse Cassegrainian Systems, A.O. Vol. 7, p. 1483 (1968).

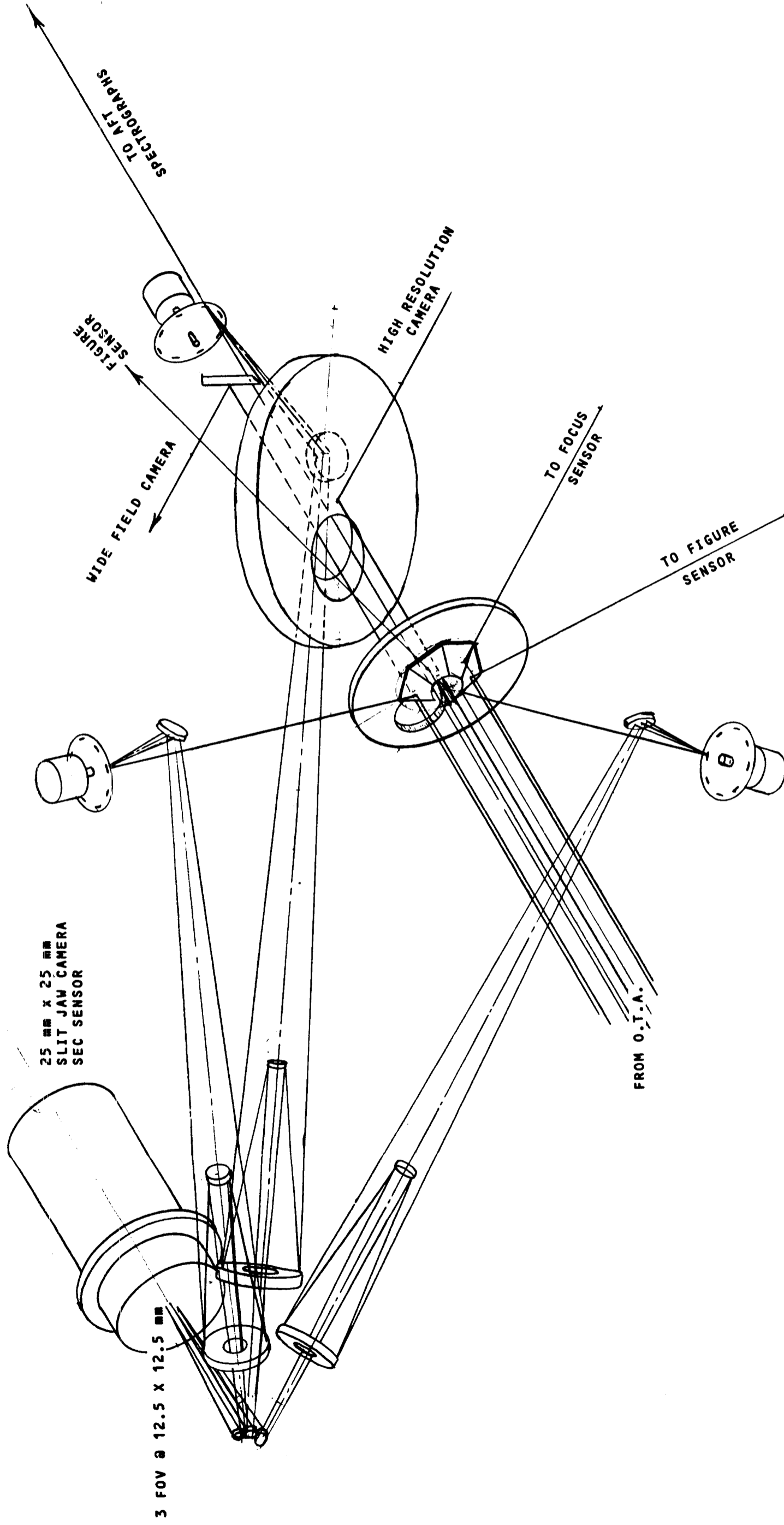


Figure 5-6. Slit Jaw Camera, Early Version

example, each sensor may have an off axis ellipsoid reflector (with its foci at the slit and at the camera tube) as the only optical surface after the reflective slit jaws. This approach has feasibility for the overall instrument arrangement presented only in the case of the two slit assemblies in the forward bay. The congestion in the area surrounding the rear instrument slit assembly will force the adoption of a two or three reflection layout. However, since the limiting case in the sensitivity analysis (highest sensitivity spectrograph) obtains in one of the forward (bay) instruments, the improvement in optical efficiency of the corresponding Slit Jaw Camera is the most desirable.

#### 5.2.4.2 Alternate Sensor Applications

Camera tubes of the SIT or EBS type, both of which employ silicon diode targets, were reviewed for properties which might eliminate the readout (amplifier) noise limitation. The latter tube types offer a gain twenty times that of the SEC tubes with an attendant reduction in amplifier noise count from 128 electrons (SEC) to 0.32 electrons (silicon). However, the silicon target has a leakage current which, referenced to the photocathode, is  $N_L \approx 2$  el/s-pixel at a target temperature of  $T = 233K$  and a 50% MTF resolution of 20 cycles/mm. From an empirical formula, the leakage current doubles with every 10K temperature increase; it follows that the target leakage count is:

$$\text{at } T = 273K, N_L = 32 \text{ el/s-pixel}$$

$$\text{at } T = 293K, N_L = 128 \text{ el/s-pixel}$$

From the above, it may be seen that the use of a silicon target vidicon will increase the integration time, previously computed for the SEC, by a factor of 5.5 when the target operates at  $T = 293K$  and will equal it when the target operates at  $T = 265K$ . Further reduction of integration time attained by operating the

targets at lower temperatures, may present major difficulties unless reduction of power dissipation is achieved (see thermal evaluation of SEC Vidicon in Section 7). From this consideration, an electrostatically focussed SIT camera tube of the RCA type C1130 was evaluated above.

#### 5.2.4.3 Image Dissector Slit Jaw Monitor

Implementation of automatic rather than ground controlled image correction to the center of a spectrograph entrance slit, to the dimmest usable target, is possible by means of an image dissector (ID) sensor. The use of three image dissectors with separate optics, one for each slit, offers the highest optical efficiency, employing only three reflecting surfaces from the slit to the detector. The high secondary electron gain of this detector eliminates the amplifier noise influence which was predominant in the SEC camera when viewing a dim target. Moreover, this detector is adaptable to photon counting techniques which, by means of a low amplitude threshold, virtually eliminate the photocathode dark noise. In addition, this solution offers savings in power dissipation, weight and size, as compared to a single SEC camera and optics.

A numerical example may be used to show the ID slit jaw monitor applicability.

Assume an ID tube with S-20 photocathode and a  $MgF_2$  window and an aperture size of  $0.22 \times 0.22$  mm, which, in an  $f/36$  focal plane, corresponds to  $2 \times 2$   $\mu$ rad or a solid angle  $\Omega = 4$  psr. Assuming a flat image distribution of about 2.5 times the diffraction spot size, an image diameter of  $1\mu$ rad is obtained at a wavelength of  $\lambda = 0.5\mu$ m.

From a comparison of the aperture and image sizes, one sees that the aperture will transmit the full image when the two are

concentric. Using the Wide Field Camera throughput data from Figure 3-18 and an optical efficiency of  $\eta = 0.8$  for the three surfaces, in addition to the ones used in the above reference, a zero magnitude star (11,000K) will yield an average photoelectron density of  $N_0 = 5 \times 10^7$  pe/s-nm in a spectral bandwidth of  $\Delta\lambda = 550$  nm. Hence, the zero magnitude star signal, referenced to the photocathode, is  $S_0 = 2.75 \times 10^{10}$  pe/s. Considering an I.D. with an aperture collecting efficiency of 65%, the resulting count is  $S'_0 = 1.8 \times 10^{10}$  pe/s. The background count is

$$N_B = \frac{11.3 \times 4}{25} \approx 1.8 \text{ pe/s}$$

with  $S_{23} = 11.3$  pe/s as an average background of one star,  $m = 23$ , in a solid angle of 25 psr. Using the same amplifier (readout) noise as before and a dark count based on the dissecting aperture, integration time was computed for assumed representative low star magnitudes. Using a common  $S/N = 2$  as criteria:

$m = +20$	$S'_{20} = 180$ pe/s	$t_{20} = 140$ ms
$m = +22$	$S'_{22} = 29$ pe/s	$t_{22} = 870$ ms
$m = +24$	$S'_{24} = 4.5$ pe/s	$t_{24} = 6.0$

If we consider next the case where the spectrograph slit is narrower than the target image leaving the spillover energy from the target to be used for guidance error signals or real time monitoring. The background ( $N_B$ ) and signal ( $S$ ) are reduced by an assumed 80% with the amplifier noise ( $n_R$ ) and dark current ( $N_D$ ) remaining the same. The following integration times are estimated using the  $S/N = 2$



FIGURE 5-7 HAS BEEN DELETED

$$S''_m = 0.2S'_m$$

m = +20	$S''_{20} = 36 \text{ pe/s}$	$t''_{20} = 0.7\text{s}$
m = +22	$S''_{22} = 5.7 \text{ pe/s}$	$t''_{22} = 4.4\text{s}$
m = +24	$S''_{24} = 0.92 \text{ pe/s}$	$t''_{24} = 29\text{s}$

From above it may be seen that the integration times obtained with the ID system remain small even when 80% of the energy is used by the spectrograph and only 20% remains for image position monitoring.

The only penalty for using the ID may be the initial acquisition time, if scan of a wide angle ( $> 25\mu\text{rad}$ ) from the slit axis is required, since a search program may be required if the initial pointing accuracy does not meet predicted values by a large margin.

### 5.3 MECHANISMS

#### 5.3.1 Servo Considerations

The mechanisms of the SIP have several characteristics in common. They do not have to track a changing input, and a response

time of several seconds is permissible. Therefore narrow bandwidth, high damping and high transformation ratios may be used in the servo design.

The number of desired positions of each mechanism is small, and the accuracy required of most of the mechanisms is not high. This permits the use of simple, reliable, moderately accurate position detectors in most cases. In those mechanisms which control sensitive parameters, the positional stability is an order of magnitude higher than the accuracy requirement. The time span between mechanism operations is large compared to the operating time. For these mechanisms, a detent is used to reach the final position, which allows power to the mechanism to be turned off once the mechanism is within the range of the detent. This not only saves power, but it makes the final position insensitive to electrical noise pickup.

The tachometer has been included in the servo because it takes little extra space, does not dissipate power, provides servo stability and design flexibility. It may be employed as a velocity controller to prevent damage to and prolong the life of components. It provides a means of maintaining a high static accuracy without high dynamic loop gains and the attendant stability problems. In some cases, such as the slit mechanism, where the rotational accuracy requirements are not stringent, it may be used in conjunction with a switch to position the mechanism. That is, the mechanism could be caused to move slowly, under the control of the motor tachometer loop, until the desired position is reached. At this point, the operation of a switch would cause the input to the tachometer loop to be zero. The arc of motor rotation before rest is  $\dot{\theta}t$  where  $\dot{\theta}$  is the initial velocity and  $t$  the tachometer loop time constant. Since both  $\dot{\theta}$  and  $t$  can be made small by proper design of the tach loop, the mechanism may be brought to rest in a short, controllable arc (distance). If rate feedback were not in the loop, neither  $\dot{\theta}$  nor the stopping arc would be controllable,

and a position detector more sophisticated than a switch would be required.

Another consideration in the servo design was the existence or non-existence of a preferred position at failure. In those mechanisms which have a preferred position in case of mechanism failure, a spring return to a center detented position is utilized. Positions other than the center position must be maintained by full time servo action. Because of the permissible use of large transformation ratios, this action will not result in the expenditure of large amounts of power, as shown in Section 9.3.2.

### 5.3.2 Mechanical Considerations

With one exception, the required output motions are attained with multi-position, rotating devices designed so that the most critical position tolerances are maintained by back-to-back ball bearing pairs. The exception in the reference design is the mirror shifter which selects one of the three cameras for each of the three different wavelength bands of the High Resolution Camera system. The linear output motion required in this case is derived by rotating a ball screw which translates the selection mirror to the proper selection position. Two typical mechanisms, the Slit Mechanism, Figure 5-8 and the Spectrograph Selector, Figure 5-9 are described in this section. The remaining mechanisms are illustrated in the instruments to which they pertain (see Figures 4-48 and 4-59). The mechanisms and their associated tolerances are listed in Table 5-1.

The mechanisms which position flat mirrors are designed to maintain their normals parallel to the shaft axis. For example, the normals to the slit mechanism's reflecting surfaces are parallel to the shaft axis, rendering the orientation of the surfaces insensitive to rotation about that axis. In the case of the Spectrograph Selector, an off-axis paraboloid collimates the light

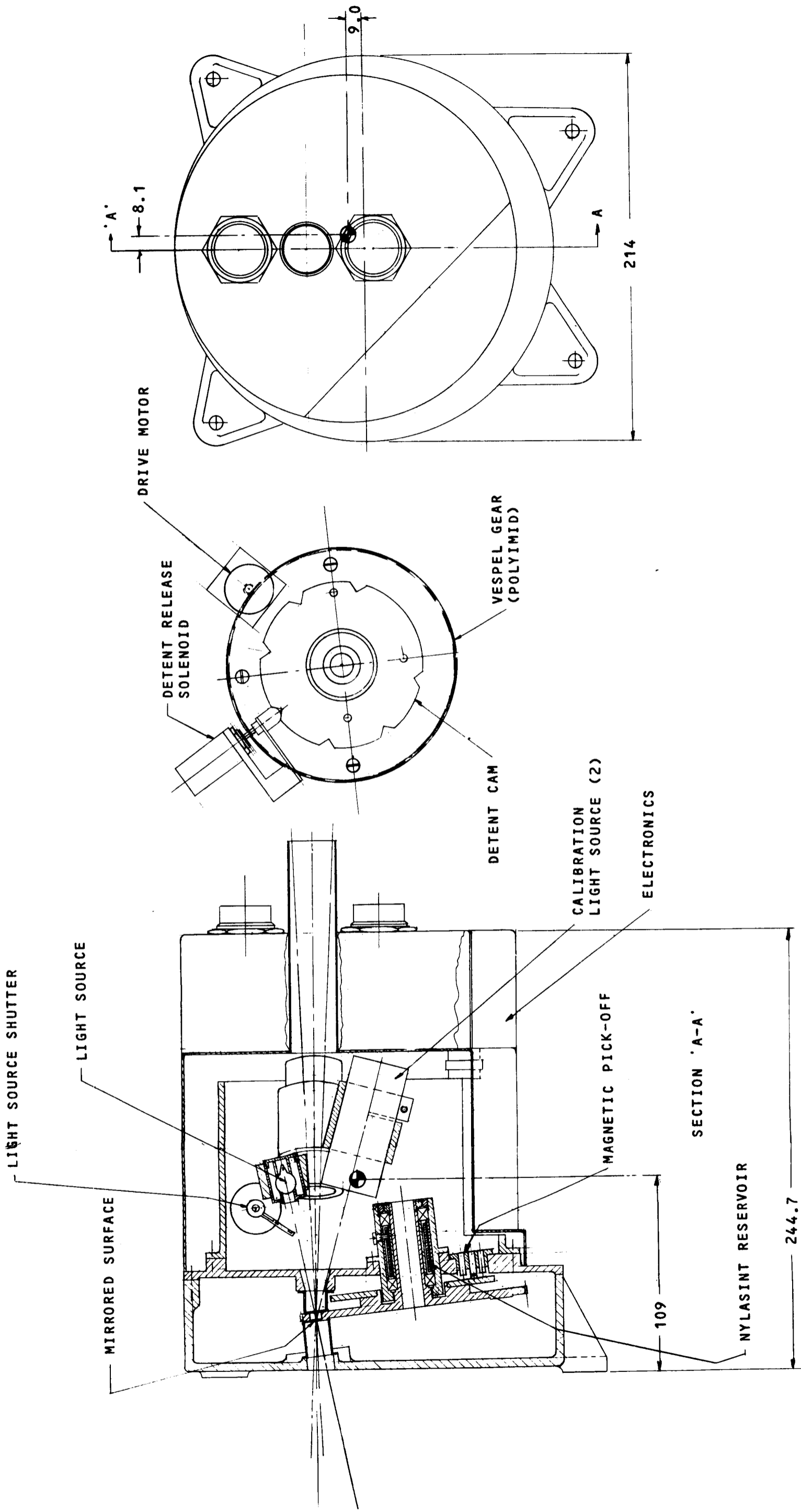
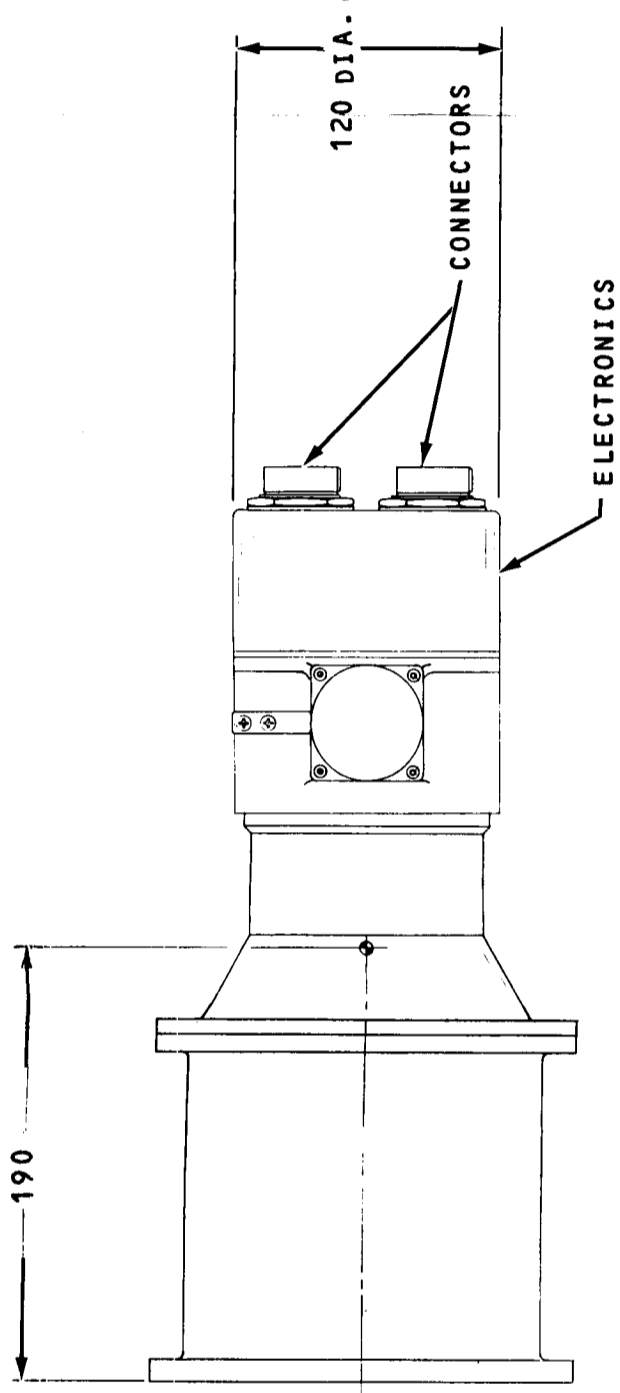
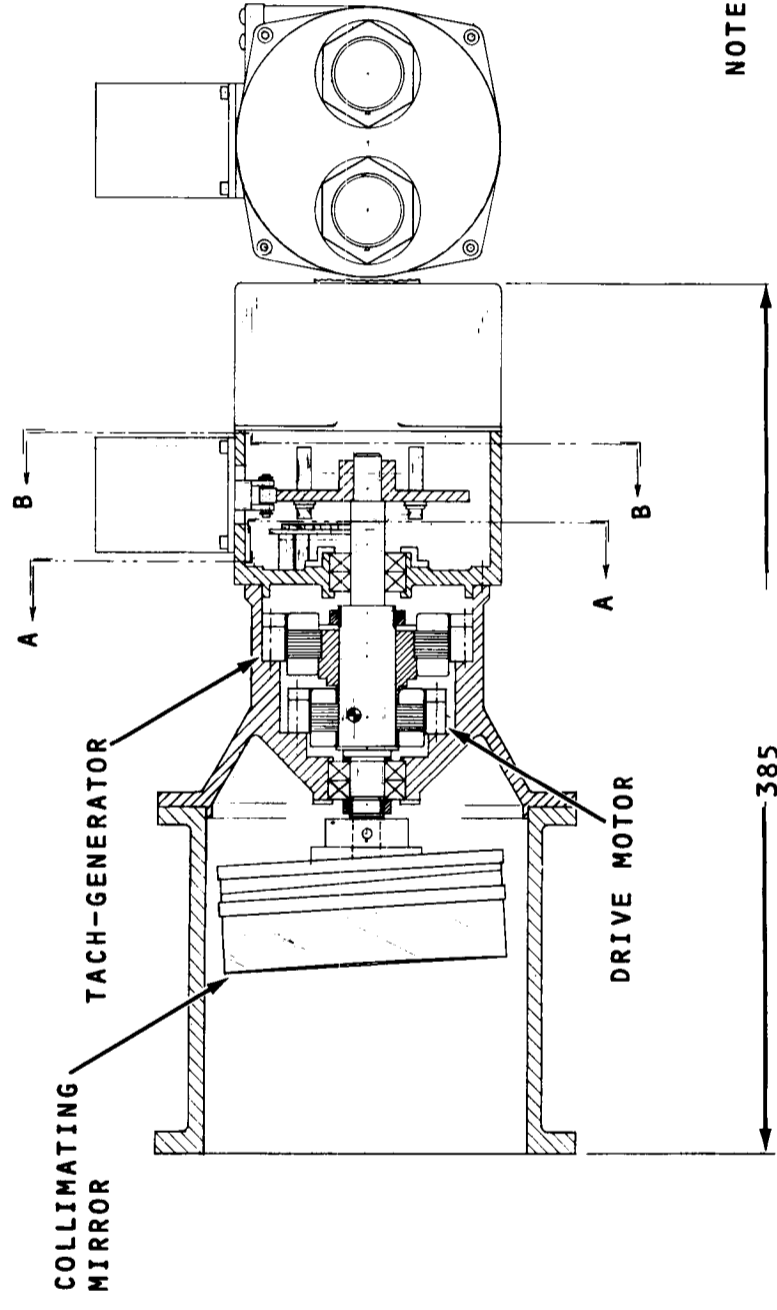
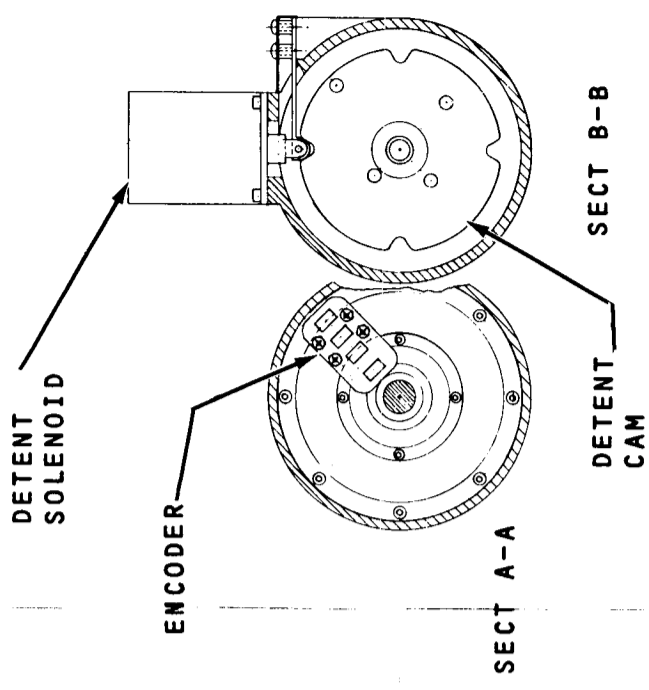
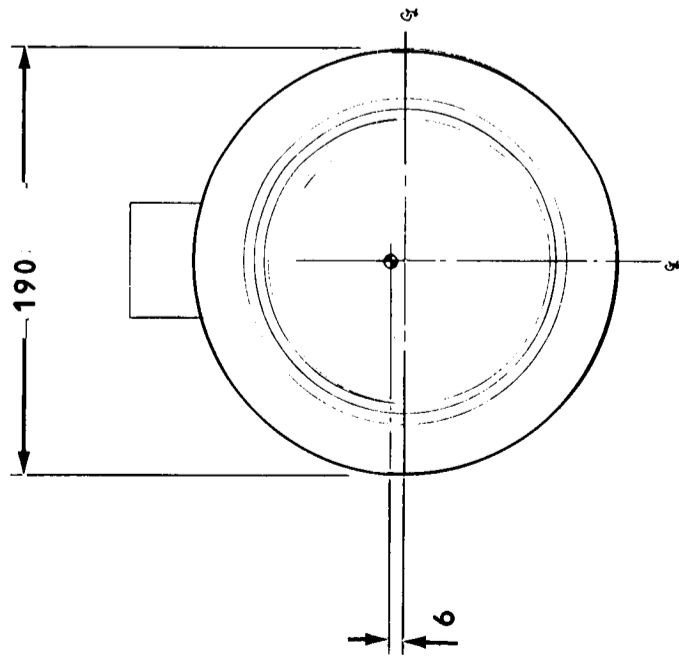


Figure 5-8. Slit Mechanism



⊕ C.G. APPROX. LOCATION  
ESTIMATED TOTAL WGT.: 7 kg



NOTE: ALL DIMENSIONS  
IN MILLIMETERS

Figure 5-9. Spectrograph Selector

Table 5-1. TOLERANCES FOR INSTRUMENT MECHANISMS

MECHANISM	FUNCTION	TOLERANCES			
		AXIS TILT		ROTATIONAL POSITION	
		MAX. ERROR	STABILITY	MAX. ERROR	STABILITY
Spectrograph Selector	Rotate off-axis paraboloid collimator; four positions	0.3 mrad	5.8 $\mu$ rad	2.4 mrad	47.5 $\mu$ rad
Grating Selector Faint Object Spectrograph 110 to 220nm	Select Grating for wavelength range; two positions	0.3 mrad	5.8 $\mu$ rad	10.0 mrad	0.4 mrad
Two Slit Changers	Rotate Slit Discs; four positions	1.0 mrad	0.5 mrad	5.0 mrad	0.33 mrad
Four Filter Selectors	Select Filters for three High Resolution Cameras and one Wide Angle Camera. Includes fail-safe return to open position	10 mrad	2 mrad	10 mrad	5 mrad
High Resolution Mirror Selector	Select Mirror, two at two positions (alt. design)	2.5 mrad	60 $\mu$ rad	10 mrad	5 mrad

from the slit and passes it to the rear bay instruments; its rotation axis must be held parallel to the OTA optical axis and must maintain focus at the entrance slit. The filter positioners, also rotating type mechanisms, have large tolerances for both position error and stability.

The Kollsman design for the critical alignment stability of shafts\* is one which has been and is performing after 20 months in orbit. Tight tolerances on position stability and low torque for continuous operation are obtained at speeds exceeding 300 rpm and with the weight of the rotating parts in the order of 1.5 kilograms. These shafts are mounted in pairs of back-to-back pre-loaded bearings with full retention of both inner and outer races. The bearings pre-load, which is controlled by the manufacturer, is achieved by a built-in offset of the inner and outer races. This offset is overcome by clamping the inner races together at assembly thus applying the pre-determined end loading. In this design, identical spacers between the inner and outer races separate the bearings so that the same offset occurs when the inner races are clamped against the spacer. Exposure of the above shaft assemblies to severe vibration, for which they were designed, has shown that bearing life is further increased by clamping the outer races. This prevented reversal of loads, widely exceeding the preload, from damaging the races.

It is important that back-to-back bearings be used rather than front-to-front. The back-to-back design supplies the most effective and largest restoring moment for the orientation of the shaft axis and reduces the variation of preload as a function of differential expansion of the parts. In critical assemblies operating over a wide temperature range with low driving torque available, it is still significant to use, for the shafts and outer race

---

\*Design similar to a classified space system.



housings, materials of nearly the same expansion coefficient as the bearings themselves.

The lubricant applied to those shafts which have been performing so well in space is F-50 oil, a silicone base lubricant. The oil is retained in porous ball separators of phenolic based plastic and in "nylasint"\* reservoirs occupying the space between the inner and outer race spacing tubes. Both the bearing separators and these nylasint reservoirs are vacuum impregnated with the lubricant.

Loss of lubricant can occur in two ways, evaporation and creeping. The F-50 oil has an extremely low vapor pressure so that by merely reducing the openings to the mechanism around the bearing, the entrapped lubricant vapors are sufficient to prevent boiling off of the lubricant indefinitely. Creeping of the lubricant is effectively prevented by use of coatings of barrier films\*\* over all the escape paths.

The detenting arrangements vary from mechanism to mechanism according to the rigor of the tolerances and the requirement for a fail-safe mechanism to take over if the normal positioning mode fails. The latter only applies to the filter change mechanisms since all of the remaining mechanisms have about the same priority at all operating positions. It is assumed here that the failure of any mechanism occurs only as a failure to initiate a change, that is, the change sequence once initiated, terminates at one of the operating positions rather than failing in transition.

The mechanisms requiring precise, stable detenting employ a leaf spring with a hard follower of cylindrical section engaging the slots in a disc on the rotating part. The engagement of the follower in the slot is of the locking type, and a solenoid in

---

\*Trade name for a porous Nylon

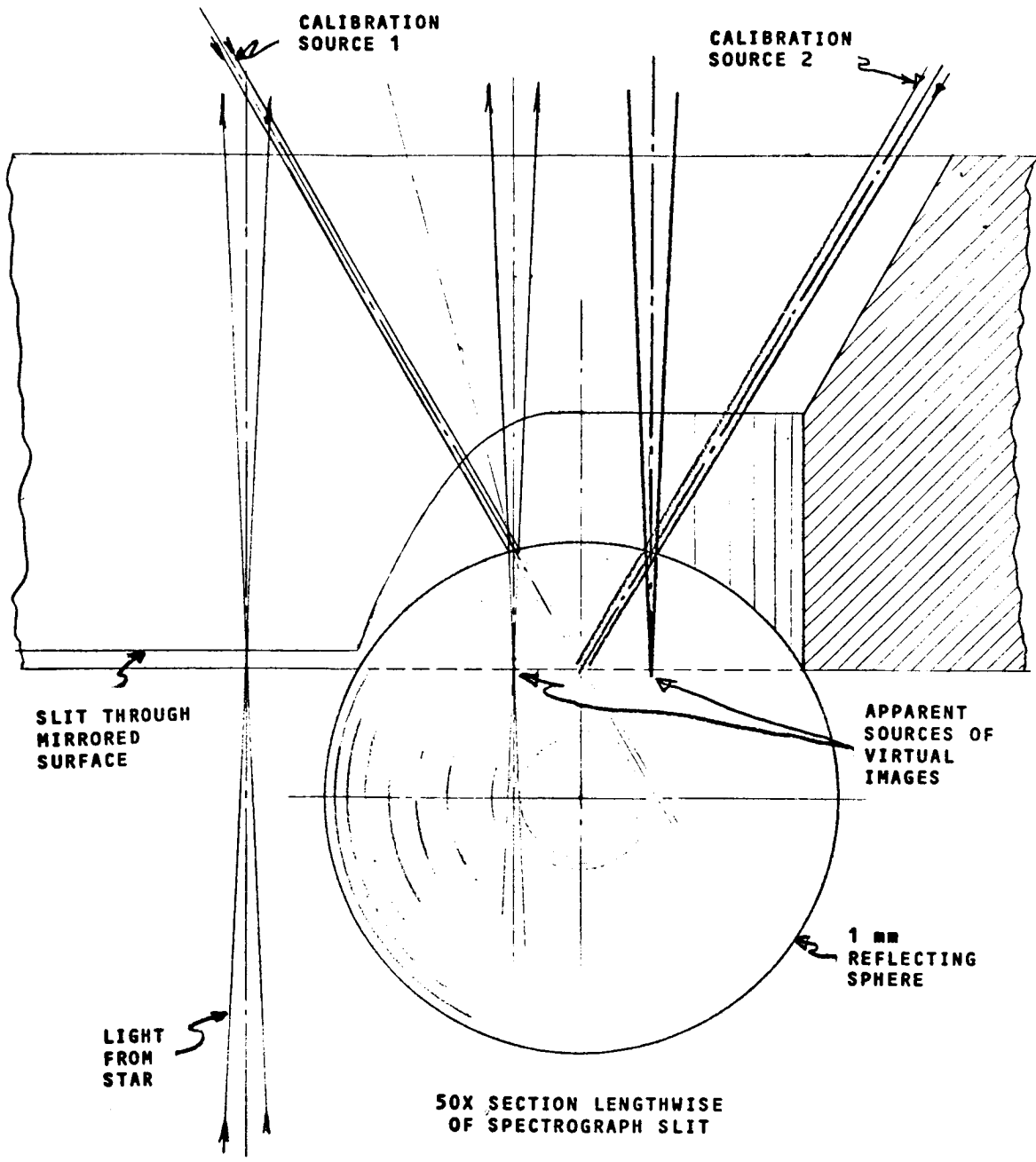
\*\*Oil migration barrier film. Dow Corning #519

series with the actuating motor pulls the follower out of engagement to permit the mechanism to move to a new position. This construction eliminates any variation in the short term repeatability and long term stability of the mechanism. The material of the follower will be one of the strong and hard composites which cannot weld to the disc. The long term wear free repeated engagements and dis-engagements will be insignificant in terms of the nominal position tolerances which are about twenty times greater than the short term repeatability and stability.

The filter mechanisms which have fail-safe return to their open positions will be actuated by servos which will continuously maintain selected positions against the centering spring of the return-to-open-position mechanism. This spring will be a leaf spring with a roller bearing on a heart shaped cam on the filter assemblies. The roller is too small to conveniently lubricate for long life operation in space, so special ball bearing materials will be utilized to prevent cold welding.

### 5.3.3 Additional Functions (Slit Mechanism)

The part played by the Slit Mechanism Assembly in the operation of the Slit Jaw Camera is described in Section 5.3.2. This mechanism also carries the spectral calibration and slit position indicators for spectrometers. Figure 5-10 schematically shows how two light sources are presented as stars off the end, and in the plane of the slit. The inevitable separation of these artificial stars from the real star shows up as separation in the camera field of view which is perpendicular to the dispersion. In order to pinpoint the calibration, a second ball at the opposite end of the slit will be used. The resulting pairs of calibration images ( $S_1$   $S_2$ ) will define lines through the calibration wavelengths and the calibration points  $P(\lambda)$ , each in an order which bisects the distance between the two respective images, as shown in Figure 5-11 for two calibration points.



THE STAR IMAGE IN THE SLIT IS SHOWN TO THE LEFT. THE CALIBRATION SOURCE IMAGE REFLECTED FROM THE 1 mm DIA. REFLECTING BALL IS PRODUCED FROM A SOURCE ILLUMINATED 25 μm DIA. APERTURE TO FORM A VIRTUAL IMAGE WITHIN THE BALL AT THE SLIT PLANE.

Figure 5-10. Spectrograph Calibration Source

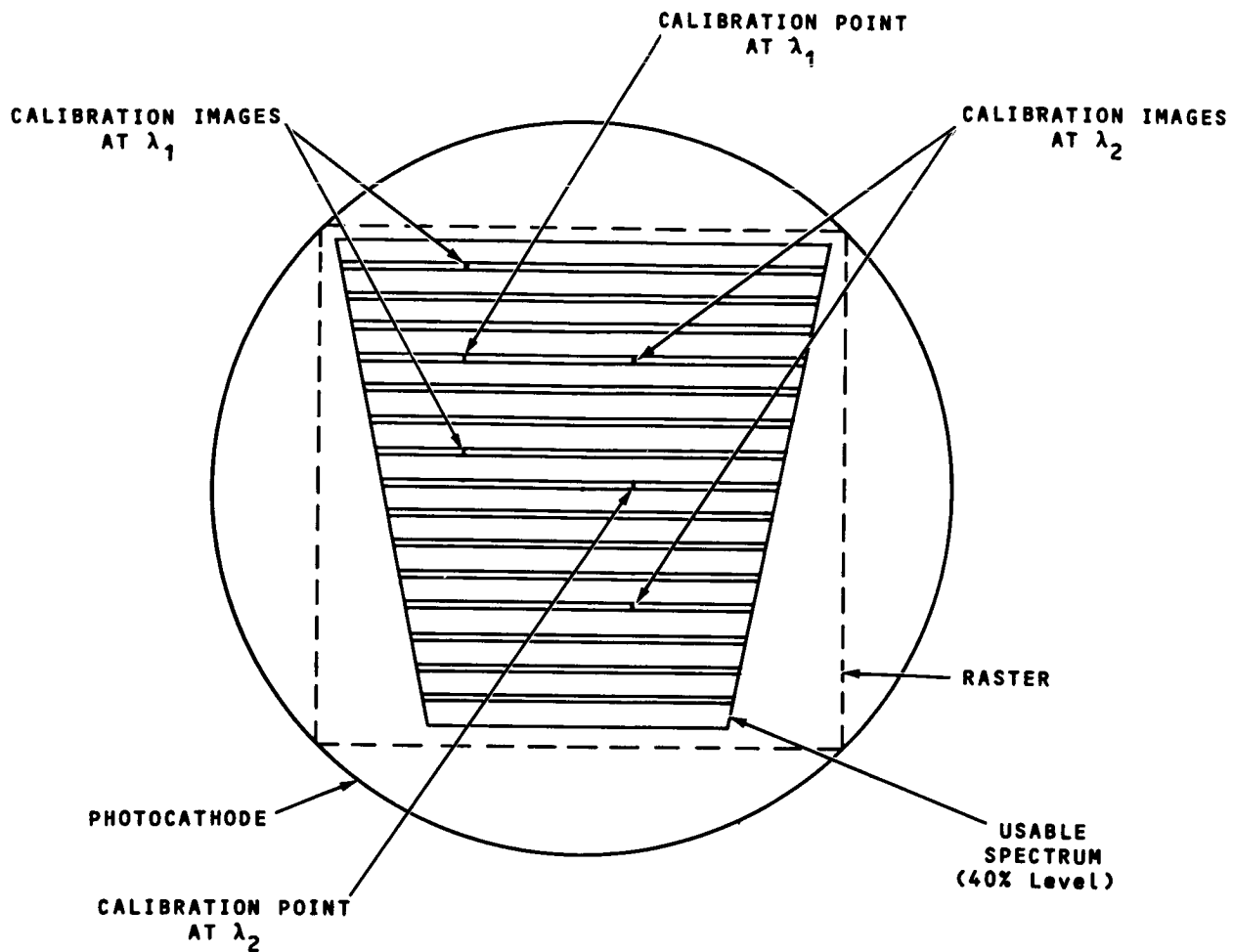


Figure 5-11. Calibration Source Display

### 5.3.4 Field Select Mirror Assembly

#### 5.3.4.1 Purpose

Located near the telescope focal plane, the Field Select Mirror Assembly is a stationary array of mirrors that apports the field of view among the various instruments.

#### 5.3.4.2 Functional Description

The completely passive role of this assembly is its most important attribute. It consists of about a dozen different mirrors whose principal requirement is to maintain the orientation. They are called out in the family tree, Figure 5-12 and shown on the layouts, Figures 5-3 and 5-5, which have already been referenced in the discussion of the Slit Jaw Camera. Working from left to right on the layout, we see first the five diagonals, in a circular array 1.1 mrad off axis, which pick off portions of the field for the five radially arrayed instruments consisting of the two Faint Object Spectrographs covering the interval from 0.22 to 1.0  $\mu\text{m}$ , the Mid IR Interferometer from 1.0 to 5.0  $\mu\text{m}$ , the Focus Sensor and the Figure Sensor. The reflecting surfaces of these five mirrors may be figured to correct the astigmatism at the center of each of the approximate 300  $\mu\text{rad}$  fields of view which they cover. These five mirrors are supported by a quartz window with a keyhole shaped cutout clearing the inputs to other instruments. On the back side of this window are mounted two more mirrors whose function is described in the Slit Jaw Camera write-up.

A large diagonal mirror, in the window cutout, reflecting the inputs to the Fine Pointing Sensor and the High Resolution Camera. This mirror also has a keyhole shaped opening, smaller than the previously described one, which passes the input to the Wide Field Camera and the rear instrument slit.

Mounted to the rear face of the large diagonal is a small diagonal, perpendicular to it, which directs the input to the

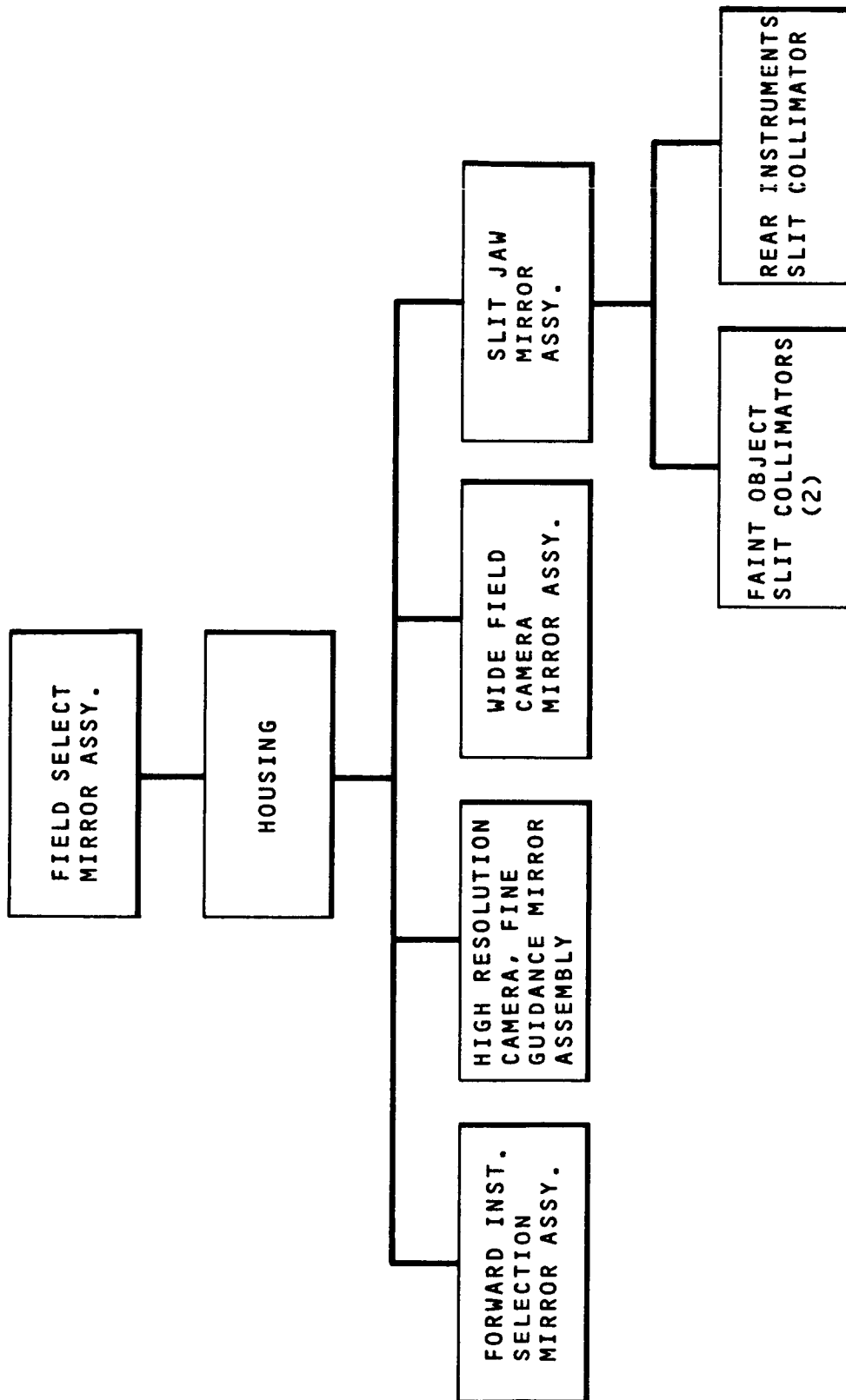


Figure 5-12. Field Select Mirror Assembly Family Tree

Wide Field Camera. A hole in the small diagonal passes the input to the rear instrument's slit.

The remaining mirrors are those already described in connection with the Slit Jaw Camera.

The design of this mirror array is dictated by the dimensions of the mirrors, resulting from the Fine Pointing field of view, and the necessity to physically separate the instruments sharing the field of view. The mirrors occupy positions far enough from the focal plane to cause the f/12 light bundles to significantly overlap. Highest priority has been given to the High Resolution Camera and the rear instruments, both of which are given completely unvignetted fields of view. Lowest in priority are the Wide Field Camera and the Fine Pointing, the first being 25% vignetted at the edge of its field and the latter by having various local vignettings plus a portion of its field assigned to the Wide Field Camera. The radially arranged instruments all have vignetting at the edges of their respective fields of view. This vignetting only affects the acquisition by means of the Slit Jaw Camera, since the instruments themselves cover a negligible field. Tolerances on the Field Select Mirror Assembly are based on the critical control necessary to maintain the focus and alignment of the star images on the slit apertures. In the position occupied by the mirror array, close to the focus, dimensional stability is paramount while angular stability is relaxed in comparison to the telescope's optics stability. The comparative compactness of this assembly and its virtual isolation from the various local heat sources suggest materials, such as aluminum in place of the quartz window.

#### 5.4 ELECTRONIC SUPPORT

##### 5.4.1 Mechanism

The inputs to all mechanisms are digital commands which originate in the SSM. There is only one source of power to any

instrument/mechanism, a +28 volt line. To simplify this system, and to do away with the need for DC to AC power converters, demodulators, etc., DC components such as error detectors, motors and amplifiers are used throughout the design of the LST mechanisms. AC encoders and motors do tend to be more reliable than DC types, but the very low duty cycles and velocities required by the mechanisms of the SIP will assure good reliability. In addition, the extra components required by an AC design would make the reliability of the mechanism electronics lower than that of the DC design.

The outputs required of the mechanisms, other than their mechanical positions are status indications. The analog outputs will be conditioned to a 0-5V range before being read by a Data Acquisition Unit. This is shown in block diagrams, Figures 5-13 through 5-18.

Most of the mechanisms are driven to their final position by a detent, and then the power is removed. This makes these mechanisms immune to electronic noise. The filter drive mechanisms, which are constantly under power, because of their preferred position of failure, are permitted the largest position error. Electronic noise is not expected to be of significance in these mechanisms.

#### 5.4.2 Packaging Approach

To enhance maintainability, each sensor, each spectrograph and each mechanism is equipped with its own electronics assembly. Each electronics package contains the signal processing, power supplies, diagnostics, data acquisition unit and interface circuits associated with the one particular opto-mechanical assembly that it supports. Consequently, each instrument may be removed from the SIP without any affect on other instruments. Further, the fact that within any given instrument the Sensor Electronics and Instrument Electronics are separate units permits replacement of the sensor in any instrument, without having to replace the entire instrument.



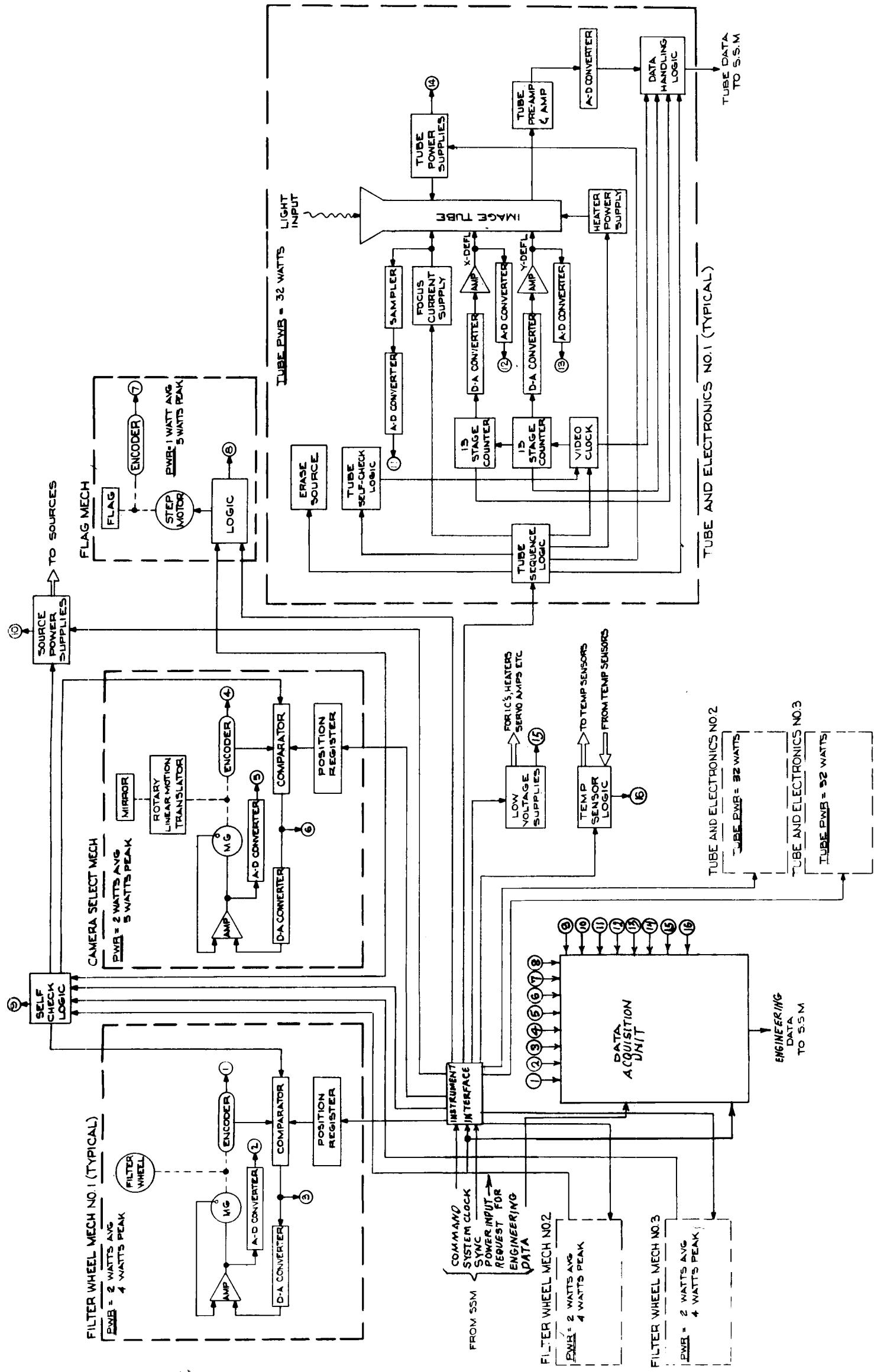


Figure 5-13. High Resolution Camera, Block Diagram

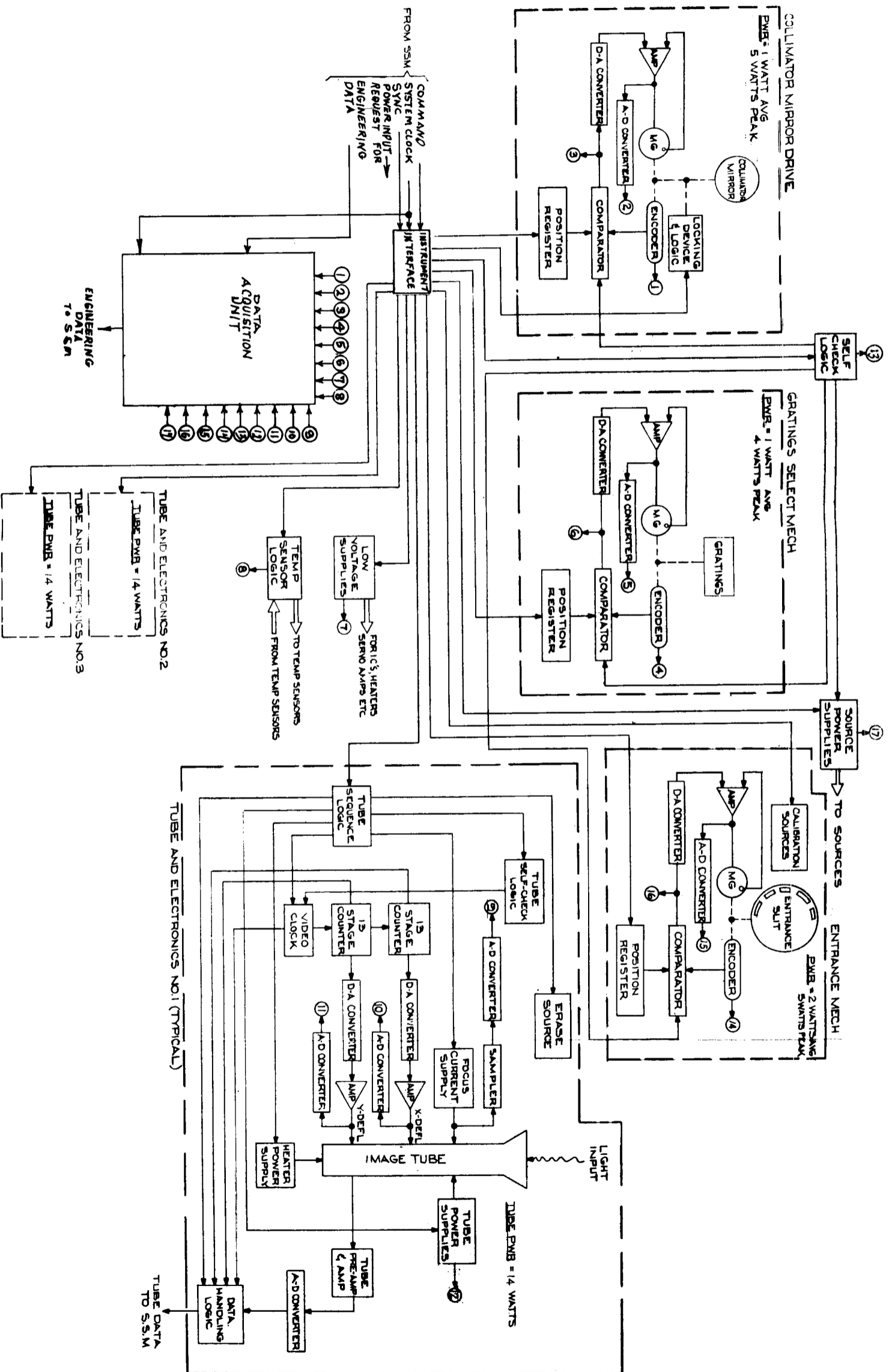


Figure 5-14. Aft Spectrographs, Block Diagram

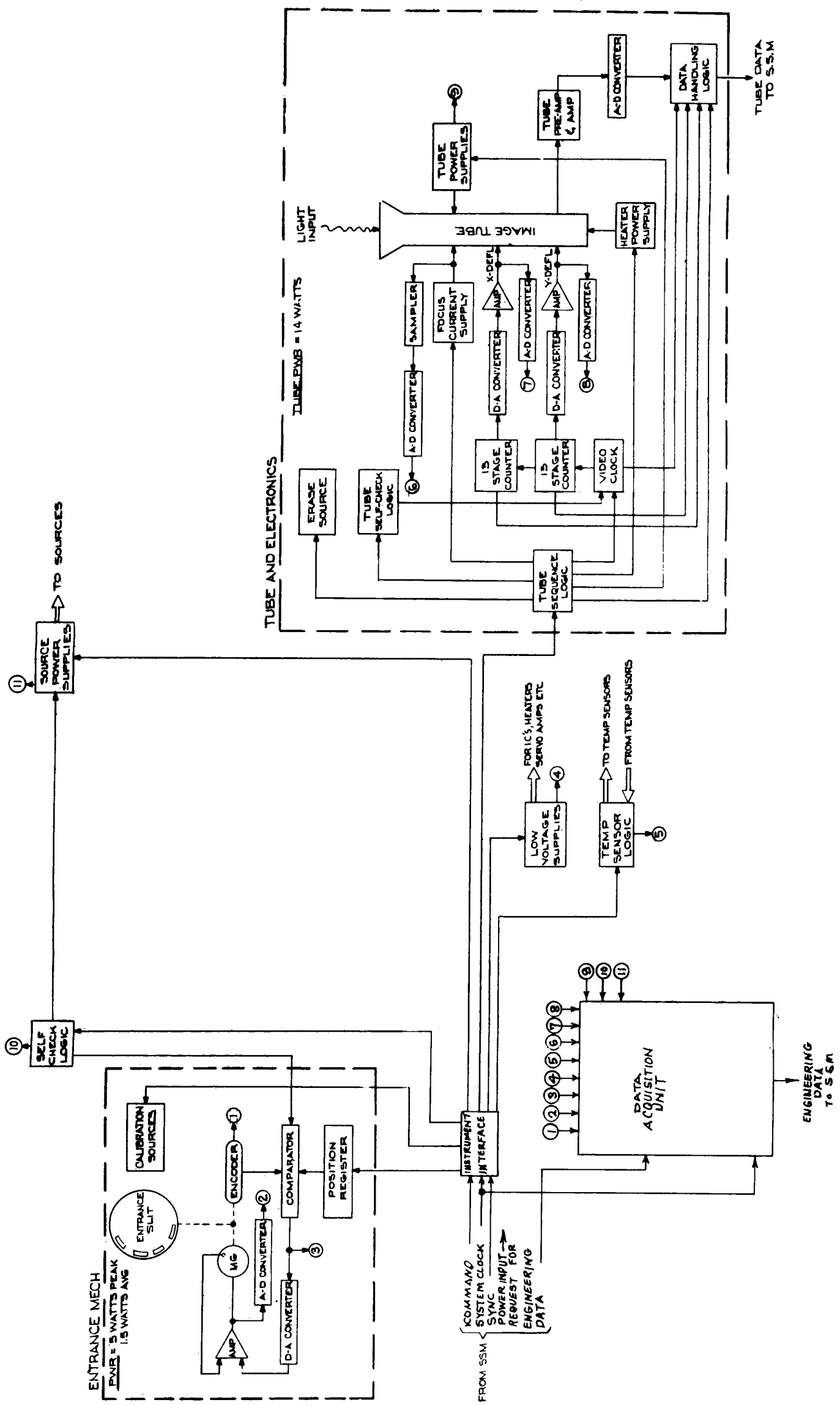


Figure 5-15. Faint Object Spectrograph No. 2, Block Diagram

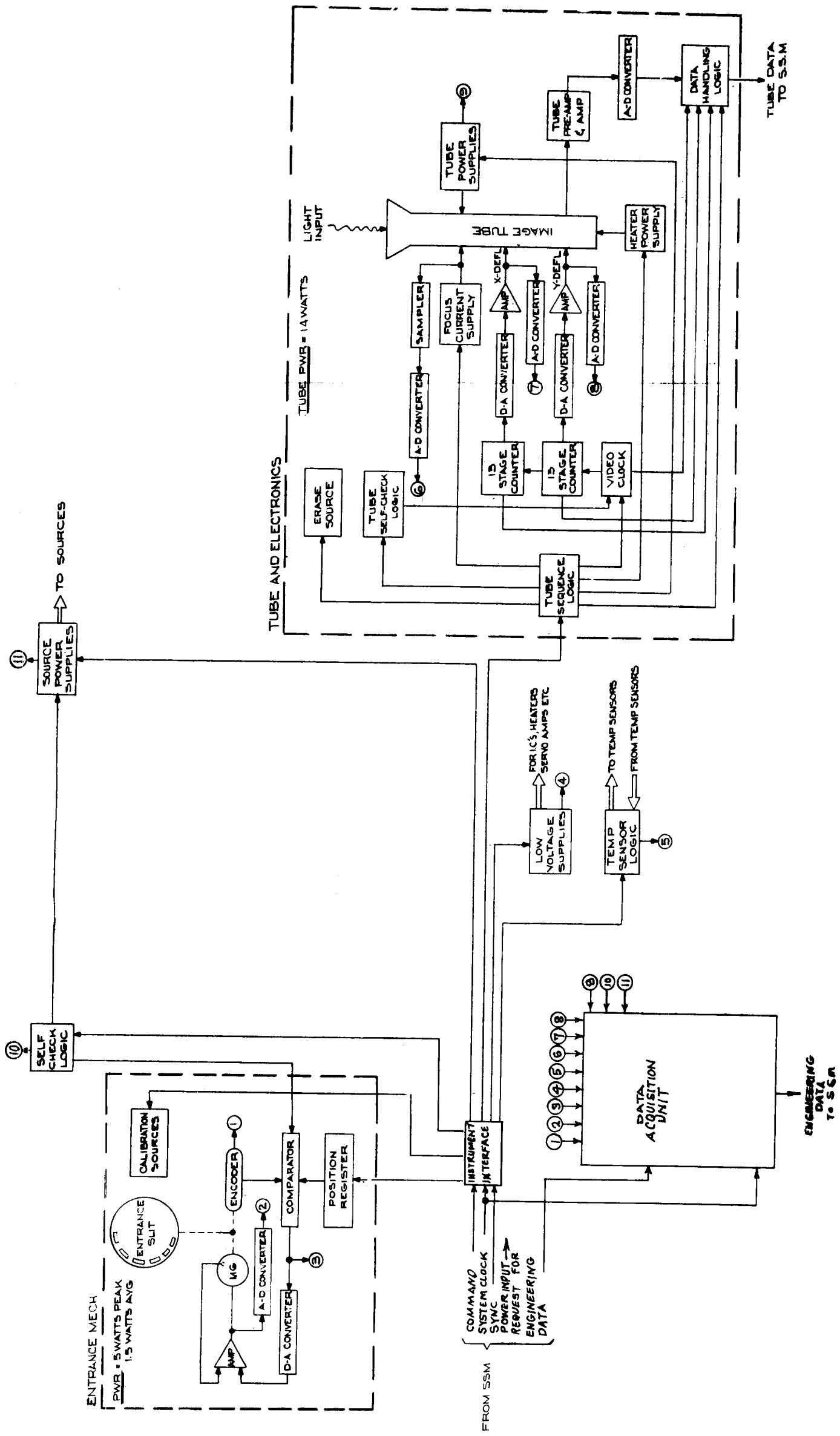


Figure 5-16. Faint Object Spectrograph No. 3, Block Diagram

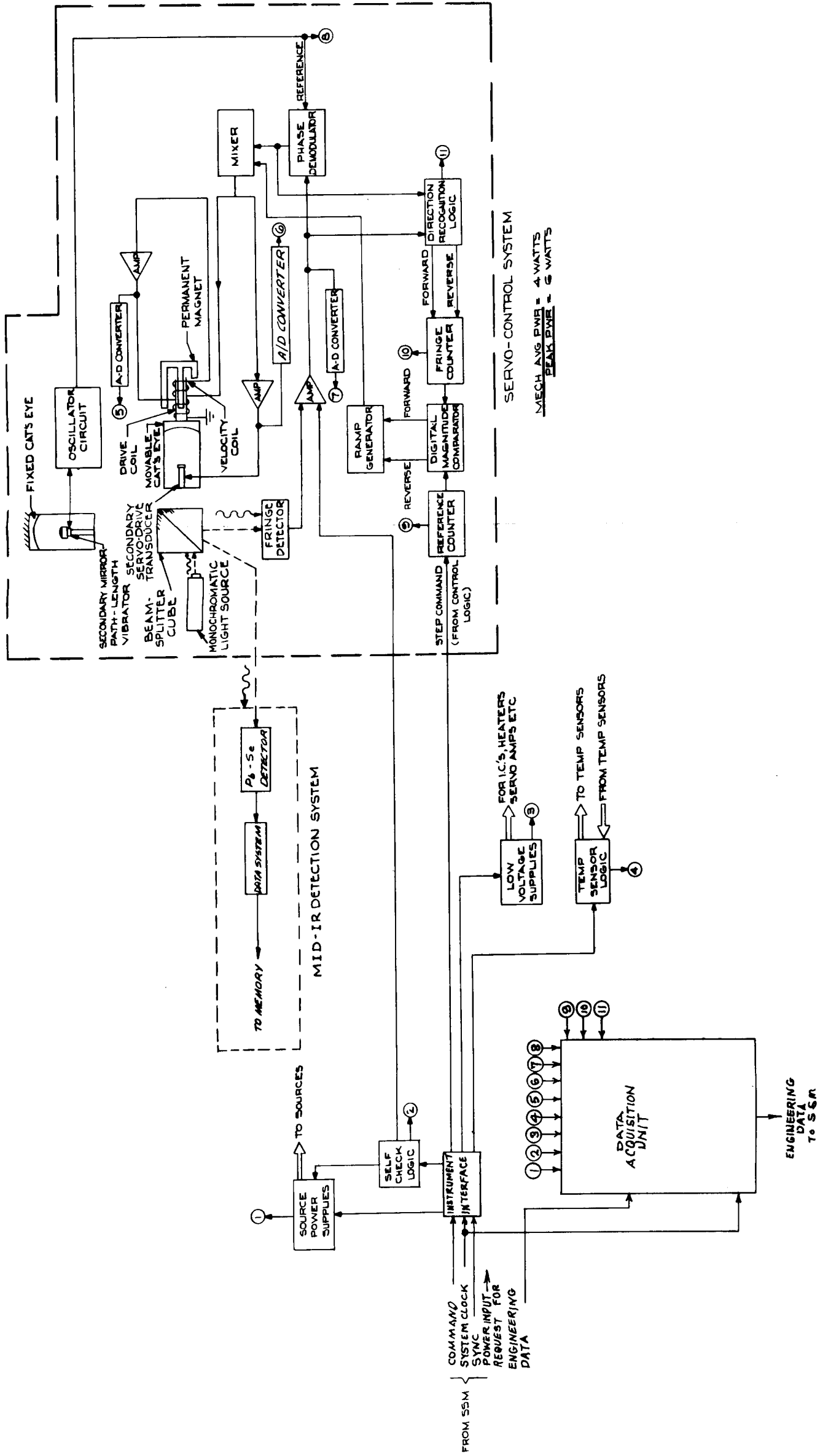


Figure 5-17. Mid-IR Interferometer, Block Diagram

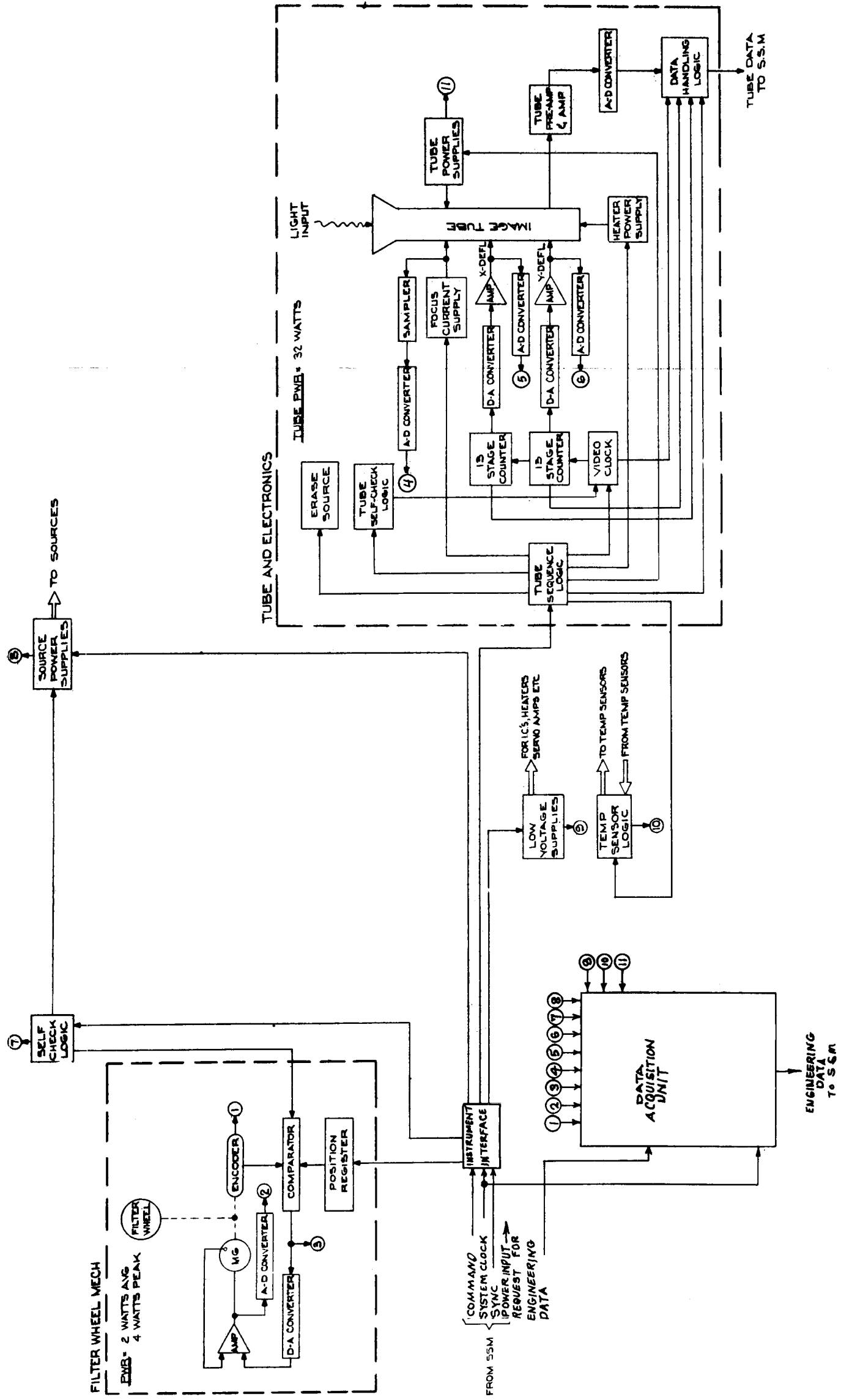


Figure 5-18. Wide Field Camera, Block Diagram

These assemblies, as typically shown in Figure 5-19, consist of printed wiring modules which are stack mounted on a mounting base. The modules will be hard wired to each other and to power, signal and instrument connectors. The power and signal connectors are as previously described for the Sensor Electronics. The instrument connector will be a center locking rectangular rack and panel type. The center lock will contain an extension shaft that will protrude through the EMI/RFI cover that encloses the package.

#### 5.4.3 Sensor Electronics

The Sensor Electronics Subassembly is a cylinder, 178 mm in diameter and 220 mm long, see Figure 5-20. It consists of eight printed wiring modules, stack mounted by means of spacers and studs in front and rear mounting rings. The rear mounting ring contains a signal connector and a power connector. The power connector is mounted to a filter-cam assembly whose purpose is to provide EMI/RFI filtering of the input power. The front mounting ring provides the necessary flanges for mounting the electronics assembly to the rear of the Sensor Assembly.

Connectors considered for use in the SIP are of the miniature type, having insertible crimp contacts and a push-pull coupling ring on the plug portion to facilitate engagement and disengagement.

Wiring of the assembly is of conventional harness type. It is dressed from the connectors down to one side of the assembly and in a relief area provided at one side of the module stack. The harness is hard wired to terminals provided on the individual modules. Hard wiring is used instead of connectors to minimize size and weight and to maximize reliability. Wiring of the various sensor coils, SEC-vidicon tube, etc., is dressed through access holes in the sensor structure to the appropriate module terminals. A retention bracket encloses the wiring harness to prevent damage during assembly or removal of the outer cover.

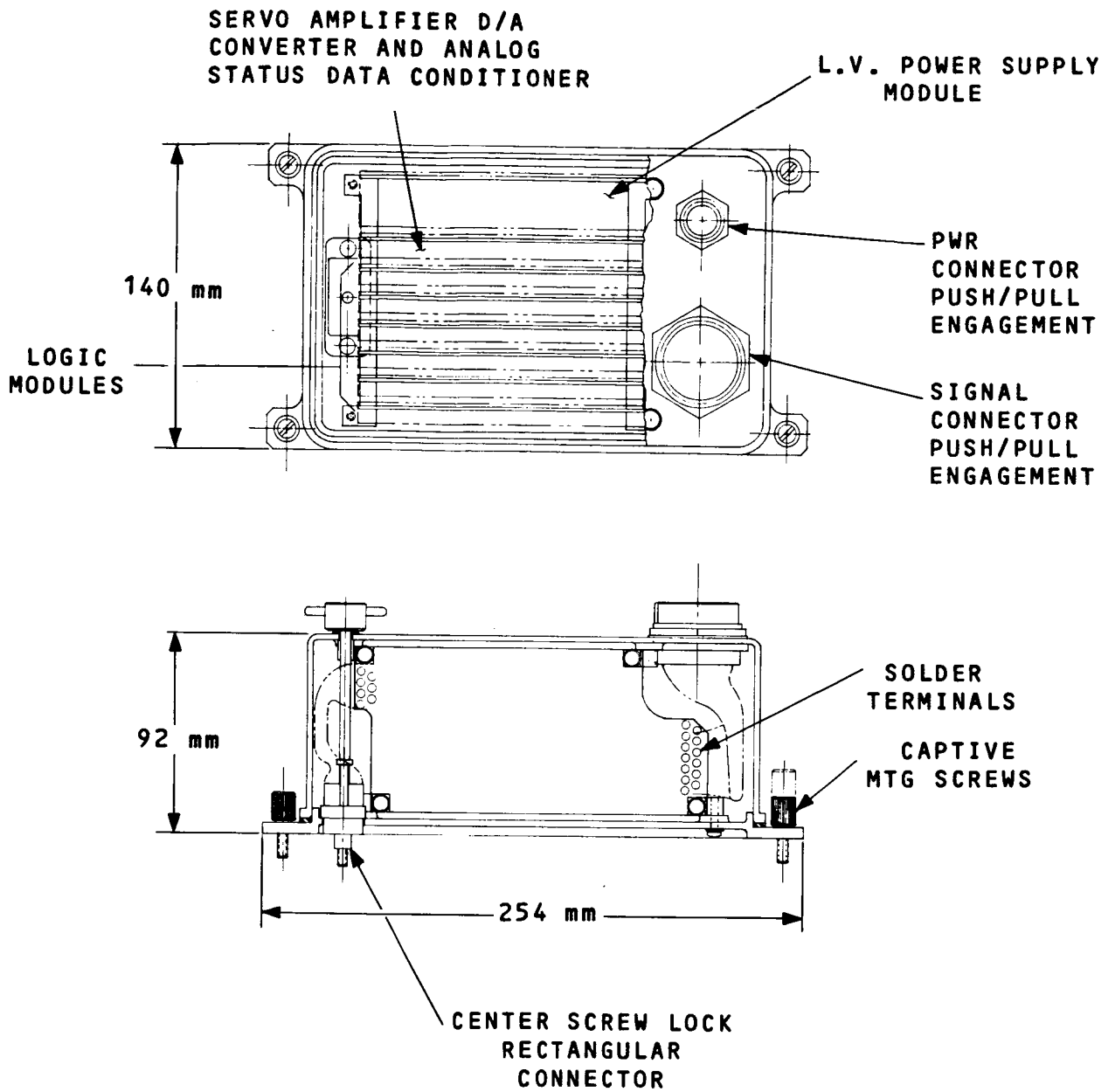


Figure 5-19. Typical Electronics Assembly



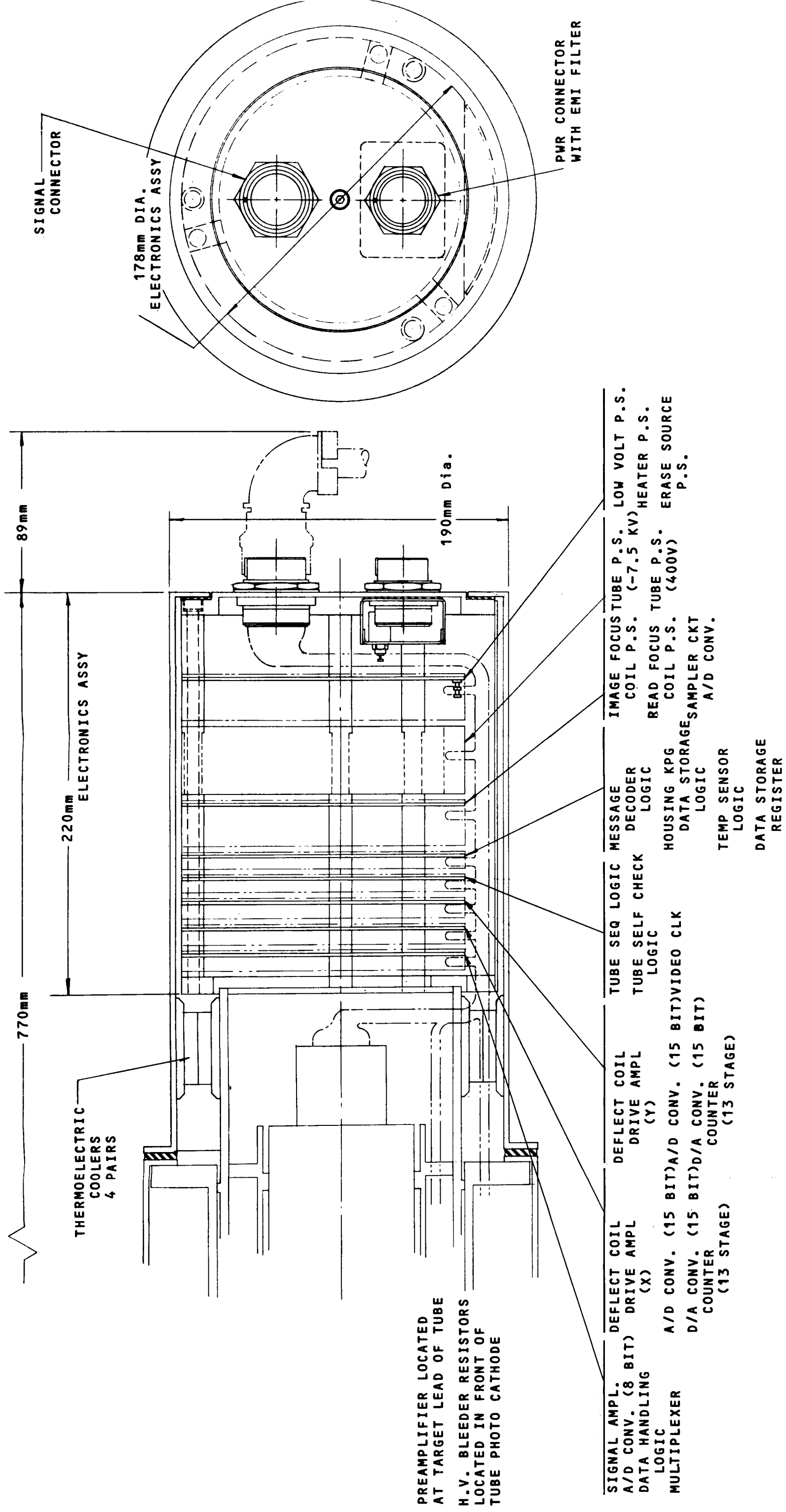


Figure 5-20. Sensor Electronics

The outer cover slips over the Sensor Electronics after all wiring has been completed. The cover is provided with EMI gaskets in front and rear, and its configuration is designed to serve as an EMI-RFI-magnetic and radiation shield. In addition, the cover acts as a radiating heat sink for the thermoelectric coolers to whose mounting plates it is attached.

The wiring modules employ boards printed on both surfaces, but with components on only one surface. Intersurface connections are made by means of plated-through holes. Circuit connectors and component terminal areas are as large as feasible within space limitations. In general, module designs meet the requirements of MIL-STD-275. Modules are conformally coated and high voltage sections fully encapsulated.

The Preamplifier and H.V. Bleeder Resistors are mounted within the sensor, separate from the Sensor Electronics. To minimize the length of the signal output lead of the SEC-vidicon target to the preamplifier, it is intended that the preamplifier be mounted forward of the deflection coils, directly at the target lead.

The H.V. Bleeder Assembly is mounted in front of the photocathode. In this location, the lengths of the leads providing the accelerator rings' voltages are minimized. The bleeder assembly is designed as a doughnut shaped encapsulated module.

#### 5.4.4 SIP Harnessing

The interconnection between instruments, ancillary equipment, the OTA and the SSM is provided by the harness shown schematically in Figure 5-21. The harness is shown as divided into five sections for ease of handling and of changes during development and to provide for future system growth. The power and signal cabling is separated as an EMC precaution. The signal cabling consists of three harnesses. Two of these carry signals from the instruments and the instrument support equipment to a connector panel on the structure. This connector panel provides for interface with the

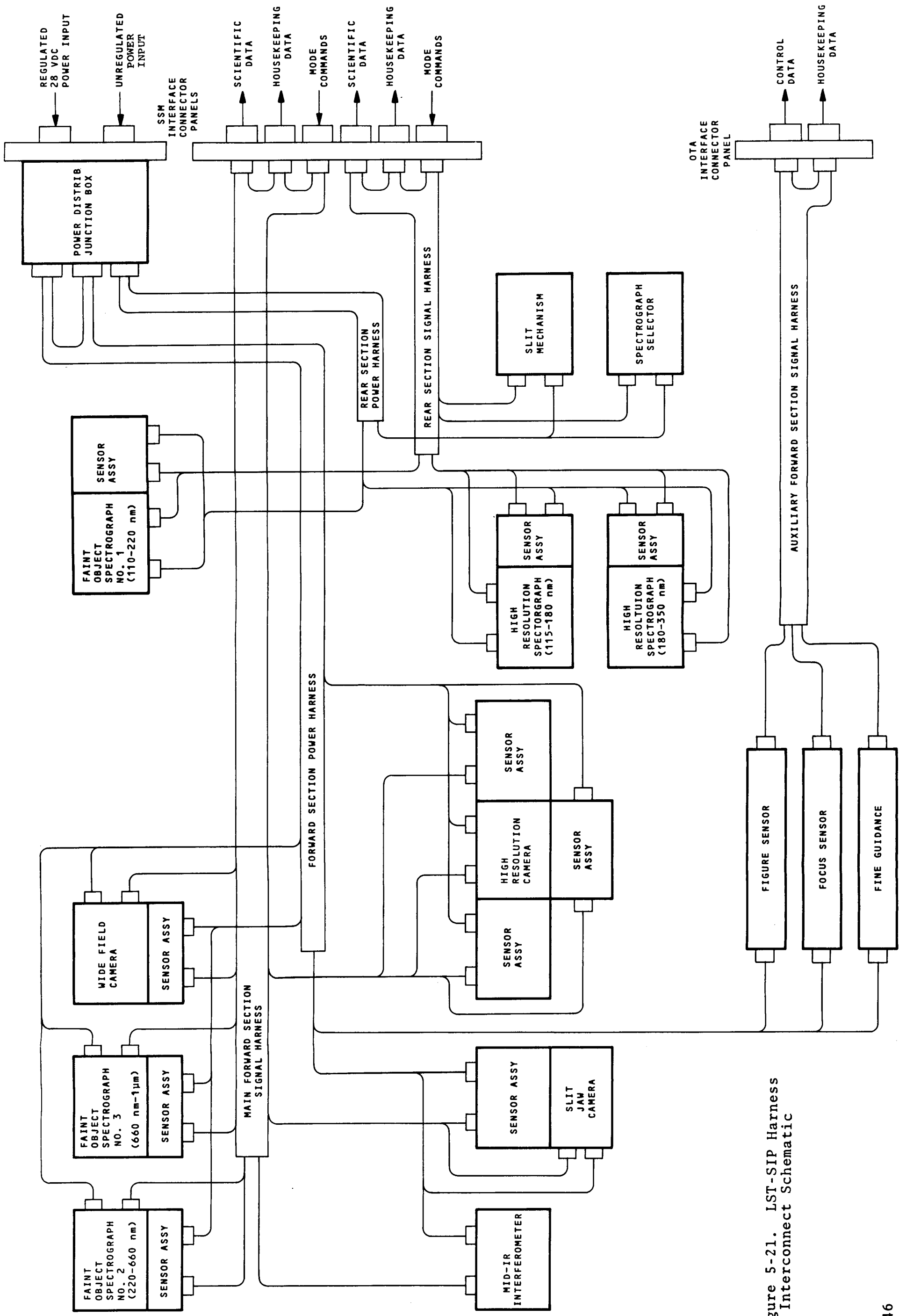


Figure 5-21. LST-SIP Harness Interconnect Schematic

SSM. The signal leads have been grouped into three categories: scientific data, housekeeping data and mode commands; and connector groupings and sizing has been based on keeping these groups integral. Twisted, shielded pairs of wire are used for the data lines. These operate as balanced lines to minimize the effect of low frequency interference.

A third signal harness is provided for the three items, located within the SIP, which provide data for telescope control. This harness terminates at a separate connector panel, where interface with the OTA is made.

Two harness sections are provided for power distribution. DC power from the SSM is distributed to the SIP equipment by means of a junction box located on the SIP structure. Mode commands to the instruments control power turn-on within each unit. Power cables are run unshielded to save weight and filtering is provided at each electronics unit.

Figure 5-22 is a layout showing general harness routing within the SIP. This layout was prepared to assure that adequate space is provided, to point out support and access requirements, and to allow more accurate weight and center of gravity calculations. The harness is never tied to any replaceable hardware to facilitate the in-flight maintenance task. This may be modified after a trade-off between added weight of cable supports and the added effort of removal and replacement of a cable clamping device. The layout also shows the interface connector mounting panels and power distribution junction box.

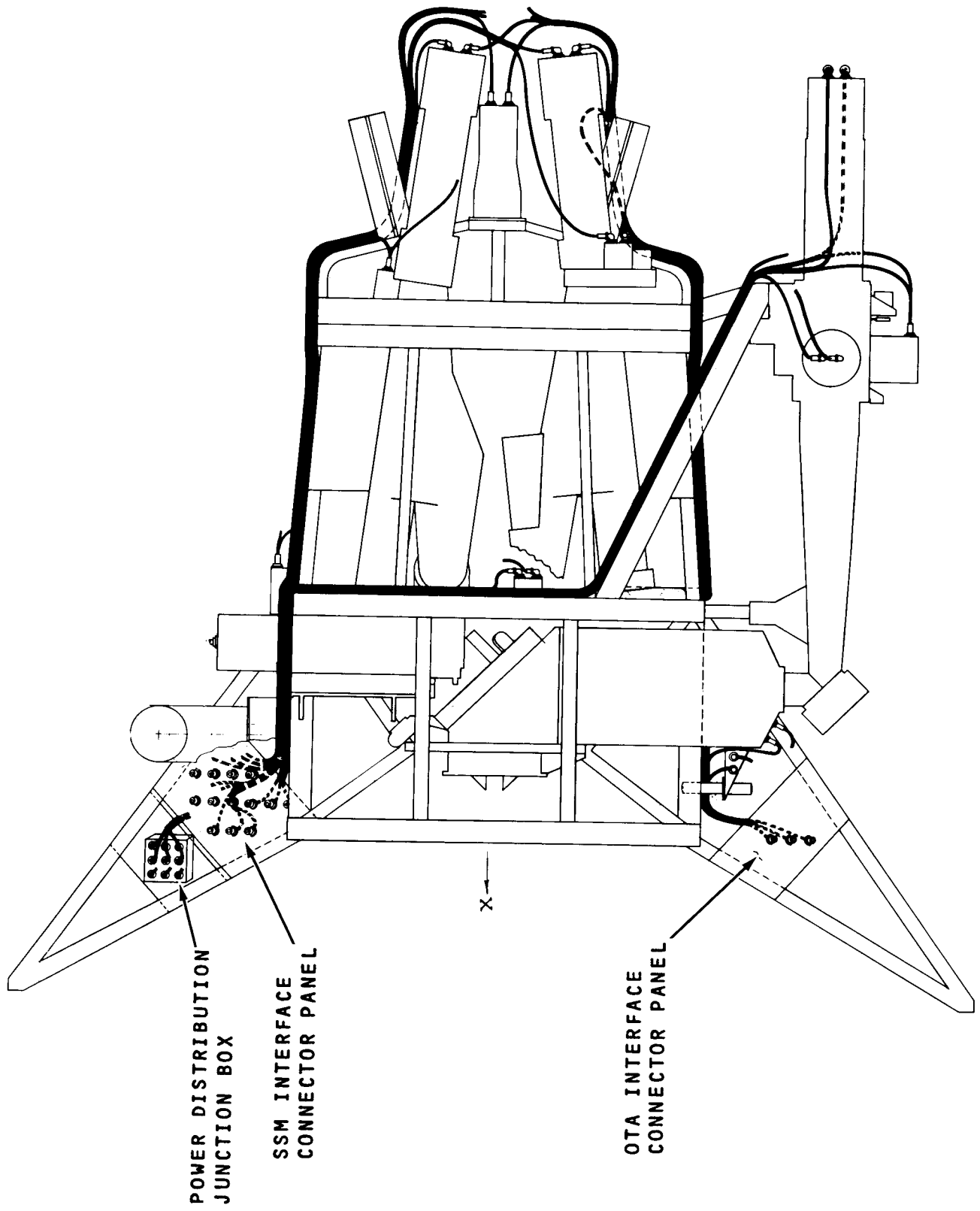


Figure 5-22. LST/SIP Harness Interconnect Layout (Sheet 1 of 2)

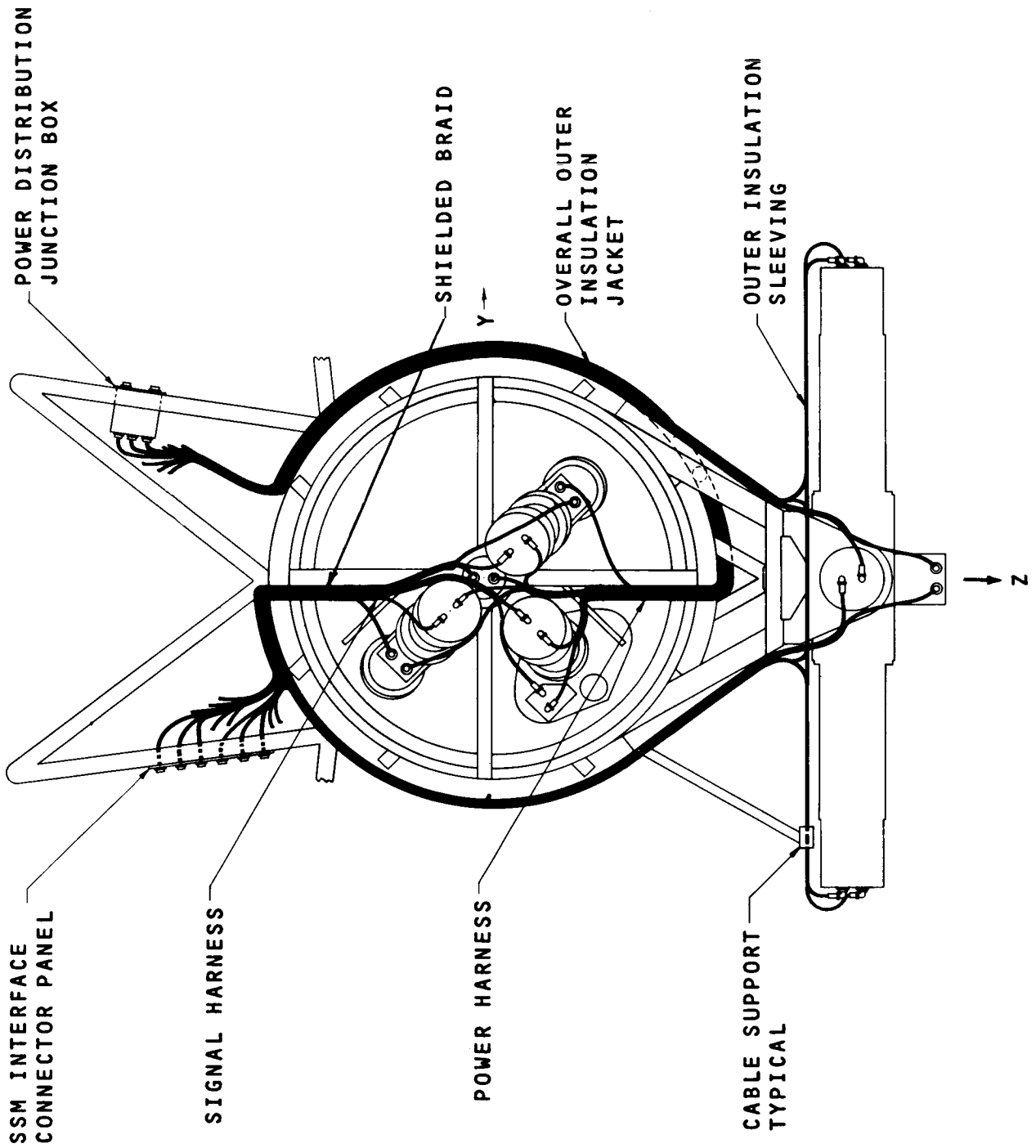


Figure 5-22. LST/SIP Harness Interconnect Layout (Sheet 2 of 2)

## Section 6

### IMAGING PHOTOELECTRIC SENSORS

#### 6.1 INTRODUCTION

This section explores the selection and performance of the instrument sensors and the materials which govern the sensor response. The initial paragraphs present the criteria for instrument sensor performance, a comparison of image tubes to photographic film, and comparisons of various image tubes.

This is followed by a discussion of the present status of the selected sensor, the SEC-Vidicon. Additional effort required to bring this sensor to the desired performance level include development of a suitable III-V semi-transparent photocathode, improved target performance, and ruggedization and qualification testing of the larger (50 mm x 50 mm) tube. Available photocathodes cut off at about 0.9  $\mu\text{m}$  thereby not providing data up to the desired 1.1  $\mu\text{m}$ .

The next several paragraphs cover photocathode and window materials with respect to the spectral response and efficiency when used in various combinations, and their suitability for each instrument application. Table 6-1 presents a summary of the sensor usage and material evaluation.

Target materials and performance are treated and a preliminary specification for the SEC-Vidicon detector tube is given. The next few paragraphs are devoted to the electron optics, magnetic interference effects on performance, and packaging considerations. The section concludes with a description of the SIT-Vidicon camera tube, which is a promising alternate for use in the Slit Jaw Camera.

#### 6.2 PERFORMANCE CRITERIA USED IN SENSOR SELECTION

The LST instrumentation requires a number of sensors for conversion of their photon images into electric signals. Each

TABLE 6-1. LST-SIP SEC-VIDICON SENSOR REQUIREMENTS

<u>Instrument</u>	<u>Format (mm)</u>	<u>Type</u>	<u>Window</u>	<u>Cathode</u>	<u>Operating Temp K</u>
1. f/96 Camera Range I	50 x 50	A	MgF <sub>2</sub>	CsTe	293
2. f/96 Camera Range II	50 x 50	B	Fused Silica	S-20	293
3. f/96 Camera Range III	50 x 50	C	Glass	III-V	250*
4. f/12 Camera	50 x 50	B	Fused Silica	S-20	293
5. Faint Object Spectrograph 1	25 x 25	D	MgF <sub>2</sub>	Bialkali	293
6. Faint Object Spectrograph 2	25 x 25	E	Fused Silica	S-20	293
7. Faint Object Spectrograph 3	25 x 25	F	Glass	III-V	250*
8. High Resolution Spectrograph 1	25 x 25	D	MgF <sub>2</sub>	Bialkali	293
9. High Resolution Spectrograph 2	25 x 25	G	Fused Silica	Bialkali	293
10. Slit-Jaw Camera	25 x 25	D	MgF <sub>2</sub>	Bialkali	293

\*III-V on NEA substrate - Operating temperature prediction is based on reflective mode of operation.



instrument has somewhat different requirements, and the matching of the detector to the instrument or optimization of both for the best possible resolution, S/N and high data collecting efficiency is the primary objective. This dictates a sensor with high resolution in conjunction with a high quantum efficiency, a high data capacity and long term data storage prior to a single readout. Although these performance criteria parameters are expressed qualitatively, the general category of sensors, developed for television cameras, clearly rates primary consideration. Although single element detectors such as photo-multipliers or solid state detectors would undoubtedly be useful for special problems, the discussion here is confined to multi-element recording camera tubes operating in a single readout mode. These tubes can much more effectively utilize the total incoming optical information resulting in a tremendous increase in data throughput.

Resolution and data capacity alone are not the only factors considered in sensor selection. Among other criteria taken into account are the following:

1. Long integration time prior to a single readout
2. High internal gain
3. High resolution
4. Low noise contribution
5. Large format size
6. Spectral selectivity
7. Development timing for LST
8. Compatibility with space application:
  - a) vibration
  - b) shock
  - c) acceleration
  - d) thermal vacuum
  - e) radiation
  - f) electrostatic/magnetic shielding

- g) cooling
- h) size
- i) weight
- j) power consumption/dissipation

### 6.3 CAMERA TUBE DISCUSSION

In the LST application, the camera tube is used as a sensor for long term single exposure, a technology which is an analogy to the film used for long exposures in ground based observatories. The camera has a number of advantages over the film, as well as some disadvantages.

The advantages are: higher quantum efficiencies, wider spectral coverage, direct signal processing into electronic data, i.e., no chemistry (development) and microdensitometry, no bulk storage, no vacuum problems, like in the Schumann emulsion for UV.

The disadvantages are: lower resolution, smaller format, susceptibility to target breakdown.

#### 6.3.1 Single Exposure Mode

In a standard television camera, a high readout rate (30 frames per second) is dictated by the human eye response time in order to preserve motion continuity perception, despite its incremental inputs. To meet this frame rate, a maximum time constant (lag) is set for TV useable target materials.

On the other hand, the SIP instrumentation requires seconds, minutes or even hours of integration time during a single frame, i.e., prior to the readout scan. This requirement is dictated by the irradiance levels, which, in the SIP are expected to be many orders of magnitude below the customary TV studio lighting.

### 6.3.2 Camera Tubes Comparison

#### a. The Vidicon Tube

The Vidicon Tube is the smallest TV camera type with diameters of 15 and 25 mm available. A semi-conductive target stores (+) charges in irradiated spots. Storage time is from a fraction to tens of seconds. The information is read off the target when the scanning beam passes the exposed areas and replenishes the missing charges.

This tube requires a very high light input level and, due to its low gain, exhibits a relatively high noise due to the pre-amplifier.

A silicon diode matrix target was lately introduced for the portable TV camera, as a replacement for the standard vidicon. It provides burn-out resistance at high signal levels and reduces the image growth as a function of light input level.

#### b. The Image Orthicon

The Image Orthicon is the workhorse of the television studio. Due to its image section gain and target secondary electron emission gain, the readout beam noise contribution is largely reduced as compared to the Vidicon. In addition, an electron multiplier amplifies the signal carrying return beam which makes the preamplifier noise effectively negligible. However, the signal carrying reflected return beam is highest at the lowest signal level. This is not too objectionable in a TV studio which uses high illuminance levels, however, is unacceptable for the SIP, where extremely low irradiances have to be sensed, particularly in the spectrograph, where each resolution element intercepts only an extremely narrow spectral bandwidth.

#### c. The Return Beam Vidicon

The Return Beam Vidicon has the most sophisticated electron optics and hence is the highest resolution camera tube ever

made. However, using the reflective return beam, this tube suffers from the high beam noise at low signal levels as the image orthicon, as a matter of fact even more so, since its ASOS target has a gain of one as compared to 15 for the  $MgO$  target used in the I.O. At high irradiance levels, such as encountered in viewing the earth from space, this tube offers the advantage of its high resolution (ERTS).

d. The Image Isocon

The Image Isocon uses the scattered rather than the reflected return beam. This beam has a reduced unmodulated component, hence provides some improvement in noise at the low irradiance levels, as compared to the I.O. and RBV. Its electron optics are improved over the I.O., however not as good as the RBV.

e. Secondary Electron Conduction Vidicon (SEC)

The SEC uses an emissive photocathode and an image section similar to the IO tube. The accelerated electrons impinge upon a potassium chloride (KCl) target which provides both high gain (100) and long term storage capability of charges, required for the single exposure mode of operation. In addition, the signal output is obtained directly from the target which secures the minimum noise at low signal levels, compared to all previously described camera tubes. The vidicon type electron beam readout scan provides a reasonably good resolution of 40 lp/mm at 3% MTF or 20 lp/mm at 50% MTF, using an all magnetic focus and deflection. This performance has qualified the SEC as the best camera tube.

#### 6.4 WINDOW AND PHOTOCATHODE COMBINATIONS

The SIP includes field cameras and spectrographs for which the ultimate goal is an extension in faint object detectivity and in spectral coverage compared to ground astronomy instrument capabilities. For reasonable signal-to-noise ratios in an ambient space background level (one +23 Mag. star in a solid angle of

$\Omega = 25$  psr typical in space<sup>(1)</sup>, data integration time of up to 10 hours is desirable, in the limiting case, assuming a SEC target with internal gain of 50 to 100. Decrease of integration time or improvement of the S/N ratio may be achieved by means of a target with higher internal gain which reduces the preamplifier noise effect. Use of solar-blind photocathodes in the far-UV range reduces both the background noise and the photocathode dark-noise contributions. Tube spectral bandwidth requirements are accommodated by appropriate combinations of detector/window materials and photocathodes. Generally, the window determines the lower wavelength cutoff and the photocathode the upper cutoff. For additional spectral selectivity of the camera, narrow band filters may be used.

The following paragraphs contain a listing and comparison of the candidate sensor front ends, i.e., the windows and semi-transparent photo emissive cathodes on their inner surface. Initially, a qualitative relative comparison of the front end candidates is made, while the actual selection, usually from the two best candidates, is made in Section 4 as part of each instrument signal-to-noise analysis.

#### 6.4.1 Window Materials

The window material is a significant factor in the signal throughput at wavelengths less than 400 nm. For the visible or near IR, any of the glass materials used in conventional camera tube envelopes is acceptable. The candidate UV transmitting materials and their relative properties are summarized as follows:

- a) Magnesium Fluoride ( $MgF_2$ ):  $\lambda_{cut-off} = 115$  nm. A hard material which can be processed into an excellent optical surface. It is water insoluble with low radiation susceptibility<sup>(2)</sup>

---

(1)"Scientific Uses of the Large Space Telescope", Ad Hoc Committee on Large Space Telescope, Space Science Board, NAS (1969).

(2)Heath, D.F., Sacher, P.A., "Effects of a Simulated High-Energy Space Environment on the UV Transmittance of Optical Materials between 105 nm and 300 nm, Applied Optics, V, 6, June 1966".

- b) Lithium Fluoride (LiF):  $\lambda_{\text{cut-off}} = 105 \text{ nm}$ . A relatively soft material which yields a relatively poor optical surface. It is adversely affected by water vapor and scintillates at low levels of particle radiation<sup>(2)(3)</sup>.
- c) Fused Silica ( $\text{SiO}_2$ ):  $\lambda_{\text{cut-off}} = 165 \text{ nm}$ . An extremely rugged material with excellent mechanical and optical surface qualities. It is water insoluble and resistant to radiation<sup>(2)</sup>.
- d) Sapphire ( $\text{Al}_2\text{O}_3$ ):  $\lambda_{\text{cut-off}} = 145 \text{ nm}$ . Mechanical and optical surface properties are good. At wavelengths greater than 200 nm, its transmission is less than fused silica. Further, it is highly susceptible to radiation<sup>(2)</sup>.

From the above candidates, Magnesium Fluoride is the selected window material for the far UV and Fused Silica is chosen for the near UV ( $\lambda > 170 \text{ nm}$ ). Where wide UV response is required in one material, magnesium fluoride is chosen.

#### 6.4.2 Photocathodes

The required photocathode materials can be divided into three classes determined by the desired spectral coverage: (1) UV only, (2) wide spectral response, and (3) near IR. The required design data, quantum efficiency and dark current, are shown here to support the sensor selection analyses in Section 4.

(1) UV only ( $\lambda < 300 \text{ nm}$ ) - This spectral region is a natural application for the "solar blind" materials. They are non-responsive in the visible range, resulting in low dark and background noises. Candidate "solar blind" materials are Cesium Iodide (CsI) and Cesium Telluride (CsTe). The overall spectral responses of these solar blind cathode materials, deposited on negative electron affinity substrates and  $\text{MgF}_2$  windows, are shown in Figure 6-1. This window cuts off at 115 nm. The other two curves in this

---

(3) Performance Evaluation of the Telescope Experiment, Smithsonian Institution (7, 1971).

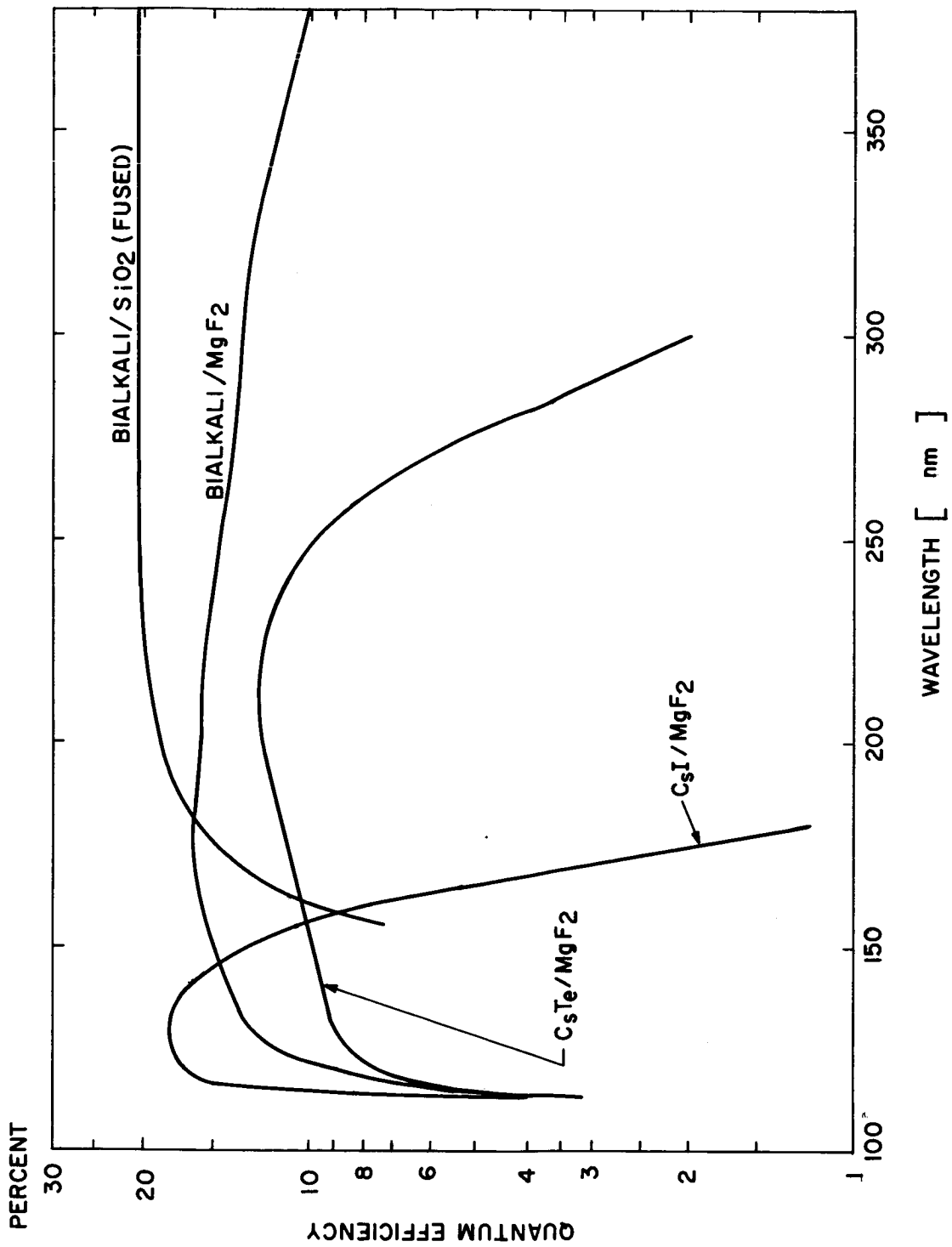


Figure 6-1. Spectral Responses, Photocathode Window in the UV

figure, given for comparison, represent spectral responses of a Bialkali photocathode in combination with two window types. This photocathode, however, better qualifies in the following type.

(2) Wide Spectral Response, near UV and Visible - The candidate wide spectral response photocathodes in this spectral range are:

- Bialkali
- Trialkali (S-20)
- ERMA III (extended red multialkali)

The spectral responses of these materials with candidate windows are shown in Figure 6-2. In general, these materials show greater dark current than the "solar blind" materials. The effect of temperature on dark current for all candidate photocathode materials is shown in Figure 6-3. Despite the increase of dark current and noise, operation up to 300K appears possible from the point of view of photocathode noise, for most cases, as shown in Section 4, S/N Analyses.

(3) Near Infrared Range (up to 1.1 micrometer) - The cesiated III-V photocathodes using negative electron affinity (NEA) substrates for improved quantum efficiency are still in the developmental stage<sup>(4)</sup>. At present, the only known results with these photocathodes are obtained in a reflective mode of operation<sup>(5)(6)(7)</sup>.

---

(4)W. Martinelli, RCA: Private Communication.

(5)Williams, B.F., and Tietjen, J.J., "Current Status of Negative Electron Affinity Devices" Proc. IEEE 59, p. 1489, (1971).

(6)Savoye, E.D., Williams, B.F. and Hughes, F.R., "Near-Infrared and Low-Light-Level Imaging Using Negative Electron Affinity Photocathodes", E-O Design Conference, Geneva, Switzerland (1972).

(7)Woodall, J.M. and Hovel, H.J., "High Efficiency  $Ga_{1-x}Al_xAsGaAs$  Solar Cells" Applied Physics Lett. 21.8 (1972)



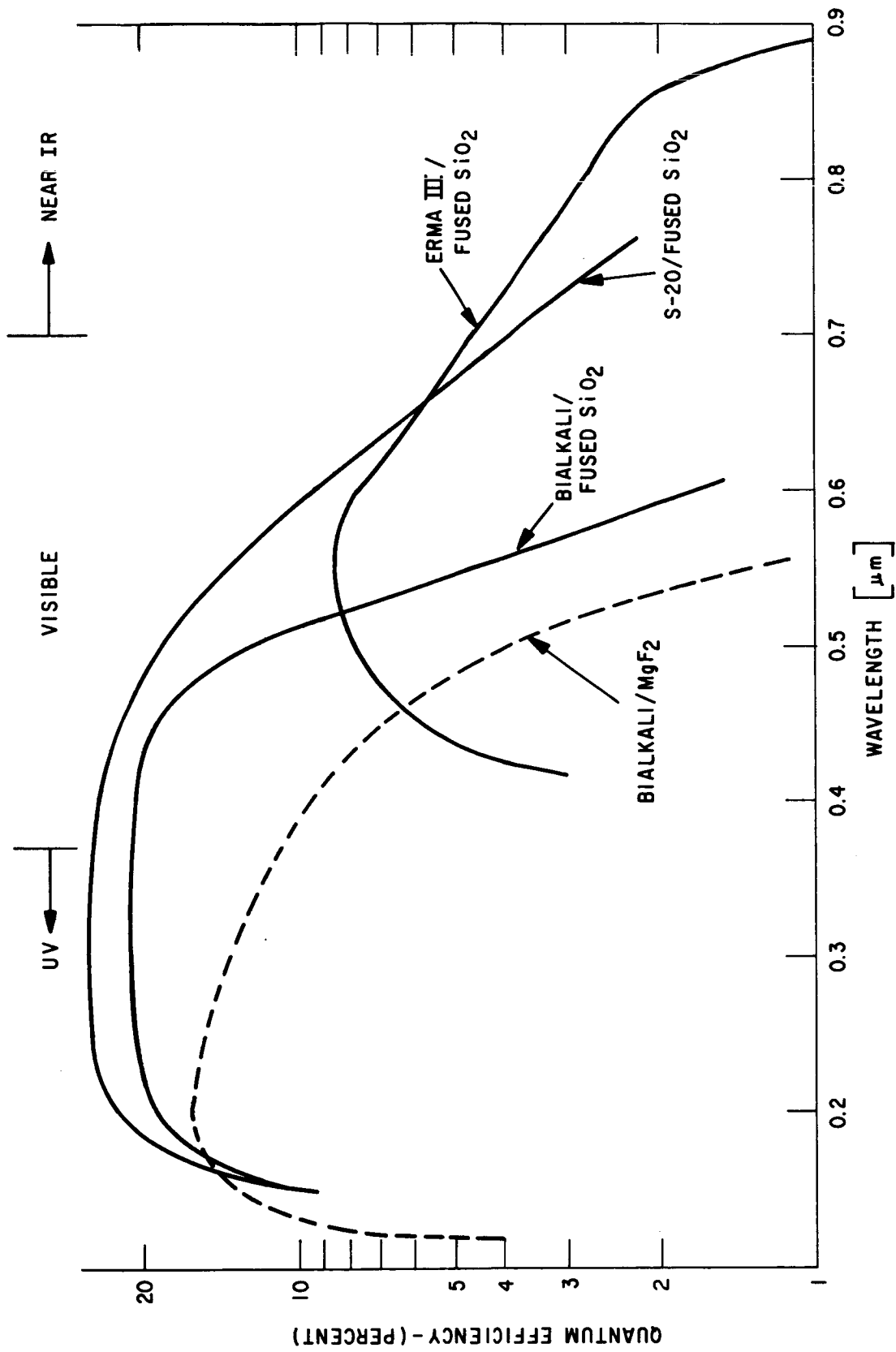


Figure 6-2. Spectral Responses, Photocathode Window in the Visible and UV

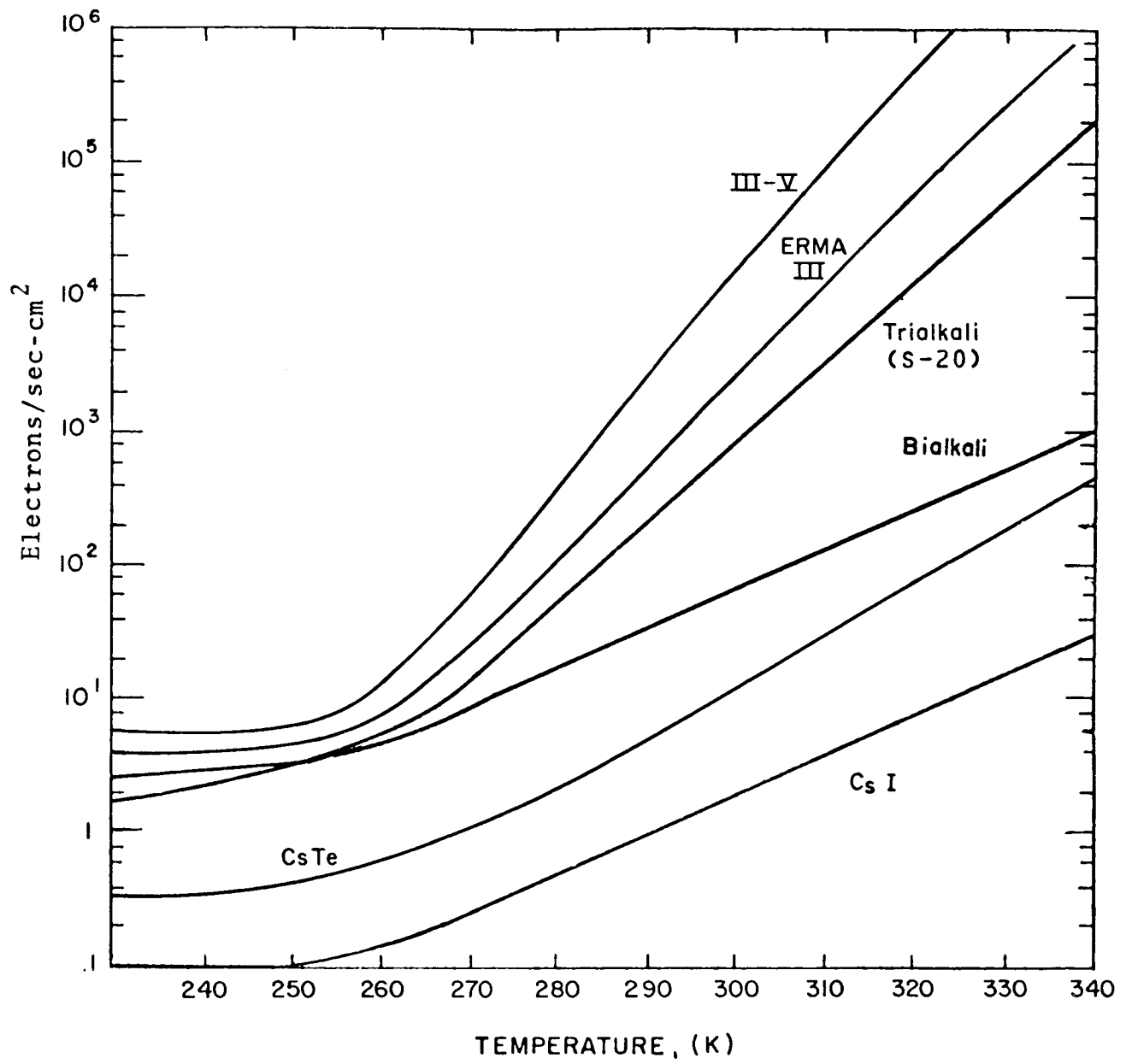


Figure 6-3. Photocathode Dark Current Vs. Temperature

The spectral responses of three different reflective III-V compounds are shown in Figure 6-4. The one with the highest response at 1.1  $\mu\text{m}$  is used for S/N analyses in Section 4.

Semi-transparent photocathodes are required by the camera tube, which at present time do not exist in the III-V material types. The semi-transparent S-1 photocathode has quantum efficiencies less than 0.1% at 1.0  $\mu\text{m}$  and less than 0.5% at 0.8  $\mu\text{m}$ , values much below any photocathode previously evaluated for the UV or visible ranges. However, development work on semi-transparent III-V photocathodes is in progress<sup>(4)</sup> and, with an additional SR & T support, reasonable results are expected from these NEA photocathodes - certainly better than obtainable with the S-1 or ERMA III.

Experience to date with reflective III-V materials with NEA substrate indicates instability at temperatures above 260K<sup>(4)</sup>. As part of the SR & T effort, operation at a cathode temperature of 300K should be a developmental goal since SIP sensors employing this material are the only ones which must be maintained below room temperature to achieve predicted performance. The optimal reflective NEA III-V photocathode is  $\text{InAs}_{0.25}\text{P}_{0.75}:\text{CsO}$  for which  $\text{QE} = 1\%$  at  $\lambda = 1.1 \mu\text{m}$  and  $\text{QE} = 10\%$  at  $\lambda = 0.6 \mu\text{m}$  were obtained.

In case this semi-transparent NEA III-V development does not provide acceptable results in the LST time schedule, an alternate photocathode, the multialkali type ERMA III will be used, rendering a quantum efficiency of only 0.1% at a wavelength of 0.92  $\mu\text{m}$  and causing the loss of operating range above this wavelength.

#### 6.4.3 Final Selections

Based on the S/N analyses performed for the individual SIP instruments and their individual optical configurations, all performed in Section 4, the SEC Vidicon Sensor characteristics listed in Table 6-1 are established. A total of seven photocathode/window/Format size combinations are used. It is obvious that

---

(4) *ibid.*

(1) (2) REF: H. SONNENBERG - APPL. PHYS. LETTERS 19, 431 (NOV. 3, 71)

(3) D. G. FISHER, RCA, D. SARNOFF RES. LAB.  
PRINCETON, DATA FOR REFLECTIVE PHOTOCATHODES

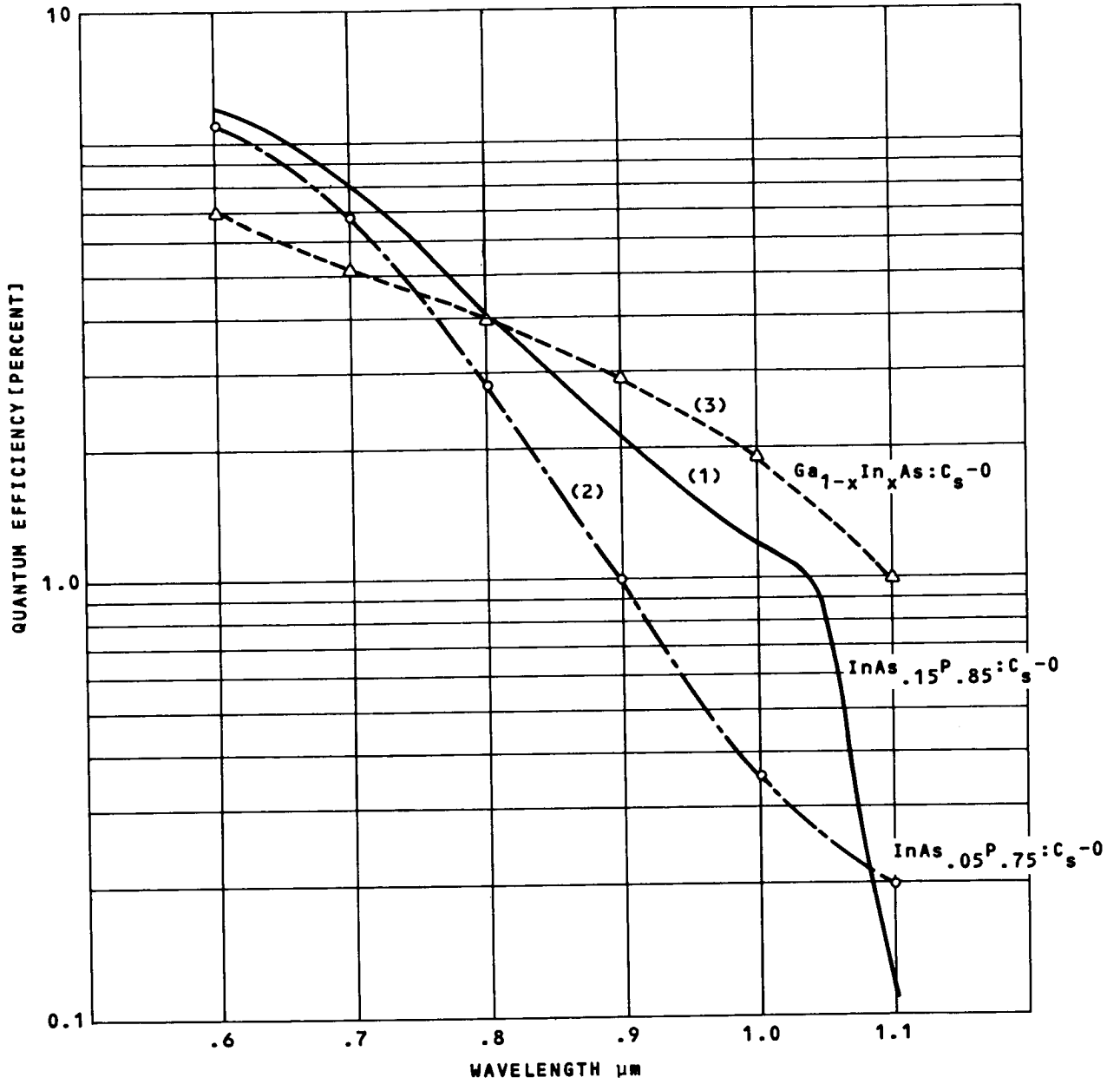


Figure 6-4. Spectral Responses, Reflective III-V Photocathodes  
6-14

reduction of the required tube assembly types will simplify procurement, manufacturing, testing and spares inventory.

## 6.5 TARGET MATERIAL

The camera tube target material determines the internal tube gain and target capacity. Increasing tube gain, which is comparatively noise free, reduces the effect of noise in succeeding amplifiers. An increase in target capacity permits the collection of a greater number of photoelectrons from the cathode without saturation. By increasing the number of electrons collected before saturation, improvements in signal-to-noise, dynamic range and/or integration time are possible.

Table 6-2 lists several properties of the candidate targets. From the preceding qualitative discussion, Table 6-2 shows potassium chloride (KCl) to be the most desirable target material at this time, and it is used in the signal-to-noise analyses of other sections. It can collect a cathode current density of 1.0 electron per  $\mu\text{m}^2$  before saturation.

The silicon diode target is potentially superior to KCl. In addition to higher gain, the resolution (MTF) of the silicon target is about twice that of KCl. However, to use this otherwise best target, intensive active cooling and on-board data storage are required. Neither of these requirements are feasible at this time. The long lag time Ebic type material may, however, be developed to a prime candidate, and its progress will be monitored.

## 6.6 ELECTRON-OPTICS

The resolution of the camera tube is a function of the sophistication placed on the image section electro-optics design and the scanning beam size. In the image section a parallel focus field is required between the photocathode and the target. The latter is placed at a single helix (electron-trajectory) distance from the cathode. Extensive work has been performed on electron-optics and beam improvements<sup>(8)</sup>. The best results to date are

---

(8)Schade, O.H., Jr.: "Electron Optics and Signal Readout of High Definition Return Beam Vidicon", RCA Rev. March 1970.

TABLE 6-2. CANDIDATE CAMERA TUBE TARGETS

<u>TYPE</u>	<u>GAIN</u>	<u>INTEGRATION TIME</u>	<u>OPERATING TEMP (K)</u>	<u>LIFE YEARS</u>	<u>CURRENT USAGE</u>	<u>REQUIRED DEVELOPMENT</u>
ASOS (Sb <sub>2</sub> S <sub>3</sub> OS)	1	0.5 hr.	225 - 300	1-2	RBV	-
KCl	50-100	over 10 hrs.	225 - 300	2-3	SEC-VID	-
Ebic (ZnS, SiO <sub>2</sub> )	200-400	TBD	TBD	TBD	CRT Storage	For SEC-VID
Silicon Diode Array	1000-2000	*	*	10	SIT, EBS	LARGE FORMAT

\*Target saturation due to leakage current. This leakage current, however, is a function of temperature. For long term integration, 4-5 hours, cooling down to 200-220K is required. Only minutes of integration time are possible at room temperature.

50% contrast at 40-50 lp/mm (on a 50 x 50 mm format ASOS target) achieved using sectional electromagnetic focus coils trimmed along the image section and over-extending the cathode and target by approximately 3cm. Application of the Schade electron optics design to the SEC tube should be attempted with partial substitution of a permanent magnet for the electromagnet for the power dissipation and generated heat reduction. This is a major effort and will require SR & T work with the large format higher gain target development. The summary of the large format (50 x 50 mm) SEC tube requirements is listed in Table 6-3.

## 6.7 MAGNETIC EFFECTS

The presently envisioned SEC Vidicon camera tube<sup>(9)</sup> uses magnetic focus in its image section with a flux density of 8 mT (80 gauss).

Experimental observations of dim celestial targets require long term data integration periods extending over a number of orbits. The earth's magnetic flux density varies approximately sinusoidally over an orbit. Its influence on the camera tube sensors is significant considering that, in an orbit with 0.5 rad inclination, the sinusoidal peak amplitude of flux density is between 23 and 35  $\mu$ T and can reach a peak of 42  $\mu$ T in an orbit with 0.9 rad inclination. The magnetic field change produces a deteriorating effect on the integrated image quality (Schade) similar to that caused by pointing instability, shown in Section 3.

In addition to the external magnetic field, internal electric and magnetic spacecraft fields will interact with the powered camera tube fields unless sufficient shielding is provided. This

---

(9)Lowrance, J. and Zucchini, P., "Development of Television Tubes for the Large Space Telescope", Princeton University Report to the LST Steering Group, September 25, 1971.

TABLE 6-3. SIP LARGE CAMERA TUBE,  
PRELIMINARY DEVELOPMENT SPECIFICATIONS

CONFIGURATION:	SEC-Vidicon. All magnetic focus and deflection with low focus power. Target material TBD based on technology in 1975.
TECHNICAL PROPERTIES:	
1. Format	50 x 50 mm; flat surface
2. Wavelengths <sup>(1)</sup> , Photocathodes and Windows	A) 115-300 nm with CsTe Photocathode, MgF <sub>2</sub> Window B) 115-600 nm with Bialkali Photocathode, MgF <sub>2</sub> Window C) 500-1,000 nm (III-V) Photocathode <sup>(2)</sup> TBD, Glass Window D) 160-600 nm with Bialkali Photocathode, Fused Silica Window
3. Quantum Efficiencies	See Figures 6-1, 6-2, and 6-4
4. Resolution	Applicable sections of Reference <sup>(9)</sup> ; in general, for k in line pairs/mm, MTF = exp <sup>-</sup> (0.039k) <sup>1.5</sup>
5. Integration	3.6 x 10 <sup>4</sup> s (10 hours) maximum
6. Readout	60s
7. Erase Cycle	160s maximum
8. Target	Ebic Type (Table 6.4-1) desirable. KCl accepted as preliminary. Silicon as a goal.
9. Temperatures <sup>(3)</sup>	A) Target 210K (for Silicon target) B) Photocathode 293K except less than 260k for type C
10. Max. Dark Current	Per Figure 6-3
11. Weight <sup>(4)</sup>	68 kg (tube, magnetics and local electronics)



TABLE 6-3. SIP LARGE CAMERA TUBE (Cont.)

12. Warm-up	3 minutes	
13. Power <sup>(5)</sup>	<u>Warmup Integration</u>	<u>Readout</u>
Image Section Focus & Bleeder	26 Watt	0 <sup>(5)</sup> Watt
Readout Focus	0	20
Deflection Coils	0	5
Filament	1	3
Circuits at Camera	<u>5</u>	<u>5</u>
	32 Watt	33 Watt
$\bar{P}^{(6)} = 32$ Watt	$P_{\max} = 40$ Watt	$P_{\min}^{(7)} = 1.0$ Watt
14. Replacement	Includes tube, coils and adjacent electronics as a unit, or electronics only.	

FOOTNOTES:

- (1) Four tube types required for this format.
- (2) III-V material on negative affinity substrate, stabilizes at or below 260K.
- (3) Maximum temperature of tube envelope
- (4) Exclusive of 9.0kg remote control box handling all cameras.
- (5) Exclusive of active cooling system and 15 watt remote control box handling all cameras.
- (6) In rare cases the average power could go to  $\bar{P} = 35$  watt for 40 minutes, then return to 32 watt for a minimum time of 55 minutes.
- (7) If a tube is not to be used for next 24 hours, it could be turned off except for the residual filament and switching electronics.

shielding naturally works both ways by also providing the required EMI shielding of other on-board equipment from the camera generated fields.

An in-depth analysis of the possibilities of local field cancellations between active and standby camera tube and other equipment, based on a detailed SIP layout and residual field levels is a recommended task for future study. However, a first cut review of the on-board magnetic fields<sup>(10)</sup>, shows the MSFC design of the Control Moment Gyro (CMG) desaturation to be much more desirable from the point of view of interaction with the SIP camera tubes than the Martin Marietta Corp. (MMC) design. The MSFC design which places the electromagnets toward the front of the spacecraft (specifically on the telescope sun shield), produces a residual flux density in the vicinity of the camera tubes of one  $\mu\text{T}$  as shown in Figure 6-5. The MMC configuration - with magnets in the SSM - produces a residual flux density of 20 mT, also shown in above figure.

The above mentioned study should consider single and double shields in conjunction with the detailed camera tube assembly design to ensure tolerable image motion during target integration time.

## 6.8 SPACE RADIATION

Tests performed within the Princeton AVF Cyclotron indicate that if the photocathode is turned off during the South Atlantic anomaly portion of the orbit a substantial reduction in the background can be achieved. The conclusions of these tests stated that there should be no problem with storing an image during the pass through the anomaly.

---

(10) Vaage, R., Swain, D. and Williams, R., "Environmental Constraints", Martin Marietta Corp. Report to the Itek Corp. (MMC-LST-T), March 1972.

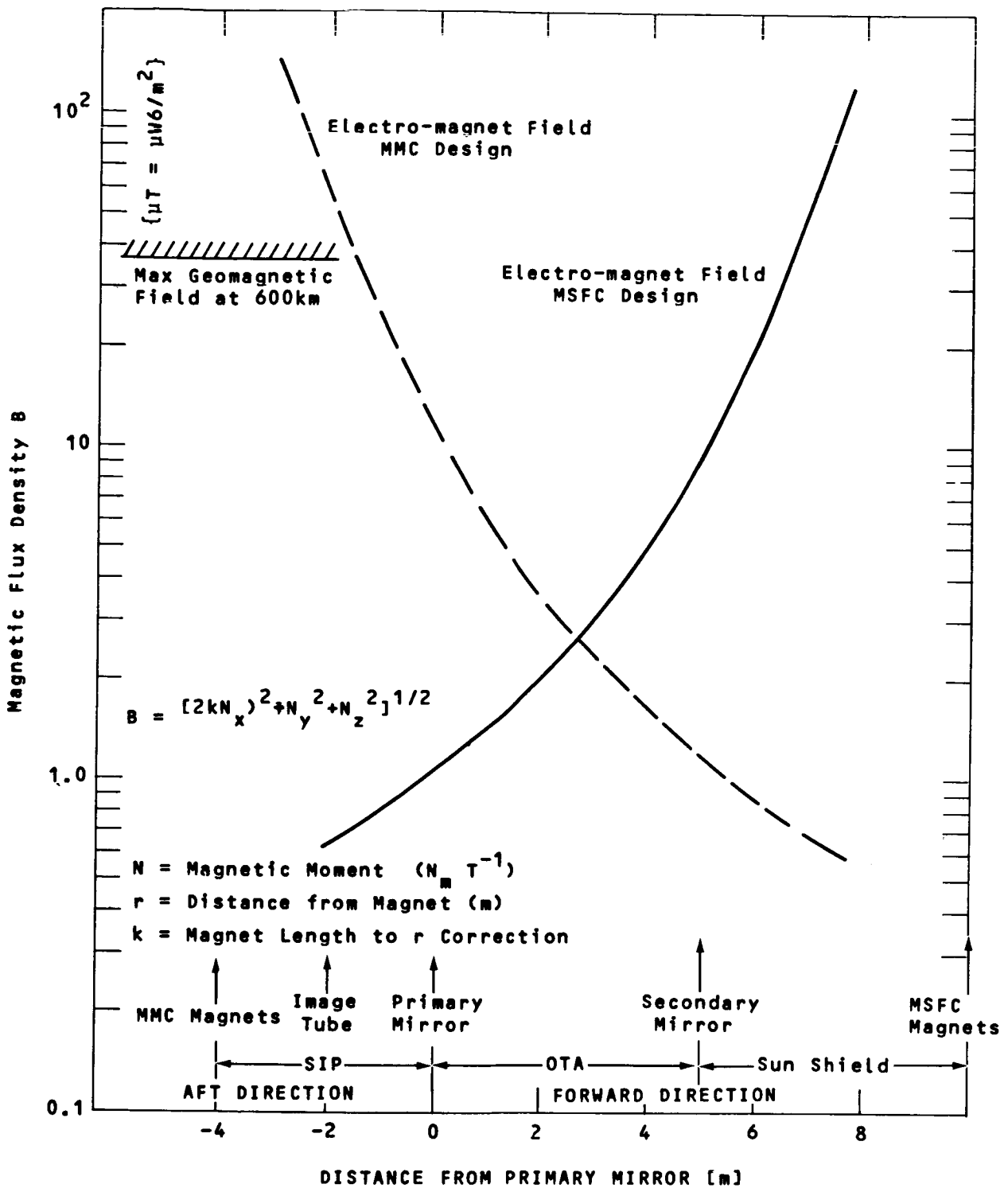


Figure 6-5. Magnetic Fields for Two LST Desaturation Magnet Designs

## 6.9 PACKAGING CONSIDERATIONS

Table 6-1 lists the reference image tube complement for the SIP instruments. Two SEC vidicon tube sizes are used in the reference design: 50 x 50 and 25 x 25 mm. Figure 6-6 shows the dimensions and physical parameters of assemblies of the two tube sizes. Each assembly consists of two major subassemblies, (1) the tube and scan subassembly and (2) the electronics subassembly.

The baseline tube and scan subassembly consists of: (1) the SEC vidicon tube, (2) the image section focus coil, (3) the readout focus and deflection coils, (4) an accelerating potential resistive divider, (5) the preamplifier, (6) Peltier coolers and (7) erase lamps. Two sizes of scan assembly are used corresponding to the 25 and 50 mm photocathode.

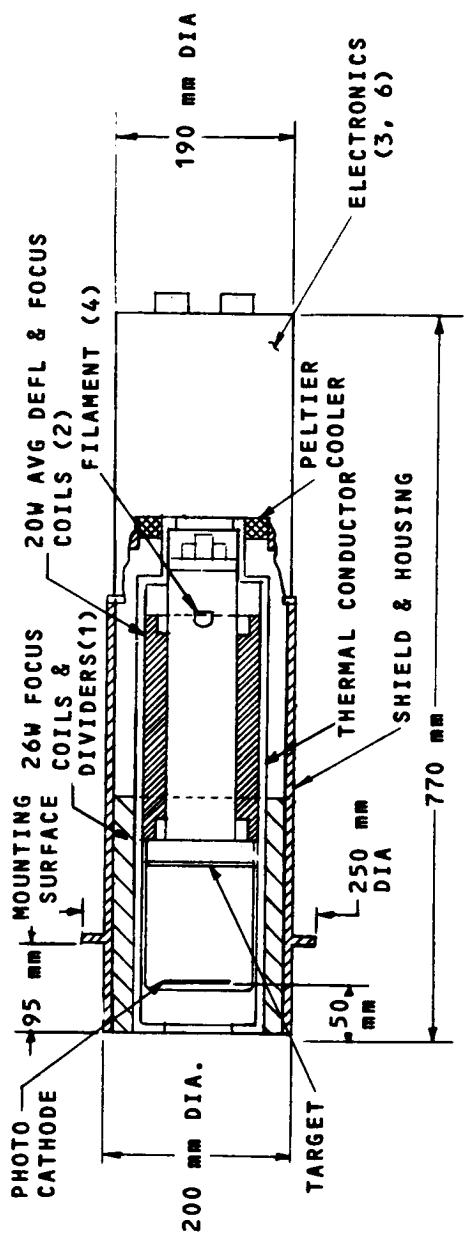
The baseline electronics subassembly is essentially the same for both cathode formats. It contains the remaining electronic components located in close proximity to the tube itself and is discussed in Section 5.4.3.

## 6.10 SIT - VIDICON CAMERA TUBE

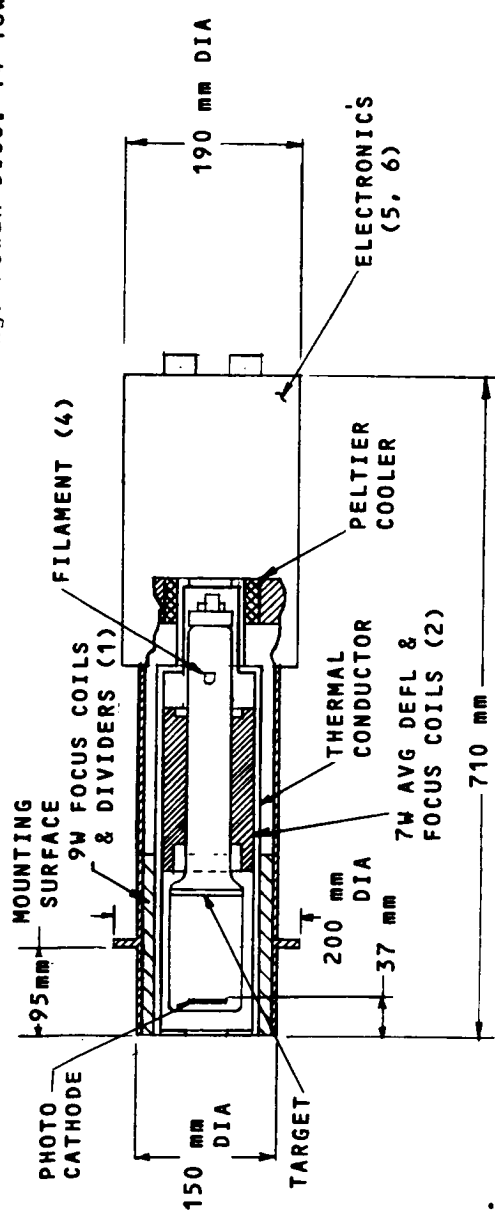
The Slit Jaw Camera, described in Section 5, could use as an alternate to the reference SEC sensor, a SIT camera tube. Application of this sensor is possible in the Slit Jaw Camera, since it operates on spectrograph targets, which are on the average 8-10 magnitudes brighter than the camera targets (approximate factor of  $10^3$  to  $10^4$ ) and, unlike the spectrographs, operate on a wide band spectrum (200-300 nm). As a consequence, only short integration times in order of seconds are required, making the leakage current contribution to noise negligible.

The SIT also consists of an image and a read section. Electrostatic, rather than magnetic focusing is used in the image section, which dictates a spherical photocathode, and a fiber optics faceplate in order to provide the conversion between the flat image plane and

A. PHOTO-CATHODE 50X50 mm, WEIGHT - 68kg, POWER DISS. 32-33W, VOL. 22.5 (dm)<sup>3</sup>



B. PHOTO-CATHODE 25X25 mm, WEIGHT 28kg, POWER DISS. 14-18W, VOL. 15 (dm)<sup>3</sup>



NOTES:

- (1) DURING DATA INTEGRATION
- (2) DURING READOUT ONLY
- (3) 5W TOTAL FOR ELECTRONICS AND P.S.
- (4) 1W FOR STANDBY & DATA INTEGRATION, 3W DURING READOUT
- (5) 4W
- (6) FOR DETAIL SEE SECT. 5.4.3.

Figure 6-6. SEC-Vidicon, Physical Parameters



## 6.11 ADDITIONAL WORK ON THE SEC-VIDICON

Advancement of the SEC by means of higher gain targets is expected to be possible by means of longer lag (Ebic) targets, since the LST mode of operation does not require rapid readouts. In addition, an increase of target capacity for extension of dynamic range prior to sensor saturation will be pursued in phase B of this study. Additional effort will be placed on solving the sensor and preamplifier cooling (see Section 7) for further improvement of dynamic range, preamplifier noise reduction, and ultimately much higher resolution. The applicable sensor is the SIT- or EBS-Vidicon, both being trade names for the same tube with an image and scan section identical to the SEC and a silicon diode mosaic target. The present problem pertains to noise due to silicon diode leakage currents, which double for every 8-10K temperature increase. For long term integration, this target would require cooling down to 210K. The reference SIP instruments call for two SEC sensor formats, as shown in Table 6-1. While the smaller format was flown in the Stratoscope III<sup>(9)</sup>, the OAO-A (Uvicon)<sup>(3)</sup>, OSO-H (White Light Spectrometer) and in a number of rockets, the larger format (50 x 50 mm) was not packaged into a space configuration<sup>(11)</sup>. This will not only require the design but, what is more involved, tests under all simulated exposures in order to make better predictions on reliability and service requirements.

The test results of a laboratory model of the large format SEC tube indicate a resolution comparable with the smaller version. Future work on resolution improvement by adaptation of the RBV electron optics<sup>(8)</sup> and a possible hybrid of a permanent magnet and electro-magnet combination is expected to provide higher resolution and lower power dissipation, thus enabling the target cooling to lower temperatures and with that the ultimate in target gain and resolution, i.e., a silicon diode mosaic-target.

---

(3) *ibid*

(8) *ibid*

(9) *ibid*

(11) J. Lowrance, Princeton University: Private Communication.

## Section 7

### ENVIRONMENTAL CONSIDERATIONS OF THE SCIENTIFIC INSTRUMENTS DESIGN

#### 7.1 INTRODUCTION

The following paragraphs describe the environmental conditions under which the SIP instruments must operate. The impact of each environment on the design, precautions that should be considered during more detailed design efforts, and areas needing additional effort are discussed. In addition, initial design and analysis calculations are presented.

#### 7.2 THERMAL CONSIDERATIONS

Thermal studies of several representative instruments associated with the Scientific Instrument Package (SIP) were conducted to determine steady-state temperature profiles of major components. Listings of the computer outputs of nodes and temperatures are included here to illustrate the method of analysis and the type of temperature results.

Three thermal models and their division into temperature nodes were used to determine the thermal behavior of the following instruments.

- a. Faint Object Spectrograph - 20 nodes
- b. High Resolution Camera Optics - 22 nodes
- c. High Resolution Spectrograph - 18 nodes

Heat transfer terms between nodes were calculated and used as input to a digital computer program adapted specifically to these problems.



The results are subsequently compared to temperature differences which are acceptable based on specific allowable changes in the optical structures. The latter differences fall into two limit classes: limits on temperature ranges based on focus and alignment tolerances, and limits on changes during observations based on permissible variations resulting in smearing.

### 7.2.1 Conditions of Investigation

The temperature distributions within the instruments were calculated for the environment and conditions, developed in Sections 8.4.2 and 7.2.9, as described below:

- a. Faint Object Spectrograph (Figure 7-1)
  1. photocathode (node 16): 264 K
  2. camera conduction cooling sleeve (node 17): 262 K
  3. camera mounting flange (node 18): 311 K
  4. radiator, camera focus coils (node 19): 311 K
  5. mounting structure and inner S/C wall (node 20): 294 K
- b. High Resolution Camera Optics, f/96 (Figure 7-2)
  1. photocathode (node 17): 265 K
  2. camera conduction cooling sleeve (node 18): 262 K
  3. camera mounting flange (node 19): 341 K
  4. radiator, camera focus coils (node 20): 332.7 K, avg.
  5. Fine Guidance Assembly (node 21): 294 K
  6. mounting structure and inner S/C wall (node 22): 294 K
- c. High Resolution Spectrograph (Figure 7-3)
  1. photocathode (node 14): 264 K
  2. camera conduction cooling sleeve (node 15): 262 K
  3. camera mounting flange (node 16): 311 K
  4. radiator, camera focus coils (node 17): 311 K
  5. mounting structure and inner S/C wall (node 18): 294 K

Two analyses were conducted for the f/96 Camera Optics, Case-1 for an aluminum housing and Case-2 for a graphite-epoxy housing.

The camera component temperatures listed above were taken from the results of the camera steady-state analyses. Since these cameras are mounted to the optical housings, their component temperatures comprise thermal inputs by conduction and radiation. Conduction is limited by thermal insulators between the camera mounting flange and the housing.

### 7.2.2 Description of the Thermal Models

The thermal models of the three instruments are shown in Figures 7-1, 7-2 and 7-3, which follow. In order to compute the temperature distributions within each unit, it was divided into temperature nodes, as indicated, to form the mathematical model of the system. Heat transfer terms by conduction and radiation, as each applies, were derived for connected nodes. The node designations assigned to each thermal model are defined in Tables 7-1, 7-2 and 7-3 for the Faint Object Spectrograph, f/96 Camera and High Resolution Spectrograph, respectively.

### 7.2.3 Input Power

There is no electrical power dissipation associated with the nodes of the three optical systems.

### 7.2.4 Method of Analysis

An exact thermal analysis of the optical instruments involves solution of nonlinear integro-differential equations of extreme complexity. A closed-form solution for any complex structure treated as a continuous system is impractical, if not impossible. Mathematical simplification results when a continuous system is replaced by a series of discrete elements that are coupled thermally. These elements, or nodes, are treated as having constant temperatures for small incremental time periods but as having a temperature different from that of the adjacent nodes. This numerical method of approach lends itself to the employment of a computer to solve the heat transfer problem.

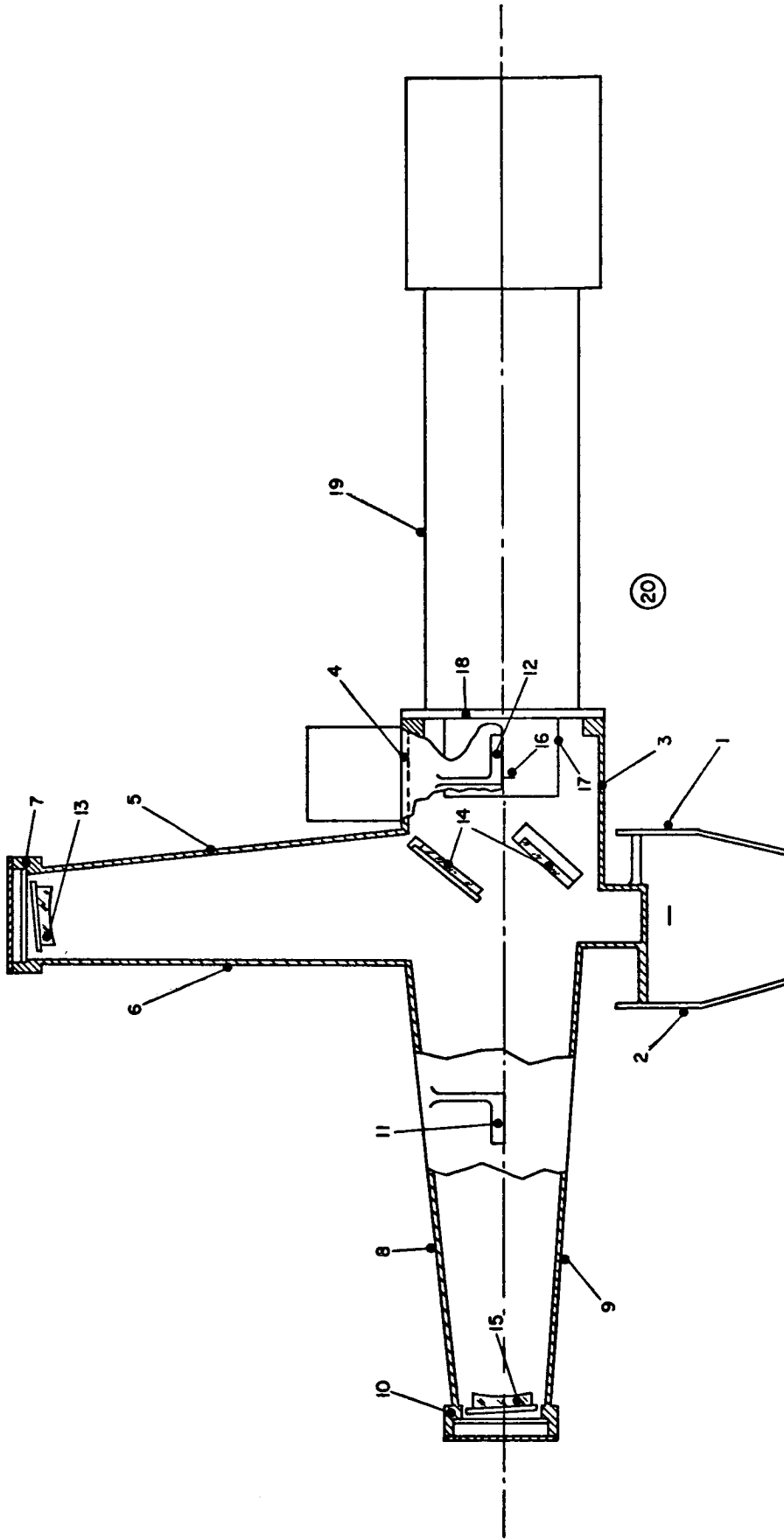


Figure 7-1. Faint Object Spectrograph, Thermal Model

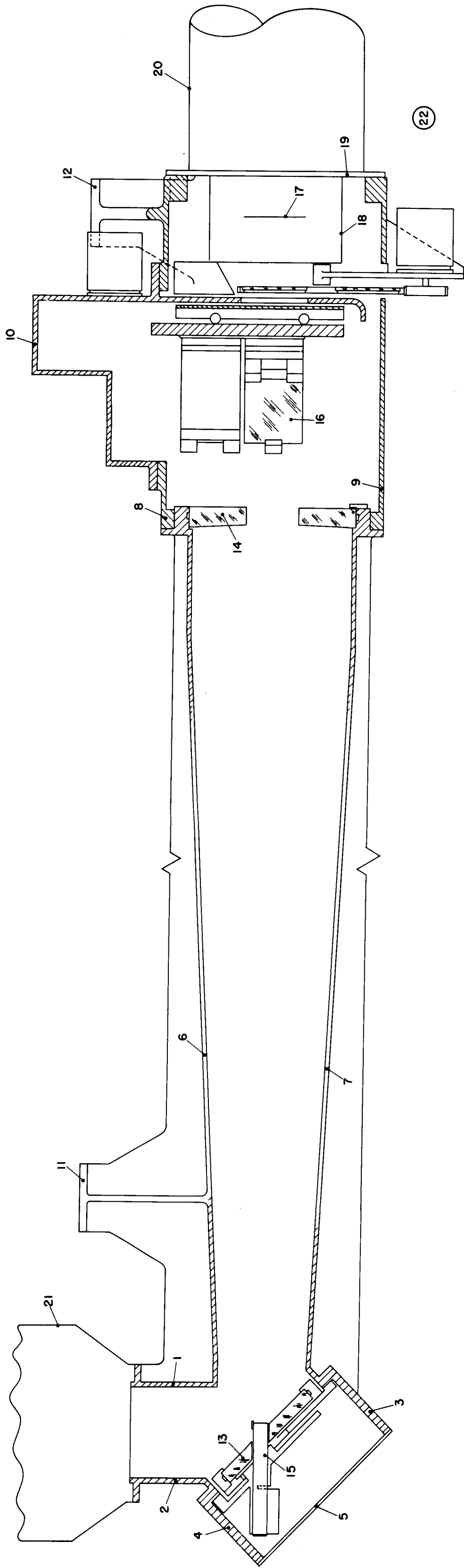


Figure 7-2. High Resolution Camera, Thermal Model

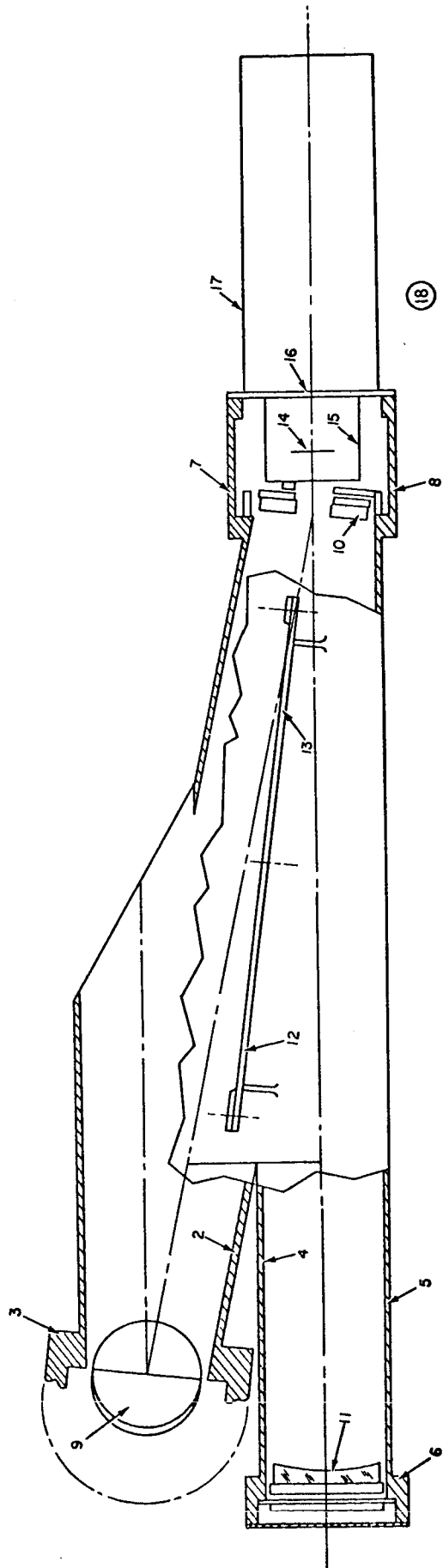


Figure 7-3. High Resolution Spectrograph, Thermal Model

TABLE 7-1. FAINT OBJECT SPECTROGRAPH-NODE DEFINITION

<u>Node</u>	<u>Description</u>
1	slit housing, rear half
2	slit housing, forward half
3	housing, camera mounting, inner half
4	housing, camera mounting, outer half
5	collimating mirror housing, rear half
6	collimating mirror housing, forward half
7	mounting ring, collimating mirror
8	relay mirror housing, outer half
9	relay mirror housing, inner half
10	mounting ring, relay mirror
11	mounting feet, forward
12	mounting feet, rear
13	collimating mirror
14	beamsplitter and angle mirror
15	relay mirror
16	photocathode
17	camera conduction cooling sleeve
18	camera mounting flange
19	radiator, camera focus coils
20	mounting structure and inner S/C wall

TABLE 7-2. HIGH RESOLUTION CAMERA-NODE DEFINITIONS

<u>Node</u>	<u>Description</u>
1	fine guidance connection, rear half
2	fine guidance connection, forward half
3	elbow housing, outer half
4	elbow housing, inner half
5	cover, elbow housing
6	tube, mounting, optics, inner half
7	tube, mounting, optics, outer half
8	housing, active relay, inner half
9	housing, active relay, outer half
10	mirror drive housing
11	mounting foot, forward
12	mounting foot, rear
13	relay mirror, stationary
14	primary mirror
15	secondary mirror
16	relay mirror, camera, active
17	photocathode
18	camera conduction cooling sleeve
19	camera mounting flange
20	radiator, camera focus coils
21	Fine Guidance Assembly
22	mounting structure and inner S/C wall

TABLE 7-3. HIGH RESOLUTION SPECTROGRAPH-NODE DEFINITIONS

<u>Node</u>	<u>Description</u>
1	Echelle grating housing, outer half
2	Echelle grating housing, inner half
3	mounting ring, Echelle grating
4	curved mirror housing, inner half
5	curved mirror housing, outer half
6	mounting ring, curved mirror
7	housing, camera mounting, inner half
8	housing, camera mounting, outer half
9	Echelle grating
10	relay mirror
11	curved mirror
12	mounting feet, forward
13	mounting feet, rear
14	photocathode
15	camera conduction cooling sleeve
16	camera mounting flange
17	radiator, camera focus coils
18	mounting structure and inner S/C wall



The data developed to describe the complex thermal interchanges between nodes involve coupling by conduction and radiation. With this information, the temperature profile for all of the nodes was obtained.

The temperature of each node is dependent upon the temperature of other nodes in the system. Thus, a temperature for a particular node results only from the solution of n simultaneous equations producing the temperature history of all the nodes in the system. The general form of the equation applicable to each node is simply a heat balance which involves the radiation interchange between the node and all others and conduction between the node and all others, electrical power dissipation associated with the node, if any, and heat loss by radiation from the node to the environment as it applies.

The vast majority of steady-state heat flow problems may be represented by a thermal resistance network with the capability of heat input at any of the discrete nodes in the system. To produce a practical temperature profile, a computer solution using finite difference techniques is employed. The computer program internally generates a series of equations, one for each unknown temperature, from the input data calculated to describe the heat balance for each node, and solves them simultaneously. The temperature of every node is determined at the end of each of a series of finite steps until steady-state is reached.

The heat balance equation which is solved for the temperature of each node is:

$$T_i = \left( \sum_j \frac{T_j}{R_{ij}} + Q_i \right) \left( \sum_j \frac{1}{R_{ij}} \right)^{-1}$$

where:

$T_i$  = the temperature of node i

$T_j$  = the temperature of node j

$\Sigma_j$  = summation over all nodes connected by a thermal resistance to node i

$R_{ij}$  = the thermal resistance between node i and any connected node j

$Q_i$  = the heat rate into node i from sources other than conduction, convection, or radiation from neighboring nodes (i.e., solar input, albedo, joule heating)

The equation above is deceptively simple, inasmuch as many  $R_{ij}$  terms apply to radiative heat transfer which is proportional to the fourth power of temperature. The mathematical complications introduced by such terms make it imperative that numerical methods be employed to solve the simultaneous equations describing the temperatures of the various nodes.

### 7.2.5 Temperature Results

The temperature results, which are shown in Tables 7-4 through 7-7, are the computer output for the instrumentation assemblies studied. They are steady-state solutions based on the current state of the reference designs. The nodes marked \* are input nodes.

TABLE 7-4. FAINT OBJECT SPECTROGRAPH, NODE TEMPERATURES

<u>Node</u>	<u>Temperature</u>	<u>Node</u>	<u>Temperature</u>
1	294.58 K	11	294.35 K
2	294.50	12	294.50
3	294.59	13	294.49
4	294.58	14	294.53
5	294.50	15	294.38
6	294.48	*16	264.00
7	294.49	*17	262.00
8	294.39	*18	311.00
9	294.39	*19	311.00
10	294.39	*20	294.00

TABLE 7-5. HIGH RESOLUTION CAMERA OPTICS, NODE TEMPERATURES  
(CASE 1, ALUMINUM HOUSING)

<u>Node</u>	<u>Temperature</u>	<u>Node</u>	<u>Temperature</u>
1	294.38 K	12	294.81 K
2	294.37	13	294.43
3	294.39	14	294.77
4	294.38	15	294.44
5	294.39	16	295.21
6	294.52	*17	265.00
7	294.54	*18	262.00
8	295.13	*19	341.00
9	295.18	*20	332.70
10	295.44	*21	294.00
11	294.38	*22	294.00

TABLE 7-6. HIGH RESOLUTION CAMERA OPTICS, NODE TEMPERATURES  
(CASE 2, GRAPHITE-EPOXY HOUSING)

<u>Node</u>	<u>Temperature</u>	<u>Node</u>	<u>Temperature</u>
1	294.40 K	12	295.13 K
2	294.39	13	294.48
3	294.42	14	295.05
4	294.40	15	294.49
5	294.41	16	295.70
6	294.58	*17	265.00
7	294.60	*18	262.00
8	295.58	*19	341.00
9	295.64	*20	332.70
10	295.98	*21	294.00
11	294.41	*22	294.00

TABLE 7-7. HIGH RESOLUTION SPECTROGRAPH,  
NODE TEMPERATURES

<u>Node</u>	<u>Temperature</u>	<u>Node</u>	<u>Temperature</u>
1	294.40 K	10	294.52 K
2	294.40	11	294.39
3	294.39	12	294.39
4	294.40	13	294.39
5	294.40	*14	264.00
6	294.39	*15	262.00
7	294.59	*16	311.00
8	294.60	*17	311.00
9	294.40	*18	294.00

#### 7.2.6 Time Response

Calculation of a normalized time constant for an optical instrument of these typical weights and specific heat indicates that, in an orbital period of 90 minutes, the steady-state temperatures will not be reached. The net temperature rise will be approximately one-half of the possible maximum.

One time constant is equal to the RC value of the system, where:

$$RC = \frac{C}{\sum \frac{1}{R}} ; \quad R = \text{resistance between the nodes and the environment}$$

C = thermal capacitance of the system

RC = 128.8 minutes, one time constant

let,  $T_{\theta}$  = temperature at time  $\theta$  = 90 minutes, orbital period

$T_{\infty}$  = maximum temperature

$T_0$  = initial temperature

then,

$$\frac{T_{\theta} - T_{\infty}}{T_0 - T_{\infty}} = e^{-\theta/RC} = e^{-90/128.8} = .497$$

or, the temperature rise at time  $\theta$  is equal to one-half the maximum temperature rise,  $T_0 - T_{\infty}$ .

### 7.2.7 Detailed Thermal Design

As more comprehensive and detailed designs of the instruments are developed, thermal models expanded to many more nodes will be used to determine specific temperatures and axial and circumferential gradients as required. Once the orbital temperature profiles of the mounting structure and the inner spacecraft wall are known, transient analyses can be conducted for all the instruments. Transient power dissipation of any associated electronic equipment can be included. Temperature profiles for any portion of the mission or steady-periodic temperatures can be derived.

Since the mathematical thermal models will be available for the instruments, parametric variations in materials, conductivities, emissivities, and insulation can be applied and answers quickly obtained from the computer. These brief, parametric studies will be the basis for making design decisions to obtain the required heat transfer and temperature levels to maintain the optical and mechanical integrity of the units.

As this process nears completion, a final thermal analysis will be made and the resultant temperature profiles will provide data for proving the efficiency and reliability of the instruments in their expected environmental extremes.

### 7.2.8 Performance Effects

The following discussions calculate the tolerances for temperature ranges and gradients based on limits for focus and dynamic shifts on the High Resolution Spectrographs and the f/96 Camera.

In these discussions the tolerance on focus is determined differently depending on the effect at the particular location. For example, slit locations are based purely on diffraction limit focus depth with the largest portion of the tolerance reserved to the OTA and the structure. At camera focus, tolerance is based on the difference between one and one-half Airy discs and the size of the camera resolution element which corresponds to 50% modulation of a 100% contrast image. If the one and one-half Airy disc value itself is larger than the camera resolution element as defined above, then the limit is the diffraction limit on defocus.

Similarly, the tolerances on variation of temperature gradients which act to produce movement of images in the focal plane have, in all cases, been based on the rather arbitrary limit of one-half of a camera resolution element.

This work was done concurrently with the thermal analysis of the preceding paragraphs. The relationship of the tolerable conditions to the predicted conditions is pointed out in each case.

#### 7.2.8.1 High Resolution and Faint Object Spectrographs

The High Resolution and Range I Faint Object Spectrographs have similar configurations, so the following discussion applies to both.

The Spectrographs have a camera mirror speed of f/9 which is the fastest of the faint object spectrographs and therefore has the least depth of focus. It also has the longest focal length camera mirror and hence, the longest path subject to thermal expansion of the housing.

The focus tolerance of the spectrographs corresponds to an image growth from one and one-half Airy disc diameters to one resolution element of the recording camera. The one and one-half Airy disc size is given by:

$$1.5 \times 2.44 \lambda f_n \text{ (meters)}$$

or  $1.5 \times 2.44 \times .115 \times 10^{-6} \times 9 \text{ (meters)}$

or  $3.8 \mu\text{m}$

The size of one resolution element is  $25 \mu\text{m}$ .

The allowable growth then is  $25 - 3.8 \mu\text{m} = 21.2 \mu\text{m}$ .

This corresponds to a defocus of  $9 \times 21.2 \mu\text{m} = 190.8 \mu\text{m}$ .

The focal length is  $1.07\text{m}$  so the fractional change in dimension al-  
is

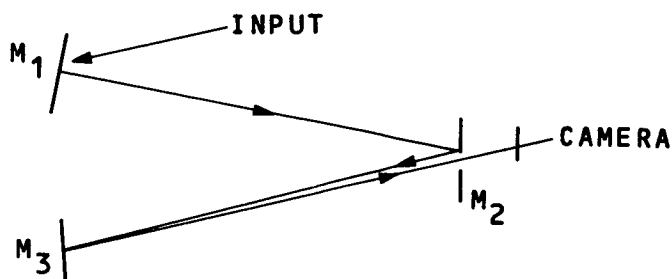
$$\frac{191 \times 10^{-6} \text{m}}{1.07\text{m}} = 178 \times 10^{-6}$$

The coefficient for aluminum is  $21 \times 10^{-6}/\text{K}$ ; dividing this into  $178 \times 10^{-6}$  gives an allowable temperature deviation of  $8.5 \text{K}$ .

This allowable deviation, which is well in excess of values predicted by the thermal analysis, establishes that no problems of focus will be experienced by the use of aluminum housings regardless of the choice of materials for the optics.

The analysis of the thermal gradient effects on the stability of the long exposure spectral image is similar for all three of the Faint Object Spectrograph instruments. All have three successive folds with the mirrors at the ends and at the point of an approximately equal sided "V", and a camera located at the point of the "V". The difference in function of the mirrors, that is, to fold, disperse, collimate or collect the light, does not change this feature of similarity. The result of particular interest for deriving the thermal requirements of the designs is that deformations which are symmetrical to this "V" configuration do not disturb the

spectrum image. The fact that the configurations are basically symmetrical relative to the heat input from the cameras is therefore a significant advantage. The designs are shown schematically in the figure below:

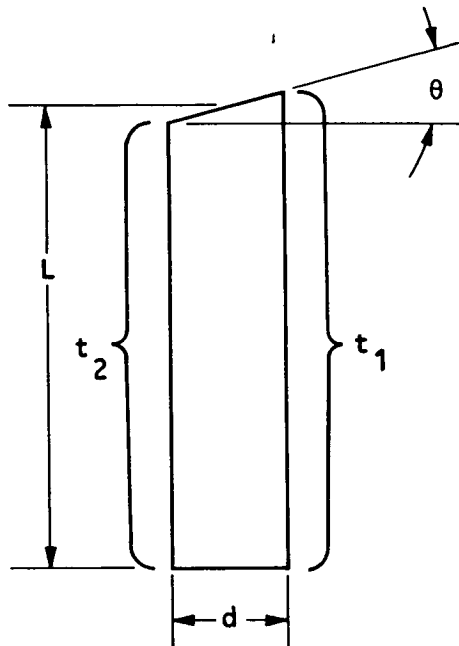


Rotations in the plane of the figure of the three mirrors must be such that the algebraic sum of the rotations of  $M_1$  and  $M_3$  is equal to the rotation of  $M_2$ . The simplest and most obvious case is when  $M_1$  and  $M_3$  are equal and opposite and  $M_2$  is zero. This is also the most likely case, but small nonsymmetries in the units may bring about the condition in which rotation of  $M_2$  comes into play.

The residual angular movement of any one mirror may be that which results in movement of the image of one-half of a resolution element or 0.025 mm. Since the camera mirror has a 1.07 meter focal length, this angle is  $\frac{.025 \text{ mm}}{2 \times 1.07\text{M}} = 11.6 \text{ } \mu\text{rad}$ .

The tolerance for the average difference in temperature from one side of a uniform section to the other is determined by the ratio of the length to the breadth and the angle variation tolerance one end from the other. This is shown below:





$$\theta = \frac{L \alpha (t_1 - t_2)}{d}$$

$$\alpha \text{ for aluminum} = 21 \times 10^{-6}/\text{K}$$

$$\theta_{\text{max}} = 11.6 \times 10^{-6} \text{ rad}$$

$$t_1 - t_2 = \frac{\theta}{\frac{L}{d} \times 21 \times 10^{-6}}$$

The length to breadth (diameter) of the longest structure path is  $1050 \text{ mm} \div 160 \text{ mm} = 6.57$ , and so the thermal gradient which is uncompensated by symmetry may be  $\frac{11.6 \times 10^{-6} \text{ rad}}{6.57 \times 21 \times 10^{-6}} \text{ K} = 0.084 \text{ K}$ . This is the circumferential thermal gradient tolerance that should be maintained during an observation. It does not mean the steady-state gradient must be this small but only the variation should be within these limits. It does not make a clear case for changing the spectrograph structures to epoxy graphite because of its low coefficient of expansion. Unlike the case discussed later of the f/96 Camera, the application in this case is not nearly as straight forward because the large hole in the side of the structure to admit the collimated beam is intuitively more disturbing to symmetry when embodied in epoxy graphite than when embodied in aluminum or any isotropic material.

The Faint Object Spectrographs for the 220 to 660 nm and the 660 to 1000 nm range, though less critical than the one for the 115 to 220 nm range, do present additional considerations because the slit mechanism is part of the instrument.

Two criteria for maintaining focus must be satisfied by the control of thermal expansion:

1. The slit to the mounting interface dimension must be controlled to a fraction of the depth of focus of the Ritchey-Chretien Telescope.

2. The collimator to slit dimension and the camera mirror to camera focus dimensions must be controlled within a fraction of the slit image defocus permissible on the camera tube.

- a. Slit to Mounting Interfaces

At  $f/12$  and  $\lambda = 220$  nm, the diffraction limit depth of focus is  $2.44 \lambda \frac{f_n^2}{n}$  or  $2.44 \times 12^2 \times .22 \times 10^{-6}$  meters =  $2.44 \times 144 \times .22 \times 10^{-6} = 80 \mu\text{m}$ . Allowing one fourth this depth of focus for thermal variation within the spectrograph, permits a swing of  $\pm 20 \mu\text{m}$ . The distance between the slit plane and the mounting plane is  $0.152$  m, so that for aluminum with an expansion coefficient of  $21 \times 10^{-6}/\text{K}$ , the temperature excursion permissible is  $\frac{20}{.152 \times 21.0} = 6.3\text{K}$ . This is ample leeway by comparison with temperature changes shown for this section. It is based on the assumption that the slit size will be equal to the diffraction star image. The smallest slit, however, will probably be about several times this size.

- b. Collimator to Slit and Camera Mirror to Camera Focus

The camera depth of focus on all of the Faint Object Spectrographs in the wavelengths from  $220$  nm upward is greater than that discussed for the  $115$  to  $220$  nm range because the longer wavelength instruments are  $f/12$  throughout. However, since their slit mechanism is part of these instruments, the combined effect of collimating the slit throughput and then re-imaging the collimated light compounds the focus shift due to the temperature change if this change is in the same direction for all parts of the system. This is quite sure to be the case so the determination of the range of acceptable temperature change must take this into account. The simplest way of doing this is to take one-half of the system and treat it as though it were  $f/6$ . Calculating the defocus limit in the same manner as in paragraph 7.2.8.1 with  $f_n = 12$  and  $\lambda = .220 \times 10^{-6}$ , the one and one-half airy disc diameter is  $9.7 \mu\text{m}$  and the growth allowance to  $25 \mu\text{m}$  leaves a tolerance of  $(25-9.7) \times 6$  or  $91.8 \mu\text{m}$ . At the focal length of the camera and collimating mirrors of  $.610$  m and for  $\alpha = 21 \times 10^{-6}/\text{K}$

for aluminum, we determine the allowable temperature excursion to be  $\frac{92}{21 \times .61} = 7.2\text{K}$ . The temperature change result of the thermal analysis is within this range.

In the discussion of allowable temperature gradients transverse to the optical axes which result in rotation of the optics for the Faint Object Spectrograph covering the 115 to 220 nm wavelength, the similarity of all three of the Faint Object Spectrographs was pointed out. The systems were described as symmetrical "V's" and the acceptable gradients were defined.

The 220 to 660 nm range instrument and the 660 to 1000 nm range instruments by the identical reasoning have a residual thermal gradient tolerance  $\frac{1070}{610}$  times as great as the 115 to 220 nm instrument based entirely on the shorter focal length of their camera mirrors with the same spatial resolution.

The construction of these two instruments is simpler because of the absence of a grating shift mechanism. The instrument with the dual gratings, that for 220 to 660 nm, demands more attention in the design of the mount for the folding mirror and beamsplitter. This mount should have an interface with the main structure at three points in a plane which has minimal thermal gradient; the angle between the two reflecting surfaces should be maintained by a one piece structure with good thermal conductivity between the surfaces that support the mirror and beamsplitter reflecting surfaces.

#### 7.2.8.2 High Resolution Camera

The optical design of the f/96 Camera has constraints on the position of optical elements to fit this unit into the SIP structure and relative to the Fine Guidance Unit. A secondary constraint, the elimination of a spider to support the secondary, was a factor in this design. One adverse consequence of the resulting arrangement, which is characteristic of all Cassagrainian systems, is to aggravate the sensitivity to variations of spacing between elements.

The Figure 7-4 shows the optical layout dimensions and the tolerance on the f/96 focus. The tolerance is based on focus shift

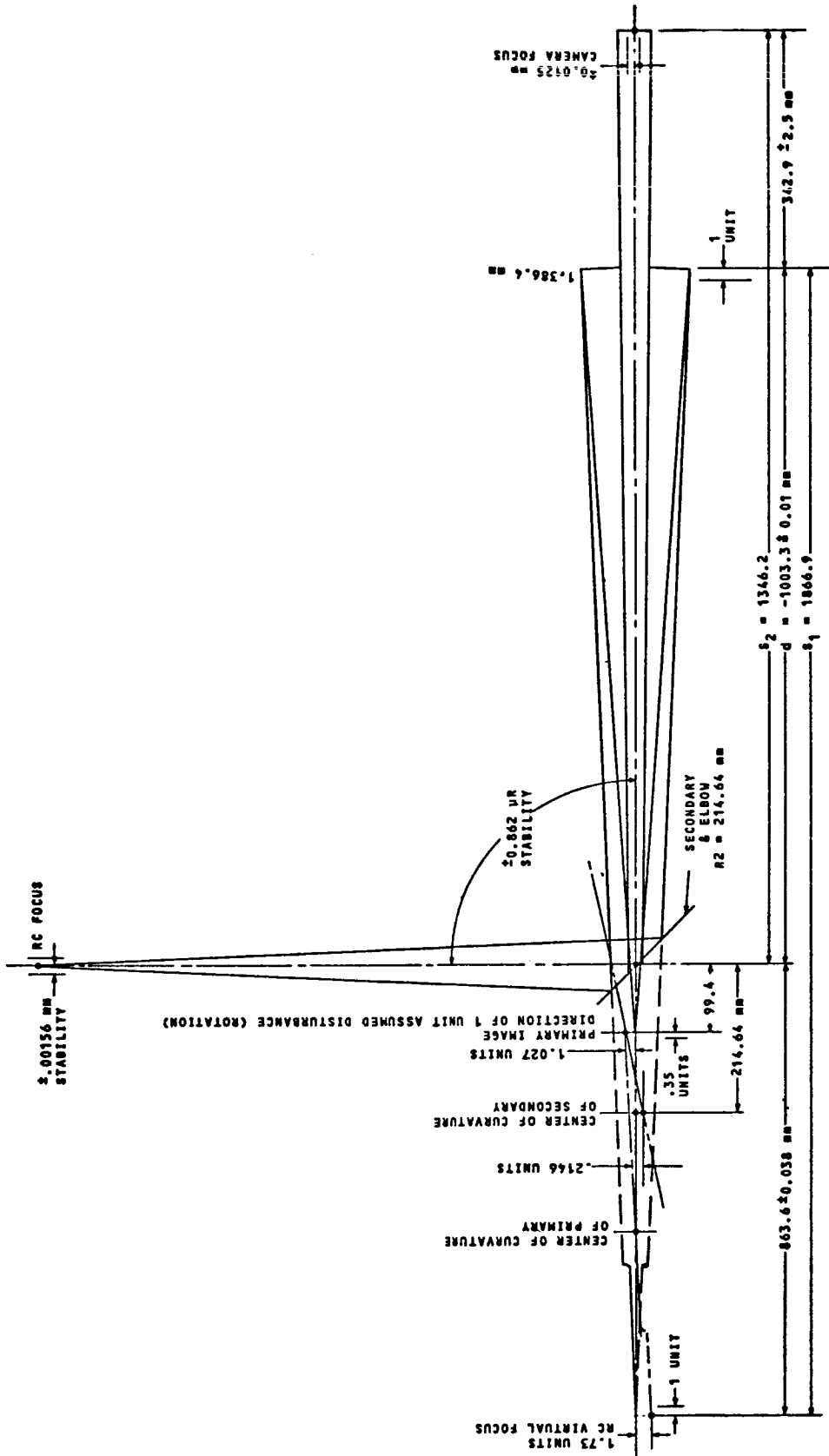


Figure 7-4. High Resolution Camera Thermal Response Diagram

equal to one-fourth of the diffraction limit on defocus, that is, 2.5 mm at the detector focal plane and a lateral shift of one-half of a camera resolution element or 0.0125 mm.

The dimensions, shown in Figure 7-4, are used to calculate the nominal location of the intermediate image using the equation  $\frac{1}{i} + \frac{1}{o} = \frac{1}{f}$  in which 'b' is the  $S_1$  dimension, 1866.9 mm; 'f' is one-half of  $R_1 = 693.2$  mm and 'i' resulting from the solution of the equation is 1102.7 mm. This places the intermediate image at 99.4 mm to the left of the secondary by subtraction of the "d" dimension from the "i" dimension.

From the ratio of image distance to object distance, 1102.7 divided by 1866.9, we find the primary magnification to be 0.591 and similarly dividing 1346.2 by 99.4, we find the secondary magnification equals 13.54. These magnification factors are then used to determine the tolerance on dimensions based on their producing the tolerable movement of 2.5 mm of the final image.

Taking the assembly of the secondary and elbow mirror as fixed we assume the primary to move one unit to the left. The primary image movement will be to the left also by one unit times the square of the magnification or  $(.591)^2 = .35$  units. This shift is also to the left and relative to the primary so that relative to the stationary secondary, it is 1.35 units to the left. The shift of the camera focus is therefore  $1.35 \times (13.54)^2 - 1$  assuming that the camera also moves with the primary; this comes to 246.5 units. Since one tolerance unit is shown to be 2.5 mm, the tolerance on the "d" dimension is  $2.5 - 246.5$  mm or 0.01 mm.

Using the same method of calculation for a unit shift in the 863.6 mm dimension with the same point of reference, that is the elbow and secondary assembly, if we decrease the dimension one unit the virtual image relative to the secondary will move 0.35 units to the right and multiplying this by  $(13.54)^2$ , we get 64 units of movement at the camera. The tolerance is therefore  $1/64$  unit or  $2.5 \text{ mm} \div 64 = 0.038$  mm.

Since the lateral magnification is 8, the allowable movement of the instrument as a whole relative to the RC focus is one-eighth of the lateral stability tolerance unit of 0.0125 mm at the focal plane, that is  $\pm 0.00156$  mm.

The equivalent of lateral shifting can take place as rotation of the combination elbow and secondary mirror. The amount of rotation which will cause a shift equal to one lateral tolerance unit is not the same as though the elbow mirror alone rotated. If that were the case, the rotation angle allowed would be  $.00156\text{mm} \div (863.6 \text{ mm} \times 2)$  rad, which works out to be 0.9 radian. In the case of the secondary moving as a unit with the elbow mirror, the center of curvature of the secondary moves in the same direction as the movement of the virtual image introduced by the elbow mirror. The movement of the intermediate image formed by the primary is in the opposite direction. Tracing out the new location of the final image formed by the secondary is a matter of extending a line through the new center of the secondary and the new location of the primary image. The angle made by this line and its height in the final image plane can be deduced from the figure. The dimensions are millimeters if the unit rotation is one milliradian.

$$\frac{.2146 + 1.027}{214.64 - 99.4} \text{ rad} \times 1346.2 \text{ mm} = .010774 \text{ rad} \times 1346.2 \text{ mm}$$

$$= 14.504 \text{ mm}$$

Since the allowable height shift in the final image plane is 0.0125 mm, the allowable rotation of the elbow and secondary assembly is  $\frac{.0125}{14.504}$  mrad or 0.862  $\mu$ rad.

Conversion of the tolerances on Figure 7-4 into allowable temperature ranges and gradients is accomplished once the material and physical proportions of the optical housing and the optics is defined. The material in the reference design is 356 cast aluminum alloy with pyrex optics with coefficient of thermal expansion of  $21 \times 10^{-6}$  per degree K and  $3.2 \times 10^{-6}$  per degree K, respectively.

The difference between these,  $17.8 \times 10^{-6}$ , determines the isothermal temperature range for acceptable focus as determined by the most sensitive "d" dimension. The tolerance in this dimension, .01 mm divided by the dimension 1346.2 mm is 1 part in 135,000 or  $7.4 \times 10^{-6}$ . This number divided by the combined expansion coefficient of  $17.8 \times 10^{-6}$  yields the temperature deviation of 0.42K. The average departure from the base temperature of 294K when the instrument reaches steady-state is 0.7K (average of nodes 1, 2, 6, 7, 8 and 9, Table 7-5). This is more than the tolerance just derived using the conservative limit of one-fourth the diffraction depth of focus. A small preset focus bias to optimize the range during use is advisable.

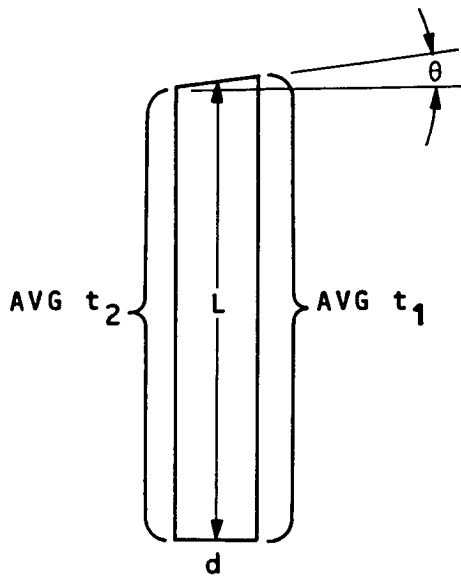
The f/96 housing made of graphite-epoxy with cervit optics will make the temperature tolerance orders of magnitude larger.

The dimension 864 mm, in Figure 7-4, from the elbow mirror to the Ritchey-Chretien focus is the next most critical, its tolerance being 0.038 mm, a change of  $43.2 \times 10^{-6}$  per unit length. All but 200 mm of this 864 mm dimension is part of the near zero expansion epoxy graphite SIP structure so the expansion tolerable per unit length for the portion within the f/96 Camera housing is  $190 \times 10^{-6}$  corresponding to a temperature departure at  $17.8 \times 10^{-6}$  units per degree of = 10.7 K, allowable in an aluminum instrument structure.

The tolerance on the back focus due to the very low convergence, f/96, is  $\pm 2.5$  mm so the thermal variation of this dimension is not significant.

The tolerance of .00156 mm on the stability of location relative to the OTA optical axis is largely a matter of placing the connection between the camera optics and the SIP structure as close as possible to the OTA optical axis. It then becomes a problem of the SIP structure stability discussed later. The camera body stability comes into the picture principally as it affects the variation of the right angle bend, the tolerance of 0.862  $\mu$ R on the figure. Variation of this angle is the result of thermal gradients as opposed to temperature range which was the ruling consideration in the preceding paragraphs.

The tolerance for the average difference in temperature from one side of a uniform section to the other with a length to cross dimension ratio of 6:1 can again be arrived at by proportionality.



$$\theta = \frac{L \alpha (t_1 - t_2)}{d} \leq 5.8 \mu\text{rad}$$

$$\frac{L}{d} = 6.0$$

$$6.0 \alpha (t_1 - t_2) \leq 1.5 \mu\text{rad}$$

$$\alpha (t_1 - t_2) \leq 0.25 \mu\text{rad}$$

using  $\alpha = 21 \times 10^{-6}/\text{K}$  for aluminum

$$t_1 - t_2 = \frac{.25 \times 10^{-6}}{21 \times 10^{-6}} = .012\text{K}$$

Using the value of  $\alpha$  for aluminum, we have a temperature gradient tolerance of 0.012K.

The thermal analyses do not indicate that reduction of transverse thermal gradients to such low values is impossible. The pairs of nodes on opposite sides of the structure have an average difference of 0.02K in the analysis for both aluminum and epoxy graphite. On the other hand, to demonstrate that they will not exist is also difficult. Neither can it be clearly demonstrated that differential expansion between the aluminum body and the epoxy graphite supporting structure will not introduce the same effect by bending the optical housing. These uncertainties must be resolved as well as the uncertainties of designing and building an epoxy graphite housing before a final choice of material is made.

## 7.2.9 Detector Tube Assembly

### 7.2.9.1 Introduction

Special attention has been given to the detector tube due to its critical relationship to the performance of most of the SIP



instrumentation, and the need for temperature control to provide the required spectral response and low preamplifier noise.

This section presents the results of the detailed thermal design effort which had as its objectives:

1. The definition of a thermal control concept
2. Supporting analysis which demonstrates the feasibility of the selected concept.
3. Suggestions for future work and/or refinements which were beyond the scope of the original task.

This analysis is an extension and elaboration of the conceptual design developed earlier. A 40 node math model of the 50 x 50 mm camera tube was developed and both steady-state and transient thermal analyses were conducted to observe the energy flows, the temperature distributions within the tube, and to estimate the thermal time constant of the tube.

Paragraph 7.2.9.6 presents a general comparison of two cooling methods. This paragraph presents arguments for and against both thermoelectrics and heat pipes and concludes that the thermoelectric concept is preferable.

#### 7.2.9.2 Design Criteria

The following thermal design criteria for the tube assembly have been developed for use with this design and analysis effort.

##### a. Focus coil, Magnetic Shield, External Structure

$T_{\text{radiating surface}}$	$325 \text{ K} \pm 25 \text{ K}$
$T_{\text{coils}}$	TBD
Circumferential Gradient (Any axial plane)	$\leq 2 \text{ K}$

b. Tube, Deflection Coil, Internal Cooling Shroud

	<u>Requirement</u>	<u>Goal</u>
$T_{\text{Photocathode and preamplifier}}$	260 K $\pm$ 4 K	250 K $\pm$ 4 K
$\Delta T$ on any point inside shroud	5 K	
Circumferential Gradient	<u>&lt;2 K</u>	

7.2.9.3 Thermal Control System

The suggested method for cooling the photocathode tube is to use a 2-stage cascaded thermoelectric cooling module located at the rear of the tube. The module is regulated by a remote electronic controller requiring approximately 10 watts of power. The thermoelectric cooler is attached to a conducting sleeve which shrouds the tube, is potted to the tube, and is stopped to a 50 mm square at the front of the tube. The analysis (one diameter sleeve extension) predicts a 2K radial temperature gradient in the photocathode. Stopping the photocathode to 50 mm will approximately halve the view factor to the ambient environment and reduce the radial temperature gradient to about 1K. The total energy absorbed by the aperture and the stop remains unchanged at 3 watts. The conduction sleeve is externally gold plated for low emittance as is the internal focus coil support structure to suppress radiation heat transfer. The tube is supported inside the focus coil structure locally by small area contacts, radially with .005 inch clearance and axially with no clearance. The hot junction of the thermoelectric device is thermally connected to the exterior surfaces of the camera which acts as the camera radiator so as to reduce temperature gradients on the external structure and keep the hot junction as cool as is practical. The supports which attach the tube assembly to the camera structure have a high thermal resistance to reduce the amount of heat conducted to the structure. Figure 7-5 presents the general camera arrangement described above.

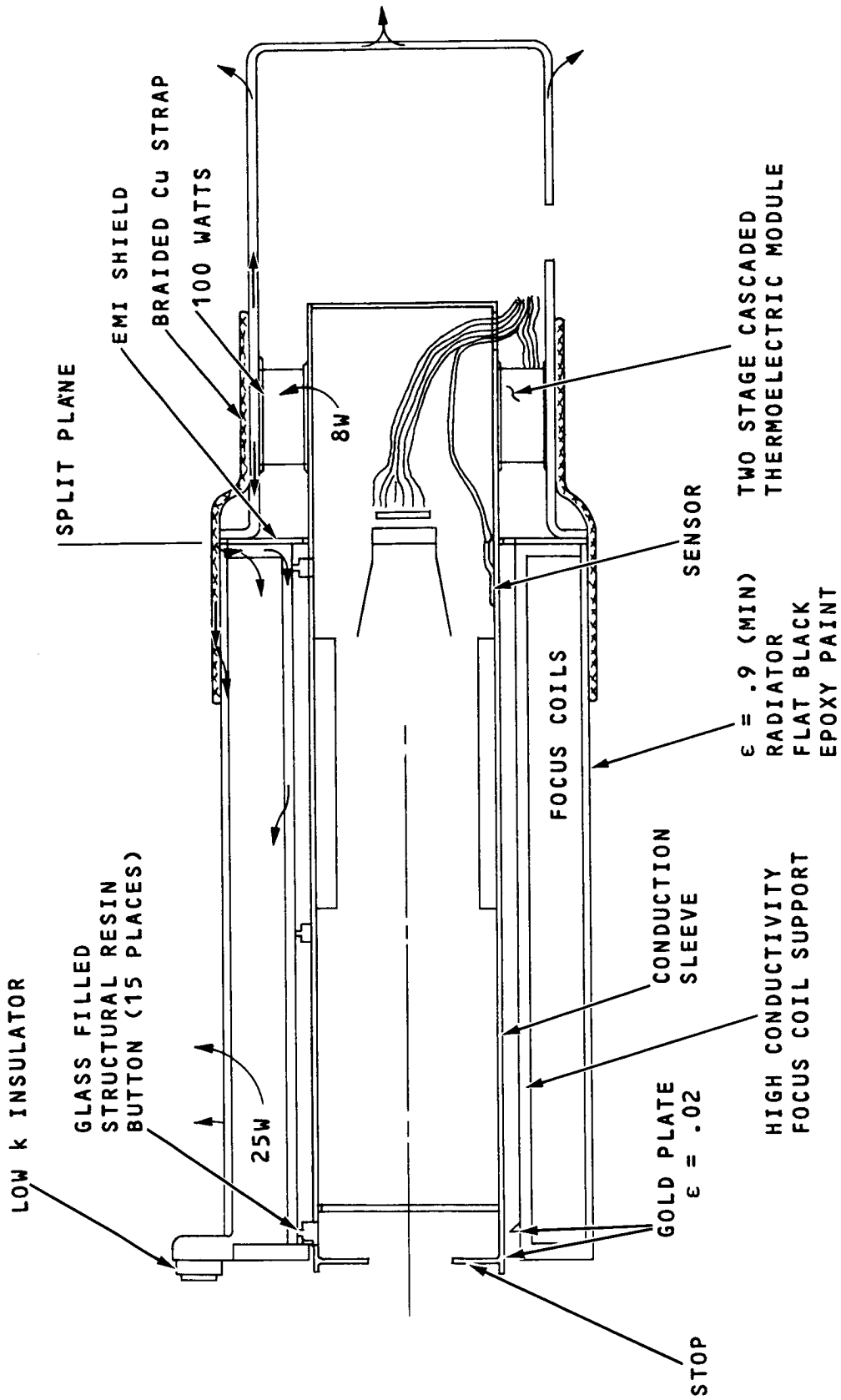


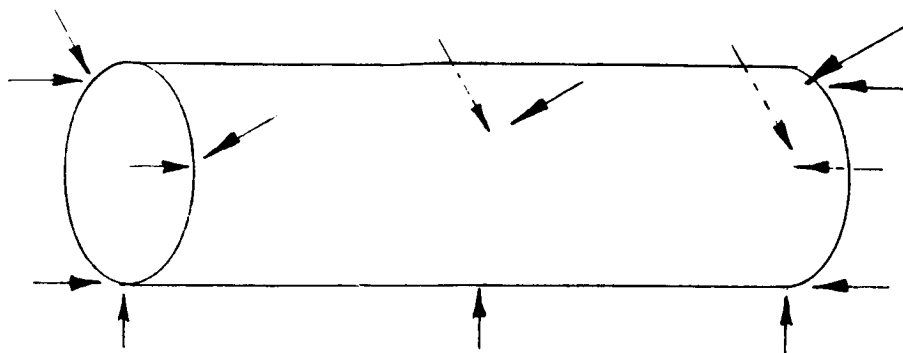
Figure 7-5. Detector Tube Assembly Model

#### 7.2.9.4 Description of Camera Thermal Model

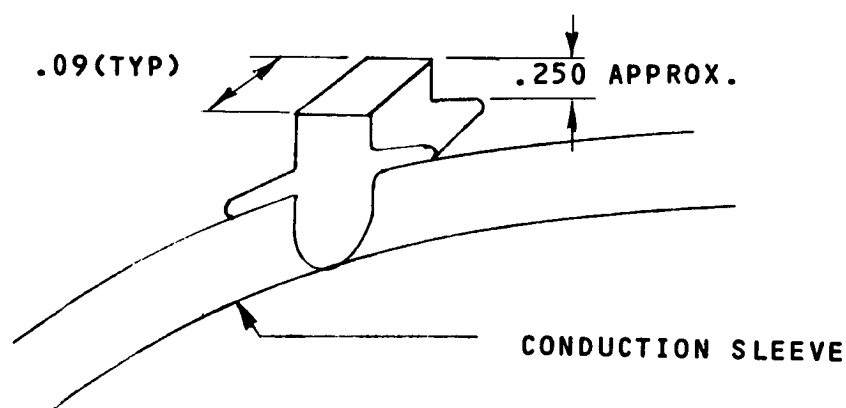
A 40 node R-C network of the photocathode tube as shown in Figure 7-6 was assembled in order to study the problem. The model consists of a gold plated conducting sleeve ( $\epsilon = 0.02$ ) which radiates and conducts to the focus coils which have an emittance of 0.02. The external surface of the focus coils radiate to an ambient of 293 K. The photocathode window in the tube was modeled as 3 nodes and was assumed to be 0.10 inch thick slab of  $\text{MgF}_2$  whose  $k$  is  $35.2 \times 10^{-3}$  cal/sec-cm-°C. The tube target was modeled as one node whose thickness is 20 microns and whose material is KCl ( $k = 41.4 \times 10^{-3}$  cal/sec-cm-°C). Conduction was included between the cold sleeve and the warm focus coils to account for heat losses through the tube supports.

Initially the conducting sleeve was extended about one diameter in front of the photocathode and extended rearward only to the target. This scheme would not cool the target which assumed the mean radiant temperature of the partial sleeve and the warm focus coils. It was then decided to sleeve the entire length of the tube in order to surround the target with a cold radiant temperature since the target's temperature level is radiation dominated. Conduction through the 20 micron target thickness is weak. The surfaces of the focus coils radiate to an ambient of 20°C with an emissivity of 0.9 (black).

The tube support conductances were estimated by assuming 1.5 x 1.5 mm contacting areas, 15 places, with a contact conductance of  $13.52 \times 10^{-3}$  cal/sec-cm<sup>2</sup>-°C. It was assumed that the tube was supported 3 places radially, center and each end, and 3 places axially each end per the following sketch.



Calculations were performed and suggest a .09 x .09 x .25 Max. glass filled structural plastic or vespel support.



The solid conduction resistance along the 6 mm support length was ignored. When estimating the thermal leak from coils to sleeve, the total resistance for the 2.2 x 2.2 mm contact areas is still representative even though the 2.2 x 2.2 mm contacting area is about twice as large as that used in the math model.

The thermoelectric module was modeled by fixing the cold junction at 260 K and dissipating an  $I^2R$  load in the external focus coil casing at the rear of the tube assembly. This should be taken as a valid assumption for the transient run since the thermal time constant of a typical Peltier cooler of this type is around 60 seconds.

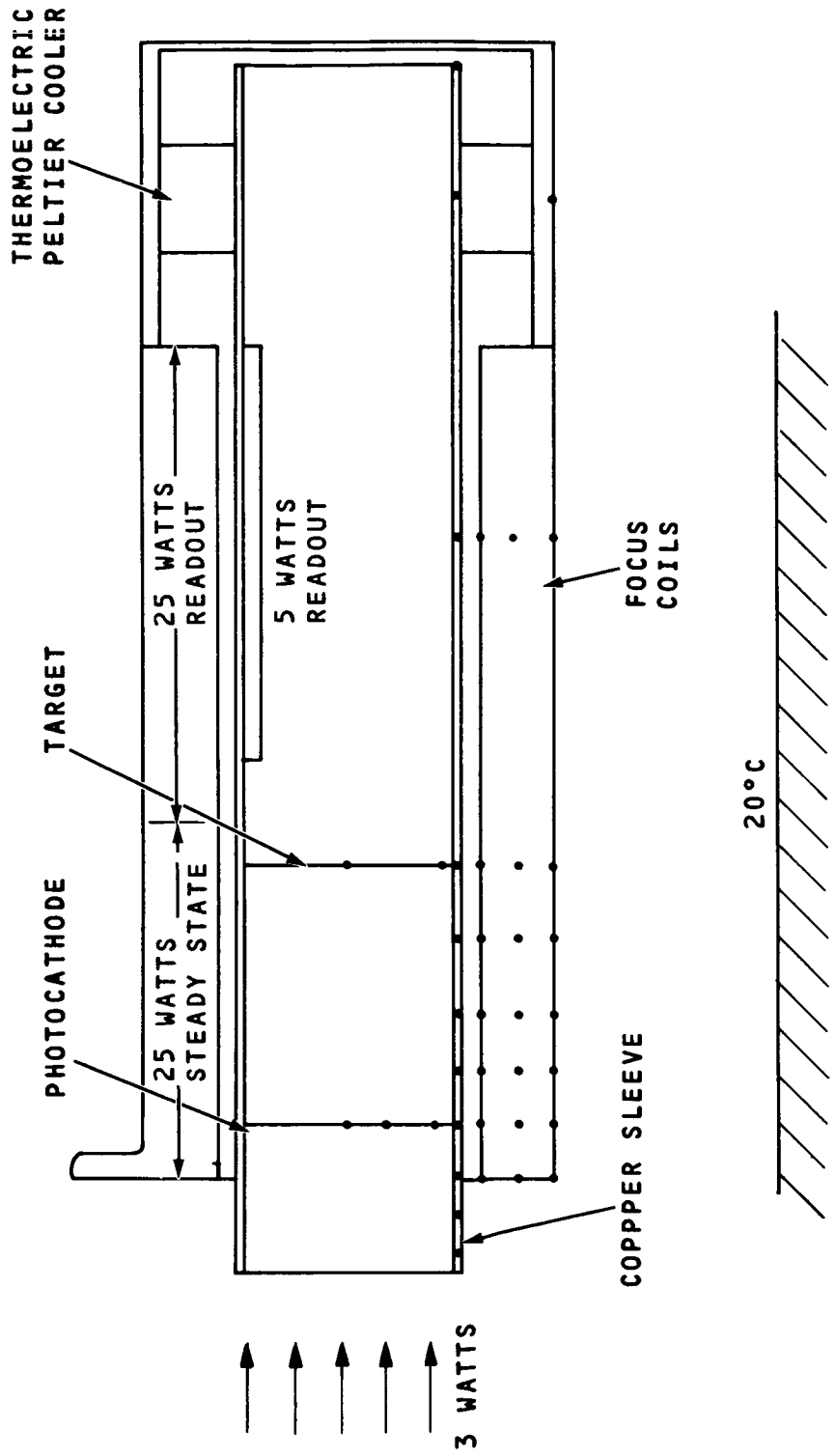


Figure 7-6. Detector Tube Assembly, Power Distribution

#### 7.2.9.5 Tube Assembly Thermal Analysis Results

The following 7 cases summarized in Table 7-8 were run to examine the thermal characteristics of the tube assembly.

Cases 1 through 4 were steady-state analyses based on fixing the right hand end of the copper cooling sleeve at 26°K (or 200 K, see case 3). Case 1 is the reference case. Case 2 shows the effect of varying the sleeve supports area (10X), and Case 4 shows the effect of reducing the sleeve thickness to 2.5 mm from 6.25 mm (1/2.5). Cases 5 and 6 show the effects of changing the Peltier device power consumption from 25 watts to 100 watts. Case 7 was run in the transient mode to develop data for estimating time constant and/or transient temperature histories for the camera. The steady-state temperature distributions are depicted in Figures 7-7 through 7-12. For all of the steady-state cases, the radial temperature gradient in the photocathode window was no greater than 2 K and the radial temperature gradient in the target was less than 1 K.

Figure 7-13 shows the thermal power leaking to the cooling sleeve vs. the contact area for a fixed  $\Delta T$ . To keep conduction losses down to about one watt, the total contacting area should be on the order of  $.58 \text{ cm}^2$  for this condition. The actual point for the small conduction area misses this curve by a fraction (.27) of a watt but since the curve must pass through zero it was so plotted. Figure 7-14 shows the effect of reducing the conduction sleeve thickness versus the axial temperature gradient along the sleeve. The actual points from the thermal model miss this curve by less than .5 K but the curve is plotted to show the best agreement with these points consistent with theory. A thickness of 2.5 mm copper would place the gradient at about 5 K.

Figure 7-15 shows the transient response of the photocathode to a step change at the end of the sleeve to a temperature from 293°K initial to 260 K. Figure 7-16 shows the mean temperature of a  $0.2 \text{ m}^2$  area x emissivity radiating to 10 and 20 C surrounding versus total watts radiated. The  $A\epsilon$  product for the 50 mm tube should be  $0.63 \text{ m}^2$  for the analysis conditions.

TABLE 7-8. TUBE ASSEMBLY THERMAL ANALYSIS RESULTS

Case No.	$Q_{fc}$ w	$Q_{pd}$ w	$Q_c$ w	$Q_w$ w	$Q_t$ w	$A_{c2}$ mm <sup>2</sup>	$t_s$ mm	$T_b$ K	$T_c$ K	$T_t$ K	$T_p$ K	$T_r$ K	$T_m$ K
1 - Fig. 7-7	25	0	.9	3	6.9	35	6.25	260	262	262	264	-	308
2 - Fig. 7-8	25	0	6.3	3	12.3	350	6.25	260	268	266	267	-	303
3 - Fig. 7-9	25	0	2.0	6	15	35	6.25	200	203	203	204	304	308
4 - Fig. 7-10	25	0	.9	3	6.9	35	2.50	260	264	263	266	-	308
5 - Fig. 7-11	25	100	1.5	3	7.5	35	6.25	260	262	262	265	345	341
6 - Fig. 7-12	25	25	1.0	3	7.0	35	6.25	260	262	262	264	313	311
7 -	25	25	-	-	-	35	6.25	260	-	-	-	-	-

where

$Q_{fc}$  = Power dissipation in front focus coils

$Q_{pd}$  = Power dissipation in Peltier device

$Q_c$  = Power conducted through tube supports

$Q_w$  = Power conducted by the wires

$Q_t$  = Power conducted to cold sink from cu. sleeve

$A_c$  = Tube support contact area

$t_s$  = cu sleeve thickness

$T_b$  = Fixed boundary temperature of cu sleeve - cold side of PD

$T_c$  = Temp. of copper sleeve - fwd

$T_t$  = Temp. of target

$T_p$  = Temp. of photocathode

$T_r$  = Temp. radiator, - warm side of PD

$T_m$  = Temp. of camera mounting surface



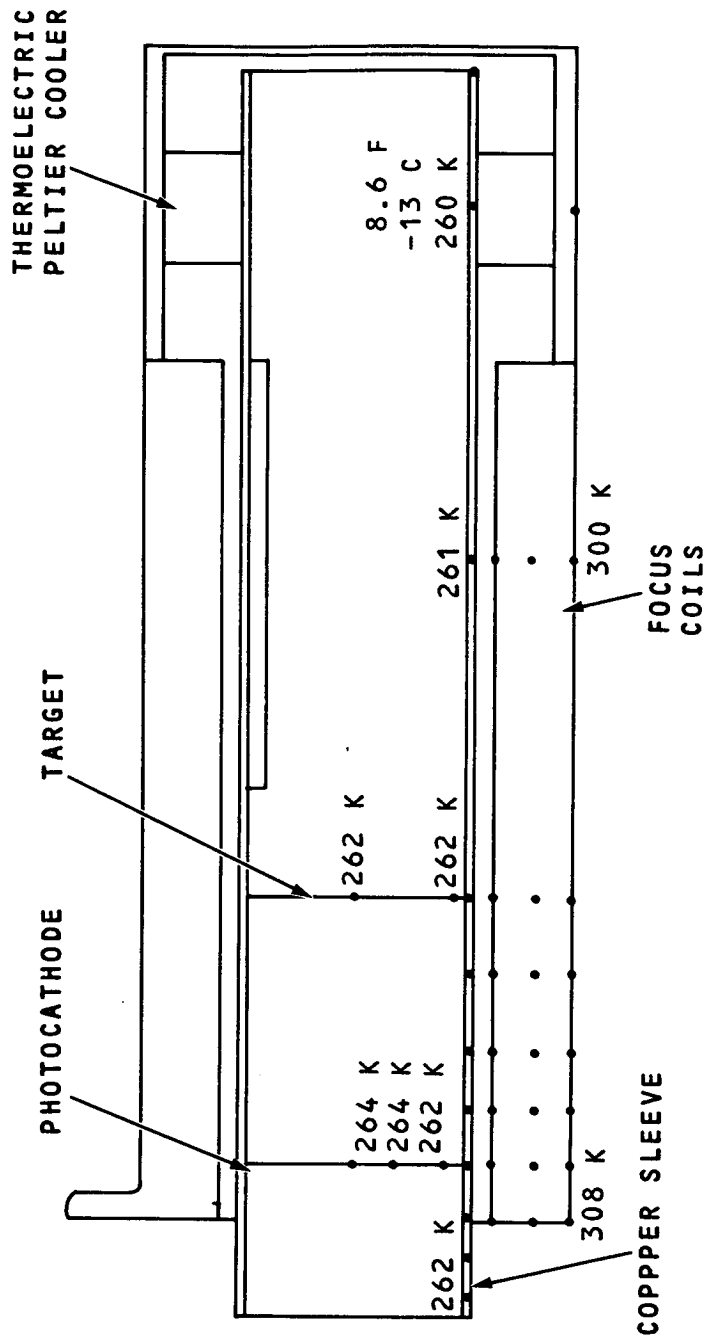


Figure 7-7. Temperature Distribution Case 1

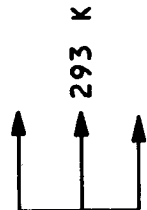
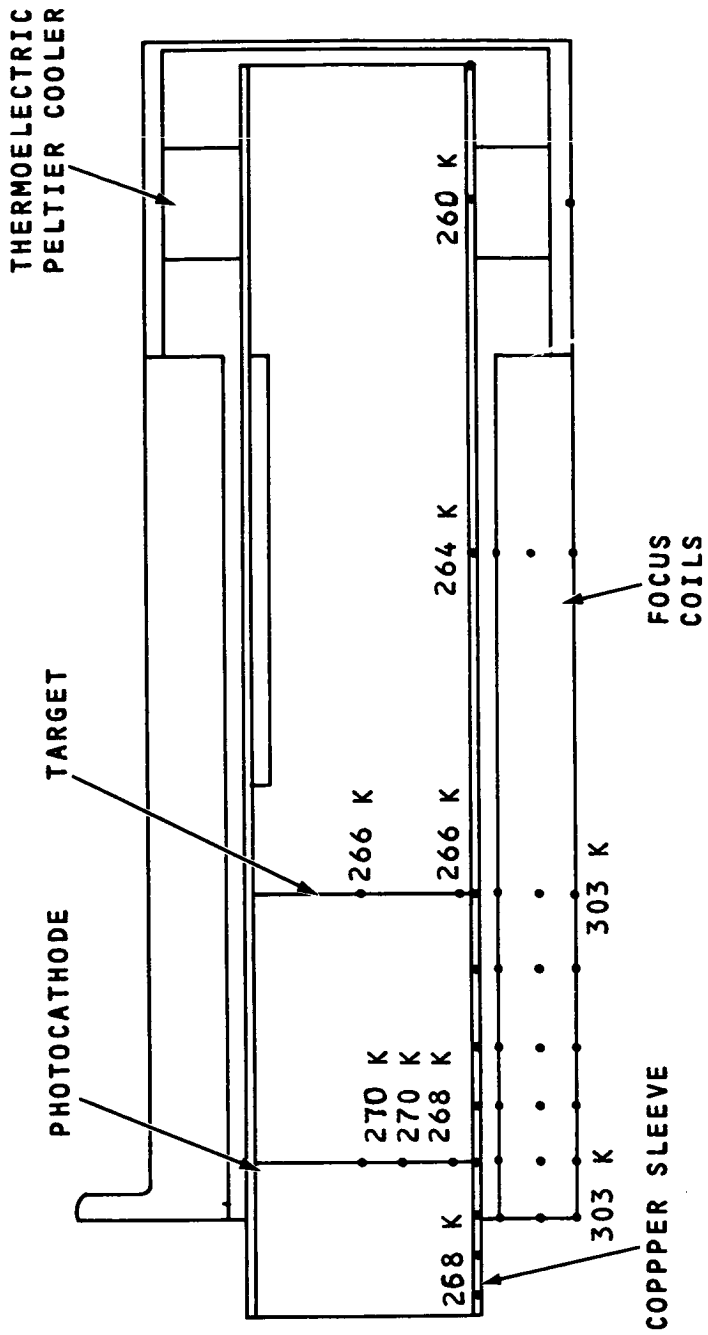


Figure 7-8. Temperature Distribution Case 2

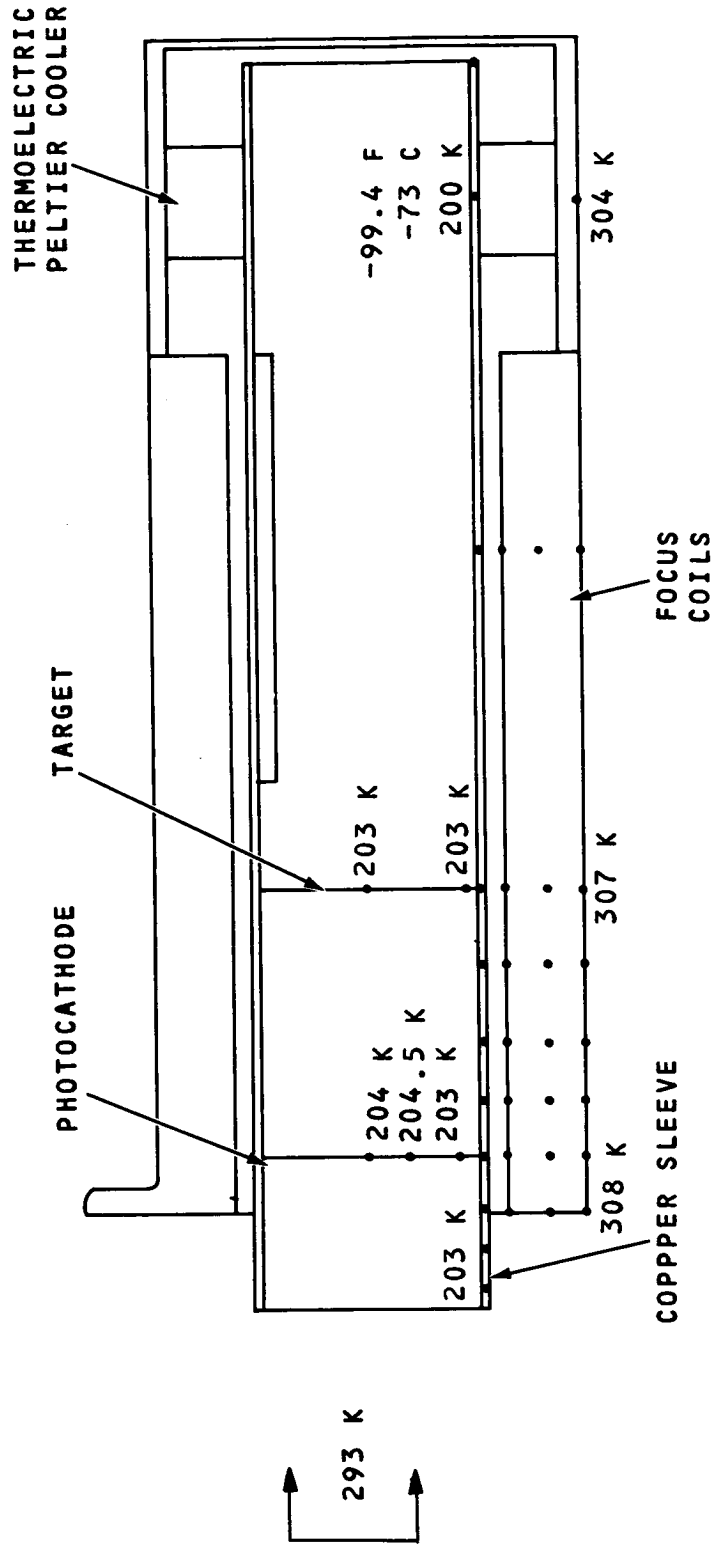


Figure 7-9. Temperature Distribution Case 3

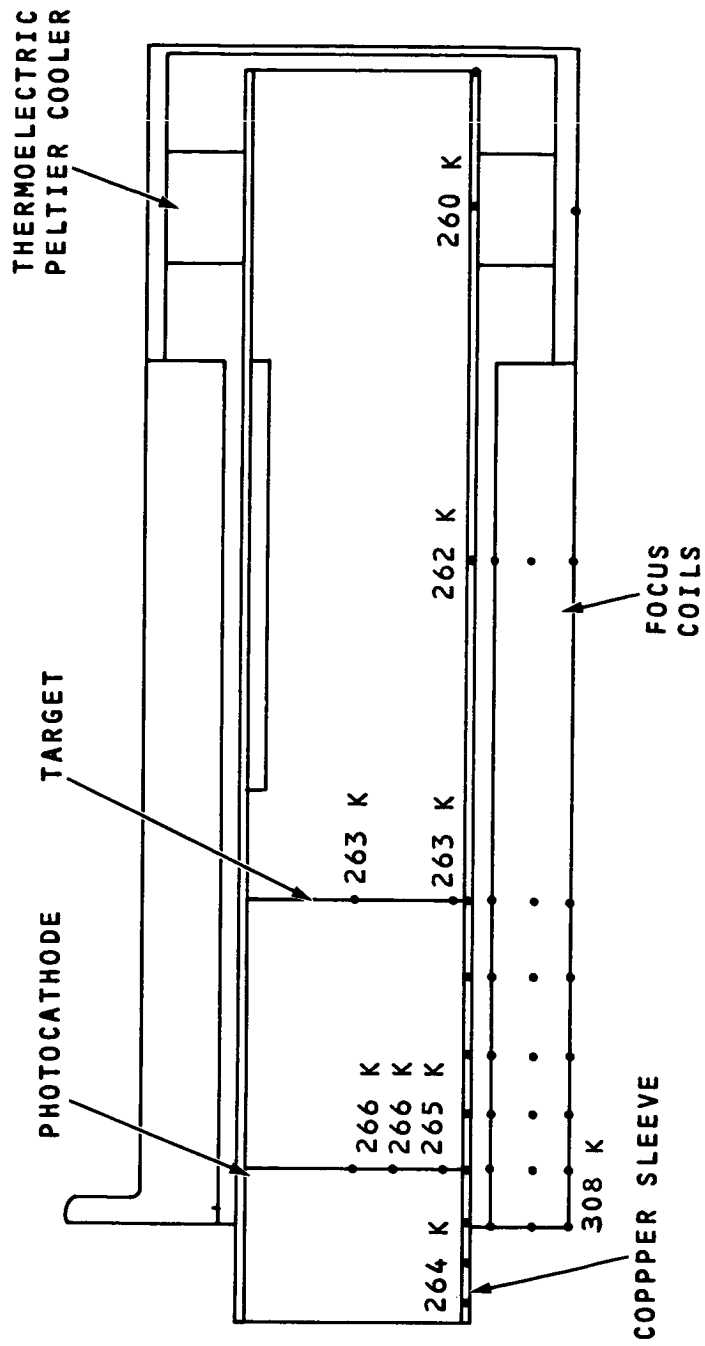


Figure 7-10. Temperature Distribution Case 4

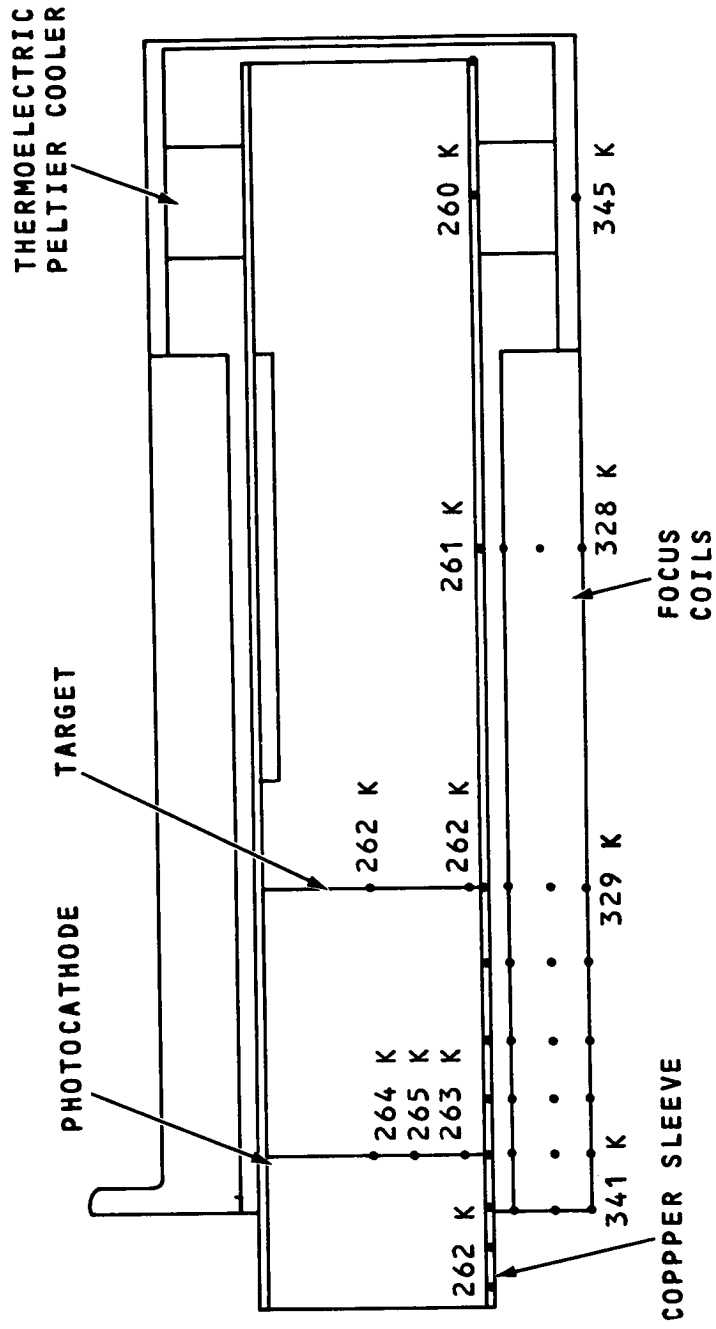


Figure 7-11. Temperature Distribution Case 5

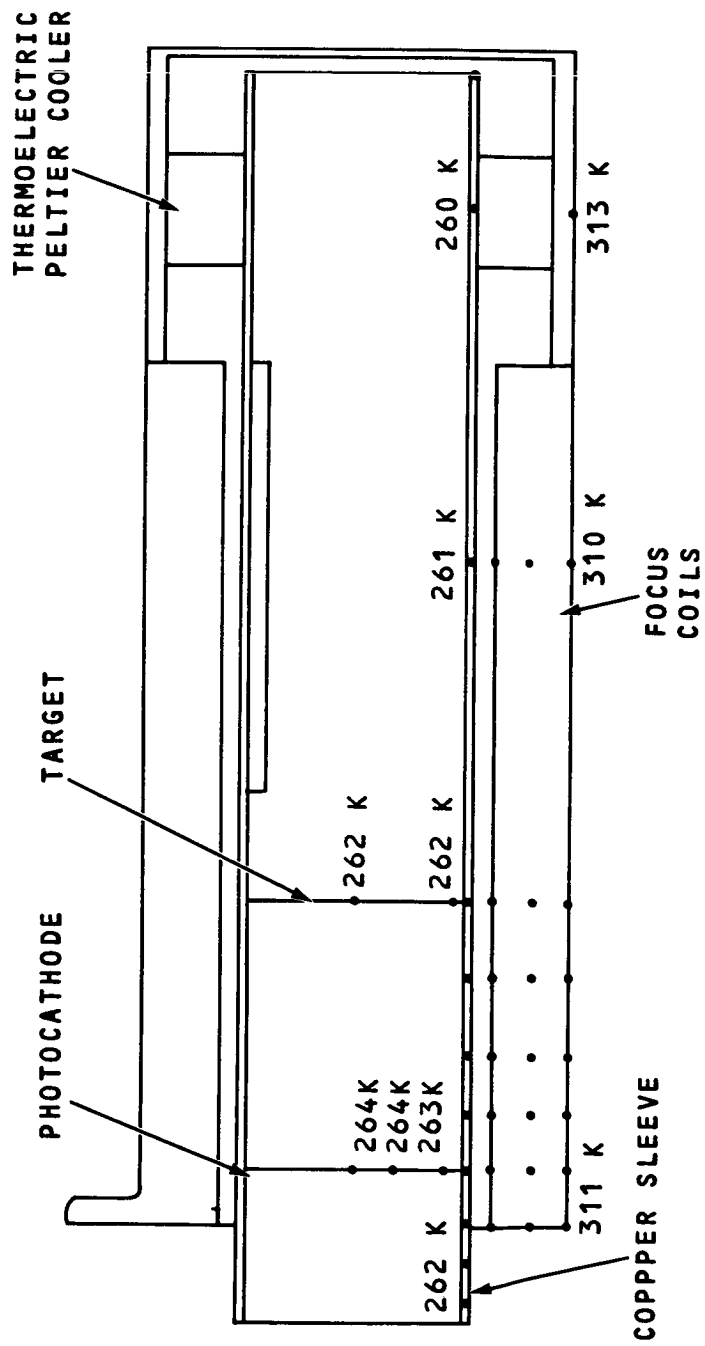


Figure 7-12. Temperature Distribution Case 6

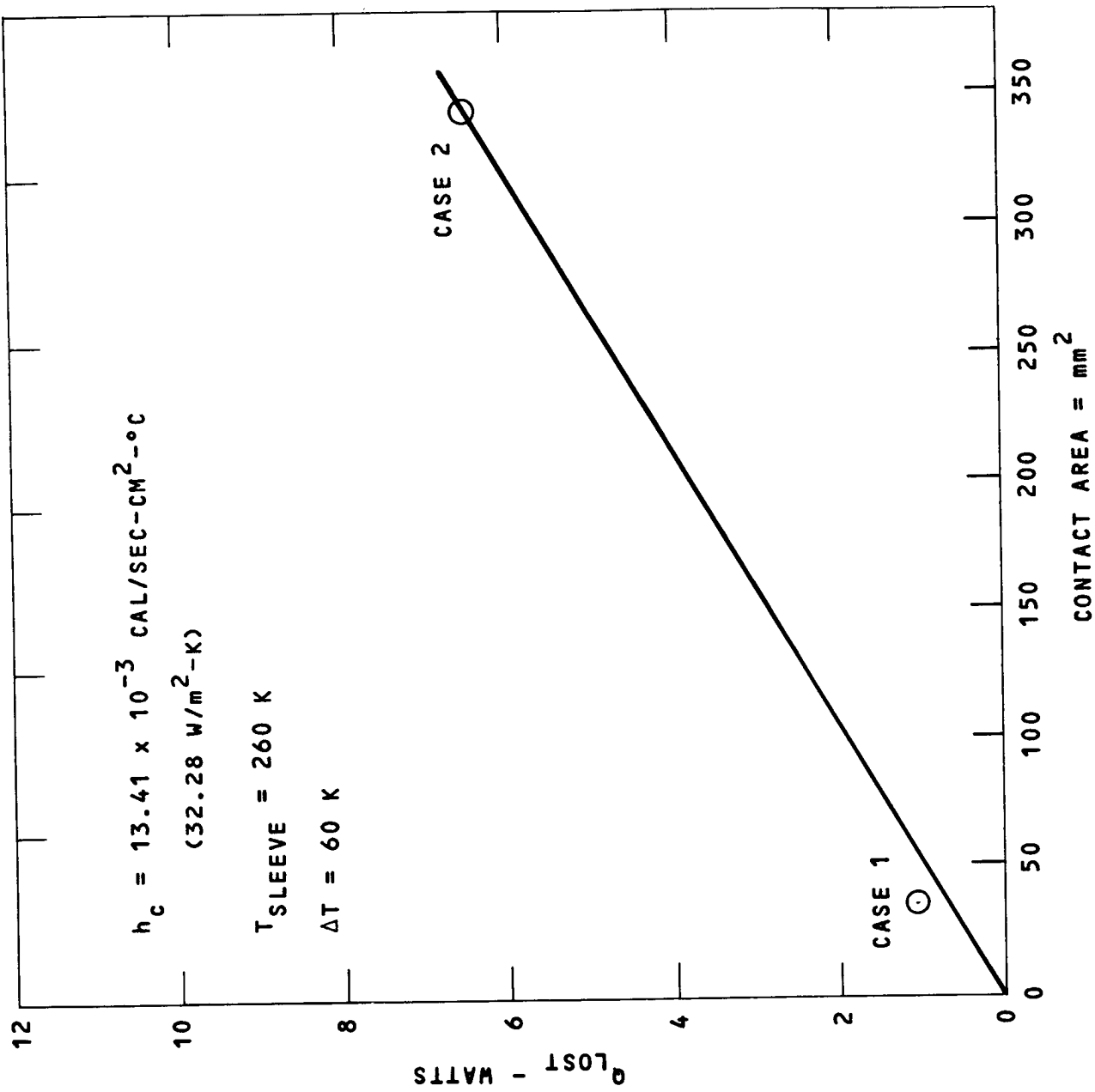


Figure 7-13. Power Lost Thru Contact Area Vs. Contact Area

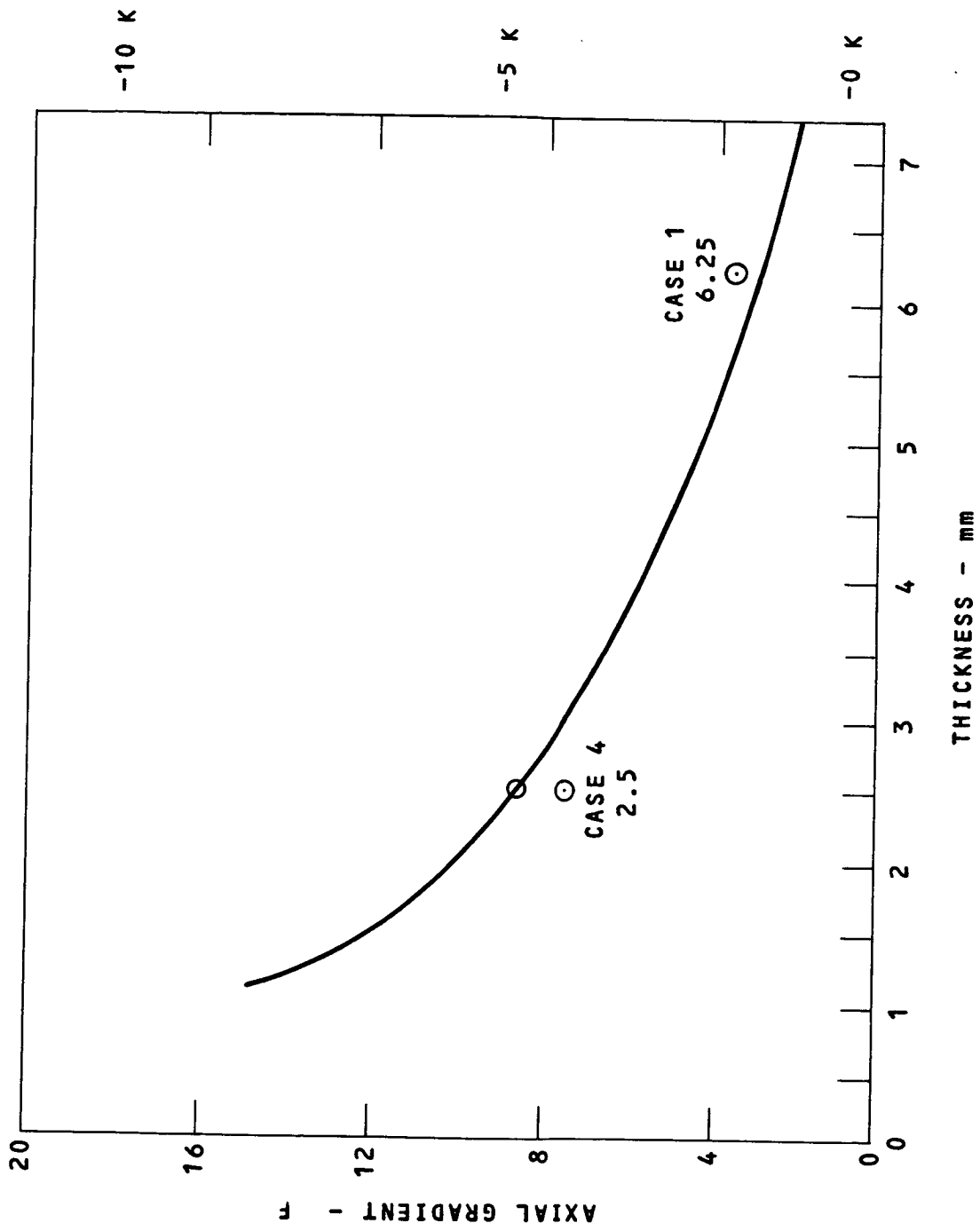


Figure 7-14. Axial Gradient on Conduction Sleeve Vs. Wall Thickness



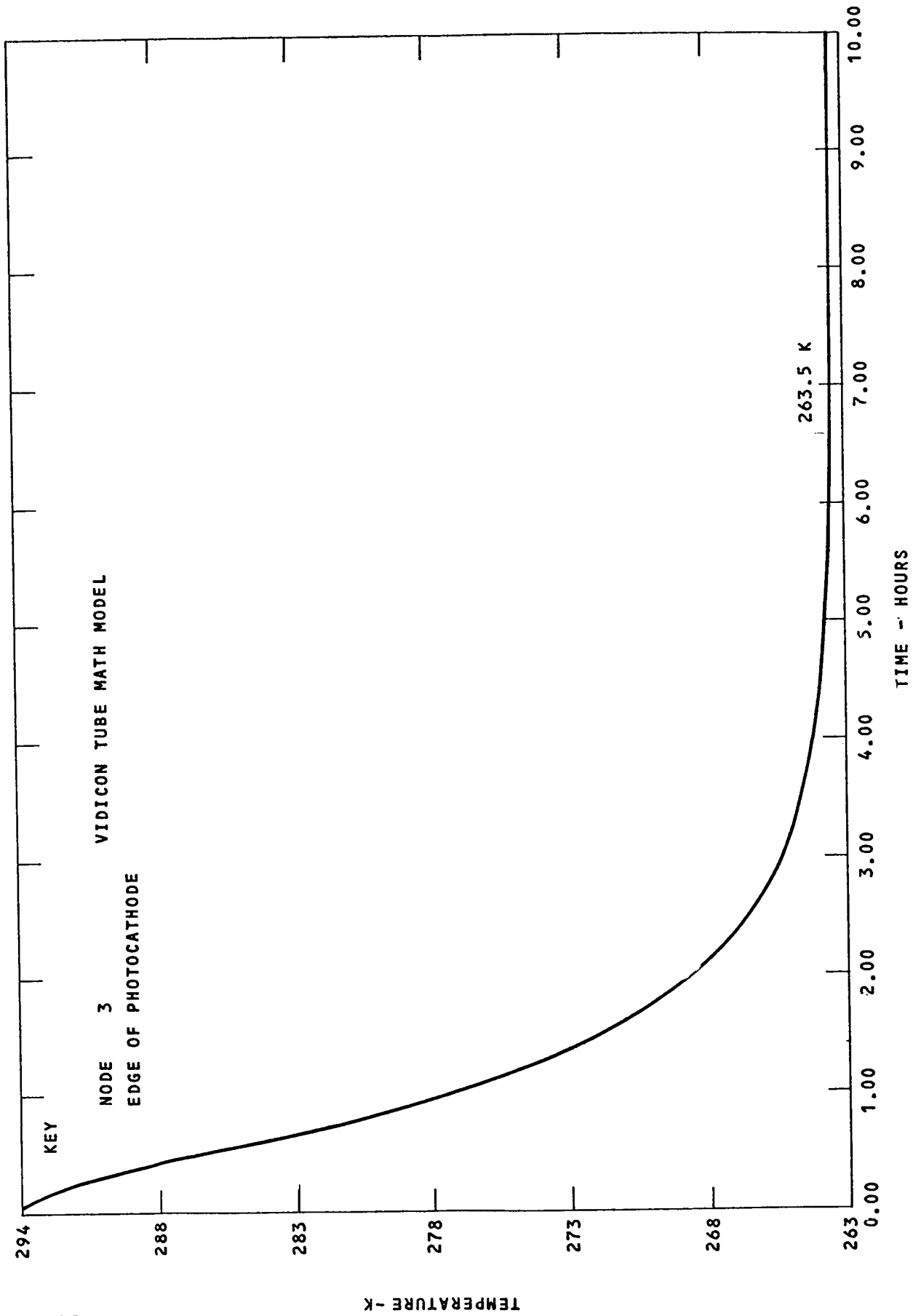


Figure 7-15. Temperature History

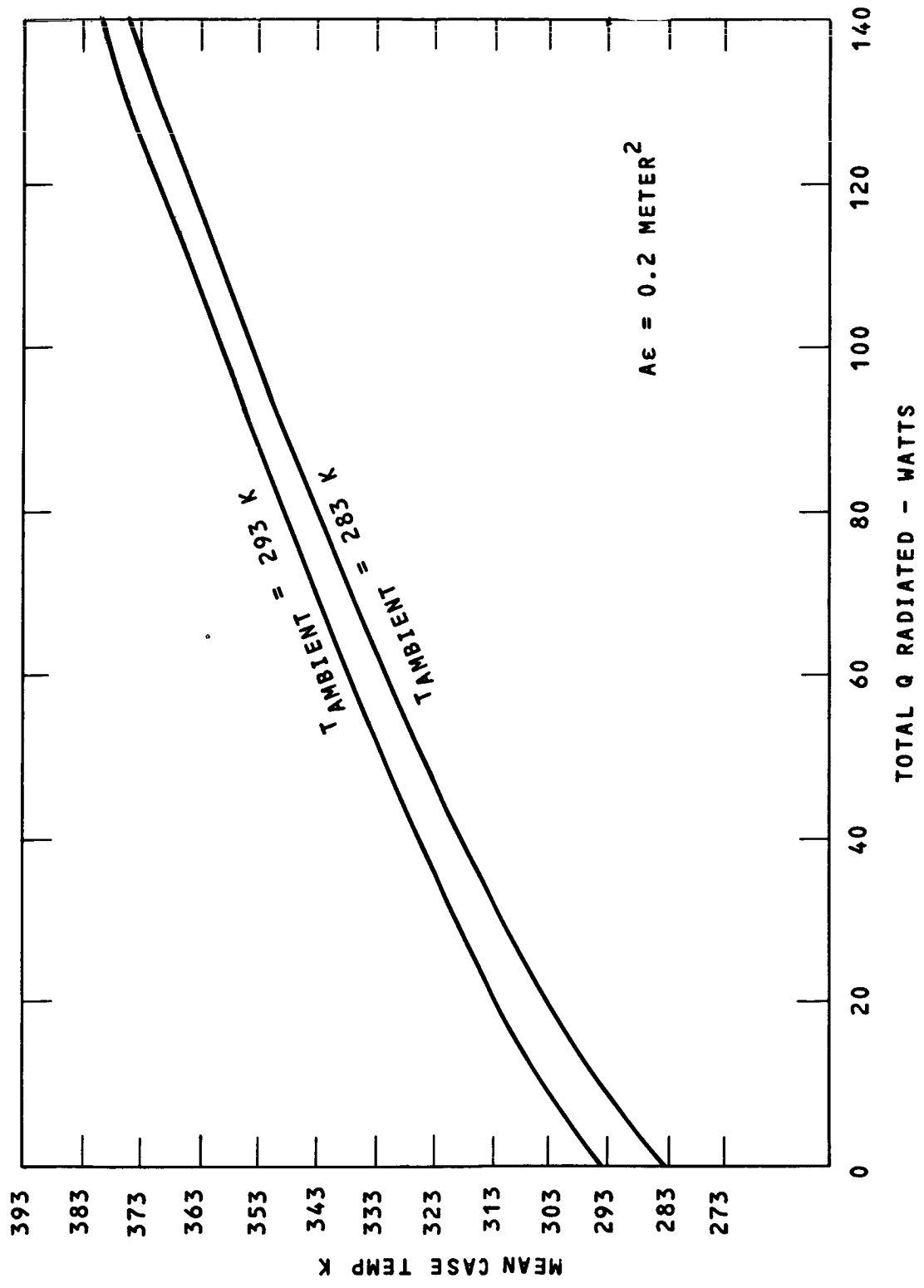


Figure 7-16. Focus Coil Case Temp. (Average Vs. P Radiated)

An energy balance on the camera assembly is shown in Figure 7-17. The total amount of cooling required has been estimated to be 8 watts. The three watts identified as lead loss (22 - #16 gage wire with a significant length of 10 inches) appears to be an area requiring further study since it is a significant contributor to the overall cooling requirement.

Referring to Figure 7-17, we note a temperature at the thermoelectric hot junction of 345 K. For an 80 K temperature drop (10 watts pumped at a 100 watt  $I^2R$  requirement) the resulting cold junction temperature would be 265 K. The cold junction estimated heat load of 8 watts would require an  $I^2R$  load of less than the assumed 100 watts. A load of less than 100 watts would lower the 345°K hot junction, and therefore move the cold junction toward the 260 ± 4 K design goal.

If the module is uncontrolled (full on-full off) with no control electronics in the system, the cold junction level will float and assume a temperature level somewhere around the design point. This level will also be influenced by the heat loss efficiency of the individual tube, the SIP temperature level (sink), and the tube duty cycle.

The question of EMI problems with large current surges near the focus and deflection coils was considered. The intention is to shield the thermoelectric cooler from the photocathode tube with MU metal. The Cambridge Thermionic Corporation has stated that the device will require 5-7 amps of current. High voltage-low current devices are currently under development and not available today. The modules can be placed in the annular volume in pairs which are 180° apart to provide for flux symmetry.

#### 7.2.9.6 Thermoelectric Vs. Heat Pipes for Camera Cooling

A theoretical solution to the problem of cooling the photocathode tube is to use heat pipes which mechanically attach to the tube sleeve, are routed through the pressure shell, and dump heat into a low temperature radiator which views deep space. The heat

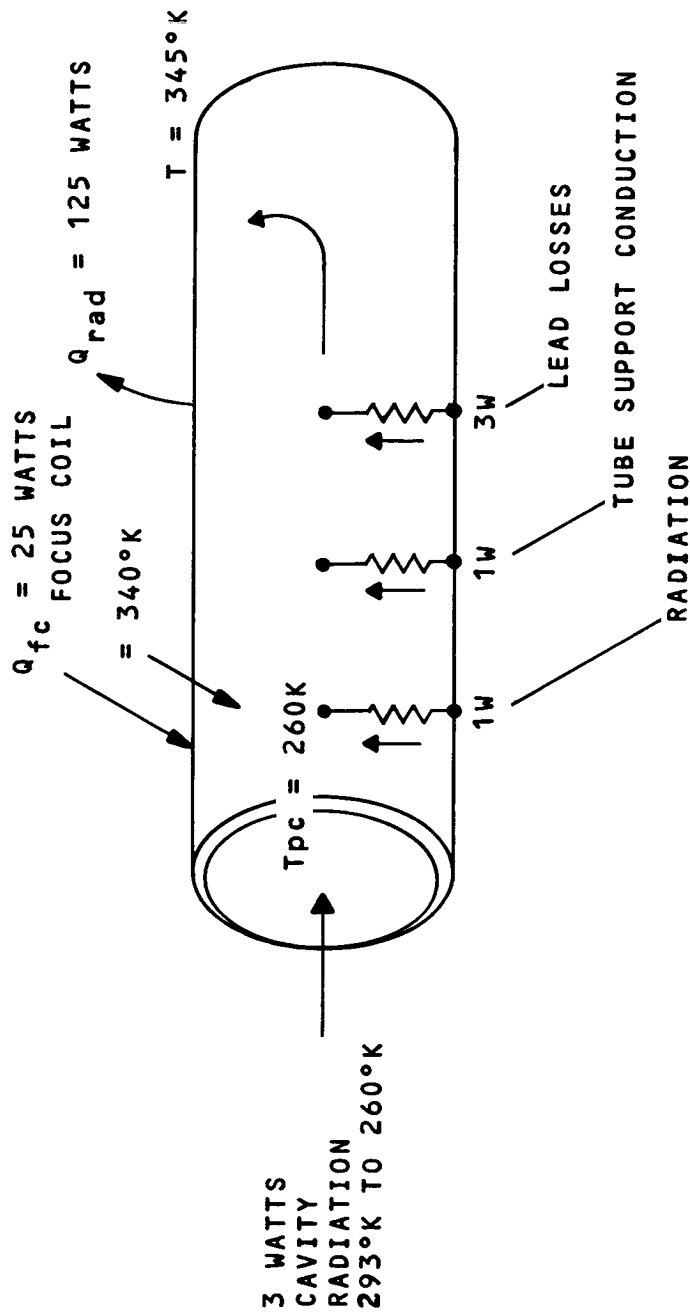


Figure 7-17. Camera Energy Balance

pipes would have to be variable conductance types for temperature control and employ feedback control. Two pipes per tube (may be required) x 10 cameras gives up to 20 heat pipes to be insulated and routed through the pressure vessel wall to various radiators which will experience variable external heat flux histories at various times in orbit. The heat pipes would have to make a dry, removable mechanical interface with each tube and would have to be flexible to a certain degree to allow for structural motions and for maintenance. Other problems with the use of heat pipes would be start-up problems, nucleate boiling in the evaporator section, unknown response, degradation of the radiator coatings, possible fluid leakage near precision optics, and detailed radiator design to allow the rejected heat to be spread from the local condenser section to the total radiator area.

As an alternate method, the implementation of a thermoelectric device to cool each tube would offer a much more sanitary design. The thermoelectric device would be soldered to both the cold tube and the hot external radiating area thus eliminating dry mechanical interface at the devices. A small electronics package, remotely mounted, and a temperature sensor at the tube would be required to modulate the electrical energy flow to the thermoelectric device. It has been estimated that the temperature controller electronics would dissipate less than 10 watts of power. A two stage cascaded thermoelectric module would be required to impress a temperature difference of 80 K hot junction to cold junction while pumping 10 watts maximum (Cambridge Thermionic Corporation).

Thermoelectrics employing a controller can maintain a temperature level of  $\pm 0.1$  K. The penalties associated with thermoelectric modules are a high power dissipation (50 to 100 watts at the device and 10 watts at the controller) and a high temperature  $340^{\circ}\text{K}$  surface on the focus coil exterior radiating to adjacent instruments. These penalties appear small when compared to heat pipe plumbing problems and heat pipes and radiator weight penalties.

#### 7.2.9.7 Suggested Future Work

At this time, basic thermal design studies have been completed and a conceptual design has been presented. It is recognized that the design is not complete and that certain possible problem areas have not been fully evaluated. The following areas of interest are suggested for future work:

1. Continue refinement of Peltier cooler design and operation to completely understand both transient and normal operating characteristics.
2. Concentrate on the design of the external camera package to reduce external gradients resulting from thermoelectric operation. Consideration of the following is suggested:
  - a. Increase the radiating area and improve view factor to cold walls.
  - b. Increase wall thickness of the focus coil external case and/or its thermal conductivity.
  - c. Bridge the mechanical gap between the focus coil split plane and the tube which is connected to the thermoelectric hot junction with braided copper straps or other means to reduce thermal resistance.
  - d. Support the focus coils by a high conductivity sleeve to help spread the  $I^2R$  power toward the front of the tube.
  - e. Decrease the  $I^2R$  power required by lowering the hot junction temperature which will thereby increase the efficiency of the thermoelectric module.
  - f. Lower the SIP compartment ambient temperature.

### 7.3 STRUCTURAL CONSIDERATIONS

Structural integrity and stability of the experiments within the instrument section will depend on the ability of the primary support structure and component support structures to survive the launch dynamic environments. These dynamic environments usually include sinusoidal vibration, random vibration, shock and acoustic noise. Representative dynamic input data is given in Section 7.3.1 for the LST payload launch.

Since these induced loads will be inputted to the spacecraft, the results of structural dynamic analysis of the spacecraft can be used to generate an equivalent dynamic environment at component locations. These local dynamic loadings will be used to evaluate the structural integrity of component modules and internal support structure within the instrument section. During the development program a detailed structural dynamic and stress analysis will be performed on each instrument package to assure the structural integrity of the instruments. A preliminary structures analysis is shown for the f/96 camera assembly to illustrate the techniques used in this analysis. Stress analyses are also shown for a typical High Resolution Spectrograph and a Faint Object Spectrograph.

#### 7.3.1 Dynamic Environments

The anticipated launch dynamic environments have been indicated in a Martin Marietta Corporation document, entitled "Environmental Constraints" MMC-LST-7, March 1972. The following levels have been given for both a Titan III-D launch and a shuttle launch and are assumed as inputs to the LST.

	<u>Titan III-D</u>	<u>Shuttle</u>
Random Vibration	50-500 Hz; +3 db/oct	20-50 Hz; +6 db/oct
	500-1000 Hz; 0.012 g <sup>2</sup> /Hz	500-300 Hz; 0.6 g <sup>2</sup> /Hz
	1000-2000 Hz; -8 db/oct	300-2000 Hz; -6 db/oct

	<u>Titan III-D</u>	<u>Shuttle</u>
Shock	150 g at 4000 Hz (SSM/LST interface)	TBD
Acoustic Pressure	145 db (overall)	152 db (overall)
Load Factors		
Longitudinal	+6.0 g	+3.5 g
Lateral	+1.5 g	-4.0 g

An evaluation of the effect of the shock requires the complete shock spectra. Therefore an assumption is made using the shock spectra for a one-half sine shock pulse. In this case, a peak shock amplitude of 150 g at 4000 Hz is equivalent to an 83 g one-half sine pulse of 0.2 millisecond duration. The peak amplitude in this shock spectra is related as follows:  $\ddot{y}_{\text{peak}}/\ddot{y}_0 = 1.8$  at

$f_n/f_p = 1.6$ , where  $f_n = 4000$  Hz,  $f_p = 1/2 (.0002) = 2500$  Hz,

$\ddot{y}_{\text{peak}} = 150$  g's.  $\ddot{y}_0 = 83$  g's.

### 7.3.2 Stability of Instruments

Due to the requirements and necessary accuracies of the optical instrumentation within the LST, the locations and orientations of the various components must be retained within the allowed optical tolerances after launch and during orbit. It is assumed that these tolerances will not be exceeded if the stresses are within the PEL of the structure material. The primary environmental factors which must be considered in assuring the stability of the instrumentation, are those structural loads induced by launch vibrations, separation shock and acoustic noise and the effects on structure and instruments due to thermal variations in orbit.

### 7.3.3 Design Criteria

While it is anticipated that the structure supporting the instrument modules can be adequately designed to survive the launch



vibrations and acoustic noise (see section 8), additional consideration must be given to assure stability of the instrument components.

Design stresses usually used to assure structural integrity are based upon a fraction of the yield strength (elastic limit) or endurance limit of the various structural materials. However, it has been established that at stresses substantially less than the elastic limit, microyielding occurs in the structure resulting in permanent deformations. The stress at which a permanent (plastic) strain of  $1.0 \times 10^{-6}$  m/m results, has been designated the precision elastic limit (PEL) of the material. Typical values of the PEL for several materials are shown in the following table compared to the yield strengths (1).

<u>Material</u>	<u>PEL</u>		<u>Yield Strength</u>	
	<u><math>10^6 \text{N/m}^2</math></u>	<u>(PSI)</u>	<u><math>10^6 \text{N/m}^2</math></u>	<u>(PSI)</u>
2024-T6 Aluminum	172.4	(25,000)	400	(58,000)
A356-T6 Aluminum	82.7	(12,000)	206.8	(30,000)
6AL-4V Titanium	482.6	(70,000)	896.3	(130,000)
Hot-Pressed Beryllium (S-200)	13.8	(2,000)	137.9	(20,000)
*Graphite-Epoxy	482.6	(70,000**)	1034.2	(150,000 (approx))

\*Added for comparison

\*\*Assumed similar to endurance limit stress ( $10^7$  cycles).

Thus to avoid this possible source of instability of the optical instruments, the component mounting structures as well as the main bulkhead interface structure, comprising structure of the radial and axial compartments, should not be stressed above the PEL of the material.

(1) Maringer, R.E., "Review of Dimensional Instability in Metals"  
DMIC Memo - Randum 213, June 23, 1966 (Table 1).

#### 7.3.4 Material Properties

For the following structural evaluation the physical and mechanical properties of aluminum casting alloy (A356-T6) are used. However graphite-epoxy composite is being considered as an alternative, in special areas, due to its excellent strength/weight ratio, high modulus of elasticity and low thermal coefficient of expansion (see discussion of this material in Section 8 ). A comparison of Aluminum Casting Alloy (A356-T6) and graphite epoxy is given in Table 7-9.

#### 7.3.5 Structural Analysis

A preliminary structures analysis is performed on the f/96 camera structure to show the structural integrity of the design and to illustrate the techniques used in performing the analysis. The results of analysis include natural frequencies and mode shapes, dynamic responses, frequency response (transmissibility), dynamic loads, and stresses.

##### 7.3.5.1 Math Model

A schematic of the f/96 camera assembly is shown in Figure 7-18-(a), which indicates a three point mount for the structure. A preliminary design concept had the two rear support tabs (B and C) located at axial location (J) in the Figure. However, a preliminary analysis indicated that stresses induced in the support tube exceeded allowable quantities. Therefore to conserve the basic geometry (i.e. avoid increases in material thickness and weight) and to reduce stresses, the rear support tabs (B and C) were located as shown in Figure 7-18-(a).

A preliminary design concept is to minimize redundant restraint induced loads at the support tab attachments by using a kinematic mounting technique. This technique will prevent warpage of the structure due to thermal variations by allowing axial movement at the rear tabs (B and C) and will minimize bending moments at tabs (B) and (C).

TABLE 7-9. COMPARISON OF ALUMINUM (A356-T6) WITH GRAPHITE-EPOXY

	Aluminum (A356-T6)		GRAPHITE EPOXY	
	<u>SI</u>	<u>ENGLISH</u>	<u>SI</u>	<u>ENGLISH</u>
Density $\text{Kg/m}^3$ ( $\text{Lb/in}^3$ )	6.96	(0.097)	4.02	(0.056)
Youngs Modulus $\text{N/m}^2$ (PSI)	$68.9 \times 10^9$	( $10 \times 10^6$ )	$137.9 \times 10^9$	( $20 \times 10^6$ (approx))
Ultimate Tensile Strength $\text{N/m}^2$ (PSI)	$275.8 \times 10^6$	(40,000)	$1379 \times 10^6$	(200,000)
Yield Strength $\text{N/m}^2$ (PSI)	$206.8 \times 10^6$	(30,000)	$1034 \times 10^6$	(150,000 (approx))
Endurance Limit - $\text{N/m}^2$ (PSI)	$89.6 \times 10^6$	(13,000)	$482.6 \times 10^6$	(70,000)
Precision Elastic Limit - $\text{N/m}^2$ (PSI)	$82.7 \times 10^6$	(12,000)	$482.6 \times 10^6$	(70,000*)
Longitudinal Coefficient of thermal expansion, $10^{-6} \text{ m/m}^\circ\text{K}$ (IN/IN $^\circ\text{F}$ )	21.4	(11.9)	-0.72	(-0.4)
Transverse Coefficient of thermal expansion, $10^{-6} \text{ m/m}^\circ\text{K}$ (IN/IN $^\circ\text{F}$ )	21.4	(11.9)	32.4	(18)
Longitudinal Thermal Conductivity, WATTS- $\text{m/m}^2/\text{K}$ (BTU-ft/ $\text{ft}^2/\text{hr}$ )	159	(92)	48.4	(28)
Transverse Thermal Conductivity, WATT- $\text{m/m}^2/\text{K}$ (BTU-ft/ $\text{ft}^2/\text{hr}$ )	159	(92)	1.38	(0.8)
Specific Heat, Joule/Kg/K (BTU/Lb/ $^\circ\text{F}$ )	921.8	(0.22)	879.9	(0.21)

\*Assumed equal to Endurance Limit Stress

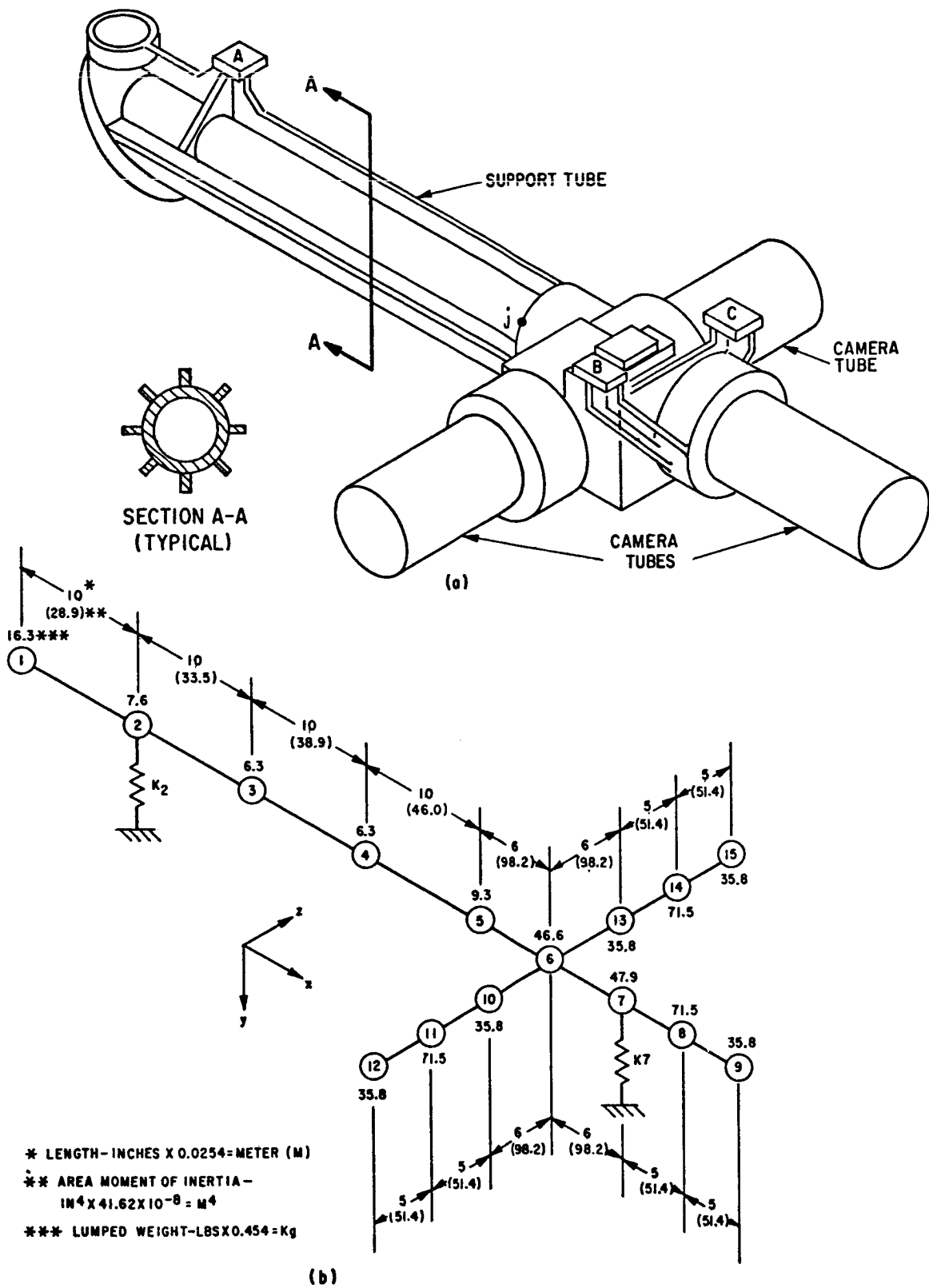


Figure 7-18. f/96 Camera Structure Model

A simplified equivalent beam lateral (y) axis structural model has been generated, which includes fifteen lumped mass degrees of freedom as shown in Figure 7-18-(b).

The following assumptions have been made:

(a) Lumped mass equivalent beam representation of support structure and cameras - only the structural envelopes are considered, treating all internal components such as mirror drive assembly, camera components, and optics as rigid masses.

(b) Simple supports at tab locations, assuming no effect of offset of tab interface from structural tube axis. Tabs (B) and (C) are combined into a single support due to Z axis symmetry of the tabs with respect to the tube centerline.  $K_2$  and  $K_7$  are tab spring rates along the y axis.

(c) Torsion about the X axis is neglected for this case and rotary inertia effects about the Z axis are also neglected at this time. However shear deformations are accounted for where applicable.

A more detailed model will be developed during Phase (B), accounting for all critical internal components and support structure.

The following analyses assume aluminum as the structural material; however, a comparison of significant results based upon use of graphite-epoxy as the structural material is shown in Section 7.3.5.9 (Table 7-10).

#### 7.3.5.2 Structural Characteristics

The structural definition of the equivalent beam model, shown in Figure 7-18-(b), was obtained using the method of influence coefficients. That is, the deflection at all mass points (j) are obtained for an applied unit load at mass point (i) and the results combined into an influence coefficient matrix.

The variable section properties (area moments of inertia) in the beam model are shown in Figure 7-18-(b). The beam cross sections from mass points (1) to (5) are typically that indicated as section (A-A) in Figure 7-18-(b). The remaining cross sections including the camera housings are considered tubular. Using the computer program (MTRIX) in conjunction with the material characteristics for aluminum (Table 7-8), and the geometry and section properties indicated in Figure 7-18-(b), the influence coefficient matrix shown in Figure 7-19 was developed.

### 7.3.5.3 Natural Frequencies and Mode Shapes

The natural frequencies and mode shapes are obtained by solving the Eigen Value problem.

$$[C] [W] \{v\} = \frac{g}{w^2} \{v\}$$

where

[C] = influence coefficient matrix - Figure 7-19

[W] = Weight matrix (Figure 7-20) Weight values at lumped mass points, shown in Figure 7-18-(b), are arranged in a diagonal matrix form; these values are based upon percentage of structural and component weights in vicinity of mass point locations.

{v} = Mode Shape (Eigenvector)

$w^2$  = frequency (rad/sec)

g = gravity constant

Results of computer program (MS3) yielded the natural frequencies and mode shapes shown in Figure 7-20, which includes the first nine modes of vibration.

COLUMN	P <sub>Y1</sub>	P <sub>Y2</sub>	P <sub>Y3</sub>	P <sub>Y4</sub>	P <sub>Y5</sub>	P <sub>Y6</sub>	P <sub>Y7</sub>	P <sub>Y8</sub>	P <sub>Y9</sub>
Y 1	0.613910	0.247620	-0.226380	-0.262810	-0.170690	-0.885270	-0.109330	0.520990	0.118400
Y 2	0.247620	0.200000	0.152380	0.104760	0.571400	0.285800	0.0	-0.238000	-0.476200
Y 3	-0.226380	0.152380	0.272860	0.294750	0.188120	0.972430	0.109330	-0.593580	-0.132920
Y 4	-0.262810	0.104760	0.294750	0.437600	0.293370	0.293370	0.219050	-0.842050	-0.196790
Y 5	-0.170690	0.571400	0.188120	0.293370	0.266050	0.142540	0.328580	-0.538340	-0.150180
Y 6	-0.885270	0.285800	0.972430	0.153050	0.142540	0.101270	0.394270	-0.649750	-0.639600
Y 7	-0.109330	0.0	0.109330	0.219050	0.328580	0.394270	0.460000	0.514740	0.569330
Y 8	0.520990	-0.238000	-0.593580	-0.842050	-0.538340	-0.649750	0.514740	0.151990	0.214930
Y 9	0.118400	-0.476200	-0.132920	-0.196790	-0.150180	-0.639600	0.569330	0.214930	0.401180
Y 10	-0.885260	0.285800	0.972430	0.153050	0.142540	0.101270	0.394270	-0.649750	-0.639600
Y 11	-0.885260	0.285800	0.972430	0.153050	0.142540	0.101270	0.394270	-0.649750	-0.639600
Y 12	-0.885260	0.285800	0.972430	0.153050	0.142540	0.101270	0.394270	-0.649750	-0.639600
Y 13	-0.885260	0.285800	0.972430	0.153050	0.142540	0.101270	0.394270	-0.649750	-0.639600
Y 14	-0.885260	0.285800	0.972430	0.153050	0.142540	0.101270	0.394270	-0.649750	-0.639600
Y 15	-0.885260	0.285800	0.972430	0.153050	0.142540	0.101270	0.394270	-0.649750	-0.639600

COLUMN	P <sub>Y10</sub>	P <sub>Y11</sub>	P <sub>Y12</sub>	P <sub>Y13</sub>	P <sub>Y14</sub>	P <sub>Y15</sub>
Y 1	-0.885260	-0.885260	-0.885260	-0.885260	-0.885260	-0.885260
Y 2	0.285800	0.285800	0.285800	0.285800	0.285800	0.285800
Y 3	0.972430	0.972430	0.972430	0.972430	0.972430	0.972430
Y 4	0.153050	0.153050	0.153050	0.153050	0.153050	0.153050
Y 5	0.142540	0.142540	0.142540	0.142540	0.142540	0.142540
Y 6	0.101270	0.101270	0.101270	0.101270	0.101270	0.101270
Y 7	0.394270	0.394270	0.394270	0.394270	0.394270	0.394270
Y 8	-0.649750	-0.649750	-0.649750	-0.649750	-0.649750	-0.649750
Y 9	-0.639600	-0.639600	-0.639600	-0.639600	-0.639600	-0.639600
Y 10	0.102270	0.102270	0.102270	0.102270	0.102270	0.102270
Y 11	0.102570	0.144490	0.157420	0.101270	0.101270	0.101270
Y 12	0.102870	0.157420	0.236220	0.101270	0.101270	0.101270
Y 13	0.101270	0.101270	0.101380	0.101380	0.101680	0.101990
Y 14	0.101270	0.101270	0.101270	0.101680	0.143640	0.156590
Y 15	0.101270	0.101270	0.101270	0.101990	0.156590	0.235450

\* IN/LB X 0.005T1 = M/N

Figure 7-19. Influence Coefficient Matrix

[W] [LBS] x 0.454 = kg

0.163000 C2 0.760000 O1 C.630000 C1 0.630000 O1 0.930000 O1 0.479000 O2 0.715000 O2 0.358000 O2  
 0.358000 C2 0.715000 C2 C.358000 O2 0.358000 O2 0.715000 O2 0.479000 O2 0.715000 O2 0.358000 O2

NATURAL FREQUENCIES (Hz)

0.145070 C3 0.212030 O3 0.336310 C3 0.376630 O3 0.563990 O3 0.796300 O3 0.959660 O3 0.596280 O3 0.114830 C4

MODE SHAPE(S(EIGENVECTORS) {V}

COLUMN	1	2	3	4	5	6	7	8	9									
1	-0.702170	00	0.157130	00	C.100000	O1	0.159850	-01	0.451770	00	0.204800	00	0.137610	00	0.890630	-02	0.800050	-01
2	0.134700	-01	-0.337850	-02	0.516510	-01	0.119830	-02	0.110750	00	0.140360	00	0.165020	00	0.122620	-01	0.187450	00
3	0.666340	00	-0.130670	00	-0.255110	00	-0.564010	-03	0.627700	00	0.884200	00	C.100000	C1	C.724830	-01	0.100000	O1
4	0.100000	O1	-0.146880	00	-0.206140	00	0.262160	-02	0.100000	O1	0.100000	O1	0.907900	00	0.557040	-01	0.511280	00
5	0.863330	00	-0.909150	-02	-0.440450	-01	0.457250	-02	0.813280	00	0.335290	00	0.118550	00	-0.256560	-02	-0.478220	00
6	0.553900	00	0.144390	00	0.152790	-01	0.436030	-02	0.469560	00	-0.924750	-01	-0.786360	-01	-0.149380	-01	-0.413560	00
7	0.139010	-01	0.323110	-01	0.267790	-03	0.238410	-03	0.229130	-01	-0.145310	-01	-0.826700	-02	-0.128670	-02	-0.327570	-01
8	-0.228510	00	0.695640	00	-0.482430	-01	0.104680	-02	0.165280	00	-0.185010	00	0.726650	00	0.365300	-01	0.204430	00
9	-0.650560	00	0.100600	O1	-0.111540	00	-0.148810	-02	-0.688690	-01	0.326680	00	-0.847830	00	-0.418540	-01	-0.232800	00
10	0.556410	00	0.146070	00	C.166240	-01	-0.109770	-01	0.459910	00	-0.930100	-01	-0.922150	-01	0.172260	-01	-0.405320	00
11	0.625450	00	0.193680	00	0.590370	-01	-0.519050	00	-0.472850	-01	-0.624700	-01	-0.364490	00	C.930680	00	0.434870	00
12	0.679260	00	0.232080	00	C.970340	-01	-0.996500	00	-0.728270	00	0.121230	00	C.411970	00	-0.567900	00	-0.346240	00
13	0.554710	00	0.144950	00	0.157520	-01	0.103460	-01	0.463540	00	-0.918960	-01	-0.799780	-01	-0.178030	-01	-0.410270	00
14	0.623610	00	0.192260	00	C.561080	-01	0.920480	00	-0.472440	-01	-0.011500	-01	-0.315730	00	-0.561490	00	0.440160	00
15	0.677330	00	0.230430	00	0.922730	-01	0.100000	O1	-0.733260	00	0.118600	00	0.356850	00	0.100000	O1	-0.350540	00

Figure 7-20. Natural Frequencies and Mode Shapes



#### 7.3.5.4 Dynamic Response

A prediction of dynamic response of the f/96 camera to random vibration and shock is made based upon the levels in Section 7.2.1. The shuttle launch random vibration and Titan III-D separation shock are examined in the following response analyses.

The actual vibration and shock levels experienced by the f/96 camera assembly will be attenuated through the SIP structure (SIP structure fundamental natural frequency is much less than that of the f/96 camera assembly) so that the resulting responses would be lower if the above vibration levels were used in the SIP structures analysis. In any case, the levels used are believed to be conservative and should be adequate to illustrate the structural integrity of the f/96 camera structure.

#### 7.3.5.5 Random Vibration

The acceleration response to random vibration can be obtained approximately, using the method of normal modes, by the expression

$$\{\ddot{q}_k\}_{\text{Peak}} = 3x \left[ \sum_{i=1}^n \frac{1.5708 f_i W_i(f) \eta_i^2 V_{ki}^2}{2\rho_i} \right]^{1/2}$$

where

- $f_i$  = natural frequency in  $i^{\text{th}}$  mode ( $i = 1, n$ )-Hz
- $W_i(f)$  = acceleration power spectral density at  $i^{\text{th}}$  mode frequency -  $G^2/\text{Hz}$
- $\eta_i$  =  $\{V_i\}^T\{W\} / \{V_i\}^T[W]\{V_i\}$  = modal participation factor in  $i^{\text{th}}$  mode.
- $V_{ki}$  = mode shape value in  $i^{\text{th}}$  mode
- $2\rho_i$  = damping factor in  $i^{\text{th}}$  mode
- $\ddot{q}_k$  = acceleration response of a particular degree of freedom,  $k$ .

Using the shuttle random PSD given in Section 7.2.1 and a damping factor,  $2\rho_i = 0.1$  for the first ten modes of vibration (note Figure 7-20), the peak accelerations computed by computer program DYNAM were obtained as shown in Figure 7-21.

#### 7.3.5.6 Shock

The shock responses are estimated, using the method of normal modes, from the following analytical expression; zero damping is assumed since this is the worst case.

$$\{\ddot{q}_k\} = \sum_{i=1}^n |\eta_i \bar{A}_i V_i| \quad (2)$$

where the symbols and subscripts are similar to those in Equation (1), except

$\bar{A}_i$  = shock spectra value at natural frequency  $f_i$ , obtained by assuming an 83 g's half sine shock pulse of 0.2 milli-second duration as discussed in Section 7.2.1.

The results of the shock analysis, obtained using computer program DYNAM are given in Figure 7-22.

#### 7.2.5.7 Frequency Response - Transmissibility

This analytical approach is based on the differential equations of motion for a damped multi-mass dynamic system, having  $n$  degrees of freedom, the solution of which can be written in the matrix form

$$\{q_i\} = [\beta]^{-1} [L]^T \{\delta_j\} + e^{-i\mu} [\beta]^{-1} [\alpha] \{\lambda_i\}$$

where

$$[\beta] = [I] - w^2 e^{-i\mu} [\alpha] [M]$$

TITL	ACCELERATION(G'S)		
	MS	RMS	PEAK
Y1	0.56071D 04	0.74880D 02	0.22464D 03
Y2	0.25978D 02	0.50969D 01	0.15291D 02
Y3	0.13285D 04	0.36449D 02	0.10935D 03
Y4	0.21436D 04	0.46299D 02	0.13890D 03
Y5	0.13376D 04	0.36573D 02	0.10972D 03
Y6	0.63348D 03	0.25169D 02	0.75507D 02
Y7	0.73528D 01	0.27116D 01	0.81348D 01
Y8	0.32368D 04	0.56893D 02	0.17068D 03
Y9	0.71631D 04	0.84635D 02	0.25391D 03
Y10	0.63872D 03	0.25273D 02	0.75819D 02
Y11	0.81918D 03	0.28621D 02	0.85864D 02
Y12	0.11910D 04	0.34511D 02	0.10353D 03
Y13	0.63443D 03	0.25188D 02	0.75564D 02
Y14	0.81068D 03	0.28472D 02	0.85417D 02
Y15	0.11798D 04	0.34349D 02	0.10305D 03

Figure 7-21. Peak Random Responses (Shuttle Launch Levels)

TITL	ACCELERATION(G'S)	DISPLACEMENT
		(IN.) x 0.0254 = Meter
Y1	0.48573D 02	0.67178D-02
Y2	0.18273D 02	0.33430D-03
Y3	0.87482D 02	0.51429D-02
Y4	0.74264D 02	0.68045D-02
Y5	0.66993D 02	0.48287D-02
Y6	0.24228D 02	0.37140D-02
Y7	0.32335D 01	0.26534D-03
Y8	0.31763D 02	0.51936D-02
Y9	0.45700D 02	0.90038D-02
Y10	0.24566D 02	0.37358D-02
Y11	0.18098D 02	0.42292D-02
Y12	0.31096D 02	0.51111D-02
Y13	0.24165D 02	0.37192D-02
Y14	0.17686D 02	0.42034D-02
Y15	0.30695D 02	0.50813D-02

Figure 7-22. Shock Response

$(q_i)_{i=1, n}$  = motion response of  $i^{\text{th}}$  degree of freedom

$(\delta_J)_{J=1, m}$  = motion input to base of structure

$n$  = number of mass point degrees of freedom

$m$  = number of motion input degrees of freedom  
( $1 \leq m \leq 6$ )

$e^{-i\mu}$  = complex damping modulus =  $\cos \mu - i \sin \mu$

$\mu$  = structural damping factor

$i$  = imaginary number  $\sqrt{-1}$

$[\alpha]$  = influence coefficient matrix ( $n \times n$ )

$[M]$  =  $\frac{1}{386}$  [W] ; [W] = weight matrix (LBS)

$\lambda_i$  = force input at  $i^{\text{th}}$  degree of freedom

$[L]^T$  = transpose of geometry matrix

$[L]$  = geometry matrix ( $m \times n$ ) - contains elements which are rigid body motions of the ( $n$ ) mass point degrees of freedom, resulting from a unit rigid body motion  $\{\delta_J = 1.0\}$  of the motion input at the base of the structure.

Computer program DYMJB is used to solve the above matrix equation for sinusoidal responses or transmissibility, based on motion or force excitation. A typical transmissibility plot is shown in Figure 7-23 for the aft end of the axial camera (mass point (9) - figure 7-18).

#### 7.2.5.8 Dynamic Loads

The dynamic load distribution is obtained by multiplying the response acceleration (g's) by the value of weight at each of the lumped mass points in Figure 7-18. Noting the acceleration responses in Figures 7-21 and 7-22, the results using the more severe

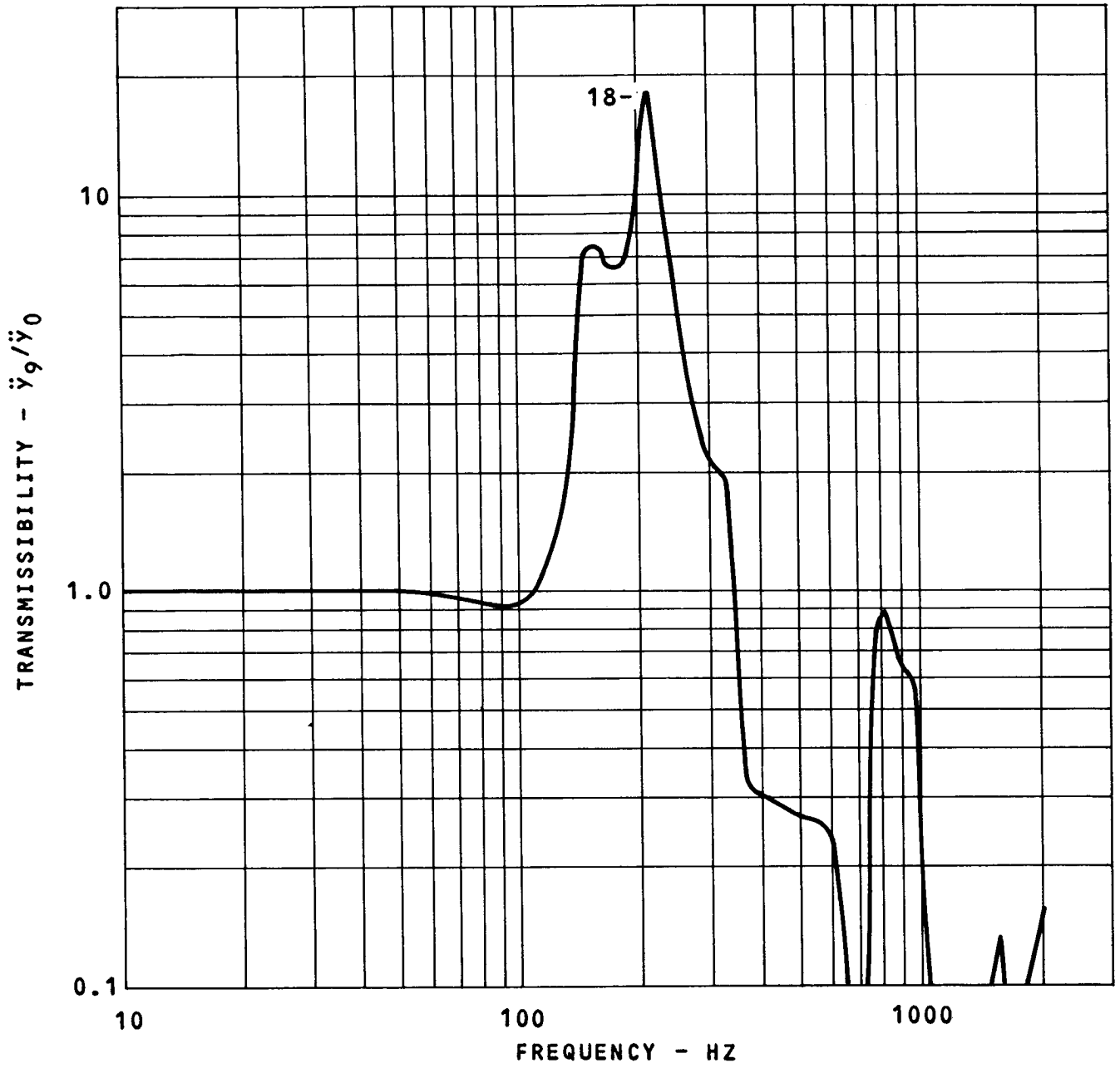


Figure 7-23. Transmissibility Plot - F/96 Camera,  
 Mass Point 9, Damping Factor =  $\mu = 2 \rho = 0.1$

W MATRIX*	$+(\ddot{Y}_R)_1$ G'S	$+(\ddot{Y}_R)_2$ G'S
0.163000 02	-0.225000 03	0.225000 03
0.760000 01	0.153000 02	-0.153000 02
0.630000 01	0.109400 03	-0.109400 03
0.630000 01	0.139000 03	-0.139000 03
0.930000 01	0.110000 03	-0.110000 03
0.466000 02	0.755000 02	0.755000 02
0.479000 02	0.810000 01	0.810000 01
0.715000 02	-0.171000 03	0.171000 03
0.358000 02	-0.254000 03	0.254000 03
0.358000 02	0.758000 02	0.758000 02
0.715000 02	0.859000 02	0.859000 02
0.358000 02	0.103500 03	0.103500 03
0.358000 02	0.756000 02	0.756000 02
0.715000 02	0.854000 02	0.854000 02
0.358000 02	0.103000 03	0.103000 03

WX $(\ddot{Y}_R)_1$	WX $(\ddot{Y}_R)_2$ *
1	2
-0.366750 04	0.366750 04
0.116280 03	-0.116280 03
0.689220 03	-0.689220 03
0.875700 03	-0.875700 03
0.102300 04	-0.102300 04
0.351830 04	0.351830 04
0.387990 03	0.387990 03
-0.122270 05	0.122270 05
-0.909320 04	0.909320 04
0.271360 04	0.271360 04
0.614180 04	0.614180 04
0.370530 04	0.370530 04
0.270650 04	0.270650 04
0.610610 04	0.610610 04
0.368740 04	0.368740 04

\* UNITS (LBS); NEWTON = 4.44822 X (LBS)

+ SIGN CONVENTION; MODES 1 AND 2

Figure 7-24. Dynamic Loads

INTERNAL LOAD * P	MODE		MODE	
	1		2	
V1 *	-0.36675D	04	0.36675D	04
V2	0.45556D	04	0.36123D	04
V3	0.81068D	04	0.61057D	02
M3 **	-0.11774D	06	0.36066D	05
V4	0.74176D	04	0.75028D	03
M4	-0.19192D	06	0.28563D	05
V5	0.65419D	04	0.16260D	04
M5	-0.25734D	06	0.12304D	05
V6	0.55189D	04	0.26490D	04
M6	-0.29044D	06	-0.35801D	04
V7	-0.87237D	03	-0.48118D	05
M7	-0.15206D	06	0.15206D	06
V7*	0.21284D	04	0.47638D	05
V8	-0.21320D	05	0.21320D	05
M8	-0.45466D	05	0.45466D	05
V9	-0.90932D	04	0.90932D	04
V10	0.12561D	05	0.12561D	05
M10	0.67762D	05	0.67762D	05
V11	0.98471D	04	0.98471D	04
M11	0.18527D	05	0.18527D	05
V12	0.37053D	04	0.37053D	04
V13	0.12500D	05	0.12500D	05
M13	0.67404D	05	0.67404D	05
V14	0.97935D	04	0.97935D	04
M14	0.18437D	05	0.18437D	05
V15	0.36874D	04	0.36874D	04

\* = SHEAR (LBS); NEWTON = 4.44822 X (LBS)

\*\* = BENDING MOMENT (IN-LBS); NEWTON-METER = 0.113 X (IN-LBS)

Figure 7-25. Internal Loads

random responses (Figure 7-21) are shown in Figure 7-24. The peak random acceleration responses (Figure 7-22) are used as load factors assuming direction of loading based upon the mode shape sign conventions in Figure 7-20 for the modes (1) and (2).

### 7.3.5.9 Stresses

Typical stresses are computed in the structural tube, support tab and camera housing based on the internal loads in Figure 7-25.

#### Structural Tube

The maximum stress occurs at point (5) in Figure 7-18, due to MODE 1 internal loads:

Bending Moment;  $M_5 = 29080 \text{ N-m (257,340 IN-lbs)}$

Shear;  $V_5 = 29091 \text{ N (6,540 LBS)}$

Section Modulus;  $Z_5 = I/C = 19.15 \times 10^{-6} \text{ m}^4 / .1201\text{m} = 158.8 \times 10^{-6} \text{ m}^3 \text{ (9.7 IN}^3\text{)}$

Area;  $A_5 = .0043 \text{ m}^2 \text{ (6.7 IN}^2\text{)}$

Bending Stress;  $\sigma_5 = \frac{M_5}{Z_5} = \frac{29080}{158.8 \times 10^{-6}} = 183 \times 10^6 \text{ N/m}^2 \text{ (26500 PSI)}$

Shear Stress;  $(S_s)_5 = \frac{V_5}{K^1 A_5} = \frac{29091}{.5(.0043)} = 13.53 \times 10^6 \text{ N/m}^2 \text{ (1950 PSI)}$

#### Support Tab

Maximum load taken by two rear tabs is  $V_7' = 211,904 \text{ N (47,638 LB)}$  (Mode 2); total tab cross section area (for two tabs);  $A_7' = .0042 \text{ m}^2 \text{ (6.5 IN}^2\text{)}$

Tensile Stress =  $(\sigma_t)_7' = \frac{V_7'}{A_7} = 50.5 \times 10^6 \text{ N/m}^2 \text{ (7,330 PSI)}$



## Camera Housing

Maximum Bending moment at mass point 7, (Mode 2);

Bending moment;  $M_7 = 17,183 \text{ N-m (152,060 IN-LBS)}$

Shear;  $V_7 = 214,039 \text{ N (48,118 LBS)}$

Section Modulus;  $Z_7 = I/C = 21.39 \times 10^{-6} \text{ m}^4 / .1092 \text{ m} =$   
 $195.8 \times 10^{-6} \text{ m}^3 \text{ (12 IN}^3\text{)}$

Area;  $A_7 = .00516 \text{ m}^2 \text{ (8 IN}^2\text{)}$

Bending Stress;  $\sigma_7 = \frac{M_7}{Z_7} = \frac{17183}{195.8 \times 10^{-6}} = 87.4 \times 10^6$   
 $\text{N/m}^2 \text{ (12,670 PSI)}$

Shear Stress;  $(S_s)_7 = \frac{V_7}{K'A_7} = \frac{214039}{.00516} = 82.9 \times 10^6 \text{ N/m}^2$   
 $\text{(12,030 PSI)}$

The above stresses indicate that the precision elastic limit stress (design allowable) of  $82.7 \times 10^6 \text{ N/m}^2$  (12000 PSI) for aluminum has been exceeded. However the loads were computed based upon vibration input levels to the f/96 camera assembly that are believed to be higher than actual, due to expected attenuation through the SIP structure, so that the actual stresses should be lower. See paragraph 7.3.5.4. In any case, the computed stress levels should not exceed the yield stress indicated in Table 7-9. Thus the structural design is shown to be feasible.

To reduce the stresses even further, an aluminum f/96 camera assembly structure can be modified by local changes in geometry; i.e. Increased wall thickness, increased tube diameter and ribbing. However, an alternative material, graphite-epoxy composite, is being considered due to the additional thermal stability requirements.

TABLE 7-10. COMPARISON OF RESULTS OF f/96 CAMERA ASSEMBLY STRUCTURES ANALYSIS

	Aluminum (A356-T6)		Graphite-Epoxy Composite	
	<u>SI</u>	<u>ENGLISH</u>	<u>SI</u>	<u>ENGLISH</u>
Density $\text{Kg/m}^3$ ( $\text{lb/in}^3$ )	6.96	(0.097)	4.02	(0.056)
Youngs Modulus $\text{N/m}^2$ (PSI)	$68.9 \times 10^6$	$(10 \times 10^6)$	$137.9 \times 10^6$	$(20 \times 10^6)$
Natural Frequencies (Hz) (Modes 1, 2, 3)		145, 212, 336		209, 300, 495
Maximum Random Response (g's) (Mass Point 9 - Figure 7-18- (b)) - Shuttle Launch Input Level		254		302
Maximum Shock Response (g's) (Mass Point 3 - Figure 7-18- (b)) - Tital III-D Launch Input Level		87		128
Maximum Bending Stress $\text{N/m}^2$ (PSI) (Mass Point 5 - Figure 7-18 (b))	$182.7 \times 10^6$	(26,500)	$211.8 \times 10^6$	(30,720)
Yield Strength ( $\text{N/m}^2$ (PSI))	$206.8 \times 10^6$	(30,000)	$1034 \times 10^6$	(150,000)
Design Allowable - Stress (Mechanical Stability) $\text{N/m}^2$ (PSI)	$82.7 \times 10^6$	(12,000)	$482.6 \times 10^6$	(70,000)

Graphite-epoxy composite not only has a higher allowable strength than aluminum, but by proper bias laying of the laminates an extremely low coefficient of thermal expansion f/96 camera structure can be developed (note Table 7-8). A structural analysis similar to that discussed above was performed using the material and physical properties of graphite-epoxy, shown in Table 7-8, and the structural model in Figure 7-18 (b). Significant results are compared to those obtained using aluminum in Table 7-9.

### 7.3.6 Structural Considerations - High Resolution Spectrograph

The following preliminary analysis considers the effect of launch loads on the axial bay high resolution spectrograph (.115 u - .18 u). An examination of stresses at structural locations experiencing the greatest effect of the external load is made, to illustrate the structural integrity of this design configuration.

A general introductory discussion is given in Section 7.2. The extent of analysis performed in Section 7.2.5 is not repeated here, but the dynamic loads used in the following analysis are based on the results of the preliminary random vibration analysis in Section 7.3.5.5.

A schematic of the high resolution spectrograph is shown in Figure 7-26. Based upon the loading shown, 244.7 N (25 Kg, mass) for the camera and approximately 253.6 N (26 Kg mass) for the remaining structure and components, stresses are obtained in the structural tube (due to camera loading) and in the mounting tabs.

#### (a) Structural Tube - Location C

$$\text{Shear Load} = V_C = 244.7 \text{ N/1g (55 LB/1g)}$$

$$\text{Bending Moment} = M_C = (244.7) (.406) = 99.4 \text{ N-m/1g} \\ (880 \text{ IN-Lb/1g})$$

$$\text{Section Modulus} = Z = \pi (.0965)^2 (.0064) = 1.84 \times 10^{-4} \\ \text{m}^3 (11.3 \text{ IN}^3)$$

$$\text{Area} = A = \pi(.193) (.0064) = 38.7 \times 10^{-4} \text{ m}^2 \text{ (6 IN}^2\text{)}$$

$$\text{Bending Stress} = \sigma_c = \frac{M}{Z} = .538 \times 10^6 \frac{\text{N/m}^2}{1\text{g}} \text{ (78 PSI/1g)}$$

$$\text{Shear Stress} = (S_s) = \frac{V_c}{KVA} = \frac{244.7}{.5(.0039)} = .124 \times 10^6 \frac{\text{N/m}^2}{1\text{g}} \text{ (18 PSI/1g)}$$

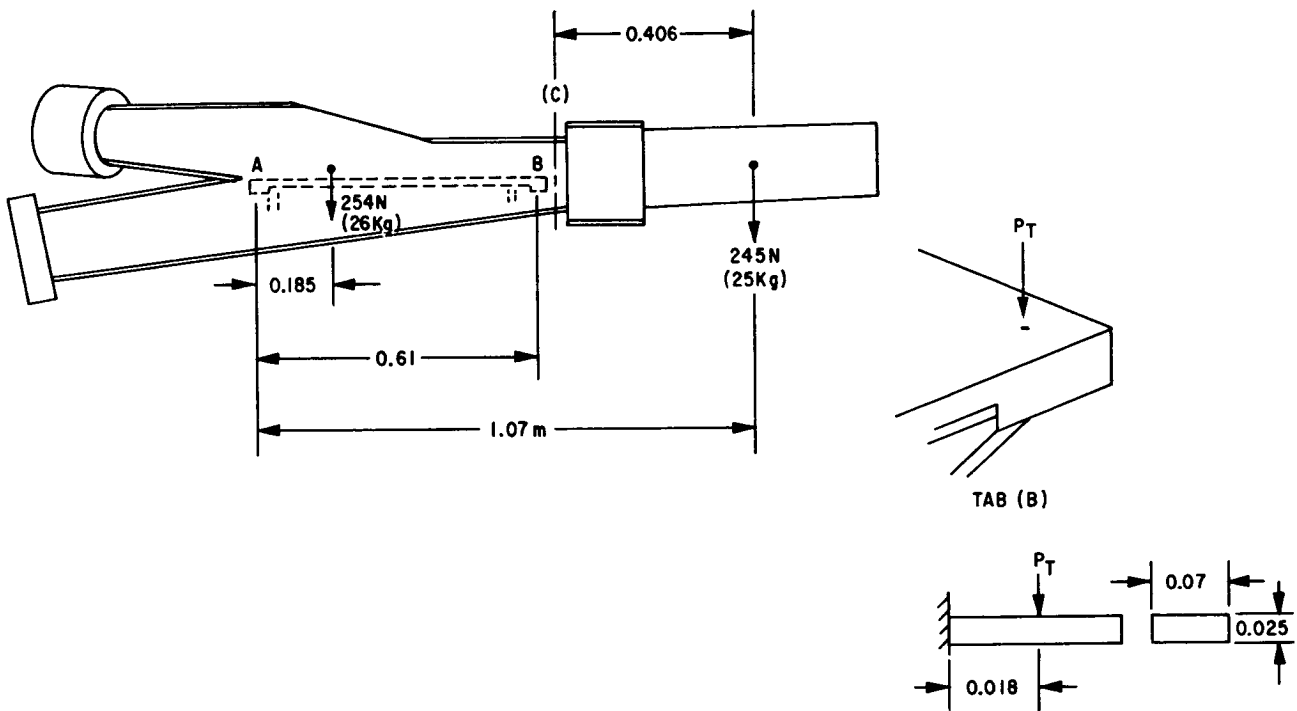


Figure 7-26. Structural Model, High Resolution Spectrograph

## Mounting Tab

Reaction at Point (B) (taken by rear two mountings tabs)

$$R_B = \frac{253.6 (.185) + 244.7 (1.07)}{.61} = 507 \text{ N/1g (114}$$

LBS/1g)

$$\text{Load/Tab} = P_t = 507/2 = 254 \text{ N/1g (57 Lb/1g)}$$

$$\text{Bending Moment} = M_t = 253.6 (.018) = 4.6 \frac{\text{N-m}}{1\text{g}} (40$$

$$\frac{\text{IN-LB}}{1\text{g}})$$

$$\text{Section Modulus} = Z = \frac{.07 (.0254)^2}{6} = 7.4 \times 10^{-6} \text{ m}^3$$

$$A (\text{minimum}) = 9.4 \times 10^{-4} \text{ m}^2 (1.4 \text{ in}^2)$$

$$\text{Bending Stress} = \sigma_t = \frac{M_t}{Z} = \frac{4.6}{7.4 \times 10^{-6}} = .62 \times 10^6$$

$$\frac{\text{N/m}^2}{1\text{g}} (87 \frac{\text{PSI}}{1\text{g}})$$

$$\text{Shear Stress} = (S_s)_t = \frac{P_t}{K'A} = \frac{254}{(.85)(.036)} = 0.33 \times$$

$$10^6 \frac{\text{N/m}^2}{1\text{g}} (48 \frac{\text{PSI}}{1\text{g}})$$

If a dynamic load factor of approximately 100g's is assumed, the resulting stresses are within the design allowable of  $82.7 \times 10^6 \text{ N/m}^2$  (12,000 psi), assumed for aluminum. If graphite-epoxy is used as the structural material, the margin of safety is substantial due to the high yield strength ( $>689 \times 10^6 \text{ N/m}^2$  (100000 psi)) for this material.

### 7.3.7 Structural Considerations - Faint Object Spectrograph

The following preliminary analysis considers the effect of launch loads on the radial bay faint object spectrograph (.220 $\mu$  - .660 $\mu$ ). An examination of stresses at structural locations experiencing the greatest effect of the external load is made, to illustrate the structural integrity of this design configuration.

A general introductory discussion is given in Section 7.3. The extent of analysis performed in Section 7.3.5 is not repeated here, but the dynamic loads used in the following analysis are based on the results of the preliminary random vibration analysis in Section 7.3.5.5.

A schematic of the Faint Object Spectrograph is shown in Figure 7-27. Based upon the loading shown, 244.7 N (25 Kg mass), for the camera and approximately 127.5N (13 Kg mass) for the remaining structure and components, stresses are obtained at the camera-structure interface and in the mounting legs.

#### a. Structure-Camera Interface - Location C

$$\text{Shear Load} = V_C = 244.7 \text{ N/1g} \left( 55 \frac{\text{LB}}{\text{1g}} \right)$$

$$\text{Bending Moment} = M_C = 244.7 (.203) = 49.7 \text{ N-m/1g} \\ (440 \text{ IN-LB/1g})$$

$$\text{Section Modulus} = Z = \pi (.102)^2 (.00508) = 1.66 \\ \times 10^{-4} \text{ m}^3 \text{ (10 IN}^3)$$

$$\text{Area} = A = \pi (.204) (.00508) = \\ 32.5 \times 10^{-4} \text{ m}^2 \text{ (5 IN}^2)$$

$$\text{Bending Stress} = \sigma_C = \frac{M}{Z} = 0.303 \times 10^6 \text{ N/m}^2/\text{1g} \\ (44 \text{ PSI/1g})$$

$$\text{Shear Stress} = (S_s) = \frac{V_C}{K'A} = \frac{244.7}{.5(.0033)} = \\ .152 \times 10^6 \text{ N/m}^2/\text{1g} \text{ (22 } \frac{\text{PSI}}{\text{1g}})$$

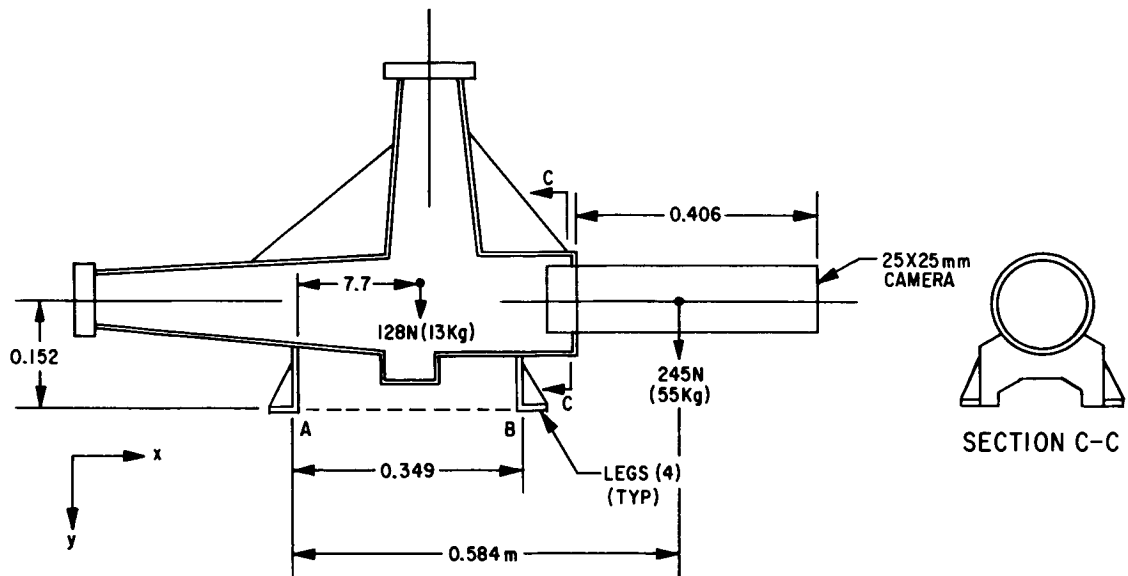


Figure 7-27. Structural Model Faint Object Spectrograph

b. Mounting Legs (y axis loading)

Reaction at point (B) [Taken by two legs]

$$R_B = \frac{127.5(.196) + 244.7(.584)}{.349} = 481 \text{ N/1g (107 LBS/1g)}$$

$$\text{Load/Leg; } P_L = R_B/2 = 240 \text{ N/1g (53.5 LBS/1g)}$$

$$\text{Area (based of leg); } A = (0.0127)(0.0508) = .00064 \text{ m}^2 \text{ (1.0 IN}^2\text{)}$$

$$\text{Tensile Stress; } \sigma_t = \frac{P}{A} = .369 \times 10^6 \frac{\text{N/m}^2}{\text{1g}} \text{ (53.5 } \frac{\text{PSI}}{\text{1g}}\text{)}$$

c. Mount Leg (x axis loading)

$$\text{Total Axial Load} = 373 \text{ N/1g} \quad (84 \text{ LB/1g})$$

$$\text{Load/Leg} = 373/4 = 93 \text{ N/1g} \quad (21 \text{ LB/1g})$$

$$\text{Bending Moment (based on leg assumed as cantilever beam)} \quad M = 93 \times (.152) = 14 \text{ N-m/1g} \quad (126 \frac{\text{IN-LB}}{\text{1g}})$$

$$\text{Section Modulus} \quad Z = \frac{(.0191)(.076)^2}{6} = 18.4 \times 10^{-6} \text{ m}^3$$
$$(1.13 \text{ IN}^3)$$

$$\text{Bending Stress} = \sigma = \frac{M}{Z} = .76 \times 10^6 \frac{\text{N/m}^2}{\text{1g}} \quad (112 \frac{\text{PSI}}{\text{1g}})$$

If a dynamic load factor of approximately 100g's is assumed the resulting stresses are within the design allowable of  $82.7 \times 10^6 \text{ N/m}^2$  (12,000 psi), assumed for aluminum. If graphite-epoxy is used as the structural material, the margin of safety is substantial due to the high yield strength ( $>689 \times 10^6 \text{ N/m}^2$  (100000 psi)) for this material.

#### 7.4 RADIATION

The LST will be in orbit at the lower edge of the inner Van Allen belt, and will pass through the South Atlantic Anomaly. Due to this environment, and based on the ten year operating life, the SIP radiation environment has been examined. The Martin Marietta Corporation has performed considerable radiation level modeling with respect to the Skylab mission at a 235 nautical mile orbit. Using that information, and data concerning the LST structure, they have estimated that the average absorption rate at the instrumentation is about one rad per day (10 m joule/kg). Since this is made up of mostly high energy protons, the additional shielding provided by the instrumentation housings will have little affect.



The dose rate of one rad per day, results in a total dose of only  $3.6 \times 10^3$  (c)rads for the 10 year mission. Since  $10^4$  rads is the normal threshold for semiconductor damage, judicious selection of standard high reliability components will satisfy this requirement. In addition, materials will be reviewed to assure safety at these levels. Little trouble is expected here since most materials exhibit almost no degradation below  $10^4$  rads (100 joule/kg).

An area of special concern is that of the SEC-Vidicon tube. Past flight experience with several types of photomultiplier and image dissector tubes (Nimbus and ATS), and simulation tests with many similar tubes indicates essentially no permanent damage below  $10^4$  rads. One area that must be guarded against however, is scintillation due to proton bombardment. Material selection must therefore include this precaution. Toward this end, lithium fluoride has been rejected as a tube window material.

Another tube effect will be the increase in tube background noise (dark current) during passage through the South Atlantic Anomaly. Tests performed within the Princeton cyclotron indicate that if the photocathode is turned off during the anomaly portion of the orbit, a substantial reduction in the background can be achieved. The conclusion of these tests stated that if this procedure were followed there should be no problem with storing an image during the pass through the anomaly.

Another area for additional investigation is the long term effect of these high energy, but low density, protons on the performance of the optical elements in the desired range of spectral response.

## 7.5 OTHER ADVERSE ENVIRONMENTS

In addition to the major environmental stresses imposed by shock, vibration, temperature and radiation as discussed above, other environments must be considered.

Environments such as sand, dust and salt fog should not reach the instruments. Contamination of this nature will degrade optical performance, and painstaking procedures will be required to remove any foreign matter. The materials and coatings used on the optics will not be permanently damaged by condensation of pure water vapor but the presence of some contaminants and particulate matter can cause the generation of corrosive droplets that will either stain or corrode optical surface coatings. Assembly and testing is to be performed in a Class 10,000 clean room, and precautions should be taken throughout the vehicle integration and launch period to prevent instrument contamination. Suitable shipping containers must also be provided to protect these instruments.

Protection from fungus is provided by selecting only materials that are not fungus nutrients. Selection of materials is also made to preclude corrosion from the atmosphere, from stress and pitting and from galvanic and electrolytic corrosion.

The earth's magnetic field affects detector tube operation only. The discussion of the variations caused, and shielding suggested are covered in Section 6, Description of Sensors.

## Section 8

### SCIENTIFIC INSTRUMENT PACKAGE OVERALL PHYSICAL DESCRIPTION

#### 8.1 INTRODUCTION

In this section, the description and development of the SIP as a whole and the Supporting Structure in particular are presented. The discussion begins with a description of the complete SIP structure reference configuration and assembly.

The second part goes into the evolution of the structural configuration, and the appendages to the basic structure to accommodate the instruments, followed by the material, construction, manufacturing and assembly details envisioned.

The next paragraphs deal with the mechanical analysis which includes thermal sensitivity and launch and re-entry loads. The final section is devoted to the thermal control philosophies and analysis of their effectiveness.

#### 8.2 DESCRIPTION OF THE SIP

The SIP structure and instrumentation mounting and location, that resulted from the phase A study, can best be seen in Figure 8-1, which is the assembly layout. Additional insight is gained when Figure 8-2, the structures drawing is examined in conjunction with the layout. The structure is made up of a series of rings and struts which serve to provide the positional integrity of all of the optical instrumentation, provide for interface to the main structural ring of the OTA. It presents a configuration that is strong, stable and light in weight and provides accessibility for implementation of both initial fabrication and alignment, and in-flight maintenance.

Referring to Figure 8-1, one sees a star shaped arrangement of support struts. There are 30 of these main support struts which

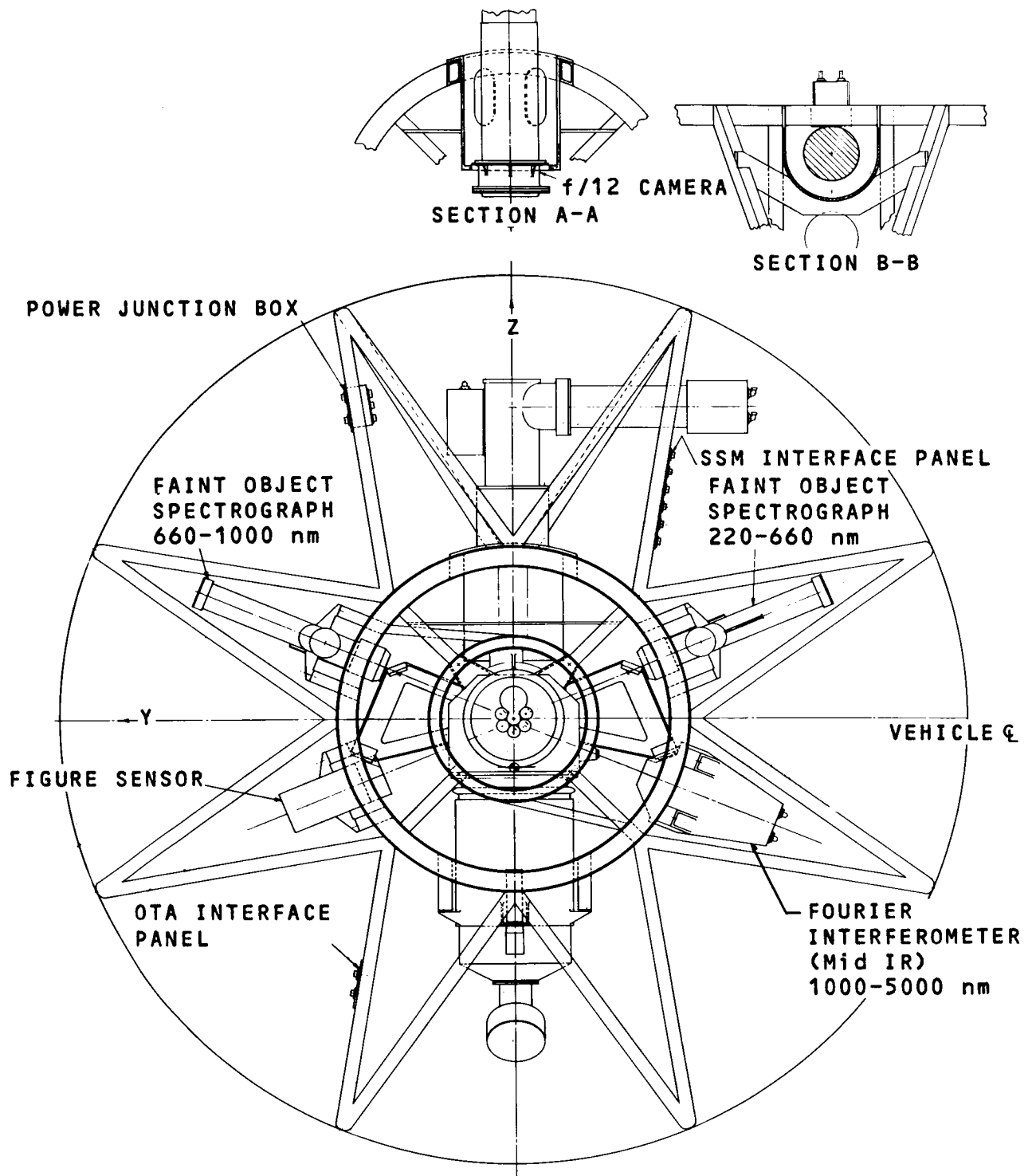


Figure 8-1. LST-SIP Assembly Layout (Sheet 1 of 2)

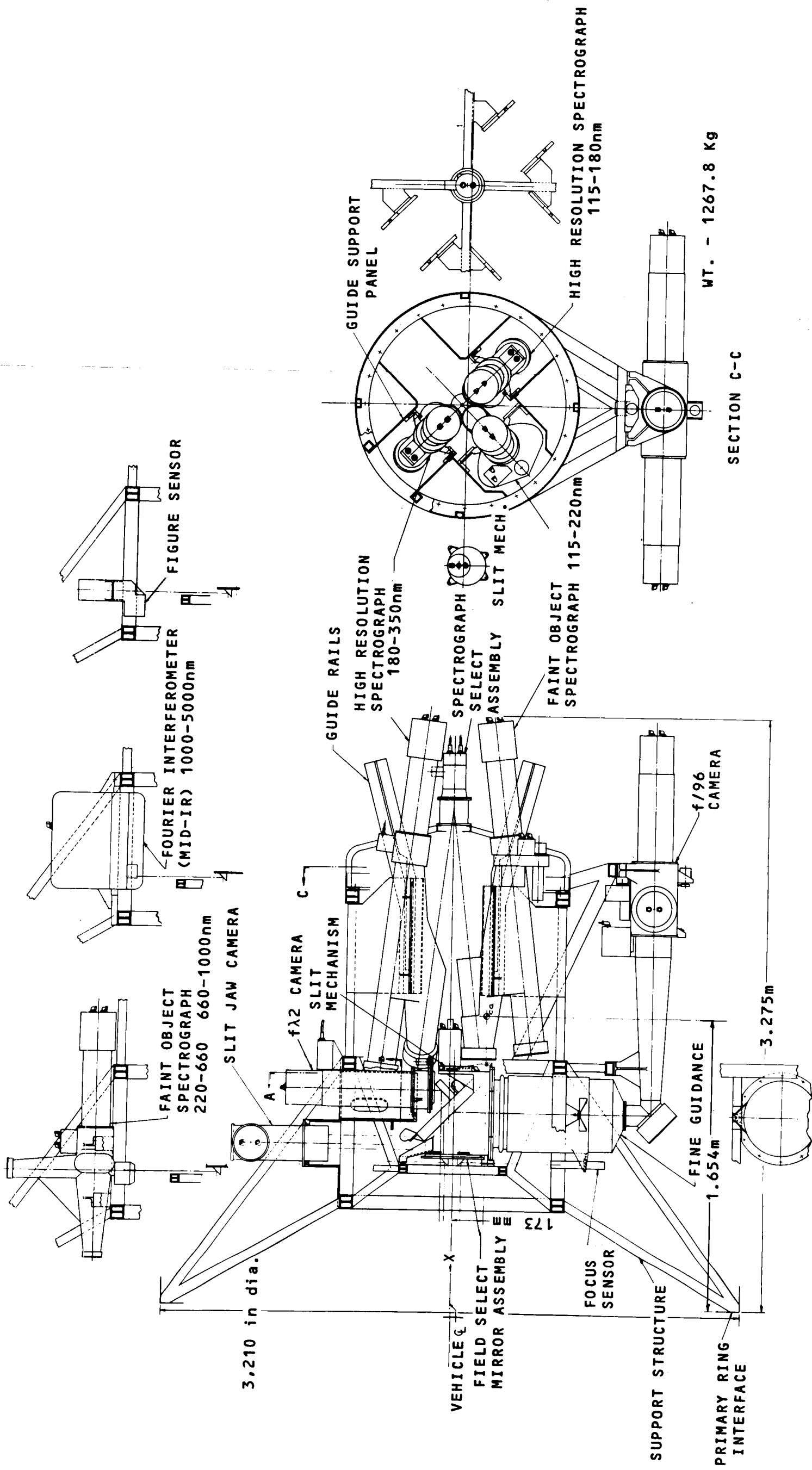


Figure 8-1. LST-SIP Assembly Layout (Sheet 2 of 2)

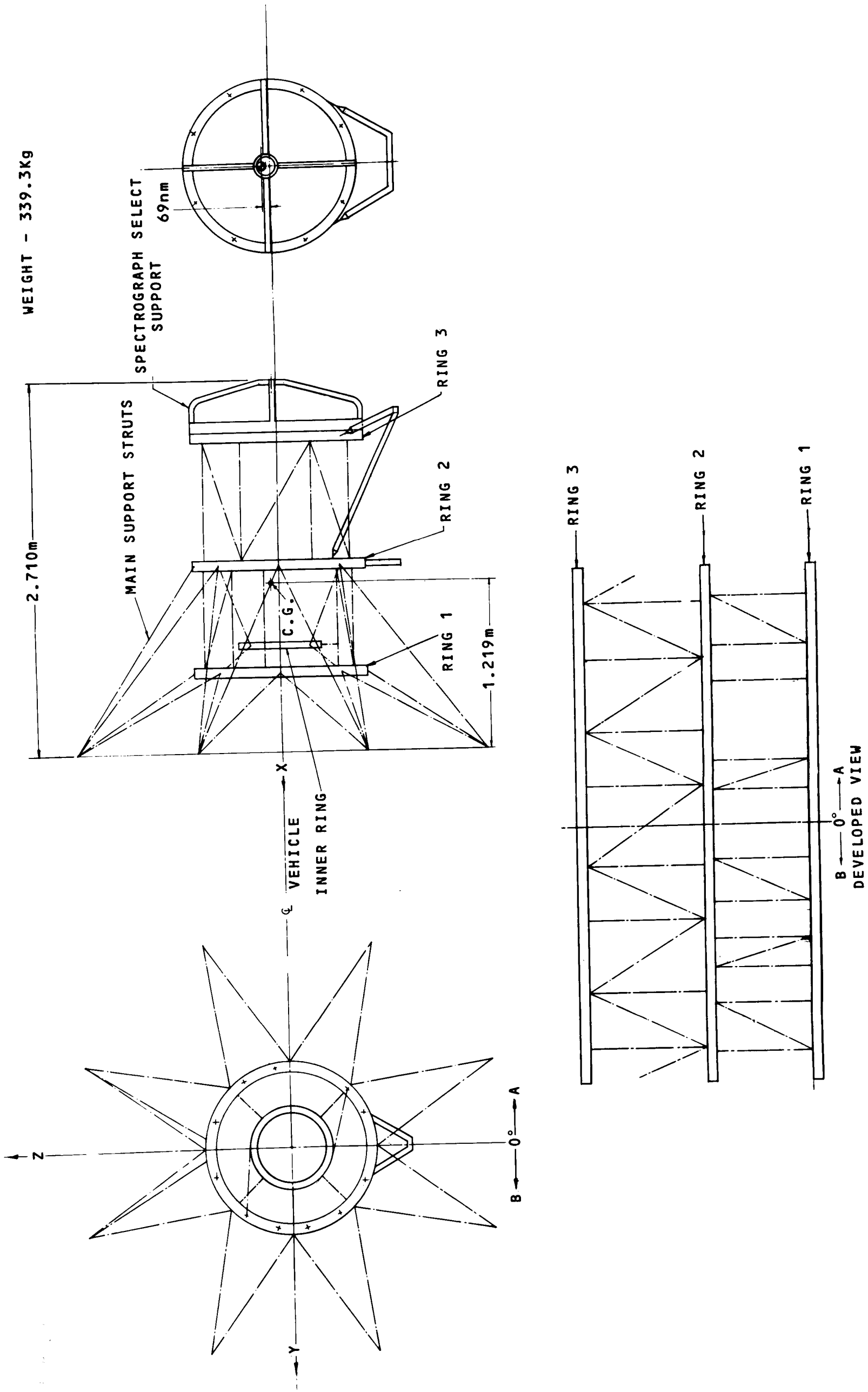


Figure 8-2. Support Structure (Sheet 1 of 2)

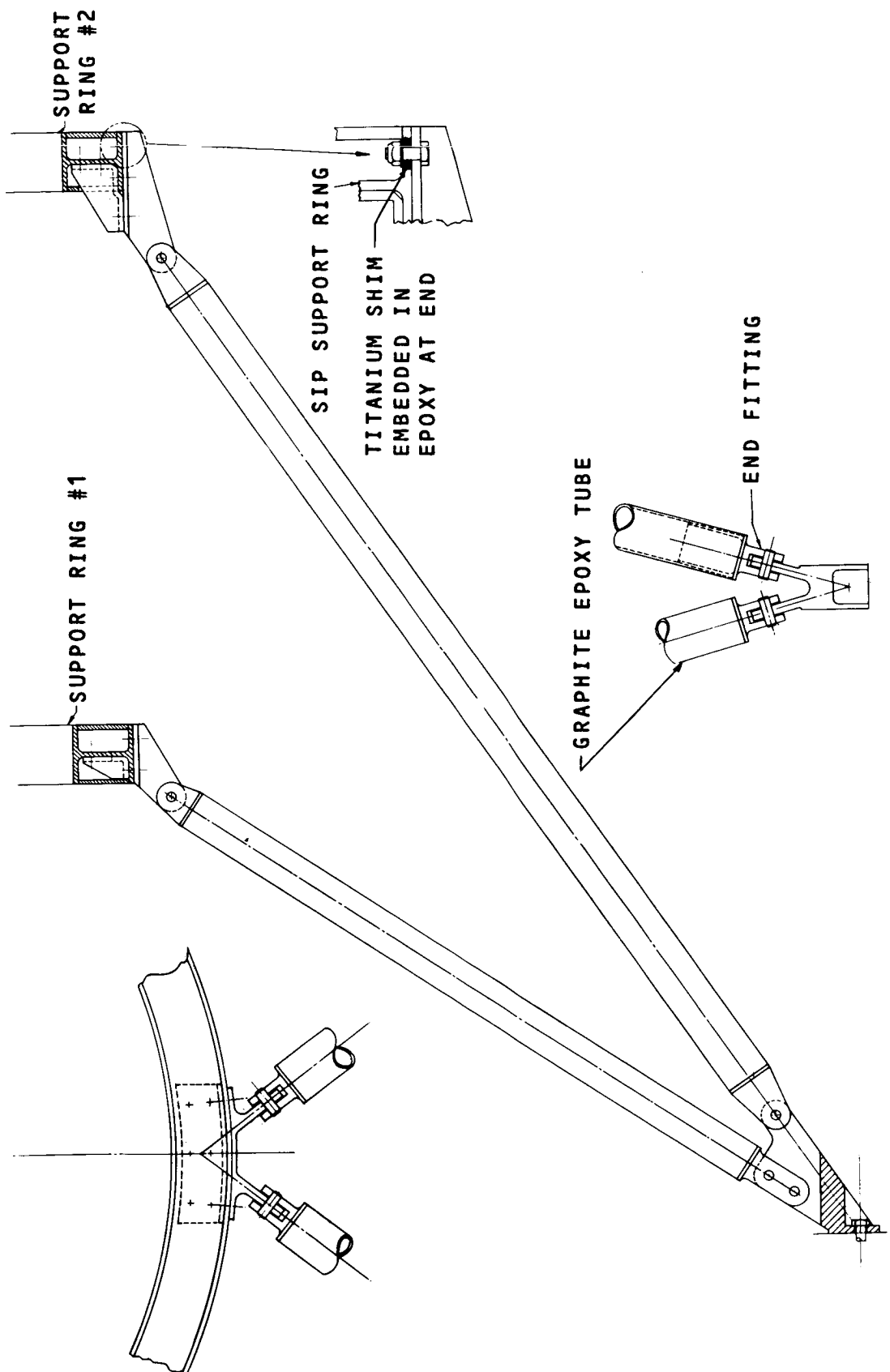


Figure 8-2. Support Structure (Sheet 2 of 2)

provide for attachment to the main ring of the OTA (at eight points). These 30 struts are fixed to the forward (1) and central (2) structural rings of the SIP. These rings are designated items 1 and 2 respectively on Figure 8-2.

The forward and central rings are also connected by 11 additional struts, and provide structural mounting for (starting at 4 o'clock and proceeding counterclockwise on the left end view of the layout) the Fourier (IR) Interferometer, the 220 to 660 nm Faint Object Spectrograph, the Slit Jaw Camera and f/12 Camera, the 660 to 1000 nm Spectrograph, the Figure Sensor, the Fine Guidance Sensor and the Focus Sensor. The f/12 Camera is held in a support half cylinder which is mounted directly to the central ring. Additional struts, attached to the forward and central rings, provide mounting for the f/96 Camera. This is seen most clearly on the bottom portion of the side view of the assembly layout.

Also attached to the forward and central rings are four "L" shaped struts. These four struts support an inner ring onto which is mounted the Field Select Mirror Assembly. The Slit Mechanism, which services the two High Resolution Spectrographs and the Faint Object Spectrograph located in the rear (axial bay) is in turn mounted to the Field Select Mirror Assembly.

A rear ring, designated number 3 on the structures drawing, is attached to the central ring with eight struts. This ring supports four guide support panels as can be seen most readily on the right end view of the assembly layout. Affixed to the guide support panels are the guide rails that are used to provide ease of in-flight replacement as well as structural mounting of the instrumentation. The 115 to 180 nm High Resolution Spectrograph, the 180 to 350 nm High Resolution Spectrograph and the 115 to 220 nm Faint Object Spectrograph are mounted on the guide rails. The fourth position is left vacant for an instrument to be selected at a later date.

The rear ring also supports a molded ring and strut structure which is seen most clearly in the right end view of the assembly



The views drawn at the top of the assembly layout are provided to show the accommodations for the radial instruments. In addition, the Power Junction Box and the two connector panels are shown mounted directly to the main support structure.

The results of the weight estimate, performed on the final phase A configuration, is shown in Table 8-1. The location of the center of gravity of the SIP is shown on Figure 8-1, and the layouts of the various hardware items, included in Sections 4 and 5, also show the center of gravity for each item.

### 8.3 DEVELOPMENT OF THE STRUCTURAL CONFIGURATION

#### 8.3.1 General Philosophy

The objective at hand was to arrive at a SIP structure that is compatible with the main structural ring and the forward end of the telescope. It should be noted that the forward end of the telescope attaches to its main structural ring and bulkhead, which is made of titanium, at eight points. These eight points represent the graphite-epoxy composite truss that separates the secondary mirror from the primary mirror, and supports the secondary mirror.

In order to reduce the number of load points into the primary ring and to take advantage of any possible negating effects from the SIP structure interacting with the OTA structure, it followed that the SIP structure should attach to the primary ring by eight points and have the same orientation as the OTA truss.

The SIP structure can be considered as consisting of two instrumentation locations; an axial bay and a radial bay. The instrumentation located in each is shown on Figure 8-1.

#### 8.3.2 Design Criteria

The primary consideration is to design a structure that will adequately support the SIP instruments. To fulfill this requirement the SIP structure will have to be relatively insensitive to a

TABLE 8-1. SIP WEIGHT SUMMARY

	<u>Lb.</u>	<u>Kg.</u>
f/96 Camera	525.9	239.0
Slit Jaw Camera	105.2	47.7
High Resolution Spectrograph 110-180 nm	137.6	62.4
High Resolution Spectrograph 180-350 nm	137.6	62.4
Faint Object Spectrograph 110-220 nm	141.5	64.2
Spectrograph Selector	17.4	7.0
Slit Mechanism	10.5	4.8
f/12 Camera	157.0	71.0
Faint Object Spectrograph 220-660 nm	108.3	49.2
Faint Object Spectrograph 660-1000 nm	104.8	47.6
Faint Object Interferometer (Mid I.R.) 1000-5000 nm	110.5	50.0
Secondary Support Structure (Titanium Fittings)	418.3	189.3
Cable and Junction Box	69.0	31.3
Cable Supports and Hardware	10.0	4.5
f/12 Electronics	<u>5.0</u>	<u>2.3</u>
Total Weight	2058.6	932.7

The following items, Field Select Mirror Assembly, Primary Support Structure, Fine Guidance Figure Sensor and Focus Sensor, are included in the OTA weight summary.

varying thermal environment in order to maintain optical alignment of the instruments during an observation. In addition, this structure must be strong enough to survive the induced dynamic loads during launch and reentry as well as being able to properly function after being exposed to these loads. Finally, the SIP structure should be stiff enough (have a high natural frequency) to avoid excitation during LST operation.

### 8.3.3 Design Evolution (Alternate Approaches)

#### Concept No. 1

Starting with the desired layout of the instrumentation in both the radial and axial bays a structure is built to support each unit considering the need for maintainability. The radial bay consists of an eight-point spider space trusswork that supports two titanium rings, as shown in Figure 8-3. These two titanium rings, which are about 1.3 m in diameter, attach to each other by an invar cylindrical shell about 1.05 m in length. The eight-point spider is connected to the primary ring opposite the OTA Truss attachments. Connected to the farthest ring (2nd ring) away from the primary ring is a Belleville shaped plate enclosing the radial bay at one end. The axial bay is formed by attaching four posts to the plate of the radial bay, with struts from the second ring laterally supporting the individual posts.

A review of the design showed that all the hardware in the radial bay would be mounted to the cylindrical invar shell but that some of the heat generating components of these instruments (e.g. f/12 camera) were contained inside the shell which is not desirable. In the axial bay easy maintainability is provided by allowing the instrument to be removed radially, but the structure is weak torsionally unless the instrument housings are used to tie the four posts together; this is not desirable. Also, the collimator sits flimsily on top of these four posts. In order to limit the excursions of the structure caused by a varying thermal environment,

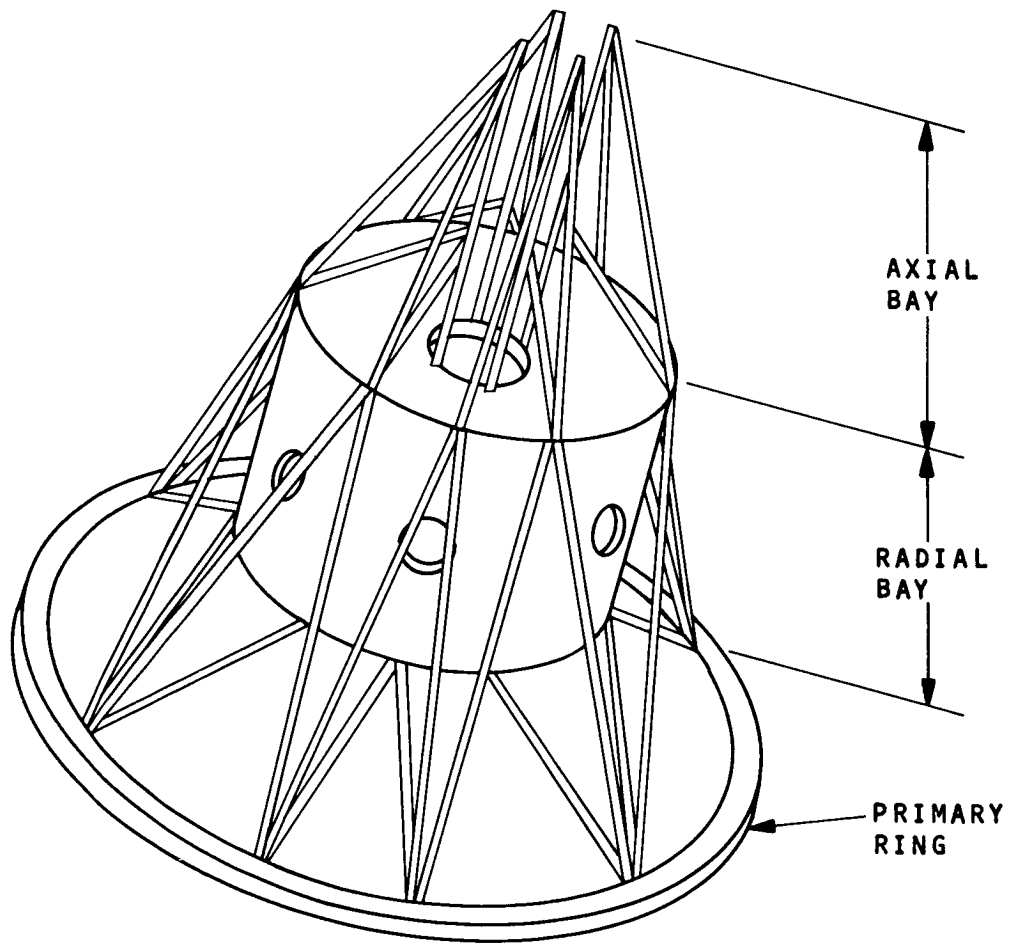


Figure 8-3. Concept No. 1

the truss is designed with invar and titanium members to create an athermalized design. This also results in a heavy structure.

#### Concept No. 2

A second concept, leaving the radial bay as it is except for removal of the Belleville shaped plate, is shown in Figure 8-4. The axial bay was changed by adding a third ring that goes around the instrumentation in the axial bay. The third ring is connected to the second ring via a trusswork made up of circular invar tubes. With this third ring around the instrumentation, removal will have to be axially instead of radially which does not present a problem. The axial bay now is structurally sound and provides a better support for the f/96 camera. The radial bay still presents some of the same thermal problems but now with the plate gone there is no means for independently supporting the Field Select Assembly.

#### Concept No. 3, Present Configuration

The present design is based upon the fact that it is desirable to have a stiff, lightweight, thermally inactive structure that would also provide ease of maintenance of the instrumentation that it supports, in both the radial and axial bays. It was therefore decided to make the SIP structure of graphite-epoxy composite materials which are light in weight and permits a design with the desired thermal properties through suitable selection of the layup of the plies. In order to prevent heat pockets in the radial bay, the invar cylindrical plate was replaced with a graphite-epoxy composite truss. Thus, the SIP structure now consists of three main rings, two in the radial bay interconnected to each other by a trusswork and supported from the primary ring by an eight point truss (Figure 8-5). The third ring is in the axial bay and is attached to the radial bay by a trusswork from the second ring in the radial bay. The three rings are graphite-epoxy composite box sections and the interconnecting and supporting trusswork are made of tubes of graphite-epoxy composites of various diameters.

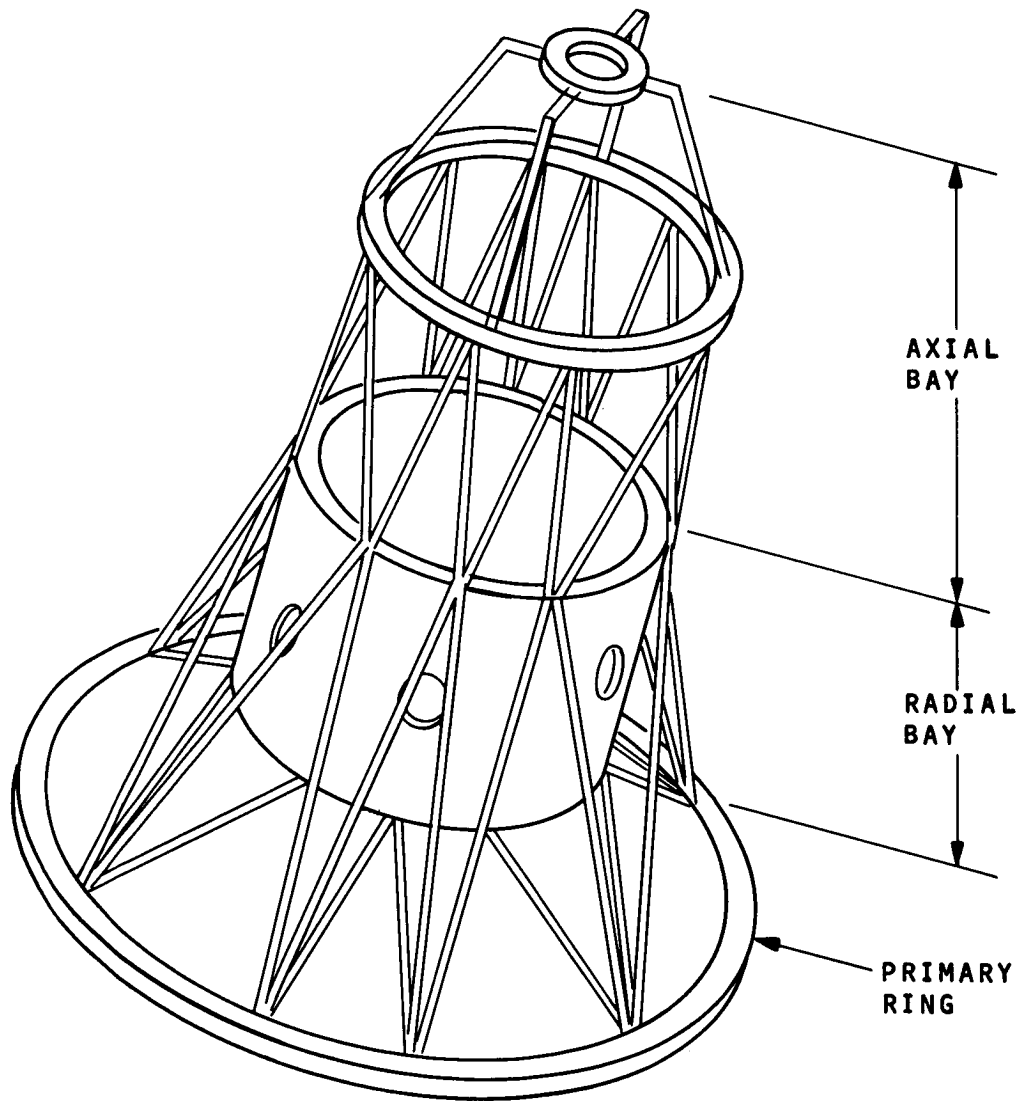


Figure 8-4. Concept No. 2

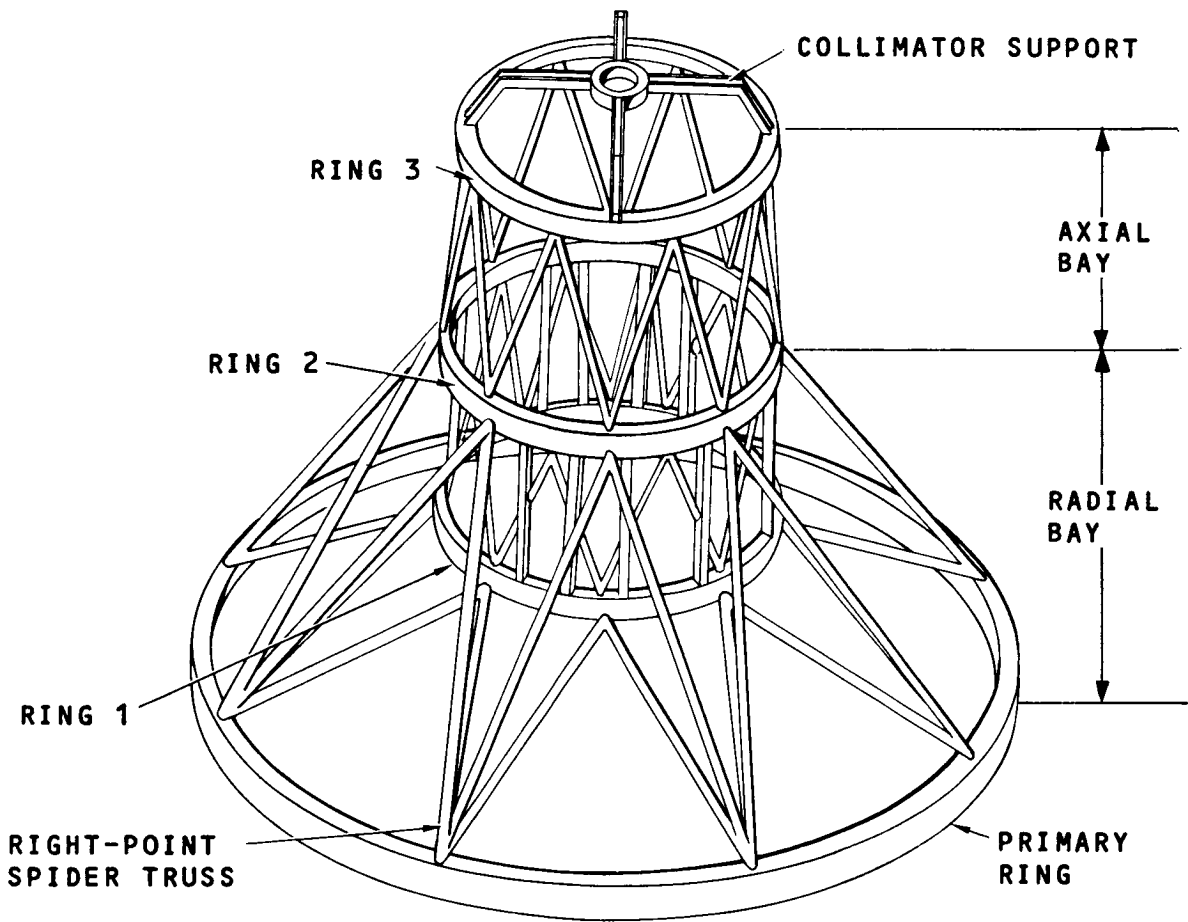


Figure 8-5. Concept No. 3, Present Design

The instruments are shown assembled within the structure on Figure 8-1. This structure is essentially the same as the "present design" structure which is the subject of analysis in the following parts of this section. The complete structure however is an amplification of the basic structure by way of inclusion of additional members for attachment of the instrument housings. The underlying structure described in the previous paragraphs and figures can readily be observed on Figure 8-2. The supporting trusswork from the primary ring to the forward and central rings defining the axial bay is shown. The rear ring and the crossed arches supporting the Spectrograph Select Assembly can also be recognized to correspond with the conceptual sketch (Figure 8-5).

The major additions are described in left to right order as they appear in the side view of Figure 8-1, Sheet 2.

A smaller box section ring just forward of the center of the axial bay supports the Field Select Mirror Assembly. This ring is supported by four inwardly reaching tubular members from rings one and two and two tangential members in the plane of the ring and connecting to axial members of the radial bay truss.

A half cylinder with inward turned flange also shown in sections A-A and B-B of Figure 8-1, Sheet 1 supports the f/12 camera. This half cylinder is attached to flanking axial struts of the lower bay truss and a pair of saddles, one attached to the same flanking axial members and one attached to the inward reaching tubular members which support the central small ring addition.

A triangle of tube sections secured to ring two supports one of the three mounting feet of the f/96 camera close to its elbow. A pair of larger tube section triangles attached from rings two and three are joined by another tubular section at their apex to support the other two feet close to the junction of the three sensor tube assemblies with the camera body, best shown in Figure 8-1, Sheet 2.



Four inwardly extending right angle walls (guide support panels) attached to the axial members of the truss connecting rings two and three support the three axial bay instruments. These panels are better understood by reference to section C-C, Figure 8-1, Sheet 2.

The actual attachment points for the axial bay instruments consist of right angle brackets attached to these four pairs of panels. These right angle brackets have grooves which serve as guide rails for leading the instruments into and out of their mounting position. These guide rails extend beyond the basic structure as can be seen in the side view. The guides are engaged by studs on the spectrograph bodies (details shown in Section 10 of this report).

The remaining additions consist of standoffs from the axial oriented truss members to the mounting flanges of the various instrument housings. They may be conical as shown for supporting the Slit Jaw Camera or merely widening of the axial members themselves as indicated for mounting the Fine Guidance and remainder of the axial bay instruments.

#### 8.4 STRUCTURAL MATERIAL

##### 8.4.1 Material Selection

The SIP support structure must be (1) thermally stable in the operating temperature range, and (2) non-magnetic. Graphite-epoxy has been selected as the principal material, with titanium fittings where loads are concentrated, to best satisfy these criteria. Upon examination of Figure 8-2, it is observed that the basic members of the support structure are frames and struts. With the proper proportions and alignment of constituents in the graphite-epoxy to compensate for the thermal coefficient characteristics of fittings, a structure, such as a strut, will exhibit essentially zero axial thermal coefficient in the temperature range of concern. Graphite-epoxy is the only material that will permit this. Boron-epoxy is

the next best material. Maintaining the extremely low coefficient of expansion requires that the fittings be as short as possible. All additions to the basic structure described above are designed so as to add minimum fitting lengths into the basic structure.

For other than tubular shapes, which are shown in Figure 8-6, special molds can be used for the layup and curing processes. For example, a four piece mold can be used for an I cross-section, as shown in Figure 8-7.

Unspecified as yet are the outgassing criteria for materials to be used in the LST. The epoxy used in construction of the SIP support structure is organic. More testing needs to be conducted to determine the outgassing characteristics of the finished composite structures in the temperature range of concern. The additional effort required to bring the graphite epoxy technology up to the level required for the LST, is outlined in Section 11 for SR & T.

#### 8.4.2 Fabrication Methods

Let us examine the production concept for a strut, as illustrated in Figure 8-6. The strut consists of a round tube and two end fittings and is fabricated in the following steps:

1. Wrap an aluminum mandrel with glass epoxy tape at  $+\pi/4$  radians (Note: the epoxy is tacky and will stick to the tube).
2. Wrap with glass epoxy tape at  $-\pi/4$  radians.
3. Wrap with layers of graphite epoxy pre-impregnated tape, with fibers in the axial direction, frequently separated with layers of glass epoxy tape.
4. Wrap with graphite epoxy pre-impregnated tape at  $+\pi/2$  radians (girth wrap) over end fitting regions.
5. Wrap with glass epoxy tape at  $-\pi/4$  radians.
6. Wrap with glass epoxy tape at  $+\pi/4$  radians.

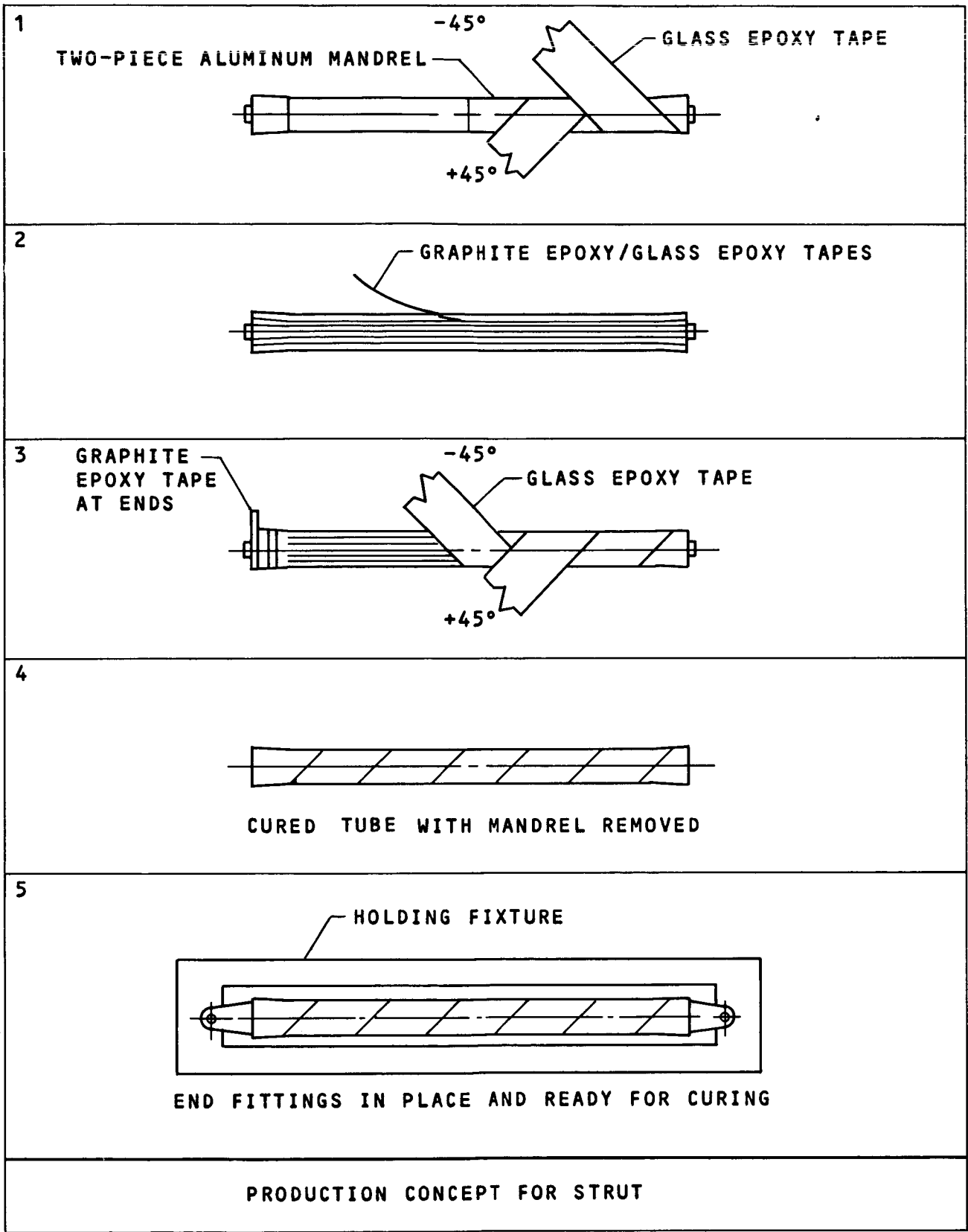


Figure 8-6. Production Concept for Strut

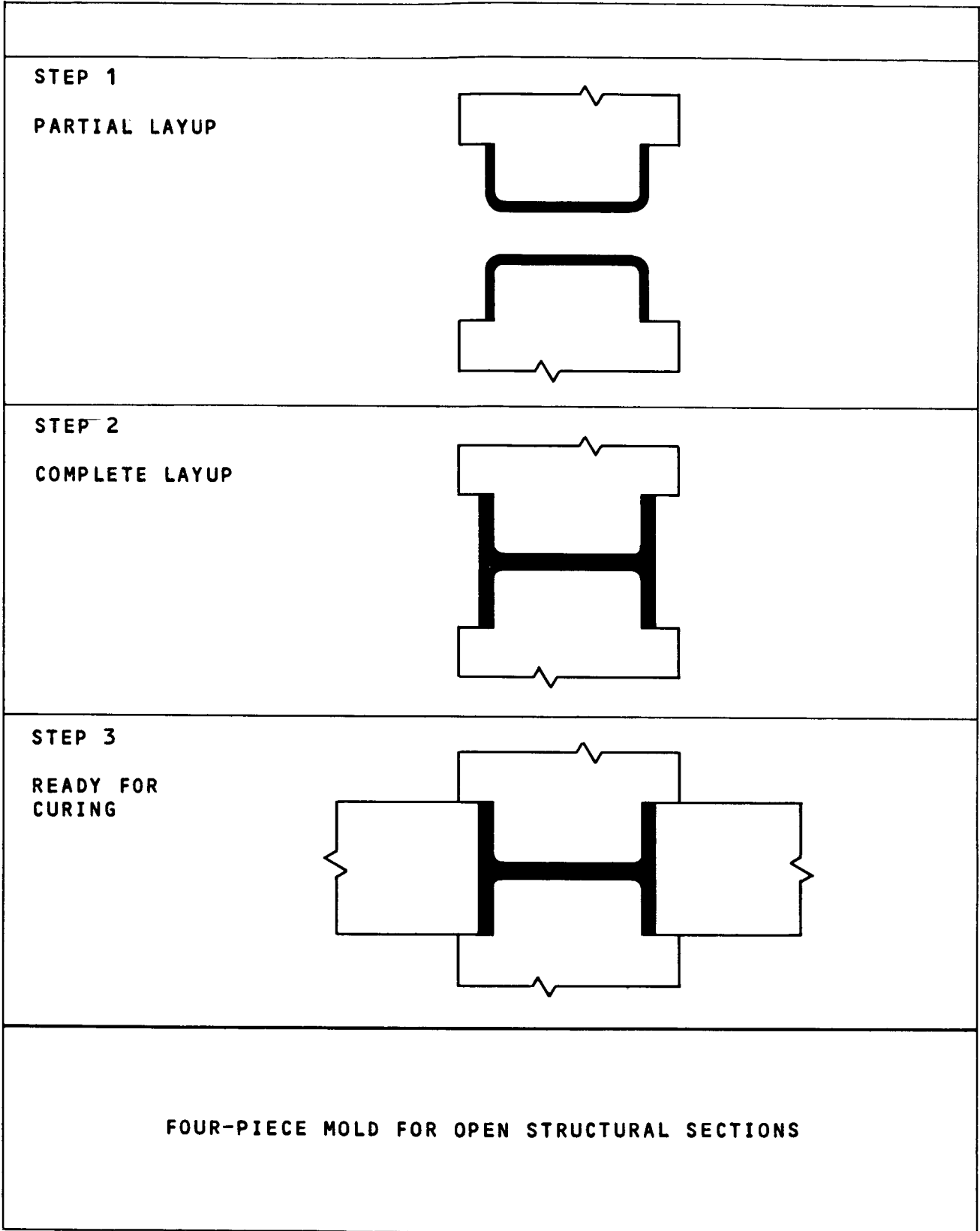


Figure 8-7. Four-Piece Mold for Open Structural Sections

7. Wrap with shrink tape to hold tight.
8. Insert in oven to cure.
9. Cool and remove mandrel (mandrel with shrink loose).
10. Peel off shrink tape.
11. Clean composite tube and end fittings.
12. Seat end fittings with epoxy into tube.
13. Insert in oven and cure.
14. Cool and clean.
15. Make final machine cuts on end fittings, if necessary.

Rings can be produced in a similar manner, in two or more segments, spliced with bolts through invar fittings. It will be somewhat difficult to remove the mandrels if the frame is of tubular cross section; an I cross section would be better, using a four-piece mold as illustrated in Figure 8-7.

The wide range of temperature experienced by a bonded member during its life will cause no separation of materials, provided careful attention is given to the direction, constituents, and thickness of each lamination.

#### 8.4.3 Assembly Concepts

Structural members should be assembled without inducing axial strain, and joints should be absolutely tight. It is expected that critically located interfaces (on frames for example) be held in a fixture and other members, such as struts, be clamped while holes between them are reamed for press fit pins. Adequate structural pads are built into the members that need clamping during assembly.

No machining of graphite-epoxy interfaces is permitted after curing. Cutting into graphite-epoxy relieves built-in stresses and results in unacceptable strain. Thus it is apparent that design

changes after fabrication (that require new equipment mounting holes for example) may require that a member be replaced rather than reworked. The pin-ended design for struts, for example, is adaptable to the replacement concept.

An alternative to the pin ended design for struts is shown in the Itek Report covering the OTA. The details accompanying the main assembly drawing of the LST show fittings into which the epoxy graphite tubes are inserted. This construction is applied to the metering truss which maintains the spacing between the primary and secondary mirrors of the OTA and results in a smaller proportion of metal in the length dimension of the truss members. No final judgement has been made on the relative merits of this assembly method for the SIP structure. The trade-off is assembly cost versus closer approach to zero expansion coefficient.

There are no unusual manufacturing problems associated with the SIP support structure. Layup and curing of graphite-epoxy members is typical fiberglass technology. Molds and mandrels are of relatively simple shapes and are easy to build. Suitable ovens are available, and curing temperature is low ( $\sim 453$  K max). Holding tools for use in the oven or autoclave are not complicated. Machining titanium is not difficult and there are no toxic materials involved.

Raw materials of course are more expensive than the usual materials of construction such as aluminum and steel. For example, graphite-epoxy prepregged tape will cost in the order of \$100 per pound, and there is considerable hand labor in laying up structural members. Preliminary design and analyses indicates that the graphite-epoxy/titanium construction may result in structure as much as 40% lighter weight than aluminum, steel, or titanium designs.

## 8.5 STRUCTURAL ANALYSIS

The graphite-epoxy composite SIP structure has been analyzed for deformations and stresses caused by a varying thermal environment, as well as launch and reentry stresses. The fundamental natural frequency is determined to show that the structure is stiff enough so as not to be disturbed by operating motor drives and launch vibration.

### 8.5.1 Analytical Model

An 89 node, 214 beam model of the SIP structure was generated for use on both the EASE and STARDYNE computer programs, as shown in Figure 8-8. To this general computer model individual modifications are made to tailor this general model for the particular analysis being performed, such as the addition of the titanium primary ring connecting nodes 1-8 in the thermal sensitivity analyses.

The following paragraphs discuss the results of using this model to establish thermal deformation, stresses and the resonant frequency of the SIP structure. Material properties used in the analyses are shown in Table 8-2.

### 8.5.2 Thermal Sensitivity Analysis

The following paragraphs discuss the effects of several thermal conditions on the SIP (Figure 8-8) structure in order to evaluate thermal deformations.

Ideally, the basis for the temperature conditions used would be derived from the thermal analysis in Section 8.6. In actuality, only one of the three modes of thermal control investigated was applied to the thermal sensitivity analysis because only one of the concepts resulted in large enough temperature spreads to make the evaluation of deformations significant. The results of the other two concepts served as a guide for the magnitude of temperature excursions which were then arbitrarily assigned to evaluate parametric changes.

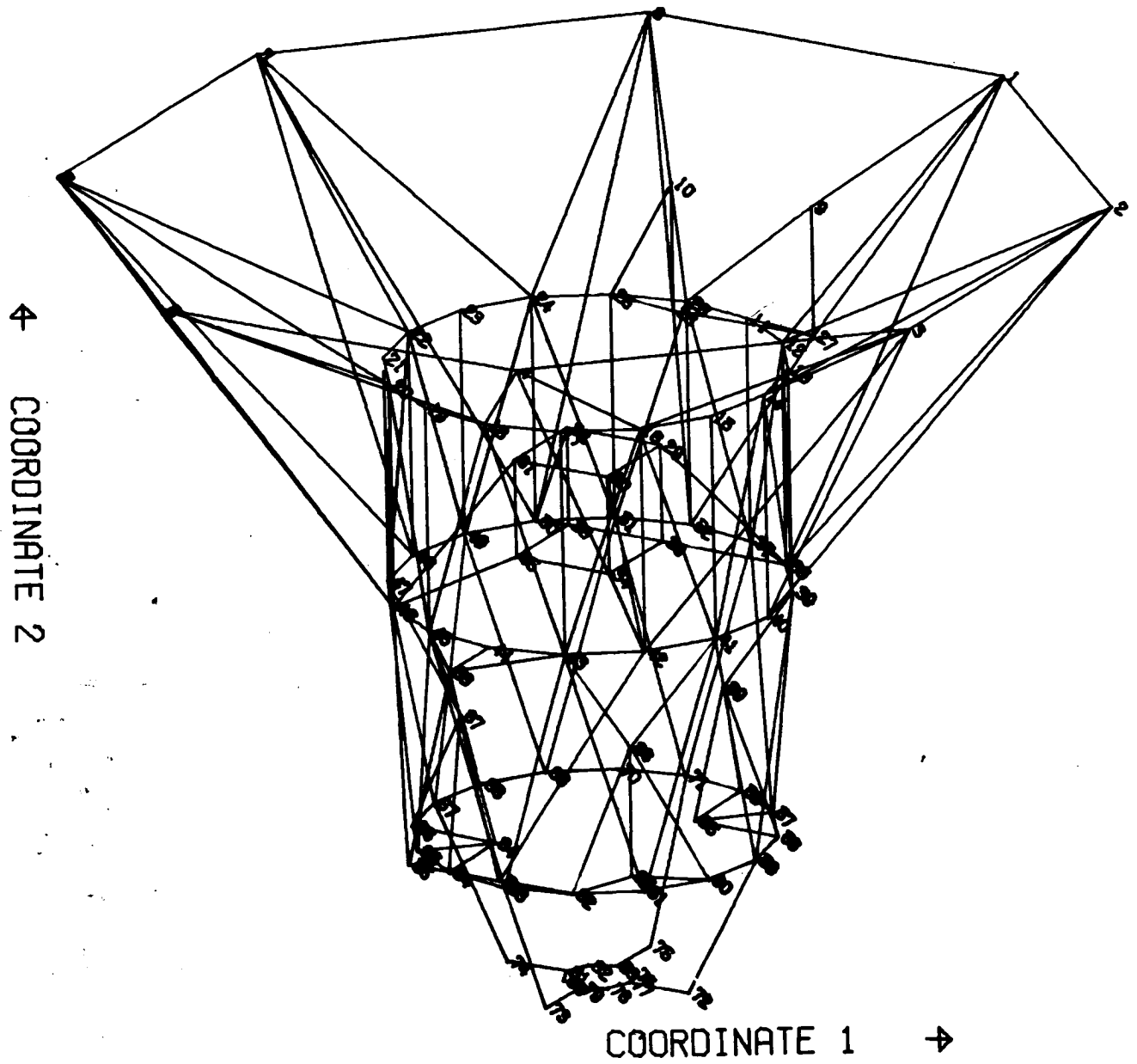


Figure 8-8. Itek Concept SIP Ease Beam Projection



TABLE 8-2. SIP ANALYSIS - STRUCTURE PROPERTIES USED

Titanium

$$E = (16.0 \times 10^6 \text{ psi}) \quad 110.3 \times 10^9 \text{ N/m}^2$$

$$\alpha = (4.8 \times 10^{-6} \text{ in./in./F}) \quad 8.6 \text{ m/m-}^\circ\text{K}$$

$$\delta = (0.16 \text{ \#/in.}^3) \quad 4429 \text{ Kg/m}^3$$

Graphite-Epoxy Composite

$$E = (15.3 \times 10^6 \text{ psi}) \quad 105.5 \times 10^9 \text{ N/m}^2$$

$$\alpha = (0.0)$$

$$\delta = (0.06 \text{ \#/in.}^3) \quad 1661 \text{ Kg/m}^3$$

Graphite-Epoxy Composite (3° Layup Error)

$$E = (15.3 \times 10^6 \text{ psi}) \quad 105.5 \times 10^9 \text{ N/m}^2$$

$$\alpha = (0.07 \times 10^{-6} \text{ in./in./F}) \quad 126 \text{ m/m-K}$$

$$\delta = (0.06 \text{ \#/in.}^3) \quad 1661 \text{ Kg/m}^3$$

The three concepts described in more detail in Section 8.6 are:

- (1) Constant "T" structure achieved by use of a shroud to isolate the structure from thermal disturbances and heaters to control the structure temperature.
- (2) Insulated structures.
- (3) Constant "Q", control of temperature by use of heaters to maintain a constant state of heat dissipation by components whether or not they are operating.

All of these concepts were analyzed using the Concept No. 1 structure in the design evolution (Section 8.3.3).

The four cases for this thermal sensitivity analysis are based on the present design structure concept No. 3 of Section 8.3.3 and Figures 8-8 and 8-9, with the following temperature and material assumptions.

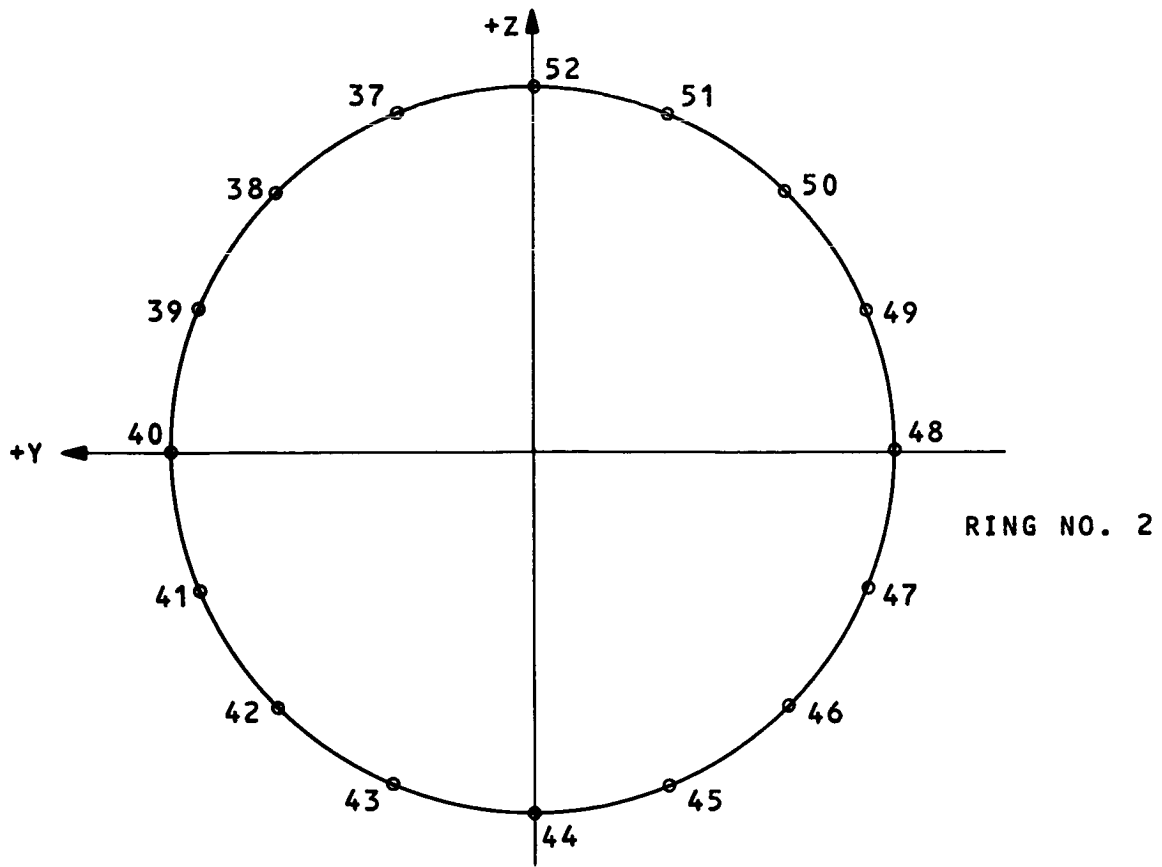
Case A - Thermal soak of the titanium primary ring, nodes 1 through 8 of Figure 8-8 at 294.6 K with the reference temperature 294.6 K applied to the remaining nodes. The mechanical properties of Table 8-2 with  $\alpha = 0.0$  for the epoxy graphite were assumed.

Case B - Thermal shock of 294.4 K of the titanium primary ring and 293 K applied to the remaining nodes. In addition, to account for a reasonable error of 5.4 mrad in the layup of the graphite fibers, the corresponding coefficient of expansion  $0.126 \times 10^{-6}/K$  was assigned to the epoxy structure.

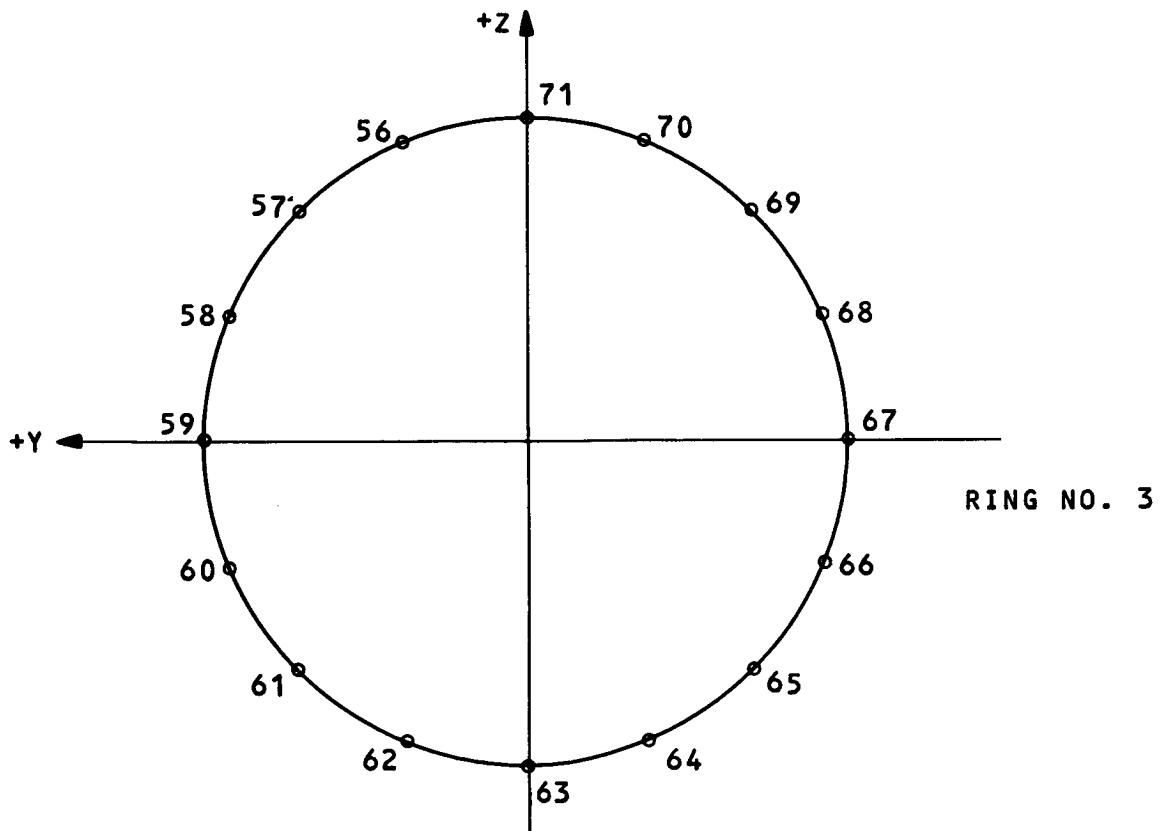
Case C - The temperatures from the number (3) Constant "Q" thermal control study of Section 8.5 were applied to the structural model of Figure 8-8 with the same material assumptions as in Case B. The temperatures are in Table 8-3.

Case D - To investigate the effect of a temperature difference crosswise of the SIP package, the same structure and material assumptions were used with the temperatures assigned in Table 8-4.

Comparison of the temperatures assigned to Cases A, B and D with the results of thermal analysis in Tables 8-18 and 8-19 shows that the cases investigated for thermal sensitivity embrace the



RING NO. 2



RING NO. 3

Figure 8-9. Thermal Model, Rings 2 and 3

temperature ranges determined by thermal analysis. The difference between the Structural Model from structure concept 3 and the thermal model from structure concept 1, while not being truly representative, are conservative. The factor by which the structures contribute to large temperature differences are low conductivity of the structure members and traps for radiation. The concept No. 3 structure is better on both of these counts.

The thermal deformation resulting are shown in Tables 8-3 through 8-16. Case C is graphically depicted in Figure 8-10.

#### 8.5.2.1 Results of Thermal Sensitivity Analysis

##### a. Summary of Results

The effects of each of the assumed thermal conditions on the structure in terms of structural deformations were indicated above in terms of tabulated displacements. This data was evaluated to establish the effect of the structural displacements on the optical instruments as shown in Table 8-17. These tabulated data include the average transverse displacements, axial displacements, and tilting of the structural rings and collimator support. The following displacement and angular errors are determined from the maximum numerical values in Table 8-17.

(a) Decentration (transverse movement) of  
Collimator Support (Case D)

$$= 6.85 \mu\text{m} \text{ (270 } \mu\text{inch)}$$

(b) Defocussing (axial movement) of  
Collimator Support (Case A)

$$= 7.62 \mu\text{m} \text{ (300 } \mu\text{inch)}$$

(c) Tilt of Collimator Support (Case D)  
= 1.9  $\mu\text{rad}$  (0.4 sec of arc)

(d) Effect on Axial Bay Instrument; assume instruments supported by Rings 2 and 3

- Maximum relative transverse displacement (Case D)

$$\Delta\delta_t = 6 - 4.62 = 1.32 \mu\text{m} \text{ (54 } \mu\text{inch)}$$

$$\text{tilt of instruments; } \theta_t = \frac{1.32 \mu\text{m}}{.84 \text{ m}} = 1.64 \mu\text{rad} (= 0.34 \text{ sec of arc})$$

TABLE 8-3. THERMAL OPERATING ENVIRONMENT  
(INSTRUMENTS OPERATING)

Radial Bay				Axial Bay	
Node	Temperature F*	Node	Temperature F	Node	Temperature F
1	70.0	36	78.0	54	101.0
2	70.0	37	81.0	55	101.0
3	70.0	38	80.0	56	110.0
4	70.0	39	79.0	57	107.0
5	70.0	40	78.0	58	106.0
6	70.0	41	77.0	59	105.0
7	70.0	42	76.0	60	105.0
8	70.0	43	75.0	61	104.0
9	71.0	44	74.0	62	103.0
10	71.0	45	74.0	63	101.0
11	73.0	46	74.0	64	101.0
12	73.0	47	74.0	65	102.0
13	73.0	48	74.0	66	102.0
14	73.0	49	75.0	67	103.0
15	72.0	50	78.0	68	103.0
16	71.0	51	80.0	69	103.0
17	73.0	52	83.0	70	107.0
18	72.5	53	74.0	71	112.0
19	72.0			72	108.0
20	71.5			73	108.0
21	71.0			74	114.0
22	71.5			75	119.0
23	72.0			76	112.0
24	72.0			77	108.0
25	72.5			78	108.0
26	73.0			79	108.0
27	75.0			80	110.0
28	75.0			81	114.0
29	75.0			82	116.0
30	76.0			83	119.0
31	76.0			84	110.0
32	76.0			85	108.0
33	77.0			86	112.0
34	78.0			87	110.0
35	78.0			88	108.0
				89	112.0

\* K = 5/9 (F - 32) + 273

TABLE 8-4. THERMAL OPERATIONAL ENVIRONMENT  
(BOUNDARY CASE)  
APPLIED TEMPERATURE\*  
CASE D

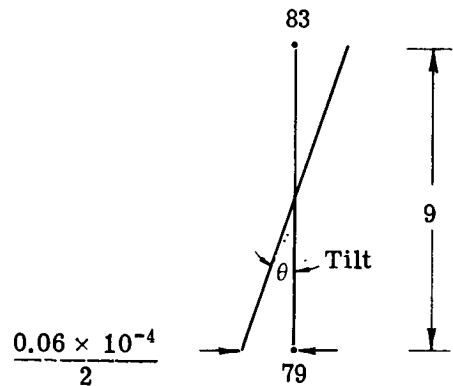
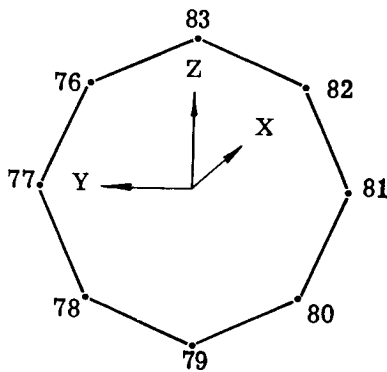
Bay	Quad.	Nodes	Input Temp.
Radial	+Z,+Y -Z,+Y	9,11-18,27, 29,30,33,34 37-44,53	293K
Radial	+Z,-Y -Z,-Y	10,19-26,28 31,32,35,36 45-52	294.1K
Axial	+Z,+Y -Z,+Y	54,56-63 72,73,76-79 85,86,88,89	293K
Axial	+Z,-Y -Z,-Y -	55,64-71,74 75,80-84, 87	294.1K
Ring	±Z,+Y	1-4	293.8K
Ring	±Z,-Y	5-8	294.4K

\* Ref. Temp. 294.1K

TABLE 8-5. COLLIMATOR SUPPORT STRUCTURE  
THERMAL SOAK PRIMARY RING

CASE A

NODE	Y DISPL.	Z DISPL.	X DISPL.
76	$1.78 \times 10^{-5}$	$-3.48 \times 10^{-5}$	$-3.06 \times 10^{-4}$
77	$2.42 \times 10^{-5}$	$-5.05 \times 10^{-5}$	$-3.04 \times 10^{-4}$
78	$1.73 \times 10^{-5}$	$-6.59 \times 10^{-5}$	$-3.02 \times 10^{-4}$
79	$1.61 \times 10^{-6}$	$-7.19 \times 10^{-5}$	$-3.01 \times 10^{-4}$
80	$-1.39 \times 10^{-5}$	$-6.54 \times 10^{-5}$	$-3.02 \times 10^{-4}$
81	$-2.03 \times 10^{-5}$	$-4.98 \times 10^{-5}$	$-3.03 \times 10^{-4}$
82	$-1.35 \times 10^{-5}$	$-3.44 \times 10^{-5}$	$-3.06 \times 10^{-4}$
83	$2.29 \times 10^{-6}$	$-2.83 \times 10^{-5}$	$-3.07 \times 10^{-4}$



$$\gamma_{\text{decenter}} \approx 5.0 \times 10^{-5} \text{ inch}$$

$$\gamma_{\text{defocus}} \approx 3.1 \times 10^{-4} \text{ inch}$$

$$\begin{aligned} \text{Maximum } \theta \text{ tilt} &= \arctan \frac{6 \times 10^{-6}}{4.5(2)} \\ &= \arctan 0.66 \times 10^{-6} \end{aligned}$$

$$\frac{3.07}{3.01} \cdot 10^{-4}$$

$$\begin{aligned} \text{MAX } \theta \text{ TILT} &= \text{ARCTAN} \frac{6 \times 10^{-6}}{4.5(2)} \\ &= \text{ARCTAN} 66 \times 10^{-6} \end{aligned}$$

$$\text{DIMENSIONS IN INCHES} \times 25.4 \times 10^3 = \mu\text{m}$$

TABLE 8-6. TEMPERATURE SOAK PRIMARY RING  
CASE A

Node	Ring No. 2 Translations		
	$\delta_Y$	$\delta_Z$	$\delta_X$
37	*5.00E-5	8.83E-5	-6.36E-5
38	9.91E-5	7.53E-5	-5.35E-5
39	1.29E-4	3.72E-5	-5.13E-5
40	1.34E-4	-1.11E-5	-4.73E-5
41	1.18E-4	-5.73E-5	-4.10E-5
42	8.67E-5	-9.48E-5	-3.76E-5
43	4.72E-5	-1.23E-4	-3.13E-5
44	6.53E-8	-1.34E-4	-2.87E-5
45	-4.70E-5	-1.23E-4	-3.15E-5
46	-8.66E-5	-9.48E-5	-3.78E-5
47	-1.18E-4	-5.73E-5	-4.12E-5
48	-1.34E-4	-1.12E-5	-4.74E-5
49	-1.30E-4	3.73E-5	-5.12E-5
50	-9.94E-5	7.50E-5	-5.36E-5
51	-5.00E-5	8.74E-5	-6.40E-5
52	-4.69E-8	8.51E-5	-7.47E-5

\*  $5.00E-5 = 5.00 \times 10^{-5}$  inches  $\times 25.4 \times 10^3 = \mu\text{m}$



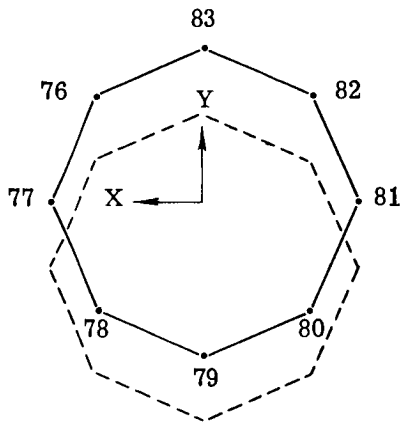
TABLE 8-7. TEMPERATURE SOAK PRIMARY RING

CASE A

Node	Ring No. 3 Translations		
	$\delta_Y$	$\delta_Z$	$\delta_X$
56	*4.61E-5	6.05E-5	-2.22E-4
57	8.51E-5	3.95E-5	-2.20E-4
58	1.13E-4	5.19E-6	-2.16E-4
59	1.22E-4	-3.77E-5	-2.09E-4
60	1.10E-4	-8.03E-5	-2.03E-4
61	8.27E-5	-1.15E-4	-1.98E-4
62	4.43E-5	-1.36E-4	-1.95E-4
63	7.99E-7	-1.43E-4	-1.94E-4
64	-4.25E-5	-1.36E-4	-1.95E-4
65	-8.05E-5	-1.13E-4	-1.98E-4
66	-1.07E-4	-7.84E-5	-2.03E-4
67	-1.18E-4	-3.56E-5	-2.08E-4
68	-1.08E-4	7.20E-6	-2.14E-4
69	-8.03E-5	4.15E-5	-2.20E-4
70	-4.11E-5	6.20E-5	-2.23E-4
71	2.66E-6	6.80E-5	-2.24E-4

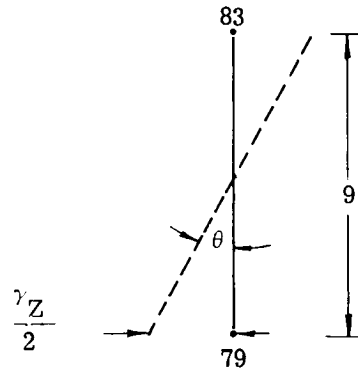
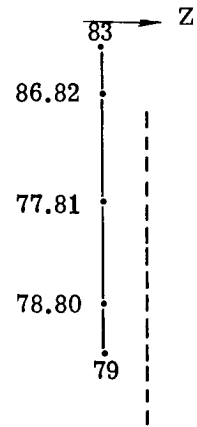
\* 4.61E-5 = 4.61 x 10<sup>-5</sup> inches x 25.4 x 10<sup>+3</sup> =  $\mu$ m

TABLE 8-8. SIP STRUCTURE THERMAL SOAK CASE B



$\gamma_{\text{decenter}} = 4.2 \times 10^{-5}$  inch

$\gamma_{\text{defocus}} = 1.5 \times 10^{-4}$  inch



Reference 21.1°C (70.0°F)  
 Soak on primary ring 21.3°C (70.5°F)  
 Soak on rest of structure 20.06°C (68.0°F)

Maximum  $\theta$  tilt =  $\arctan \frac{4.7 \times 10^{-6}}{4.5(2)}$   
 =  $\arctan 0.52 \times 10^{-6}$

Across	$\gamma_Z$ , inches
76-80	$0.033 \times 10^{-4}$
77-81	$0.00058 \times 10^{-4}$
78-82	$0.034 \times 10^{-4}$
79-83	$0.047 \times 10^{-4}$

DIMENSIONS IN INCHES  $\times 25.4 \times 10^{+3} = \mu\text{m}$

TABLE 8-9. TEMPERATURE SOAK SIP STRUCTURE  
CASE B

Node	Ring No. 2 Translations		
	$\delta_Y$	$\delta_Z$	$\delta_X$
37	*1.01E-8	-3.81E-6	1.48E-4
38	-1.59E-6	-5.38E-6	1.46E-4
39	-4.54E-6	-6.72E-6	1.53E-4
40	-1.21E-5	-7.80E-6	1.53E-4
41	-1.31E-5	-7.19E-6	1.61E-4
42	-1.07E-5	-8.45E-6	1.60E-4
43	-2.06E-6	-2.14E-5	1.74E-4
44	8.05E-9	-2.92E-5	1.81E-4
45	2.11E-6	-2.12E-5	1.74E-4
46	1.08E-5	-8.28E-6	1.60E-4
47	1.32E-5	-7.02E-6	1.61E-4
48	1.24E-5	-7.59E-6	1.54E-4
49	4.95E-6	-6.65E-6	1.53E-4
50	1.79E-6	-5.08E-6	1.46E-4
51	1.16E-7	-3.43E-6	1.48E-4
52	1.01E-7	-5.47E-6	1.45E-4

\* 1.01E-8 = 1.01 x 10<sup>-8</sup> inches x 25.4 x 10<sup>+3</sup>  $\mu\text{m}$

TABLE 8-10. TEMPERATURE SOAK SIP STRUCTURE  
CASE B

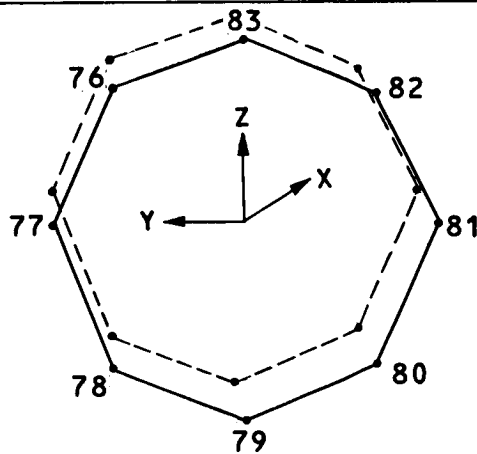
Node	Ring No. 3 Translations		
	$\delta_Y$	$\delta_Z$	$\delta_X$
56	*-2.25E-7	-1.89E-5	1.43E-4
57	-2.13E-6	-2.39E-5	1.45E-4
58	-6.03E-6	-2.80E-5	1.49E-4
59	-8.59E-6	-2.99E-5	1.53E-4
60	-7.02E-6	-3.17E-5	1.59E-4
61	-2.51E-6	-3.63E-5	1.63E-4
62	2.13E-7	-4.25E-5	1.65E-4
63	-3.18E-7	-4.55E-5	1.67E-4
64	-9.01E-7	-4.28E-5	1.65E-4
65	1.76E-6	-3.67E-5	1.63E-4
66	6.14E-6	-3.21E-5	1.59E-4
67	7.32E-6	-3.04E-5	1.53E-4
68	4.34E-6	-2.84E-5	1.48E-4
69	2.68E-7	-2.42E-5	1.46E-4
70	-1.66E-6	-1.92E-5	1.44E-4
71	-9.65E-7	-1.68E-5	1.43E-4

\* -2.25E-7 = 2.25 x 10<sup>-7</sup> inches x 25.4 x 10<sup>+3</sup> =  $\mu$  m

TABLE 8-11. OPERATIONAL THERMAL ENVIRONMENT  
(INSTRUMENTS OPERATING) COLLIMATOR  
SUPPORT STRUCTURE

CASE C

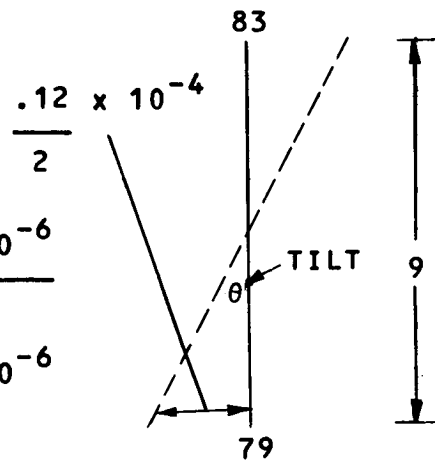
NODE	Y DISPL.	Z DISPL.	X DISPL.
76	$2.60 \times 10^{-6}$	$3.18 \times 10^{-5}$	$1.44 \times 10^{-4}$
77	$-1.61 \times 10^{-7}$	$4.11 \times 10^{-5}$	$1.39 \times 10^{-4}$
78	$4.22 \times 10^{-6}$	$4.93 \times 10^{-5}$	$1.36 \times 10^{-4}$
79	$1.28 \times 10^{-5}$	$5.27 \times 10^{-5}$	$1.34 \times 10^{-4}$
80	$2.19 \times 10^{-5}$	$5.00 \times 10^{-5}$	$1.35 \times 10^{-4}$
81	$2.69 \times 10^{-5}$	$4.11 \times 10^{-5}$	$1.38 \times 10^{-4}$
82	$2.31 \times 10^{-5}$	$3.10 \times 10^{-5}$	$1.43 \times 10^{-4}$
83	$1.24 \times 10^{-5}$	$2.69 \times 10^{-5}$	$1.46 \times 10^{-4}$



$$\delta \text{ DECENTER} \approx 4.0 \times 10^{-5}$$

$$\delta \text{ DEFOCUS} \approx 1.45 \times 10^{-4}$$

$$\begin{aligned} \text{MAX } \theta \text{ TILT} &= \text{ARCTAN} \frac{.06 \times 10^{-6}}{4.5} \\ &= \text{ARCTAN} 1.33 \times 10^{-6} \end{aligned}$$



DIMENSIONS IN INCHES  $\times 25.4 \times 10^3 = \mu\text{m}$

TABLE 8-12. OPERATIONAL THERMAL ENVIRONMENT  
(INSTRUMENTS OPERATING, RING NO. 2)

CASE C

Node	Translations		
	$\delta_Y$	$\delta_Z$	$\delta_X$
37	*-5.43E-6	-1.26E-5	3.88E-5
38	-1.09E-5	-7.65E-6	3.83E-5
39	-1.32E-5	-1.19E-6	3.61E-5
40	-1.24E-5	4.99E-6	3.29E-5
41	-9.21E-6	9.74E-6	2.91E-5
42	-4.71E-6	1.23E-5	2.56E-5
43	-4.94E-7	1.32E-5	2.17E-5
44	2.90E-6	1.25E-5	1.85E-5
45	5.43E-6	1.06E-5	1.78E-5
46	7.50E-6	8.44E-6	1.87E-5
47	1.00E-5	6.62E-6	1.96E-5
48	1.24E-5	4.13E-6	2.22E-5
49	1.39E-5	5.82E-7	2.69E-5
50	1.39E-5	-4.85E-6	3.18E-5
51	1.03E-5	-1.06E-5	3.53E-5
52	2.78E-6	-1.35E-5	3.88E-5

\* -5.43E-6 = 5.43 x 10<sup>-6</sup> inches x 25.4 x 10<sup>3</sup> =  $\mu$ m

TABLE 8-13. OPERATIONAL THERMAL ENVIRONMENT  
(INSTRUMENTS OPERATING, RING NO. 3)

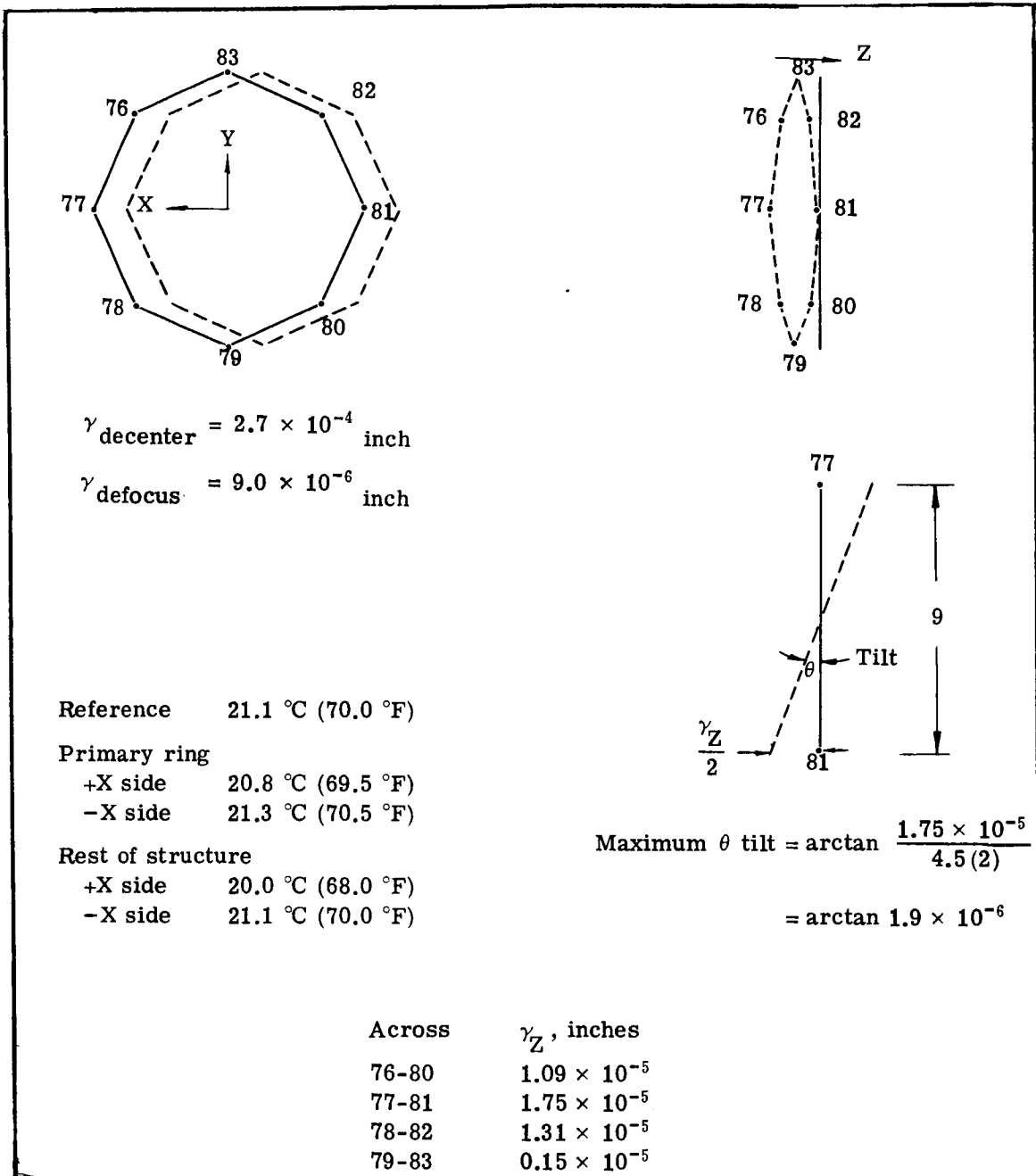
CASE C

Node	Translations		
	$\delta_Y$	$\delta_Z$	$\delta_X$
56	*-1.24E-5	-3.34E-5	1.01E-4
57	-3.24E-5	-1.98E-5	9.64E-5
58	-4.57E-5	-1.07E-6	9.20E-5
59	-4.93E-5	2.09E-3	8.68E-5
60	-4.22E-5	4.18E-5	8.19E-5
61	-2.72E-5	5.79E-5	7.62E-5
62	-8.51E-6	6.80E-5	7.08E-5
63	1.14E-5	7.05E-5	6.59E-5
64	3.03E-5	6.54E-5	6.42E-5
65	4.66E-5	5.41E-5	6.47E-5
66	5.94E-5	3.85E-5	6.75E-5
67	6.62E-5	1.90E-5	7.07E-5
68	6.47E-5	-1.75E-6	7.51E-5
69	5.47E-5	-1.99E-5	8.23E-5
70	3.70E-5	-3.31E-5	9.25E-5
71	1.28E-5	-3.85E-5	1.00E-4

\* -1.24E-5 =  $1.24 \times 10^{-5}$  inches  $\times 25.4 \times 10^3 = \mu\text{m}$

TABLE 8-14. OPERATING THERMAL ENVIRONMENT  
(BOUNDARY CASE)

CASE D



DIMENSIONS ARE IN INCHES X  $25.4 \times 10^3 = \mu\text{m}$



TABLE 8-15. OPERATIONAL THERMAL ENVIRONMENT  
(BOUNDARY CASE, RING NO.2)

CASE D

Node	Translations		
	$\delta_Y$	$\delta_Z$	$\delta_X$
37	*-1.76E-4	7.54E-7	-2.15E-5
38	-1.74E-4	3.93E-7	-3.55E-5
39	-1.72E-4	3.04E-7	-4.52E-5
40	-1.70E-4	-1.04E-6	-4.76E-5
41	-1.73E-4	-2.21E-6	-4.57E-5
42	-1.76E-4	-1.77E-6	-3.61E-5
43	-1.79E-4	-8.97E-7	-2.27E-5
44	-1.81E-4	-7.33E-7	-6.26E-6
45	-1.81E-4	-8.87E-7	1.06E-5
46	-1.80E-4	-9.47E-8	2.48E-5
47	-1.78E-4	1.60E-6	3.43E-5
48	-1.75E-4	1.96E-6	3.68E-5
49	-1.76E-4	1.92E-6	3.47E-5
50	-1.77E-4	2.68E-6	2.54E-5
51	-1.77E-4	2.62E-6	1.15E-5
52	-1.77E-4	1.66E-6	-4.68E-6

\* -1.76E-4 =  $-1.76 \times 10^{-4}$  inches  $\times 25.4 \times 10^3 = \mu\text{m}$

TABLE 8-16. OPERATIONAL THERMAL ENVIRONMENT  
(BOUNDARY CASE, RING NO. 3)

CASE D

Node	Translations		
	$\delta_Y$	$\delta_Z$	$\delta_X$
56	*-2.33E-4	2.40E-6	-2.28E-5
57	-2.31E-4	2.15E-6	-3.71E-5
58	-2.30E-4	1.40E-6	-4.63E-5
59	-2.30E-4	1.75E-7	-4.95E-5
60	-2.31E-4	-8.79E-7	-4.67E-5
61	-2.33E-4	-1.11E-6	-3.81E-5
62	-2.35E-4	-5.71E-7	-2.50E-5
63	-2.36E-4	2.35E-7	-9.19E-6
64	-2.37E-4	1.19E-6	7.34E-6
65	-2.36E-4	1.98E-6	2.15E-5
66	-2.35E-4	2.56E-6	3.07E-5
67	-2.34E-4	2.74E-6	3.38E-5
68	-2.34E-4	2.61E-6	3.08E-5
64	-2.34E-4	2.42E-6	2.24E-5
70	-2.33E-4	2.29E-6	9.45E-6
71	-2.33E-4	2.28E-6	-6.33E-6

\* -2.33E-4 = -2.33 x 10<sup>-4</sup> inches x 25.4 x 10<sup>3</sup> =  $\mu$ m

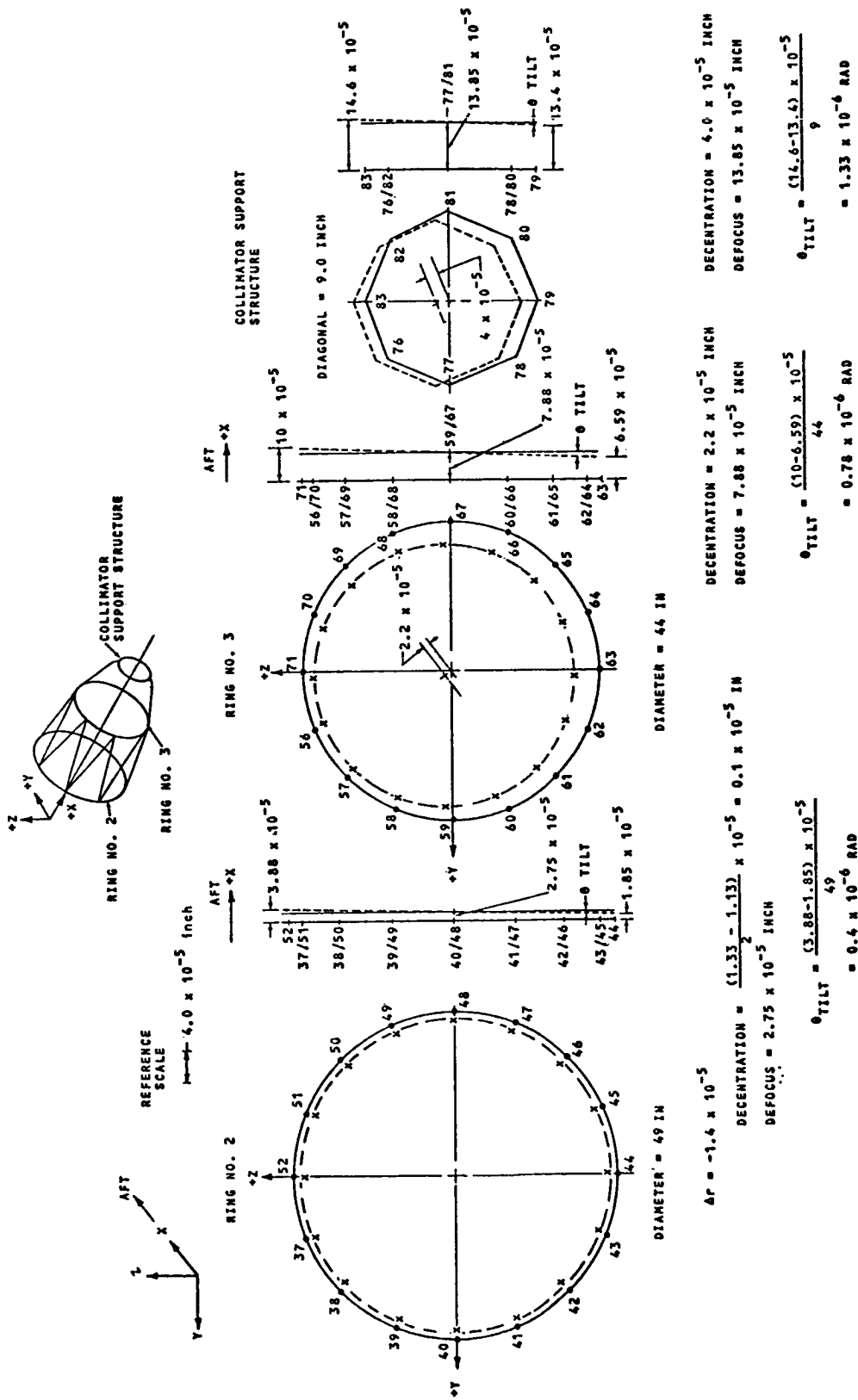


Figure 8-10. Structure Deformations  
CASE C

TABLE 8-17. RESULTS OF SIP THERMAL DEFORMATION ANALYSIS

Case	Description	Ring No. 2			Ring No. 3			Collimator Support		
		$\delta_T^*$ $\mu\text{m}$	$\delta_A^{**}$ $\mu\text{m}$	$\theta_t^{***}$ $\mu\text{rad}$	$\delta_T$ $\mu\text{m}$	$\delta_A$ $\mu\text{m}$	$\theta_t$ $\mu\text{rad}$	$\delta_T$ $\mu\text{m}$	$\delta_A$ $\mu\text{m}$	$\theta_t$ $\mu\text{rad}$
A	Thermal Soak (Primary Ring)	.64	1.19	.94	.97	5.3	.68	1.27	7.72	0.66
B	Thermal Soak (SIP Structure)	.43	3.88	.73	.79	3.88	.55	1.07	3.81	.52
C	Operating Thermal Environment (Instruments Operating)	.025	.71	0.4	.56	2.0	.78	1.02	3.53	1.33
D	Operating Thermal Environment (Boundary Case)	4.62	.15	1.72	6.0	.20	1.89	6.85	.23	1.9

\* Transverse Displacement of central axis (Decentration in the case of the Collimator Support).

\*\* Axial Displacement along center axis (Defocussing in the case of the Collimator Support).

\*\*\* Tilt about transverse axis.

b. Effect of Structural Deformations on Instrument Performance

In the following assessments of effects of thermal shifts it is assumed that the operational cycles will span all conditions from nominal temperature to the extremes used in the analysis.

The movements of the collimator support structure for the four cases in the structures thermal analysis can be directly compared to the tolerances for alignment, focus and centering of the collimator assembly. These movements are summarized in Table 8-17. The decentration and the tilt both have the same kind of effect on the collimated output direction. These two effects should not be root mean square added because they are systematically rather than randomly related. The significant movement to observe is the movement of the center of curvature of the collimator mirror as a function of tilt and decentration of the support surface relative to the slit assembly which is assumed to be stationary. The tilts shown in Tables 8-3, 8-6, 8-10 and 8-14 are all clockwise around an axis approximately parallel to the direction of the "Y" axis. The decentration adds to the shift of the center of curvature when it is in the +"Z" direction. Since the change in direction of the collimated beam, which is twice the tilt of the mirror, is the variable of interest for the spectrographs, the lateral shifts are converted to equivalent tilts of the mirror by dividing them by the mirror focal length. The summation is algebraic in all cases except Case D in which the lateral movement vector is at right angles to the tilt vector where the addition is vectorial. The axial shifts are repeated from Table 8-17 for evaluation of the effects on focus.

<u>Case</u>	<u>Tilt</u>	<u>Decentration/EFL</u>	<u>Collimated Beam Tilt = 2 x Sum</u>	<u>Collimator Focus Shift</u>
A	0.66 $\mu$ rad	-0.88 $\mu$ rad	-0.44 $\mu$ rad	7.62 $\mu$ m
B	0.52 $\mu$ rad	-0.74 $\mu$ rad	-0.44 $\mu$ rad	3.81 $\mu$ m
C	1.33 $\mu$ rad	+0.71 $\mu$ rad	+4.08 $\mu$ rad	3.53 $\mu$ m
D	1.9 $\mu$ rad	+4.75 $\mu$ rad	+10.2 $\mu$ rad	0.23 $\mu$ m

$$\text{Sum} = (\text{Tilt}) + \frac{\text{Decentration}}{\text{EFL}}$$

The lateral shift at the spectrograph camera focal planes has been assigned a tolerance of one-half of a camera resolution element, 0.0125 mm, in the individual instrument discussions. The tilt of the collimated beam multiplied by the respective camera mirror focal length gives the shift resulting from these beam tilts. The longest focal length is in the two High Resolution Echelle Spectrographs and is 1205 mm. The Faint Object No. 1 Spectrograph has a camera mirror focal length of 1080 mm.

The beam tilts for the four cases result in shifts of 0.000265, 0.00256, 0.00188 and 0.0123 mm. The very worst case exactly equals the tolerance which has been allowed, which indicates that the structural concept is adequate even for the unusual temperature distribution assumed.

The focus tolerance has its smallest value in the case of the lowest f number which is the Faint Object Spectrograph operating at f/9. In this case, the defocus tolerance, developed in Section 4, is 0.250 mm. The tolerance which is even greater at the f/12 collimating mirror is far larger than the few microns shifts predicted in the four thermal cases (Tables 8-17  $\delta A$  of collimator support).

The angular movements which will show up at the mountings of the three rear spectrographs are a function only of the relative decentration of rings 2 and 3 assuming that the extension from these rings to the actual mounting interface does not add significantly to the results from analysis of the rings. Since these spectrographs have their optical interface in collimated light, only angular shifts at the mechanical interface have significance. It has been seen in the preceding paragraphs that the High Resolution Spectrographs have the smaller tolerance for rotation relative to the collimated beam because of their longer focal length camera mirrors.

The previous analysis of tilts and shifts of the collimator support, which is the most responsive part of the structure to thermal changes, indicates that the shifts at the spectrograph mountings will be negligible, therefore only the worst of the four cases is used for analysis. Inspection of Table 8-17 shows that Case D is the most severe for lateral shifts of both rings individually and differentially. Further, by inspection of Tables 8-15 and 8-16 it can be seen that the lateral shifts are uniform within a few percent in the "Y" direction for both rings. Therefore, the value of the maximum decentration in Table 8-17 is directly applicable to determining the tilt for all three of the instruments in the rear bay. The tilt movement is then the difference in the maximum decentrations divided by the spacing from ring to ring.

Case D Decentration of Ring No. 2	= 4.6 $\mu\text{m}$
Case D Decentration of Ring No. 3	= 6.0 $\mu\text{m}$
Difference	= 1.4 $\mu\text{m}$
Ring to Ring Spacing	960 mm
Tilt of Spectrograph Mounting	$\frac{1.4 \mu\text{m}}{960 \text{ mm}} = 1.46 \mu\text{rad}$

This tilt can be quite safely neglected, as in the previous section the beam tilt of 10.2  $\mu\text{rad}$  was found equal to the tolerance.

There is one more important interface with the axial bay SIP Structure which seems to be more critical. That is the mounting of the f/96 Camera. This unit has its optical interface at the OTA Central focal point and the tolerable lateral shift measured at this point was developed in Section 4 to be 0.00156 mm. Variation of this registration is a function of tilts and translations of the f/96 camera optics housing. The combined effects of movements of the two mountings which are extensions of rings 2 and 3 at nodes 44 and 63 is most directly measured by graphical analysis. This analysis is shown on Figure 8-11. The f/96 camera is indicated by lines OPS which connect the object, the pinning point of the mounting and the sliding point of the mounting. Node 44 of ring 2 and node 63 of ring 3 are shown in section connected by zero expansion struts to the mounting support members at P and S. The movement of the supports at points P and S for cases A, B, and C are taken from Tables 8-4, 5, 7, 8, 11 and 12 and are shown to a scale of 1 inch =  $10^4$  inch. Case D is not shown because even at this scale the movements are too small to plot. The camera is made to follow the movements of point "P" and remain in contact with the mounting at "S". The departures at "O" are compared to the tolerance value of .00156 mm (62.4  $\mu$  inches) lateral deviation and 0.0187 mm (750  $\mu$  inches) focus deviation. All other dimensions are shown in inches to agree with the tables from which they were taken. From inspection of the figure it can be seen that all three cases shown are within the focus tolerance, but that Case B falls out of the lateral shift tolerance. The consequence of this shift being beyond the assigned tolerance cannot be determined until further work relating the simultaneous changes in the camera itself to those of the supporting structure is accomplished. It can generally be predicted that simultaneous shifts of this nature will tend to compensate each other.



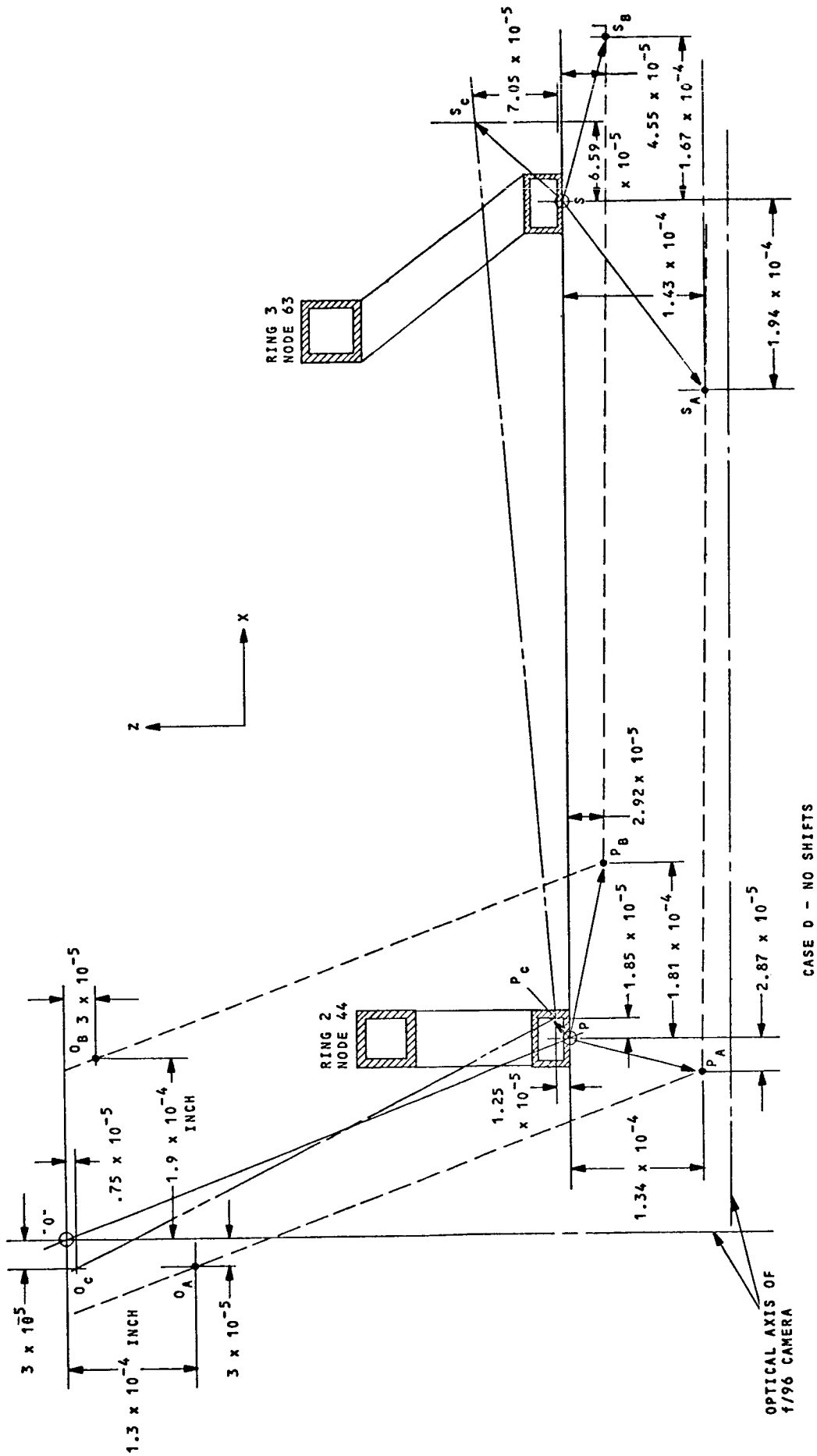


Figure 8-11. Structural Shifts at f/96 Camera Mounting

### 8.5.3 Launch and Reentry Loads

In order to perform a stress analysis of the SIP structure the computer model was revised in the following manner; the eight points that attach to the primary ring were restrained from translation in the X, Y and Z directions and the masses of the instruments were added in their respective places. To obtain unit stresses a 1g load was applied individually in each direction. Taking the 1g loads and applying the given design limit load factors of 6.0, 1.5, 1.5 in the appropriate directions, stresses less than 10,000 psi, well below the allowable ultimate design stresses of graphite-epoxy composites, were determined.

### 8.5.4 Resonant Frequency

The same graphite-epoxy composite model that was used for the stress analysis was also analyzed for stiffness. Based on the weight of the instrumentation and the dead weight of the structure in conjunction with the stiffness of the graphite-epoxy composite structure, a first frequency of 28.6 Hz was obtained.

## 8.6 SIP THERMAL DESIGN AND ANALYSIS

### 8.6.1 Introduction

The following is a description of the thermal control concepts developed for the SIP, and a summary of supporting analysis performed to verify the adequacy of the approach. Response of specific instrumentation to thermal perturbations are discussed in Section 7, and the response of the SIP structure is discussed in Section 8.4 above.

It is required that, as part of the overall thermal design effort of the LST, to develop a thermal control concept for the SIP. This design must take into account, not only the thermal perturbations resulting from orbital operation and orientation but also, the random operation of individual instruments as well. Specific requirements for the instruments cameras have been discussed in Section 7.

## 8.6.2 Thermal Control Concepts

### 8.6.2.1 Constant "T" System

This thermal control method proposes to enclose the entire instrument compartment structure and instruments within an aluminum shell which is thermostatically controlled at 21.1C. The major thermal power sources, the cameras, are outside of this thermal shroud and are free to radiate to the pressure shell wall. The thermal shroud is polished on the external surfaces to provide a low emittance ( $\epsilon = .04$ ) to the pressure shell walls and thus reduce thermal control power. The interior of the shroud is coated to provide a high emittance and thus closely couple the internal structure to the temperature controlled walls of the shroud.

In order to provide thermal control, the pressure shell walls are insulated with a low performance insulation ( $\epsilon^* \approx .09$ ) which provides a cold background. The insulation characteristics were initially selected to provide a thermally balanced system rejecting 300 watts from the shroud.

This concept provides a close control on the temperature of the structure and the associated instruments or structure mounted components. Because of this control, the design is quite insensitive to material substitutions or variations in the thermal coefficient of expansion. Since this concept encloses the entire structure within a metal shroud, it is obvious that maintenance problems may be encountered. This shroud requires careful design to allow for the removal of various sections for access to specific instruments or components. The cameras however, are fully exposed and there appears to be no access problems. This design is fully compatible with a laminar airflow concept. It should also be noted that supplementary pressure shell wall heaters may be required if, during maintenance operations, parts of the thermal shroud have been removed.

#### 8.6.2.2 Insulated Structure System

This concept is based on the idea that the structure and instruments can be isolated from the walls of the pressure shell with multilayer insulating blankets while allowing the cameras to radiate to the wall in order to reject the operating power. Since the primary structure is thermally decoupled from the cooler pressure shell it will experience attenuated thermal transients which may occur at the wall.

The pressure shell wall is thermally decoupled from the outer wall of the vehicle by means of a high performance multi-layer insulation (MLI) blanket ( $\epsilon^* \approx 0.01$ ) which reduces the overall thermal leakage and external temperature transients.

In contrast to the thermal shroud concept discussed previously, manned maintenance does not appear to present a problem. Access to all instruments and components can be accomplished by careful removal of a MLI blanket. Compatibility with the laminar airflow requirement will require some design effort and this may be accomplished by enclosing the open regions of the light bundle in thin metal shells to provide a continuous air path from end-to-end. The use of supplemental wall heaters during maintenance may be required.

#### 8.6.2.3 Constant "Q" System

This thermal control method proposes to maintain the SIP inner wall at temperatures below or near 293 K while radiating the power dissipated in the scientific instruments and in the thermoelectric coolers to the wall. When certain instruments are switched off, their power dissipation will have to be made up by  $I^2R$  heaters. The heaters may be on the compartment wall or on the instruments. The compartment walls will be insulated with a low performance insulation system whose average  $\epsilon^*$  will produce a system energy balance and maintain the wall temperature near 293 K maximum for hot conditions. The use of heaters will provide a near constant energy source within the SIP. If the heaters are located in the photocathode camera radiators the temperature distribution will remain nearly constant on

the truss structure and cancel displacements caused by duty cycling of the cameras. Because of the low coefficient of expansion of the graphite epoxy material ( $.13 \times 10^{-6} \text{K}^{-1}$ ), the philosophy in building the math model was to leave all radiating surfaces black and allow the support structure temperatures to run hot with gradients. Adding a low  $\epsilon$  surface finish would have no significant impact in this case.

The manned maintenance of this system presents no problems in terms of accessibility since it is similar to the insulated structure. The laminar airflow may also be solved in a fashion identical to that suggested for the insulated structure. The remaining problems in terms of maintenance is the effect of turning off the constant power sources within the compartment.

This results in a cooldown of the pressure shell from its nominal value of 293 K. Supplemental heaters must be provided to account for the heat being released by the cameras. The alternate systems, which incorporate more efficient insulation systems require less power for the same condition.

#### 8.6.2.4 SIP Thermal Model

A detailed thermal model of the instrument compartment was made, and consists of 147 nodes with approximately 840 radiation connections and 230 conduction connections depending on the specific configuration. The detailed thermal model of the SIP can be categorized into the following areas:

##### a. Outer Thermal Control Surface (meteoroid shell)

As shown in Figure 8-12, this surface was divided into 16 nodes (nodes 500 - 515). The material of the structure was assumed to be aluminum (6061-T6) and subject to the following boundary conditions:

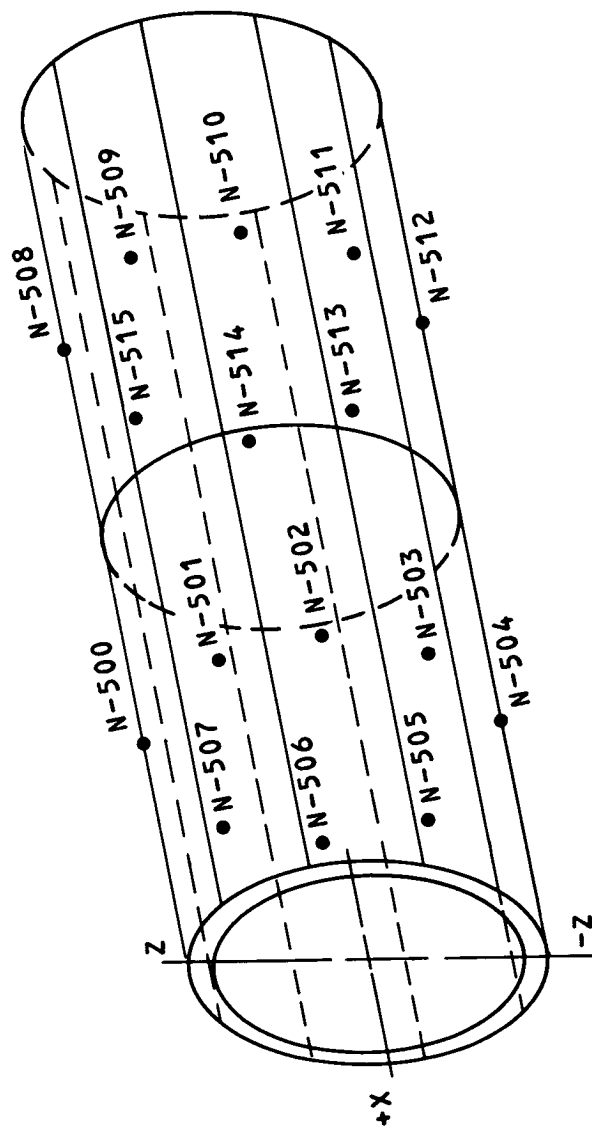


Figure 8-12. Outer Thermal Control Surface - Nodal Network

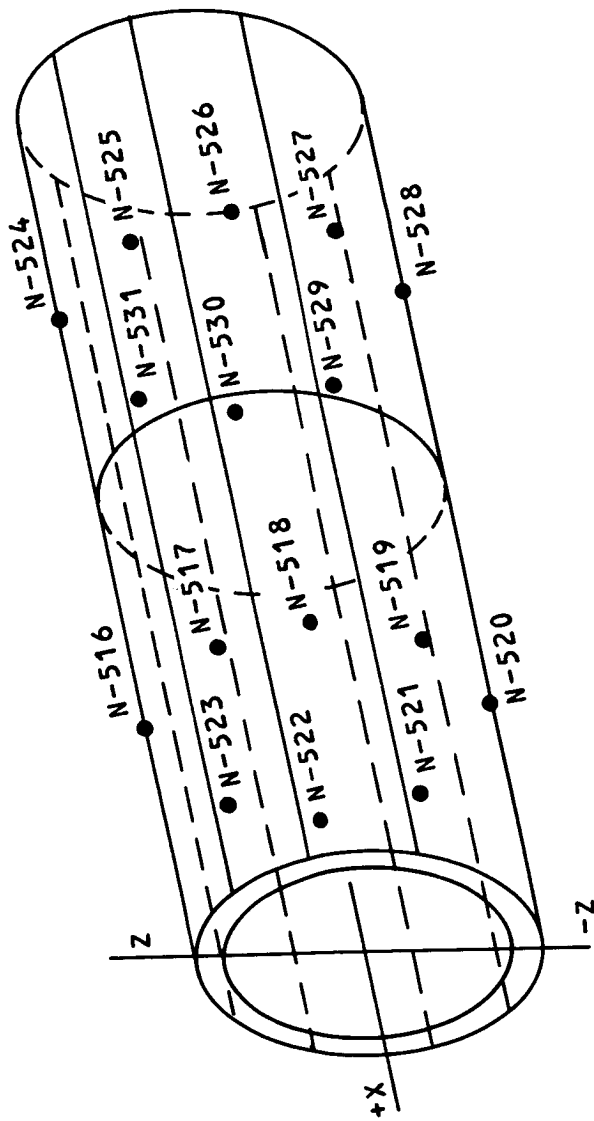


Figure 8-13. Pressure Cylinder Wall - Nodal Network

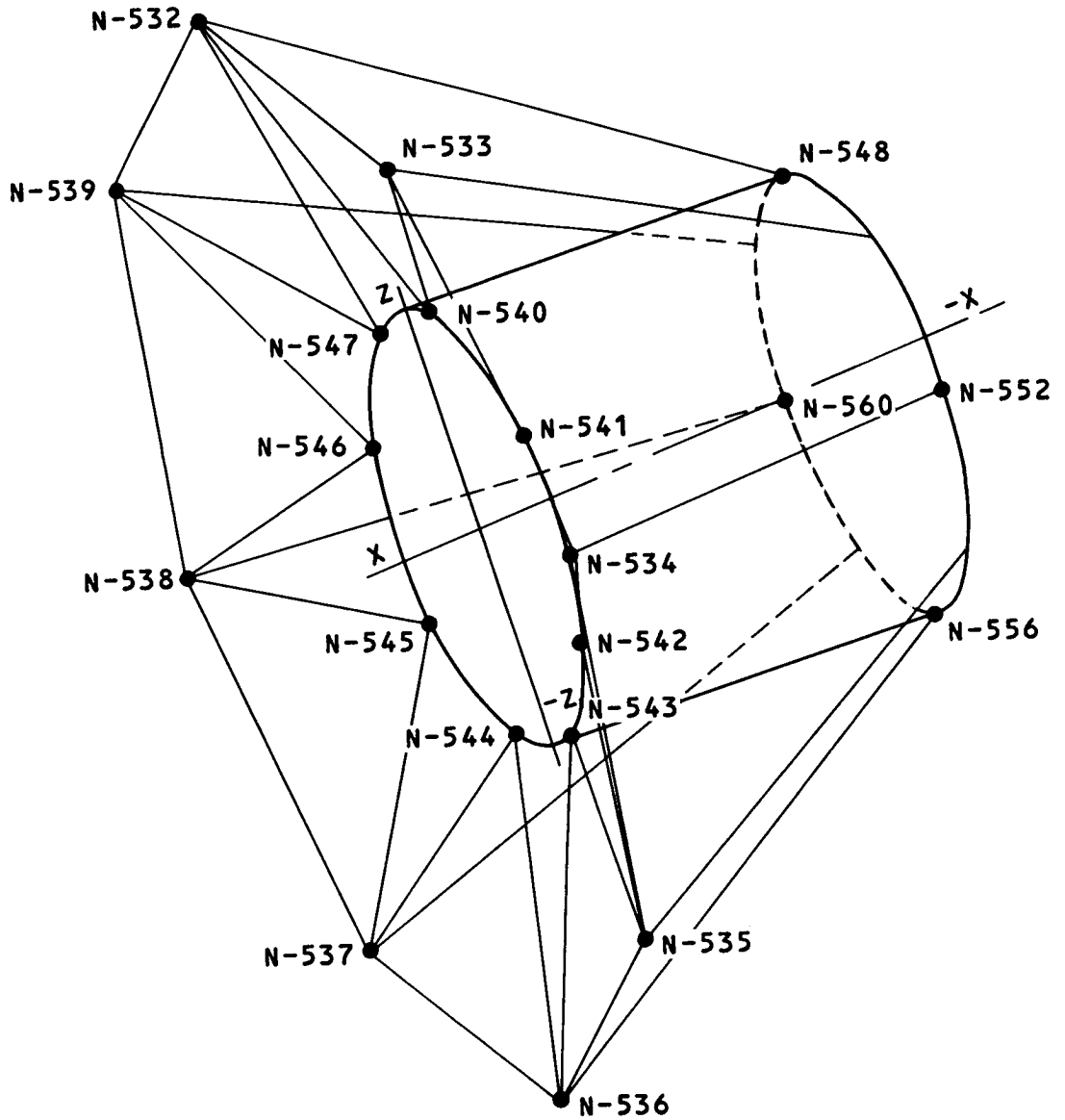


Figure 8-14. Radial Truss Nodal Network



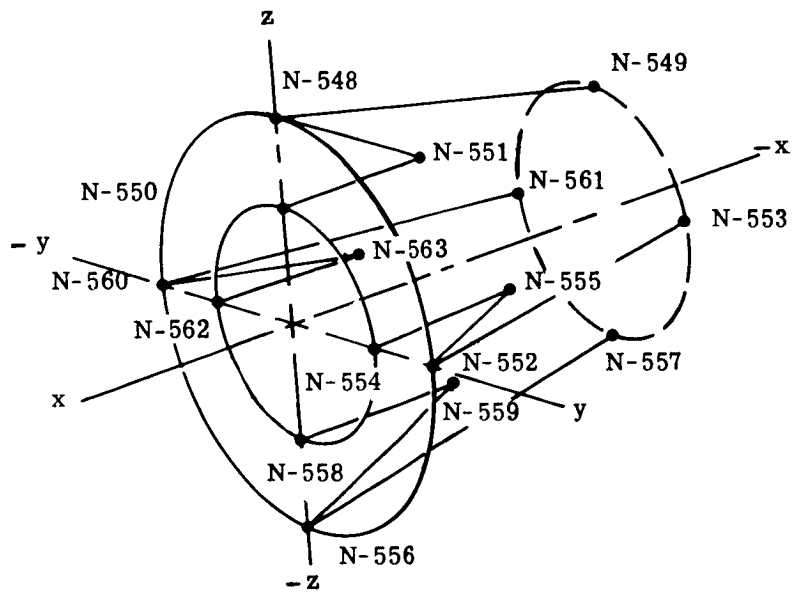


Figure 8-15. Nodal Network - Axial Truss

1. Orbital beam fluxes for a 400 nm orbit.
2. Heat loss from surface to 4 K space.
3.  $\alpha S/\epsilon = .135/.92 = .146$

b. Pressure Shell Wall

As shown in Figure 8-13 this surface was divided into 16 nodes (node 516-531), the material of the structure was assumed to be aluminum (6061-T6).

c. SIP Support Structure Radial Truss

Nodal identification of this structure is shown in Figure 8-14. The structure was divided into 28 nodes and consisted of a titanium primary ring, (nodes 532-539) and a graphite epoxy truss network. The primary ring temperature was held at 295 K while the remainder of the structure was not controlled directly and received heat input from operating cameras and the surroundings. An axial conductivity of  $43.8 \frac{\text{BTU}}{\text{hr-ft-F}}$  (4.33 W/m-K) and  $49.4 \frac{\text{BTU}}{\text{hr-ft-F}}$  (4.88 W/m-K) was used for various graphite layups.

The contact resistance encountered in all truss connections was neglected because preliminary analysis indicated that this resistance was negligible in comparison to the axial resistance of the members.

d. SIP Support Structure - Axial Truss

Nodal identification of this structure is shown in Figure 8-15. An axial conductivity of 253.1 W/m-K was used for truss members. The purpose of this truss network was to support the echelle spectrographs and a Faint Object Spectrograph (110 to 220 nm); heat inputs to the truss were produced by conduction from these instruments and radiation from the surroundings. A contact conductance of  $1.91 \times 10^4$  W/m-K was assumed for all instrument mounting connections.

e. Node Identification

The nodal identification for the instrumentation contained in the scientific instrument package are as follows:

<u>Node</u>	<u>Camera</u>
597	High Resolution Spectrograph (110 to 180 nm)
602	High Resolution Spectrograph (180 to 350 nm)
606	f/96 Camera(High Resolution Camera)
607	f/96 Camera(High Resolution Camera)
608	f/96 Camera(High Resolution Camera)
617	Faint Object Spectrograph (110 to 220 nm)
620	Faint Object Spectrograph (220 to 660 nm)
622	Faint Object Spectrograph (660 to 1000 nm)
624	Mid-Ir Interferometer
625	Slit Jaw Camera
614	f/12 Camera

For analysis purposes, the following camera power dissipations were used: 76 watts for the 50 mm format cameras (f/96 and f/12) and 59 watts for the 25 mm format cameras. This power is based on the instrument integration time only since the readout is assumed to be negligible. It includes an estimate for thermo-electric cooling power lower than mentioned in Section 7 due to a cooler environment for the detector cooler radiators.

#### f. Structural Changes

The current SIP structure is not reflected in the thermal model as the structural concept was modified after the model had been made. The major region of divergence is the radial bay internal region. The model is based on the prior concept of a cylindrical shell supported between two truss and ring members (see Figure 8-4), whereas the current structural concept has replaced the cylindrical shell with a truss structure.

In terms of the concepts previously discussed and subsequently evaluated, the thermal model results, in terms of temperature distributions and heater power, are considered valid for the shroud concept and the insulated structure concept. The validity of the temperature distributions calculated for the constant power output system are subject to some doubt, however this is of minor concern since that concept is considered the least promising thermal control approach.

### 8.6.3 Results of Thermal Model Studies

#### 8.6.3.1 Constant "Q" System

As indicated in the previous discussion, the temperature distributions determined for this system are questionable. Structure temperatures in excess of 310K were calculated. Even if we ignore these structural temperatures, this concept is considered to be least promising for a thermal control system due to the high power required to maintain a constant thermal power output.

#### 8.6.3.2 Constant "T" System

The constant temperature system has been examined for both the "hot" and "cold" orbital conditions representing the extremes in terms of induced thermal gradients and maximum thermal control power respectively. A camera operational duty cycle was imposed on the model to examine transient thermal effects.

The duty cycle consisted of an initial period of 24 hours with no instrument power followed by a 10 hour operation of all three f/96 cameras. The system was then unpowered for 6 hours at which time one of the aft spectrographs was powered for 10 hours.

Typical results of this operation for the enclosed shroud approach, in terms of structural temperature response are presented in Table 8-18 for the initial and final structural temperatures during the operation of the f/96 camera complement in the "hot" orbit. Temperature changes in no case exceed 0.1K during this period. During this period, the camera temperatures increase from 286K to 313K (56F) to (105F), however, they are isolated from the instrument and structure radiatively by the thermal shroud and conductively by a high thermal resistance mounting configuration

The thermal power required to maintain the thermal shroud at 294.1K (70F) is estimated to be 65 watts average.

TABLE 8-18. TRANSIENT STRUCTURAL TEMPERATURE DISTRIBUTION -  
THERMAL SHROUD CONCEPT

Node and Description	24 Hrs.	34 Hrs.	Node and Description	24 Hrs.	34 Hrs.
540	70.0	70.0	552	69.6	69.6
541	70.2	69.9	553	69.5	69.5
542	70.0	70.0	554	69.5	69.4
543	70.0	70.1	555	69.6	69.5
544	70.0	69.9	556	69.6	69.7
545	70.0	69.9	557	69.6	69.6
546	70.1	70.0	558	69.4	69.4
547	70.1	70.1	559	69.6	69.6
548	69.6	69.8	560	69.6	69.7
549	69.6	69.6	561	69.5	69.5
550	69.5	69.5	562	69.4	69.4
551	69.6	69.6	563	69.5	69.5

TABLE 8-19. TRANSIENT STRUCTURAL TEMPERATURE DISTRIBUTION -  
INSULATED TRUSS CONCEPT

Node and Description	24 Hrs.	34 Hrs.	Node and Description	24 Hrs.	34 Hrs.
540	69.35	69.30	552	68.82	68.75
541	69.38	69.40	553	68.71	68.46
542	69.48	69.64	554	68.17	68.13
543	69.53	69.85	555	68.53	68.25
544	69.47	69.84	556	68.98	69.22
545	69.38	69.49	557	68.80	68.70
546	69.35	69.35	558	68.25	68.29
547	69.34	69.28	559	68.57	68.32
548	68.72	68.53	560	68.79	68.69
549	68.68	68.34	561	68.74	68.46
550	68.51	68.26	562	68.57	68.39
551	68.53	68.14	563	68.58	68.22

### 8.6.3.3 Insulated Structure System

The insulated structure system was investigated in a manner identical to that used for the constant temperature system discussed above. The identical duty cycle was imposed on the camera complement. Table 8-19 presents the structural temperatures both immediately before and at the termination of f/96 Camera operation. Although the temperatures are slightly lower (reflecting the lack of thermal control on the structure), the characteristic change during this period is less than 0.25K. It is also interesting to note that an axial gradient of approximately .7K from the main mounting ring is seen. Again this is due to the lack of direct thermal control on the structure. The direct thermal control power to maintain the instrument array at 294.1K has been estimated to be 14 watts average.

To illustrate the effects of instrument duty cycle on the cameras and their respective instruments, Table 8-20 presents the temperature history of the baseline instrument complement during the previously mentioned 50 hour time period. This particular run did not include instrument heaters. The results indicate that the f/96 Camera temperature increases approximately 33K during the ten hour time span. Examination of the detailed data also reveals that the Cameras are almost at a steady state temperature at this time (temperature increase less than .5K per hour). Over the last 16 hours of the run, the Cameras cool down and are within 1K of their initial temperature.

It is interesting to observe the secondary effects on the other instruments within the system after the release of 2780 watt hours of power within the SIP. All cameras increase in temperature with the largest effects appearing at the three aft mounted cameras closest to the f/96 array.

TABLE 8-20. TRANSIENT CAMERA AND INSTRUMENT  
TEMPERATURE DISTRIBUTION - INSULATED TRUSS CONCEPT

Node Description	Temperature °F			
	24 Hrs.	34 Hrs.	40 Hrs.	50 Hrs.
596	68.1	67.4	67.3	66.9
597	58.2	62.2	61.0	60.0
601	68.1	67.4	67.2	68.8*
602	56.1	60.3	60.2	93.9*
606	61.9	113.3	70.8	63.7**
607	62.1	115.1	71.7	63.9**
608	62.1	113.8	71.1	64.0**
609	69.3	70.7	71.1	70.8
614	69.9	69.4	09.9	09.8
616	68.5	68.3	68.2	67.8
617	56.2	63.0	61.4	60.0
620	63.5	64.5	64.9	64.4
621	69.0	68.6	68.4	68.1
622	63.4	64.3	64.7	64.3
623	69.1	68.5	68.4	68.0
625	62.3	64.0	64.4	64.0
626	69.1	68.7	68.6	68.5

\* On 40-50 hrs.  
 \*\* On 24-34 hrs.  
 $K = 5/9 (°F - 32) + 273$

#### 8.6.4 Discussion of Results

Based on the results reported, it is recommended that the constant "T" SIP thermal control system be studied further. This recommendation is based primarily on the fact that the system is thermally feasible, offers reasonably positive control of structural temperatures, and is currently compatible with the laminar air flow concept. The two outstanding problems with this concept are:

1. The maintenance requirements imposed by an additional fixed structure surrounding the truss to the primary ring and enclosing the instrument complement are increased (probably solvable by design of a multi-panel shroud with suitable removable access ports).
2. Heat rejection requirements for the f/12 camera (in its present location) require more detailed design and analysis. This problem must be resolved in concert with the design of the thermal shroud indicated above.

Present indications are that the insulated structure concept is also feasible, with greatly improved service access. As such, it provides us with an alternate which, although not providing direct thermal control, appears viable with an ultra low expansion structure (graphite epoxy composite).

It also has the advantage of lower total power requirements shown in Table 8-21, a power saving that pays doubly since it results in a lower average temperature that in turn decreases the power input to the Peltier coolers for the detector tubes discussed in Section 7.

In the process of evaluating and reviewing the thermal model data, it was observed that the predicted thermal control power for the recommended baseline concept was much lower than expected. A review of the model revealed a major heat leak from the main support ring to the pressure shell wall causing the wall to run warm. An examination of the structural design indicates that this is the



case since the pressure shell wall is hard mounted to the main ring for load carrying purposes. The magnitude of this leak measured by the heat input to the main support ring is shown in Table 8-21. The actual leak seems to vary with the different methods of temperature control but what is indicated is whether the heat is supplied to the ring from the warm SIP, as in the case of the Constant "Q", or from the ring to the SIP, as in the other two cases in which the structure temperatures are cooler.

TABLE 8-21. THERMAL POWER REQUIREMENTS

	Constant "Q" System	Constant "T" System	Insulated Structure System
SIP Thermal Control Power	660 watts	65 watts	14 watts
Primary Ring Control Power	0 watts	356 watts	160 watts
Total Power	660 watts	421 watts	174 watts

If this leak is reduced (for example, by increasing the thermal resistance to the shell), the direct thermal power required for maintaining the shroud at 294K will be increased and the net power reduction will be minimal. In the case of the insulated structure, reduction of the thermal leak will reduce the wall temperature secondary power and the "floating" structural temperatures accordingly. This area should be given careful study as soon as possible since it does impact the overall design. Wall temperatures in the 283 ±5K range will result.

A comparison of the results of this study with the camera cooling study, Section 7, indicates that the cameras are operating significantly cooler than predicted. In part, this is the result of sink temperatures below the 293K postulated in that analysis,

i.e., 283  $\pm$ 5K. It is also the result of the use of a lower power consumption estimate for the thermal model cameras. This lower dissipation is based on later discussions with a thermoelectric module manufacturer wherein it was determined that module efficiency of 20% was attainable for our application. For this analysis, an efficiency (COPR), coefficient of performance, of 16% was used.

## Section 9

### INTERFACE CONSIDERATIONS

#### 9.1 INTRODUCTION

This section is a summary of the SIP interface considerations and specifications. The optical, pointing, and mechanical considerations have been examined in detail in Sections 3, 4 and 5. Therefore, only the interface specifications are presented in this section.

The data handling falls into two categories, scientific data and diagnostic data. Scientific data is examined for the impact of tube resolution, sampling rate, sensor bandwidth, and required transmission time. Table 9-2 summarizes the scientific data requirements. The diagnostic data is examined for its impact upon performance monitoring, troubleshooting, and the effect on ground control and mission planning. Table 9-3 is a detailed and summarized estimate of the diagnostic data bits and average bit rates required.

General power consumption and distribution problems are discussed. Because power consumption is a function of instrument usage, "typical" power profiles are shown and a per instrument breakdown is given. Based on the data and power handling considerations, an interface summary specification is presented. The concluding paragraphs cover EMC considerations for the SIP.

The salient points of this section can be summarized as follows:

The wavefront error has been specified as 0.1 wavelength at 300 nanometers, and the pointing error as 25 nanoradians, one sigma. The mechanical interface between the OTA and SIP is defined as the rear surface of the OTA structural ring.

With one exception, the scientific data is integrated and stored on the SEC vidicons. The maximum number of scientific data

bits is  $8 \times 10^7$  bits for the field cameras, which use an area presentation format. The data transmission time required is 80 seconds. For line presentation instruments such as the faint object spectrographs,  $8 \times 10^5$  bits and 0.8 seconds are needed. The scientific data bit capacity required for the mid-IR spectrograph is  $2 \times 10^6$  bits, and an on-board storage is required for this instrument. It has been determined that the tape system within the data acquisition system of the SSM can be utilized for this purpose.

The SIP requires an on-board storage capability of 2600 bits for input commands, and 2100 bits for status data.

A single, regulated power supply voltage is used by all instruments. Any other voltages required will be generated within a particular instrument.

#### 9.1.1 Optical Interface

One of the factors which determine the performance of the SIP is the image presented to it by the telescope. The following paragraphs outline an optical interface which should insure the proper operation of the instruments of the SIP.

The clear aperture of the telescope is  $3.0 \pm .1$  meters, with an obscuration which is not to exceed 30% of the diameter of the aperture. The optical efficiency conforms to Figure 3-13 for  $n = 2$ . This efficiency may be obtained with the Haas coating outlined in Section 3.6.

The f/number is specified as  $12 \pm 0.1$ , and the field of view exceeds 2.7 milliradians, diameter.

The size of the image and its stability is such that the encircled energy curve conforms to Figure 3-9. This curve is the

result of a  $0.1\lambda$  W.F.E. and 25 nanoradian  $1\sigma$  pointing, but any combination of telescope optical and pointing error which produces this encircled energy curve is permissible.

The focal plane is located a predetermined distance from the primary ring interface, and the focus of the telescope image is within  $\pm 70 \mu\text{m}$  of the nominal focal plane.

The focal plane shall be flat as follows:

<u>Field Angle (mrad)</u>	<u>Local Field (mrad)</u>	<u>Flatness (<math>\mu\text{m}</math>)</u>	<u>Instrument (type)</u>
0	0.1	80	f/96 Camera
2	1.4	160	f/12 Camera
0.78	0.3	80	Axial Spectrograph
1.2	0.3	160	Radial Spectrograph

To protect the sensitive devices in the SIP, the incoming energy must be prevented from entering the SIP whenever it would produce an energy density exceeding  $100 \text{ nW/mm}^2$  at the f/12 focal plane.

### 9.1.2 Mechanical Interface

The SIP includes eight mountings which engage the inside diameter and the rear surface of the OTA structural ring. The ring's center is 780 mm from the primary mirror's vertex. Three of the eight mountings define the plane and the center of the mounting. The remaining five mountings are shimmed to conform.

The characteristics required at this interface are as follows:

- (1) The optical axis of the OTA shall be coincident with the mechanical axis of the interface within 10 mrad, assuming a wavefront error (WFE)  $\leq 0.1\lambda$ .

- (2) The structural/thermal stability of the OTA focal plane, measured with respect to the SIP interface ring along a line parallel to the telescope axis, shall be within 25  $\mu\text{m}$ .
- (3) The absolute positioning error of the image shall be less than 300 micrometers in the f/12 focal plane.

## 9.2 FINE GUIDANCE ASSEMBLY

The fine guidance, in conjunction with the slit jaw camera, is used to bring the selected target into the center of the spectrograph slits. It also determines the center of the F.O.V. of the field cameras. Errors in the fine guidance manifest themselves in two ways. Instability in the fine guidance will result in smearing of the image. Positioning, or accuracy errors will result in gathering data on a different part of the sky than intended, or could cause the image to fall out of the FOV of the slit jaw camera.

Table 9-1 summarizes the requirements placed upon the fine guidance for various modes of operation, assuming a  $0.1\lambda$  W.F.E.

Table 9-1

LST/OTA TARGET POINTING REQUIREMENTS  
 BASED ON TELESCOPE WFE = 0.1

SIP INSTRUMENT	Pointing Error Initial ( $\mu$ rad)	Pointing Error Final ( $\mu$ rad)	One Sigma Stability Pointing (p+y) ( $\mu$ rad)	Roll ( $\mu$ rad)
<u>f/96 Camera</u>				
Range I @ 150 nm	10	10	25	5
Range II @ 300 nm	10	10	25	5
Range III @ 500 nm	10	10	40	5
<u>Faint Object Spectrograph</u>				
			Slit Width	
			<u>250</u>	<u>500</u>
110-220 nm	10	0.1	25	250
220-660 nm	10	0.1	25	250
660-1000 nm	10	0.1	40	250
<u>High Resolution Spectrograph</u>				
110-180 nm	10	0.1	25	250
180-350 nm	10	0.1	25	250
<u>f/12 Camera</u>				
@ 300 nm	10	10	200	40

p = pitch  
 y = yaw

### 9.3 DATA HANDLING AND ELECTRONICS DATA

The data handling and electronics interface is broken into three main sections: Data (both scientific and diagnostic), power, and a summary document section which contains a model electronic and data handling interface document.

#### 9.3.1 Data

##### a. Scientific Data

The scientific data of the SIP, bit-wise, represents the vast majority of the SIP data transmitted. The basis for the scientific data requirements are shown in Figure 9-1. The readout analog signal cycles every two TV lines or every resolution element. If a function is sampled at a frequency  $f_s$ , the spectrum of the sample is reproduced centered around 0,  $f_s$ ,  $2f_s$ ,  $3f_s$ , . . . ., as shown in Figure 9-2. To prevent aliasing errors, the sample frequency must be at least twice the highest frequency present in the sampled data, also known as the Nyquist frequency. Associated with the sampling is an MTF response. Sampling at the Nyquist frequency results in an MTF of 0.63, sampling at twice the Nyquist frequency results in an MTF of 0.9. A sampling rate of twice the Nyquist frequency means sampling twice for every TV line. If the entire tube is scanned off, the total number of elements is equal to  $(2 \times \text{resolution} \times \text{tube width})^2$  where the resolution is given in line pairs per millimeter. For a 50 mm square tube with a resolution of 20 line pair/mm, the total number of elements is  $(2 \times 20 \times 50)^2$  or  $4 \times 10^6$  resolution elements. If twice the Nyquist frequency is used for sampling, and each sample is encoded into a 10 bit word, the total number of bits is  $4 \times 10^6 \times 2 \times 10$  or  $8 \times 10^7$  bits. If the tube resolution were to triple to 60 line per/mm, the number of elements would increase by a factor of 9, and  $7.2 \times 10^8$  bits would be required for a 50 x 50 mm tube.



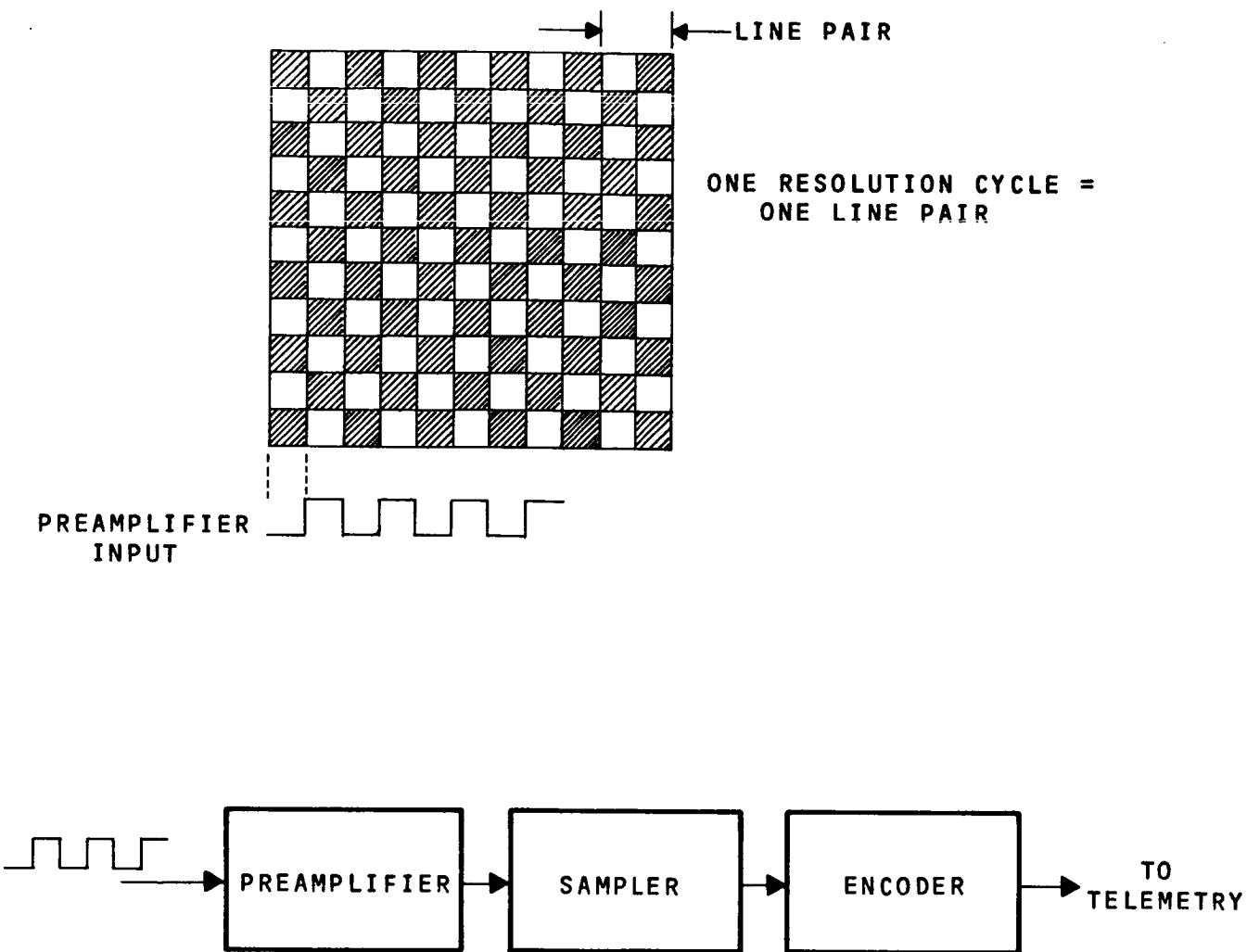
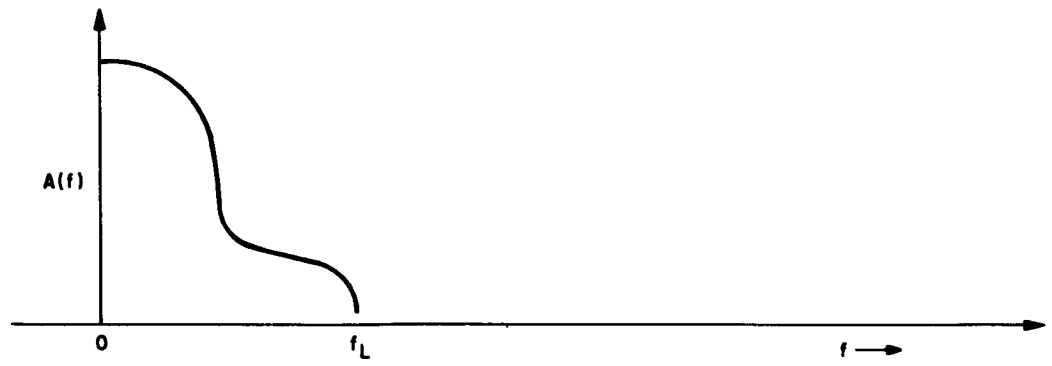


Figure 9-1. Scientific Data Flow



DATA SPECTRUM

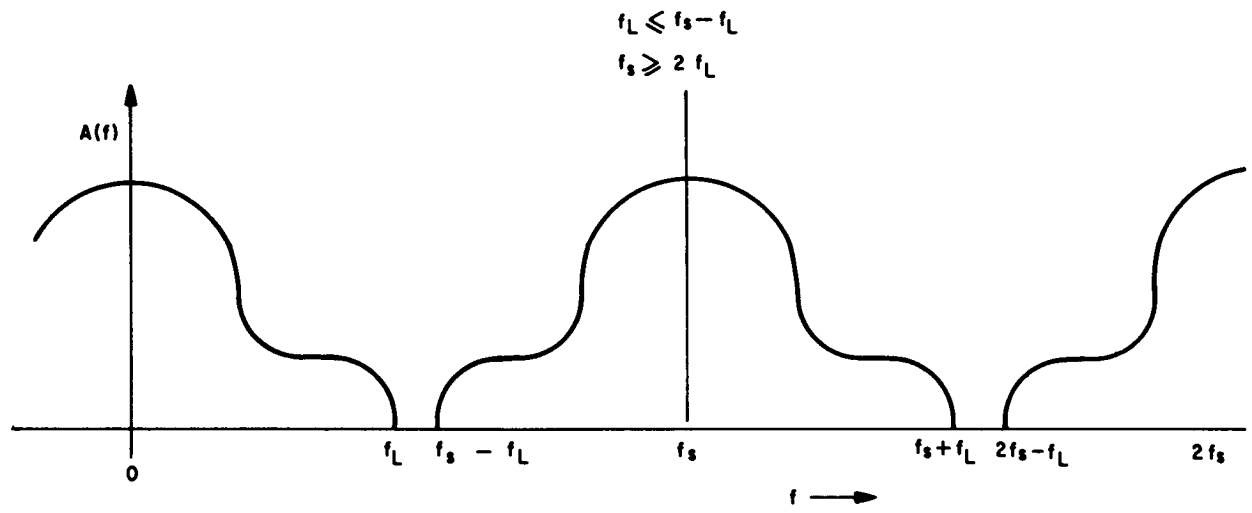


Figure 9-2. Sampled Data Spectrum

The time required for transmission to ground is determined by two considerations. It has been shown that there is an optimum rate of 25 kilohertz/second x sampling of the tube data to achieve the maximum S/N ratio. The sample frequency is not critical however; an order of magnitude increase in sample rate results in a 20% decrease in S/N ratio. The second limitation is the maximum transmission rate of the spacecraft data handling system, at present two channels of  $0.5 \times 10^6$  bits/second each.

The criteria of maximum S/N limits the preamplifier bandwidth to 25 kilohertz, or  $50 \times 10^3$  lines per second. Each line is sampled twice, and each sample is encoded as a 10 bit word, therefore the maximum S/N criteria establishes a limit of  $10^6$  bits/second. The time required to transmit a picture to ground is then  $\frac{8 \times 10^7}{10^6} = 80$  seconds for a 20 cycle/mm tube resolution.

It is expected that in the future, larger tubes of greater resolution will evolve. For example, if a 75 x 75 mm tube of 40 line pair/mm is used, the maximum S/N criteria would require  $80 \text{ sec} \times \left(\frac{40}{20}\right)^2 \times \left(\frac{75}{50}\right)^2$  or 12 minutes. If less than seven minutes is to be consumed in transmitting scientific data, the bit transmission rate must be increased. Note that the bit transmission rate limitation imposed by S/N considerations and the limitation of the spacecraft data handling system are the same. If it is desired to lessen the transmission time by increasing the preamplifier bandwidth, the S/N ratio will degrade slightly. In addition, either the number of bits used to encode a sample must be reduced, or the spacecraft data handling capability must be increased. Since it is doubtful that less than 7 bits would ever be used to encode a sample, a 30% decrease in transmission time is the most that could be expected unless the spacecraft data handling bit rates are increased.

If it is not desired to readout the entire tube, the time required to transmit the information to the ground will be less.

For example, if a narrow slit is placed around an image in the High Resolution Camera, it is not necessary to readout the entire tube, since most of it will be masked off. In all of the Faint Object Spectrographs, line presentations of the data are employed, and most of the tube contains no information. In both cases, transmission time and the required bit handling capacity may be saved by reading off a part of the tube. For the case of a reduced readout area, the equation for the number of elements to be sampled is  $(2 \times \text{Resolution} \times \text{Area Width}) (2 \times \text{Resolution} \times \text{Area Height})$ . Using a sample rate equal to twice the Nyquist, and encoding each sample with 10 bits yields a total bit requirement of  $80 \times (\text{Resolution})^2 \times \text{Area Width} \times \text{Area Height}$ , for each tube area encoded.

Table 9-2 is a summary of the total number of bits and the transmission time required for each instrument. These calculations are based on the assumption of 20 line pair per millimeter resolution, sampling at twice the Nyquist frequency, transmission rate of  $10^6$  bits/second, and a height of 1 mm for the line presentation formats.

If it is desired to approach the diffraction limited performance of the field cameras, either a small loss in sampling MTF must be acceptable, or the number of scientific data bits increased. For example, a resolution of 1.33 Airy discs, or 160 nanoradians, corresponds to a spatial frequency of  $6.25 \times 10^6$  cycles/radian. A frequency of 20 line pair/millimeter at the detector corresponds to a spatial frequency of  $5.75 \times 10^6$  cycles/radian. If the tube is to be sampled at twice the Nyquist frequency, the number of bits must be increased by a factor of  $\left(\frac{6.25}{5.75}\right)^2$  or 1.19.

If the sampling frequency is not increased, the detector will be sampled at  $2 \left(\frac{5.75}{6.25}\right)$  or 1.84 times the Nyquist frequency. The sampling MTF associated with this rate is 0.88, compared with 0.9 of twice the Nyquist frequency.

TABLE 9-2. REQUIRED BITS AND TRANSMISSION TIME

<u>Instrument</u>	<u>Presentation Type</u>	<u>Tube</u>	<u>Total Bit Count</u>	<u>Time of Transmission</u>
High Resolution Camera*	Area	(3) 50 x 50 mm	$8 \times 10^7$	80 seconds
Wide Field Camera	Area	(1) 50 x 50 mm	$8 \times 10^7$	80 seconds
High Resolution Spect. 110-180 nm	Area	(1) 25 x 25 mm	$2 \times 10^7$	20 seconds
High Resolution Spect. 180-350 nm	Area	(1) 25 x 25 mm	$2 \times 10^7$	20 seconds
Faint Object Spect. 110-220 nm	Line	(1) 25 x 25 mm	$8 \times 10^5$	0.8 seconds
Faint Object Spect. 220-660 nm	(2) Lines	(1) 25 x 25 mm	$16 \times 10^5$	1.6 seconds
Faint Object Spect. 660-1000 nm	Line	(1) 25 x 25 mm	$8 \times 10^5$	0.8 seconds
Faint Object Spect.** 1-5 $\mu$ m	-	-	$2 \times 10^6$	2 seconds
Slit Jaw Camera	Area	(1) 25 x 25 mm	$2 \times 10^7$	20 seconds

\*High Resolution Camera uses 3 tubes, but only one is employed at a given time.

\*\*From Report: Small High Speed Interferometer for Aircraft, Balloon and Spacecraft applications: Schindler Feb. 1970 Applied Optics.

The mid IR Fourier Interferometer presents a problem that the other instruments do not. In the other experiments, a TV tube integrates the incoming energy and stores it for readout. When the experiment is over, the integration is stopped and the contents of the tube transmitted to ground. The mid-IR Interferometer utilizes PbSe as a total power detector, and the PbSe detector is read out at each of the many positions that the cat's eye mechanism assumes. The data output of the mid-IR Interferometer is a digital number representing the total power impinging upon the detector and the position of the mechanism. Since this type of equipment does not have a storage capability, an on-board memory is required. It has been determined that the tape system within the data acquisition system of the SSM can be utilized for this purpose.

A Fourier Interferometer which has been developed for spacecraft use is discussed in "A Small High Speed Interferometer for Aircraft, Balloon and Spacecraft Applications" by Schindler in the February 1970 edition of Applied Optics. It is estimated that a memory with the capacity for storing  $2 \times 10^6$  bits is required for this application. The data rate specified in the article is 50 kilobits/sec, which is greater than the tape recorders can handle. But the high data rate is due to the high speed capability of the instrument, which is not required for the SIP application. The stepping rate of the cats eye can be cut by a factor of 20 or more, which will cut the data rate by the same factor and bring it within the capability of the tape recorder.

#### b) Diagnostic Data

##### Introduction

In addition to the prime scientific data, that is the output of the spectrographs and cameras, other data is to be made available. This other data, called diagnostic data, can be classified into the following categories:

1. Pre-experiment checks
2. Secondary data to improve accuracy of scientific data
3. Performance monitoring and troubleshooting data.

Section 3.7 provides a detailed description of the considerations involved in the choice of the diagnostic data system. To summarize the essence of Section 3.7, the diagnostic system chosen was one which contains a good deal of monitoring. This was done because it maximizes the confidence in a diagnosis, minimizes the probability that failures in the monitoring system will cause improper diagnosis, and yields the best chance of pinpointing the actual source of trouble. In addition, estimates (shown at the end of this section) indicate a total of approximately 2000 bits of status information are required from the SIP. This data will be acquired through Data Acquisition units (DAU) in two modes, real-time and stored. In the realtime mode the data will be acquired from the DAU's, formatted, and stored on tape at a rate of 1.6 K bits/sec. This stored data will be sent to ground later at a rate of 51.2 K bits/sec. Comparing this number with the numbers shown in Table 9-2 shows that the entire number of bits required for the diagnostic system is only 0.006% to 0.6% of the bit requirements of a single instrument. Packaging studies have shown that the volume of a typical diagnostic section of an instrument's electronics is 1 cubic decimeter, and consumes about 1 watt. Compared to the volume and power consumption of a single 50 x 50 mm vidicon, which is 22.5 cubic decimeters and 32 watts, the requirements of the diagnostic data is small. Since the cost of this monitoring system is relatively low, and it yields the before-mentioned benefits, it was selected for use in the LAST

Of the three categories mentioned, the pre-experiment checks and the secondary data to improve accuracy of the scientific data are actually part of the performance monitoring and troubleshooting data. They have been broken into separate categories because they are utilized at different times and have differing

impacts upon system operation in both the realtime and non-real-time modes. The reasons for this are discussed in the following sections.

### Pre-Experiment Checks

Prior to starting the data gathering phase of any experiment, verification of satisfactory performance of all hardware to be employed, is carried out during the "warm-up" period. This will include verification of performance of all mechanisms, detector tube operation and support electronics. This testing is to be performed several hours before the experiment is scheduled to start, so that any apparent malfunction can be verified, and also that possible work-arounds or schedule changes can be implemented. This is particularly important since some of the experiments will require several days to gather meaningful data so that much time will be lost before it is known that the scientific data is 'bad'. In addition, the fact that a large number of instruments and long experiment times could mean some of the hardware will not be operated for extended periods of time, reinforces the need for pre-experiment checkout.

This verification will be quite extensive, but is also implemented to be performed quickly through go-no-go type checks in many areas. In addition, complete checks while previous experiments are in process, will not be possible in all cases. This is due to the fact that shared mechanisms will sometimes be involved, and some of the testing will mean disturbing existing experiments. Thus, the planning stages of each experiment must consider the ongoing experiment to avoid such conflicts.

Categories of tests for pre-experiment verification will be similar, and in some cases, identical to those used throughout the experiment and will include:



1. Exercising of related mechanisms
2. Detector tube assembly operation
3. Temperature conditions
4. Electronic processing circuit operation
5. Electronic interface functions

In many cases, groups of parameters are combined to provide Go-No-Go indications in the interest of minimizing test time and required ground analysis time.

#### Secondary Data

The purpose of the secondary data is to enable improvement of the precision of the scientific information. The most obvious data in this category is temperature of the detector tube cathode, but additional data relevant to circuit processing will also be identified as adding to data precision when the camera circuits and performance are evaluated further. It is expected that this data will be continually transmitted and stored on the ground where access to any segment of this data can be examined when and if desired.

#### Performance Monitoring and Troubleshooting

The maintenance concept anticipated for the LST involves in-flight replacement of major subassemblies based on analysis of telemetered data. Due to the timing problems and cost of sending up maintenance flights, it is imperative that fault isolation to replaceable major hardware items be accurate.

Performance monitoring can also serve another purpose other than troubleshooting to determine the cause of a failure. The possibility exists that a particular mechanism or instrument may not fail catastrophically, but gradually deteriorate into an unacceptable level of performance. By careful monitoring such conditions can be detected, and experiments rescheduled to get the

maximum use of the device before performance falls below an acceptable level. Monitoring of conditions such as this may also be useful in predicting future maintenance missions, if a trend can be established from existing data.

To do this, it is necessary to transmit all of the diagnostic data. The reason for this is that the deterioration may not be immediately noticeable from an examination of the scientific data, and part or even all of the diagnostic data. If a trend in performance is to be established, several sets of data must be available. There is no way to know in advance what will deteriorate, hence, there is no prior knowledge of what part of the diagnostic data must be saved, and what part may be discarded. Therefore, if performance monitoring is to be effective, all of the diagnostic data must be transmitted and stored. Otherwise, it is lost and unavailable for future reference. Considering that the diagnostic data is only 0.006% to 0.6% of the scientific data, it seems a small price to pay for the advantages gained.

Table 9-3 lists the diagnostic data presently considered and an estimate of the number of data bits required for adequate information content. It should be kept in mind that hard detailed information is lacking in most of the areas which impact on the estimates, such as tube electronics. The estimates reflect the desire to provide an adequate bit handling capacity for the present system, with an allowance for possible future growth. While the estimate may be somewhat high, it is in the right "ballpark", and it was felt that at this stage in the program, a conservative estimate is preferable to an optimistic one.

Table 9-3

LST COMMAND AND STATUS DATA ESTIMATE:  
BY INSTRUMENT AND SUMMARY

---

The bit error rate will be less than  $10^{-8}$  for uplink data, and less than  $10^{-5}$  for downlink data. Therefore, it will not be necessary to code each message with identification bits followed by the message bits. Instead, the bits will be counted, and certain bit positions will be reserved for specific information. For example, the 1st seven bits of the message to the F/12 camera would control the target voltage of the vidicon tube, the next two bits would control the heater voltage, etc. Every 50 bits will be used for a parity check to help check the quality of transmission. An estimate of the bit count by the instrument follows:

## I. Wide Field

## A. Input Command Bits

1. Tube Commands	2 bits
heater on & off	2 bits
Focus on & off	2 bits
Scan start	13 x 2 = 26 bits
Scan stop	13 x 2 = 26 bits
High Voltage Control	13 bits
Self check	40 bits
Readout Speed Control	4 bits
target voltage control	<u>4 bits</u>
	117 bits
2. Filter Wheel Mechanism	
position	6 bits
power on & off	<u>2 bits</u>
	8 bits

---

Table 9-3 (Cont.)

---

3.	Power Supply Control	
	4 supplies at 3 bits =	12 bits
4.	Self Check	70 bits
5.	Redundant Electronics	2 bits
6.	Temp Sensor & Control	10 bits
	Total for F/12 Camera	219 bits
	+4 for parity =	223 bits total
B. Status Data Bits		
1.	Mechanism	
	position	10 bits
	power supply monitors	
	(4 at 10 bits)	40 bits
	Error signal monitor	8 bits
	Amp Output	8 bits
	Amp Monitor	<u>2 bits</u>
		68 bits
2.	Tube	
	High Voltage Monitor	20 bits
	Self Check	30 bits
	Low Voltage Monitor	<u>8 bits</u>
		58 bits
3.	Temp Sensor	
	6/inst. at 10 bits per =	60 bits
	Total for f/12 Camera =	186 bits
	+4 for parity =	190 bits total

---

Table 9-3 (Cont.)

---

II.	High Resolution Camera I	
	A. Input Command Bits	
	1. Tube Commands	117 bits
	2. Filter Wheel Mech.	8 bits
	3. Power Supply Control	12 bits
	4. Self Check	70 bits
	5. Redundant Electronics Command	2 bits
	6. Temp. Sensor & Control	<u>10 bits</u>
		219 bits
	+4 for parity =	223 bits total
	B. Status Data Bits	
	1. Filter Wheel Mech.	68 bits
	2. Tube	58 bits
	3. Temp Sensors	<u>60 bits</u>
		186 bits
	+4 for parity =	190 bits total

---

III.	High Resolution Camera II	
	A. Input Command Bits	
	1. Tube Commands	117 bits
	2. Filter Wheel Mech.	8 bits
	3. Power Supply Control	12 bits
	4. Self Check	70 bits
	5. Redundant Electronics Command	2 bits

---

Table 9-3 (Cont.)

---

6.	Temp Sensor & Control	10 bits
7.	Camera Select Mechanism	<u>8 bits</u>
		227 bits
	+4 for parity =	231 bits total
B. Status Data Bits		
1.	Filter Wheel Mech.	68 bits
2.	Tube	58 bits
3.	Temp Sensor	60 bits
4.	Camera Select Mech.	<u>68 bits</u>
		254 bits
	+5 for parity =	259 bits total

---

IV. High Resolution Camera III

A. Input Command Bits

1.	Tube Commands	117 bits
2.	Filter Wheel Mech.	8 bits
3.	Power Supply Control	12 bits
4.	Self Check	70 bits
5.	Redundant Electronics Command	2 bits
6.	Temp. Sensor & Control	<u>10 bits</u>
		219 bits
	+4 for parity =	223 bits total

---

Table 9-3 (Cont.)

---

B. Status Data Bits	
1. Filter Wheel Mech.	68 bits
2. Tube	58 bits
3. Temp. Sensor	<u>60 bits</u>
	186 bits
+4 for parity =	190 bits total

---

V. High Resolution Echelle Short $\lambda$	
A. Input Command Bits	
1. Tube Commands	117 bits
2. Power Supply Control	12 bits
3. Self Check	70 bits
4. Redundant Electronics Command	2 bits
5. Temp Sensor & Control	<u>10 bits</u>
	211 bits
+4 for parity =	215 bits total
B. Status Data Bits	
1. Tube	58 bits
2. Temp Sensor	<u>60 bits</u>
	118 bits
+4 for parity =	122 bits total

---

Table 9-3 (Cont.)

---

VI.	High Resolution Echelle, Long $\lambda$	
	A. Input Command Bits	
	1. Tube Commands	117 bits
	2. Power Supply Control	12 bits
	3. Self Check	70 bits
	4. Redundant Electronics Command	2 bits
	5. Temp. Sensor & Control	<u>10 bits</u>
		211 bits
	+4 for parity =	215 bits total
	B. Status Data Bits	
	1. Tube	58 bits
	2. Temp. Sensors	<u>60 bits</u>
		118 bits
	+4 for parity =	122 bits total

---

VII.	Faint Object Spectrograph 110 nm - 220 nm	
	A. Input Command Bits	
	1. Tube Commands	117 bits
	2. Grating Select Mech.	18 bits
	3. Power Supply Control	12 bits
	4. Self Check	70 bits
	5. Redundant Electronics Command	2 bits
	6. Temp. Sensor & Control	<u>10 bits</u>
		229 bits
	+4 for parity =	233 bits total

---



Table 9-3 (Cont.)

B. Status Data Bits

1. Tube	58 bits
2. Grating Select Mech.	68 bits
3. Temp Sensors	<u>60 bits</u>
	186 bits
+3 bits for parity =	189 bits total

---

VIII. Faint Object Spectrograph 220-660 nm  
(Same as IX.)

---

IX. Faint Object Spectrograph 660-1000 nm

A. Input Command Bits

1. Tube Commands	117 bits
2. Slit Mech.	8 bits
3. Power Supply Control	12 bits
4. Self Check	70 bits
5. Redundant Electronics Command	2 bits
6. Temp. Sensor & Control	<u>10 bits</u>
	219 bits
+4 for parity =	223 bits total

B. Status Data Bits

1. Tube	58 bits
2. Mech.	68 bits
3. Temp. Sensors	<u>60 bits</u>
	186 bits
+3 for parity =	189 bits total

---

Table 9-3 (Cont.)

---

X.	Faint Object Spectrograph 1 $\mu$ - 5 $\mu$	
	A. Input Command Bits	
	1. PbSe Detector & Controls	20 bits
	2. Servo Control	140 bits
	3. Power Supply Controls	25 bits
	4. Self Check	70 bits
	5. Redundant Electronics	2 bits
	6. Temp. Sensor & Control	<u>10 bits</u>
		267 bits
	+5 for parity =	272 bits total
	B. Status Data Bits	
	1. Secondary Drive Voltage	16 bits
	2. 2 Magnetic Drives	30 bits
	3. PbSe Output	15 bits
	4. Ref. Cntr. Output	24 bits
	5. Fringe Cntr. Output	24 bits
	6. Direction Recognition Logic	16 bits
	7. Reference	16 bits
	8. Temp. Sensor	<u>60 bits</u>
		201 bits
	+4 for parity =	205 bits total

---

Table 9-3 (Cont.)

---

XI.	Slit Mechanism Aft. Spectrographs	
	A. Input Command Bits	
	1. Servo Commands	30 bits
	2. Self Check	70 bits
	3. Redundant Electronics	2 bits
	4. Temp. Sensor & Controls	<u>4 bits</u>
		106 bits
	+2 for parity =	108 bits total
	B. Status Data Bits	
	1. Mech.	68 bits
	2. Temp. Sensor	<u>10 bits</u>
		78 bits
	+1 for parity =	79 bits total

---

XII.	Spectrograph Selector	
	A. Input Command Bits	
	1. Servo Commands	25 bits
	2. Self Check	70 bits
	3. Redundant Electronics	2 bits
	4. Temp. Sensor & Controls	<u>4 bits</u>
		101 bits
	+2 for parity =	103 bits total

---

Table 9-3 (Cont.)

B. Status Data Bits		
1. Mechanism		68 bits
2. Temp. Sensor		<u>10 bits</u>
		78 bits
	+1 for parity =	79 bits total
<hr/>		
XIII. Slit Jaw Camera		
A. Input Command Bits		
1. Tube		117 bits
2. Temp. Sensor & Controls		<u>2 bits</u>
		119 bits
	+2 for parity =	121 bits total
B. Status Data Bits		
1. Tube		58 bits
2. Temp. Sensor		<u>10 bits</u>
		68 bits
	+1 for parity	69 bits total
<hr/>		
XIV. Sources		
A. Input Command Bits		
1. On-Off Control		10 bits total
B. Status Data Bits		
		10 bits total
<hr/>		

Table 9-3 (Cont.)

TOTALS			
	<u>Device</u>	<u>Input Command Bit</u>	<u>Status Data Bits</u>
I.	Wide Field Camera	223	190
II.	High Resolution Camera I	223	190
III.	High Resolution Camera II	231	259
IV.	High Resolution Camera III	223	190
V.	High Resolution Echelle Short $\lambda$	215	122
VI.	High Resolution Echelle Long $\lambda$	215	122
VII.	Faint Object Spect. 110-220 nm	233	189
VIII.	Faint Object Spect. 220-350 nm	223	189
IX.	Faint Object Spect. 350-660 nm	223	189
X.	Faint Object Spect. 1 $\mu\text{m}$ - 5 $\mu\text{m}$	272	205
XI.	Slit Mechanism, Aft Spect.	108	79
XII.	Spectrograph Selector	103	79
XIII.	Slit Jaw Camera	121	69
XIV.	Sources	<u>10</u>	<u>10</u>
Total		2622*	2082*
Total average bit rate		$\frac{2622 \text{ bits}^*}{1800 \text{ sec}}$	$\frac{2082^*}{1800 \text{ sec}}$
		$\approx 1.5 \text{ bits/sec}$	$\approx 1.2 \text{ bits/sec}$

\* This data is not expected to be transmitted more often than once per 30 minutes.

### 9.3.2 Power

#### a) General

The power consumption, voltage level, regulation, ripple, etc., will vary according to instrument, and future instruments may require a source of power not needed by any of the present instruments. To keep cabling and connectors to a minimum, and to provide the maximum flexibility for the present and future instruments, the power provided to an instrument will be in the form of a single regulated voltage. The electronics for each instrument will contain the power supplies necessary for the operation of that instrument, and the necessary filters to prevent electrical transients and noise generated within the instruments from appearing on the power line. Although one power line is needed, several power returns are available to prevent cross-talk and ground noise problems between sensitive signal devices and apparatus such as motors or heaters.

The largest single consumer of power is the SEC Vidicon. The present assessment for the tube is 32 watts, including power supplies. The assessment is based on the assumption that the single power input is +28V regulated. If an unregulated voltage (which could drop as low as 20 volts) were used, the regulator for the SEC Vidicon power supply would consume an additional 15 watts under normal conditions.

The power consumed by the SIP is a function of the number of devices that are operational at a given time and is a function of the status of the instrument. The total power drawn will vary with the use sequence, observation time and warm-up time required for each sensor. For instance, if the warm-up time for a sensor is considerably longer than the observation time, two or more sensors will be powered simultaneously. Since we have no a priori knowledge of what the "average" sequence will be, or even if one exists, it is difficult to arrive at an "average" power consumption. Instead, two indications of power consumption will be given. This section contains the detailed power consumption on a per instrument basis. Using the detailed numbers, power profiles of several "typical" operational

sequences are shown in Figure 9-3. Case I is for a 3 hour observation using the High Resolution (50 mm Vidicon) Camera, and a 5 hour observation using the High Resolution Spectrograph (25 mm Vidicon). Case II is for three successive 45 minute exposures using a 25 mm sec Vidicon, and Case III is for three successive 45 minute exposures using a 50 mm Vidicon. The assumptions upon which the profiles are based are:

- (1) The tubes require a 2 hour warm-up.
- (2) Occultation occurs from 0.75 to 1.5 hr, 2.25 to 3 hr, etc.
- (3) At time  $t = -2$  hr, the first tube focus coil is energized, and the power consumption exclusive of the tube, is 20 watts due to
  - a) 10 watts for 10 tube cathode heaters
  - b) 5 watts for all mechanisms
  - c) 5 watts standby power for unused instruments
- (4) The Peltier coolers (which require 50 watts to cool the cathode of a 50 mm Vidicon) are not needed.

At  $t = -2$  hours, the power consumption is equal to the power consumed by the tube plus 20 watts. For Case I, the power at  $t = -2$  hours is 52 watts; for Case II, 34 watts, and for Case III, 52 watts.

If a dim target is being observed, then the Peltier coolers must be used, and 50 watts of additional power per 50 mm tube and 25 watts per 25 mm tube is consumed. This would cause a peak power of 66 watts for Case I, 76 watts for Case II, and 148 watts for Case III.

b) Detailed Power Consumption, per Instrument

The power dissipated in each instrument can be broken into three major categories: The tube and its associated

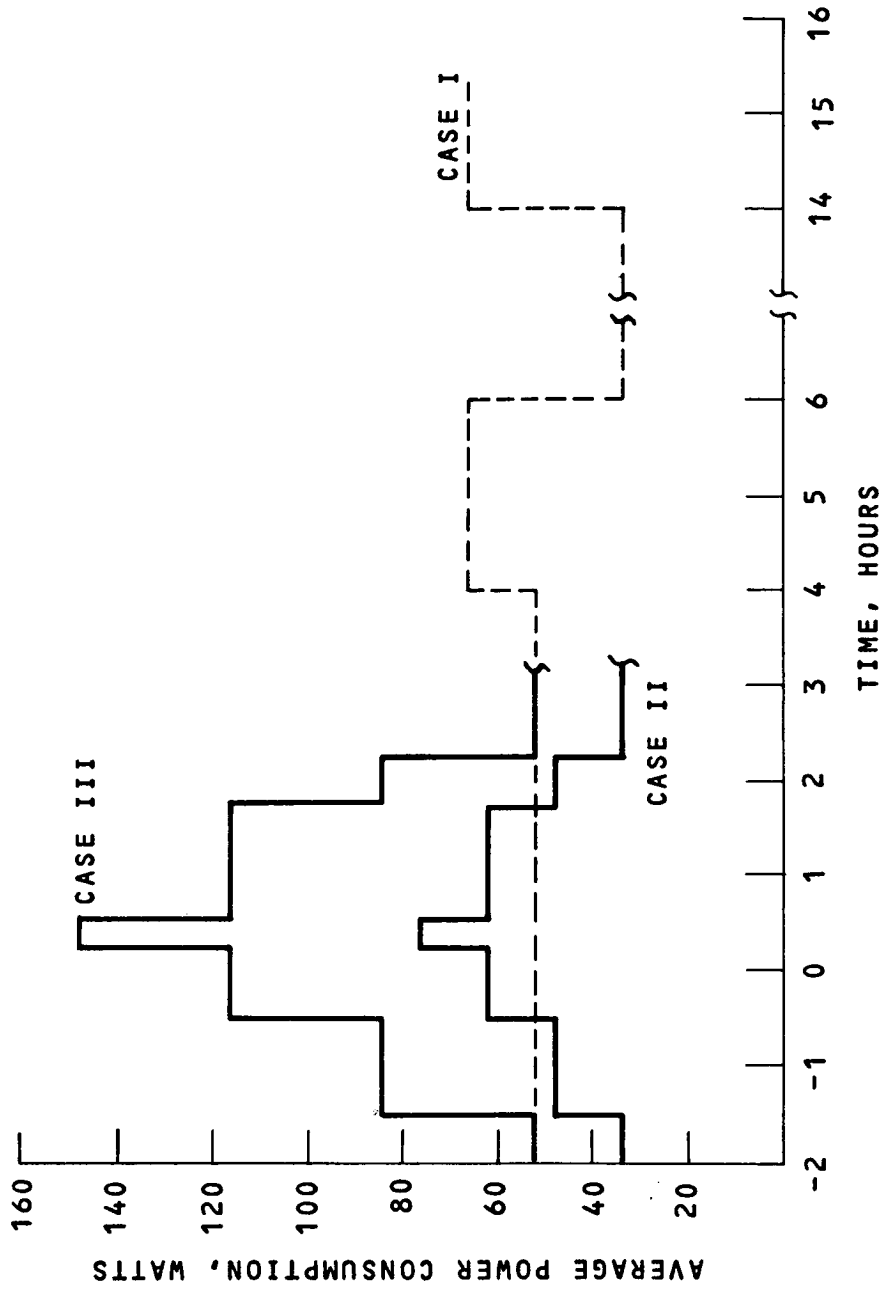


Figure 9-3. Power Profile Examples



electronics, the instrument electronics, and the mechanism power. In addition, power is calculated for those mechanisms which are common to several instruments.

A 50 mm tube and its associated electronics is discussed in detail in Section 6. The power dissipation for this tube is 32 watts. The 25 mm tube, which dissipates 14 watts, is also discussed in the same section.

The electronics for an average instrument requires 100 flat packs, which dissipate 10 milliwatts each, and other associated electronics such as D/A converters and power supplies. The total average electronic power for an instrument is taken as 2 watts.

The mechanism power dissipations are shown on the block diagrams. A breakdown of power on a per instrument basis is shown in the following:

I. Wide Field Camera

Tube	32
Filter Wheel Mechanism	2
Inst. Electronics	<u>2</u>
Total	36 watts

II. High Resolution Camera I

Tube	32
Filter Wheel Mechanism	2
Inst. Electronics	<u>2</u>
Total	36 watts

III. High Resolution Camera II

Tube	32
Filter Wheel Mechanism	2
Inst. Electronics	2
Camera Select Mechanism	<u>2</u>
Total:	38 watts

IV.	High Resolution Camera III	
	Tube	32
	Filter Wheel Mechanism	2
	Inst. Electronics	2
	Flag Mechanism	<u>1</u>
	Total	37 watts
V.	High Resolution Spect. Short	
	Tube	14
	Inst. Electronics	<u>2</u>
	Total	16 watts
VI.	High Resolution Echelle Long	
	Tube	14
	Inst. Electronics	<u>2</u>
	Total	16 watts
VII.	Faint Object Spectrograph 110-220 nm	
	Tube	14
	Grating Select Mech.	1
	Inst. Electronics	<u>2</u>
	Total	17 watts
VIII.	Aft Spectrograph Slit Drive	
	Mechanism	2
	Electronics	<u>1.5</u>
	Total	3.5 watts

IX.	Collimator Mirror Drive	
	Mechanism	1
	Electronics	<u>1.5</u>
	Total	2.5 watts
X.	Faint Object Spectrograph No. 2 220-660 nm	
	Tube	14
	Entrance Mechanism	1.5
	Inst. Electronics	<u>2</u>
	Total	17.5 watts
XI.	Faint Object Spectrograph No. 3 660 nm - 1 $\mu$ m	
	Tube	14
	Entrance Mechanism	1.5
	Inst. Electronics	<u>2</u>
	Total	17.5 watts
XII.	Mid-IR Interferometer 1-5 $\mu$ from JPL space programs summary 37-43 volume IV	10 watts
XIII.	Sources for the mid-IR, 0.1 watts. For the visible and UV, lamps will be required, which will consume 6-10 watts while operating. Their duty cycle is expected to be less than 1%.	
XIV.	Slit Jaw Camera	
	Tube	14
	Electronics	<u>2</u>
	Total	16 watts

### 9.3.3 Summary Document

Thus far, Section 9.3 has discussed drivers which have the greatest impact on the data handling and electronics interface, as regards the requirements for power and data bit rates. Section 5 discusses the packaging and hardware considerations for the electronics. The paragraphs which follow are an electronics interface document which is a logical result of subsections 9.3.1 and 9.3.2.

Since it is difficult to predict an "average" power consumption, the power interface has been specified in terms of an absolute maximum power and the total energy over a ten hour period. This will permit the experimenter the maximum flexibility in planning his experiment, and still limit the drain on the spacecraft batteries.

The numbers used represent the best estimates presently available and are subject to change. In those cases where it is felt that numbers are either premature or unavailable, the designation TBD for "to be determined" is used.

#### Electrical & Data Interface

##### 1. Required of SSM

a) The SSM shall supply power to the SIP in the form of +28 VDC.

b) The SSM shall be capable of furnishing 2000 watt hours over a 10 hour period with a maximum power capability of 400 watts. The duration of the maximum power shall not exceed 15 minutes of time. The SSM +28V line shall be capable of withstanding a short circuit for TBD seconds.

c) The +28 VDC shall be regulated to  $\pm 2\%$ .

d) The transients on the +28V line shall not exceed  $\pm 50$  volts for 10 microseconds of time.

e) The noise on the +28V line shall not exceed 5 millivolts rms.

f) Transients on the ground return shall not exceed that specified for the +28 volt lines.

g) Noise on the 28V return line shall not exceed 5 millivolts rms.

h) Three separate return lines shall be provided. One will be used by the TV tubes, one by the data handling electronics, and one by devices such as motors, heaters, etc.

j) The SSM shall be in conformance with RFI specification MIL-STD-461A, MIL-E-6051, MIL-STD-462.

k) Each instrument of the SIP and those mechanisms which are not contained within an instrument should be capable of being operated independently. Therefore, each instrument requires sync lines, message lines and one clock pulse line. The clock pulse line will be common to all instrument/mechanisms. A sync and message line will be paired to accomplish commanding of each instrument. Message lines will also be used to transmit experiment status data to the data acquisition units of the SSM. In addition, message and sync lines will be used to transmit the data stored on the image tube to the SSM. Both the sync and message lines will be synchronized to the clock pulse line. All sync and clock pulses will be provided by the SSM.

l) The total number of bits needed for command of the SIP shall be 3000 bits.

m) The SSM must be capable of accepting 3000 bits of diagnostic information from the SIP.

n) The SSM must be capable of accepting  $10^8$  bits in a scientific data readout message.

o) The SSM shall be capable of providing message, sync, and clock pulses while working into a load of TBD ohms and TBD P.F. or greater, or into TBD gates of type TBD and TBD P.F.

p) The SSM shall impose a load of not less than TBD ohms and greater than TBD P.F.; or not more than TBD type TBD gates and TBD P.F. on the message lines which the status and scientific data readout messages are sent.

## 2. Required of SIP

a) The electronics of the SIP instruments/mechanisms shall be capable of working from a single +28V line which meets the specifications outlined in paragraphs 1.a through 1.g. Any other sources of D.C. or A.C. power needed by any instrument/mechanism shall be produced within that instrument/mechanism.

b) The SIP shall not draw more than 2000 watt hours over a 10 hour period, and the maximum power drain shall not exceed 400 watts over a period of 15 minutes.

c) The SIP electronics shall be designed such that a single component failure will not cause a short circuit on the +28V line. In the event of a short circuit, the short circuit condition shall be removed within 20 milliseconds, otherwise SSM-EDU will remove it within 50 milliseconds.

d) The SIP electronics shall be in conformance with RFI specification MIL-STD-461A Notice 3, MIL-STD-462 Notice 2 and MIL-E-6051.

e) The SIP electronics shall be designed such that it shall not generate transient disturbances (such as inductive kick-backs) on the +28V line of greater than TBD volts in series with TBD ohms, for greater than TBD seconds. The minimum time between these transient disturbances shall be TBD seconds.

f) The data acquisition units, supplied by the SSM, will provide 64 lines for the collection of diagnostic data. These lines will accept either digital or analog information. Digital diagnostic data will be accepted by the Data Acquisition Units in parallel on eight discrete lines. Analog data supplied over a single line will be conditioned to a zero to five volt scale before transmission to the data acquisition units.

g) The SIP must be capable of generating  $10^8$  bits in a scientific data readout message, and must be capable of transmitting these  $10^8$  bits in TBD minutes.

h) The SIP must be capable of accepting 3000 bits of command message, in a period not to exceed TBD minutes.

i) The SIP must present a load of not less than TBD ohms and not more than TBD P.F., or not more than TBD type TBD gates and TBD P.F. to the clock pulses.

j) The SIP must present a load of not less than TBD ohms and not more than TBD P.F., or not more than TBD type TBD gates and TBD P.F. to the sync pulses.

k) The SIP must present a load of not less than TBD ohms and not more than TBD P.F., or not more than TBD type TBD gates and TBD P.F. to the message pulses.

l) The SIP must be capable of generating the message pulses while driving a load of greater than TBD ohms and less than TBD P.F.; or driving a load of less than TBD type TBD gates and TBD P.F.

m) Connectors - Each instrument/mechanism shall transmit or receive all electrical signals through standard connectors per MSFC Spec. 40M39569 and 40M38286. Each instrument/mechanism shall be allotted TBD coax pins, TBD shielded wire pins, and TBD plain wire pins. The wire gauge used on the connectors will be no less than size AWG #24 coax cabling in accordance with MSFC Spec. 40M38286.

#### 9.3.4 EMC

As in all systems of this type, it is important to assure that system performance is not degraded by electromagnetic interference. EMC control is provided most effectively and most economically when applied during the engineering development phase, and is further enhanced by a uniform, coordinated EMC program for the entire LST. Overall EMC criteria for the SIP, OTA and SSM should be established early in the program, and an EMC review board should be set up to resolve questions, modify and add to design guide lines and interference levels and to provide general EMC coordination among all contractors.

In the case of the SIP equipment, the basic guideline documents for design and testing are MIL-STD-461A Notice 3 and MIL-STD-462 Notice 2, respectively, for Class 1C equipment. These guideline specifications provide for the setting of interference and susceptibility limits commensurate with the system configuration involved. In addition, it is recommended that an overall EMC test be performed on the completed LST, of the type described in MIL-E-6051, to prove the compatibility of the entire system.

The baseline SIP equipment design includes such EMC provisions as balanced lines consisting of twisted shielded pairs for data transmission to reject low frequency induced interference, filtering at the power connector of all electronic packages and EMI gasketing of all electronic packages to contain both conducted and radiated interference as well as a susceptibility precaution.



## Section 10

### RELIABILITY AND MAINTAINABILITY

#### 10.1 RELIABILITY

##### 10.1.1 Introduction

The following paragraphs deal with the development of some insight into the reliability that can be achieved with a SIP of a configuration such as that described in the preceding sections. In addition, those areas which require additional effort and/or special attention are identified.

The discussion starts with a description of the organization of the SIP hardware for reliability analysis purposes, followed by a description of the operational bases and ground rules used. Failure rates for individual items are then presented, and reliability block diagrams and math models are developed based upon those rates.

Reliability predictions are then developed for one and two year missions and for 100 and 1,000 observation hours. Since many items of instrumentation do operate independently of various other items, and no absolute definition of mission success or failure can be made, based on any one or group of hardware, no single reliability figure tells a meaningful story. Therefore, to provide a basis for evaluation, Table 10-4 was prepared to show the reliability of 25 different SIP hardware combinations. The reliability predictions shown vary from a high of 0.999 for the probability that at least one faint object spectrograph will complete its mission during a two year orbit, to a low of 0.607 that there will be no failures in any item over a two year period (SIP series model).

The final paragraphs, devoted to this subject, discuss the reliability critical items, the SEC Vidicon tube and the Vidicon

and Support Electronics, and list those areas requiring further effort.

#### 10.1.2 Bases for Reliability Analysis

Unlike previous space programs, the LST-SIP corrective/preventive maintenance will be performed in-orbit. A crew of one or more men and replacement units will be shuttled into space to perform this function. The techniques required for in-orbit maintenance have to be pioneered and developed in the near future, SKY-LAB will be the first major effort in this area. Reliability and Maintainability (R/M) are critical LST-SIP design parameters. The primary R/M objectives throughout the entire LST-SIP Program will be:

- Minimize overall program costs by optimizing an integrated model of reliability/maintenance design, hardware, and logistic costs over the useful life of the LST.
- In the event of a failure, provide the assurance that a malfunctioning instrument can be identified via ground diagnostics, readily replaced on-orbit and subsequently verified as operational.

The LST-SIP instrumentation is divided into the following functions for purposes of the reliability analysis:

- f/96 (High Resolution) Camera "A" (115 - 300 nm)
- f/96 (High Resolution) Camera "B" (160 - 600 nm)
- f/96 (High Resolution) Camera "C" (500 - 1100 nm)
- High Resolution Spectrograph #1 (110 - 180 nm)
- High Resolution Spectrograph #2 (180 - 350 nm)
- Faint Object Spectrograph FOS #1 (110 - 220 nm)
- Faint Object Spectrograph FOS #2 (220 - 660 nm)

- Faint Object Spectrograph #3 (660 - 1000 nm)
- Faint Object Spectrograph #4 (1000 - 5000 nm)
- f/12 (Wide Field) Camera Assembly

It is assumed in the Reliability analysis that each of these instruments performs independent experiments; hence, in the event of failure of a basic instrument, its experiment is terminated and the remaining experiments continued. After the failure of "X" basic instruments, corrective maintenance action will be mandatory.

The Slit Jaw Camera is not considered a basic experimental instrument; this unit is used in conjunction with five spectrographs, and there is a useful degraded mode of spectrograph operation in the event of Slit Jaw Camera failure.

The Reliability analysis contained herein is based on the design described in earlier sections of this document and concerns only the in-orbit phase of the LST-SIP. The launch phase reliability is presently considered to be less significant than the in-orbit phase and has been deferred for later consideration; the LST-SIP will not be operational during the launch phase. During those in-orbit periods when an instrument/component is non-operational, its failure rate is assumed zero; this assumption also warrants future consideration.

A previous Kollsman design, employing only established reliability parts for a space application similar to the LST, was utilized in establishing the complexity (piece part count) of the electronic/electromechanical portion of the SIP instruments. Part failure rates were determined using the methods and data contained in the RADC Reliability Notebook (Vol II, 1967). The failure rates were calculated using an orbital temperature of 25°C and appropriate temperature rises due to power dissipation. Mechanical piece parts are not considered in the initial reliability predictions because experience indicates that the electronic/electromechanical components have a far more significant reliability impact.

The operating time for each of the ten independent instruments in the LST-SIP was derived from the operational priorities implicit in the steering committee recommendations. The amount of warm-up time required for the instruments is significant and was integrated into the reliability analysis.

The reliability analysis also assumes a 50% occultation (earth obscuration of an experiment's objective) with the consequence that instrument "on time" is doubled for a prescribed experimental observation period. This is a worst case assumption from the point of view of instrument usage to accumulate a given amount of data.

### 10.1.3 LST-SIP Operational Reliability Block Diagram

The basic LST-SIP Operational Reliability block diagram used in the Reliability Analyses is presented in Figure 10-1. Included in the Support System Module (SSM) are the following assemblies which are part of the telescope control system:

- Fine Guidance
- Focus Sensor
- Figure Sensor

These items, though vital to proper LST operation, are not included in the Reliability Analyses of the instrumentation. They are considered in the document covering OTA performance. The present calculated failure rates for these three units are, in failures per million operating hours, 9.06 for the Guidance Sensor, 3.10 for the Focus Sensor and 3.50 for the Figure Sensor. The Itek Corporation developed these failure rates as part of the Phase A Telescope study.

As shown in Figure 10-1, there are ten basic LST-SIP instruments in parallel, each one required for independent, individual experiments. None of the experiments will be performed concurrently, hence only one instrument performs experimental

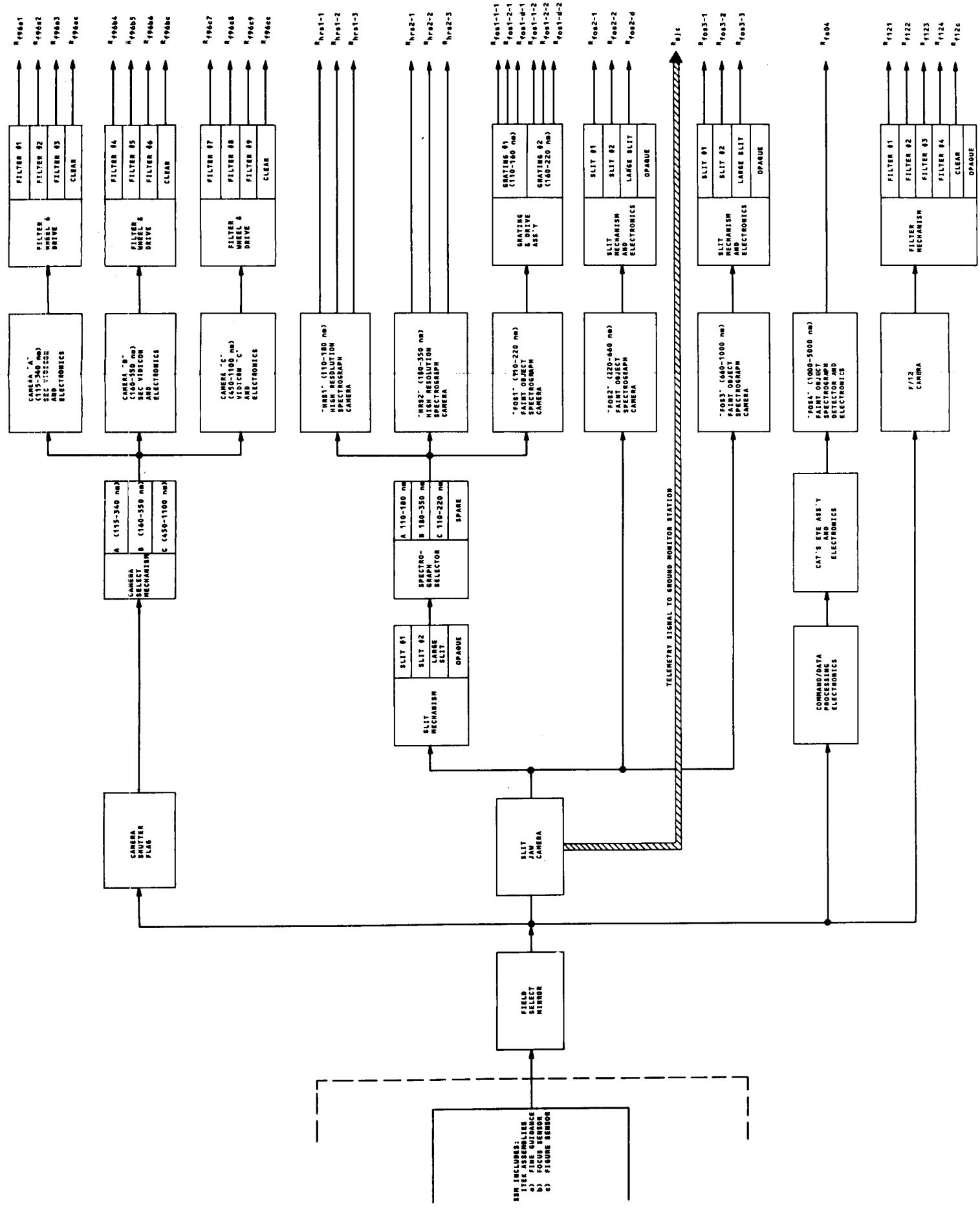


Figure 10-1. LST-SIP Operational Reliability Block Diagram

observations at a time. Upon command via ground telemetry, a second instrument will be placed in "warm up" status; as previously noted, "warm up" is treated in the analysis as if the instrument were fully operational.

For purposes of the Reliability Analyses, the basic instrumentation is functionally grouped as follows:

- High Resolution Cameras (F96A, F96B, F96C)
- Spectrographs (HRS1, HRS2, FOS1, FOS2, FOS3, and FOS4)
- Wide Field Camera (F12)

Success/failure criteria have not been defined at this time as the priority/nature of the LST-SIP experiments and their corresponding instruments are not fully defined. The Reliability Analysis has considered the operation of the functional groups and specific instruments within the group.

The Field Select Mirror is the sole series element of the LST-SIP and a catastrophic failure of this unit would preclude operation of any of the ten basic LST-SIP instruments. The Slit Jaw Camera is indicated to be a series element of the five basic instruments (HRS1, HRS2, FOS1, FOS2 and FOS3) but a catastrophic failure of this item would not have disastrous consequences. Ground monitoring equipment can detect a Slit Jaw Camera malfunction and has the capability, via telemetry, to command the Camera to assume a configuration which permits the five instruments to operate in a degraded mode. The remaining critical chain of components consists of the Camera Shutter Flag and the Camera Select Mechanism which is in series with the three parallel f/96 Cameras.

The use of redundancy to improve reliability is not included in the present configuration. The cost, power and weight of duplicate electronics, the incompatibility of any optical design with reliable focal plane hardware switching and the relatively low failure rates of individual electronics subassemblies has led to the initial conclusion that redundancy is not a satisfactory approach.

However, detailed trade-off analyses considering incremental costs of maintenance flights, SIP hardware costs, impact of increased size and weight and reliability of switching devices should be performed before a final decision is made.

#### 10.1.4 LST-SIP Instrument Utilization Profile

Table 10-1 presents the percentage usage assumed for the ten basic LST-SIP instruments. The ensuing reliability predictions are predicated on this usage.

Table 10-2 enumerates the failure rates, observation hours, the stress (power on) to observation time ( $t/t_{obs}$ ) ratio, and the stress hours for the ten basic instruments and their individual components for a one year orbit. The  $t/t_{obs}$  ratio includes warm-up time, readout time and the 50% occultation period and was used to derive the actual operating or "stress" hours of each instrument component.

Table 10-2 indicates that the SEC Vidicon is obviously the most critical component since it has a high failure rate and long usage hours. The RADC Reliability Notebook indicates a failure rate of 130 failures per million hours for a Vidicon. With the imposition of severe pre-conditioning and burn-in requirements a desired failure rate of 15 failures per million hours on a specially configured tube should be achievable in the time frame of the program. During consultation with a potential supplier, five possible SEC Vidicon failure modes were identified and explored with the following results.

- Photo-cathode Degeneration - data accumulated to date does not indicate this will be a significant problem.
- Thermionic Gun Life - presently a useful life of 10 to 20 thousand operating hours can be expected.
- SEC Target Degradation - for LST-SIP application with its corresponding low light level a life of 10 thousand hours can reasonably be expected before objectionable degradation (due to electron bombardment) occurs, the effects of the radiation environment must be further evaluated.

TABLE 10-1. ANTICIPATED LST/SIP  
INSTRUMENT UTILIZATION PROFILE

Item	Instrument	Observation Usage %
1	F/96 Camera - Range I (115-300 nm)	13.33
2	F/96 Camera Range II (160-600 nm)	13.33
3	F/96 Camera Range III (500-1100 nm)	13.33
4	F/12 Camera	5.0
5	High Resolution Spectrograph "HRS1" (110-180 nm)	5.0
6	High Resolution Spectrograph "HRS2" (180-350 nm)	5.0
7	Faint Object Spectrograph "FOS1" (110-220 nm)	22.0
8	Faint Object Spectrograph "FOS2" (220-660 nm)	14.0
9	Faint Object Spectrograph "FOS3" (660-1000 nm)	6.0
10	Faint Object Spectrograph "FOS4" (1000-5000 nm)	3.0
	Total	<hr/> 100.0 <hr/>
11	Slit Jaw Camera 20% of Item 5 thru 9 Total	10.4%



TABLE 10-2. LST/SIP COMPONENT  
FAILURE RATES AND DUTY CYCLES

Item	Instrument/Component	Failure Rate (Failures/ $10^6$ Hrs)	Observation Hours* Per 1 Yr. Orbit "t <sub>obs</sub> "	Stress (Power On) Time "t" To Observation Time "t <sub>obs</sub> " Ratio
1	<u>F/96 Camera Assembly</u>			
1.1	Field Select Mirror	0.000114	1752	2.0
1.2	Camera Shutter	0.3	1752	1.0
1.3	Tracking Detector Electronics	4.5	1752	1.0
1.4	Camera Select Mechanism	0.3	1752	0.03
1.5	SEC Vidicon	15.0	584	3.2
1.6	Vidicon Electronics	3.0	584	3.2
1.7	Supporting Electronics	2.0	584	0.07
1.8	Filter and Drive	0.3	584	0.03
2	<u>Slit Jaw Camera</u>			
2.1	Field Select Mirror	0.000114	456	1.0
2.2	SEC Vidicon	15.0	456	3.2
2.3	Vidicon Electronics	3.0	456	3.2
2.4	Supporting Electronics	2.0	456	0.07
3	<u>F/12 Camera</u>			
3.1	Field Select Mirror	0.000114	219	2.0
3.2	SEC Vidicon	15.0	219	3.2
3.3	Vidicon Electronics	3.0	219	3.2
3.4	Support Electronics	2.0	219	.07
3.5	Filter and Drive Mechanism	0.3	219	.03

TABLE 10-2. LST/SIP COMPONENT  
FAILURE RATES AND DUTY CYCLES (Cont.)

Item	Instrument/Component	Failure Rate (Failures/ $10^6$ Hrs)	Observation Hours* Per 1 Yr. Orbit "t <sub>obs</sub> "	Stress (Power On) Time "t" To Observation Time "t <sub>obs</sub> " Ratio
4	<u>Faint Object Spectrograph "FOS1"</u> (110-220 nm)			
4.1	Field Select Mirror	0.000114	964	2.0
4.2	Slit Mechanism	0.3	964	1.0
4.3	Spectrograph Selector	0.3	964	0.02
4.4	SEC Vidicon	15.0	964	2.42
4.5	Vidicon Electronics	3.0	964	2.42
4.6	Support Electronics	2.0	964	0.06
4.7	Grating Drive	0.3	964	0.02
5	<u>Faint Object Spectrograph "FOS2"</u> (220-660 nm)			
5.1	Field Select Mirror	0.000114	613	2.0
5.2	SEC Vidicon	15.0	613	2.42
5.3	Vidicon Electronics	3.0	613	2.42
5.4	Support Electronics	2.0	613	0.06
5.5	Slit Mechanism	0.3	613	1.0
6	<u>Faint Object Spectrograph "FOS3"</u> (660-1000 nm)			
6.1	Field Select Mirror	0.000114	263	2.0
6.2	SEC Vidicon	15.0	263	2.42
6.3	Vidicon Electronics	3.0	263	2.42
6.4	Support Electronics	2.0	263	0.06
6.5	Slit Mechanism	0.3	263	1.0

TABLE 10-2. LST/SIP COMPONENT  
FAILURE RATES AND DUTY CYCLES (Cont.)

Item	Instrument/Component	Failure Rate (Failures/ $10^6$ Hrs)	Observation Hours* Per 1 Yr. Orbit " $t_{obs}$ "	Stress (Power On) Time " $t$ " To Observation Time " $t_{obs}$ " Ratio
7	Faint Object Spectrograph "FOS4" (1000-5000 nm)			
7.1	Field Select Mirror	0.000114	131.5	2.0
7.2	Electronics	5.0	131.5	2.42
8	High Resolution Spectrographs "HRS1" (110-180 nm) "HRS2" (180-350 nm)			
8.1	Field Select Mirror	0.000114	438	2.0
8.2	Slit Mechanism	0.3	438	1.0
8.3	Spectrograph Selector	0.3	438	0.02
8.4	SEC Vidicon	15.0	219	2.42
8.5	Vidicon Electronics	3.0	219	2.42
8.6	Support Electronics	2.0	219	0.06

\* NOTE: In the above 50% occultation was assumed  
hence, 4380 hours of observation are available  
for each year of orbit.

- Gas content due to imperfect vacuum - this appears to be a remote possibility since SEC Vidicons have demonstrated a four/five year shelf life.
- Mechanical deficiencies such as cracks, bubbles, improper seams, etc. - proper design, manufacture and quality control techniques relegate to a remote possibility.

As an initial requirement criteria, the SEC Vidicon must exhibit a life of 4,000 hours during which no more than 10% degradation is tolerable when cycled to saturation once every two hours followed by a two minute readout period.

#### 10.1.5 Reliability Block Diagrams and Mathematical Models

The Reliability block models and the math models derived therefrom are presented as Figures 10-2 thru 10-5. Three general approaches were used in formulating the models, namely:

- LST-SIP Series Reliability Model wherein all instruments and components are considered to be one single chain.
- Conditional probability models where the survival and corresponding experiment completion of "N" of "M" instruments was considered.
- Normalized models where the Reliability was determined for 100 and 1000 experiment observation hours.

The glossary of Table 10-3 is provided herein as an aid to interpreting the math models.

The LST-SIP Series Model was formulated to provide a maintainability reference since it indicates the probability that at least one failure will occur ( $Q = 1-R$ ) for the stipulated orbit duration. From a Reliability view point, this model is unacceptable since one failure cannot be presumed catastrophic as several instrument failures may be tolerated. This model is useful for planning the maintenance missions and in determining spares requirements.

TABLE 10-3. MATH MODEL GLOSSARY

The following summarizes the R subscripts used in the Math Models.

12E	F/12 Camera Electronics
96E	F/96 Camera Electronics
CSF	F/96 Camera Shutter Flag
CSM	F/96 Camera Select Mechanism
FM	F/12 Camera Filter Mechanism
FOE	Faint Object Spectrograph Electronics
FOS	Faint Object Spectrograph (any one of the four)
FOS1	Faint Object Spectrograph (110 - 220 nm Range)
FOS1/S/G	Faint Object Spectrograph (110 - 220 nm Range) with a specified slit and a specified grating
FOS2	Faint Object Spectrograph (220 - 660 nm Range)
FOS2/S	Faint Object Spectrograph (220 - 660 nm Range) with a specified slit
FOS3	Faint Object Spectrograph (660 - 1000 nm Range)
FOS4	Faint Object Spectrograph (1000 - 5000 nm Range)
FOSM	Faint Object Spectrograph Slit Mechanism and Electronics
FSM	Field Select Mirror
FWD	F/96 Camera Filter Wheel and Drive
HRE	High Resolution Spectrograph Electronics
HRS	High Resolution Spectrograph (either of the two)
HRS/FOS	Spectrograph (either of the two High Resolution Spectrographs, or one of the four Faint Object Spectrographs)
HRS1	High Resolution Spectrograph (110 - 180 nm Range)
HRS2	High Resolution Spectrograph (180 - 350 nm Range)
HRS+S	High Resolution Spectrograph (either of the two specified) with a corresponding slit specified
HRS1/2	High Resolution Spectrograph (110 - 180 nm Range) or High Resolution Spectrograph (180 - 350 nm Range)

TABLE 10-3. MATH MODEL GLOSSARY (Cont.)

SEC	Vidicon, Secondary Electron Conduction
SJC	Slit Jaw Camera
SM	Slit Mechanism (Spectrograph Control)
SS	Spectrograph Selector
TD	F/96 Camera Target Detection Electronics

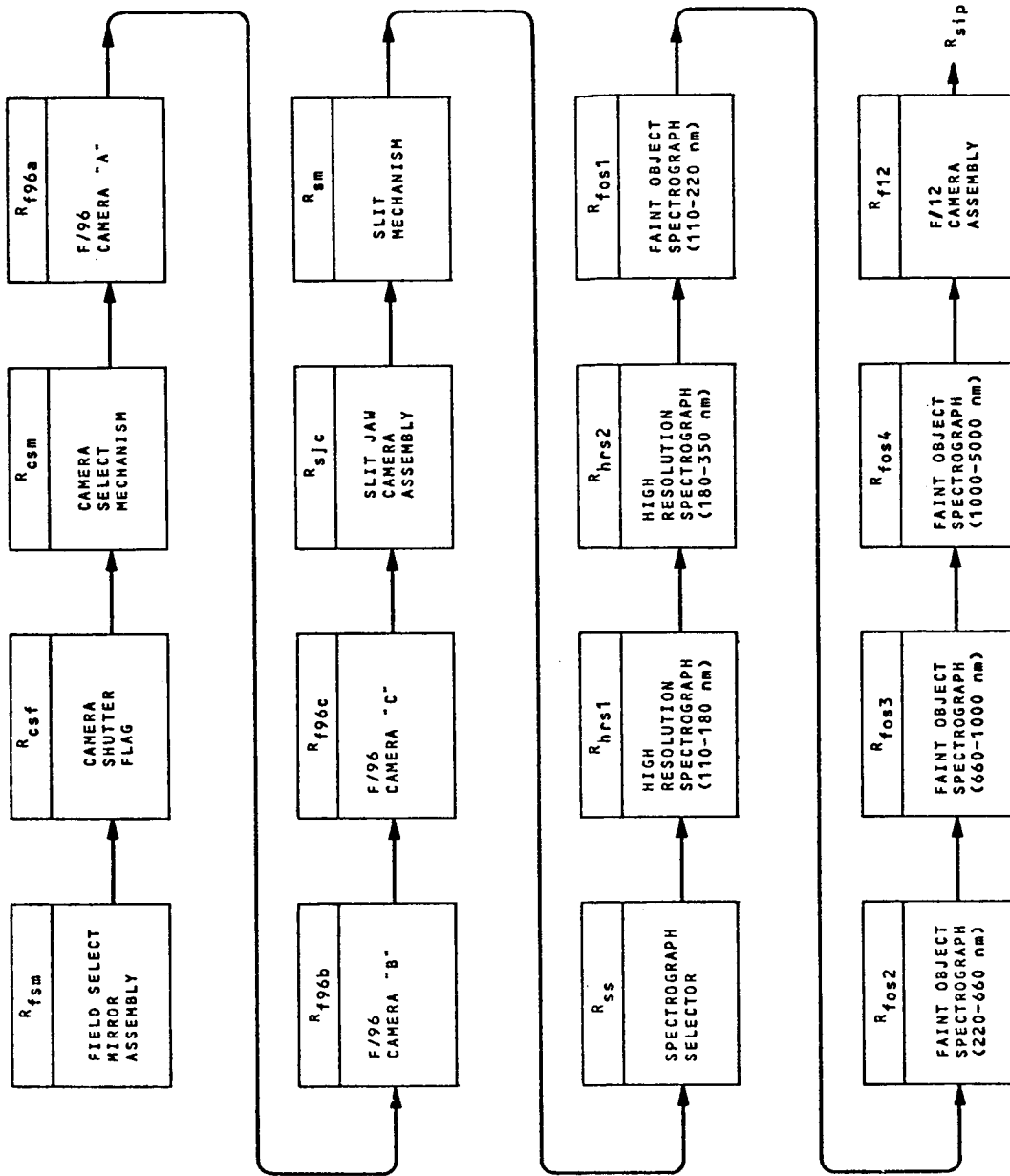
The conditional probability models represent a realistic Reliability approach. The models presented do not represent all the possibilities - for example: a model for the probability of two (2) of the three (3) F/96 Cameras and the ramifications of each having four filters was not considered. Further, no attempt was made to consider the impact resulting from instrument failures whereby the surviving instruments would be subjected to increased operation (stress). It is to be noted that Models 10-4N and 10-4P were derived using Bayes' Theorem; active redundancy appears to apply to these models, but this is not so because in the event of an instrument failure(s), its corresponding experiment(s) is terminated.

Figure 10-2 is the LST-SIP Series Model while Figures 10-3, 10-4 and 10-5 correspond to the functional grouping of the F/96 Camera Assembly, Spectrographs, and the F/12 Camera respectively. More precise models are required in the future when a more detailed definition of experiment sequence and duration and possible experimental alternatives in the event of a given instrument failure is available.

The LST-SIP design includes appropriate features to preclude jamming between operational positions of the filter, grating and slit mechanisms of the Cameras and Spectrographs. In the formulation of the models this feature was translated as a certainty that a filter, grating or slit would always be available.

#### 10.1.6 Reliability Predictions

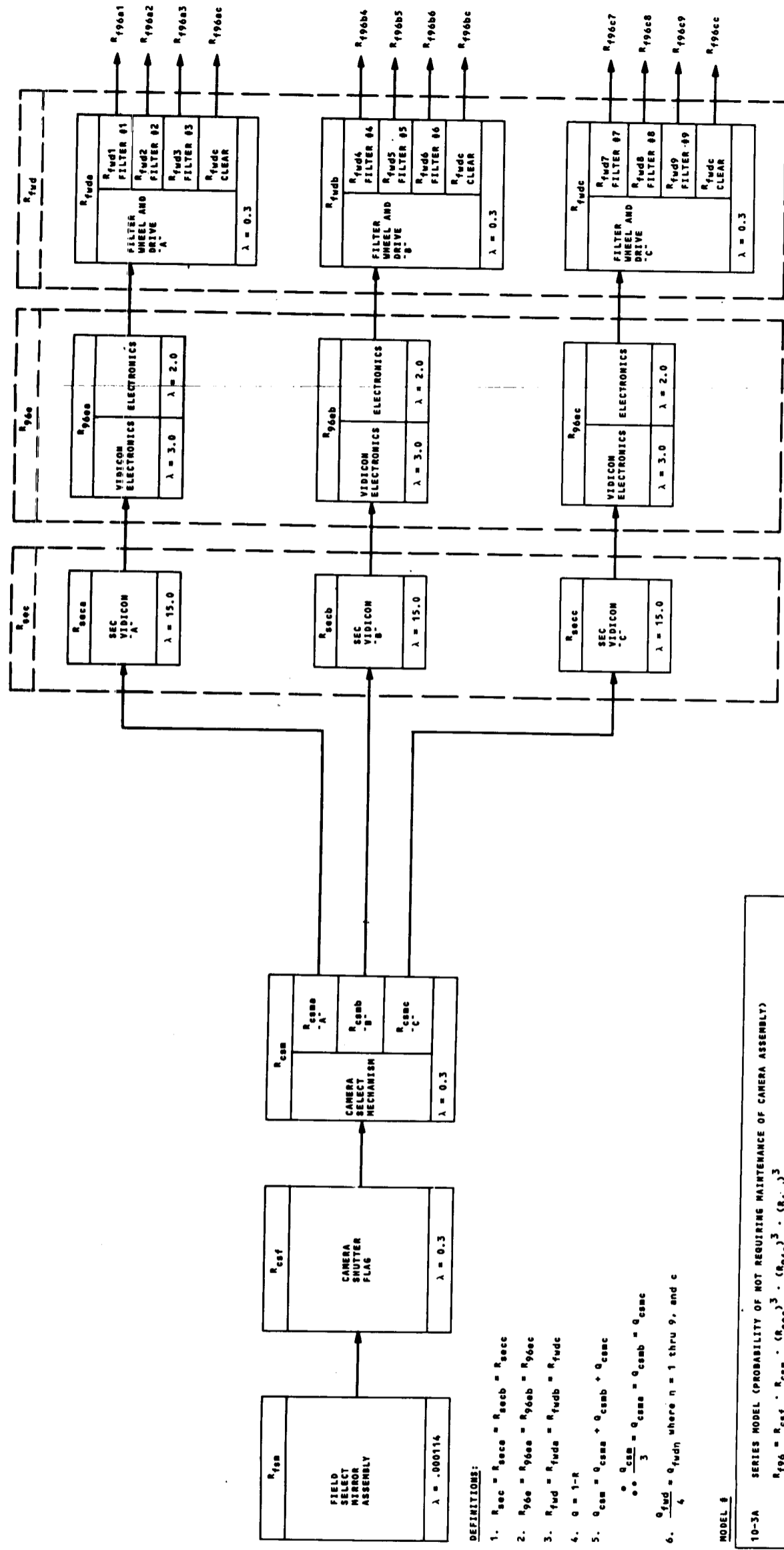
The evaluations of the LST-SIP Series Model for one year of orbit and two years of orbit are presented in Figures 10-6 and 10-7, respectively; the predicted reliability of each element in the series chain is indicated thereon. The higher failure rate of the SEC Vidicon, relative to other system components, coupled with its projected long hours of usage is reflected, as expected, in the lower reliabilities of the spectrograph and camera blocks. It is to be remembered that for the  $R_{SIP}(1 \text{ YR})$  and  $R_{SIP}(2 \text{ YR})$  calculations all the LST-SIP instruments/components will perform properly



MODEL 10-2  $R_{sip} = R_{fsm} \cdot R_{f96} \cdot R_{sjc} \cdot R_{sm} \cdot R_{ss} \cdot R_{hrs1} \cdot R_{hrs2} \cdot R_{fos1} \cdot R_{fos2} \cdot R_{fos3} \cdot R_{fos4} \cdot R_{f12}$

Figure 10-2. SIP Series Model





**DEFINITIONS:**

1.  $R_{sec} = R_{seca} = R_{secb} = R_{sec}$
2.  $R_{96} = R_{96a} = R_{96b} = R_{96c}$
3.  $R_{fud} = R_{fuda} = R_{fudb} = R_{fudc}$
4.  $Q = 1-R$
5.  $Q_{csm} = Q_{csm} + Q_{csm} + Q_{csm}$
6.  $\frac{Q_{fud}}{4} = Q_{fud}$  where  $n = 1$  thru  $9$ , and  $c$

**MODEL 8**

10-3A	SERIES MODEL (PROBABILITY OF NOT REQUIRING MAINTENANCE OF CAMERA ASSEMBLY)
$R_{f96} = R_{csm} \cdot R_{csm} \cdot (R_{96})^3 \cdot (R_{96})^3 \cdot (R_{fud})^3$	
10-3B	PROBABILITY THAT A SPECIFIC F/96 CAMERA IS OPERABLE
$R_{f96a} = R_{f96b} = R_{f96c} = R_{fm} \cdot R_{csm} \cdot R_{csm} \cdot (R_{csm} + \frac{Q_{csm}}{3}) \cdot R_{sec} \cdot R_{96} \cdot R_{96} \cdot R_{fud}$	
10-3C	PROBABILITY THAT A SPECIFIC F/96 CAMERA OUTPUT IS AVAILABLE
$R_{f96an} = R_{f96bn} = R_{f96cn} = R_{fm} \cdot R_{csm} \cdot R_{csm} \cdot (R_{csm} + \frac{Q_{csm}}{3}) \cdot R_{sec} \cdot R_{96} \cdot (R_{fud} + \frac{Q_{fud}}{4})$	
10-3D	PROBABILITY THAT AT LEAST ONE OF THE F/96 CAMERAS IS OPERABLE:
$R_{f96(1.3)} = R_{fm} \cdot R_{csm} \cdot (R_{csm} + \frac{Q_{csm}}{3}) [1 - (1 - R_{sec} \cdot R_{96} \cdot R_{fud})^3]$	

Figure 10-3. F/96 Camera Assembly Operational Reliability Block Diagram and Math Models

II. MATH MODELS	
HIGH RESOLUTION SPECTROGRAPH RELIABILITY: MODEL 10-4A $R_{hrs} = R_{hrs1} \cdot R_{hrs2} \cdot R_{sec} \cdot R_{hre}$	
FAINT OBJECT SPECTROGRAPH RELIABILITY: MODEL 10-4B $R_{fos1} = R_{sec} \cdot R_{fos} \cdot R_{fog}$	
10-4C $R_{fos2} = R_{fos3} \cdot R_{sec} \cdot R_{fos}$	
SERIES SPECTROGRAPH MODEL (PROBABILITY THAT NO MAINTENANCE WILL BE REQUIRED): MODEL 10-4D $R_{spec} = R_{fam} \cdot R_{sjc} \cdot R_{ss} \cdot (R_{hrs})^2 \cdot R_{fos1} \cdot R_{fos2} \cdot R_{fos3} \cdot R_{fos4}$	
PROBABILITY THAT A SPECIFIED HIGH RESOLUTION SPECTROGRAPH IS OPERATIONAL: MODEL 10-4E $R_{hrs} = R_{hrs1} \cdot R_{hrs2} \cdot R_{hrs3} \cdot R_{hrs4}$	
PROBABILITY THAT BOTH A SPECIFIED HI RES SPECTROGRAPH AND SLIT IS OPERATIONAL: MODEL 10-4F $R_{hrs66} = R_{hrs} \cdot R_{sjc} \cdot (R_{ss} + Q_{ss}/\lambda) \cdot (R_{ss} + Q_{ss}/\lambda) \cdot R_{hrs}$	
PROBABILITY THAT AT LEAST ONE OF THE TWO HI RES SPECTROGRAPHS IS OPERATIONAL: MODEL 10-4G $R_{hrs1/2} = R_{hrs1} \cdot R_{hrs2} \cdot R_{hrs3} \cdot R_{hrs4} \cdot (R_{hrs1} + R_{hrs2} + R_{hrs3} + R_{hrs4})$	
PROBABILITY THAT FAINT OBJECTS SPECTROGRAPH FOS1 (110-220 nm) IS OPERATIONAL: MODEL 10-4H $R_{fos1} = R_{fam} \cdot R_{sjc} \cdot R_{ss} \cdot (R_{ss} + Q_{ss}/\lambda) \cdot R_{fos1}$	
PROBABILITY THAT FOS1 WITH A SLIT AND A GRATING BOTH SPECIFIED IS OPERATIONAL: MODEL 10-4I $R_{fos1/6} = R_{fam} \cdot R_{sjc} \cdot R_{ss} \cdot (R_{ss} + Q_{ss}/\lambda) \cdot (R_{ss} + Q_{ss}/\lambda) \cdot R_{sec} \cdot R_{fog} \cdot (R_{fog} + Q_{fog}/\lambda)$	
PROBABILITY THAT FOS2 IS OPERATIONAL: MODEL 10-4J $R_{fos2} = R_{fam} \cdot R_{sjc} \cdot R_{fos2}$	
SIMILARLY FOR MODEL 10-4K $R_{fos3} = R_{fam} \cdot R_{sjc} \cdot R_{fos3}$	
PROBABILITY THAT FOS2/S WITH A SPECIFIED SLIT IS OPERATIONAL: MODEL 10-4L $R_{fos2/s} = R_{fam} \cdot R_{sjc} \cdot R_{sec} \cdot R_{fog} \cdot (R_{fog} + Q_{fog}/\lambda)$	
THIS RELATIONSHIP IS ALSO VALID FOR FOS3/S.	
PROBABILITY THAT FOS4 IS OPERATIONAL: MODEL 10-4M $R_{fos4} = R_{fam} \cdot R_{fos4}$	
PROBABILITY THAT AT LEAST ONE OF THE FAINT OBJECT SPECTROGRAPHS IS OPERATIONAL: MODEL 10-4N $R_{fos} = R_{fam} \cdot \left\{ 1 - \left[ R_{sjc} \cdot Q_{fos2} \cdot Q_{fos3} \cdot \left[ R_{ss} \cdot (R_{ss} + Q_{ss}/\lambda) + Q_{ss} \right] + Q_{sjc} \cdot Q_{fos4} \right] \right\}$	
PROBABILITY THAT AT LEAST ONE OF THE SIX SPECTROGRAPHS IS OPERATIONAL: MODEL 10-4P $R_{hrs/fos} = R_{hrs} \cdot \left\{ 1 - \left[ R_{sjc} \cdot Q_{fos2} \cdot Q_{fos3} \cdot \left[ R_{ss} \cdot (R_{ss} + Q_{ss}/\lambda) + Q_{ss} \right] + Q_{sjc} \cdot Q_{fos4} \right] \right\}$	

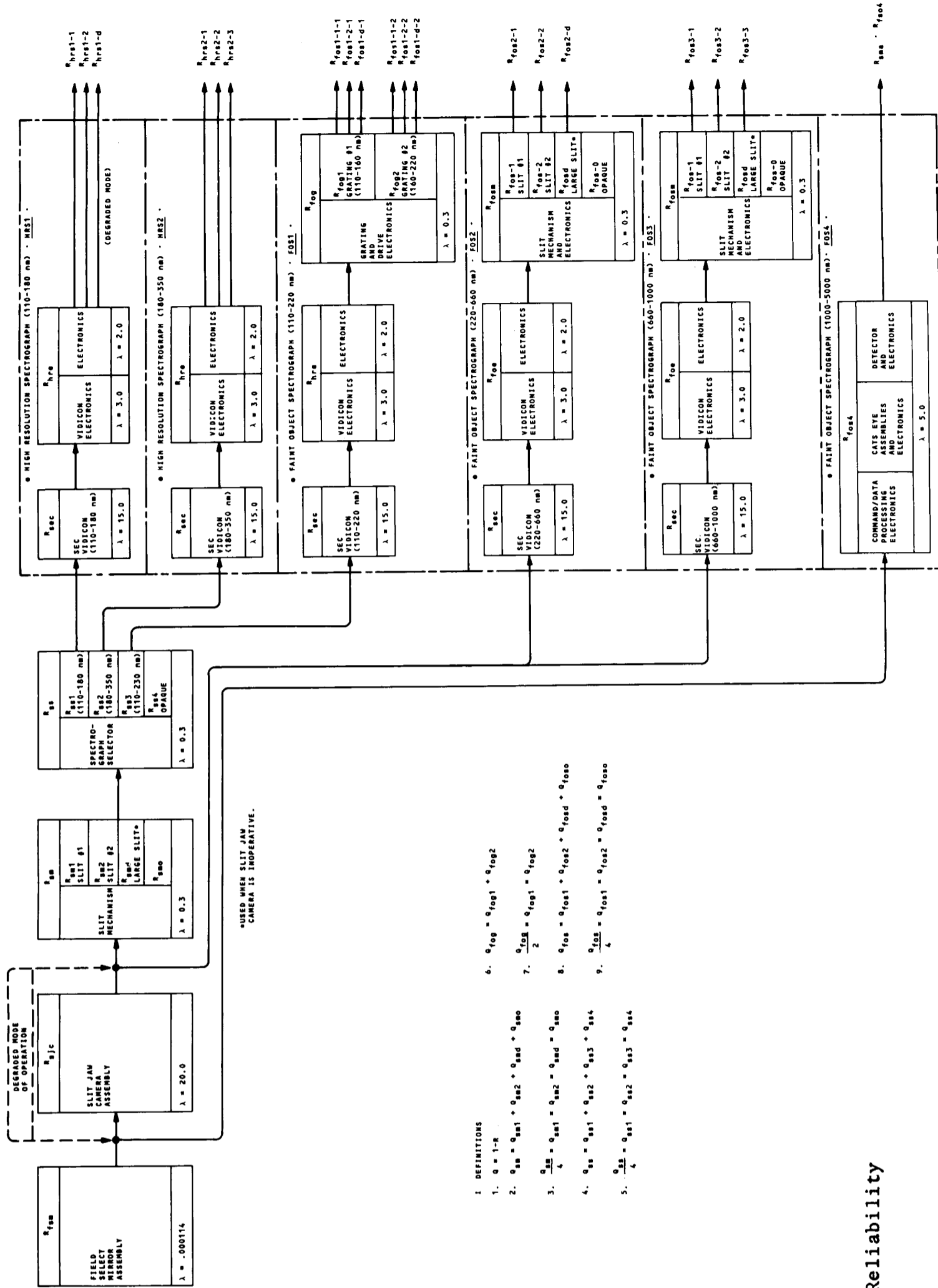
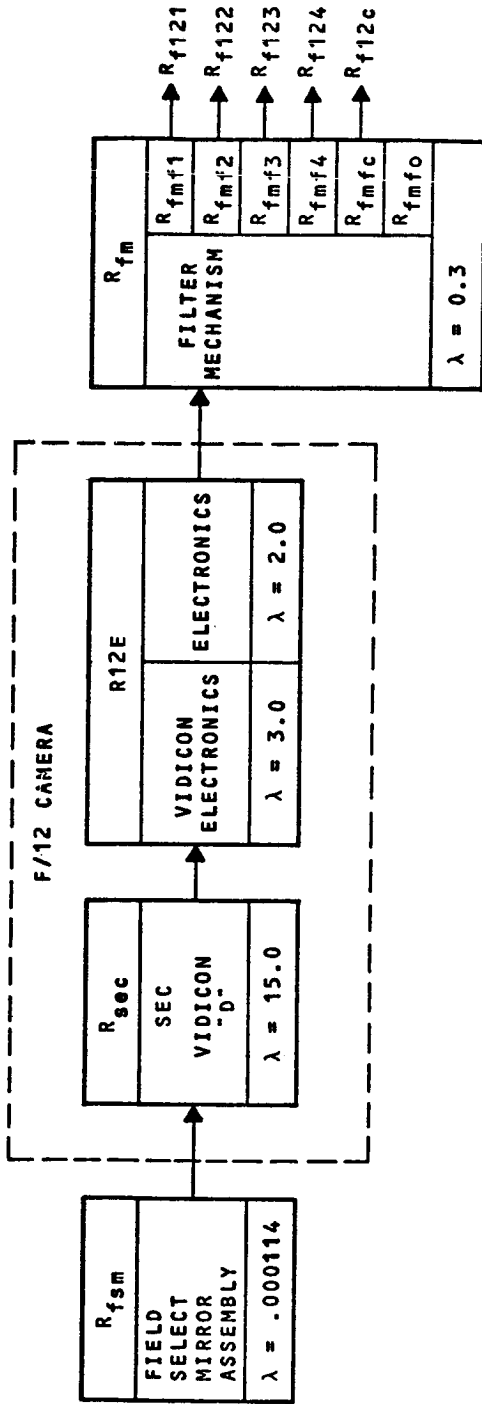


Figure 10-4. Spectrography Operational Reliability Block Diagram and Math Models



DEFINITION:  $R_{fmf} = R_{fmf1} = R_{fmf2} = R_{fmf3} = R_{fmf4} = R_{fmfc} = R_{fmfo}$

MODEL NO.

10-5A SERIES MODEL (PROBABILITY THAT F/12 CAMERA WILL NOT REQUIRE MAINTENANCE):

$$R_{f12} = R_{sec} \cdot R_{12E} \cdot R_{fm}$$

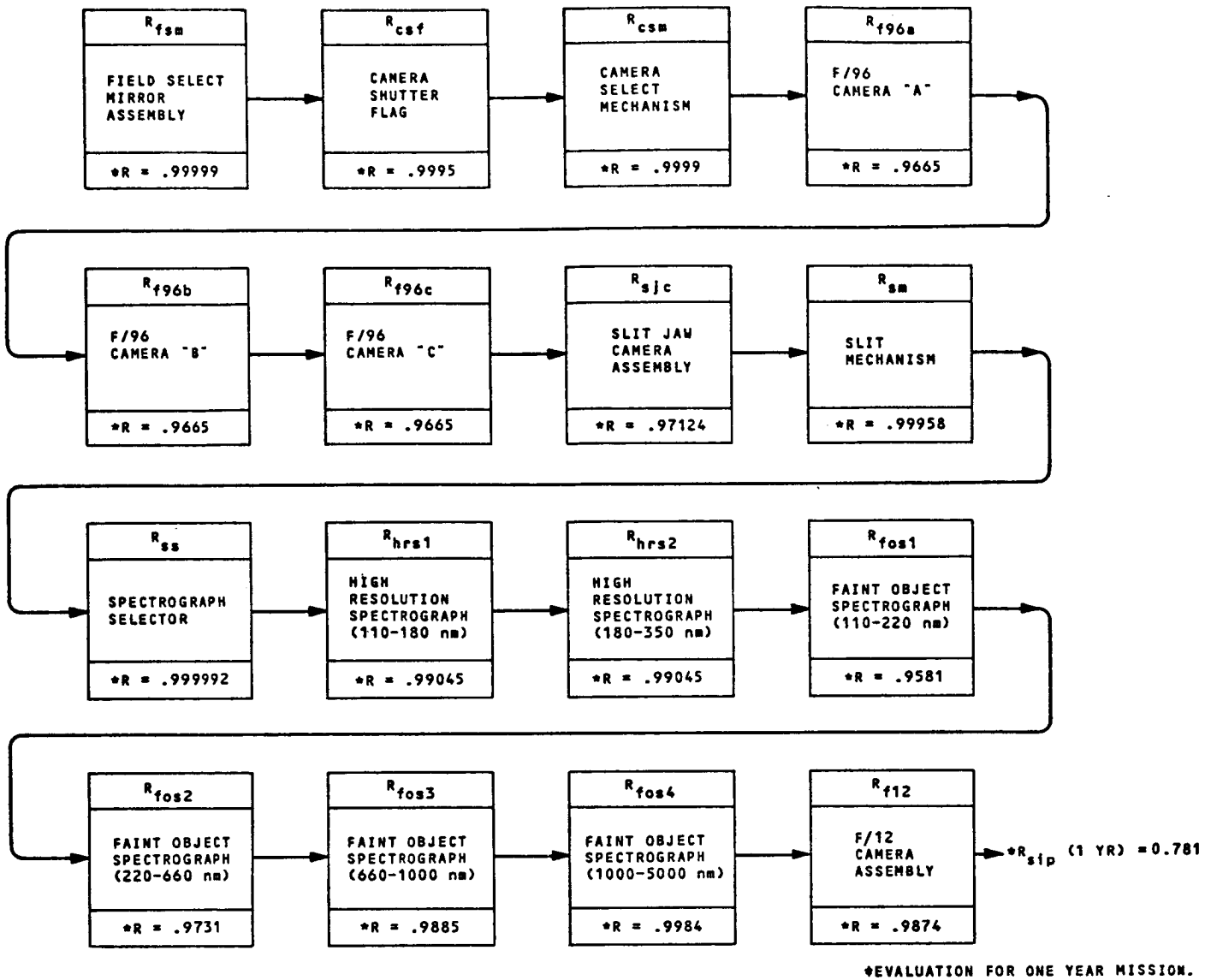
10-5B PROBABILITY THAT THE F/12 CAMERA SYSTEM IS OPERABLE:

$$= R_{fsm} \cdot R_{sec} \cdot R_{12E} \cdot R_{fm}$$

10-5C PROBABILITY THAT A SPECIFIED F/12 SLIT IS AVAILABLE:

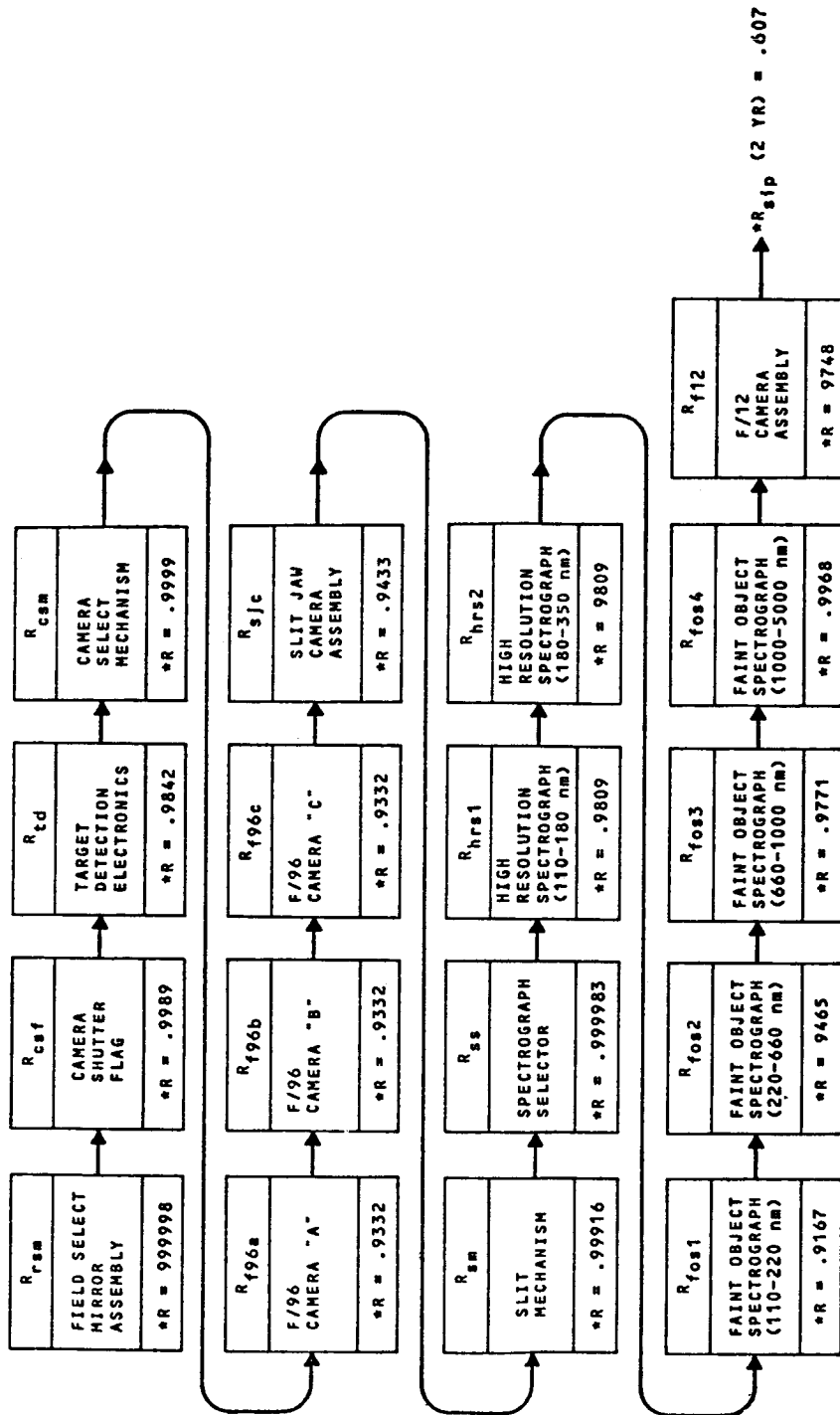
$$= R_{fsm} \cdot R_{sec} \cdot R_{12E} \cdot (R_{fm} + \frac{Q_{fm}}{6})$$

Figure 10-5. F/12 Camera Assembly Operational Reliability Block Diagram and Math Models



MODEL 10-2  $R_{sip} = R_{fsm} \cdot R_{f96} \cdot R_{sjc} \cdot R_{sm} \cdot R_{ss} \cdot R_{hrs1} \cdot R_{hrs2} \cdot R_{fos1} \cdot R_{fos2} \cdot R_{fos3} \cdot R_{fos4} \cdot R_{f12}$

Figure 10-6. SIP Series Model Evaluation



\* EVALUATION FOR TWO YEAR ORBIT WITH 50% OCCULTATION.

$$MODEL\ 10-2\ R_{slp} = R_{fsm} \cdot R_{f96} \cdot R_{sjc} \cdot R_{sm} \cdot R_{ss} \cdot R_{hrs1} \cdot R_{hrs2} \cdot R_{fos1} \cdot R_{fos2} \cdot R_{fos3} \cdot R_{fos4} \cdot R_{f12}$$

Figure 10-7. SIP Series Model Evaluation

for the prescribed period of operation. Conversely,  $(1-R_{SIP})$  is the probability that a failure will occur; hence there are probabilities of 21.9% and 39.3% that a failure will occur in one year and two years of orbit respectively,

Table 10-4 is a summary of the quantitative evaluation of the math models using the previously enumerated failure rates and the operating (stress) hours anticipated during one year and two years in orbit. Selected models have been evaluated for experiment observation periods of 100 and 1000 hours to provide reliability indexes for some instruments and instrument groupings.

The Spectrograph Series configuration (Item 10 Model 10-4D) has the lowest projected reliabilities, 87.7 and 76.7% for one and two years of orbit. This result is not surprising since there is a SEC Vidicon in each of the five (5) Spectrographs that have a combined operational usage of 5513 hours. Further, the Slit Jaw Camera, which also contains a SEC Vidicon with 1459 hours use per orbit year, has been considered as a series element in this model. If it is assumed the degraded failure mode of the Slit Jaw Camera is acceptable in LST experiments, the projected reliabilities for one and two years are 90.3% and 81.3%, respectively.

The f/96 Camera Series configuration (Item 2, Model 10-3A) has a projected reliability of 90.2% and 81.2% for one and two years of orbit respectively. The f/96 Camera Assembly utilizes three SEC Vidicons for a projected 5607 hours of operation and is the principal factor impacting reliability.

#### 10.1.7 Conclusions

##### 10.1.7.1 Series Elements

Figure 10-1 indicates the critical elements by virtue of their position in the reliability configuration.

TABLE 10-4. RELIABILITY PREDICTION SUMMARY

Item No.	Math Model Description	Reliability Math Model Figure No.	Operational Reliability (50% Occultation Assumed)			
			One Year Orbit	Two Year Orbit	100 Hrs. of Observation	1000 Hrs. of Observation
1	S.I.P. Series Model (probability that no maintenance will be required)	10.2	.781	.607	-	-
2	F/96 Camera Ass'y Series Model (probability of not requiring camera ass'y maintenance)	10.3A	.902	.812	-	-
3	Probability that a specified F/96 camera is operational	10.3B	.967	.935	.995	.944
4	Probability that a specified F/96 camera output is available	10.3B	.992	.983	-	-
5	Probability that at least one of the three F/96 camera experiments will be completed	10.3D	.972	.944	-	-
6	High Resolution Spectrograph Reliability	10.4A	.990	.981	-	-
7	Faint Object Spectrograph Reliability "FOS1"	10.4B	.958	.917	-	-
8	FOS2 Reliability (probability no maintenance will be req'd.)	10.4C	.973	.947	-	-
9	FOS3 Reliability	10.4C	.989	.977	-	-
10	Series Spectrograph Model (probability that Spectrograph maintenance will not be required)	10.4D	.877	.767	-	-
11	Probability that a specified high resolution Spectrograph is operational	10.4E	.977	.954	.989	.898
12	Probability that both a specified high resolution Spectrograph and a slit is operational	10.4F	.977	.954	-	-
13	Probability that at least one of the two high resolution Spectrographs remains operational	10.4G	.994	.989	-	-
14	Probability that Faint Object Spectrograph (110-220 nm) "FOS1" is operational	10.4H	.946	.894	.987	.8976
15	Probability that "FOS1" with a slit and a grating both specified as operational	10.4I	.947	.869	-	-
16	Probability that "FOS2" (220-660 nm) is operational	10.4J	.965	.932	.989	.898
17	Probability that "FOS3" is operational	10.4K	.985	.971	.989	.898
18	Probability that "FOS2" and a specified slit is operational	10.4L	.966	.933	-	-
19	Probability that "FOS3" and a specified slit is operational	10.4L	.985	.971	-	-
20	Probability that "FOS4" (1000-5000 nm) is operational	10.4M	.998	.997	.999	.988
21	Probability that at least one of the four faint object Spectrographs completes its scheduled mission (experiment)	10.4N	.999	.999	-	-
22	Probability that at least one of the six Spectrographs completes its scheduled mission (experiment)	10.4P	.999	.999	-	-
23	F/12 Camera Ass'y. Series Model (probability that F/12 Camera maintenance will not be required)	10.5A	.987	.974	-	-
24	Probability that F/12 Camera System is operational	10.5B	.987	.975	.995	.944
25	Probability that the output from a specified F/12 Camera slit is available	10.5C	.977	.954	-	-

- Field Select Mirror Assembly: this is the sole LST/SIP series element and a catastrophic failure of same would disable all ten basic instruments. A failure of this item is not expected as it will be solely a fixed position, opto-mechanical structure.
- F/96 Camera Controls: this group includes the Camera Shutter Flag and Camera Select Mechanism which are series elements of the three F/96 Cameras. The Shutter Flag and Select Mechanism will be simple devices similar in design to those used successfully in space; these items have low failure rates and low duty cycles and are not expected to be a problem.
- Spectrograph Controls: this group includes the Slit Mechanism and the Spectrograph Selector which are series elements and a catastrophic failure of either would disable High Resolution Spectrographs "HRS1" and "HRS2" and the Faint Object Spectrograph "FOS1". Both items will be simple devices with low failure rates and are not expected to pose a reliability problem.
- Slit Jaw Camera: this element is in series with the High Resolution Spectrographs "HRS1" and "HRS2" and Faint Object Spectrographs "FOS1", "FOS2" and "FOS3", but is not reliability critical since it is provided with a feature whereby ground control can command it to assume "degraded mode" status so experiments can continue. The capability of the ground station to determine improper operation and to have the command to degraded mode executed is important with respect to LST/SIP reliability.

#### 10.1.7.2 Thermal Environment

An orbital temperature of 300K and a nominal electronic part temperature rise of 10K due to power dissipation was assumed in the analysis. Significant deviations from this criteria could impact reliability, hence these assumptions should be reviewed during final design activities.



The SEC Vidicon tubes will employ Peltier Cooling devices to maintain the desired photocathode temperatures. In the event these devices do not have the desired efficiency, the SEC Vidicon tube life is adversely effected and maintenance actions will be increased. Further study of this item is warranted as a more detailed design is developed.

#### 10.1.7.3 Mission Profile (Instrument/Component Duty Cycle)

The instrument/component duty cycle is the ratio of the operating (stress) hours to the hours of experimental observation. The duty cycles used in the Reliability Analysis are indicated in Table 10-2. The duty cycles were derived from the instrument time-phased operating sequences as developed from the steering committee guidelines. Any significant alteration of the assumed duty cycles will necessitate a revision of the Reliability prediction.

Table 10-2 indicates the duty cycle varies from 0.02 for several items to 3.2 for the Camera SEC Vidicons. The latter duty cycle includes a 50% occultation (earth obscuration of the instrument objective) time and a two hour warm-up/stabilization period. The 50% occultation assumption is a worst case situation and in some instances will improve, dependent on the position of the experimental objective. The necessity for the lengthy warm-up period must be further reviewed.

Possible back-up experiments that can be performed in the event of specific instrument failures should be identified in order that they may be factored into the reliability analyses.

#### 10.1.7.4 Math Models

Math models can be developed for conditional probabilities not treated herein - for example, five of six, or four of six Spectrographs performing successfully.

#### 10.1.7.5 Reliability Critical Components

Those components with high failure rates and duty cycles are herewith designated as "reliability critical". The data in Table 10-2 indicates three components are in this category, namely: SEC Vidicon, Vidicon/Support Electronics and Tracking Detector Electronics.

- SEC Vidicon

The LST/SIP will employ ten SEC Vidicon tubes that will be operational for 13,280 hours per year of orbit. A rate of 15.0 failures per million hours has been allocated for this component. The RADC Reliability indicates a 130 failures per million hours for SEC Vidicon tubes, however a significant improvement is expected to result from design improvements and a rigorous screening and pre-conditioning program. The achievement of a 15.0 failures per million hours rate is a major LST/SIP Reliability objective.

Six 25 X 25 mm Vidicon tubes are being used in the SIP Spectrographs and four 50 X 50 mm tubes in the f/96 and f/12 Cameras. Both tubes are in the development phase and corresponding usage data has not been generated. Accordingly, Phase B efforts must include the detailed formulation of a design verification/test program to assure the stipulated failure rate requirement is achieved. The failure mechanisms of smaller tube types should be reviewed as part of this effort.

- Vidicon/Support Electronics

Using the baseline that the Vidicon and Support Electronics will be similar to a previous Kollsman space program design, failure rates of 3.0 and 2.0 failures per million hours was projected for the Vidicon Electronics and for the Support Electronics respectively. The former has a duty cycle some 400 times greater than the latter and hence, is of much greater reliability significance. Established reliability parts only will be used in the Vidicon/Support Electronics and the indicated failure rates are achievable. Further, it is anticipated that the Vidicon/Support Electronics units will be very similar and this commonality will minimize the effort to achieve the stipulated reliability.

#### 10.1.8 Recommendations

The following areas should be further investigated during future LST-SIP Reliability efforts as more information is developed:

- Equipment failure during the launch phase.
- Mechanical failures.
- In-orbit non-operational electronic failure rates.
- Useful life and wearout mechanisms of components and piece parts.

The following should be continuing efforts through all program phases:

- SEC Vidicon reliability improvement.
- Mission profile definition.
- Reliability prediction update.

## 10.2 MAINTAINABILITY

### 10.2.1 Introduction

The following paragraphs cover the consideration of maintainability in the design concepts of the SIP. The discussion begins with the basic approach and reasons for a maintainability program. Following are a list of required inputs for a detailed analysis, and a consideration of maintenance scheduling based on reliability predictions and SIP usage.

Using the results of past investigations by other organizations, the overall maintenance concept chosen for present emphasis is that of manual replacement of major units, in orbit, in a pressurized environment. Using this concept, the hardware design features, to provide ease of maintenance, are described. This area includes layouts showing access to instruments and clearance for astronaut maneuvering. The results of two such layout investigations are shown. In addition, the guide rail and alignment pin provisions for optical assembly mounting, the method of electronics package mounting and connection and a list of required mounting surface tolerances for replaceability are presented.

The concluding paragraphs cover the related areas of growth provisions, failure identification, provisioning, and training, and presents a list of conclusions and recommendations. The main thrust of these conclusions and recommendations is that the selected maintenance concept is compatible with the SIP design as presented, but re-evaluations, with more detailed inputs, should be made, especially with respect to new information relative to Skylab, Space Shuttle and human engineering in a zero-g environment.

### 10.2.2 Basic Approach

The LST will be a pioneer in the development of the concept of in-orbit maintenance of scientific instrumentation. The LST-SIP is to have a projected five year useful life, and later Shuttle launched NAS observatory a ten year lifetime; hence, on-orbit maintenance offers an attractive lower-cost alternative to the development of ultra-high reliability (redundant)/long life instruments or to launching several LST-SIP's. Further studies are required to minimize overall program costs by optimizing an integrated model reliability/maintenance design, hardware, and logistic costs over the useful life of the LST. LST-SIP on-orbit maintenance will utilize the Space Shuttle Orbiter and visiting astronaut personnel will perform the following functions:

- Corrective maintenance - malfunctioning instruments or components are replaced
- Scheduled (preventive) maintenance - life limited instruments or components are replaced.
- New instrument installation - improved or newly developed, will replace present instruments.

The LST-SIP is equipped with groups of basic instrumentation. In the event of a failure, a particular experiment is terminated until corrective maintenance action is taken. From the Reliability analysis, a moderately high reliability can be anticipated for each instrument; there is therefore, the opportunity to combine corrective maintenance and scheduled maintenance in a single visit. For purposes of efficiency, maintenance planning should be directed toward concurrent performance of, at least two of the three on-orbit functions and, ideally, all three.

### 10.2.3 Maintainability Analysis

Detailed Maintainability Analysis of the LST-SIP should be performed when the detailed design information required for the development of a meaningful analysis is available. Specifically,

the following information is required:

- Reliability analysis of the actual design identifying failure rates modes and mechanisms;
- Human engineering study establishing the capabilities of an astronaut performing in-orbit maintenance in a zero-g environment;
- Final selection of the maintenance action environment (pressurized in-orbit, unpressurized manual or manipulator);
- Definition of the test points/data incorporated that will permit ground control station monitoring of instrument performance.

#### 10.2.4 Maintenance Action Schedule

The Reliability analysis indicates that there is a 22% and 40% probability that at least one item failure would have occurred during a 1 year and a 2 year orbit, respectively. Further, a review of the instrument/component duty-cycle operating (stress) time data listed in Table 10-2 indicates that preventive (scheduled) maintenance actions resulting from those failure mechanisms associated with, among others, wear out, useful life and material consumption, will not occur during the first four years of orbit. Projections of anticipated corrective/scheduled maintenance actions beyond the first four years of orbit are premature at this time due to a lack of sufficient stress/time vs. failure-mode details.

The failures expected during the early orbit periods are random catastrophic ones, independent of accumulated operating time, rather than gradual degradations characteristic of wear out. The LST-SIP schedule has the flexibility of deferring completion of an experiment when a given instrument fails and opting to perform other experiments; hence corrective maintenance can be implemented as convenience dictates.

Based on the foregoing, the LST-SIP Maintenance Concept relative to the first four years of use is:

- Perform the LST-SIP corrective/scheduled maintenance actions concurrently and replace only those assemblies that have malfunctioned.

This concept imposes stringent requirements for the ground based diagnostic capability. Some catastrophic failures will be quickly identified but other failures and degradations are more difficult to determine. The telemetered data from component test points must provide the identification of these problems.

#### 10.2.5 Maintenance Action Environment

Four maintenance action environments were reviewed in previous studies for LST-SIP application, namely:

- Ground - LST-SIP returned to earth for ground maintenance and subsequently relaunched
- Unpressurized - Manipulator: Mechanical manipulators aboard the Space Shuttle Orbiter or Tug would be used for instrument/component replacement
- Unpressurized - Manual: On orbit maintenance performed by a suited astronaut
- Pressurized - On-orbit - the LST would be docked to the Space Orbiter/Tug and then pressurized to permit the astronaut to perform maintenance in a "shirt sleeve" environment

The first approach is not promising and will not be considered here. More complete trade off analysis relative to the latter three approaches must be made in order to reach a final decision.

At this time the pressurized on-orbit environment seems preferable because of the freedom of motion and the dexterity offered the astronaut.

Special tools may be required to permit the astronaut to apply bi-directional torques in the zero g environment that will be necessary for the removal and reinstallation of the larger instruments.

A Human Engineering investigation must be performed to determine how an astronaut(s) can best perform maintenance functions in a zero-g environment. Maintenance area layout, equipment and tool designs, work schedules and procedures, housekeeping, potential safety hazards, human functions and limitations must be thoroughly evaluated and optimized.

As a projected worst expected maintenance case, a procedural analysis of an f/96 Camera Assembly was performed based upon experience with Apollo optical systems. Removal and replacement actions require some four plus hours of work in a pressurized in-orbit situation. Special tools would be used for the removal and installation of five items (three camera tube assemblies, the front end optical section and the front end electronics package).

This is now followed by a considerable period for depressurization outgassing, warmup and ground controlled check out.

This maintenance is obviously an imposing task and points up the necessity for additional study and trade off analyses in both the Human Engineering and operational planning areas.

#### 10.2.6 General Design Features for In-Orbit SIP Maintenance

The unpressurized in-orbit concepts will dictate a set of design requirements relative to compatibility with the mechanical manipulator or suited maintenance operations; they will not be explored herein as it is presently assumed that the pressurized on-orbit concept will be employed.



The present LST-SIP design layouts were reviewed and all desired removable hardware was found to be readily accessible for maintenance removal/reinstallation; the f/12 Camera is the most difficult to access.

A full scale mock-up of the entire LST is being built to facilitate examination of accessibility and define removal and reinstallation procedures. The mock-up should be structurally sound so as to provide support for an experimenters weight, and should be rotatable to permit access from all directions.

Some of the design features incorporated to facilitate in-orbit maintenance are:

- Insertion and removal of assemblies by means of positive locking/unlocking lever mechanisms;
- Snubbers and other friction devices to preclude excessive shocks as components engage their stops;
- Oversized guides and tracks to facilitate positioning of replacement units;
- Pins and guides used in conjunction with the locking mechanism to assure proper positioning/seating of instrumentation;
- Proper replacement unit mechanical/optical alignment established upon insertion by a combination of mounting surface guides and pins; a metal model fabricated as a master template to assure this feature is obtained on all provisioned components;
- Electrical connectors of the linear motion positive locking type and connections are accomplished either manually or by the locking mechanism;
- Incorporation of test points to monitor the performance of each component; data from tests will be telemetered to the ground control station on command.

#### 10.2.7 SIP Layout and Hardware Mounting Considerations

To assure adequate access for replacement of hardware, layout studies were performed taking the anthropometry of the astronaut into account. Figure 10-8 shows the results of the first layout evaluation. The open ring structure permits access to all mounting hardware, and the instrumentation form factors were controlled to permit guiding each item from its mounting location through the



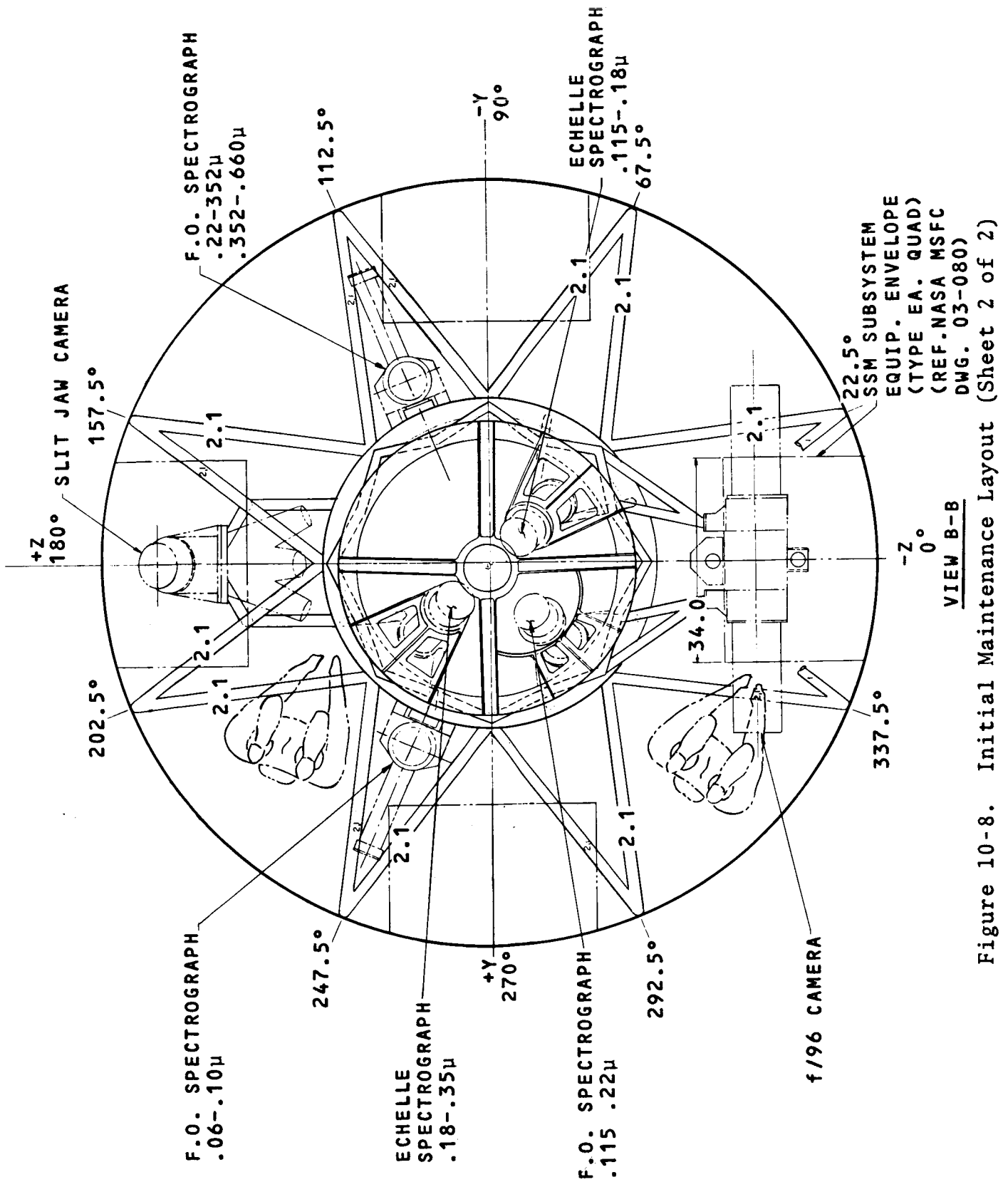


Figure 10-8. Initial Maintenance Layout (Sheet 2 of 2)

opening of the SSM. (Figures 10-12 through 10-16 show maximum instrument form factors.)

The results of the first study and the many additions and modifications to both the SIP and SSM resulted in a second set of accessibility layouts which are shown in Figure 10-9. Locations of mechanisms, electronics packages, mounting provisions, etc., were in many cases established from access needs. The constraints imposed by the SSM structure and subsystem are in accordance with Marshall Space Flight Center drawing number 03-091 dated September 6, 1972. It is believed that adequate space for maneuvering of the astronaut and for the astronaut to control the instrument position, has been provided. Provisions for turning, hand and arm access to fasteners and connectors and astronaut constraints (handholds, and foot constraints) have been considered.

The following additional areas require detailed study. From the SIP layout point of view, dynamic dimensions coupled with visibility, luminance, dynamic response of the weightless astronaut, eye-hand coordination and force emission must be known and evaluated with respect to hardware configuration. From the overall LST systems point of view, the maintenance provisions must be coordinated with requirements for life support both with respect to astronaut physiology and possible safety hazards. The interactions of life support system design with the metabolic cost of each task, and the need to prevent instrumentation contamination are vital to both mission success and program cost.

Figure 10-10 illustrates the means of mounting those axially located instruments. Each instrument is provided with a pair of guide/mounting flanges. These flanges fit, rather loosely, into fixed guide rails on the SIP structure. These guide rails provide control as the astronaut pushes the instrument forward until it hits a stop then settles down into place, hitting another stop. Alignment marks are placed on the instrument and the structure to provide quick assurance to the astronaut that the unit has been pushed far enough. At this point he reaches past the structural

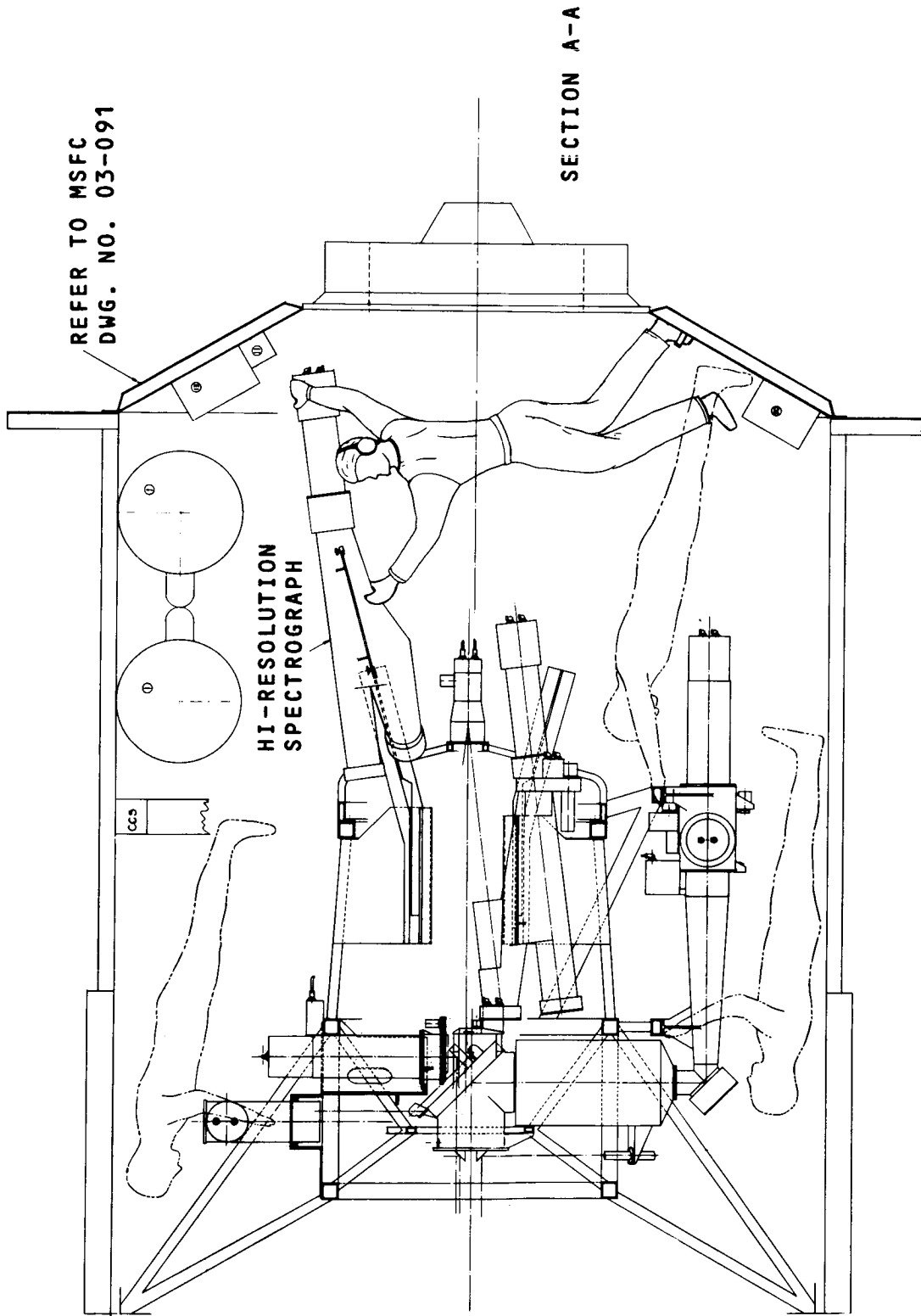
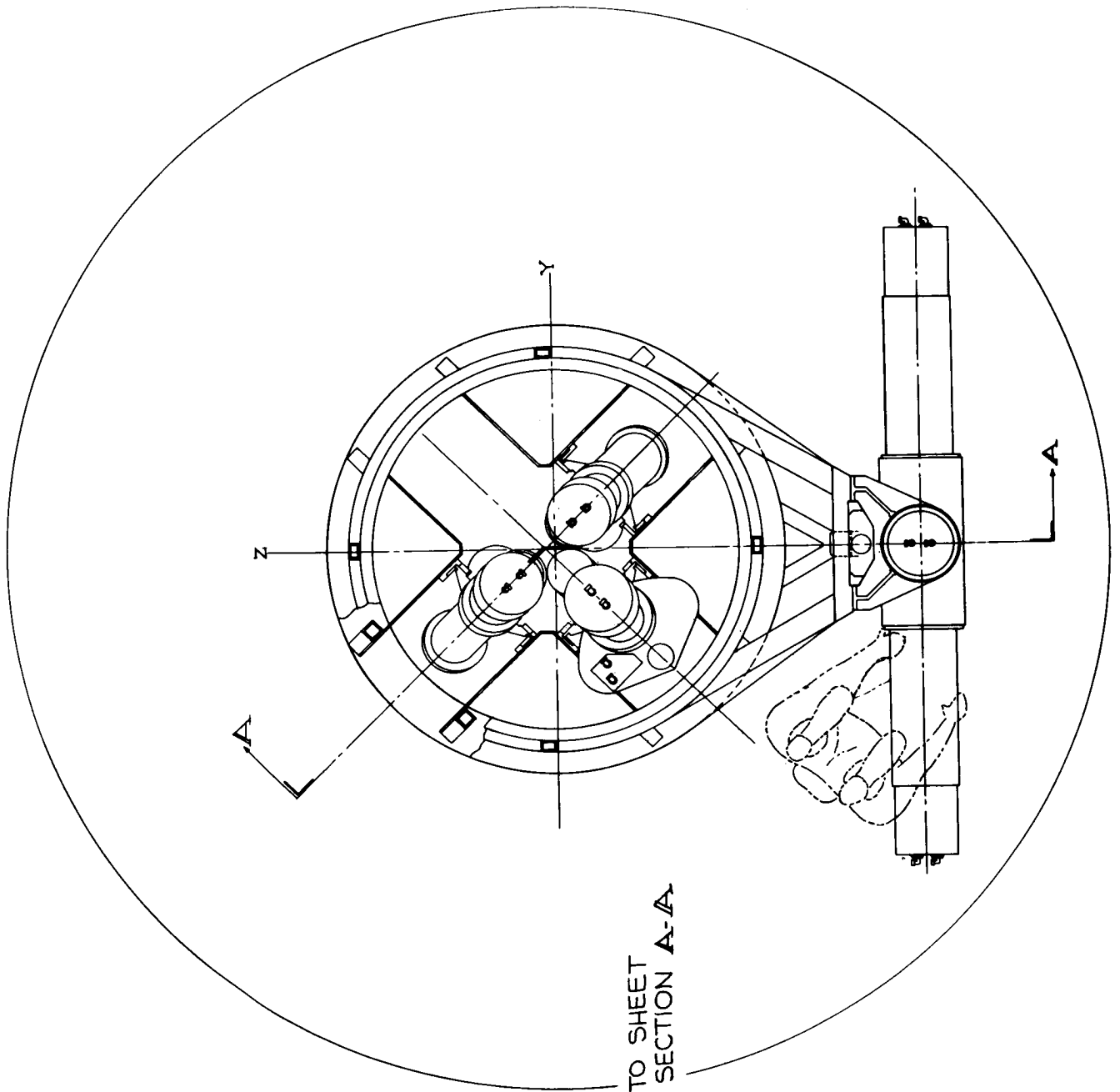


Figure 10-9. Maintenance Layout (Sheet 1 of 2)



REFER TO SHEET  
1 FOR SECTION A-A

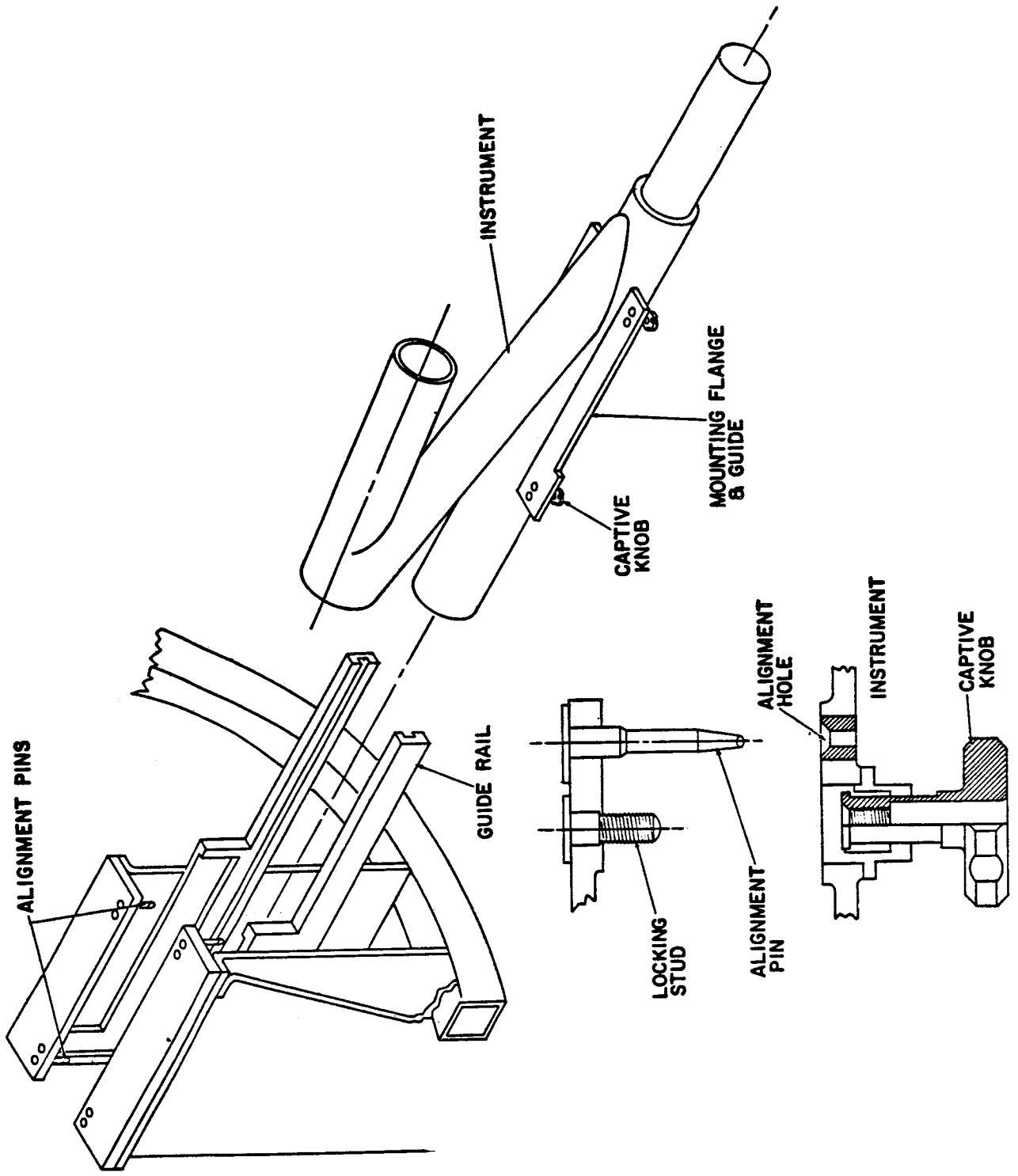
Figure 10-9. Maintenance Layout (Sheet 2 of 2)

ring to tighten the captive thumb knobs. The alignment pins help assure proper instrument location and ease of positioning. The detailed arrangement of the thumb knob and guide pin is also shown on Figure 10-10. Figure 10-9 shows an astronaut positioning a High Resolution Spectrograph by means of the guide rails. Here can be seen the intent of the guide rails to minimize astronaut maneuvering in the relatively crowded area.

These instruments which are mounted radially do not suffer from the access problems of the axial units. There are no obstructions and no support rings to pass. Therefore the guiderails were not included here. Guidepins and captive hardware are provided for positioning and fastening. This arrangement is shown in Figure 10-11. The captive hardware, whether threaded thumbknobs or a lever configuration, can be decided on a human engineering basis since access for either is available.

The provision for attachment of the removable camera tube assemblies consists of two locating guidepins to maintain angular orientation of the photocathode with respect to the instrument optical axis and of three captive bolts to secure the camera to the instrument. The mounting surface of the camera tube assembly is premachined to assure proper placement of the photocathode along the optical axis within the tolerance dictated by the depth of focus. Access and maneuvering space is provided in all cases.

To minimize the possibility of misjudging failure locations, the electronics associated with each major hardware item is packaged separately. Figure 5-21 is the SIP interconnection schematic; it also illustrates the electronics packaging division approach taken. For example, all of the electronics associated with the SEC vidicon camera tube assemblies, including data processing, power supplies, diagnostics, and data interface formatting that are associated with each SEC vidicon, are contained within its housing. Therefore, replacement of any detector tube assembly replaces all associated electronics. In addition, all of the circuits related to an



LOCKING PROVISION DETAIL

Figure 10-10. Installation Provisions for Axially Located Instrumentation



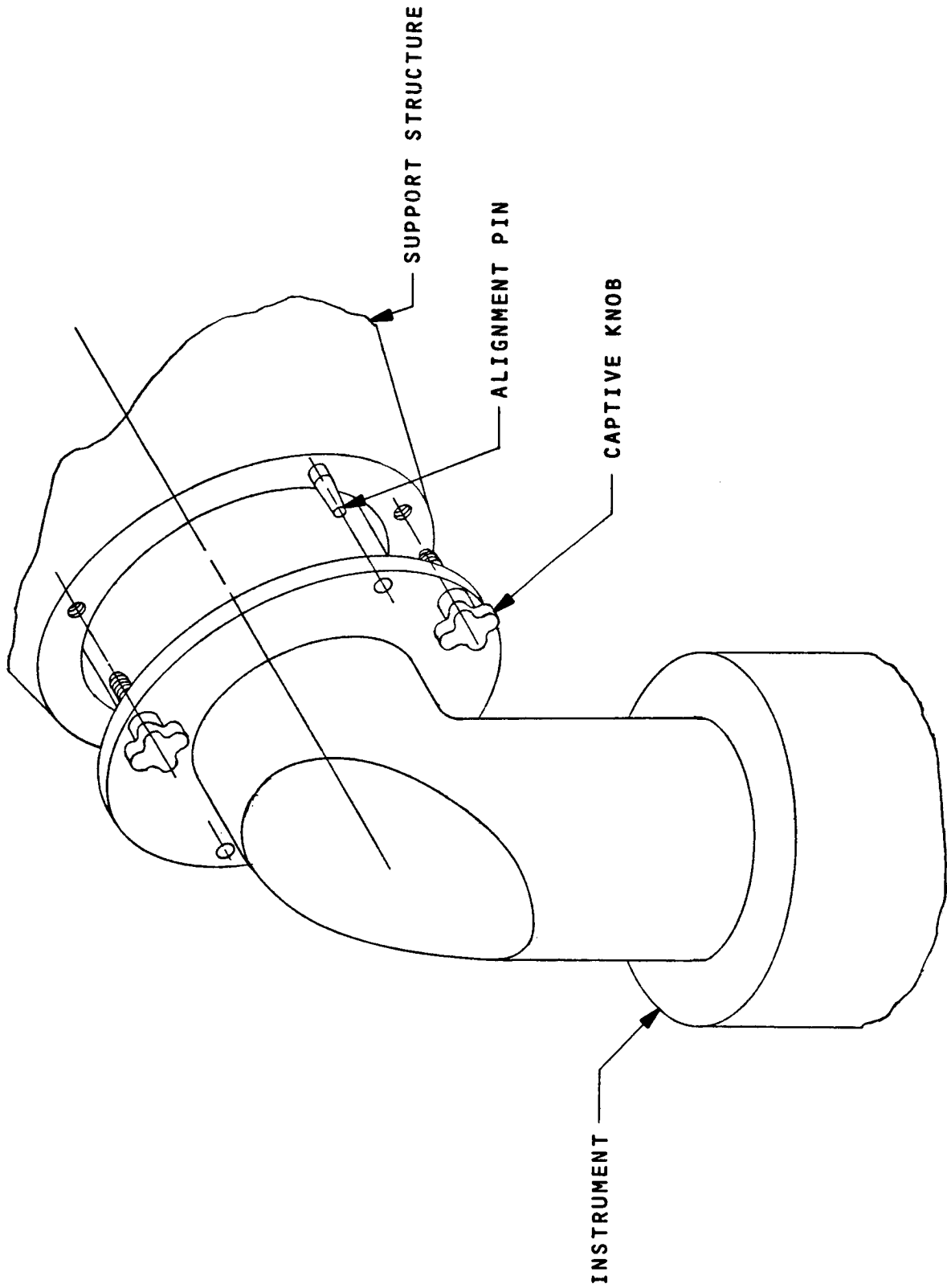


Figure 10-11. Radial Instrument Installation

instrument "front end" are included in a removable package. That is to say, if an instrument malfunction is traced to an electronic failure for a filter position control, replacement can be made of that instrument's support electronics package. This package is located on its particular instrument and contains the control, power supply, diagnostics, and data formatting and interface circuits associated with that particular instrument.

The electrical interface between each electronics package and its associated instrument is made through a center locking, rectangular, rack and panel type of connector as shown on Figure 5-10. The center lock contains an extension shaft that protrudes through the gasketed cover that encloses the electronics. Removal of the electronics package requires the following steps:

- Disengage the Signal & Power connectors (SIP harness connections) with a straight pull on the plug coupling rings (Lanyards are provided for this purpose).
- Rotate the Instrument connector knob that will cause that rack and panel connector to disengage while being jacked into the electronics unit.
- Loosen captive mounting screws and lift electronics package.

Reverse this procedure to replace the electronics.

The following summarizes the in flight maintenance aspects of the electronics packaging:

- All SEC Vidicon circuits are packaged within its corresponding tube housing.
- All instrument support and ancillary circuits are housed in individual package adjacent to the mechanism serviced by it.
- Linear motion type connectors are used at all SIP harness/electronics package interfaces.
- Electronics package to mechanism interface is made by a rack and panel type of connector with screw type ejection provisions.

### 10.2.8 Tolerances for In-Service Replaceability

Table 10-5 defines additional restrictions on variations of assemblies to insure their replaceability with others of the same kind and their adherence to the same performance criteria as the original instruments.

The tolerances given are for the coordinates of focal plane interfaces relative to mechanical mounting interfaces. The de-centration limits are measured at the focal interface, which is often remote from the mechanical interface. The projection of the focal plane centration to the mounting plane assumes that the measurement is made perpendicular to the mounting plane within 0.1 mrad.

TABLE 10-5. TOLERANCES FOR REPLACEABILITY

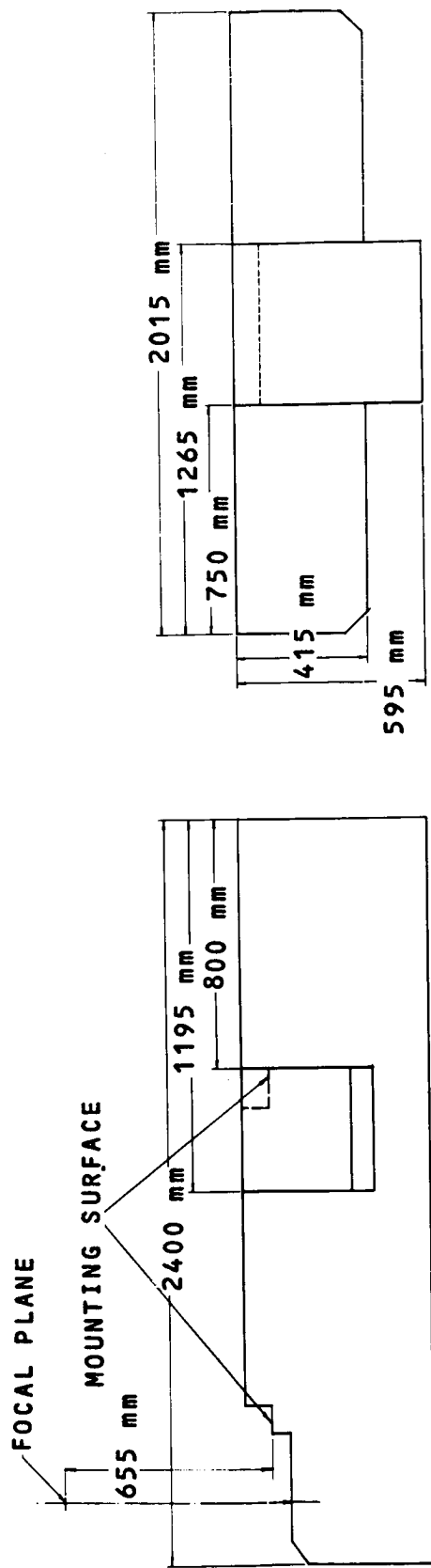
<u>Instrument and Location</u>	<u>Defocus Tolerance</u>	<u>Decentration Tolerance</u>
f/96 Camera at f/12 focus	0.07 mm	0.1 mm
Slit Assembly for Axial Bay Instruments	0.08 mm	0.3 mm
Spectrograph Select Collimator Assembly	0.17 mm	0.3 mm
Faint Object Spectrograph in Radial Bay	0.08 mm	0.5 mm
f/12 Camera	0.15 mm	0.5 mm
Sensor Tubes for Spectrographs	0.10 mm	0.5 mm
Sensor Tube for f/96 Camera	1.0 mm	1.0 mm
Axial Bay Instruments	Not Applicable	0.2 mrad tilt max.

### 10.2.9 Growth Provisions

The design of the SIP configuration provides for growth to permit this national resource to keep pace with both changes in the state of technology and future astronomy objectives. Toward that end, the opto-mechanical interfaces have been designed for hardware replacement without need for alignment, and electrical interfaces have been configured for ease of instrument replacement. In addition, one extra instrument location has been provided in the axial bay. It is also recognized that instruments will be replaced by others of different capabilities. Figure 10-12 shows the maximum outline for an instrument that could fit into the f/96 Camera location. Figure 10-13 shows the maximum outline for the 220 to 660 nm and the 660 to 1000 nm Faint Object Spectrograph locations. Figure 10-14 shows the maximum outline for the spare location, the 115 to 180 nm High Resolution Spectrograph and the 180 to 350 nm High Resolution Spectrograph locations, and Figure 10-15 shows the maximum outline for the 115 to 220 nm Faint Object Spectrograph location.

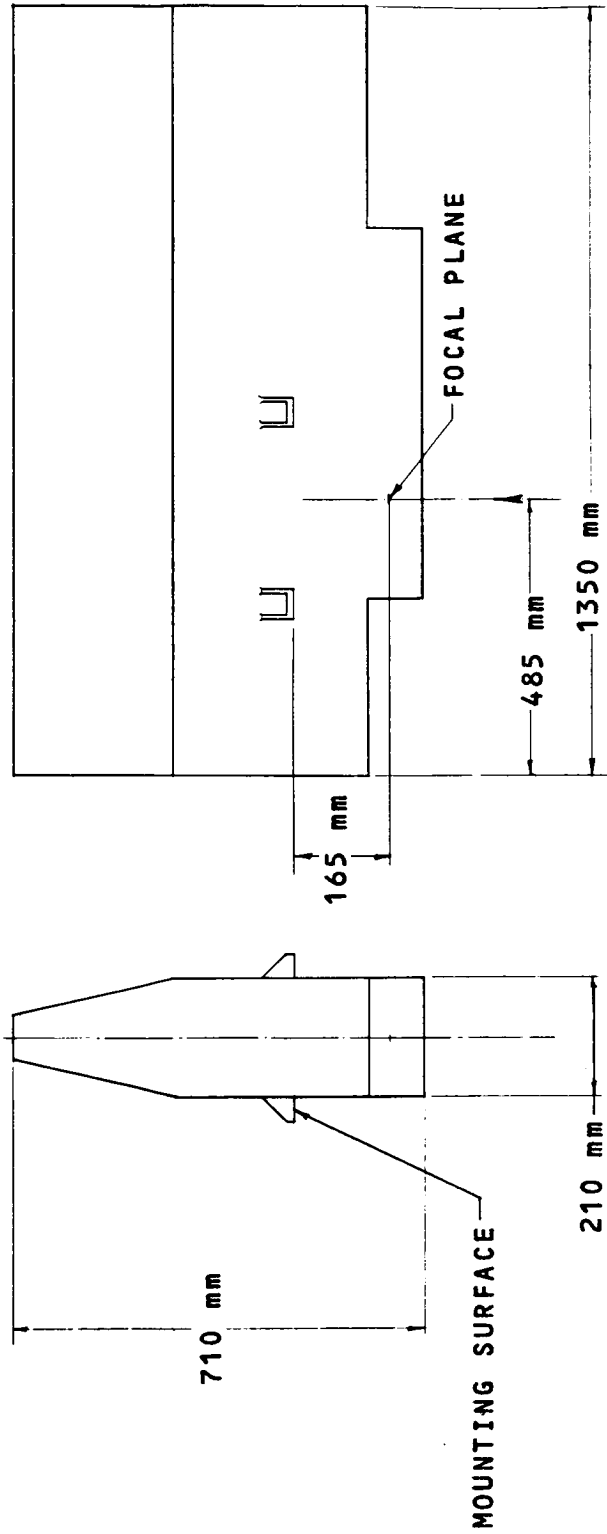
### 10.2.10 Failure Identification

In-orbit malfunctioning hardware is identified by ground diagnostics. Telemetered experiment and ancillary sensor data transmitted by the LST to ground monitoring stations provides the capability of monitoring in-orbit performance. As the equipment design requirements are finalized, provision will be included to provide feedback to ground control from test points which monitor the function of each component. Identification of the malfunctioning component may be accomplished by a Fault-Tree Logic analysis, computer simulation/analysis, or simulation of the malfunction in a ground based LST. In general, the determination of a malfunctioning item does not require "quick reaction" as corrective action can only be implemented at the next scheduled maintenance mission.



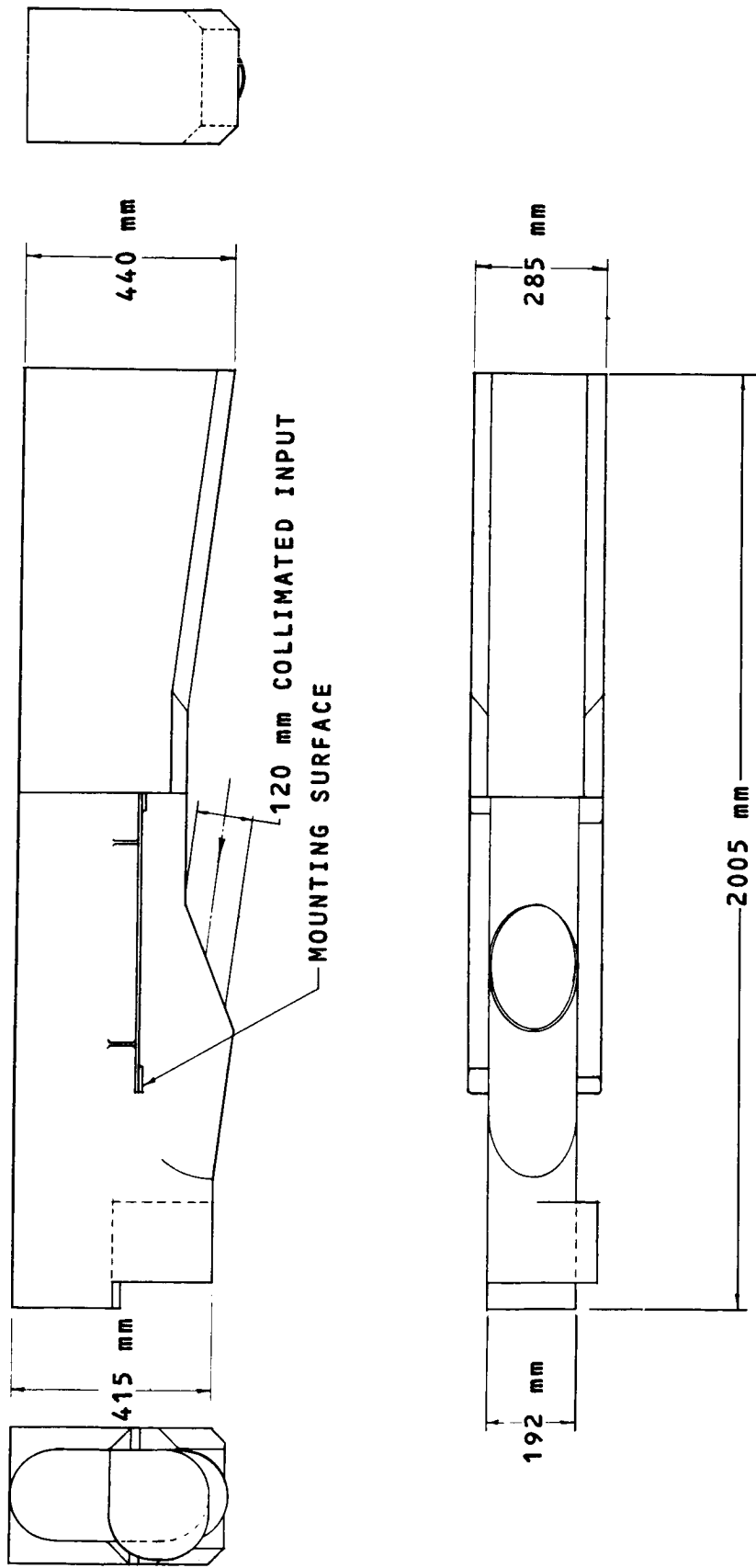
NOTE  
 ANY UNASSIGNED INSTRUMENT CONFORMING TO THIS  
 MAX. OUTLINE DWG. WILL REPLACE THE f/96 CAMERA

Figure 10-12. f/96 Camera, Maximum Outline



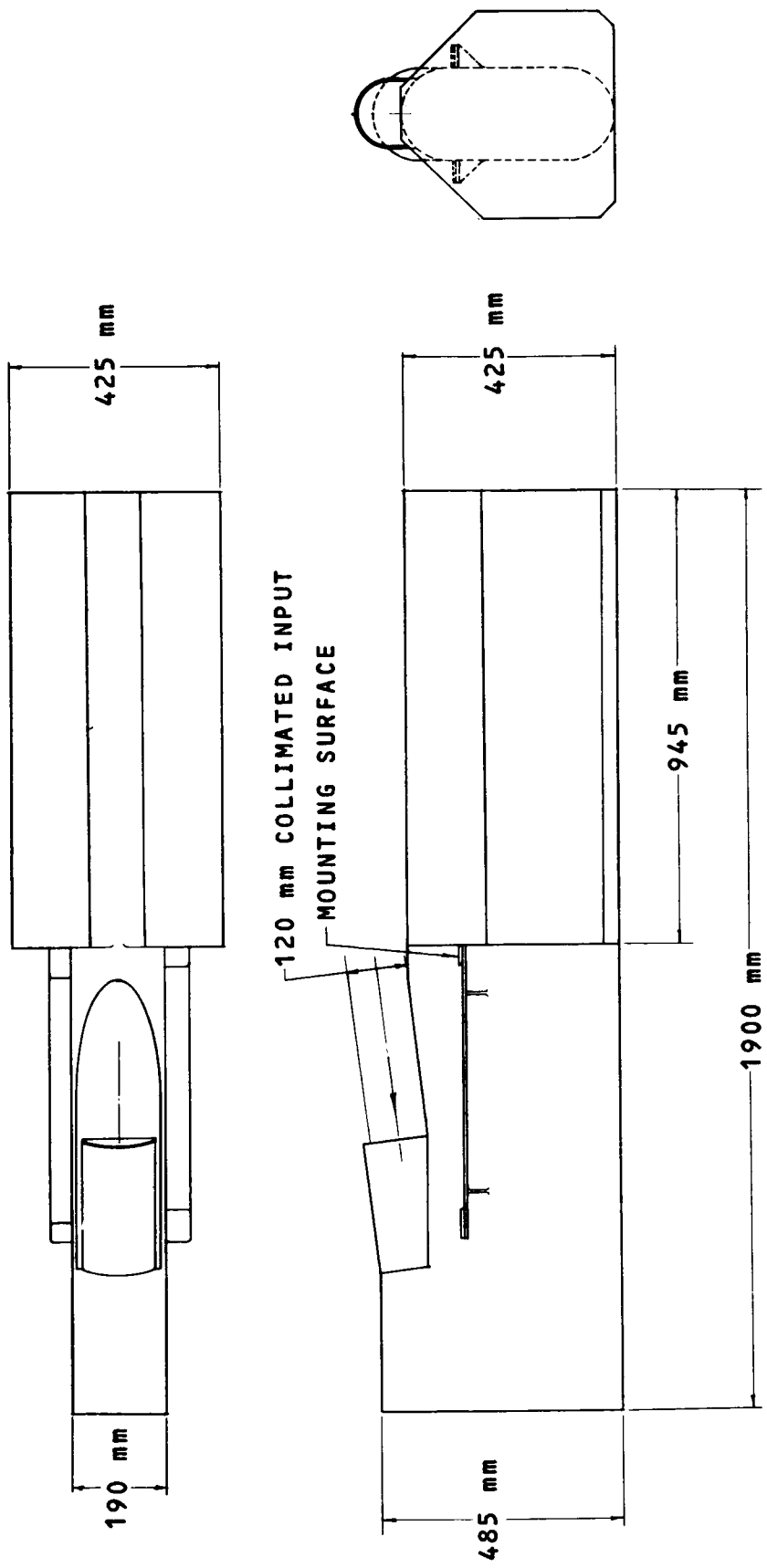
NOTE: ANY UNASSIGNED INSTRUMENT CONFORMING TO THIS MAX. OUTLINE DWG. WILL REPLACE THE FAINT OBJECT SPECTROGRAPH (RADIAL) (2)

Figure 10-13. Radial Instrument, Maximum Outline



NOTE: UNASSIGNED EXPERIMENT MAX.  
 OUTLINE ALSO HIGH RESOLUTION  
 SPECTROGRAPH MAX. OUTLINE.

Figure 10-14. High Resolution Spectrometer Instrument Replacement,  
 Maximum Outline



NOTE: ANY UNASSIGNED INSTRUMENT CONFORMING TO THIS MAX. OUTLINE DWG. WILL REPLACE THE FAINT OBJECT SPECTROGRAPHS (AXIAL).

Figure 10-15. Faint Object Spectrograph Instrument Replacement, Maximum Outline



In-orbit performance of diagnostics or analyses is not planned for the astronaut maintenance crew. Check out procedures are employed after the replacement of a failed item. Replacements for those components established to be malfunctioning via ground diagnostics are launched for in-orbit maintenance.

#### 10.2.11 Provisioning

The following is the tentative list of in-orbit replaceable assemblies, the numbers in parenthesis indicate the quantity of units of one type located in a SIP:

- f/96 Camera Assembly (1)
  - SEC Vidicon and Electronics (3)
  - Support Electronics (1)
- High Resolution Spectrographs (2)
  - SEC Vidicon and Electronics (2)
  - Support Electronics (2)
- Faint Object Spectrographs (4)
  - SEC Vidicon and Electronics (3)
- Support Electronics (3)
- MID-IR Spectrophotometer
- F/12 Camera Assembly (1)
  - SEC Vidicon and Electronics (1)
  - Support Electronics
- Slit Jaw Camera Assembly (1)
  - SEC Vidicon and Electronics (1)
  - Support Electronics (1)
- Spectrograph Selector (1)
  - Support Electronics (1)
- Slit Mechanism Electronics (1)

It is not expected during the orbital life of the SIP that servicing will be required for the optical elements, mechanical mechanisms, slits, shutters, or filters. The benign environment of zero weight; controlled and relatively low operational temperatures; dustless, vapor free, vacuum atmosphere; and virtually zero shock and vibration, eliminate the major causes of failure of these components. Coupled with in orbit alignment complexities, it must be concluded that all replacements of these items or of the SIP package must be performed on the ground. The probability that this will be required during the mission life due to a predictable failure mode is considered zero. Further consideration is required to determine the effect of low quantity, high energy protons on the long term performance of the optical components.

#### 10.2.12 Training

Detailed training requirements will be established during the Human Engineering study wherein problems peculiar to the zero-g environment will be investigated. A full size, rotatable mockup is used to permit the astronaut maintenance crew to become familiar with LST-SIP component removal/replacement procedures.

#### 10.2.13 Conclusions

The following preliminary conclusions have been made as a result of this initial maintainability review:

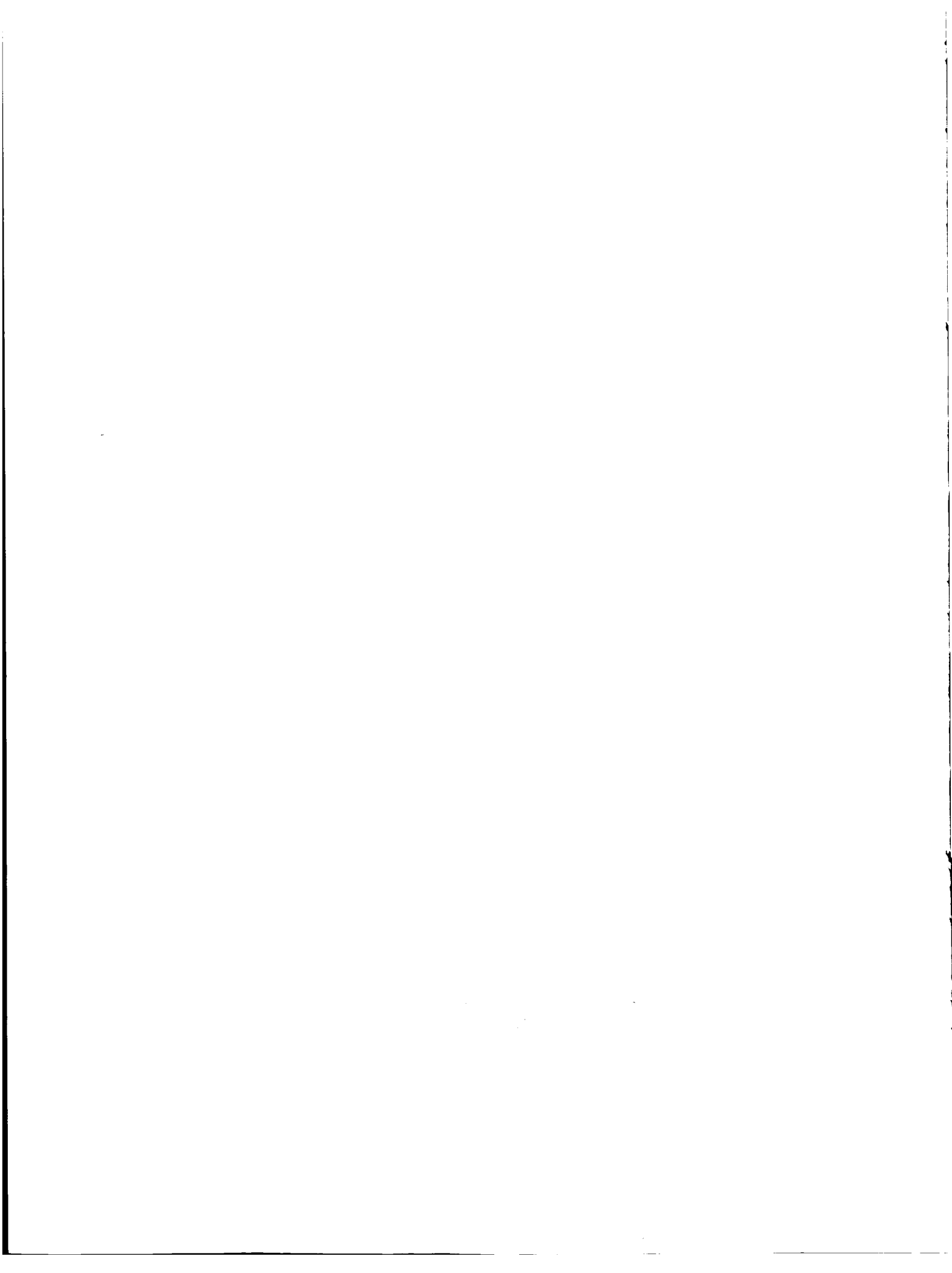
- LST-SIP scheduled maintenance actions may not be required for the first four years of orbit.
- The shirt sleeve environment of the pressurized in-orbit maintenance concept appears the most attractive at this time.
- The LST-SIP design as presently conceived by Kollsman provides adequate accessibility for in-orbit replacement/reinstallation.

- Adequate design features will be incorporated to facilitate the interchange of components and to obtain automatic registration of replaceable components and, thus to preclude adjustments to obtain the required optical/mechanical alignment.
- Astronaut training to perform in-orbit maintenance of the LST-SIP will be minimal as it will be limited to a simple interchange of major subassemblies.

#### 10.2.14 Recommendations

LST-SIP maintainability represents a significant portion of the LST financial budget. For cost effectiveness purposes, a future effort should be directed toward integrating the Maintainability effort and planning with the OTA/SSM and other space programs, particularly Space Shuttle and SKYLAB. Relative to the LST-SIP, the following recommendations apply:

- An early decision on the maintenance concept/environment is required as it has major impact on the design features required.
- A Human Engineering study concerning astronaut maintenance activities in a zero-g environment must be initiated as early as possible.



## APPENDIX A

### RESOLVABLE ELEMENT SIZE VS POINTING PARAMETRIC ANALYSIS

The purpose of this appendix is to derive the equations to be used in a parametric study of resolvable element size vs. pointing error. The parameter is the telescope f number (f#). Several other parameters such as telescope aperture (D) and wavelength ( $\lambda$ ) are taken as fixed values, but by careful scrutiny of the derivation it is possible to rewrite the equations and use them as parameters if it so desired.

The first step in the parametric analysis is to list the following assumptions:

- (1) The limiting resolvable image size corresponds to the inverse of the spatial frequency at which the overall modulation transfer function is 3%.
- (2) The MTF of each element of the system is independent of the others, which means that the overall MTF is the product of the element MTF's.
- (3) The pointing MTF is Gaussian  $A_p(\omega) = e^{-\frac{\omega^2}{2\sigma^2}}$  where  $\omega$  is the spatial frequency in cycles/radian.
- (4) The detector MTF is exponential of the form  $A_d(f_d) = e^{-b(f_d)^{1.5}}$  where  $f_d$  is the detector spatial frequency in cycles/millimeter
- (5) The MTF of the telescope is as shown in Figure A-1.

The first assumption is the result of defining a resolvable image size as the smallest distance two equal intensity point images may be separated, and still be recognizable as two images. Since many of the system elements which tend to smear the image have Gaussian or near Gaussian MTF's, the final image is a good approximation to Gaussian. If two equal intensity Gaussian image functions

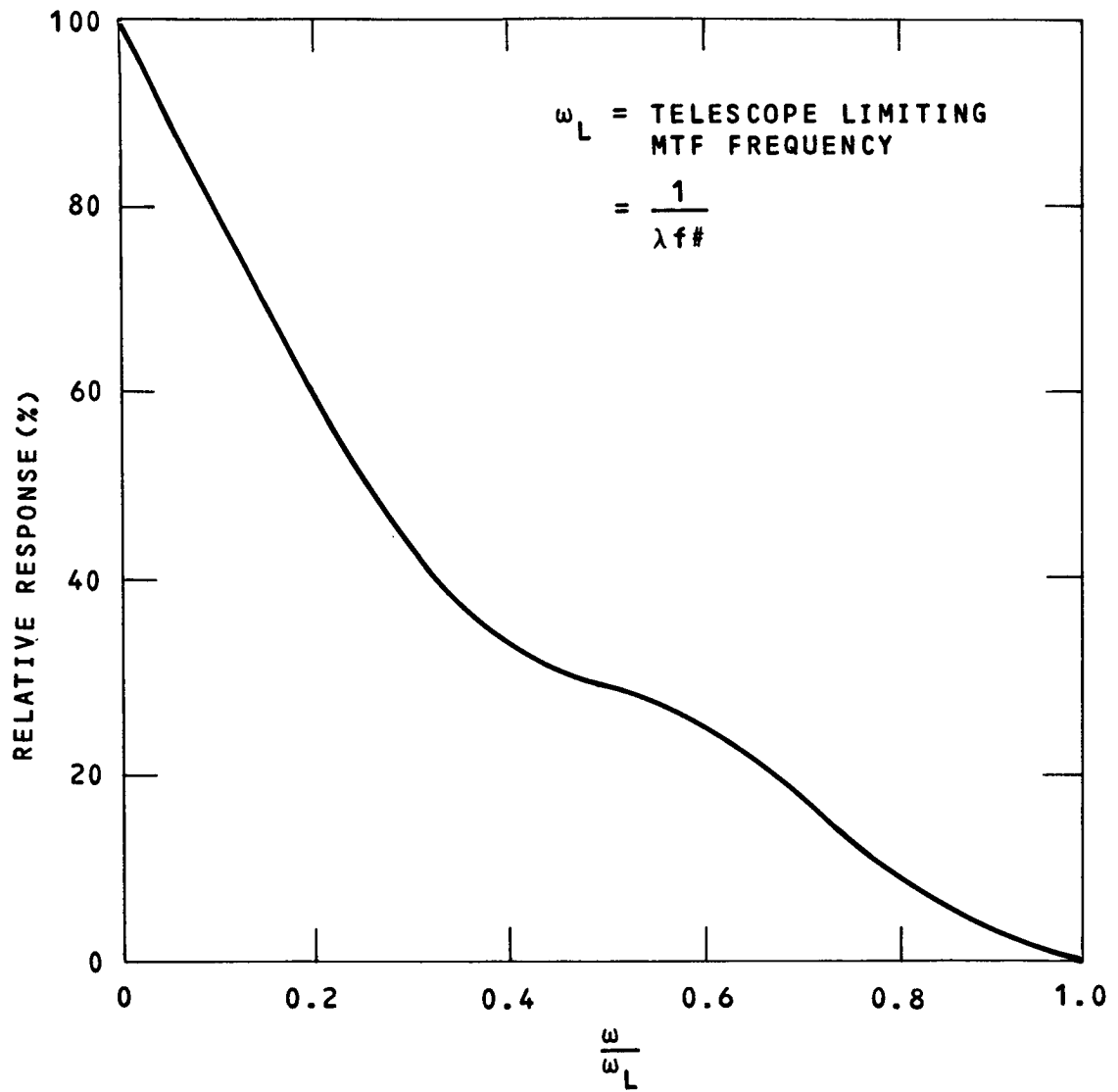


Figure A-1. Telescope MTF

are separated by a distance equal to the inverse of the three percent MTF frequency, the result is the curve shown in Figure A-2, with a contrast ratio of 5%. Thus, it may be seen that assumption (1) is valid whenever the S/N ratio exceeds 20.

The second assumption is based on the fact that the MTF's of the system elements are due to different phenomena.

The third assumption is that the fine guidance error is due predominantly to random noise or servo errors. Fixed errors do not concern us here because they result in offsets, not image smears.

The detector MTF is extrapolated from data on an actual tube.

The final assumption is the result of computerized studies of a three meter diameter telescope with a 30% obscuration ratio and a  $0.1\lambda$  W.F.E. (wavefront error).

The next step is to solve the necessary mathematical equations. For a resolvable angular image size  $\Delta\theta$ , there exists a spatial frequency

$$\omega = \frac{1}{\Delta\theta} \text{ in cycles/radian} \quad (1)$$

If  $\Delta X$  is a distance on the detector,

$$\Delta\theta = \frac{\Delta X}{F.L.} = \frac{\Delta X}{Df\#} \quad (2)$$

where

D = telescope aperture diameter

f# = camera f/number

F.L. = camera focal length

Corresponding to a distance  $\Delta X$  on the tube is a spatial frequency

$$f_d = \frac{1}{\Delta X} \quad (3)$$

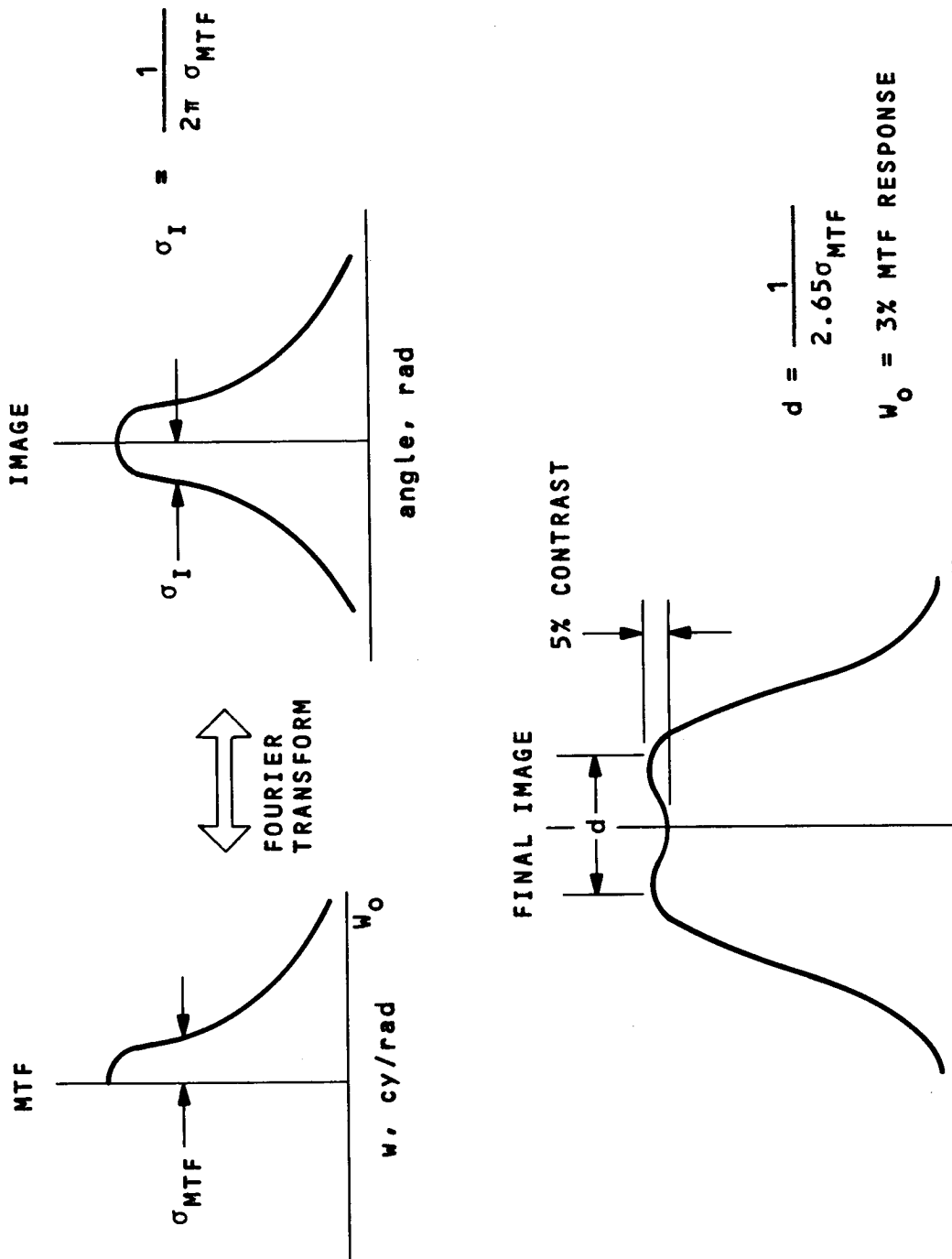


Figure A-2. Gaussian MTF, Its Associated Image, and Result of Bringing Two Images Close Together



Combining equations 1, 2 and 3, the detector MTF becomes

$$A_d(\omega) = e^{-b \left( \frac{\omega}{Df\#} \right)^{1.5}}$$

where

$$\frac{\omega}{Df\#} = f_d$$

For a detector with  $A_d(f_d) = 0.5$  at 20 lp/mm,  $b = 7.75 \times 10^{-3}$

The telescope response  $R_T(\omega)$  is obtained from Figure A-1 and from the fact that  $\omega_L = \frac{D}{\lambda}$ , where  $\lambda$  is the wavelength of interest and  $\omega_L$  is the limiting MTF frequency in cycles/radian.

$$\text{The pointing MTF is } A_p(\omega) = e^{-\frac{\omega^2}{2\sigma^2}}$$

The resolvable image size is taken as the point where the product of the MTF's = 3% or

$$0.03 = \left[ e^{-7.75 \times 10^{-3} \left( \frac{\omega}{Df\#} \right)^{1.5}} \right] \left[ R_T(\omega) \right] \left[ e^{-\frac{\omega^2}{2\sigma^2}} \right] \quad (4)$$

Solving (4) for  $\sigma$

$$\sigma = \frac{\omega}{\sqrt{2 \ln \left[ 33.3 R_T(\omega) e^{-7.75 \times 10^{-3} \left( \frac{\omega}{Df\#} \right)^{1.5}} \right]}}$$

This is the  $1\sigma$  pointing MTF spatial frequency. It may be shown that for a Gaussian pointing MTF with a one sigma frequency of  $\sigma$  cycles, there exists a Gaussian pointing motion whose  $1\sigma$  value,  $\sigma_p$ , is  $\sigma_p = \frac{1}{2\pi\sigma}$

$$\sigma_p = \frac{\sqrt{2 \ln \left[ 33.3 R_T(\omega) e^{-7.75 \times 10^{-3} \left( \frac{\omega}{Df\#} \right)^{1.5}} \right]}}{2\pi\omega} \quad (5)$$

$R_T(\omega)$  is obtained from an extrapolation subroutine which was part of the computer program which solved equation (5). A partial result of the study is shown in Figure 3-7.

APPENDIX B  
SIGNAL-TO-NOISE RATIO

GENERAL

The LST-SIP capability to detect faint objects, in a given amount of time, depends upon several factors including the number of photons received per second from the object, the background noise, the properties of the optical train and of the sensor/amplifier subsystem used.

This capability is usually expressed in terms of the signal-to-noise ratio (SNR or S/N).

$$\text{SNR} = \frac{S}{n_{\text{rms}}}$$

Its reciprocal is a measure of photometric accuracy of the obtained data ( $\zeta = \frac{n}{S}$ ).

Computation of the S/N for individual SIP instruments in Section 4 is based on the general relationships developed in the following subsections.

Neither the signal nor the noise will be multiplied by the MTF, because the models which are used to determine resolution are based upon image point spread functions, which already include the effects of MTF. For a further discussion of this subject, see Appendix A, and Sections 3.4.1 and 3.4.3.

SIGNAL

The Signal (S) denotes the information in the celestial object and is expressed here in terms of the total number of photoelectrons (pe) at the photocathode output.

$$S = A n(\lambda) N_i t$$

where

A = clear telescope aperture

$\eta$  = overall system efficiency, including light losses in the telescope (OTA) and instrument optics and the quantum efficiency of the photocathode over the entire wavelength spectrum.

$N_i$  = LST photon input rate from the object.

$$N_i = \int_{\lambda_1}^{\lambda_2} N_i(\lambda) d\lambda$$
 with  $\lambda_1$ , and  $\lambda_2$  the spectral limits of the data (spectrograph) or instrument (camera)

t = integration time

In Section 3.6, the values of  $N_o(\lambda) = An N_i(\lambda)$  are computed for the individual baseline SIP instruments using as an input a zero magnitude star (black body at various temperatures T). For the signal-to-noise prediction, the values of  $N_o(\lambda)$  for a black body at  $T = 11,000K$  are used. Hence, for each instrument, the signal for an object star of zero magnitude is

$$S_o = t \int_{\lambda_1}^{\lambda_2} N_o(\lambda) d\lambda$$

and for an object of magnitude m

$$S_m = (2.51)^{-m} S_o = (2.5)^{-m} t \int_{\lambda_1}^{\lambda_2} N_o(\lambda) d\lambda \quad (1)$$

## NOISE

The noise (n) is a square root of the sum of squares (rss) of all internal and external noise contributions, (i) where P is the number of noise sources.

$$n_{rms} = \left[ \sum_{i=1}^P n_i^2 \right]^{1/2} \quad \text{these include}$$

$n_{sm} = S_m^{1/2}$  is the quantum noise due to statistical arrival of photons

$n_B = S_B^{1/2} = \left[ (S_{23}) \frac{\Omega}{25} \right]^{1/2}$  is the background noise due to sources other than the object. To describe an average background in space we use one + 23rd magnitude star ( $S_{23}$ ) in a solid angle  $\Omega_B = 25$  psr (one arc second square) and  $\Omega$  is the solid angle (in psr), subtended by the star image, for which the noise is computed.

$n_D = N_D^{1/2}$  The photocathode dark noise ( $n_D$ ) is the variance caused uncertainty by the dark charge  $N_D$ ; the product of dark current and integration time. Section 6, Figure 6-3, lists the selected photocathodes and their dark current densities as a function of operating temperature.

$n_R = \frac{N_R^{1/2}}{G}$  The readout noise, obtained from the total noise at the target which, divided by the target gain  $G$ , becomes referenced to the photocathode. Evaluation of readout target voltage shift and read beam switching noise were found negligible in comparison with the preamplifier noise<sup>(1)</sup>  $n_p$ . Hence,

$$n_R \approx n_p = 8 \text{ photoelectrons/half cycle of spatial frequency } W_s$$

$n$  8 pe/resolution element for a single sample or  $8\sqrt{2}$  for two samples (Nyquist criteria)

---

(1) Lowrance, J. L. and Zucchini, P.: Development of Television Tubes for the Large Space Telescope. Proc. International Conf. on Space Appl. of Camera Tubes, Paris (1971)

## LIMITING SIGNAL-TO-NOISE RATIO

$(S/N)_{lim} = 2$  is assumed as a reasonable value for target detection.

From this

$$S^2 = 4 (S + S_B + N_D + (n_R)^2)$$

and solving for S, the limit signal with  $S_B$ ,  $N_D$  and  $n_R$  remaining the same as above.

$$S_{lim} = 2 \left[ 1 + \sqrt{1 + S_B + N_D + (n_R)^2} \right]$$

The limiting magnitude

$$m_{lim} = 2.5 \log \left( \frac{S_0}{S_{lim}} \right)$$

where  $S_0$  is the zero magnitude signal, described above.

Both the S/N for various star magnitudes  $m$  and integration times,  $t$ , the limiting magnitude for an assumed maximum integration time are used in Section 4 for individual instruments performance computation.

APPENDIX C  
 SIGNAL-TO-NOISE ANALYSIS  
 FAINT OBJECT SPECTROGRAPH NUMBER 3

The general discussion and S/N analyses for Faint Object Spectrographs 1 and 2 are presented in Section 4. The calculations are based on the throughput values developed in Section 3 and a selected slit length of 75 microradians.

Mean Wavelength	$\lambda_m = 830 \text{ nm}$
Spectral Bandwidth	$\Delta\lambda_m = 0.83 \text{ nm}$
Integration Time	$t = 3.6 \times 10^4 \text{ s}$
Spectral Density (From Figure 3-27)	$N_o = 4 \times 10^6 \text{ pe/s-nm}$
Slit Width to produce $E_W/E_T = 0.7$	$W = 1.0 \text{ } \mu\text{rad}$
Zero Magnitude Signal	$S'_o = 8.4 \times 10^{10} \text{ pe}$
+23 Magnitude Signal	$S_{23} = 53$
Solid Angle for $W = 1 \text{ } \mu\text{rad}$ and height of resolution element	$\Omega = 1.4 \text{ psr}$
Background Signal	$S_B = S_{23} \frac{\Omega}{25} = 3 \text{ pe}$
$N_D = aNt$	$N_D = 3600 \text{ pe}$
$a = 2.5 \times 10^{-5} \text{ cm}^2$	
$N = 4000 \text{ pe/s-cm}^2$	
Readout Noise Count	$(n_R)^2 = 128$
Limiting Signal for $S/N = 2$	$S_{lim} = 124$
Limiting Magnitude for $S/N = 2$	$M_{lim} = 22$

Cooling the cathode to 260K, which may be necessary for cathode material stability, increases  $M_{lim}$  to 23.5 magnitude. Figure C-1 shows the S/N ratio as a function of star magnitude for various integration times.



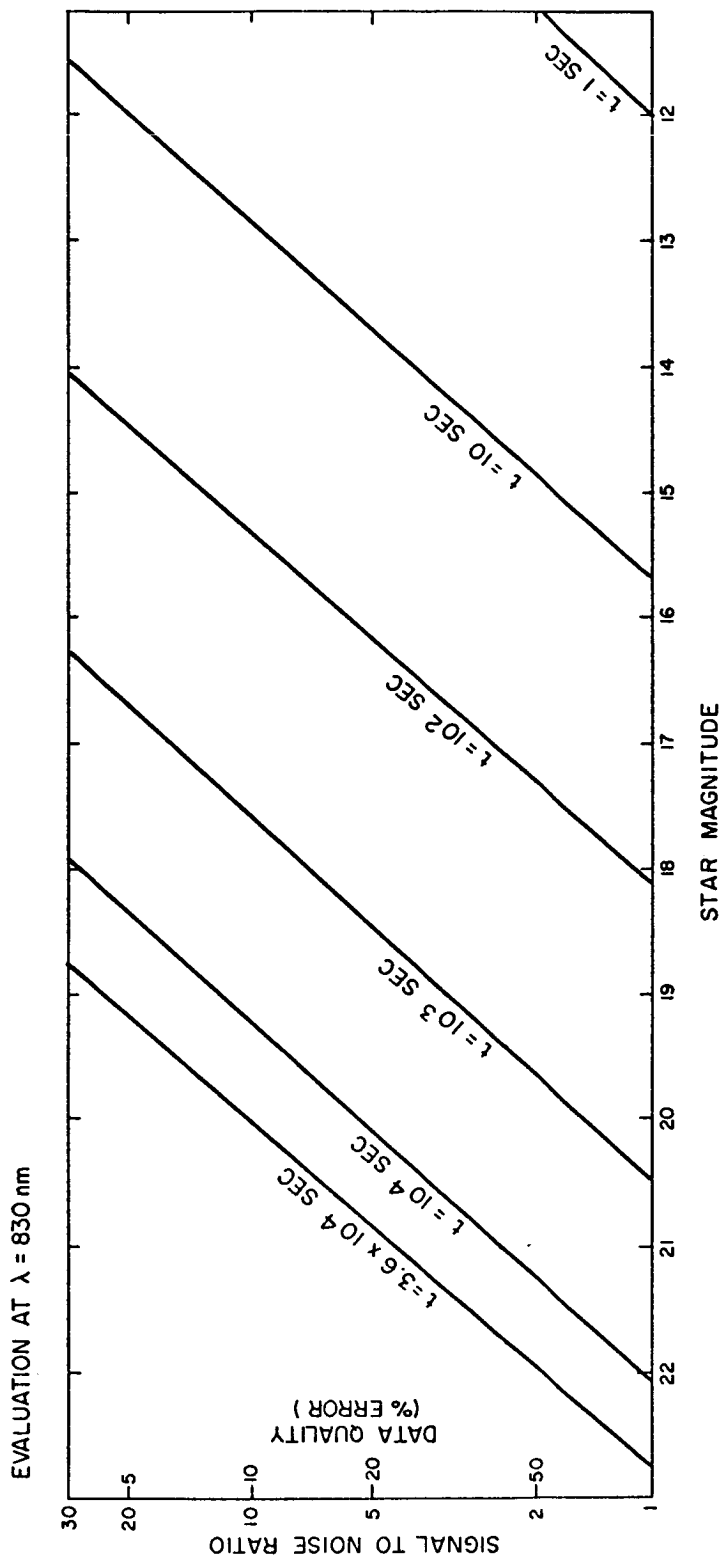


Figure C-1. Faint Object Spectrograph No. 3, S/N Ratio as a Function of Star Magnitude (11,000K) and Integration Time (t). SEC-Vidicon Operating Temperature = 293K; 20 LP/mm at 50% MTF

APPROVAL

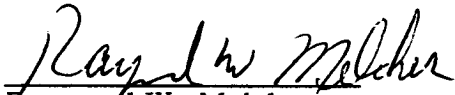
LARGE SPACE TELESCOPE  
PHASE A FINAL REPORT

Volume IV -- Scientific Instrument Package


By Program Development

(This volume prepared by Kollsman Instrument Corporation under  
contract to the Goddard Space Flight Center)

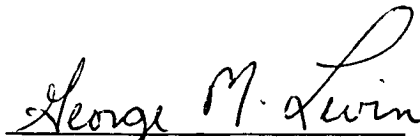
This document has been reviewed and approved for technical accuracy.



Raymond W. Melcher  
Technical Officer  
Laboratory for Optical Astronomy



Stanley Sobieski  
Instrumentation Scientist  
LST Study Office



George M. Levin  
Manager, LST Study Office

DISTRIBUTION

INTERNAL

DIR  
Dr. Petrone

DEP-T  
Dr. Lucas

AD-S  
Dr. Stuhlinger

PD-DIR  
Mr. Murphy  
Mr. Jean  
Dr. Mrazek

PD-LST  
Mr. Downey  
Dr. O'Dell  
Mr. McCulloch  
Mr. Olivier (8)  
Mr. Heyer (8)  
Mr. Hamilton  
Mr. Perry  
Mr. Nelson (6)  
Mr. Ealy  
Mr. Conway  
Mr. Teuber

PD-PL  
Mr. Huff

PD-MP  
Mr. Gierow (3)  
Mr. Emanuel  
Mr. Bradford

PD-PP  
Mr. Sneed (3)

PD-SL  
Mr. Trott

PD-DO  
Mr. Goerner  
Mr. Marshall  
Mr. Laue  
Mrs. Kozub  
Mr. Darwin  
Mr. Butler  
Mr. Blumrich  
Mr. Colley  
Mr. Love  
Mr. Nixon  
Mr. Fritz  
Mr. Mordan  
Mr. Goldsby  
Mr. Burton  
Mr. French  
Mr. Fults  
Mr. Kromis  
Mr. Digesu (10)  
Mr. Fikes  
Mr. Schultz  
Mr. Davis  
Mr. Green  
Dr. Steincamp  
Mr. Sanders  
Mr. W. Price  
Mr. Boehme

PD-DO (Cont'd)  
Mr. Rood  
Mr. Arsement  
Mr. Reed

SS-H  
Dr. Speer  
Mr. Fichtner  
Mr. Dailey  
Mr. Shields  
Mr. Wiesenmaier  
Mr. Carlile

SP-EM  
Mr. Harden  
Dr. Thomason

MO  
Mr. Kurtz (2)

S&E-DIR  
Dr. Weidner  
Mr. Richard

S&E-S&P  
Mr. Vreuls (2)

S&E-R  
Dr. Johnson

S&E-AERO  
Dr. Geissler  
Mr. Horn  
Mr. Dahm (2)  
Mr. Baker (3)  
Mr. Lindberg (3)  
Dr. Lovingood (5)

S&E-ASTR  
Mr. Moore  
Mr. Horton  
Mr. Powell  
Mr. Mack (3)  
Mr. Barr (8)  
Mr. Hosenthien (3)  
Mr. Wojtalik (3)  
Mr. Swearingen (3)  
Mr. Taylor (3)  
Mr. Boehm (3)  
Mr. Aden (3)  
Mr. Dugan (3)  
Mr. Justice  
Mr. Counter  
Mr. Zurasky  
Mr. Shearer  
Dr. Clarke  
Mr. Tutt  
Mr. Golley

S&E-ASTN  
Mr. Heimburg  
Mr. Kingsbury  
Mr. Kroll (2)  
Mr. Isbell (2)  
Mr. Sterett (2)  
Mr. Paul (2)  
Mr. Connor (2)  
Mr. Swinghamer (2)

S&E-SSL  
Dr. Haeussermann  
Dr. Naumann (2)  
Dr. Decher  
Dr. Sieber (2)  
Mr. Snoddy (2)

A&PS-MS-D  
Mr. Garrett

A&PS-MS-I  
Mr. Ziak

A&PS-MS-IP  
Mr. Ledbetter (2)

A&PS-MS-IL  
Miss Robertson (8)

A&PS-MS-H  
Mr. Akens

A&PS-PAT  
Mr. Wofford

A&PS-TU (6)

EXTERNAL

NASA Headquarters  
MH/Mr. Donlan (Vol I only)  
MK/Mr. Culbertson (Vol I only)  
MTL/Mr. Armstrong (Vol I only)  
SG/Dr. Nancy Roman (Vol I only)  
SG/Mr. Aucremanne (3 complete sets plus 10 of Vol I)  
WX/Mr. Krueger (3 complete sets plus 6 of Vol I)

Goddard Space Flight Center  
Code 604/Mr. Meese (80)

Johnson Space Center  
LP/Mr. Heberlig  
LP/Mr. Battey  
ER-4/Mr. Davis  
ER-4/Mr. Hirasaki  
ER-4/Mr. Casey

Kennedy Space Center  
FP-B/Mr. McCoy  
LL-OPN-2/Mr. Sheppard  
FP-B/Mr. Engle  
FP-B/Mr. Bailey

Dr. Herbert Flicker  
L-DOT TA-35  
Los Alamos Scientific Lab  
Los Alamos, N. W. 87544

Dr. Robert E. Danielson  
Princeton University Observatory  
Peyton Hall  
Princeton, N. J. 08540

Scientific and Technical  
Information Facility  
College Park, Maryland 20740  
Attn: NASA Representative (S-AK/RKT) (25)